# Three-Dimensional Constraint Based Fracture Mechanics

by
Feizal Yusof

A thesis submitted for the degree of
Doctor of Philosophy
to the
Department of Mechanical Engineering
Faculty of Engineering, University of Glasgow

May 2006

# Abstract

The structure of three-dimensional crack tip fields has been examined under elastic perfectly-plastic conditions using both three-dimensional boundary layer formulations and full-field solution of single edge notched bend bars and centre cracked tension panels. The nature of the stress fields was examined at the crack tip ($r = 0$) and at a distance of $r = 2J/\sigma_o$ as a function of load level and thickness. The three-dimensional nature of the crack tip fields has been compared with the limiting cases of plane strain and plane stress. The proximity to plane strain has been assessed using a parameter related to the out-of-plane stress deviator. The proximity to plane stress has been assessed using a parameter related to the radial stress deviator. At the intersection of the free surface and the crack tip, an elastic perfectly-plastic corner field which is different to the plane stress field is shown to develop. Along the crack front, in specimens of different thickness, a family of asymptotic fields develop which feature a constant stress sector. Within this sector the fields differ both hydrostatically and deviatorically but are similar in respect of the maximum stress deviator. This allows the level of the constraint to be assessed by a single parameter which quantifies both the change in the maximum principal stress and the mean stress.

A simple expression for out-of-plane constraint loss in SENB and CCP specimens is proposed. In CCP specimens, constraint loss arises from both in-plane and out-of-plane effects. In-plane constraint loss can be estimated using the T-stress and this effect is then combined with out-of-plane constraint loss. At any given section, constraint loss in any thickness specimen can be unified into a single relationship. This allows the quantification of out-of-plane constraint loss through a parameter based on J and the plate thickness.

Finally, a three-dimensional constraint based failure methodology based on Failure Assessment Diagrams has been proposed using the analytical expression for constraint loss. The failure assessment scheme has been validated using experimental data on the effect of thickness on toughness.

# Acknowledgements

My deepest gratitude goes to Professor John W. Hancock for his expert guidance, enthusiasm and support which made possible the task to complete the research and the thesis. I believed he has taught me the real meaning of research through his approach in problem solving, attention to detail and his words of wisdom will always be my source of inspiration. It is a great privilege to have him as my supervisor.

Thanks are due to the Faculty of Engineering staff particularly Mrs. Patricia Duncan and Miss Evelyn MacDonald and Mrs. Marion Richardson for their friendliness and assistance.

Acknowledgements are also due to University of Science Malaysia for an academic training fellowship award which enabled the research to be carried out in University of Glasgow and the Faculty of Engineering, University of Glasgow for their support during the latter phases of the research.

Of a more personal nature, I am indebted to my wife, Nazirah Hamzah who has made sacrifices so that this research can be completed. Her constant love and encouragement has been the source of my strength. On many occasions, my children, Haikal, Irfan and Isyraf have been the source of motivation and always bring joy to offset the weight of the tasks. Finally, I would like to dedicate this thesis to my mother and my late father who tirelessly strive to ensure the best for me.

# Contents

# List of Figures

# List of Tables

# Introduction

Fracture mechanics is intended to ensure the integrity of structures or components which contain defects and cracks. The subject is based on the similarity of the stress and strain fields at the tip of a crack in a laboratory specimen and a real flaw or defect. Similarity of the crack tip fields ensures the transferability of toughness data between the two geometries, and as such is a central requirement of fracture mechanics. A parameter that characterises crack tip fields under largely elastic conditions is the stress intensity factor, K, which was introduced by Irwin (1957). A critical value of the stress intensity factor can be used to describe the toughness ($K_c$) of structures containing cracks and defects. Although structures are designed to behave broadly in an elastic manner, plasticity has been shown to precede failure at the crack tip and limit the applicability of the stress intensity factor approach. In a key development, based on the energetics of crack advance, Rice (1968) proposed a scheme to quantify the elastic-plastic deformation field at the crack tip through the J-Integral. This extended the application of fracture mechanics to tough structural materials.

However, when fracture occurs with substantial levels of plastic deformation, the toughness becomes geometry dependent, McClintock (1971). The dimensions of the body affect the level of hydrostatic or mean stress in the crack tip field. This is known as the level of constraint. A constrained crack tip field exhibits a lower toughness than unconstrained field. In an early piece of research Irwin demonstrated that the thickness of a cracked body affected its toughness. Thick specimens exhibited a lower bound plane strain toughness which could be regarded as a material property and used to provide a conservative estimate of failure. However, failure assessment schemes based on lower bound toughness often caused the unnecessary repair of structures and outages of plant. Similarly, defects were often prematurely sentenced as critical.

The conservatism associated with lower bound toughness fracture assessment can be avoided when in-plane geometry effects are quantified by two-parameter fracture

mechanics (Betegón and Hancock (1991) and O'Dowd and Shih (1991)). The first parameter reflects the scale of crack tip deformation as measured by J while the second parameter is used to identify the triaxiality or the level of constraint at crack tip

Although significant progress has been made on the application of two-parameter fracture mechanics, it is limited to in-plane effects in thick specimens to the neglect of out-of-plane or thickness effects. However, a practical analytical model to quantify out of plane constraint loss, and express the effect of thickness on toughness is still lacking.

This thesis discusses opportunities to further reduce conservatism intrinsic to plane strain failure assessments by incorporating out-of-plane constraint loss. As a first step, it is necessary to understand the nature of three-dimensional elastic-perfectly plastic crack tip fields. The next step is to quantify how constraint is lost. Finally, the loss of constraint is used to develop a three-dimensional constraint based failure assessment scheme.

Following the current introduction, the relevant literature is reviewed in Chapters 2 and 3. Chapter 2 introduces a review of the governing equations of elastic and plastic deformation. This is followed by a review of single parameter and two parameter fracture mechanics for linear elastic and elastic-plastic solids focussing on two-dimensional plane strain and plane stress deformation. In Chapter 3, the key studies in the development of three-dimensional fracture mechanics are discussed within the context of crack tip constraint. This allows the current research to be placed on the context of previous developments.

Chapter 4 introduces the numerical techniques used in the current research, which is based on numerically stable, credible three-dimensional finite element models of a series of cracked specimens. A three-dimensional boundary layer formulation was benchmarked based on the work of Nakamura and Parks (1988a) to ensure that the configuration was a valid representation of the critical annulus around the tip of crack. Full-field SENB and CCP solutions were generated from the boundary layer formulations and benchmarked by comparing solutions of stress intensity factor and T-stresses with standard solutions.

In Chapter 5, the nature of the elastic-perfectly plastic three-dimensional crack tip stress field of boundary layer formulations, full-field SENB and CCP are investigated in the context of two-parameter fracture mechanics. The large amount of data presented in Chapter 5 is analysed to establish a systematic pattern of constraint loss in Chapters 6 and 7.

Chapter 6 discusses constraint loss as a function of a plane strain parameter. A constraint estimation scheme based on deformation and geometry is addressed in Chapter 7. This leads to the introduction of a deformation parameter to unify constraint loss at different sections through the thickness.

In Chapter 8, constraint loss in three-dimensional field has been used to develop three-dimensional constraint based failure assessment diagrams. The failure assessment schemes have been validated using experimental data. Constraint loss in constrained and unconstrained geometries has been united by the proposed failure assessment scheme. Out-of-plane constraint loss can now be related using a simple procedure depending on the level of constraint for structural defects.

# Fundamentals of Deformation and Fracture

This chapter introduces the basic concepts of solid mechanics and the fundamentals of fracture mechanics. Fracture mechanics is discussed starting with linear elastic fracture mechanics and extending into elastic-plastic fracture mechanics. Two-parameter fracture mechanics is then introduced within the context of the loss of crack tip constraint. Finally, the application of constraint based fracture mechanics is discussed.

## 2.1 Stress

The theory which underlies the deformation of elastic solids is described in standard texts such as Timoshenko and Goodier (1971), Crandall, Dahl and Lardner (1978) and McClintock and Argon (1966). A body subject to a system of external loads experiences an internal field of varying forces which act on an arbitrary section through the body. The ratio of components of the force to the area on which they act defines the components of force intensity or stress. When referred to a set of Cartesian co-ordinate axes $x_i$ ($i$ = 1, 2, 3), stress $\sigma_{ij}$, which is a second order tensor may be defined as:

$$\sigma_{ij} = \lim_{\Delta A_j \to 0} \frac{\Delta F_i}{\Delta A_j} \qquad (i,j, = 1, 2, 3) \qquad (2.1)$$

The relationship $i = j$, defines normal stress components while $i \neq j$, defines the shear stresses. Stress components may be referred to Cartesian co-ordinates axes as shown in Figure 2.1(a), but for solutions in axisymmetric bodies, it is often convenient to use cylindrical co-coordinates ($r$, $\theta$, $z$) as shown in Figure 2.1(b). It may also be necessary to transform the components of the stress tensor from one set of orthogonal axes $x_j$ to a new set $x_i'$. The new set of axes $x_i'$ is related to from old axes $x_j$ by a set of angles $\theta_{ij}$, where $\theta_{ij}$ is the angle between the new $x_i'$ axes and the old $x_j$ axes. The direction cosines of the new axes with respect to the old axes are $l_{ij}$:

$$l_{ij} = \cos \theta_{ij} \tag{2.2}$$

The transformation law for components of the stress tensor $\sigma'_{ij}$ can then be expressed as:

$$\sigma'_{ij} = l_{ip}\, l_{jq}\, \sigma_{pq} \qquad (i, j, p, q = 1, 2) \tag{2.3}$$

where repetition of suffices in the same term implies summation as described by Nye (1985).

At every point within the body, there are three mutually perpendicular planes on which the shear stresses are zero. The normals to these planes form the principal axes of the stress tensor. In this co-ordinate system, the corresponding stresses are principal stresses which will be denoted $\sigma_1$, $\sigma_2$, $\sigma_3$ with the convention ($\sigma_1 \leq \sigma_2 \leq \sigma_3$). The hydrostatic or mean pressure, $\sigma_m$, is an important stress invariant that is independent of the choice of co-ordinate axes:

$$\sigma_m = \frac{1}{3}(\sigma_1 + \sigma_2 + \sigma_3) = \frac{\sigma_{kk}}{3} \tag{2.4}$$

In a three-dimensional body, 18 components of stress act on an infinitesimal cell such as that shown in Figure 2.1. However, in the absence of distributed couples, equilibrium requires that $\sigma_{ij} = \sigma_{ji}$. This reduces the number of independent stress components to six. For a body in static equilibrium, the stresses acting on the body must satisfy the equilibrium equations, which in the absence of body forces are:

$$\sigma_{ij} = \sum_{i=1}^{3} \frac{\partial \sigma_{ij}}{\partial x_i} \quad = \sigma_{ij}, x_i = 0 \tag{2.5}$$

where the comma denotes differentiation. For crack problems with cylindrical symmetry, it is convenient to refer the equations of equilibrium to cylindrical coordinates:

$$\begin{aligned}
&\frac{\partial \sigma_{rr}}{\partial r}+\frac{1}{r}\frac{\partial \sigma_{r\theta}}{\partial \theta}+\frac{\partial \sigma_{zr}}{\partial z}+\frac{\sigma_{rr}-\sigma_{\theta\theta}}{r}=0\\
&\frac{\partial \sigma_{r\theta}}{\partial r}+\frac{1}{r}\frac{\partial \sigma_{\theta\theta}}{\partial \theta}+\frac{\partial \sigma_{z\theta}}{\partial z}+2\frac{\sigma_{r\theta}}{r}=0\\
&\frac{\partial \sigma_{zr}}{\partial r}+\frac{1}{r}\frac{\partial \sigma_{z\theta}}{\partial \theta}+\frac{\partial \sigma_{zz}}{\partial z}+\frac{\sigma_{zr}}{r}=0
\end{aligned} \tag{2.6}$$

## 2.2 Strain

The effect of stress on a solid body is to cause deformation and rigid body motion. To quantify deformation, it is initially useful to introduce a deformation tensor $D_{ij}$:

$$D_{ij}=u_i\,,x_j; \qquad (i,j:1,2,3) \tag{2.7}$$

This can be divided into symmetric and anti-symmetric components:

$$D_{ij}=\varepsilon_{ij}+\omega_{ij} \tag{2.8}$$

The symmetric component, $\varepsilon_{ij}$, is the strain tensor;

$$\varepsilon_{ij} \;=\; \frac{1}{2}\left(u_i,x_j+u_j,x_i\right) \tag{2.9}$$

while the antisymmetric component, $\omega_{ij}$, is the associated rotation;

$$\omega_{ij} \;=\; \frac{1}{2}\left(u_i,x_j-u_j,x_i\right) \tag{2.10}$$

Normal components of strain occur when $i = j$, and shear components when $i \neq j$. Engineers frequently define the components of shear strain $\gamma_{ij}$ without the factor of ½.

$$\gamma_{ij} = 2\varepsilon_{ij} \qquad (i \neq j) \tag{2.11}$$

Allowable functions of stress, strain and displacement must satisfy both the governing equations and the boundary conditions and hence preserve continuity. In two-dimensions $(x_1, x_2)$ the strain-displacement equations are:

$$\varepsilon_{11} = \frac{\partial u_1}{\partial x_1}, \qquad \varepsilon_{22} = \frac{\partial u_2}{\partial x_2}, \qquad \varepsilon_{12} = \frac{1}{2}\left(\frac{\partial u_1}{\partial x_2} + \frac{\partial u_2}{\partial x_1}\right) \tag{2.12}$$

Since the three strains are written in terms of two displacements, a relation must exist between the three strains. Differentiating twice and eliminating the displacements gives the compatibility equations. For example:

$$\frac{\partial^2 \varepsilon_{11}}{\partial x_2^{\,2}} + \frac{\partial^2 \varepsilon_{22}}{\partial x_1^{\,2}} = 2\frac{\partial^2 \varepsilon_{12}}{\partial x_1 \partial x_2} \tag{2.13}$$

**2.3 Elastic Constitutive Relations.**

Elastic deformation is reversible and instantaneous and when the applied loads are removed, the body returns to its original state. Linear elasticity implies that the stresses are proportional to the strains. In the most general case, this implies:

$$\sigma_{ij} = C_{ijkl}\, \varepsilon_{kl} \qquad (i, j, k, l = 1, 2, 3) \tag{2.14}$$

This general anisotropic relation involves 81 elastic constants, $C_{ijkl}$. However, due to the symmetry of the stress tensor $C_{ijkl} = C_{jikl} = C_{ijlk} = C_{jilk}$, and in view of the existence of a strain energy density $C_{ijkl} = C_{klij}$, this reduces the elastic constants to 21. Symmetry

considerations further reduce the elastic constants to 3 for cubic symmetry and 2 for an isotropic solid. In a linear elastic isotropic solid, the stress-strain relation can be written in terms of the shear modulus, $G$, and Poisson's ratio, $\nu$:

$$\sigma_{ij} = 2G\left(\varepsilon_{ij} + \frac{\nu}{1-2\nu}\delta_{ij}\,\varepsilon_{kk}\right) \tag{2.15}$$

and $\delta_{ij}$ is the Kronecker delta.

$$\begin{aligned} \delta_{ij} &= 1 \qquad i = j \\ \delta_{ij} &= 0 \qquad i \neq j \end{aligned} \tag{2.16}$$

The summation convention for repeated subscripts will only be considered to apply to Cartesian coordinate and not to cylindrical polar r, θ, z.

The strain-stress relation for a linear elastic isotropic solid can also be written in terms of Young's modulus $E$, where $E = 2G\,(1 + \nu)$:

$$\begin{aligned} \varepsilon_1 &= \frac{1}{E}\left[\sigma_1 - \nu(\sigma_2 + \sigma_3)\right] \\ \varepsilon_2 &= \frac{1}{E}\left[\sigma_2 - \nu(\sigma_1 + \sigma_3)\right] \\ \varepsilon_3 &= \frac{1}{E}\left[\sigma_3 - \nu(\sigma_1 + \sigma_2)\right] \end{aligned} \tag{2.17}$$

Relations between common isotropic elastic constants are given in McClintock and Argon (1966).

Important modes of deformation occur in pure shear and hydrostatic states of stress. In consequence, it is often advantageous to separate the stress tensor into hydrostatic and deviatoric components, $s_{ij}$:

$$s_{ij} = \sigma_{ij} - \frac{\sigma_{kk}}{3}\delta_{ij} \tag{2.18}$$

This allows the elastic stress-strain relations to be written as:

$$\varepsilon_{ij}^{e} = \frac{1}{E}\left((1+\nu)\sigma_{ij} + \left(\frac{1-2\nu}{3}\right)\delta_{ij}\ \sigma_{kk}\right) \tag{2.19}$$

## 2.4 Plane States of Stress and Strain

Mathematical solutions to the deformation of three-dimensional bodies are frequently intractable. In consequence, two-dimensional idealisations have been introduced to provide an approximation to the deformation of three-dimensional solid bodies.

Generalised plane stress conditions in the $x_3$ direction are assumed to apply when the stress components $\sigma_{33}$, $\sigma_{13}$, $\sigma_{23}$ and their derivatives with respect to $x_3$ are negligible in comparison to the other components of stress. As a result, a state of plane stress is expected to be realised in thin plates. If the thickness of the plate is small compared to its transverse dimensions the stress components $\sigma_{11}$, $\sigma_{22}$, $\sigma_{12}$ can vary only slightly across the thickness while the stress components involving $x_3$ are:

$$\begin{aligned} &\sigma_{i3} = 0 \\ &\qquad (i = 1, 2, 3) \\ &\sigma_{13}, x_3 = 0 \end{aligned} \tag{2.20}$$

In plane strain, displacements are assumed to occur in the $x_1$-$x_2$ plane and are independent of $x_3$. This implies that strain in the thickness direction is restrained and the out of plane strain, and its derivatives in the out of plane direction, are zero:

$$u_1 = u_1\left(x_1, x_2\right), \quad u_2 = u_2\left(x_1, x_2\right), \quad u_3 = 0$$

$$\varepsilon_{i3} = 0 \qquad (i = 1, 2, 3) \qquad (2.21)$$

$$\varepsilon_{13}, x_3 = 0$$

Plane strain is taken to occur in long prismatic bodies subject to loads which are normal to the lateral surface and independent of $x_3$. For plane strain in the $x_3$ direction, the linear elastic stress-strain relations expressed in terms of the principal stresses give:

$$\varepsilon_3 = \frac{\sigma_3}{E} - \nu\left(\frac{\sigma_1}{E} + \frac{\sigma_2}{E}\right) = 0; \qquad (2.22)$$

hence,

$$\sigma_3 = \nu\left(\sigma_1 + \sigma_2\right) \qquad (2.23)$$

## 2.5 Closed Form Solutions: Airy Stress Function

In two-dimensional deformation, Airy (1862), demonstrated the existence of a stress function, $\phi$, which satisfies equilibrium and compatibility, and enables the stresses to be related to the applied loads. The stresses in cylindrical coordinates arc:

$$\sigma_{rr} = \frac{1}{r}\frac{\partial\phi}{\partial r} + \frac{1}{r^2}\frac{\partial^2\phi}{\partial\theta^2}; \qquad \sigma_{00} = \frac{\partial^2\phi}{\partial r^2}; \qquad \sigma_{r\theta} = -\frac{1}{r^2}\frac{\partial^2\phi}{\partial\theta^2} - \frac{1}{r}\frac{\partial^2\phi}{\partial r\partial\theta} \qquad (2.24)$$

Substitution in the equilibrium equation shows that equilibrium is satisfied. Compatibility requires:

$$\left(\frac{\partial}{\partial r^2} + \frac{1}{r}\frac{\partial}{\partial r} + \frac{1}{r^2}\frac{\partial^2}{\partial\theta^2}\right)\left(\frac{\partial^2\phi}{\partial r^2} + \frac{1}{r}\frac{\partial\phi}{\partial r} + \frac{1}{r^2}\frac{\partial^2\phi}{\partial\theta^2}\right) \equiv \nabla^2\left(\nabla^2\phi\right) \equiv \nabla^4\phi = 0 \qquad (2.25)$$

Since the bi-harmonic equation satisfies the equilibrium equations, its solution with appropriate boundary condition defines the complete state of stress.

For a circular hole in an infinite plate as illustrated in Figure 2.2 with $a$ the radius of the hole, the stress function which satisfies the equilibrium equations, compatibility conditions and the boundary conditions is:

$$\phi = \left( -\frac{\sigma}{4} r^2 - \frac{a^4}{4} \frac{\sigma}{r^2} + \frac{a^2}{2} \sigma \right) \cos 2\theta \tag{2.26}$$

Direct differentiation of equation (2.24) shows that, the maximum value of hoop stress is obtained when $\theta = \pi/2$ and $r = a$ and given by:

$$\sigma_{\theta\theta} = \sigma \left( 1 + \frac{a^2}{2r^2} + \frac{3a^4}{2r^4} \right) \tag{2.27}$$

This gives a maximum elastic stress concentration factor of 3 for a circular hole in an infinite plate.

## 2.6 Plasticity

The discussion of plasticity essentially follows the definitive texts of Hill (1950) and Kachanov (1974). Yielding in metals is associated with permanent irreversible deformation. Yielding and plastic flow depends on the magnitudes of the component of stress and is a function of the invariants of the deviatoric stress tensor, $J_2$ and $J_3$:

$$J_2 = \frac{1}{2} s_{ij} s_{ij} \tag{2.28}$$

$$J_3 = \frac{1}{3} s_{ij} s_{jk} s_{ki} \tag{2.29}$$

where $s_{ij}$ are the stress deviators. Plastic deformation in metals depend on the shear components of stress and the differences of the normal stress components, but not on the mean or hydrostatic pressure, $\sigma_{kk}$, which does not produce dislocation motion.

For metals undergoing purely plastic deformation, the volume remains constant because deformation occurs by slip, Hill (1950). If small strain plastic deformation occurs at a constant volume, $V$;

$$\frac{\nabla V}{V} = \varepsilon_{kk} = 0 \tag{2.30}$$

The Tresca (1864) and von Mises (1913) yield criteria are widely used to describe isotropic plastic deformation, Hill (1950). The Tresca criterion argues that yielding occurs when the maximum shear stress, $\tau$, reaches a critical value, $k$, which can be related to the yield stress in uniaxial tension $\sigma_o$.

$$\frac{\sigma_3 - \sigma_1}{2} = k = \frac{\sigma_o}{2} \qquad (\sigma_1 \le \sigma_2 \le \sigma_3) \tag{2.31}$$

The Mises criterion suggests that yielding occurs when the elastic strain energy of distortion reaches a critical value which can be expressed in terms of stresses, $\sigma_{ij}$

$$\bar{\sigma} = \sqrt{\frac{1}{2}\left[(\sigma_{11}-\sigma_{22})^2 + (\sigma_{22}-\sigma_{33})^2 + (\sigma_{33}-\sigma_{11})^2 + 3\sigma_{12}^2 + 3\sigma_{23}^2 + 3\sigma_{31}^2\right]} \tag{2.32}$$

or more compactly using stress deviators, $s_{ij}$

$$\bar{\sigma} = \sqrt{\frac{3}{2} s_{ij}\, s_{ij}} \tag{2.33}$$

Yield occurs when the equivalent stress $\bar{\sigma}$ reaches the yield stress in tension $\sigma_o$:

$$\bar{\sigma} = \sigma_o \tag{2.34}$$

Alternatively the yield criterion can be expressed in terms of the yield stress in shear, $k$

$$\bar{\sigma} = \sqrt{3}\, k \tag{2.35}$$

### 2.6.1 Elastic – Plastic Constitutive Relations

In elastic-plastic deformation, the incremental strains $d\varepsilon_{ij}$, are sums of the elastic strain increments $d\varepsilon_{ij}^{e}$ and the plastic strain increments $d\varepsilon_{ij}^{p}$.

$$d\varepsilon_{ij} = d\varepsilon_{ij}^{e} + d\varepsilon_{ij}^{p} \tag{2.36}$$

The plastic strain increments can be derived from a plastic potential $g\ (J_2,\ J_3)$, which defines the ratios of components of the plastic strain increment through a flow rule:

$$d\varepsilon_{ij}^{p} = \frac{\partial g}{\partial \sigma_{ij}}\, d\lambda \tag{2.37}$$

where $d\lambda$ is a scalar factor of proportionality which is not a material constant but varies during deformation. For the plastic potential, $g = J_2 = s_{ij}\ s_{ij}/2$, the incremental plastic strains can be written through an associated flow rule:

$$d\varepsilon_{ij}^{p} = s_{ij}\, d\lambda \tag{2.38}$$

where $d\lambda = 3d\bar{\varepsilon}^{p} / 2\bar{\sigma}$. Assuming isotropy is maintained under plastic deformation, the flow stress may increase as a function of the equivalent plastic strain due to strain or work

hardening. The equivalent plastic strain $\bar{\varepsilon}^p$ is obtained by integration of the strain increments $d\bar{\varepsilon}^p$ over the loading history:

$$d\bar{\varepsilon}^p = \sqrt{\frac{2}{9}\left[\left(d\varepsilon_{11}^p - d\varepsilon_{22}^p\right)^2 + \left(d\varepsilon_{22}^p - d\varepsilon_{33}^p\right)^2 + \left(d\varepsilon_{33}^p - d\varepsilon_{11}^p\right)^2 + \frac{1}{3}\left(d\gamma_{12}^{p\,2} + d\gamma_{23}^{p\,2} + d\gamma_{31}^{p\,2}\right)\right]} \tag{2.39}$$

$$\bar{\varepsilon}^p = \int d\bar{\varepsilon}^p \tag{2.40}$$

The total strain increment which includes the elastic and plastic components can be expressed compactly as:

$$\begin{aligned} d\varepsilon_{ij} &= d\varepsilon_{ij}^e + d\varepsilon_{ij}^p \\ &= \frac{1}{E}\left[(1+\nu)\,d\sigma_{ij} - \left(\frac{1-2\nu}{3}\right)\delta_{ij}\,d\sigma_{kk}\right] + \frac{3}{2}\,d\bar{\varepsilon}^p\,\frac{s_{ij}}{\bar{\sigma}} \end{aligned} \tag{2.41}$$

In classical plasticity the relationship between the equivalent plastic strain and the equivalent stress is independent of the stress or strain rate, and can be determined from a single uni-axial tensile test. Yield and plastic flow is independent of the hydrostatic or mean stress. The mean and equivalent stress can be combined into a single non-dimensional parameter ($\sigma_m/\bar{\sigma}$), which defines the triaxiality of the stress state. At yield in pure shear, ($\sigma_1 = k = -\sigma_2$, $\sigma_3 = 0$) the triaxiality is zero, while in perfect hydrostatic tension or compression, the triaxiality is infinite ($\sigma_1 = \sigma_2 = \sigma_3 = \sigma_m$).

In uniaxial tension elastic-plastic stress-strain relationship is often approximated by a pure power law of the form:

$$\left(\frac{\varepsilon}{\varepsilon_o}\right) = \alpha\left(\frac{\sigma}{\sigma_o}\right)^n \tag{2.42}$$

where $n$ is the strain hardening exponent and $\varepsilon_o$ is a reference strain and $\sigma_o$ is reference stress, $\sigma$ and $\varepsilon$ are the tensile stress and strain respectively and $\alpha$ is a material constant. As the exponent $n$ can vary from 1 to $\infty$, a range of responses varying from linear elastic to rigid-perfectly plastic can be described. A Ramberg-Osgood law is also frequently used to describe nonlinear stress-strain responses in uniaxial tension:

$$\frac{\varepsilon}{\varepsilon_o} = \frac{\sigma}{\sigma_o} + \alpha\left(\frac{\sigma}{\sigma_o}\right)^n \tag{2.43}$$

The curve fitting constant $\sigma_o$ is often associated with yield stress however, when $\sigma = \sigma_o$, $\varepsilon_o$ does not correspond to yield strain. The corresponding strain is $\varepsilon = \varepsilon_o (1+\alpha)$, and the relation does not model linear elasticity accurately. However, this relation gives good overall description of the stress-strain relation at large plastic strains. The relations given by Equations (2.42) and (2.43) can be generalised into multi-axial states of stress by a yield criterion and an associated flow rule.

### 2.6.2 Elastic-Perfectly Plastic Deformation: Slip Line Fields

In elastic-plastic fracture mechanics, the deformation field directly ahead the crack tip warrants an approach that focuses primarily on the plastic strain to the neglect of the elastic strain components. The material is effectively assumed to be elastically rigid with an infinite Young's modulus. This simplification in conjunction with the assumption that material does not strain harden defines a response described as elastic-perfectly plastic. This allows the application of plane strain slip line fields which were initially used for large plastic strain deformation processes as described in Hill (1950) and Johnson Sowerby and Venter (1982).

The theory is based on the fundamental governing equations: equilibrium, stress-strain relations, the yield criteria and finally the compatibility relations. In plane strain incompressibility allows the stress-strain relations to define the out-of-plane stress $\sigma_{33}$ in plane strain as:

$$\sigma_{33} = \frac{1}{2}(\sigma_{11} + \sigma_{22}) = \sigma_m = \frac{\sigma_{kk}}{3} \tag{2.44}$$

Equation (2.44) can be rearranged to define a parameter which controls the out-of-plane stress in plane strain, ρ:

$$\rho = \frac{\sigma_{33}}{\sigma_{11} + \sigma_{22}} = \frac{1}{2} \tag{2.45}$$

The Mises yield criterion limits the difference of the in-plane stresses to $2k$

$$\sigma_1 - \sigma_2 = 2k \tag{2.46}$$

as is illustrated by Mohr's circle in Figure 2.3. This allows the three principal stresses to be written in terms of the mean stress, $\sigma_m$

$$\begin{aligned} \sigma_1 &= \sigma_m + k \\ \sigma_2 &= \sigma_m - k \\ \sigma_3 &= \sigma_m \end{aligned} \tag{2.47}$$

while the angular positions of the principal stresses are determined through:

$$\begin{aligned} \tan 2\phi &= \frac{2\sigma_{xy}}{(\sigma_{xx} - \sigma_{yy})} \\ \tan 2\theta' &= \frac{(\sigma_{yy} - \sigma_{xx})}{2\sigma_{xy}} \end{aligned} \tag{2.48}$$

Here, θ' is the angle between $x_1$-axis and first shear line denoted α. Plane strain shear line or slip line fields can be represented as two orthogonal sets of curvilinear curves defined as α and β axes. The α, β axes are the characteristics of the governing differential equations. Physically these are the directions of zero extension, which in plane strain correspond to the directions of maximum and minimum shear stress. The maximum principal stress lies in the first and third quadrants of the α, β axes. The shear stress on the lines is equal to $k$, the yield stress in shear. Hencky's first theorem, which is a statement of the equilibrium equations in the α, β co-ordinate system, gives the change in mean normal stress in terms of the rotation of a slip line direction:

$$\begin{aligned} d\sigma_m &= 2k\, d\phi \qquad \text{on an } \alpha \text{ line} \\ d\sigma_m &= -2k\, d\phi \qquad \text{on a } \beta \text{ line} \end{aligned} \tag{2.49}$$

A given slip line field can then be analysed by following the rotation of the slip lines from free surface where the stress state is known and the slip lines necessarily are inclined at π/4 to the surface. The compatibility of displacements is completed by Geiringer's equations Hill (1950):

$$\begin{aligned} du - v d\theta' &= 0 \\ dv - u d\theta' &= 0 \end{aligned} \tag{2.50}$$

where $u$ and $v$ are displacements along α and β axes.

## 2.7 Linear Elastic Fracture Mechanics

### 2.7.1 Stress Concentrations.

The fundamental concepts of fracture mechanics were established in the early 20th century by the early work of Inglis (1913) who identified the nature of stress concentrations such as notches and cracks. The central problem is the stress field of an elliptical hole as illustrated in Figure 2.4. Using complex potentials to satisfy the boundary problem, Inglis showed that the maximum stress $\sigma_{22}$ in the opening direction is:

$$\sigma_{22} = \sigma_{22}^{far}\left(1+2\frac{a}{b}\right) \tag{2.51}$$

where $a$ is major semi-axis of the ellipse, $b$ is semi-minor axis and $\sigma_{22}^{far}$ is the remotely applied uniaxial stress. The stress concentration can also be written in terms of the radius of curvature, $\rho$, at the end of the semi-major axis.

$$\sigma_{22} = \sigma_{22}^{far}\left(1+2\sqrt{\frac{a}{\rho}}\right) \tag{2.52}$$

As the radius of curvature approaches zero, the stresses at the tip of a sharp crack in an elastic body become infinite, independent of the applied load or crack length. This presented a dilemma which prompted an energetic approach to the analysis of sharp cracks.

### 2.7.2 Griffiths Criterion

The energetics of crack advance were first discussed by Griffiths (1920) in response to the paradox that crack tip stresses in an elastic material are infinite. Griffiths argued that the energy ($W$) required to extend a crack is a balance between the change in the potential energy ($U$) in the cracked body and surface energy ($S$) absorbed during crack growth. The change in energy which occurs if the half crack length $a$ of a centre cracked panel is

extended by an infinitesimal amount $\delta a$ can be considered in either fixed displacement or fixed load conditions as shown in Figure 2.5. The corresponding load-displacement curves are shown in Figure 2.6. In fixed displacement conditions (OACO), crack extension produces a release of strain energy, ($U^{FD}_{strain}$):

$$U^{FD}_{strain} = -\frac{1}{2}(P_1 - P_2)u_1 \quad = -\frac{1}{2}\Delta P\, u \tag{2.53}$$

where $P$ and $u$ are load and displacement. In fixed load conditions (OABO), crack extension results in an increase in strain energy, but a release of potential energy, ($U^{FL}_{potential}$):

$$U^{FL}_{potential} = -\frac{1}{2}P_1(u_1 - u_2) \quad = -\frac{1}{2}P\,\Delta u \tag{2.54}$$

It can be shown that in both conditions the potential energy release is the same through the relationship between the displacement $u$ and load $P$.

$$u = C\,P \tag{2.55}$$

where $C$ is the compliance of the system. As the change in crack length $\delta a$ tends to zero, $C_{(a)}$ approaches $C_{(a+\delta a)}$ and Equation (2.55) becomes:

$$\Delta u = C\,\Delta P \tag{2.56}$$

Using Equation (2.55) and (2.56) in Equations (2.53) and (2.54) respectively, it can be shown that:

$$U^{FD}_{strain} = -\frac{1}{2}\Delta P\, CP \quad = U^{FL}_{potential} = -\frac{1}{2}P\,C\,\Delta P \tag{2.57}$$

Using the calculations of Inglis (1913), Griffiths expressed the strain energy, $U_{strain}$ under fixed displacement conditions as:

$$U_{strain}^{FD} = -\frac{1}{2}\frac{\pi\sigma^2 a^2 B}{E'} \tag{2.58}$$

$$-\frac{1}{B}\frac{\partial U}{\partial a} = \frac{\pi\sigma^2 a B}{E'} \tag{2.59}$$

where $E'=E$ in plane stress and $E/(1-\nu^2)$ in plane strain. In an ideally brittle material, Griffiths assumed that the energy of crack advance was equal to the surface energy, $S$, to form the new free surface,

$$S = 2\gamma a B \tag{2.60}$$

$$\frac{1}{B}\frac{\partial S}{\partial a} = 2\gamma \tag{2.61}$$

Here $\gamma$ is the surface energy per unit area. The Griffiths criterion states that for crack to advance, the decrease in potential energy must be greater or equal to energy required to create the crack surfaces such:

$$\frac{\partial U}{\partial a} \geq \frac{\partial S}{\partial a} \tag{2.62}$$

Equating the potential energy release rate to the work done in cracking fresh surface, gives the fracture stress, $\sigma_f$, as:

$$\sigma_f = \sqrt{\frac{2\gamma E'}{\pi a}} \tag{2.63}$$

Until the 1940s, Griffiths' (1920) pioneering work was not considered to be relevant to engineering structures because of the inherent brittleness of the material (glass) which was used to validate the theory. The work of Orowan (1945) led to the generalisation of Griffiths' work to less brittle materials. Orowan modified Griffiths' energy balance criteria to include materials that undergo plastic flow as:

$$\sigma_f = \sqrt{\frac{E(2\gamma + \gamma_p)}{\pi a}} \tag{2.64}$$

where $\gamma_p$ represents the energy per unit area to break a solid when plastic flow occurs at the crack tip. Experimentally it is found that $\gamma_p >> 2\gamma$, which shows that crack tip plasticity dominates the fracture process even in highly brittle materials. Irwin (1948) noted that the energy expended in plastic deformation could be estimated from Orowan's result and concluded that Griffiths' theory could be used if the plastic work were substituted for the surface energy. Irwin (1957) defined the potential energy released for a unit increase in crack area as the crack extension force $G$.

$$G = \frac{\pi \sigma^2 a}{E'} \tag{2.65}$$

where $E'=E$ in plane stress and $E/(1-\nu^2)$ in plane strain. $G$ quantifies the energy to propagate a crack and a critical value of the strain (potential) energy release rate, $G_c$ can be used as a material property which quantifies fracture toughness:

$$G_c = \frac{\pi \sigma_f^{\,2} a_c}{E'} \tag{2.66}$$

where $\sigma_f$ is the fracture stress and $a_c$ is the half crack length.

### 2.7.3 Stress Intensity Factor

The nature of the asymptotic elastic crack tip field was established by Westergaard (1939) and Williams (1957). Westergaard (1939), developed asymptotic solutions from algebraic stress functions which identified the leading term of a series expansion of the crack tip stress field. The Westergaard stress field for a central crack in an infinite plate can be given using Cartesian stresses and cylindrical coordinates ($r$, $\theta$) centred at the crack tip as defined in Figure 2.7.

$$\begin{aligned}
\sigma_x &= \frac{\sigma\sqrt{a}}{\sqrt{2r}}\cos\frac{\theta}{2}\left(1+\cos\frac{\theta}{2}\sin\frac{3\theta}{2}\right)\\
\sigma_y &= \frac{\sigma\sqrt{a}}{\sqrt{2r}}\cos\frac{\theta}{2}\left(1-\cos\frac{\theta}{2}\sin\frac{3\theta}{2}\right) \qquad (r \ll a)\\
\sigma_{xy} &= \frac{\sigma\sqrt{a}}{\sqrt{2r}}\sin\frac{\theta}{2}\cos\frac{\theta}{2}\cos\frac{3\theta}{2}
\end{aligned} \tag{2.67}$$

Here $a$ is the half crack length. Irwin et al. (1958) expressed the Westergaard equations in a generalised form:

$$\sigma_{ij} = \sigma\sqrt{\frac{a}{2r}}\,f_{ij}(\theta) = \frac{K'}{\sqrt{2r}}\,f_{ij}(\theta) \qquad (r \ll a),(i,j=1,2) \tag{2.68}$$

The term $K' = \sigma\sqrt{a}$, was originally termed the stress intensity factor, however, modern notation defines the stress intensity factor, K for a Griffiths crack as:

$$K = \sigma\sqrt{\pi a} \tag{2.69}$$

The elastic dominant singularity in asymptotic crack tip fields can now be written in the form:

$$\sigma_{ij}(r,\theta) = \frac{K}{\sqrt{2\pi r}} f_{ij}(\theta) \tag{2.70}$$

The stress intensity factor, K, can be related to the Griffiths theory of potential strain energy release rate, G, by the relation:

$$K^2 = \frac{E'G}{\pi} \tag{2.71}$$

where $E' = E/(1-\nu^2)$ for plane strain and E for plane stress. The stress intensity factor, K, characterises the strength of the elastic crack tip singularity, and quantifies the strain potential energy release rate in virtual crack extension.

Under arbitrary loading, a crack in a solid can deform in three different modes (Irwin (1960b)) as shown in Figure 2.8. Mode I is the opening mode. In this mode the body is subjected to a normal stress and the displacement of the crack surface are symmetric about the crack plane. In-plane shear results in the mode II or the edge-sliding mode when displacements are anti-symmetric with respect to the crack plane. The shearing mode or mode III is caused by out-of-plane shear such that the displacements are in the plane of the crack parallel to the leading edge of the crack. In practice, Mode I is usually the most important. Each mode features the $1/\sqrt{r}$ stress singularity at the crack tip, but the angular functions $f_{ij}(\theta)$ depend on the mode. The stress field and associated displacement field ahead of a crack tip in an isotropic linear elastic material in mode I can be written following Rice (1968a):

$$\begin{Bmatrix}\sigma_{11}\\ \sigma_{12}\\ \sigma_{22}\end{Bmatrix} = \frac{K_I}{\sqrt{2\pi r}}\cos(\theta/2)\begin{Bmatrix}1-\sin(\theta/2)\sin(3\theta/2)\\ \sin(\theta/2)\cos(3\theta/2)\\ 1+\sin(\theta/2)\sin(3\theta/2)\end{Bmatrix} \tag{2.72}$$

$$\begin{Bmatrix}u_1\\ u_2\end{Bmatrix} = \frac{K_I}{2G}\left(\frac{r}{2\pi}\right)^{1/2}\begin{Bmatrix}\cos(\theta/2)\left[\kappa-1+2\sin^2(\theta/2)\right]\\ \sin(\theta/2)\left[\kappa+1-2\sin^2(\theta/2)\right]\end{Bmatrix} \tag{2.73}$$

where $\kappa = (3 - 4\nu)$ for plane strain and $\kappa = (3 - \nu)/(1 + \nu)$ for generalised plane stress. The corresponding stress and displacement fields for mode II and mode III can also be found in Rice (1968a).

The definition of the stress intensity factor given in Equation (2.70) applies to a central crack in an infinite plate, however for finite plates, K can be expressed in a similar form:

$$K = \sigma_{app}\sqrt{\pi a} \quad f\left(\frac{a}{W}\right) \tag{2.74}$$

where W is the plate width and $f(a/W)$ is a non-dimensional function of geometry. The non-dimensional function of geometry for single edge notch bend (SENB) specimens given by Tada et al. (1985):

$$f\left(\frac{a}{W}\right) = 1.122 - 1.4\left(\frac{a}{W}\right) + 7.33\left(\frac{a}{W}\right)^2 - 13.08\left(\frac{a}{W}\right)^3 + 14.0\left(\frac{a}{W}\right)^4 \tag{2.75}$$

The form function for a centre crack panel (CCP) as a function of a/W is given in Table 2.1.

The stress intensity factor, K, characterises crack tip deformation when plasticity can be regarded as a minor perturbation of a largely elastic field. For this state, Rice (1968a) introduced the term small-scale yielding. Linear elastic fracture mechanics (henceforth LEFM) deals with deviations from linearity which are limited to a region that is small compared to the dimensions of the cracked body. Identical values of stress intensity factor ensure that cracks of different lengths in geometrically different bodies have the same crack tip stress, strain and displacement fields. This allows the failure conditions measured from a laboratory test specimen to be applied to an engineering structure.

The critical stress intensity factor, $K_c$, associated with the onset of crack growth under monotonic loading depends on the material, its temperature and possibly its environment.

It also depends on the mode of loading and on whether plane strain or plane stress conditions apply. The value of $K_c$ for any given set of conditions can only be obtained by experiment using a calibrated precracked test specimen which meets the restrictions of small scale yielding at the onset of fracture. The critical stress intensity factor in mode I, plane strain conditions, designated $K_{Ic}$, is called the fracture toughness.

### 2.7.4 Limits of LEFM

The application of LEFM is subject to severe size limitations intended to ensure that plasticity is restricted to a local perturbation of the elastic field. When materials fail in a macroscopically elastic manner, $K_{Ic}$ is a measure of fracture toughness. A valid $K_{Ic}$ test according to ASTM (E399-83, 1988) can be performed using several types of specimen subject to the size requirement:

$$a \geq 2.5\left(\frac{K_{Ic}}{\sigma_o}\right)^2; \quad W-a \geq 2.5\left(\frac{K_{Ic}}{\sigma_o}\right)^2; \quad B \geq 2.5\left(\frac{K_{Ic}}{\sigma_o}\right)^2 \tag{2.76}$$

where $a$ is the crack length, W is the width of the specimen and B is the thickness of the specimen. The value of $K_{Ic}$ is calculated from a critical applied load $P_Q$ given in ASTM (E399-83, 1988):

$$K_{Ic} = \frac{P_Q}{B\sqrt{W}} f\left(\frac{a}{W}\right) \tag{2.77}$$

These limits ensure that radius of the plastic zone, which is proportional to $(K_I/\sigma_o)^2$, is very much smaller than the relevant in-plane dimensions of the body. The thickness requirement ensures plane strain conditions while the requirements on the in-plane dimensions: $a$, W-$a$, ensure that the macroscopic response is linear elastic and that plasticity is a minor perturbation of a largely elastic field characterised by $K_I$.

Structural metals and alloys frequently exhibit extensive plasticity before failure, and as the thickness reduces, the fracture toughness increases as shown in Figure 2.9. This limits the practical application of LEFM, as tough structural materials require large test specimens which are very expensive to prepare and difficult to test.

## 2.8 Elastic-Plastic Fracture Mechanics

The applicability of LEFM is severely limited by the restrictions on the size of the plastic zone compared to the dimensions of the cracked body. In tough structural steels, this limits the use of LEFM in assessing structural integrity, and establishes the need for elastic-plastic fracture mechanics henceforth EPFM to characterise crack tip fields and define the energetics of crack extension in non-linear materials.

### 2.8.1 Crack Tip Plasticity

Linear elastic stress analysis of bodies containing sharp cracks feature crack tip singularities. However in real materials, the stresses at the crack tip are finite because the crack tip radius becomes finite after deformation. More importantly in non-linear materials, plastic deformation leads to relaxation of the crack tip stresses. Crack tip plasticity was initially discussed by Irwin (1960b) and Dugdale (1960) as a correction to the linear elastic solution. Irwin suggested that the crack length could be regarded as being enhanced by plasticity so that the effective crack length, $a_{eff}$ can be regarded as the length of the crack, $a$, plus a correction due to the plastic zone size:

$$a_{eff} = a + r_y \tag{2.78}$$

where $a$ is half crack length, $r_y$ is the radius of plastic zone as in Figure 2.12.

The size and shape of crack tip plastic zone can be estimated by applying the Von Mises or Tresca yield criterion, Hill (1950), to the elastic field. In the current work the Von Mises criterion is used to estimate the boundary of plastic zone. In terms of principal stresses:

$$(\sigma_1 - \sigma_2)^2 + (\sigma_2 - \sigma_3)^2 + (\sigma_3 - \sigma_1)^2 = 2\sigma_o^2 \tag{2.79}$$

where $\sigma_o$ is the uniaxial yield stress. The stress field of a mode I crack can be expressed in terms of principal stresses using Mohr's circle:

$$\sigma_1, \sigma_2 = \frac{\sigma_{11}+\sigma_{22}}{2} \pm \sqrt{\left(\frac{\sigma_{11}-\sigma_{22}}{2}\right)^2 + \sigma_{12}^2}$$
$$\sigma_3 = \nu(\sigma_1+\sigma_2) \quad \text{for plane strain} \qquad (2.80)$$
$$\sigma_3 = 0 \quad \text{for plane stress}$$

substituting equation (2.72) into (2.80) gives:

$$\sigma_1 = \frac{K}{\sqrt{2\pi r}}\cos\left(\frac{\theta}{2}\right)\left(1+\sin\left(\frac{\theta}{2}\right)\right)$$
$$\sigma_2 = \frac{K}{\sqrt{2\pi r}}\cos\left(\frac{\theta}{2}\right)\left(1-\sin\left(\frac{\theta}{2}\right)\right) \qquad (2.81)$$
$$\sigma_3 = 2\nu\frac{K}{\sqrt{2\pi r}}\cos\left(\frac{\theta}{2}\right) \quad \text{for plane strain}$$
$$\sigma_3 = 0 \quad \text{for plane stress}$$

Substitution of equation (2.81) into (2.79) gives a first estimate of the extent of plastic zone as a function of the angular co-ordinate θ:

$$r_p(\theta) = \frac{K^2}{4\pi\sigma_o^2}\left[\frac{3}{2}\sin^2(\theta) + (1-2\nu)^2(1+\cos(\theta))\right] \quad \text{for plane strain}$$
$$r_p(\theta) = \frac{K^2}{4\pi\sigma_o^2}\left[1+\frac{3}{2}\sin^2(\theta)\cos(\theta)\right] \quad \text{for plane stress} \qquad (2.82)$$

The shape of these plastic zones is shown in Figure 2.13. More accurate analyses were first contributed by Tuba (1976) using a relaxation method as shown in Figure 2.14.

### 2.8.2 Asymptotic Crack Tip Fields: Slip Line Fields.

In elastic-perfectly plastic non-hardening materials, the crack tip stresses are finite. This allows the stresses to be discussed in terms of slip line fields. The slip lines fields for plane strain and plane stress assuming plasticity completely surrounds the crack tip have been

discussed by McClintock (1971) and Rice (1982). In this thesis, Rice (1982) approach has been adopted.

### 2.8.2.1 Plane Strain Slip Lines

For plane strain, it is convenient to use polar coordinates which allow the equilibrium equation (2.6) to be reduced to;

$$\begin{aligned}\frac{\partial \sigma_{rr}}{\partial r}+\frac{1}{r}\frac{\partial \sigma_{r\theta}}{\partial \theta}+\frac{\sigma_{rr}-\sigma_{\theta\theta}}{r}=0\\ \frac{\partial \sigma_{r\theta}}{\partial r}+\frac{1}{r}\frac{\partial \sigma_{\theta\theta}}{\partial \theta}+2\frac{\sigma_{r\theta}}{r}=0\end{aligned} \tag{2.83}$$

Multiplying through by r, the assumption of finite crack tip stress suggests that $\frac{\partial \sigma_{rr}}{\partial r}\cdot r$ and $\frac{\partial \sigma_{r\theta}}{\partial r}\cdot r \rightarrow 0$ as $r \rightarrow 0$ allowing the equilibrium equations to be further reduced to:

$$\sigma_{rr}-\sigma_{\theta\theta}+\frac{\partial \sigma_{r\theta}}{\partial \theta}=0 \tag{2.84}$$

$$2\sigma_{r\theta}+\frac{\partial \sigma_{\theta\theta}}{\partial \theta}=0 \tag{2.85}$$

The Mises yield condition may be rewritten in polar coordinates for plane strain as:

$$\overline{\sigma}^2=\frac{1}{4}(\sigma_{rr}-\sigma_{\theta\theta})^2+\sigma_{r\theta}^2+\frac{1}{12}(\sigma_{rr}+\sigma_{\theta\theta}-2\sigma_{33})^2=\sigma_o^2 \tag{2.86}$$

Differentiating equation (2.86) with respect to 0 and using the equilibrium equations (2.84-2.85), simplifies the result to:

$$6\left[\frac{\partial\sigma_{r\theta}}{\partial\theta}\right]\left[\frac{\partial(\sigma_{rr}+\sigma_{\theta\theta})}{\partial\theta}\right]=\frac{\partial(\sigma_{rr}+\sigma_{\theta\theta}-2\sigma_{33})^2}{\partial\theta} \tag{2.87}$$

Using the flow rule with the plane strain conditions requires that:

$$\sigma_{33}=\frac{\sigma_{rr}+\sigma_{\theta\theta}}{2} \tag{2.88}$$

Using equation (2.88), the right side of equation (2.87) vanishes and the stress state at the crack tip (r = 0) satisfies either:

$$\begin{aligned}&(\mathrm{a})\ \frac{\partial(\sigma_{rr}+\sigma_{\theta\theta})}{\partial\theta}=\frac{\partial\sigma_m}{\partial\theta}=0\\&(\mathrm{b})\ \frac{\partial\sigma_{r\theta}}{\partial\theta}=0\end{aligned} \tag{2.89}$$

In sectors in which condition (a) holds, the mean stress does not change with angle around the crack tip. This defines a constant stress sector in which the slip lines are straight and the stress components ($\sigma_m$, $\sigma_{11}$, $\sigma_{22}$, $\sigma_{33}$) in Cartesian coordinates are constant. Such sectors occur directly ahead of the crack tip and in region adjacent to the crack surfaces in the Prandtl field, illustrated in Figure 2.15.

Condition (b) corresponds to a situation in which the shear stress $\sigma_{r\theta}$ does not change with angle. Substituting $\frac{\partial\sigma_{r\theta}}{\partial\theta}=0$ in equation (2.84) gives:

$$\sigma_{\theta\theta}=\sigma_{rr} \tag{2.90}$$

which reduces the yield criterion expressed in terms of shear stress, $k$, to:

$$\sigma_{r\theta}^2-k^2=0 \tag{2.91}$$

The other stress components can be determined from equation (2.84):

$$\frac{\partial \sigma_{\theta\theta}}{\partial \theta} = -2\sigma_{r\theta} = \mp 2k \tag{2.92}$$

which on integration with respect to θ gives:

$$\sigma_{\theta\theta} = \mp 2k\theta + C \tag{2.93}$$

The asymptotic stresses around the crack tip can be expressed as the Prandtl field which is an important limiting crack tip field in which plasticity is assumed to completely surround the crack tip. On this basis, the stresses can be solved from the traction free crack surface region denoted I in Figure 2.15. In this region, the yield criterion and the free surface require that the stress field is a homogenous tensile field parallel to the crack flanks.

$$\sigma_{11} = 2k \tag{2.94}$$

$$\sigma_{22} = 0 \tag{2.95}$$

$$\sigma_{33} = \sigma_m = k \tag{2.96}$$

$$\sigma_{12} = 0 \tag{2.97}$$

Cylindrical coordinates ($r$, θ) are employed to describe the stress field in region I as:

$$\sigma_{rr} = k\left(1 + \cos 2\theta\right) \tag{2.98}$$

$$\sigma_{\theta\theta} = k\left(1 - \cos 2\theta\right) \tag{2.99}$$

$$\sigma_{r\theta} = -k \sin 2\theta \tag{2.100}$$

$$\sigma_m = k \tag{2.101}$$

The Hencky equations, Hill (1950), express the equilibrium requirements in terms of the rotation of the slip lines and allow the stress state in region II to be given as:

$$\sigma_{\theta 0} = \sigma_{rr} = \sigma_{zz} = \sigma_m = k\left(1 + \frac{3\pi}{2} - 2\theta\right) \tag{2.102}$$

$$\sigma_{r0} = k \tag{2.103}$$

The constant stress sector III ahead of the crack comprises a stress system which consists of a simple stress state given by:

$$\sigma_{\theta\theta} = k(\pi + 1 + \cos 2\theta) \tag{2.104}$$

$$\sigma_{rr} = k(\pi + 1 - \cos 2\theta) \tag{2.105}$$

$$\sigma_{zz} = \sigma_m = k(1 + \pi) \tag{2.106}$$

$$\sigma_{r\theta} = k \sin 20 \tag{2.107}$$

The plane strain Prandtl mode I asymptotic stress field in Cartesian and cylindrical coordinates are shown in Figure 2.16.

### 2.8.2.2 Plane Stress Slip Lines

A state of plane stress is said to exist in the $x_3$ direction if:

$$\sigma_3 = 0 \quad \text{and} \quad \frac{\partial \sigma_{3i}}{\partial x_3} = 0 \tag{2.108}$$

A plane stress crack field can be developed assuming either that plasticity surrounds the crack tip at all angles (Hutchinson (1968b)), or incomplete plasticity is permitted, Sham and Hancock (1999). Both solutions are similar in the critical area ahead of the crack front. In this thesis, incomplete plastic solution has been adopted to compare with the numerical three-dimensional solutions.

Hill (1950) demonstrated that the characteristics of stress and velocity are the same in plane stress and their directions coincide with that of zero rate of extension as in plane strain. However in plane stress, the stress state will dictate whether the directions of zero rate extension can exist in the $x_1$-$x_2$ plane. The state of stress is governed by the partial differential equations of equilibrium and compatibility which can either be hyperbolic, parabolic or elliptic. Under hyperbolic conditions, plane stress slip-lines comprise a non-orthogonal grid in which the direct stress across the line is twice that along the lines. Consequently, the slip lines are lines of zero extension. The angle between the lines depends on the stress state, but in the limit may become zero to give a single set of characteristics when the equilibrium equations are parabolic.

In plane stress, the Mises yield criterion in cylindrical coordinate system conditions is given as:

$$\overline{\sigma}^2 = \sigma_{rr}^2 + \sigma_{\theta\theta}^2 - \sigma_{rr}\sigma_{\theta\theta} + 3\sigma_{r\theta}^2 = \sigma_o^2 \tag{2.109}$$

Differentiating the Mises yield criterion with respect to θ gives:

$$2\sigma_{\theta\theta}\frac{\partial \sigma_{\theta\theta}}{\partial \theta} - \sigma_{rr}\frac{\partial}{\partial \theta}(\sigma_{rr}\sigma_{\theta\theta}) + 6\sigma_{r\theta}\frac{\partial \sigma_{r\theta}}{\partial \theta} = 0 \tag{2.110}$$

Substituting the equilibrium equations as in equation (2.84 and 2.85), gives:

$$\frac{\partial \sigma_m}{\partial \theta} \cdot \frac{\partial s_{rr}}{\partial \theta} = 0 \tag{2.111}$$

where $\sigma_m$ is the mean stress and $s_{rr}$ is the radial stress deviator. The equations have two solutions subject to the condition that the yield criterion is satisfied.

$$\text{(a)}\frac{\partial \sigma_m}{\partial \theta} = 0$$

or (2.112)

$$\text{(b)}\frac{\partial s_{rr}}{\partial \theta} = 0$$

Rice (1982) has shown that two possible types of plastic sectors may exist at the crack tip in plane stress: constant stress sectors and centred fans. Condition (a) implies that mean stress does not vary with angle and defines constant stress sector in which the slip lines are straight but non-orthogonal. Condition (b) implies that the radial stress deviator does not vary with angle and identifies centred fan sectors which comprise straight radial lines intersected by a set of curved characteristics with equations of the form:

$$r^2 \sin(\theta - \phi) = \text{constant} \tag{2.113}$$

where $\phi$ is the angle to which the curved lines are asymptotic. For isotropic Mises materials, the centred fan condition $\partial\sigma_{rr}/\partial\theta = 0$ reduces to $2\sigma_{rr} = \dot{\sigma}_{\theta\theta}$ and the equilibrium equations in equations (2.84-2.85) can be integrated to give:

$$\sigma_{rr} = \pm k \cos(\theta - \phi) \tag{2.114}$$

$$\sigma_{\theta\theta} = \pm 2k \cos(\theta - \phi) \tag{2.115}$$

$$\sigma_{r\theta} = \pm k \sin(\theta - \phi) \tag{2.116}$$

When the stresses are assumed to be bounded in the elastic sector at the crack tip, the stresses in the elastic can be expressed in terms of the semi-infinite wedge solution given by Timoshenko and Goodier (1970) subject to the requirement that the yield criterion is not violated:

$$\sigma_{rr} = A_1 \sin 2\theta + A_2 \cos 2\theta + (A_3\theta + A_4)/2 \tag{2.117}$$

$$\sigma_{\theta\theta} = A_1 \sin 2\theta - A_2 \cos 2\theta + (A_3 + A_4)/2 \tag{2.118}$$

$$\sigma_{r\theta} = A_1 \cos 2\theta - A_2 \cos 2\theta - A_3/4 \tag{2.119}$$

where $A_1$, $A_2$, $A_3$ and $A_4$ are constants that satisfy the conditions of equilibrium and compatibility at the crack tip in plane stress.

The plane stress asymptotic mode I field for incomplete crack tip plasticity discussed by Sham and Hancock (1999) can be regarded as a limiting case for a near mode-I field. The field consists of a curved fan sector directly ahead of the crack in the angular range $\theta_1 = \pm 39.126^{\circ}$ complemented by elastic sectors extending to the crack flanks as shown in Figure 2.17. The mode I plane stress asymptotic stress field for Cartesian and cylindrical coordinates are shown in Figure 2.18.

### 2.8.3 Crack Tip Opening Displacement (CTOD)

Wells (1961) observed that initially sharp crack tips are blunted by plastic deformation. This observation led to the introduction of the crack tip opening displacement concept (CTOD) to characterise fracture under conditions of large plastic deformation. Wells (1961) argued that the degree of crack blunting at failure increases with the toughness of the material. From the Dugdale (1960) analysis, the CTOD, $\delta_t$, is given by:

$$\delta_t = \frac{8\sigma_o a}{\pi E}\ln\left[\sec\frac{\pi}{2}\frac{\sigma}{\sigma_o}\right] = \frac{\pi\sigma^2 a}{E\sigma_o} + \cdots \qquad (2.120)$$

If the applied stress $\sigma$ is very small compared to $\sigma_o$, a series expansion of the (ln sec) term reduces to the small scale yielding relationship including a constant $m$ to distinguish plane stress ($m = 1$) and plane strain ($m = 2$):

$$\delta_t = \frac{\sigma^2 \pi a}{\sigma_o E}\frac{1}{m} = \frac{K^2}{E\sigma_o}\frac{1}{m} = \frac{G}{\sigma_o}\frac{1}{m} \qquad (2.121)$$

This relates the CTOD approach to the elastic potential energy release rate, G, and stress intensity factor, K, which are all equivalent in small-scale yielding. Experimentally, $\delta_t$ can

be determined through the crack mouth opening displacement (CMOD) by measuring the surface displacement across the crack front, as shown in Figure 2.19(a). Computationally, $\delta_t$ is usually determined by the 90° line intercept construction as illustrated in Figure 2.19(b) following Shih (1981).

### 2.8.4 The Path Independent Integral (J)

A key unifying concept which enables the characterisation of elastic and elastic-plastic crack tip fields for rate-independent materials under monotonic loading is the J-Integral. J is a path independent integral, that describes the potential energy released during an increment of virtual crack extension in non-linear elastic materials. Path independent integrals were proposed independently by Cherepanov (1967), Eshelby (1968) and Rice (1968b). However, it was Rice (1968b) who established their relevance to fracture mechanics beyond the validity limits of LEFM.

For a crack in a two-dimensional field, Rice (1968b) defined a path independent line integral, J:

$$J = \int_{\Gamma} \left[ W_{\varepsilon}\, dx_2 - \sigma_{ij}\, n_i \frac{\partial u_j}{\partial x_1}\, ds \right] \tag{2.122}$$

The arbitrary path $\Gamma$ starts at any point on the lower crack surface and ends at an arbitrary point on the upper surface as illustrated in Figure 2.20. without including any other singularities apart from the crack tip. The first term in the integral is the strain energy density, $W_c$ or work of deformation per unit volume:

$$W_{\varepsilon} = \int_0^{\varepsilon} \sigma_{ij}\, d\varepsilon_{ij} \tag{2.123}$$

The second term is the work done by the external forces where $n_i$ is the outward normal unit vector to the path $\Gamma$, and $\sigma_{ij}$ and $u_i$ are the stress and displacement fields, $ds$ is the

differential arc length of the virtual contour around the crack tip. Consequently, J represents the change in potential energy during incremental crack extension *da* in a fixed load-displacement curve. The area between the curves corresponds to the potential energy loss when the crack length is extended to $a + \delta a$:

$$J = -\frac{1}{B}\left(\frac{\partial U}{\partial a}\right) \tag{2.124}$$

and $U$ is total potential energy in a plate of thickness, B. Under linear elastic conditions J is directly equivalent to the potential energy release rate, $G$, as shown in Figure 2.21. Experimentally, J can be measured at the load points of a two specimens which have incrementally different crack lengths, a and a + δa but otherwise are identical (Landes and Begley (1972)). However this is a very impractical, and ASTM (E813-87, 1988) argues that J can be determined from deeply cracked bend geometries ($a/W \geq 0.45$) in which J is decomposed into elastic and plastic components:

$$J = J^E + J^P \tag{2.125}$$

The elastic component $J^E$ is most simply calculated from stress intensity factor $K_I$:

$$J^E = \frac{K_I^2}{E'} = G \tag{2.126}$$

where $E' = E/(1-\nu^2)$ for plane strain while K is obtained from the applied load relation given in ASTM (E399-83, 1988):

$$K_I = \frac{P_Q S}{B\sqrt[3]{W}} f\left(\frac{a}{W}\right) \tag{2.127}$$

Here $P_Q$ is the applied load, S is the span between the loading points, while the function $f(a/W)$ is given in ASTM (E399-83, 1988). In general, J becomes:

$$J = \frac{K^2\left(1-\nu^2\right)}{E} + \frac{\eta_{pl}}{B\left(W-a\right)} A_{pl}^{LLD} \tag{2.128}$$

where $\eta_{pl}$ is the non-dimensional plastic eta factor and $A_{pl}^{LLD}$ is the plastic area under the load-displacement curve. Comprehensive discussions of experimental methods for the determination of J and CTOD from laboratory testpieces are given in Karstensen and Hancock (2002).

Usefully, the J-integral can also be related to the CTOD, $\delta_t$ through the relation, Shih (1981):

$$J = \delta_t \, \sigma_o \frac{1}{d_n} \tag{2.129}$$

where $d_n$ is a constant which depends strongly on the strain hardening exponent, n, but weakly on $\alpha\sigma_o/E$. For nonhardening cases $n \rightarrow \infty$, $d_n$ is 1 and 0.78 for plane stress and plane strain, Shih (1981).

### 2.8.5 HRR Field

Path independence of the J-integral requires that the integrand in equation (2.122) has a $1/r$ dependence:

$$r\left(W_\varepsilon - \sigma_{ij} n_j u_{i,1}\right) = f(0) \quad as \quad r \rightarrow 0 \tag{2.130}$$

This allows J to be independent of the radius of the contour.

$$J = \int_{-\pi}^{\pi} f(\theta) \quad d\theta \tag{2.131}$$

Path independence allows J to quantify the strength of crack tip singularities and characterise crack tip deformation. A more explicit connection between J and crack tip deformation is revealed using a power law relation between stress and strain. In nonlinear elastic solids, material deformation can be approximated by a Ramberg-Osgood relationship for uniaxial deformation equation (2.43). As the crack tip is approached asymptotically, contributions to the strains that depend linearly on stress are negligible compared to power law terms which approximate to a power law such as that given in equation (2.42). $J_2$ deformation theory can be used to generalise equation (2.42) to multiaxial states,

$$\frac{\varepsilon_{ij}}{\varepsilon_o} = \frac{3}{2}\alpha\left(\frac{\sigma_e}{\sigma_o}\right)^{n-1}\frac{s_{ij}}{\sigma_o}; \qquad \sigma_e = \sqrt{\frac{3}{2}s_{ij}\,s_{ij}} \tag{2.132}$$

where $s_{ij}$ are the stress deviators. Using this non-linear relationship with the J integral, Hutchinson (1968a) and Rice and Rosengren (1968), identified the dominant crack tip singularity for nonlinear deformation and showed that J characterises crack tip stress and strain field which are known as the HRR fields. The stress, strain and displacement fields associated with the dominant singularity are of the form:

$$\sigma_{ij} = \sigma_o\left[\frac{J}{\varepsilon_o\sigma_o\alpha I_n r}\right]^{\frac{1}{1+n}}\tilde{\sigma}_{ij}(\theta;n); \tag{2.133}$$

$$\varepsilon_{ij} = \frac{\sigma_o\alpha}{E}\left[\frac{J}{\varepsilon_o\sigma_o\alpha I_n r}\right]^{\frac{n}{1+n}}\tilde{\varepsilon}_{ij}(\theta;n) \tag{2.134}$$

$$u_i = \alpha\varepsilon_o r\left[\frac{J}{\alpha\sigma_o\varepsilon_o I_n r}\right]^{\frac{n}{1+n}}\tilde{u}_i(\theta;n) \qquad (i = 1, 2) \tag{2.135}$$

where $I_n$ is an integration constant that depends on the strain hardening exponent $n$, loading mode and on whether plane strain or plane stress. The functions $\tilde{\sigma}_{ij}(\theta,n)$, $\tilde{\varepsilon}_{ij}(\theta,n)$ and $\tilde{u}_i(\theta;n)$ are non-dimensional angular functions tabulated by Shih (1983). Examples of

plane strain and plane stress asymptotic angular functions for $n = 3$ and $n = 13$, are shown in Figures 2.22 – 2.23 after Hutchinson (1968b)

### 2.8.6 Limits of Single Parameter Fracture Mechanics

With increased levels of deformation, the strict requirements of LEFM are invalidated by the size of the plastic zone compared to dimensions such as the ligament, or the crack length. However the crack tip field can be characterised by J from small-scale yielding into full plasticity. Nevertheless, in full plasticity, McClintock (1971) first suggested that the asymptotic plastic fields in the absence of strain hardening are not unique but are functions of the geometry, loading mode. This is illustrated by comparing the slip line field for centre crack panels, shallow and deeply cracked bend bars and shallow and deeply double edge cracked bars as shown in Figure 2.24-2.27.

Crack tip fields for large scale yielding in tension are entirely different from those of bending geometries which are associated with the Prandtl field as shown in Figure 2.24 and 2.25. For the tension geometry, McClintock (1971) argued that intense shear deformation is confined to slip planes emanating at 45 degrees from the tensile direction. A state of plane strain tension exists ahead of the crack in the 90 degree wedge where the stresses which satisfy equilibrium and yield criterion are given by:

$$\sigma_{22} = 2k \tag{2.136}$$

$$\sigma_{11} = 0 \tag{2.137}$$

$$\sigma_{12} = k \tag{2.138}$$

$$\sigma_{33} = \sigma_m = k \tag{2.139}$$

The stress levels in tension elastic-perfectly plastic crack tip are much lower than the levels in bending. McClintock's (1971) observation implies that elastic-perfectly plastic crack tip fields are not unique, but depend on geometry and loading. As a result fracture cannot be characterised by a single parameter such as J or $\delta_t$.

### 2.8.7 J-Dominance

McMeeking (1977) and McMeeking and Parks (1979) describe the ability of a single parameter, such as J, to uniquely define the crack tip field as J-Dominance.

To assess J-Dominance, McMeeking and Parks (1979) compared large geometry change finite strain solutions for deep crack bend bar with the corresponding small scale yielding solution. At distance greater than $2J/\sigma_o$ (or 2 to $3\delta_t$), the effect of the crack tip blunting diminishes and the stress field of a large geometry change solution is similar to a small geometry change solution at distance greater than $2J/\sigma_o$ as illustrated in Figure 2.28.

McMeeking and Parks (1979) calculated the stresses in edge cracked bend bars and centre crack tension panel into full plasticity and compared with small-scale yielding solutions. For the edge cracked bend bars, it was found that the non-dimensionalised stresses and strains field were independent of J even with non-hardening solutions. However, the centre crack tension panel deviated from the small-scale yielding solution. Based on this result, the requirements of J-dominated zone in a crack tip field were expressed through a non-dimensional grouping, $\mu$:

$$\frac{c\,\sigma_o}{J} = \mu \tag{2.140}$$

where $c$ is a critical dimension of the cracked body. For deeply cracked bars $c = (W\text{-}a)$ while for shallow cracked bars $c = a$. For deeply cracked plane strain centre crack tension panel, J-dominance is maintained as long as the ligament is greater than $200J/\sigma_o$ (or $\mu = 200$), (McMeeking and Parks (1979). While for bend type configuration, the J is maintained as long as the ligament is greater than $25J/\sigma_o$.

Shih and German (1981) repeated the work of McMeeking and Parks (1979) comparing the full field solution for deeply cracked bend and centre crack tension panel in plane strain with small strain formulations and proposed that, for J-dominant fields the hoop stress

directly ahead the crack at a distance $r = 2J/\sigma_o$ must be within 10 percent of the HRR field. On this basis, the local stress field in deeply cracked plane strain edge notched bend bars, scales in the same way as the small-scale yielding solution as long as the ligament ($W$-$a$) is greater than $25J/\sigma_o$ (or $\mu = 25$). For deeply cracked plane strain CCP, J-dominance is maintained as long as the ligament is greater than $200J/\sigma_o$ (or $\mu = 200$).

Al-Ani and Hancock (1991) examined the J-Dominance criteria of deeply cracked and shallow cracked bars in tension and bending. For shallow cracked bars J-dominance was lost before $a\sigma_o/200$. More importantly, they demonstrated that at different crack length the plastic flow fields are not unique. For shallow cracked bending specimens, the plastic field spreads to the face of the cracked ligament in accord with slip line field discussed by Ewing and Hill (1967). At deformation levels at which J-Dominance is lost, two parameter characterisation is required.

Although the full plastic plane strain crack tip fields are not unique, Hancock and co-workers (Al-Ani and Hancock (1991), Betegón and Hancock (1991) and Du and Hancock (1991)) have argued that the lack of uniqueness is not associated with the sudden development of the fully plastic flow field but rather evolves from the small-scale yielding and the geometry dependent nature of the elastic field. Specifically, Betegón and Hancock (1991) and Du and Hancock (1991) identify the role of higher order terms in the elastic asymptotic expression (T-stress) as having a critical role in determining J-Dominance. Within this context it is now appropriate to introduce the T-stress as a precursor to a discussion of two-parameter fracture mechanics.

## 2.9 Two-Parameter Fracture Mechanics

### 2.9.1 T-Stress

Williams (1957) expressed the asymptotic elastic stress field of a crack as a polynomial series of the form:

$$\sigma_{ij}(r,\theta) = A_{ij}(\theta)r^{-1/2} + B_{ij}(\theta)r^{0} + C_{ij}(\theta)r^{1/2} + \cdots \tag{2.141}$$

where $A$, $B$, $C$ combine the angular functions and intensities and $r$ is distance from the crack tip. In classical LEFM, interest is focused on the first term of the asymptotic William expansion, which incorporates the stress intensity factor. Larsson and Carlsson (1973) demonstrated that under contained yielding conditions, the second term of the Williams expansion has a pronounced effect on the size and shape of the plastic zone at the crack tip. Rice (1974) denoted the second term of the Williams expansion, as the T-stress. The T-stress is independent of the radial distance from the crack tip and corresponds to a uniaxial stress parallel to the crack flanks,

$$\begin{bmatrix}\sigma_{11} & \sigma_{12}\\ \sigma_{21} & \sigma_{22}\end{bmatrix} = \frac{K}{\sqrt{2\pi r}}\begin{bmatrix}f_{11}(\theta) & f_{12}(\theta)\\ f_{21}(\theta) & f_{22}(\theta)\end{bmatrix} + \begin{bmatrix}T & 0\\ 0 & 0\end{bmatrix} + \text{higher order terms} \tag{2.142}$$

where higher order terms vanish at the crack tip. Methods to determine the T-stress have been reviewed in Sherry et al. (1995) and Karstensen and Hancock (2002). These include the direct method used by Larsson and Carlsson (1973) which allows the T-stress to be evaluated directly from the stress on the crack flanks, $\theta = \pm\pi$ using a refined crack tip finite element mesh:

$$T = \lim_{r\to 0}\sigma_{11}(r, \theta = \pi), \qquad f_{11}(\pm\pi) = 0 \tag{2.143}$$

Sham (1991) developed generalised weight functions to calculate T for a given geometry. Kfouri (1986) used Eshelby's theorem to determine T by the difference in J-integral of two solutions with and without a superimposed crack tip point load in the direction of crack advance. In the line-spring method Rice and Levy (1972), T is calculated through the finite element procedure by superimposing results of cracked two-dimensional elastic T from bending and tension calculated independently under the action of membrane force and bending moment.

The T-stress has now been tabulated for a wide range of geometries for which the results are either expressed in terms of a T-stress concentration factor, $T/\sigma$, or as a biaxiality parameter, $\beta$, following Leevers and Radon (1983):

$$\beta = \frac{T\sqrt{\pi a}}{K} \tag{2.144}$$

Tables 2.2(a-c) show the value of $K_I$ and $\beta$ for a range of a/W ratios for single edge crack bars under tension and bending following Sham (1991). The results of Leevers and Radon (1983) for centre cracked panels are shown in Table 2.3. Two-dimensional studies (Larsson and Carlsson (1973), Leevers and Radon (1983), Cardew et al. (1984), Kfouri (1986), Sham (1991)) show that the T-stress depends strongly on the type of loading as well as the geometry. However in all cases the T-stress is proportional to the applied load and at asymptotically small load levels T = 0 for all geometries. The effects of the specimen thickness on the T-stress in three-dimensional fields are discussed in chapter 3.

### 2.9.2 Boundary Layer Formulations

Boundary layer formulations were introduced by Rice (1966, 1967a, 1967b) to analyse crack tip plasticity in contained yielding without having to model the geometry of the whole cracked body. Small scale yielding occurs when crack tip plasticity is small compared to the dimensions of the finite element model allowing the asymptotic elastic field to be used as the boundary conditions on a domain around the crack tip. Figures

2.29(a), (b) show schematically how the full field geometry may be replaced by the boundary-layer formulations where $K_I$ is the stress intensity factor for the associated elastic crack problem.

Tractions or displacements corresponding to the K field are applied on the outer boundary of a region around the crack tip using equations (2.112) or (2.113) as shown schematically in Figure 2.29(b). Boundary layer formulations are mathematically exact in the limit of a vanishingly small plastic zone, but are accurate as long as plasticity is confined to less than one tenth of the mesh radius.

### 2.9.2.1 Modified Boundary Layer Formulations

The addition of the non-singular T-stress to the remote K field in the boundary condition is known as a modified boundary layer formulation (MBLF). As the T-stress is directly proportional to the load applied in an isotropic linear elastic body, the load in modified boundary layer formulations can be added using the superposition principle. The displacement in $u_i^{mblf}$ plane strain under the load due to K and T is therefore:

$$u_i^{mblf} = u_i^{K_I} + u_i^{T} \tag{2.145}$$

In plane strain deformation, $\varepsilon_{zz} = 0$ :

$$\sigma_{11} = T, \quad \sigma_{22} = 0, \quad \sigma_{zz} = \nu T \tag{2.146}$$

Figure 2.30 schematically shows the components of distance around a circular boundary layer formulation mesh which is used to derive the displacement $u_1^{T}$ and $u_2^{T}$. Consequently, the remote displacements field for a mode I plane strain MBLF in terms of cylindrical representation are:

$$u_1^{mblf}(r,\theta)=K_I\frac{1-\nu}{E}\sqrt{\frac{r}{2\pi}}\cos\frac{\theta}{2}(3-4\nu-\cos\theta)+T\frac{1-\nu^2}{E}r\cos\theta$$
$$u_2^{mblf}(r,\theta)=K_I\frac{1-\nu}{E}\sqrt{\frac{r}{2\pi}}\sin\frac{\theta}{2}(3-4\nu-\cos\theta)-T\frac{\nu(1+\nu)}{E}r\sin\theta \quad (2.147)$$

The remote displacement field for plane stress modified boundary layer formulations can also be given for a state of remote plane stress. In plane stress, $\sigma_{zz} = 0$:

$$\sigma_{11}=T,\quad \sigma_{22}=0 \quad (2.148)$$

The mode I displacement field for plane stress in terms of cylindrical representation are:

$$u_1^{mblf}(r,\theta)=K_I\frac{1-\nu}{E}\sqrt{\frac{r}{2\pi}}\cos\frac{\theta}{2}(3-4\nu-\cos\theta)+\frac{T}{E}r\cos\theta$$
$$u_2^{mblf}(r,\theta)=K_I\frac{1-\nu}{E}\sqrt{\frac{r}{2\pi}}\sin\frac{\theta}{2}(3-4\nu-\cos\theta)-\frac{\nu T}{E}r\sin\theta \quad (2.149)$$

### 2.9.3 J-T approach

Larsson and Carlsson (1973) have shown that the second term in the William's expansion has a significant effect on the shape and size of the plastic zone which develops at the crack tip. Rice (1974) denoted the second term in the Williams expansion as the T-stress. Significantly, the T-stress has no effect on the J-integral.

In an important development, Bilby et al. (1986) showed the effect of the second-order term on the large geometry change solution (LGC) within $2J/\sigma_o$ of the crack tip. Negative *T*-stresses were shown to reduce triaxial stress level ahead of the crack. However, the effect of *T* on crack tip fields was made clear through systematic analyses by Hancock and co-workers (Betegón and Hancock (1991), Al-Ani and Hancock (1991), Du and Hancock (1991)).

Betegón and Hancock (1991) modelled plane-strain elastic-plastic crack tip fields using modified boundary layer formulations and a strain hardening material response. The results indicate that the geometries characterised by zero and positive T stress cause the stress field to approach the HRR field, while geometries with a negative T cause the direct stresses directly ahead the crack to fall significantly. The effect of T stresses is to reduce the direct stresses ahead of crack by an amount that depends only on T and is independent of distance $r\sigma_o/J$. Based on these results, Betegón and Hancock proposed a family of stress field differing only by a distance independent higher order term which depends on T:

$$\left(\frac{\sigma_{\theta\theta}}{\sigma_o}\right)_{(r,T)} = \left(\frac{\sigma_{\theta\theta}}{\sigma_o}\right)_{(r,T=0)} + A_n\left(\frac{T}{\sigma_o}\right) + B_n\left(\frac{T}{\sigma_o}\right)^2 \qquad (2.150)$$

where $A_n$, and $B_n$ are constants dependent on the strain hardening exponent $n$ where values $A_n$, and $B_n$ for $n$ = 13 and $\infty$ are shown in Table 2.4. Betegón and Hancock (1991) argued that $J$-Dominance should be maintained for T stresses greater than -0.2 $\sigma_0$ for $n$ = 13. Wang (1993) reinforced the findings of Betegón and Hancock (1991), using three-term polynomial fit to describe the effect. The important development from Betegón and Hancock (1991) was that the problems of J-Dominance in different geometries were unified. Geometries that show positive T-stress can be described by the HRR field and characterised by J alone. Geometries that lose J-Dominance feature negative T-stresses and can be characterised by two-parameters, J and T.

Al-Ani and Hancock (1991) studied the transition of crack tip fields from deep to shallow edge crack bend bars. J-Dominance was retained or lost according to the sign of T. Fully constrained flow fields were found in deeply crack bars when plasticity is limited to uncracked ligament and $T \geq 0$, while shallow cracked specimen showed unconstrained flow field in which plasticity spreads across uncracked and cracked ligament with $T \leq 0$. These observations imply that the stress fields can be characterised by two terms J and T. This two-parameter fracture mechanics approach uses the T-stress to quantify constraint while the applied load is scaled by J.

Du and Hancock (1991), demonstrated the effect of T on structure of crack tip field in plane strain under elastic perfectly-plastic conditions. Crack tip deformation was represented as slip line fields within small-strain theory as shown in Figure 2.31. The analysis clearly showed that in the leading sector of the crack tip field, T is similar deviatorically but hydrostatically different as illustrated in Figure 2.32. Compressive (negative) T-stresses reduce the level of stress triaxiality and cause the plastic zone to swing forward. Tensile (positive) T-stresses increase level of crack tip stress triaxiality towards the Prandtl field while the plastic zone decreases and rotates towards the crack flank. The change of plastic zone shape due to T-stress is illustrated in Figure 2.33, where the stress field is compared with the Prandtl field. For tensile T-stresses, plasticity envelops the crack tip corresponding to the complete Prandtl field which is the limiting HRR field characterised by J. Under compressive T-stresses, the triaxiality of stress state was shown to reduce and cause the appearance of elastic wedges at crack flanks so that plasticity does not completely surround the crack tip.

Although the fully plastic crack tip fields are not unique, Hancock and co-workers (Al-Ani and Hancock (1991), Betegón and Hancock (1991) and Du and Hancock (1991)) have argued that the lack of uniqueness is not associated with the sudden development of the fully plastic flow field but rather evolves from the small-scale yielding and the geometry dependent nature of the elastic field as characterised by T.

### 2.9.4 J-Q Approach

Following Bilby et al. (1986) and Hancock and co-workers, O'Dowd and Shih (1991, 1992) presented a related approach to quantify the evolution of constraint from small-scale yielding to full plasticity. O'Dowd and Shih (1991) carried out finite element studies using large geometry change analyses (LGC) as well as small-strain, small geometry change solutions (SGC). In an annular region surrounding the tip between $J/\sigma_0 < r < 5J/\sigma_0$, the stress field was expressed as:

$$\frac{\sigma_{ij}}{\sigma_o} = \left(\frac{J}{\alpha \varepsilon_o \sigma_o I_n r}\right)^{1/(n+1)} \tilde{\sigma}_{ij}(\theta, n) + Q\left(\frac{r}{J/\sigma_o}\right)^q \hat{\sigma}_{ij}(\theta, n) \tag{2.151}$$

The first term is the HRR field in which the r and θ are polar co-ordinates centered at crack tip, n is strain hardening exponent, $\varepsilon_o$ the yield strain and $\alpha$ is a material constant and, $\tilde{\sigma}_{ij}(\theta)$ and $\hat{\sigma}_{ij}(\theta)$ are angular functions that depend on θ. This can be expressed as:

$$\sigma_{ij} = (\sigma_{ij})_{HRR} + Q\sigma_o \delta_{ij}; \qquad \text{for } r > J/\sigma_o \qquad |\theta| \le \frac{\pi}{2} \tag{2.152}$$

setting $Q = 0$ defines the HRR reference field and the perturbations are purely hydrostatic in the leading sectors ahead of the crack tip. Physically Q measures the change in crack tip triaxiality from a reference field. In the context of contained yielding, $T/\sigma_o = \tau$ is uniquely related to Q. This can be written explicitly comparing equation (2.152) with the modified boundary layer solution in three-term with constants $C_n$. Q then becomes:

$$Q = Q_o + A_n \tau + B_n \tau^2 + C_n \tau^3 \tag{2.153}$$

where $Q_o$ represents the difference between HRR and small scale yielding crack opening stress at a reference distance from the tip normally $2J/\sigma_o$. A refinement to equation (2.152) arises if the reference field is taken as the small scale yielding field resulting in a modified definition of the constraint parameter $\tilde{Q}$:

$$\sigma_{ij} = (\sigma_{ij})_{SSY} + \tilde{Q}\sigma_o \delta_{ij} \tag{2.154}$$

$$\tilde{Q} = A_n \tau + B_n \tau^2 + C_n \tau^3 \tag{2.155}$$

Using Q = 0 as the reference field, the constraint of any stress component in full-field solutions can be determined through:

$$Q = \frac{\sigma_{ij} - (\sigma_{ij})_{SSY}}{\sigma_o} \quad \text{at } \theta = 0, \qquad r = 2J/\sigma_o \tag{2.156}$$

O'Dowd and Shih (1991) numerical solutions show that the stress distribution with the same $Q$-value collapse onto a single curve when the distance is normalized by $J/\sigma_o$. $Q$ is a hydrostatic stress parameter in which negative values indicate that the hydrostatic stress is reduced while positive values imply the hydrostatic stress is increased by $Q\sigma_o$.

The viability of two-parameter characterisation of fracture has been reviewed by Parks (1992). The parametric descriptions correlated with the $T$-stress largely used by Hancock and co-workers (Betegón and Hancock (1991), Al-Ani and Hancock (1991), Du and Hancock (1991)) has been shown to provide good correlations in small to moderate plasticity but the rigorous application diminishes at large scale plasticity because the MBLF itself is based on a assumption of SGC plasticity occurrence however $T$-stresses are easily obtainable for a wide range of geometries, (Leevers and Radon (1983), Kfouri (1986), Sham (1991)). The $J$-$Q$ method provide complete description from small to large scale plasticity however it entails detailed finite element modelling for every geometry at all deformation levels.

## 2.10 Constraint Effects on Toughness

### 2.10.1 In-plane Constraint Effects on Cleavage Failure

The effect of constraint parameter T on cleavage fracture toughness has been discussed by Betegón and Hancock (1990) and Sumpter and Forbes (1992). Both examined the critical value of J for geometries with different levels of constraint. Betegón (1990), Betegón and Hancock (1990) tested shallow cracked bend geometries with $a/W < 0.3$ and deep crack for which $a/W > 0.3$. The shallow cracks exhibit negative T-stresses while deeply bend specimens showed positive T-stresses. Specimens with negative T were systematically found to be tougher than positive T specimens. For deep cracks in bending ($a/W > 0.3$) the

critical value of toughness, $J_c$, is constant and independent of the T-stress as shown in Figure 2.34.

Similar effects of constraint on cleavage toughness due to T were found by Sumpter (1993) using centre cracked tension panels and bend bars of high strength weld steel at –30°C as shown in Figure 2.35.

Sumpter and Hancock (1994) reanalysed the Sumpter (1993) data using Q as shown in Figure 2.36. Sumpter and Hancock (1994) also showed the toughness of high strength weld metal with a yield stress 700 MPa at test temperature –30°C. Figure 2.37 shows $J_c$ as a function of $T/\sigma_o$ while Figure 2.38 shows the same data as a $J_c$-Q locus. Constraint enhanced toughness were found to be more marked for this type of material than for the mild steel, and both J-T and J-Q loci describe the data well. Kirk, Koppenhoefer and Shih (1993) presented cleavage toughness data for A515 steel at room temperature with different a/W ratios showed toughness can be classified based on $T/\sigma_o$. However, attempts to show effect of constraint on thickness were inconclusive because the range of specimen thicknesses used were not sufficient to show the effect of out-of-plane constraint loss associated with the reduction of thickness. The specimen thickness to ligament ratio B/(W-a) ranged from 1.6 to 2 which broadly correspond to plane strain geometries.

In cleavage failure, the fracture toughness can be expressed within the context of two-parameter fracture mechanics by expressing the toughness as a function of the T-stress or Q-parameter:

$$J_c = f(T,Q) \tag{2.157}$$

### 2.10.2 In-plane Constraint Effects on Ductile Tearing.

The resistance to stable ductile tearing has been addressed experimentally by Hancock, Reuter and Parks (1993). Hancock, Reuter and Parks (1993) examined constraint effects in stable ductile tearing using an A710 steel in a series of cracked configurations. CTOD and

J were measured as a function of the T-stress for crack extensions $\Delta a$ = 0, 200μm and 400μm as shown in Figures 2.39-2.40. The initiation toughness was taken to be the critical value of J at a crack extension $\Delta a$ = 200μm. At any finite crack extension, ($\Delta a > 0$) the toughness increased with constraint loss, however at ($\Delta a = 0$), the initiation toughness become constraint independent as $\frac{\sigma_m}{\sigma} = \frac{1}{\sqrt{3}}$ for all geometries (Figure 2.41).

For geometries with compressive T-stresses such as CCP, the initiation toughness was approximately four times greater than that of deeply cracked bend bar and compact tension specimens as indicated in Figure 2.41. The effect of constraint was even more significant for higher crack extensions. An important result from the work of Hancock, Reuter and Parks (1993) is that the tearing resistance of all cracked geometries is correctly ordered by the T-stress, while Q has no meaning for growing cracks.

Figures 2.41 and 2.42 show that the effect of constraint loss in ductile tearing is due to the effect of T on the slope of the resistance curves. This data may be discussed with the numerical solutions of Varias and Shih (1993), which model the effect of constraint loss on the resistance to stable tearing.

## 2.11 Application of Constraint in Structural Integrity Assessments.

Structural integrity assessments in structures containing cracks have been traditionally based on single parameter toughness data $K_{Ic}$ or $J_{Ic}$ acquired from highly constrained flow field in deeply cracked bend specimens. This provides a lower bound conservative toughness, but may lead to unnecessary repairs and outage of engineering structures which develop unconstrained flow fields. The observation that constraint parameters such as T/Q can order experimental toughness data on cleavage and ductile crack failure in constrained and unconstrained flow field led to application of J-T/Q toughness loci in structural integrity assessments. Two parameter fracture mechanics is applied by the constraint matching or the failure assessment diagrams (FADs).

### 2.11.1 Constraint Matching

In constraint matching, the toughness that corresponds to the constraint experienced by the structural defect is used to predict failure. The conditions at failure can be inferred for specific geometry and load dependent toughness by matching the constraint at fracture with laboratory tests at the same constraint level. Constraint matching is illustrated in Figure 2.43. Here a $J_c$-Q loci is develop through the result of experiment on highly constrained and unconstrained geometries. Failure is predicted when the applied driving force curve J-T/Q passes through the toughness locus ($J_c$-T/Q):

$$J(T \text{ or } Q) \geq J_c(T \text{ or } Q) \tag{2.158}$$

### 2.11.2 Failure Assessment Diagrams

Failure Assessment Diagrams evolved from work at Central Electricity Generation Board (CEGB) in the United Kingdom (Dowling and Townley (1975)). The proximity to failure is quantified by the ratio of the applied stress intensity factor, K to experimentally measured material fracture toughness $K_{Ic}$:

$$\frac{K}{K_{Ic}} = K_r \tag{2.159}$$

The proximity to plastic collapse is given as:

$$\frac{P}{P_o} = L_r \tag{2.160}$$

Dowling and Townley (1975) proposed the first failure assessment diagram as a simple square box in Figure 2.44. Interpolation between the extreme values of proximity of failure $K_r$ and $L_r$ either based on failure at a critical value of J or a pragmatic approach to experimental data shows the bound of safe operation of structure. Any load and crack

combination that fall outside the region enclosed by a Failure Assessment Line (FAL) may lead to failures.

The original R6 code was based on a non-hardening material and did not include the strain hardening capability of real structural materials. To address this problem, R6 provides three options for failure assessment: (1) A general failure assessment line (FAL) which can be used for materials which do not exhibit a yield discontinuity:

$$K_r = \left(1 - 0.14L_r^2\right)\left(0.3 + 0.7\exp\left(-0.65L_r^6\right)\right) \quad \text{for } L_r \le L_r^{\max} \tag{2.161}$$

(2) A material specific FAL curve based on J-Integral analysis described by the equation:

$$K_r = \sqrt{\frac{E\varepsilon_{true}}{L_r\sigma_o} + \frac{L_r^3\sigma_o}{2E\varepsilon_{true}}} \tag{2.162}$$

(3) The FAL is based on the J-integral to calculate the $K_r$ which was originally introduced by Bloom (1983) and Shih et al. (1983).

$$K_r = \sqrt{\frac{J_e}{J_{Ic}}} \tag{2.163}$$

The J-integral was calculated based on the explicit formulation given by the EPRI estimation scheme, Kumar, German and Shih (1981) in which J is decomposed into elastic and plastic components as equation (2.125). The elastic component of J, $J_e$ is proportional to $(P/P_o)^2$, while the plastic component of J, $J_p$ is proportional to $(P/P_o)^{n+1}$. The total value of J can thus be expressed as a function of $L_r$. Failure at a critical value of J can then be represented by a FAL for a specific hardening rate. To ensure calculations are not invalidated by necking, the $L_r$ is truncated at $L_r^{\max}$:

$$L_r^{max} = \frac{\sigma_o + \sigma_{UTS}}{2\sigma_o} \tag{2.164}$$

### 2.11.3 Constraint Modified Failure Assessment Diagrams

Constraint based fracture mechanics has been used to modify failure assessment diagrams (FADs) to take advantage of enhanced levels of toughness associated with constraint loss in unconstrained flow field (MacLennan and Hancock (1995) and Ainsworth and O'Dowd (1995)). MacLennan and Hancock (1995) adopted an approach based on T. The effect of constraint on toughness was described by a relation of the form:

$$\begin{aligned} \frac{J_c(T)}{J_c(T=0)} &= \left(\frac{1}{\exp(T/\sigma_o)}\right)^m & \frac{T}{\sigma_o} &< 0 \\ \frac{J_c(T)}{J_c(T=0)} &= 1 & \frac{T}{\sigma_o} &\geq 0 \end{aligned} \tag{2.165}$$

where *m* defines the constraint sensitivity of fracture. Constraint insensitive materials are identified by m = 0 such that the toughness is both T and Q insensitive and non-zero values of m correspond to increasing constraint sensitivity for negative value of T. Constraint sensitive toughnesses are denoted $J_{(T)c}$ to indicate that the critical value of J at failure initiation is a function of T (T < 0). The fully constrained field is identified with T = 0 field and denoted as $J_{(T=0)c}$. Failure initiation is taken to occur at the intersection of a (J-T) loading history with the failure locus. Figure 2.45 illustrates the effect of constraint for a hardening exponent n = 6 and SENB a/W < 0.3 which indicate that enhanced toughness in constraint sensitive material to increase safety margins. Although the FAL in Figure 2.45 are weakly sensitive to geometry but strongly dependent on constraint sensitivity of the material. MacLennan and Hancock (1995) proposed a modified FAD where $K_r$ is modified and redefined as the square root of the elastic component of J to the constraint matched toughness $J_c$ (T):

$$K_r^{modified} = \sqrt{\frac{J_e}{J_{c(Q/T)}}} \tag{2.166}$$

Figure 2.46 show the modified FAD proposed by MacLennan and Hancock (1995) which measures the toughness of shallow and deeply cracked bend bars as a function of T or Q and the FAD is constructed using the constraint matched toughness as given in equation (2.166).

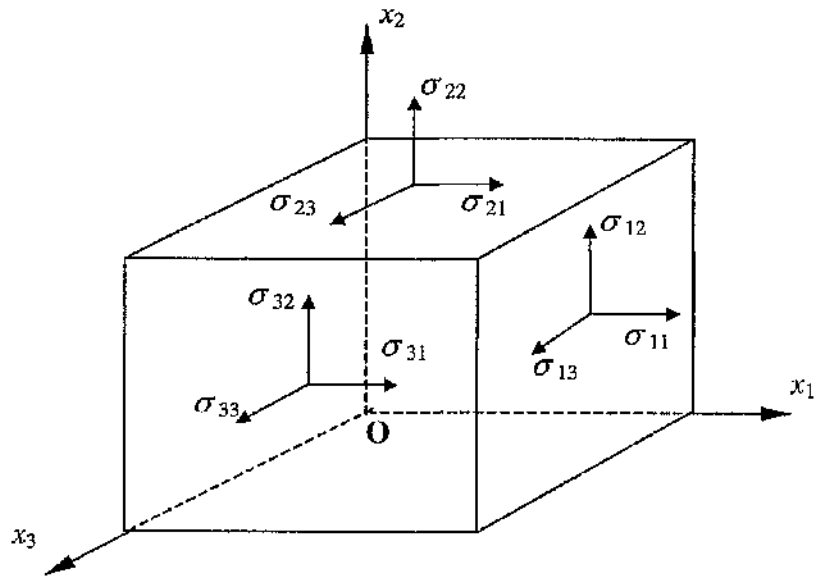


(a)

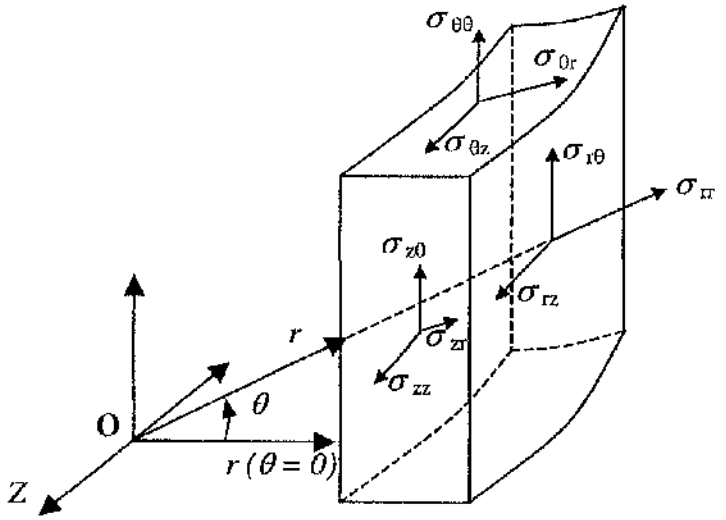


(b)

Figure 2.1: A three-dimensional body showing the stresses in (a) Cartesian and (b) cylindrical co-ordinate systems.

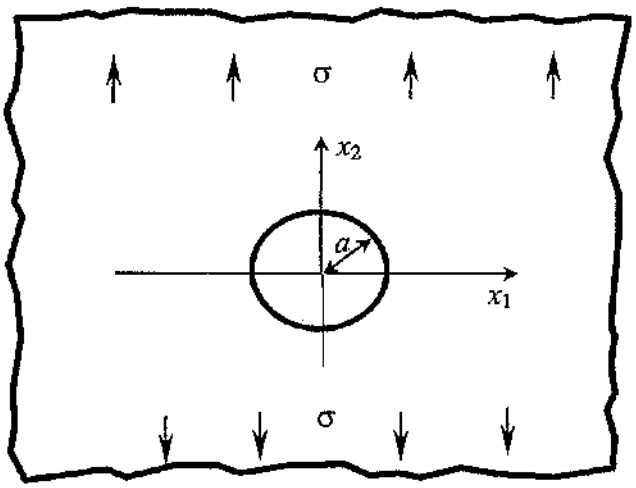


Figure 2.2: Stress concentration due to a circular hole in an infinite plate.

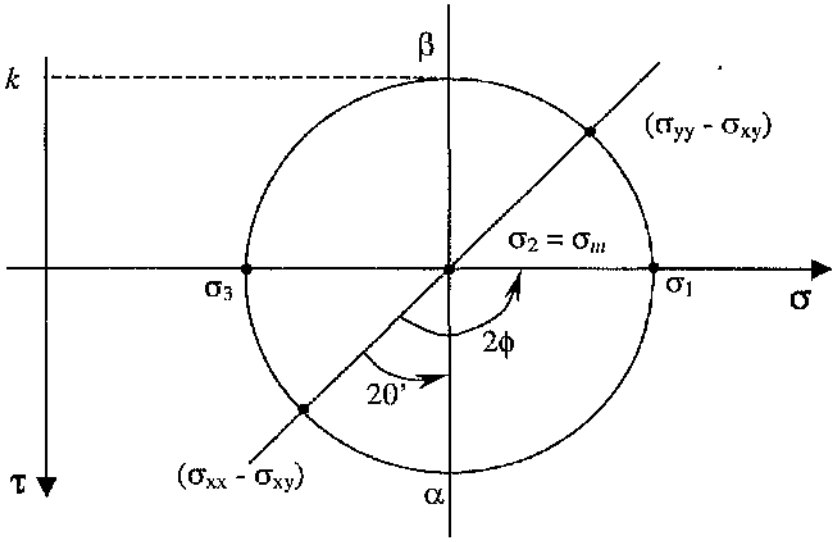


Figure 2.3: Mises yield criterion expressed using Mohr's circle.

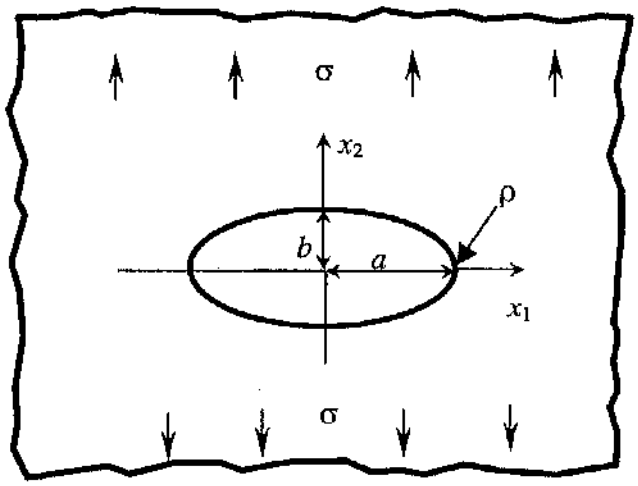


Figure 2.4: Elliptical hole in an infinite plate.

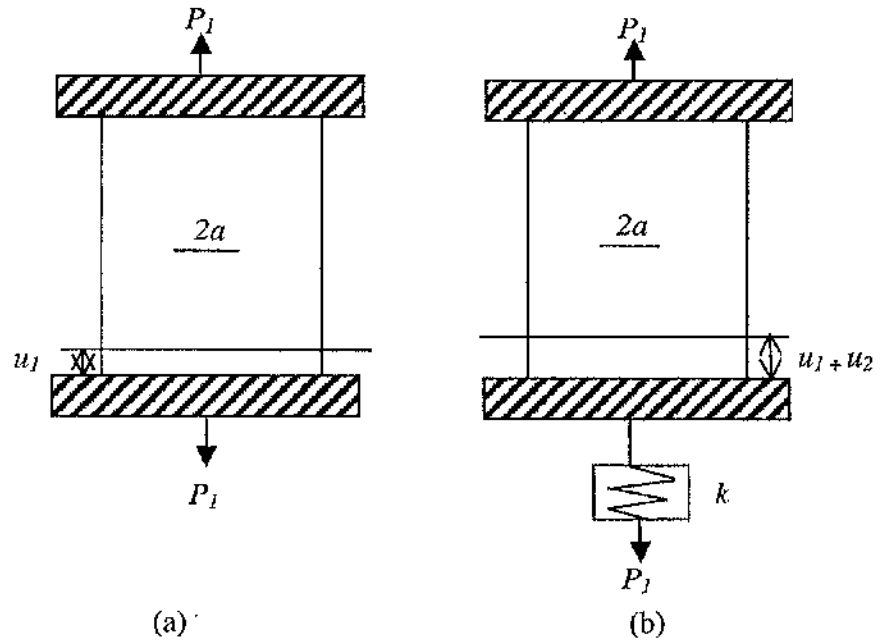


Figure 2.5: Cracked bodies in (a) Fixed displacement conditions and (b) fixed load conditions.

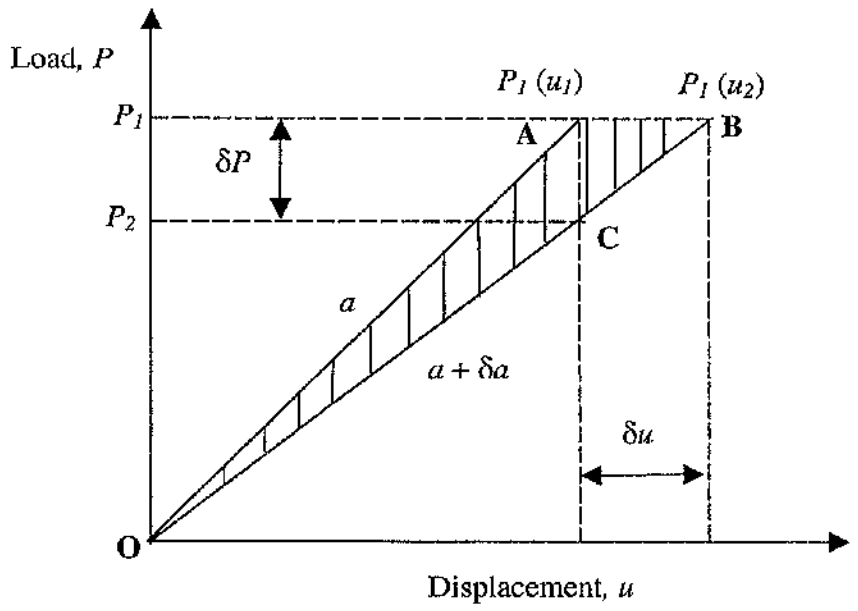


Figure 2.6: Elastic Load-Displacement curves under fixed displacement conditions (OACO) and fixed load conditions (OABO).

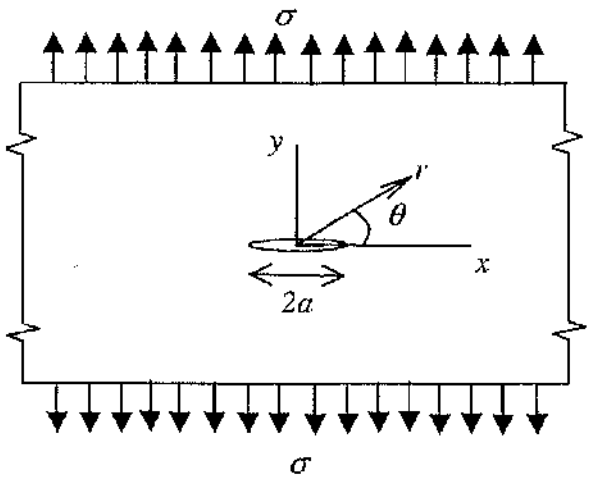


Figure 2.7: Co-ordinates used in Westergaard's asymptotic solution.

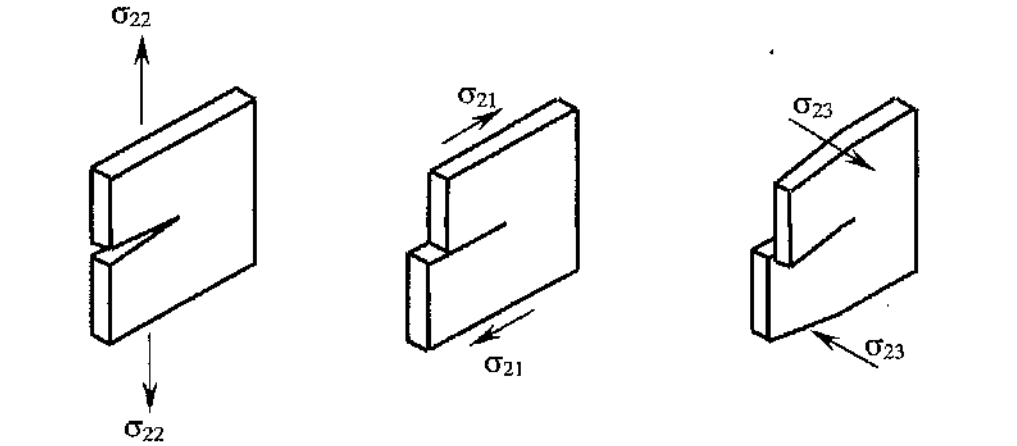


Mode I - Opening

Mode II – In-plane Shear

Mode III – Out-of-Plane Shear

Figure 2.8: Modes of Deformation.

| a/W | f (a/W) |
|---|---|
| 0.0 | 1.0000 |
| 0.1 | 1.0060 |
| 0.2 | 1.0246 |
| 0.3 | 1.0577 |
| 0.4 | 1.1094 |
| 0.5 | 1.1867 |
| 0.6 | 1.3033 |
| 0.7 | 1.4882 |
| 0.8 | 1.8160 |
| 0.9 | 2.5776 |

Table 2.1: Numerical values of $f$(a/W) for centre crack panels after Tada et al. (1973).

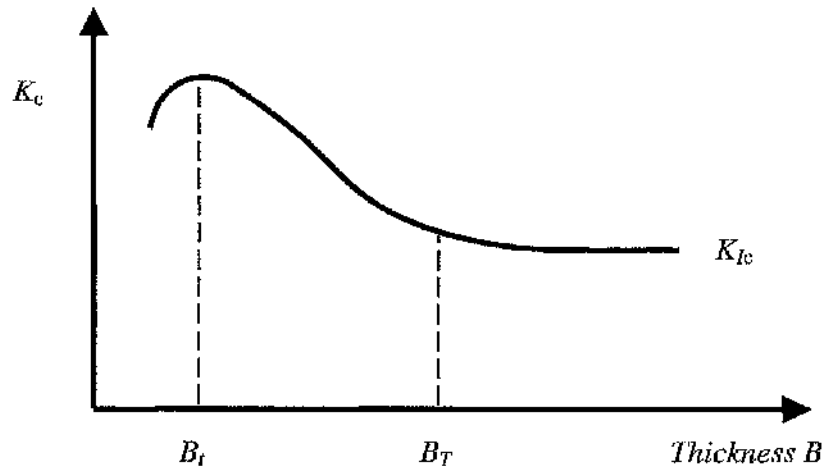


Figure 2.9: Toughness as a function of thickness, $B_t$ = thin specimen, $B_T$ = Thick specimen after Broek (1974).

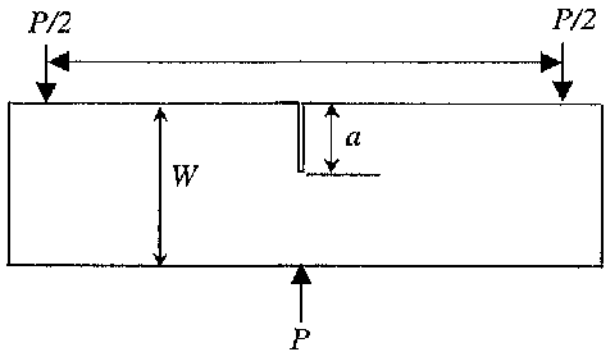


Figure 2.10: Single edge notch in bending (SENB).

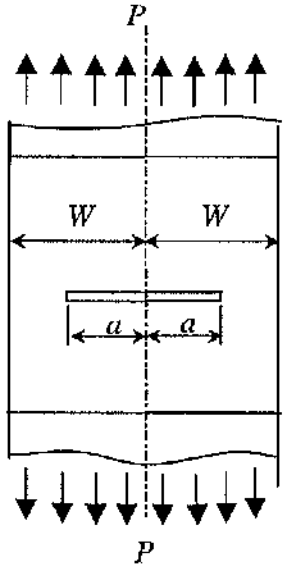


Figure 2.11: Centre cracked tension panel (CCP).

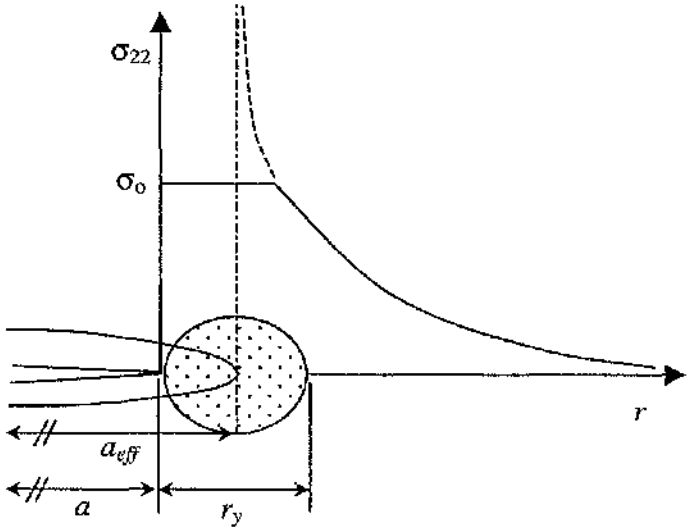


Figure 2.12: Plastic zone correction after Irwin (1961).

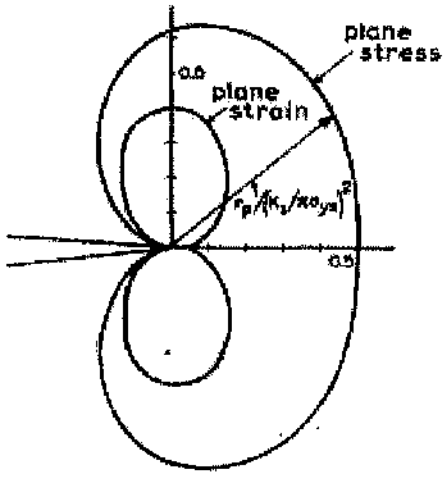


Figure 2.13: Approximate plastic zone shapes using Mises criterion for $\nu = 0.3$ after Kanninen and Popelar (1985).

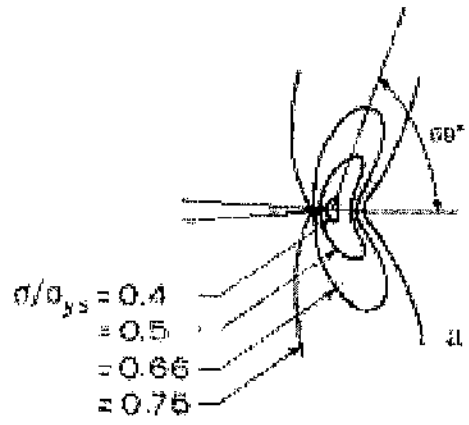


Figure 2.14: More accurate numerical calculations of the plastic zone shape in mode I deformation after Tuba (1976).

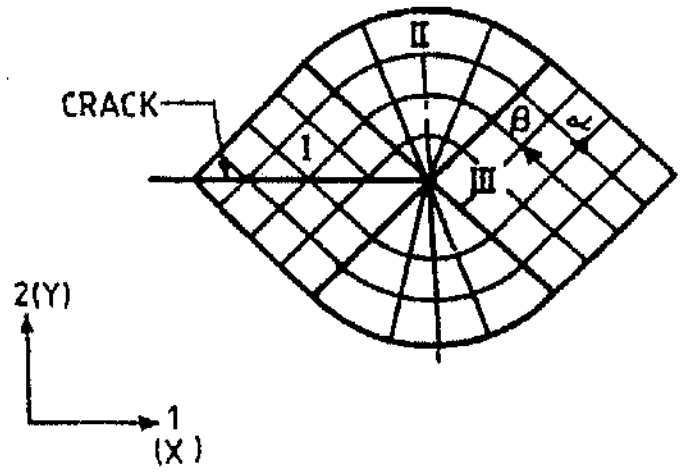


Figure 2.15: Prandtl field.

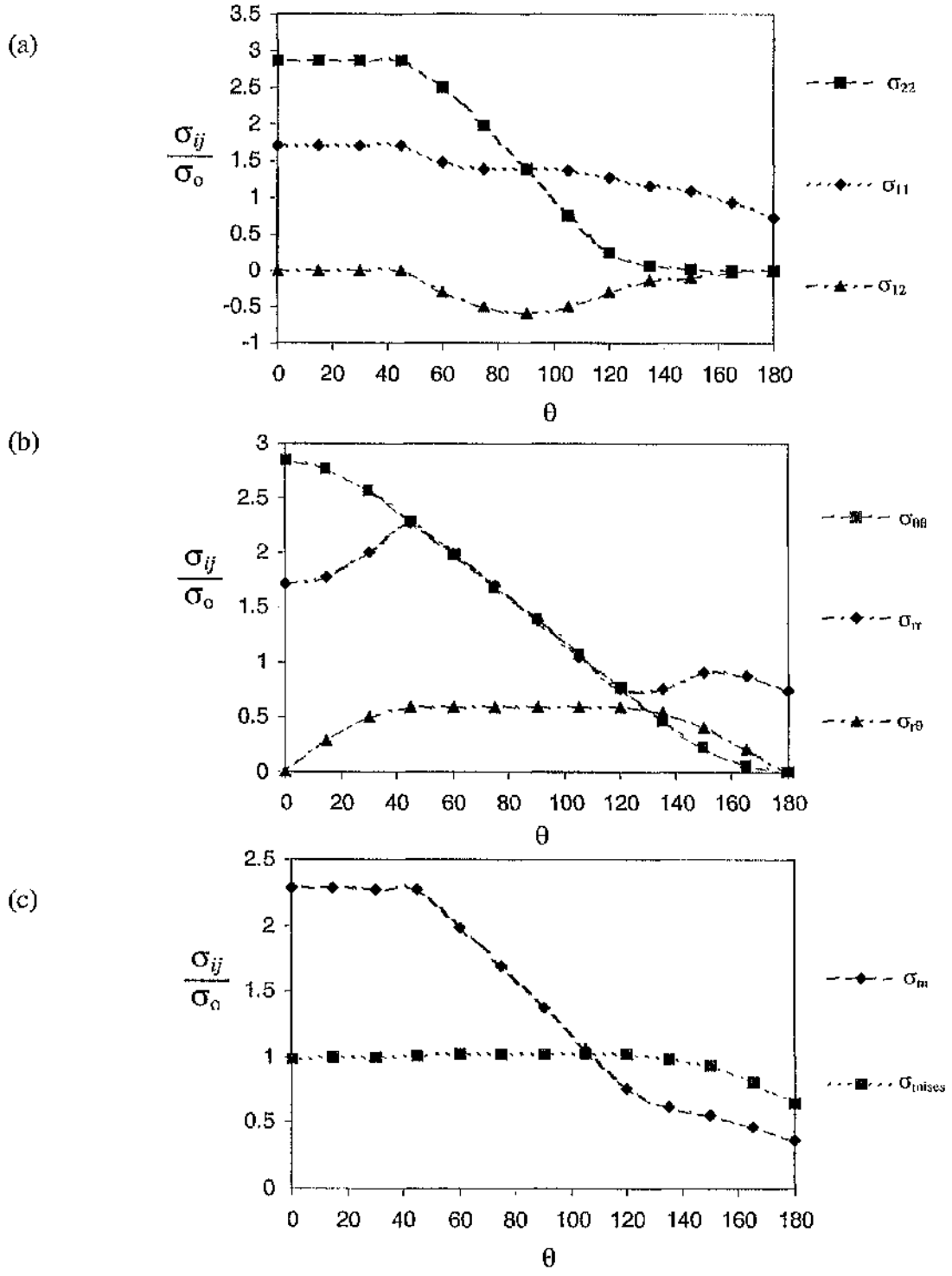


Figure 2.16: The small scale yielding asymptotic crack tip stresses for plane strain perfect plasticity determined from two-dimensional boundary layer formulations.

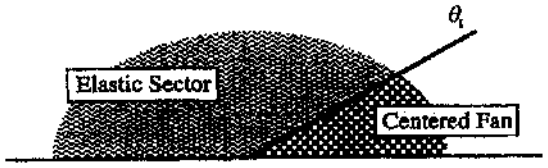


Figure 2.17: Plane stress mode-I asymptotic field configuration after Sham and Hancock (1999).

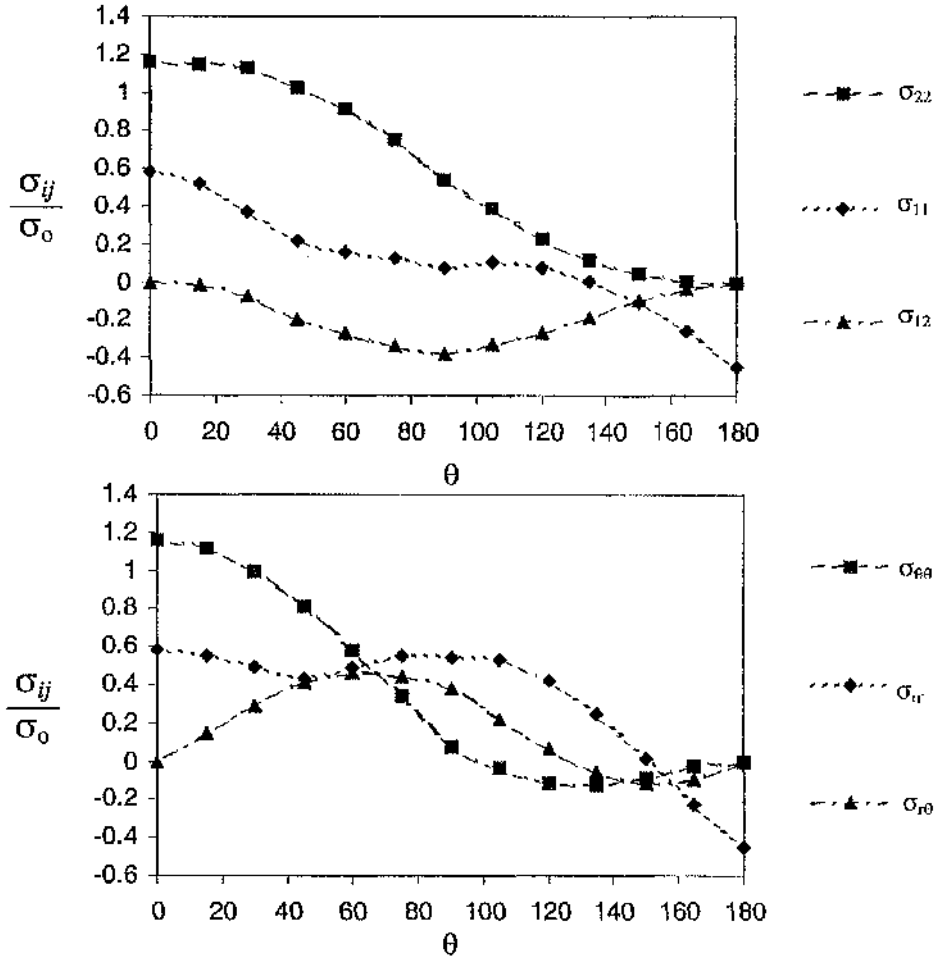


Figure 2.18: The small scale yielding asymptotic crack tip stresses for plane stress perfect plasticity determined from a two-dimensional boundary layer formulation.

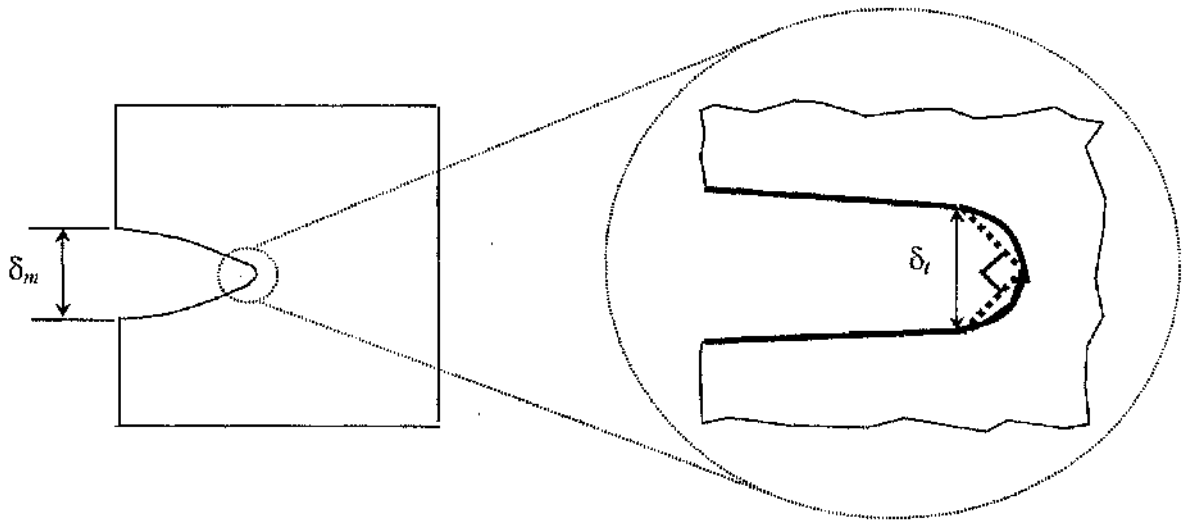


Figure 2.19: The crack tip opening displacement $\delta_t$ measured from (a) crack mouth opening displacement (CMOD) (b) The 90° intercept construction method.

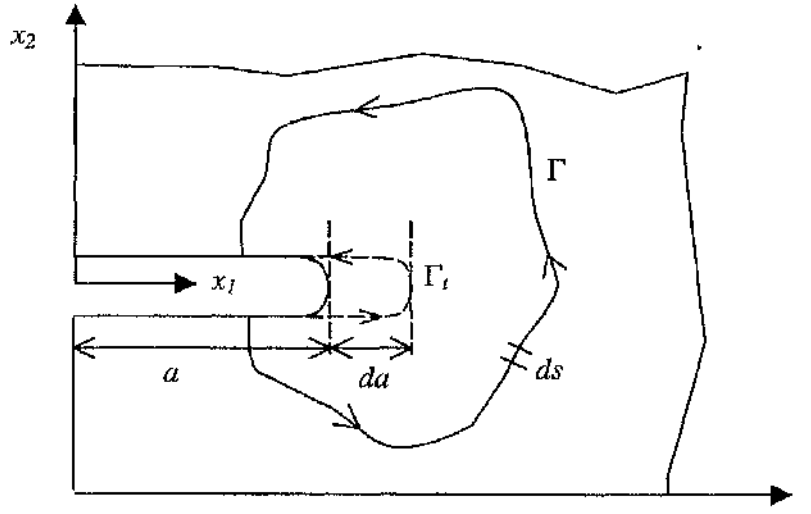


Figure 2.20: $J$ – Contour Integral for a flat surfaced notch in a 2-D deformation field. $\Gamma$ is an arbitrary contour surrounding the notch tip; $\Gamma_t$ denotes the curved notch tip.

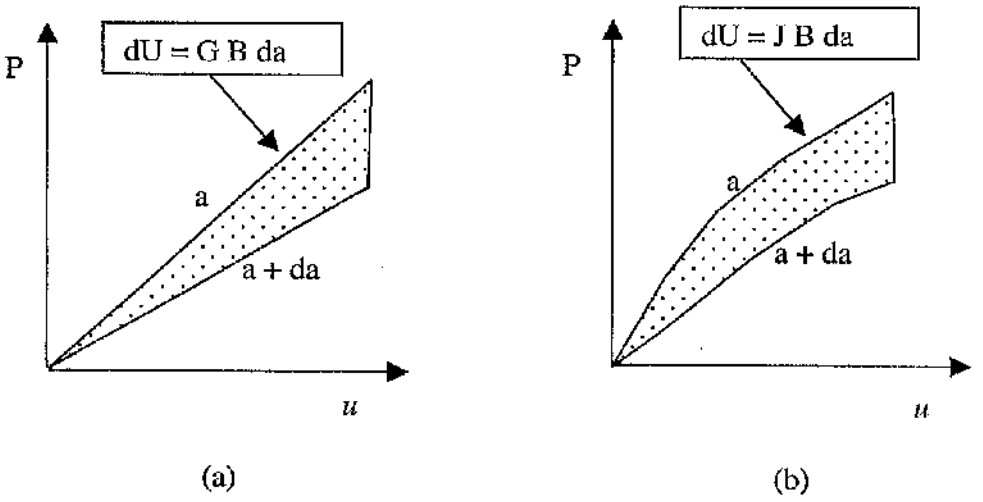


Figure 2.21: The load-displacement relations for crack advance $\delta a$ under fixed displacement condition for (a) linear elastic material (b) non-linear elastic material. The shaded area indicates the loss in potential energy.

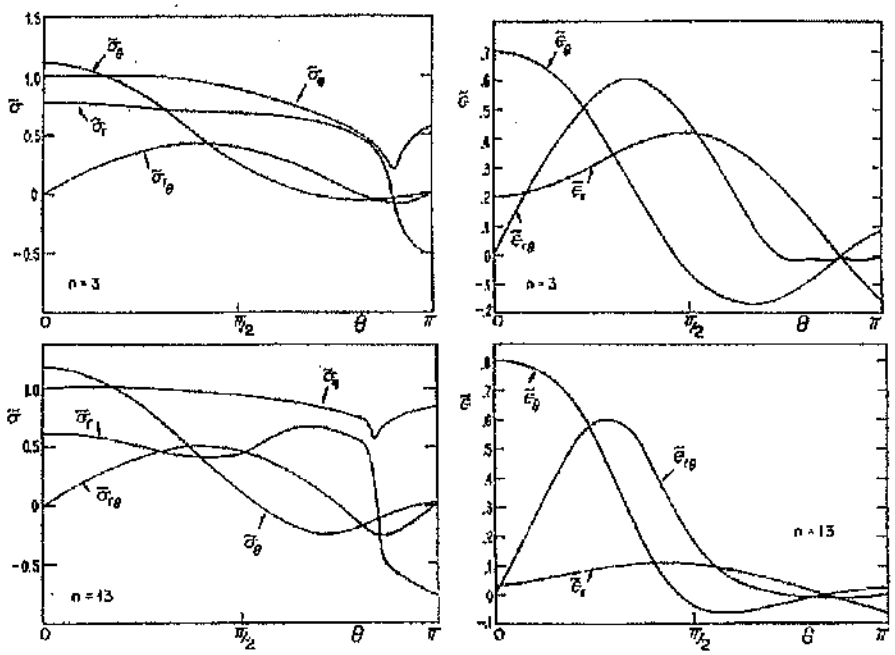


(a)

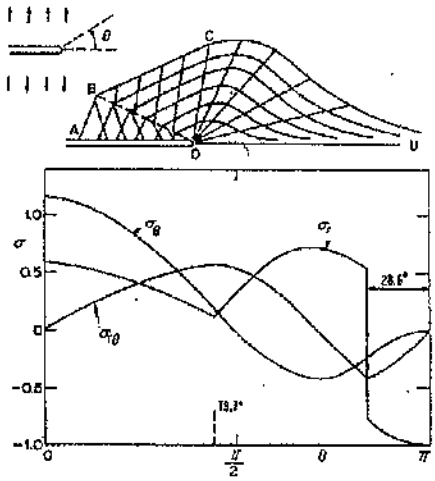


(b)

Figure 2.22: Plane stress asymptotic stresses after Hutchinson (1968b) (a) Strain Hardening field, (b) Elastic Perfectly-Plastic field.

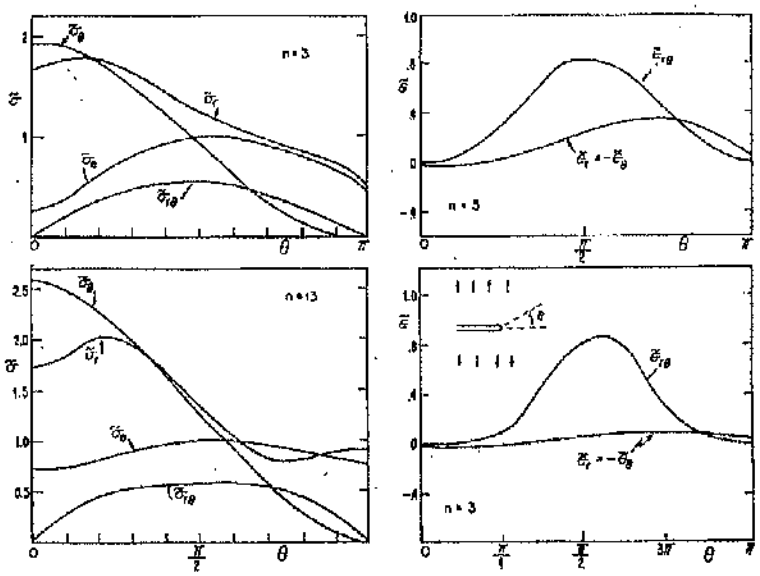

(a)

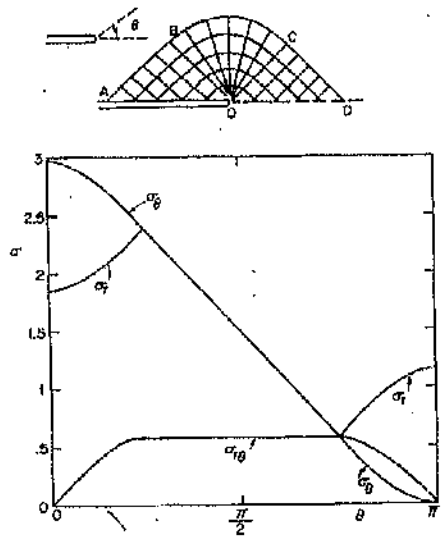

(b)

Figure 2.23: Plane strain asymptotic stresses after Hutchinson (1968b) (a) Strain Hardening field, (b) Elastic Perfectly-Plastic field.

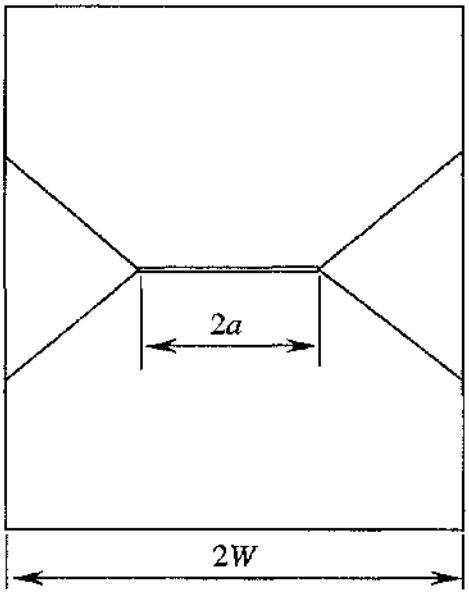


Figure 2.24: Slip line field for a centre crack panel (CCP) in tension.

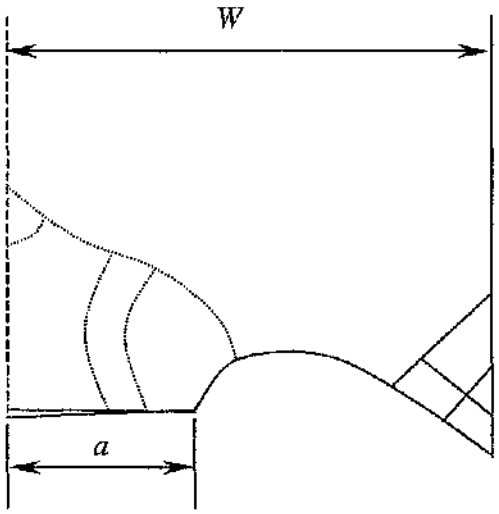


Figure 2.25: Slip line fields for deep and shallow-cracked bars in bending after Ewing (1968) and Green (1953). The solid and dotted lines represent the deep and shallow-cracked bars slip line fields.

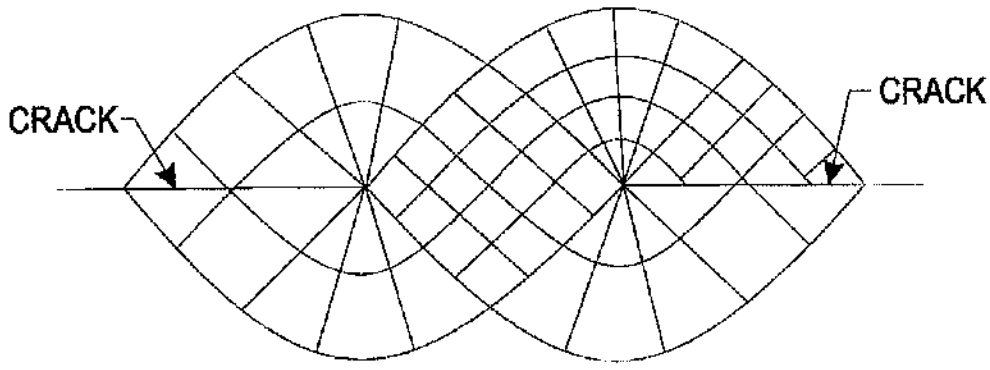


Figure 2.26: Prandtl slip line field for a deeply double edge cracked bar.

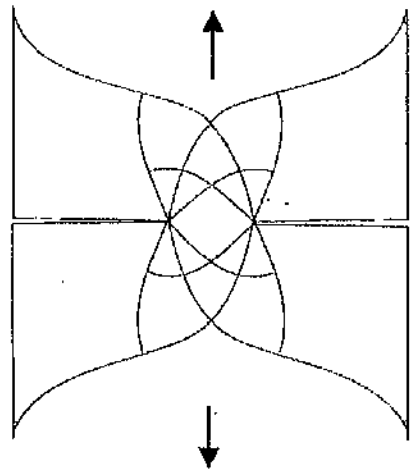

Figure 2.27: Slip line field for a shallow double edge cracked bar after Ewing and Hill (1967).

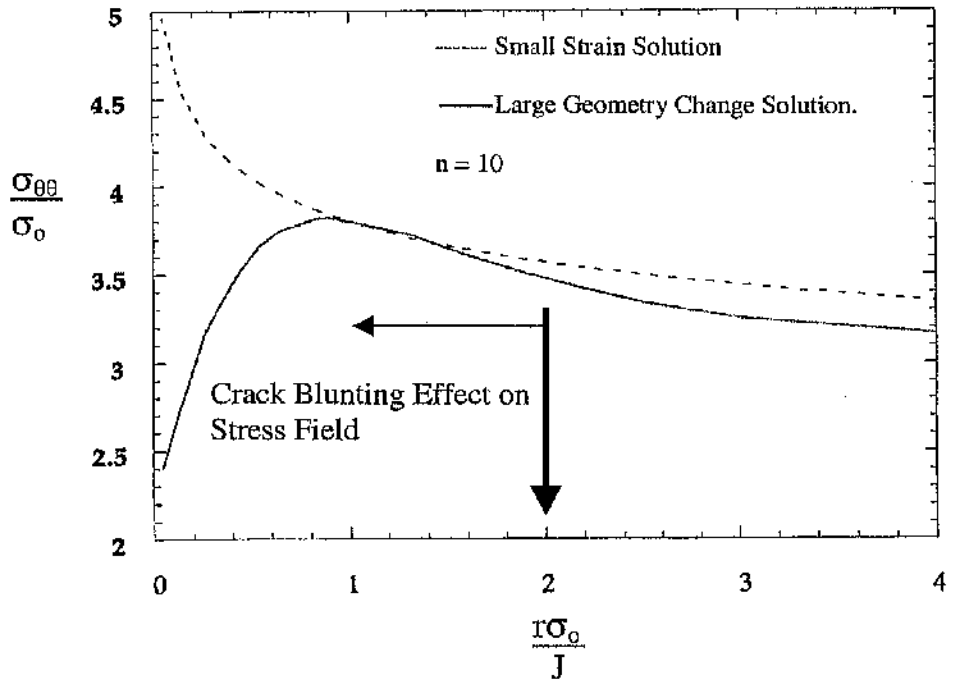


Figure 2.28: The difference between large geometry change and small geometry change solution at distance within $0 < r < 2J/\sigma_o$.

| a/W | $\frac{K}{\sigma\sqrt{\pi a}}$ | $\beta = \frac{T\sqrt{\pi a}}{K}$ |
|---|---|---|
| 0.1 | 0.11877E1 | -0.46436E0 |
| 0.2 | 0.13650E1 | -0.43362E0 |
| 0.3 | 0.16570E1 | -0.37070E0 |
| 0.4 | 0.21083E1 | -0.27762E0 |
| 0.5 | 0.28210E1 | -0.15293E0 |
| 0.6 | 0.40254E1 | 0.69027E-2 |
| 0.7 | 0.63457E1 | 0.21010E0 |
| 0.8 | 0.11926E2 | 0.50105E0 |
| 0.9 | 0.34485E2 | 0.10306E1 |

(a)

| a/W | $\frac{K}{\sigma\sqrt{\pi a}}$ | $\beta = \frac{T\sqrt{\pi a}}{K}$ |
|---|---|---|
| 0.1 | 0.10458E1 | -0.36263E0 |
| 0.2 | 0.10534E1 | -0.22852E0 |
| 0.3 | 0.11220E1 | -0.73444E-1 |
| 0.4 | 0.12586E1 | 0.92115E0 |
| 0.5 | 0.14951E1 | 0.26160E0 |
| 0.6 | 0.19100E1 | 0.43325E0 |
| 0.7 | 0.27210E1 | 0.61041E0 |
| 0.8 | 0.46642E1 | 0.83862E0 |
| 0.9 | 0.12406E2 | 0.12675E1 |

(b)

| a/W | $\frac{K}{\sigma\sqrt{\pi a}}$ | $\beta = \frac{T\sqrt{\pi a}}{K}$ |
|---|---|---|
| 0.1 | 0.10234E1 | -0.36062E0 |
| 0.2 | 0.10272E1 | -0.23295E0 |
| 0.3 | 0.10937E1 | -0.90071E-1 |
| 0.4 | 0.12290E1 | 0.60928E01 |
| 0.5 | 0.14647E1 | 0.21685E0 |
| 0.6 | 0.18787E1 | 0.37921E0 |
| 0.7 | 0.26880E1 | 0.55311E0 |
| 0.8 | 0.46270E1 | 0.78585E0 |
| 0.9 | 0.12358E2 | 0.12273E1 |

(c)

Table 2.2: (a) Values of $K_I$ and $\beta$ for single edge notched bars in tension, (b) Values of $K_I$ and $\beta$ for single edge notched bars in pure bending, (c) $K_I$ and $\beta$ for single edge notched bars in three-point bending after Sham (1991).

| a/W | $\frac{K}{\sigma\sqrt{\pi a}}$ | $\beta = \frac{T\sqrt{\pi a}}{K}$ |
|---|---|---|
| 0.1 | 0.1006E1 | -0.1017E1 |
| 0.2 | 0.1025E1 | -0.1034E1 |
| 0.3 | 0.1058E1 | -0.1051E1 |
| 0.4 | 0.1109E1 | -0.1068E01 |
| 0.5 | 0.1187E1 | -0.1085E1 |
| 0.6 | 0.1303E1 | -0.1102E1 |
| 0.7 | 0.1488E1 | -0.1261E1 |
| 0.8 | 0.1816E1 | -0.1460E1 |
| 0.9 | 0.2312E1 | -0.1930E1 |

Table 2.3: Values of $K_I$ and $\beta$ for centre cracked panels after Levers and Radon (1983).

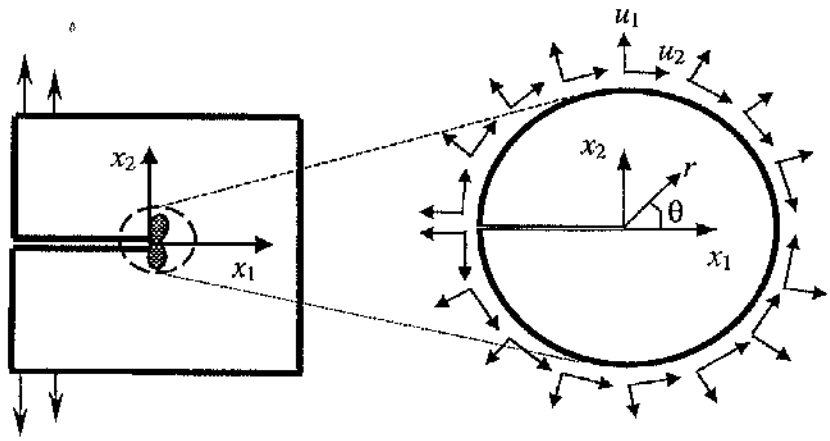


Figure 2.29 (a), (b) : Boundary layer formulation Rice (1968a)

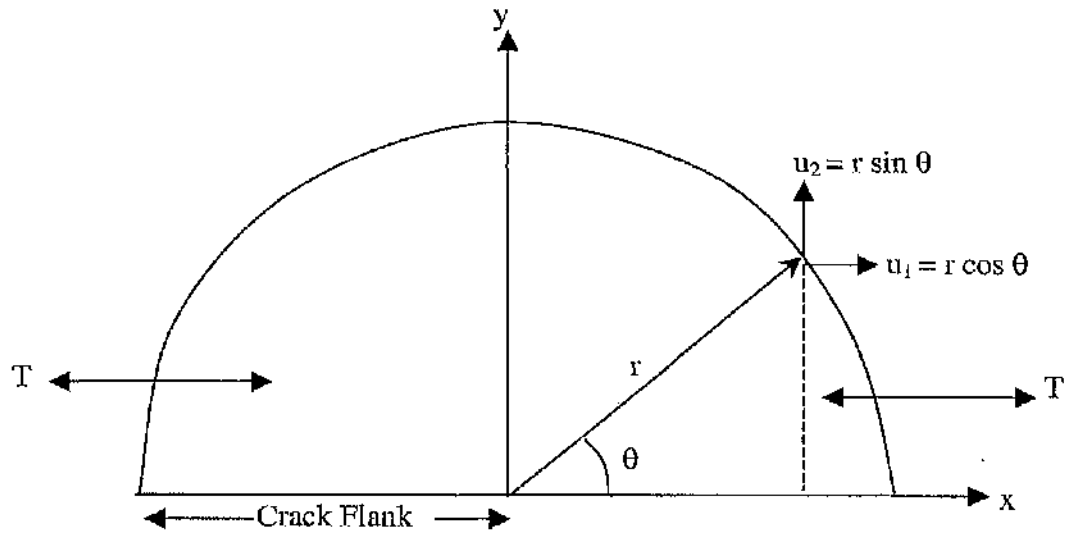


Figure 2.30: Components of distance around a circular boundary layer formulation mesh in terms of cylindrical axes.

| $n$ | $A_n$ | $B_n$ |
|---|---|---|
| 13 | 0.64 | -0.4 |
| ∞ | 0.6 | -0.75 |

Table 2.4: Curve fitting constants after Betegón and Hancock (1991).

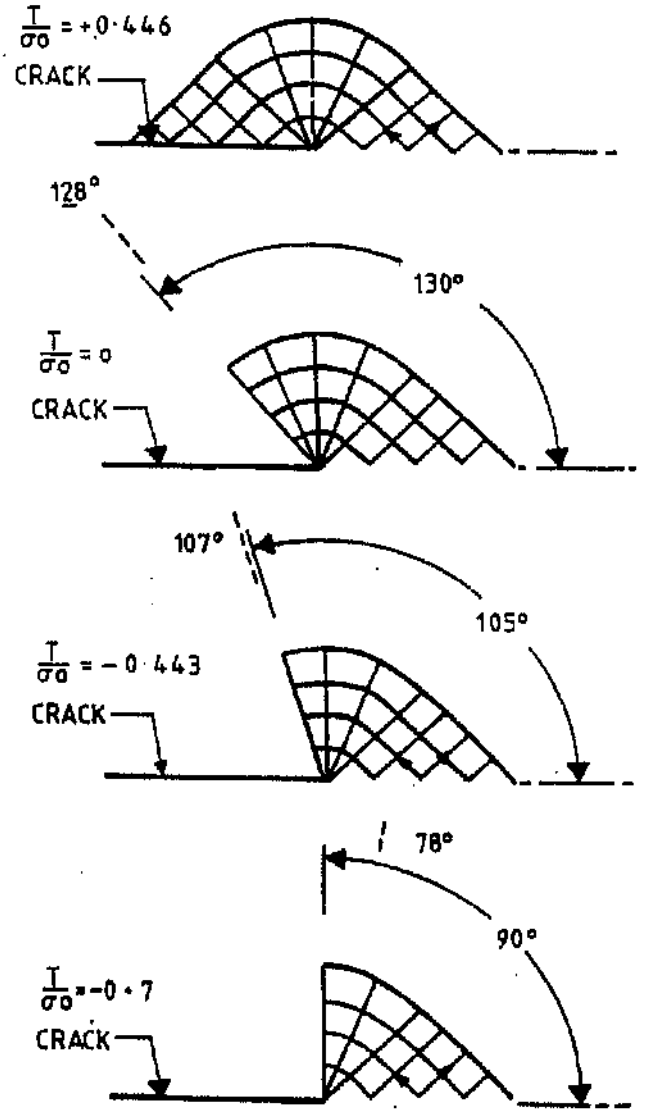


Figure 2.31: Slip line field after Du and Hancock (1991).

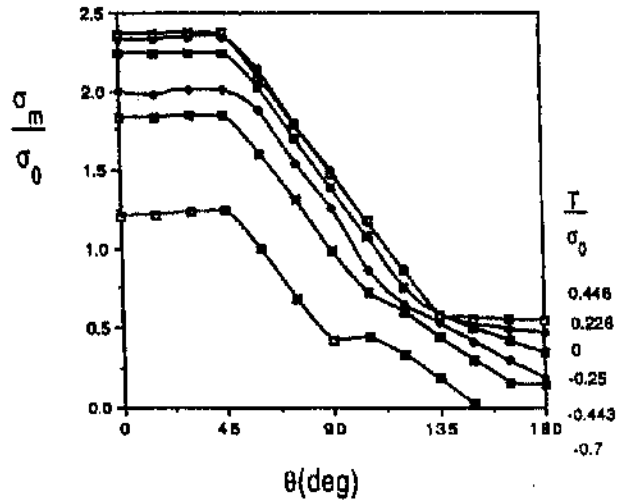


Figure 2.32: Angular variation of the mean stress around a crack tip as a function of $T/\sigma_o$ after Du and Hancock (1991).

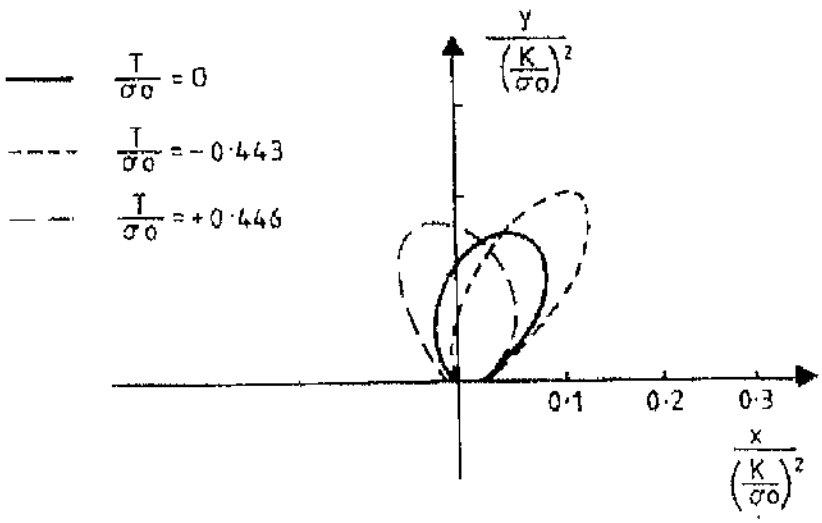


Figure 2.33: Plastic zone shape after Du and Hancock (1991).

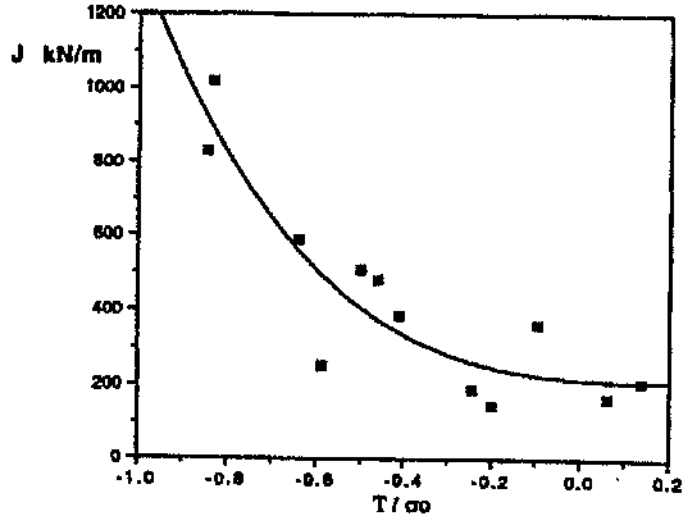


Figure 2.34: Toughness of edge cracked bend bar as a function of $T/\sigma_o$ after Betegón (1990) and Betegón and Hancock (1990).

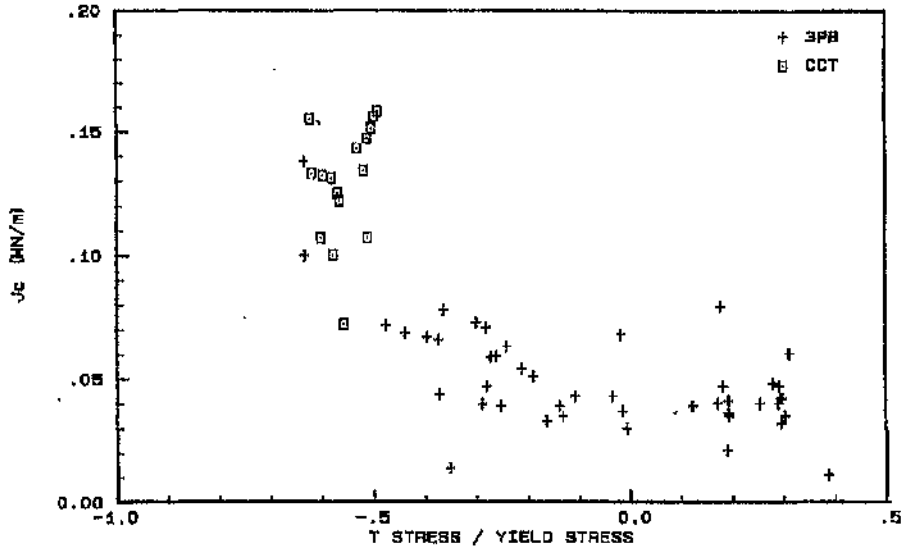


Figure 2.35: $J_c$ as a function of non-dimensionalised T-stress for three-point-bend and centre crack tension specimens of at –30°C after Sumpter (1993).

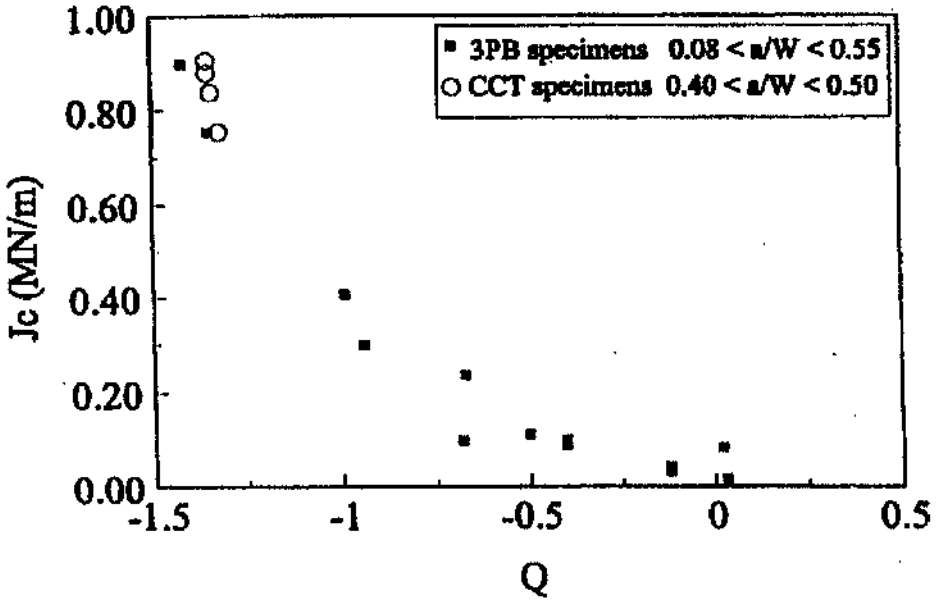


Figure 2.36 : Critical value of J as a function of Q for 3PB and CCT specimens of high strength weld metal at –30°C after Sumpter and Hancock (1994).

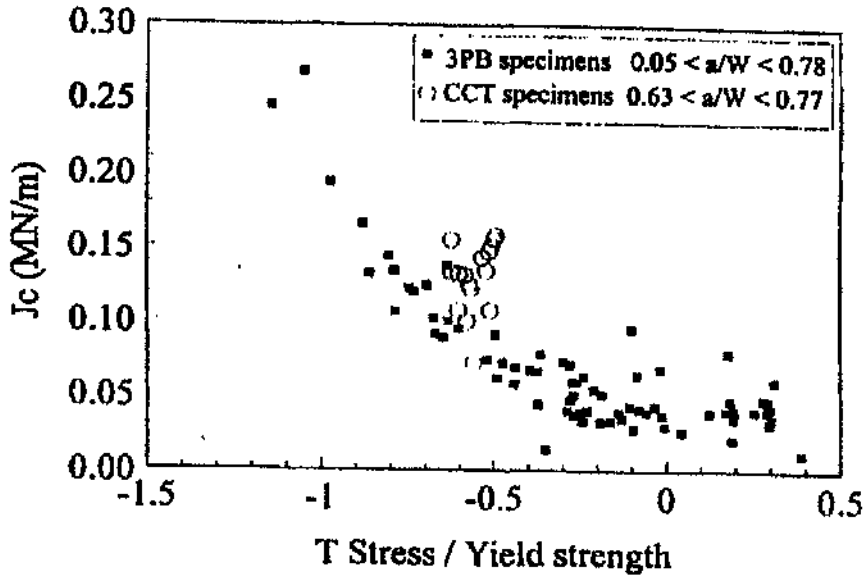


Figure 2.37: Critical value of J as a function of $T/\sigma_o$ for 3PB and CCT specimens, low-grade mild steel at –50°C after Sumpter (1993).

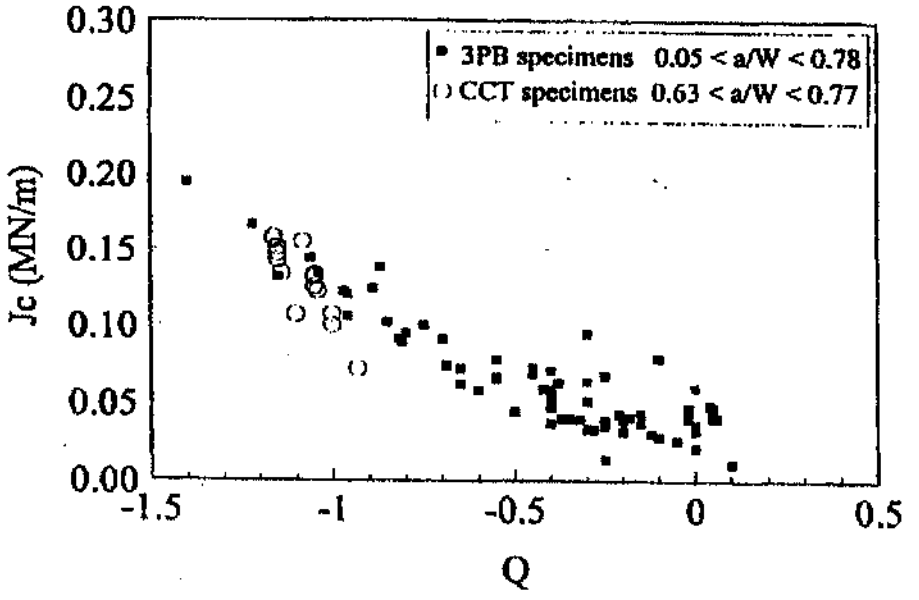


Figure 2.38: Critical value of J as a function of Q for 3PB and CCT specimens, low-grade mild steel at –50°C after Sumpter (1993).

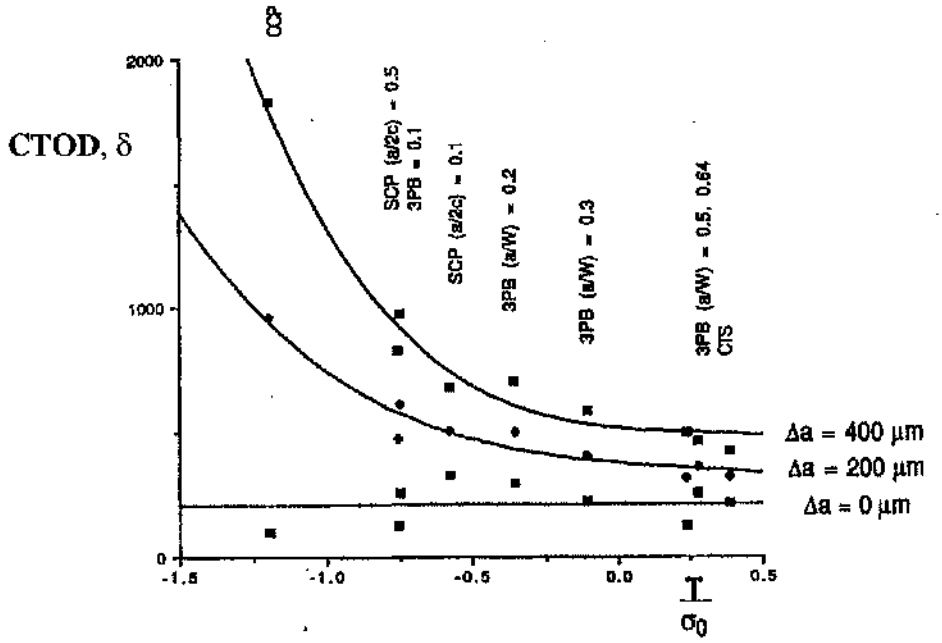


Figure 2.39: CTOD as a function of the T-stress at crack extension of 0, 200 and 400 μm after Hancock, Reuter and Parks (1993).

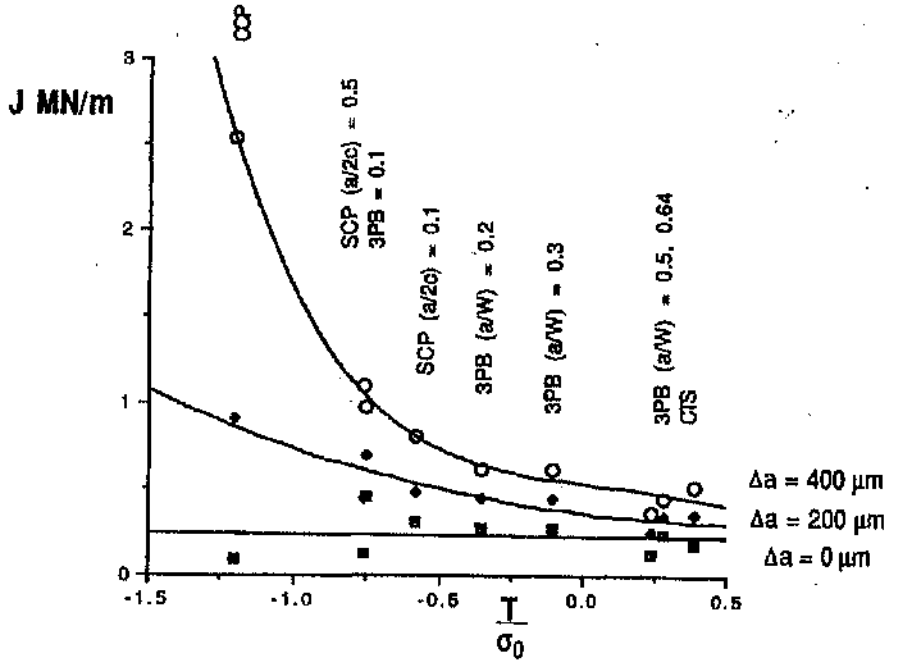


Figure 2.40: J as a function of the T-stress at crack extensions of 0, 200 and 400μm after Hancock, Reuter and Parks (1993).

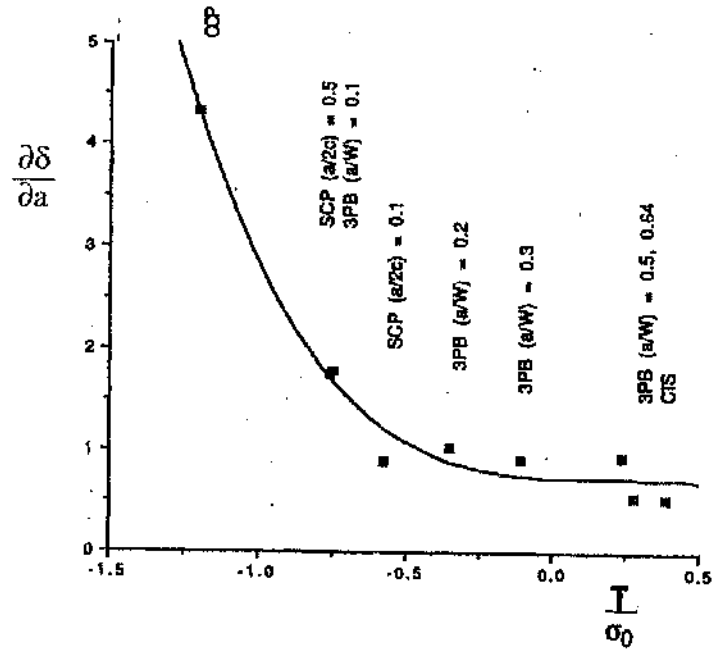


Figure 2.41: The initial slope of the CTOD-Δa resistance curve as a function of T after Hancock, Reuter and Parks (1993).

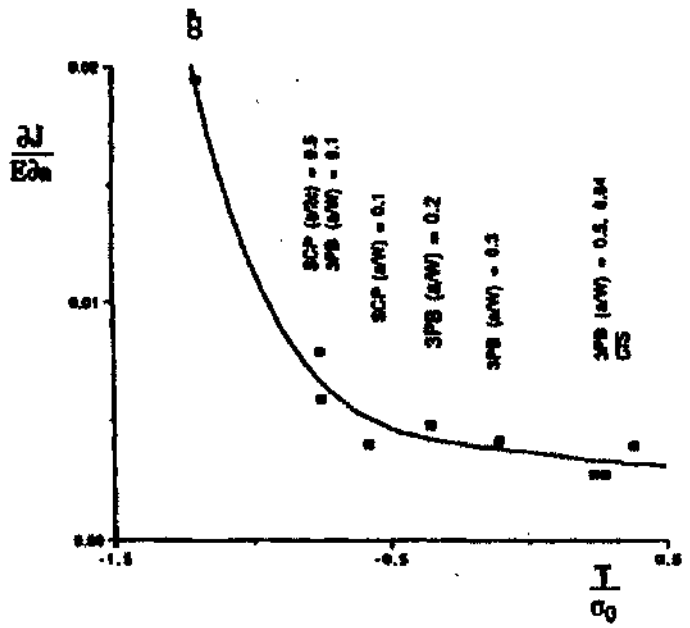


Figure 2.42 : The initial slope of the J-Δa resistance curve as a function of T after Hancock, Reuter and Parks (1993).

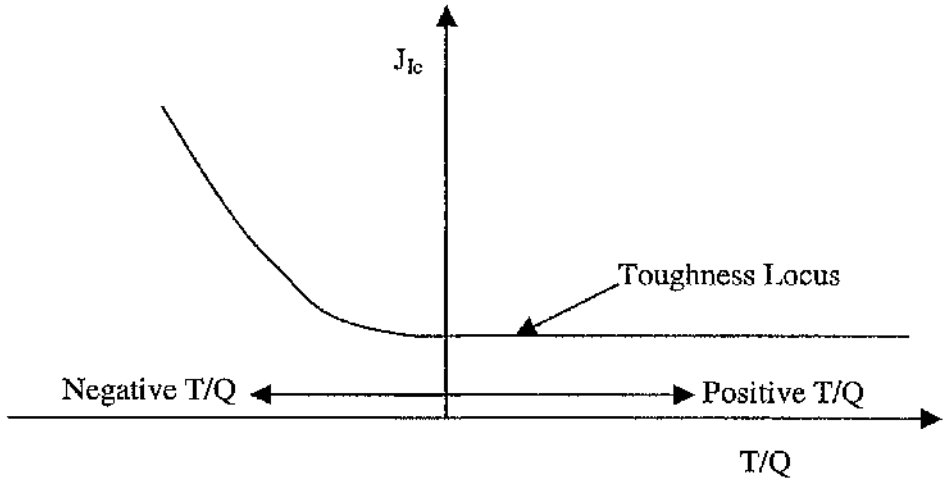


Figure 2.43: General representation of the effect of constraint on the cleavage fracture toughness.

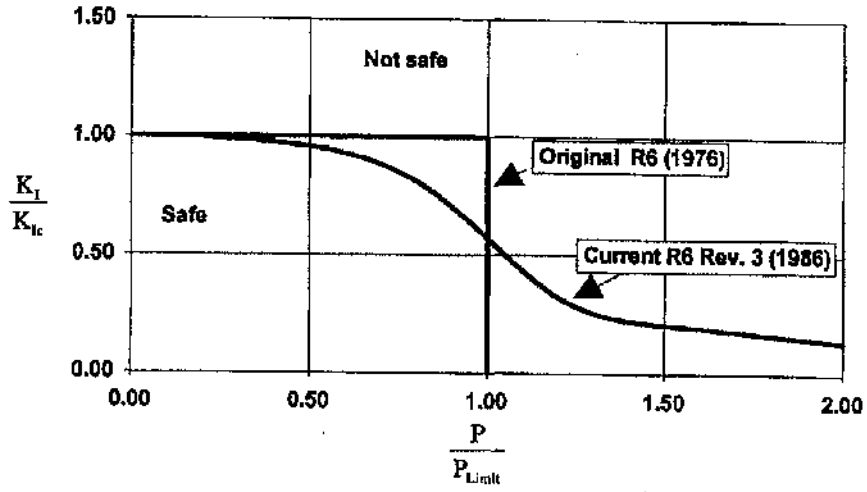


Figure 2.44: Failure assessment lines as given by R6 Rev3 (1986) and the original (1976) form.

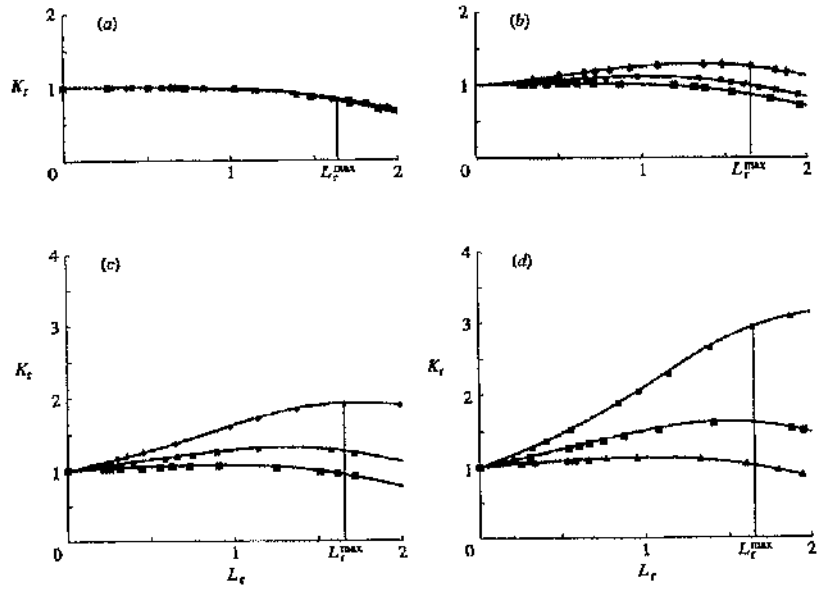


Figure 2.45 : FADS for a SENB with (a) constraint insensitive material, m= 0, n = 6, (b) slightly constraint sensitive material m = 1, n = 6, (c) constraint sensitive material, m = 2, n = 6, (d) highly constraint sensitive material, m = 3, n = 6 after MacLennan and Hancock (1995).

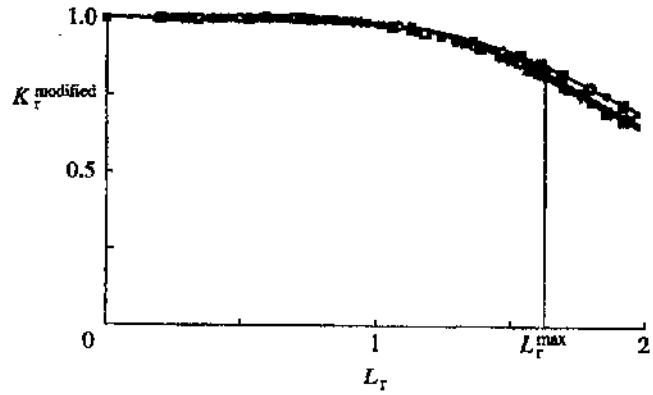


Figure 2.46: A modified FAD for a SENB with constraint sensitivity indices (m = 0, 1, 2, 3) and hardening exponent, n = 6 after MacLennan and Hancock (1995).

# Three-Dimensional Crack Tip Fields

Although real structural integrity problems are fully three-dimensional, classically, fracture problems have been largely analysed using two-dimensional idealisations based on plane strain or plane stress. Initial studies of three-dimensional crack problems focused on the determination of the nature of stress and strain fields close to the crack tip. The review in this chapter emphasises on the development of the features of crack tip fields in three-dimensions and the effect of thickness on constraint and toughness. Finally, a review of thickness effect on toughness is given as a precursor to three-dimensional crack constraint failure assessment.

## 3.1 Three-Dimensional Elastic Analyses

### 3.1.1 Elastic Stress Solutions

Sih and Liebowitz (1968) discussed the mathematical theories of brittle fracture including the theory of elastic cracks in three-dimensions. Several approaches to the determination of the singular behaviour of crack tip in three-dimensional geometries were discussed. In an ensuing work, Hartranft and Sih (1970) suggested an approximate three-dimensional stress solution at the crack tip:

$$
\begin{aligned}
\sigma_x &= \frac{K_I}{\sqrt{2r}}\left(\cos\frac{\theta}{2}+\frac{1}{2}\sin\theta\sin\frac{3\theta}{2}\right)+0(r^0)\\
\sigma_y &= \frac{K_I}{\sqrt{2r}}\left(\cos\frac{\theta}{2}-\frac{1}{2}\sin\theta\sin\frac{3\theta}{2}\right)+0(r^0)\\
\sigma_{xy} &= \frac{K_I}{\sqrt{2r}}\left(\frac{1}{2}\sin\theta\cos\frac{3\theta}{2}\right)+0(r^0)\\
\sigma_z &= \frac{K_I}{\sqrt{2r}}\left(\cos\frac{\theta}{2}\right)+0(r^0)\\
\sigma_{yz} &= \sigma_{zx} = 0(r^0), \qquad \text{as} \quad r\to 0
\end{aligned}
\tag{3.1}
$$

where $\sigma_x$, $\sigma_y$, $\sigma_{xy}$ and $\sigma_z$ become infinite along the crack edge when $r^{-0.5}$ while the transverse shear stress $\sigma_{yz}$ and $\sigma_{zx}$ remain finite at the crack tip through the thickness. The

angular variation of the in-plane stresses is identical to the two-dimensional asymptotic crack tip stress field equation (2.67). However, equation (3.1) may not be applicable to the singularity problem at the free surface field.

Paris and Sih (1965) reviewed early developments in the stress-intensity factor approach for three-dimensional elastic crack problems and provided some standard solutions for important configurations including ellipsoidal cracks in infinite bodies. This work initiated the collection of stress-intensity factors solution in compendia as exemplified by Sih (1973), Rooke and Cartwright (1976), Tada et al. (1985) and more recently by Murakami (1987). A collection of work carried out by Soviet scientists on three-dimensional linear elastic crack problems has been reviewed by Panasyuk et al. (1980, 1981).

The Sih and Liebowitz (1968) and Rice (1968a) reviews highlighted the importance of clarifying the three-dimensional features of crack tip deformation, and specifically understanding the effect of finite thicknesses and the accompanying plane strain to plane stress transition.

Cruse and Vanburen (1971) provided an early discussion of three-dimensional elastic stress analysis of a finite thickness compact tension fracture specimen using direct potential methods. The nature of the three-dimensional state of stress as the crack tip was discussed and argued that the out-of-plane stress, $\sigma_z$ is a function of the thickness co-ordinate, $x_3$. In a subsequent paper, Cruse (1970) drew out the importance of out-of-plane constraint effects and presented some numerical results on plasticity effects in small scale yielding. Out-of-plane constraint factor was quantified by a factor $\rho$ as given in equation (2.45) which measures the proximity to plane strain. The degree of plane strain as measured by equation (2.45) increases as crack front is approached. However the results only provided general trends and were not sufficiently accurate to quantify the magnitude of the stresses. Although accuracy of the solutions is debatable, Cruse (1971) showed that three-dimensional crack problems comprised of two types of singularity: the usual two-dimensional crack front stress singularity and a crack front-free surface intersection singularity.

Finite element techniques have proved to be a powerful tool with which to address the intractable nature of three-dimensional crack analysis. Levy, Marcal and Rice (1971) formulated an early elastic finite element approach to three-dimensional crack tip problems in which the near tip elements featured coincident but independent nodes. This allows the crack tip to exhibit the necessary $r^{-0.5}$ stress singularity. For a straight through thickness crack, the proximity to plane strain was measured by the plane strain parameter, ρ. At distances less than $0.5t$ from the crack front, ρ was close to 1 on the midplane, indicating that the elastic field in the three-dimensional problem is similar to the two-dimensional plane strain singularity.

### 3.1.2 Elastic Stress Field

Many analyses have been carried out to understand out-of-plane effects in finite thickness plate and to identify the size of the three-dimensional field in cracked plates.

Yang and Freund (1985) employed an approximate method based on a boundary layer approach for a crack in a thin plate to assess the effect of out-of-plane effects in thin elastic plates. The model assumed the three-dimensional crack front to be surrounded by a plane stress field controlled by a remote stress intensity factor. The out-of-plane displacements were taken to be identical to the corresponding plane stress solution at radial distances from the front greater than half to three quarters of the plate thickness.

The analytical approach of Yang and Freund (1985) can be compared to an experimental method developed by Rosakis and Ravi-chandar (1986). Rosakis and Ravi-chandar (1986) investigated the three-dimensional stress field at the vicinity of a through crack using transmitted and reflected caustics in Plexiglas specimens and in 4340 steel specimens. The nature of the stress field as the crack front was approached was analysed using shadow spot method. They proposed an analytical expression for the local stress intensity factor from the analysis of caustics as:

$$K^{EXP} = \frac{9.34E-2}{z_o\, ch} D^{5/2} \tag{3.2}$$

where $K^{EXP}$ is the stress intensity factor determined from caustics experiments, $z_o$ is a reference distance, $t$ is plate thickness, $D$ is the maximum transverse diameter of the caustic and $c$ is the appropriate optical constant dependent for plane stress or plane strain conditions. $K^{EXP}$ is non-dimensionalised by the plane stress stress-intensity factor $K_{2D}$ given by Tada et al. (1985).

At distances r/t > 0.5 both materials demonstrate $K^{EXP}/K_{2D}$ approaching 1 which indicates a plane stress field. At r/t < 0.5, $K^{EXP}/K_{2D}$ continued to decrease instead of reaching a constant value which demonstrated that the plane strain region is not clearly identified. Rosakis and Ravi-Chandar concluded that plane strain was only achieved at $r/t = 0$, and suggested that in the range $0 < r/t < 0.5$ the three-dimensional stress gradients were weaker than the corresponding two-dimensional gradients.

The most complete stress analysis of the out-of-plane effects in thin plate has been given by Nakamura and Parks (1988a). Nakamura and Parks (1988a) studied the stress field of a thin cracked plate under mode I loading using three-dimensional finite element boundary layer formulations. The problem was defined by applying displacements corresponding to the two-dimensional plane stress K field given by equation (2.73) to the perimeter of a thin domain surrounding the crack tip. The transition from a two-dimensional to a three-dimensional field occurred within an annulus r/t <1.5. At r/t > 1.5, the in-plane stresses started to merge with the dominant plane stress solution. The transition from two-dimensional to three-dimensional fields was independent of Poisson's ratio (ν) although, the amplitude of the opening stress was greatly affected by ν. In nearly incompressible solids, Poisson's ratio affected the variation of opening stress, $\sigma_{22}$, from the midplane ($x_3/t = 0$) to the free surface ($x_3/t = 0.5$)

Within the near tip field, Nakamura and Parks showed that the characterising parameter J varied along the crack front. As the midplane field approached plane strain conditions, Nakamura and Parks (1988a) determined local K values using the plane strain conversion:

$$K_{loc} = \sqrt{\frac{EJ_{loc}}{(1-\nu^2)}} \tag{3.3}$$

At the midplane ($x_3/t = 0$), the local values of K and J were amplified, while near the free surface the values were attenuated depending on the magnitude of ν. The normalised local J curves at different Poisson's ratio intersected at $x_3/t = 0.35$ where $J_{loc}/J_{far} = 1$. Similar behaviour was observed for the normalised local K with curves for different Poisson's ratios intersecting near $x_3/t = 0.47$ where $K_{loc}/K_{far} = 0.99$. Based on the linear elastic condition, K and J should be similar and the variation along the crack front should also be identical. However, the results showed that the local K and J values intersect at different positions. This could be due to the use of the local J values driven from an outer plane stress field to extract a local K values using the plane strain condition of equation (3.3).

Nakamura and Parks (1988a) used the plane strain parameter defined in equation (2.45), to characterise the three-dimensional nature of the stress field ahead of the crack front. The three-dimensional field was found to approach plane strain within distances of $r/t < 0.5$ with the highest tendency towards plane strain at the midplane ($x_3/t = 0$). At $r/t = 0.0015$, $\nu = 0.3$, and $x_3/t = 0$, the three-dimensional field exactly matched the angular distributions of stress in the asymptotic plane strain solution.

## 3.2 Fracture Characterising Parameters

### 3.2.1 J-Integral in Three-Dimensional Analyses

Levy, Marcal and Rice (1971) have discussed finite element methods to model three-dimensional elastic-plastic crack tip fields. While the development of the energy release rate to obtain J has been implemented in finite element approach using the virtual crack extension method, Hellen (1975) and Parks (1974, 1977).

In three-dimensional crack analyses, J can be extracted using virtual domain integral methods Shih et al. (1986) in which the line integral form of J given in equation (2.122) is expressed in terms of a volume/domain integral, $J_D$:

$$J_D = \int_A [\sigma_{ij} u_{j,1} - W \delta_{1i}] q_{1,i} \, dA \tag{3.4}$$

This is identical to the potential energy release rate given in Li et al. (1985) and Nakamura et al. (1986b) and is consistent with path-independent integral J of Rice (1968b). Equation (3.4) is domain independent when evaluated over an arbitrary annular area $A$, surrounding the crack tip.

In the limit, the three-dimensional crack analyses show that path-independent is not achieved (Nakamura and Parks (1988b, 1990) and Yusof and Hancock (2005)). For a given section ($x_3/t$) along the crack front of a boundary layer formulation, the J-integral value remains path-independent for a limited distance ahead of the crack front. At large distances from the crack front, the J-integral approaches the applied values which drive the displacement field. Therefore, the local J that varies along the crack front approaches the uniform applied stress intensity factor on the perimeter of the boundary layer formulation. Nevertheless, the local J can still be regarded as a parameter which characterises the near tip field.

### 3.2.2 T-stress in Three-Dimensional Analyses

Given the significance of the effect of the T-stress in two-dimensional crack tip analyses, Nakamura and Parks (1992) developed a method for extracting the T-stress along three-dimensional crack fronts from moderately detailed finite element solutions. The method is based on an interaction integral given by Kfouri (1986). Instead of a point load, a line load is introduced, and T is calculated from the difference in J, with and without the line load:

$$T(s)=\frac{E}{f\left(1-\nu^2\right)}\left[I(s)+\nu\varepsilon_{33}(s)\right] \tag{3.5}$$

Here $f$ is the line load in the $x_1$ direction, I(s) is the interaction integral. Nakamura and Parks (1992) used the interaction integral method to extract the T-stress in elastic three-dimensional specimens and showed that the T-stress was influenced by the plate thickness as well as ν. The thickness dependence of the T-stress distribution can be expressed as:

$$\frac{T(x_3/t,\nu)}{K_I(x_3/t,\nu)/\sqrt{\pi a}} \approx \sqrt{\frac{t}{a}}B^{2D}+B^{thin}(x_3/t,\nu) \tag{3.6}$$

where B is the biaxiality factor and the two-dimensional biaxiality parameter $B^{2D}$ has been tabulated for various crack configurations by Sherry et al. (1995). The function $B^{thin}$ is the inherent biaxiality parameter of a thin plate which is independent of any loading conditions. Figure 3.1 shows the dimensionless biaxiality function $B^{thin}$, of a thin plate. As Poisson's ratio, ν, increases, there is a marked increase in the biaxiality factor for nearly incompressible solutions as the free surface plane is approached. In thick plates the T-stress coincides with the two-dimensional solution where the first term on the right-hand side of equation (3.6) dominates, while the first term vanishes for an infinitely thin plate. Nakamura and Parks' (1992) work demonstrates that thickness-dependence can elevate the negative biaxiality of two-dimensional crack configurations ($B^{2D} < 0$) as the thickness is reduced providing $\sqrt{t/a} <\sim B^{thin}/\left|B^{2D}\right|$.

### 3.3 Three-Dimensional Elastic-Plastic Analyses

Fracture processes in engineering structures are dominated by plastic deformation even for materials that exhibit cleavage. Two-dimensional elastic-plastic crack analyses are widely available but are usually based on plane strain conditions and focus on in-plane effects. However, crack tip deformation in the fracture process zone is affected by the combination of in-plane and out-of-plane effects. This section of the literature, reviews progress in understanding three-dimensional elastic-plastic crack tip fields.

#### 3.3.1 Elastic-Plastic Stress Field in Finite Thickness Plates

Rice (1968a) has argued that the three-dimensional field in a finite thickness specimen should be bounded by the states of plane strain and plane stress. However the transition between the two states has not conclusively been quantified.

A three-dimensional finite element analysis of a test specimen configuration has been given by Wellman et al. (1985). Three-point-bend plane strain specimens were analysed from elastic to full plasticity using data derived from a uniaxial tension test of a pressure vessel steel. The plane strain and plane stress solutions provided upper bound and lower bounds to the load-displacement characteristics as shown in Figure 3.2. In the three-dimensional three-point-bend model, the occurrence of plane strain was shown at midplane. Although the Wellman et al. (1985) models were based on thick deeply cracked plane strain crack configurations (B/(W-a) = 1), they anticipated that plane stress should occur at the free surface. However, plane stress conditions were not shown to occur conclusively as illustrated in Figure 3.3.

Nakamura and Parks (1988b) analysed small scale yielding fields in a thin plate using boundary layer formulations. The material response was elastic-plastic with a strain hardening exponent, $n = 10$ in a Ramberg-Osgood power hardening law. The objective was to quantify $J$-Dominance conditions in thin plates. Three-dimensional fields occurred

within an annulus r < t independent of load. The opening stress, $\sigma_{22}$, merged with the plane stress field at r =1.5$t$, while a significant variation of through-thickness field quantities only occurred within r ≤ 0.5$t$.

A comparison of the local J along crack front at different load levels showed amplified values at the midplane ($x_3/t = 0$), and attenuated values at the free surface ($x_3/t = 0.5$). At low loads, the plastic zone shape was similar to the two-dimensional plane strain plastic zone shape both at the midplane and the free surface. As the load increased, the midplane plastic zone shape changed towards the two-dimensional plane stress plastic zone shape but the free surface plane retained the two-dimensional plane strain shape. These effects were attributed to the competition between the crack front singularity and the corner singularity. Nakamura and Parks (1988b) argued that under small scale yielding conditions, the coexistence of a plane strain HRR-field and a plane stress HRR-field along the crack front was very unlikely. A plane strain field was developed much more readily at the midplane than near the free surface. In the boundary layer formulation, the level of load to maintain a local plane strain HRR field at the distance ($r = 2J/\sigma_o$) was proposed to be $J_{far}/\sigma_o\varepsilon_o t \leq 10$.

Hom and McMeeking (1990) employed large geometry change solutions to study a thin cracked plate modelled by boundary layer formulations at load levels of $J/\sigma_o t = 2$ for a nonhardening material and $J/\sigma_o t = 2.7$ for a hardening material response. The state of stress near the crack tip was quantified through the difference between the midplane and free surface hoop stresses at corresponding positions ahead of the crack front. The stress field was considered to be dominated by the plane stress field if the hoop stress ratio was less than 5 percent:

$$\frac{\sigma_{\theta\theta}^{\text{midplane}} - \sigma_{\theta\theta}^{\text{free surface}}}{\sigma_{\theta\theta}^{\text{free surface}}} \leq 5\% \qquad (3.7)$$

On this basis, the three-dimensional features of the stress field extended a distance of 6t ahead crack tip in non-hardening solution and 2t in the strain hardening solution.

Nakamura and Parks (1990) extended the three-dimensional boundary layer formulations studies of a thin cracked plate to model the transition from small scale yielding to large scale yielding. In this study, substructured three-dimensional meshes were constructed so that contained yielding could be extended to multiple plate thickness distances. Small scale yielding and moderate yielding were identified to occur when the plastic zone is $r_y << t$ and $r_y \cong t$. A strong three-dimensional effect was observed at $r < 0.5t$ accompanied by relatively weaker through thickness variations of field quantities between $0.5 < r/t < 1.5$ and a nearly plane stress region at $r = 1.5t$ were observed as the load increased to moderate yielding.

Plastic zone shapes were studied beyond small scale yielding and the results were presented at the midplane and the free surface. A plane stress plastic zone shape occurred through the thickness at load levels $J/\sigma_o\varepsilon_o t > 5$. However, at low loads, the plastic zone shape took a plane strain shape at the free surface but approached plane stress at the midplane. This was argued to be due to the local J values which were higher at the midplane than the free surface.

In the transition from small scale to moderate yielding, the level of hoop stress decreased with increase in distance r/t as illustrated in Figure 3.6. Plane strain dominance was attained at the crack tip but decreased with distance from the crack tip as shown in Figure 3.7. A dominance parameter, $\rho$, was defined to determine the proximity to a local plane strain HRR field:

$$\rho = \frac{\left\| \sigma_{ij} - \sigma_{ij}^{HRR(pl.strain)} \right\|}{\left\| \sigma_{ij}^{HRR(pl.strain)} \right\|} \tag{3.8}$$

Near the midplane at moderately high load levels, the local plane strain HRR-dominated field was lost as shown in Figure 3.8.

Results for $n = 3, 5, 10$ were given in the fully plastic analysis in which a plane stress HRR field with plastic strains that exceeded the elastic strain was imposed on the tip-model.

Three-dimensional effects occurred at distances less than r/t < 1 while the transition from a three-dimensional to two-dimensional field occurred within the range of 1< r/t <1.5. Using the plane strain dominance parameter given in equation (3.8) showed that, plane strain constraint was lost along the crack front as shown in Figure 3.9. The result is similar to that obtained from the boundary layer formulations.

Nakamura and Parks (1988b and 1990) indicated that in small strain hardening elastic-plastic solution the three-dimensional zone extends to r/t = 1.5. Hom and McMeeking (1990) used a large geometry change solution to characterise crack tip field in thin plates but showed the three-dimensional field range from 2t in hardening to 6t in non-hardening materials.

The zone where the crack tip field is fully characterised by the J-integral is known as the J-Dominated zone. In three-dimensional crack tip fields, there are three zones along the crack front; a local near-plane strain, a plane stress and a corner field. Nakamura and Parks (1988b and 1990) showed the load to maintain the local plane strain J-Dominated HRR zone in a boundary layer formulation is $\Omega_{far} \leq 10$. A local plane stress field at the crack front has not been conclusively shown to exist, while the existence of a corner field in elastic-plastic field is still unresolved analytically and numerically.

### 3.3.2 Constraint Effects in Three-Dimensional Crack Tip Fields

It is now appropriate to focus on the effect of constraint in three-dimensional crack tip fields. In-plane constraint effects associated with the T/Q have been usefully adopted to increase margins associated with conservative plane strain fracture methodologies in problems of geometries dependent/non-dependent on J-Dominance. This has led to the engineering concepts of constraint matching and modified failure assessment diagrams which have been discussed in Chapter 2. However, an important aspect which has not been addressed is the effect of constraint in finite thickness specimens.

Three-dimensional elastic-plastic crack solutions using finite element methods became viable when efficient finite element formulations were combined with the computing capability to handle problems with many large degrees of freedom in the early eighties. The development of the numerical techniques has been described by Levy, Marcal and Rice (1971).

The development of plasticity and the evolution of crack tip parameters such as the J-Integral and CTOD were initially given by deLorenzi and Shih (1983) for compact tension (CT) specimens with thickness to ligament ratio B/(W-a) = 1.25. They analysed three-dimensional elastic-plastic crack fields using deformation plasticity with a hardening exponent, $n$ = 10. The energy release rates along crack the front were amplified at the midplane ($x_3/t = 0$) and attenuated at the free surface ($x_3/t = 0.5$). For loads ranging from small scale yielding to full plasticity, the crack opening stress normalised by the opening stress at the midplane was uniform at the midplane and reduced toward the free surface. This indicated that the opening stress reached a fully constrained value at midplane and reduced with increasing loads towards the free surface as shown in Figure 3.4. As the load increased, the plane strain constraint parameter ($\sigma_z/\sigma_x+\sigma_y$), approached 0.5 at the midplane and zero at the free surface as indicated in Figure 3.5.

Brocks and Olschewski (1986) also analysed three-dimensional compact tension (CT) specimens in thicknesses ranging in thickness from the standard plane strain fracture toughness, (2a = W, 2B = W) B/(W-a) = 1, to thin specimens, using incremental plasticity. The effects of thickness on the stress field were studied by varying the thickness of CT specimen using the HRR field as a reference. The results showed a loss of constraint when the thickness of the CT specimens was reduced from the plane strain standard geometry (B/(W-a) =1. However, even in the thickest specimen, stress components did not compare well to the two-dimensional HRR stresses leading to the conclusion that plane strain two-dimensional solution might not be applicable in three-dimensional fracture analyses. This result may be questionable because the fineness of the mesh was far less than the two-dimensional studies used in their paper.

Nevalainen and Dodds (1995), investigated constraint effects in the context of brittle fracture using SENB and CT specimens. For shallow cracked bend bars, a/W = 0.1 at the midplane, a loss of constraint was observed at very low deformation levels. Deeply notched thick specimens in bending, (a/W = 0.5 W/B = 1), showed a small increase in constraint at the midplane at high deformation levels due to in-plane effects. Thin deeply notched specimens showed a severe loss of constraint on the midplane while shallow notched specimens showed less severe constraint loss at the midplane. For deeply notched SENB and CT specimens, midplane levels of stress triaxiality were maintained to higher deformation levels in contrast to two-dimensional plane strain analyses.

The effect of constraint on a ductile austenitic steel has been investigated by Yuan et al. (1995) using the J-Q methodology. The paper can be divided into two-dimensional and three-dimensional crack tip analyses. In three-dimensional analyses of CT specimens, they showed that the stress field tended toward the plane stress field in both thick, B/(W-a) = 1 and thin B/(W-a) = 0.2 specimen as the load increased. In the thick specimen, the direct stresses at the midplane remained similar to the plane strain stress level even at high levels of deformation. However the free surface did not show conclusive evidence of a plane stress field. In the thin specimen, the midplane stresses were close to plane strain levels at low loads but developed toward a plane stress field with increasing load. Another important result showed that Q, varied significantly along the crack front and with distance from the crack tip which has profound implications to the applications of J-Q methodology to three-dimensional crack tip analyses, as Q should be distance independent.

The applicability of the J-Q approach in three-dimensional analyses has been discussed by O'Dowd (1995). O'Dowd (1995) argued that the J-Q method was applicable to three-dimensional crack in thick plates but is limited to midplane ($x_3/t = 0$) where out-of-plane strain components are negligible compared to the in-plane singular terms.

Although the J-Q methodology may not be able to fully characterise the effect of finite thickness crack, it is useful to determine constraint effects at the midplane where crack propagation is normally expected to initiate in straight through crack problems. Henry and

Luxmoore (1997) performed three-dimensional crack analyses on high and low constraint geometries to evaluate the effect of constraint in a low hardening response material using the J-Q methodology. The specimens dimensions for the high constraint geometry varied between B/(W-a) = 0.8 to 1.01 while the low constraint specimens dimensions varied from B/(W-a) = 0.8 to 5.6. All data were extracted at the midplane ($x_3/t = 0$) but at two different in-plane distances ($r\sigma_o/J$ = 1 and 2). The triaxiality factor defined as the mean stress divided with equivalent Mises stress ($\sigma_m / \overline{\sigma}$ = h) varied linearly with $Q$ as shown in Figure 3.10. Figure 3.11 shows the triaxiality parameter as a function of Q indicating that for different hardening exponent, n, the triaxiality, h, increases at a fixed Q.

Yuan and Brocks (1998) analysed mode I cracks using both three-dimensional modified boundary layer formulations and full field bending and tension geometries with strain hardening responses similar to those used by Nakamura and Parks (1990). The full-field specimens used thickness to ligament ratios of B/(W-a) = 1 and 0.2. The T-stresses in the modified boundary layer formulations varied in the range of $-1 \leq \tau \leq 1$ ($\tau = T/\sigma_o$). Q values were defined as differences between the hoop stress of the three-dimensional field and the plane strain reference solution near midplane ($x_3/t = 0.033$) and near free surface ($x_3/t$ = 0.994). Their results showed that the crack front stress fields were dominated by the plane strain solution at small plastic zone sizes, but the stress field approached the plane stress field as the plastic zone increased in size. Near the crack tip, Q depended on distance from the crack front and on the distance from the free surface. This suggests that Q parameter cannot describe the crack front constraint as the load increases. However, it was found that Q was related to the normalise hydrostatic stress, $\sigma_m/\sigma_o$ uniquely through a linear relationship for a particular constraint level as shown in Figure 3.12-3.14. They noted that the three-dimensional crack fields fall between the plane strain and plane stress idealisations although plane stress behaviour was not clearly identified. Finally they argued that any parameter defined under plane strain condition cannot characterise in-plane and out-of-plane constraint loss.

Kim et al. (2001) carried out three-dimensional analyses on a thin cracked plates using boundary layer formulations and correlated the numerical solutions with a three-term

asymptotic crack tip expansion J-$A_2$. The numerical results from their analyses essentially follow a J-T/Q approach and can be used in part to demonstrate three-dimensional crack tip constraint effects. The *T*-stress was applied to simulate the effect of geometries in boundary layer formulations. The results were compared with HRR plane strain and plane stress fields. For the low and high loads, data gathered at the midplane and near the free surface fell between the HRR plane strain and plane stress field, indicating a plane strain like field at midplane, and near plane stress field close to the free surface. The effect of T was similar to the effects which have been demonstrated in two-dimensional analyses. The effect of the plane strain parameter equation (2.45) was evaluated with varying T-stress as illustrated in Figure 3.15. It was found that the T-stress does not affect the plane strain parameter. In subsequent work, Kim et al. (2003) examined the effect of constraint on three-dimensional SENB specimens. The specimens had crack to width ratio of a/W = 0.5 and 0.15 with an identical thickness B. In order to relate the results to the experimental cleavage toughness data of Sorem et al. (1989) and Wellman et al. (1988), specimens with B = W and W = 2B were selected. The results showed that at the midplane, the HRR plane strain field is approached and remained close to the HRR field for all load levels much more nearly in the W = 2B specimen when compared to the B = W specimen. With increasing load, the physical location of $r = 2J/\sigma_0$ moves toward the global bending field and this affects the crack tip constraint field in the square specimen much earlier than the rectangular specimen at the same deformation level. At the free surface for the B = W specimen, the stress field did not approach the plane stress field. The shallow cracked B = W specimen showed a constraint loss similar to the effect seen in two-dimensional shallow crack bend specimens.

Three-dimensional crack analyses require a very detailed finite element mesh to bring out the characteristics of the crack tip field. In order to accommodate a stable stress gradient change from the midplane to the free surface, the mesh must have a build up of element layers through the thickness but weighted to the surface and away from the crack front, but weighted towards the crack tip. Three-dimensional crack problems are further complicated by the need to have significant computing resources to solve problems with many degrees of freedom. Brocks and Olschewski's (1986) results are questionable as highlighted by

Parks (1991) because the three-dimensional mesh was coarse compared to two-dimensional solutions. A reference three-dimensional analysis by Nakamura and Parks (1988b and 1990) provided initial results on the elastic-plastic constraint effect. The three-dimensional analyses of a thin plate largely focused in characterising the three-dimensional field and extent of J-Dominance. Subsequent work focused on applying two-parameter fracture methodology to full-field solutions. However the results were only given at the midplane and the free surface field from small scale to large scale yielding (Sorem et al. (1991), Yuan et al. (1995), Nevalainen and Dodds (1995), Henry et al. (1996), Henry and Luxmoore (1999), Kim et al. (2001), Kim et al. (2003)). The results centre on in-plane geometry effects rather than the effect of thickness on constraint. Yuan and Brocks (1998) attempted to quantify thickness effect on constraint by showing results in boundary layer formulations and full-field solutions from small scale yielding to full plasticity. However, they concluded that a parameter based on plane strain cannot fully describe both in-plane and out-of-plane constraint loss.

Although the application of J-T/Q methodology in three-dimensional analyses is suspect, a detailed discussion on the limits has never been provided. J-T/Q theory requires the field to be deviatorically similar which means the shear stresses must remain identical under constraint loss, but direct stresses differ hydrostatically. An important requirement is that within the microstructural-separation distance ahead of the crack front normally within $2J/\sigma_0 \leq r \leq 5J/\sigma_0$, the stress difference Q is distance independent. Yuan et al. (1995) and Yuan and Brocks (1998) showed that Q is not distance independent. In contrast, O'Dowd (1995) and Pardoen et al. (1999) argued that in very thick specimen when out-of-plane constraint is bounded, J-T/Q theory suffices to describe the constraint loss. A detailed investigation on out-of-plane constraint effect is needed to show limits of two-parameter methodology in three-dimensional analysis.

### 3.4 Experimental Data on Toughness

The effect of thickness on fracture toughness is a fundamental issue in fracture mechanics. Irwin et al. (1958) found that fracture toughness varied with thickness. Using bend bars and centre cracked tension panels in aluminium alloys (7075-T6 and 2024-T3) which ranged in thicknesses from 0.016 to 1 inch: they showed that the critical crack extension force, $G_c$ increased as the thickness decreased as shown in Figure 3.16. An important outcome from this work was the identification of the plane strain fracture toughness, $K_{Ic}$, as a material property.

Any discussion of the effect of thickness on fracture toughness requires fractographic analysis, such as that given by Knott (1973). Figure 3.17(b) illustrates the effect of thickness on fracture toughness. The fracture profiles can be divided into 3 regions: A, B and C. The C region is associated with plane strain fracture, B is associated with transition from plane strain to plane stress and A is region where necking precedes failures.

Fractographically C is the region where flat fracture occurs in the centre of relatively thick specimens with very small shear lips at the edges. Flat fracture occurs because lateral contraction is constrained under near plane strain conditions and a triaxial stress system is developed. However at the free surface, the lateral stress is zero and the stress state approaches plane stress causing a shear lip. Thickness-toughness data in this region are widely available as exemplified by Hudson and Seward (1978 and 1982). However, fracture toughness data for the same material seems to vary greatly as critically remarked by Chambers and Sinclair (1986) raising doubts about the safe application of fracture toughness data to structural integrity assessment by inexpert personnel. The variation of cleavage fracture toughness can be resolved by applying statistical methods. Wallin (1984) demonstrated that the scatter in the cleavage $K_{Ic}$ data can be described by a Weibull distribution. The relative scatter described through the Weibull modulus is constant and equal to four. In ductile tearing, Wallin (1985) argued that valid fracture toughness data should be identified at the initiation of crack extension. Ductile fracture initiation is thickness independent if $B \geq \alpha(J/\sigma_o)$. For bend specimens, the factor $\alpha$ is usually suggested

to be 25. Wallin (1985) showed typical experimental data on thickness effect on ductile crack initiation taken from (Keller and Munz (1977), Gilmore et al. (1983), Huang and Gehes (1984) and Druce (1980)) in Figures 3.18 – 3.20. When $B \leq 25J/\sigma_o$, the toughness increases with reduction in thickness and corresponding to the transition to region B of Figure 3.17(a).

In region B the toughness increases with a reduction of the thickness and reaches a maximum critical crack extension force, $G_c$. Experimental data in the transition region from plane strain to plane stress have been shown by Irwin (1964), Tiffany and Masters (1965), Kaufmann and Hunsicker (1965), Brothers and Yukawa (1966), Srawley and Brown (1967), Rolfe and Novack (1970) and Jones and Brown (1970) in Figure 3.21-3.27. All data show that fracture toughness increases with reduction in thickness. The fracture profile in the intermediate thickness is shown in Figure 3.28. At low load levels, the stress field at the crack front is triaxial and specimens exhibit flat fracture surfaces, however, as plastic deformation increases, the lateral stress, $\sigma_{zz}$ relaxes and the flat surfaces tunnels between the shear lips. Krafft, Sullivan and Boyle (1965) developed a hypothesis to explain the behaviour in the transition of plane strain to plane stress in terms of the energy necessary to deform in the transition plane strain and plane stress. Plane strain fracture was associated to energy required to form new surfaces while plane stress fracture is the plastic energy contained in the shear lips. This established the crack resistance R-curve concept. Currently, ASTM-E1152 (1988) specifies the method to determine the fracture toughness in stable tearing using J-R curves. However, toughness testing based on crack resistance R-curve may not be practical because of problems associated with the accuracy of results. Landes and Brown (1998) reported round robin results on the standard method for measurement of fracture toughness and concluded that the J-R curves method could not provide a valid initiation fracture toughness data because of the difficulty of obtaining valid initiation toughness values from the R curve.

In region A, the fracture toughness reduces with a reduction of thickness. The effect of thickness on fracture toughness in region A have been inferred, (Knott (1973), Broek (1974), McClintock (1971)) although the literature usually concentrates on qualitative

rather than quantitative explanation because of the complex nature of deformation and fracture. McClintock (1971) explained the behaviour in region A qualitatively by attributing the decrease in fracture toughness with the decrease in thickness to the effect of thinning of the specimen at the crack tip under deformation. This behaviour affects foils and very thin sheet metals.

Pardoen et al. (1999) studied the influence of thickness on thin aluminium 6082T0 plates in double edge cracked tension (DENT) specimens experimentally and numerically. The specimens thicknesses range from 1 to 6 mm, while the crack length, a, ranged from 20 to 27.5 mm, and the ratio a/W ranged from 0.66 to 0.91. The effect of thickness showed a decreasing toughness with reducing thickness as shown in Figure 3.29. The thickest specimen (B/(W-a) = 0.3) showed the toughness started to decrease with increasing thickness. A similar trend of reducing thickness and reducing toughness effect was also shown by Wang et al. (2003) as illustrated in Figure 3.30 using copper foils in DENT configuration with specimen thickness ranging from 20 micron to 1 mm and a/W = 0.4 (a = 5 mm and W = 12.5 mm). Figure 3.30 also shows that the maximum toughness is attained at thickness 0.3 mm. The toughness undergoes a drastic reduction with further increase in thickness as shown in region II. However Wang et al. (2003) argued that region II occurs because of the transition from plane stress to plane strain without giving fractographic details on the fracture modes.

Collectively the thickness-toughness relation for wide range of materials is qualitatively similar to Figure 3.17(a) which shows a constant fracture toughness in region C followed by an increasing fracture toughness with decreasing thickness in region B and a reducing fracture toughness with further thickness reduction in region A. However, the discussion on the effect of thickness on fracture toughness has largely been centred on region C because of the opportunity to identify the fracture toughness as a material property.

Most textbooks on fracture mechanics (Knott (1973), Broek (1974), Anderson (1995)) have discussed qualitatively the thickness effect on toughness. A consensus has emerged

which agrees that reduction of thickness caused the fracture toughness to increase corresponding to change from plane strain to plane stress fracture.

It is clear that toughness in plane strain is dependent on the state of flow field or constraint. The level of constraint in plane strain specimens can be indexed by the T-stress. A highly constrained geometry has positive T-stresses while geometry which loses constraint develop negative T-stresses. However a review of experimental data is still needed now because existing data were mostly obtained prior to the establishment of theory of constraint effect on fracture.

### 3.5 Corner Singularity Fields

Cruse (1970) identified the existence of a singularity field at the intersection of the free surface and the crack front which is known as a corner field. Benthem (1977, 1980) developed analytical solutions of the elastic corner singularity field in a quarter-half space using a separation variable technique. Bazant and Estenssoro (1978) used a potential energy technique in finite element analysis to identify corner singularity solution in Mode II and III and elastic interface crack problems.

The corner field is usually discussed as a vertex formed by the intersection between the crack front and the free surface plane as illustrated in Figure 3.31 using spherical co-ordinates ($\rho$, $\theta$, $\phi$). Without loss of generality, the corner singularity asymptotic field can be expressed following Riedel (1987) in the form:

$$\sigma_{ij} = \beta \rho^{-s} \, g_{ij}(\theta, \phi) \tag{3.9}$$

Here $g_{ij}$ is a dimensionless angular function and the spherical coordinates centred at the vertex are:

$$\rho = \sqrt{r^2 + z^2}, \quad \phi = \tan^{-1}\left(\frac{r}{z}\right), \quad z = \frac{t}{2} - x_3 \tag{3.10}$$

equation (3.9) is analogous to the two-dimensional linear elastic crack tip problem solved by Benthem (1977, 1980) using variational principles and Bazant and Estenssoro (1978) using energy theorems. Both found that s = 0.5, 0.452 and 0.332 when Poisson's ratio is $\nu$ = 0, 0.3 and 0.5 respectively. This implies that the vertex singularity is weaker than the usual inverse square root singularity except when $\nu = 0$. If $\nu = 0$, the surface field plays no particular role. For small $\phi$, the vertex field approaches the plane strain crack tip field as:

$$g_{ij} \rightarrow \frac{f_{ij}(\theta)}{\sqrt{2\pi\phi}} \qquad \text{as } \phi \rightarrow 0 \tag{3.11}$$

where $f_{ij}(\theta)$ describes the angular stress distribution of the linear elastic crack tip fields. The factor $\beta$ is undetermined by asymptotic analysis, and requires a full three-dimensional finite element analysis of the whole specimen. However, from the scaling laws for power-law materials, $\beta$ is shown to be related to the applied stress and the specimen thickness:

$$\beta \propto \sigma_{net}\, T_{total}^{s} \tag{3.12}$$

where $T_{total}$ is the full specimen thickness. From equations (3.9) and (3.11), the coefficient of the $1/\sqrt{r}$ crack tip singularity approach 0 at the free surface according to:

$$K_I \propto \beta\,(z)^{(1/2-s)} \tag{3.13}$$

This behaviour is shown numerically in Figure 3.32 following deLorenzi and Shih (1983), for the local $J$, $J \propto (K_I)^2$ which indicate that at the free surface, $J$ approaches 0.

Burton et al. (1984) presented a three-dimensional finite element analysis of a through cracked elastic plate and found a decay in the energy release rate through the plate thickness. This indicated that the drop in energy release rates as the free surface is

approached is probably not significant from a fracture toughness testing point of view with the exceptions of residual stress fields near the crack surface intersection problems.

Nakamura and Parks (1988b) elucidated the effect of intersection of a crack front with free surface in three-dimensional boundary layer formulation. Using the stress intensity factor along the crack front with the asymptotic form of equation (3.9), Nakamura and Parks (1988a) showed that for small z,

$$K_{local}(z) = \beta\, z^{\lambda+1/2} \tag{3.14}$$

where $\beta$ is a constant which represents the stress intensity of corner singularity field. The coefficient, $\lambda+1/2$ can be determined from the gradient of curves for different Poisson's ratio plotted in a log-log scale, and from the values of computed three-dimensional local stress intensity factor very near the corner vertex ($z/t<0.03$). The normalised values of corner stress intensity factor $\beta$ plotted against Poisson's ratio $\nu$ are shown in Figure 3.33. The stress tensor for the corner singularity field can be expressed as:

$$\sigma_{ij} = \frac{\beta}{\sqrt{2\pi}} \rho^{\lambda}\, g_{ij}(\lambda;\theta,\phi) \tag{3.15}$$

Here the strength of the as exemplified by the exponent $\lambda$ depends on Poisson's ratio. $\beta$ is the corner stress intensity factor representing the magnitude of singularity field and its dependence on geometry and load. Equation (3.14) is similar to Riedel (1987) equation (3.9) with the addition of the term $1/\sqrt{(2\pi)}$. From equations (2.70), (3.13) and (3.14), the dimensionless function $g_{ij}$ must behave as:

$$f_{ij}(\theta) = \lim_{\phi \to 0} \sqrt{\phi}\; g_{ij}(\lambda;\theta,\phi) \tag{3.16}$$

where the in-plane components of $f_{ij}(\theta)$ are given in equation (2.72). The asymptotic corner field matched with Benthem dimensionless function $g_{ij}$ is shown in Figure 3.34 for $\nu = 0.3$

at a spherical radius of $\rho/t = 0.48 \times 10^{-2}$. The corner singularity region appears to dominate a spherical radius of approximately 3 percent of the plate thickness from the intersection of the free surface and the crack front.

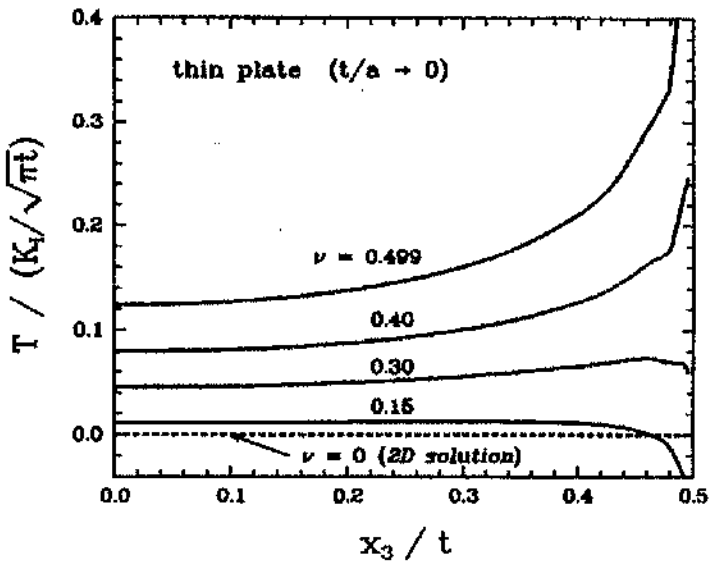


Figure 3.1: Biaxiality factor for thin elastic plate for various Poisson's ratios along the crack front after Nakamura and Parks (1992).

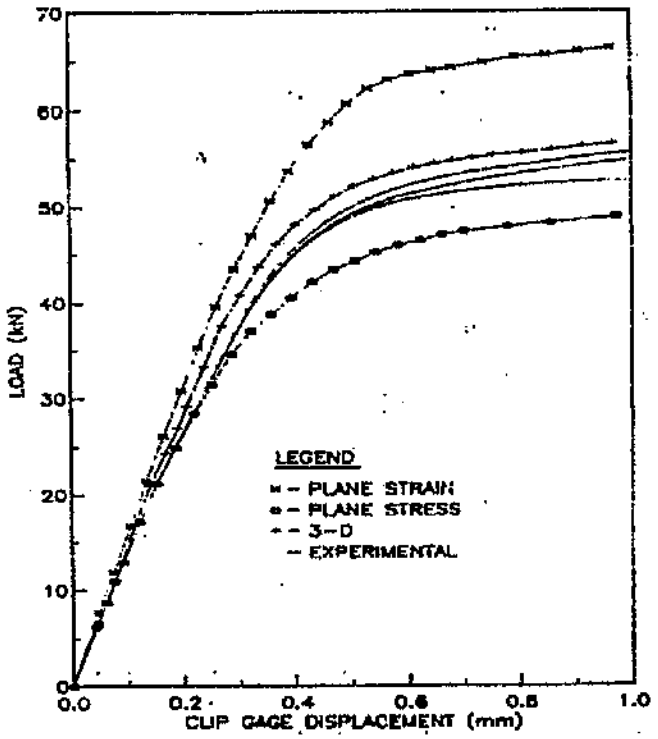


Figure 3.2: Load versus clip-gauge displacement for an A508 steel after Wellman et al. (1985).

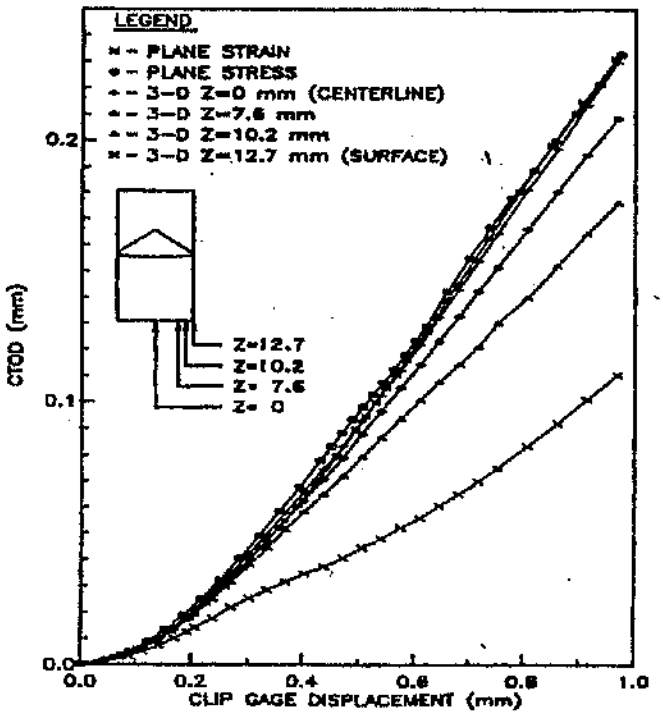


Figure 3.3: CTOD versus clip-gauge displacement for an A508 steel after Wellman et al. (1985).

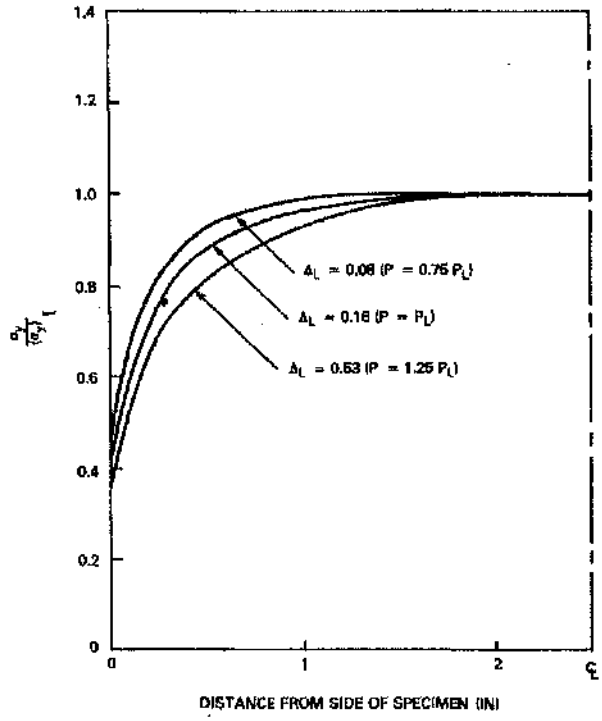


Figure 3.4: Variation of crack opening stress along the crack front for compact tension specimens after deLorenzi and Shih (1983).

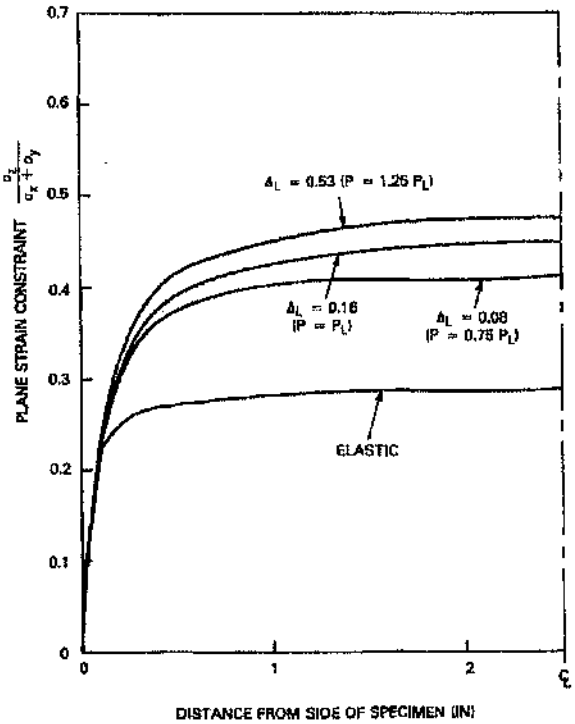


Figure 3.5: Variation of plane strain constraint along crack front for un-sided notched compact tension specimens after deLorenzi and Shih (1983).

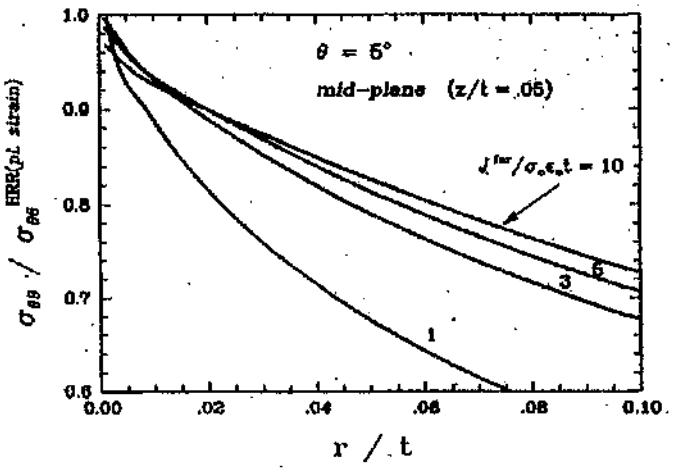


Figure 3.6: Opening stress normalised by the local plane strain HRR solution for various load levels after Nakamura and Parks (1990).

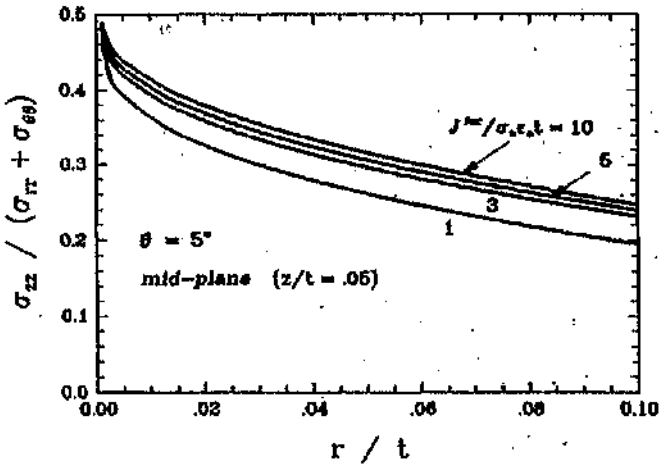


Figure 3.7: The constraint parameter ahead of the crack front at $\theta = 5°$ on the midplane for various load levels after Nakamura and Parks (1990).

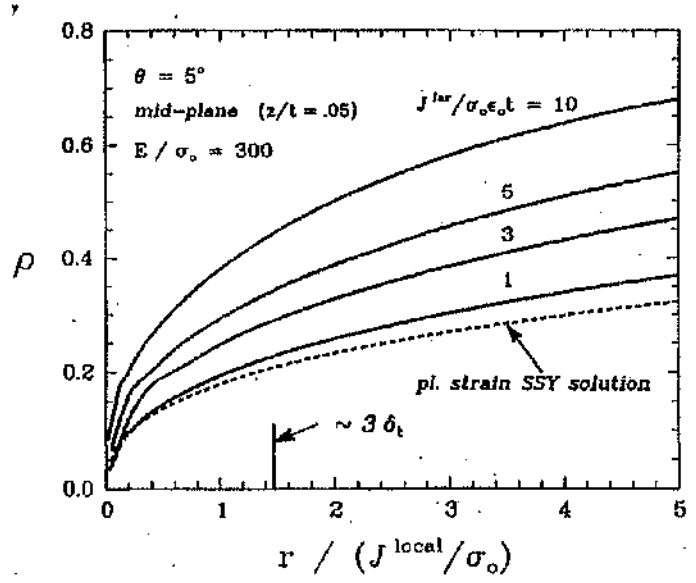


Figure 3.8: Plane strain J-Dominance parameter at the midplane ($x_3/t = 0.05$) ahead of the crack front, normalised by the local J at various load levels after Nakamura and Parks (1990).

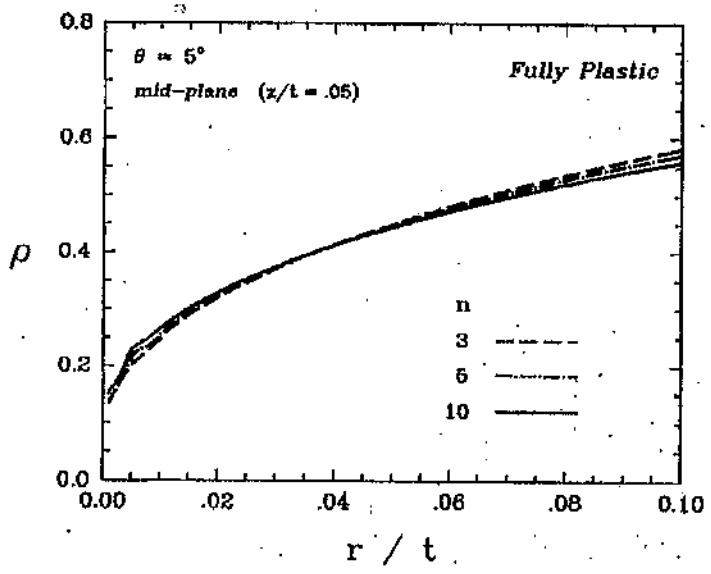


Figure 3.9: Plane strain J-Dominance parameter ρ near the midplane ($x_3/t = 0.05$), ahead crack front, in full plasticity solutions in materials with strain hardening exponents n = 3, 5, 10 after Nakamura and Parks (1990).

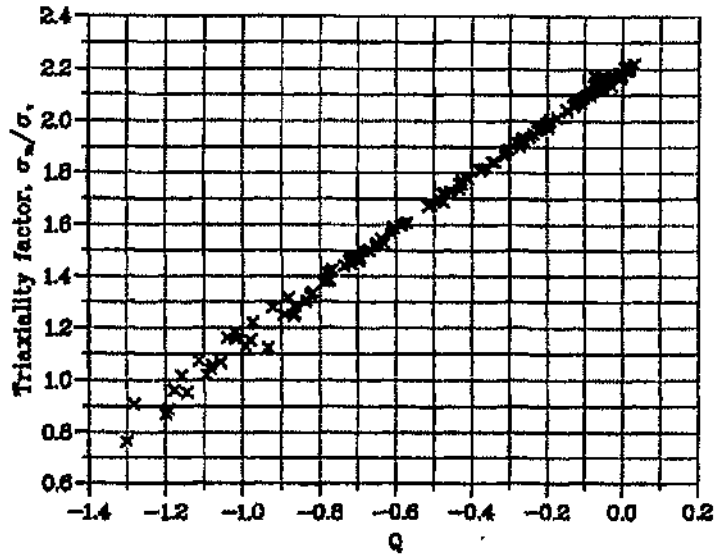


Figure 3.10: Variation of the triaxiality factor with the Q-value at $r\sigma_o/J = 2$ on the midplane ($x_3/t = 0$) for different 3-D three-point-bend and 3-D centre crack tension panel at different load levels after Henry and Luxmoore (1997).

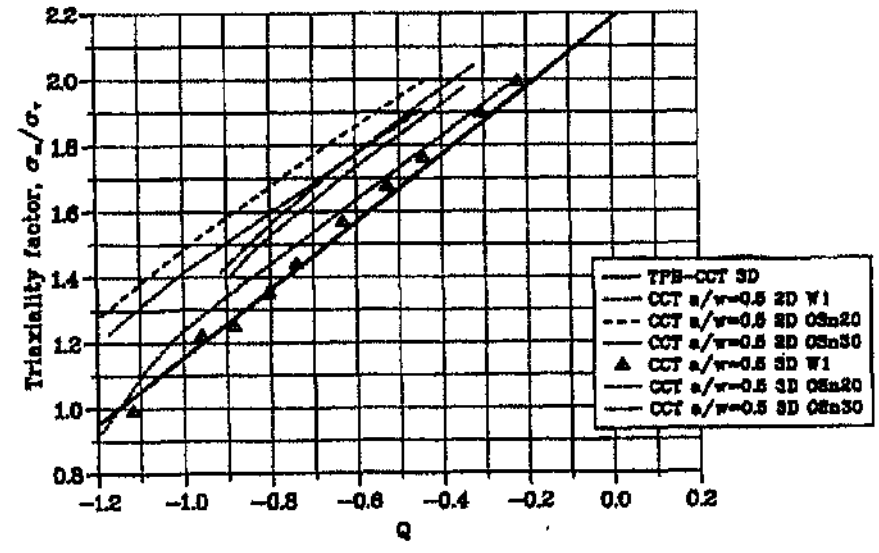


Figure 3.11: Variation of the triaxiality factor with the Q-value at $r\sigma_o/J = 2$ at midplane ($x_3/t = 0$) for three-dimensional three-point-bend and centre crack tension panel as well as 2-D three-point-bend and centre crack tension panel for different material hardening exponent, $n$, at different loads after Henry and Luxmoore (1997).

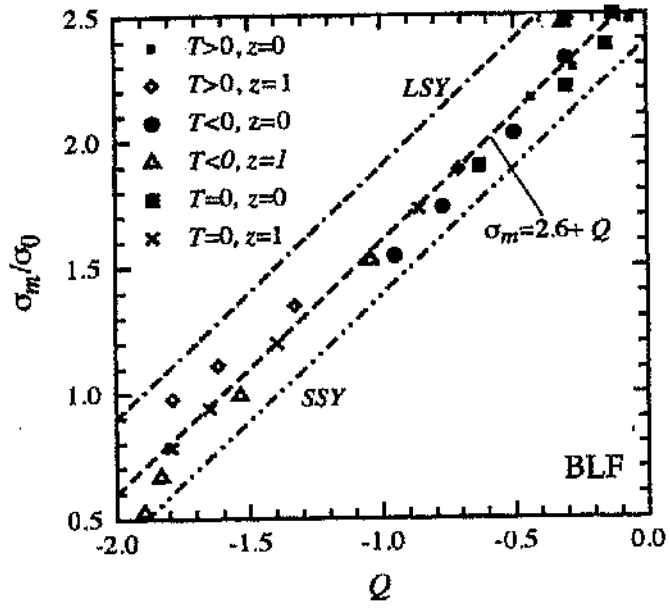


Figure 3.12: Boundary layer formulation crack tip triaxiality parameter with Q ahead of the crack front $\theta = 0^{\circ}$ at $r\sigma_o/J = 2$ and at the midplane ($x_3/t = 0.056$) and the free surface ($x_3/t = 0.996$) under different loads. Broken lines denote plane strain estimates for small scale and large scale yielding after Yuan and Brocks (1998).

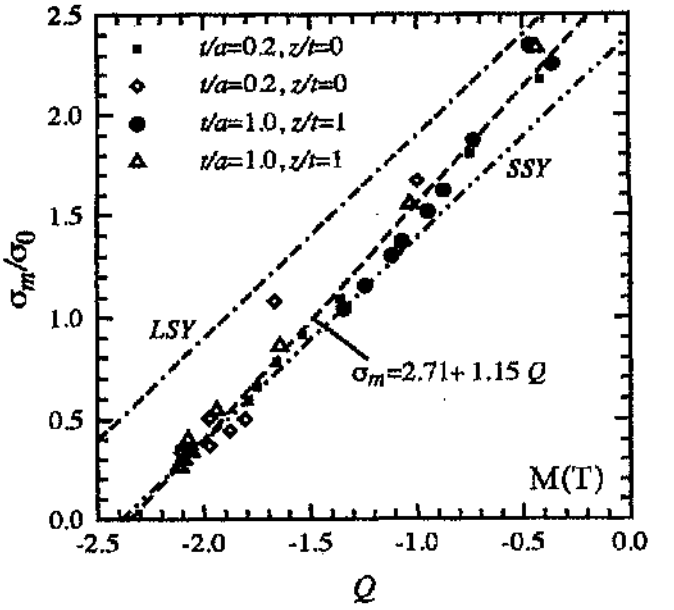


Figure 3.13: Centre crack tension panel crack tip triaxiality parameter with Q ahead of the crack front $\theta = 0^{\circ}$ at $r\sigma_o/J = 2$ and at the midplane ($x_3/t = 0.056$) and the free surface ($x_3/t = 0.996$) under different loads. Broken lines denote plane strain estimates for small scale and large scale yielding after Yuan and Brocks (1998).

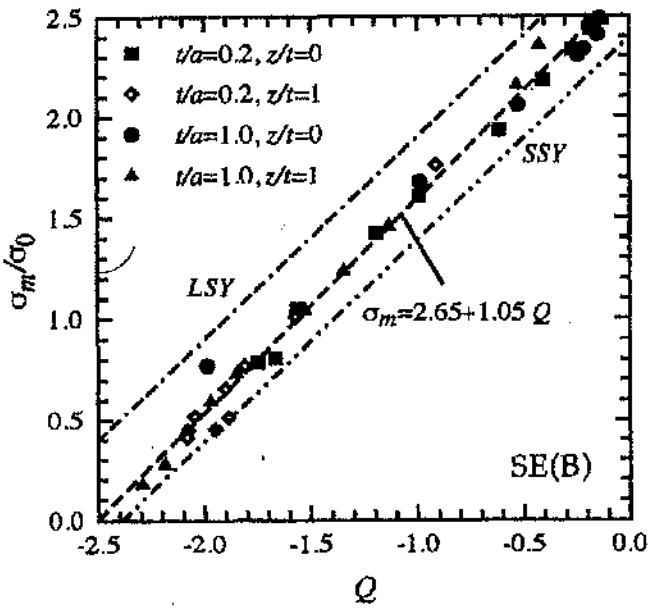


Figure 3.14: Edge crack bend bar crack tip triaxiality parameter with Q ahead of the crack front $\theta = 0^\circ$ at $r\sigma_o/J = 2$ and at the midplane ($x_3/t = 0.056$) and the free surface ($x_3/t = 0.996$) under different loads. Broken lines denote plane strain estimates for small scale and large scale yielding after Yuan and Brocks (1998).

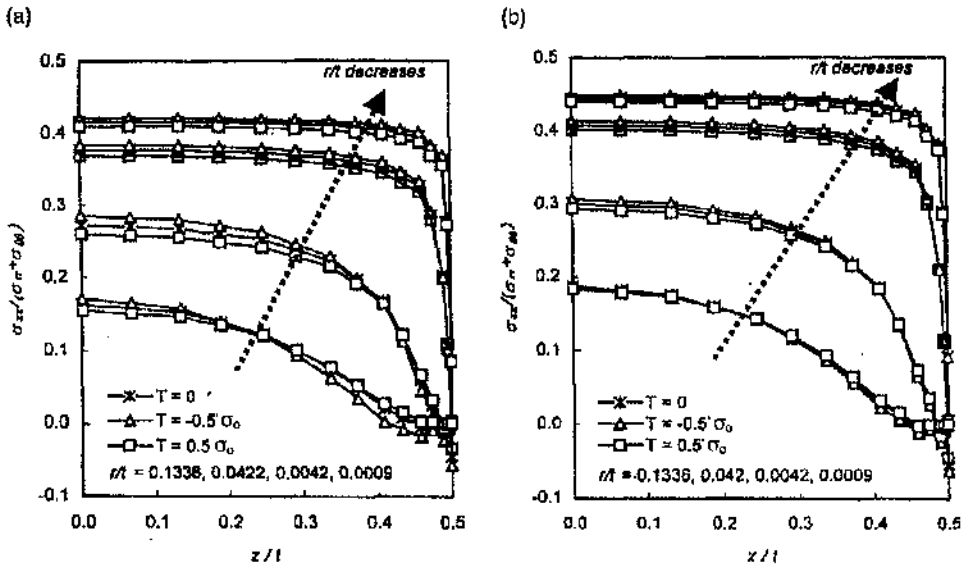


Figure 3.15: Variation of plane strain constraint parameter through the thickness at $\theta = 0^\circ$ for (a) low load and (b) high load after Kim et al. (2001).

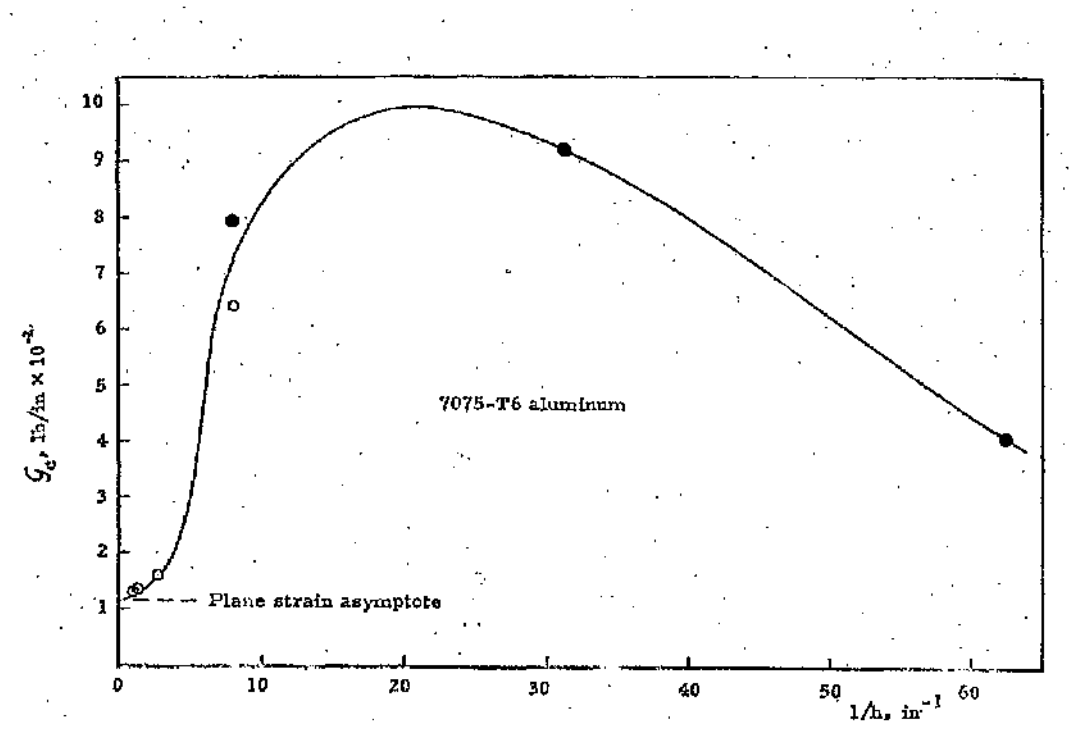


Figure 3.16: Effect of thickness on critical crack extension force, $G_c$, after Irwin et al. (1958). The black and white dots indicate centre crack panel in tension and bend specimens.

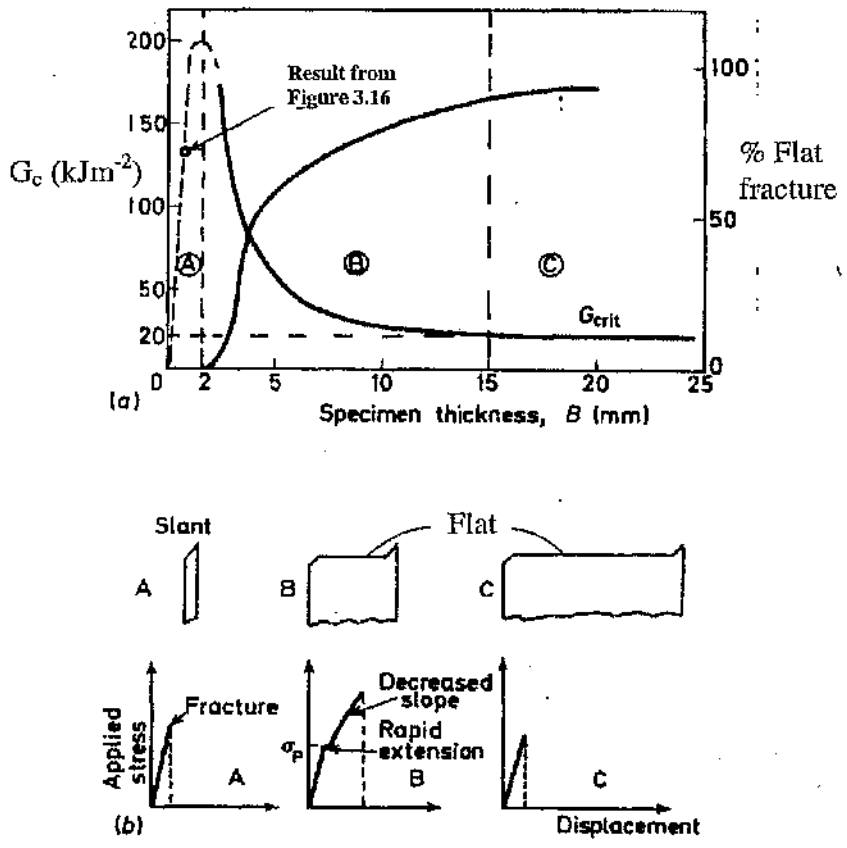


Figure 3.17: (a) Variation of fracture toughness with thickness for an 7075-T6 aluminium alloy from Irwin et al. (1958) as shown in Figure 3.16 and (b) Fracture profiles and stress-displacement curves typical of regions A, B and C after Knott (1973).

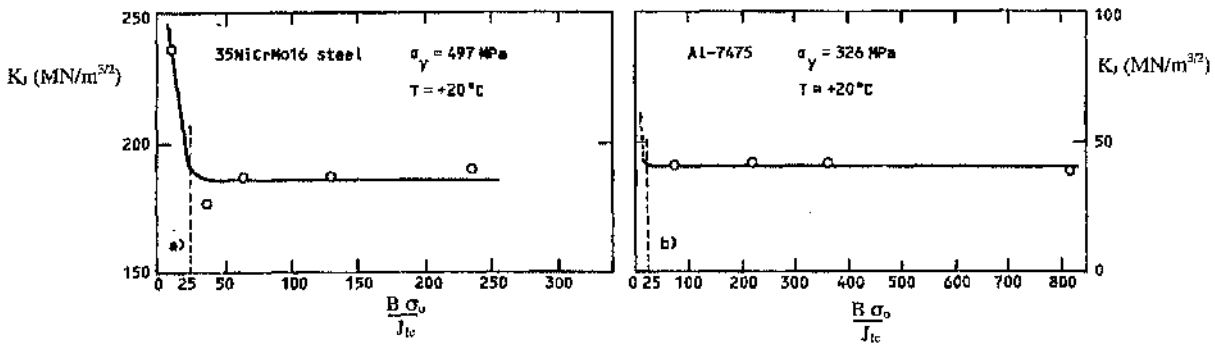


Figure 3.18: The effect of thickness on ductile fracture initiation after Wallin (1985) from Keller and Munz (1977) for (a) 35NiCrMo16 steel and (b) Al-7475.

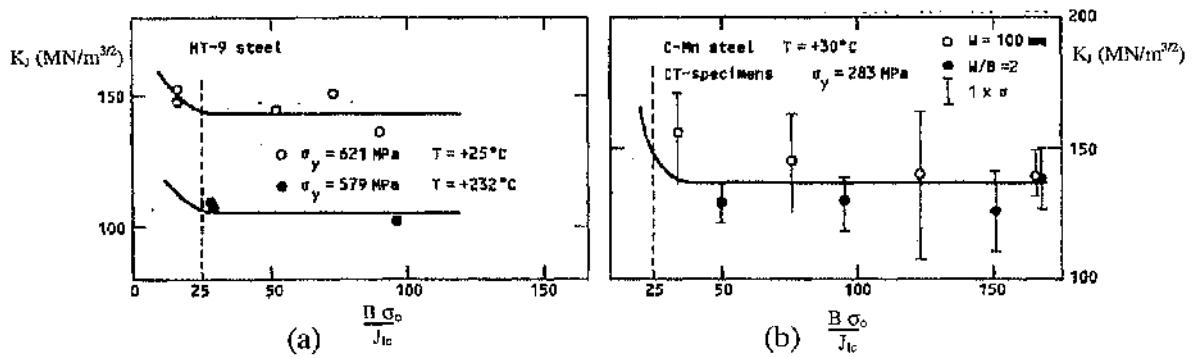


Figure 3.19: The effect of thickness on ductile fracture initiation after Wallin (1985) from (a) Huang and Gehes (1984) and (b) Druce (1980).

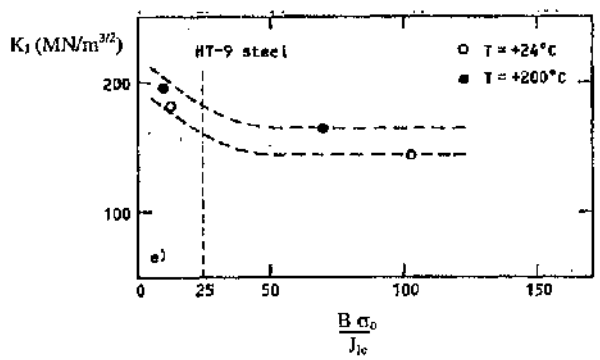


Figure 3.20: The effect of thickness on ductile fracture initiation for HT-steel after Wallin from Gilmore et al. (1983).

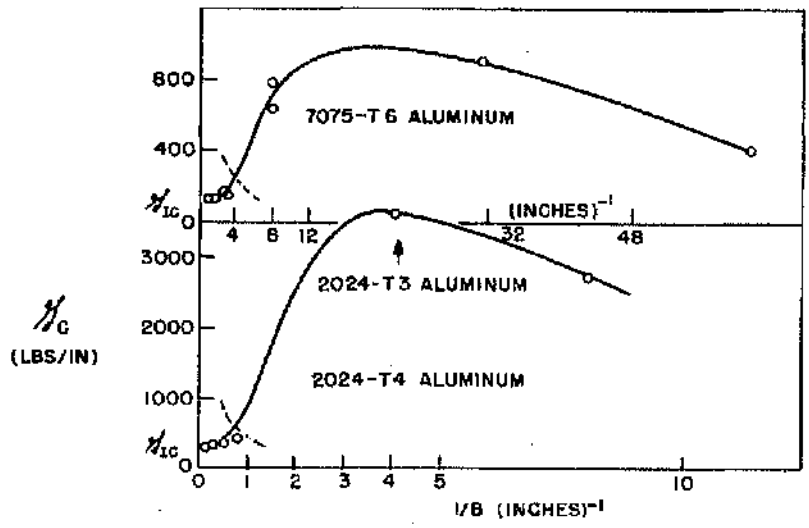


Figure 3.21: Thickness effect on toughness after Irwin (1964) for 7075-T6, 2024-T3 and T4 Aluminium alloys for cracked bend bars and centre cracked tension specimens.

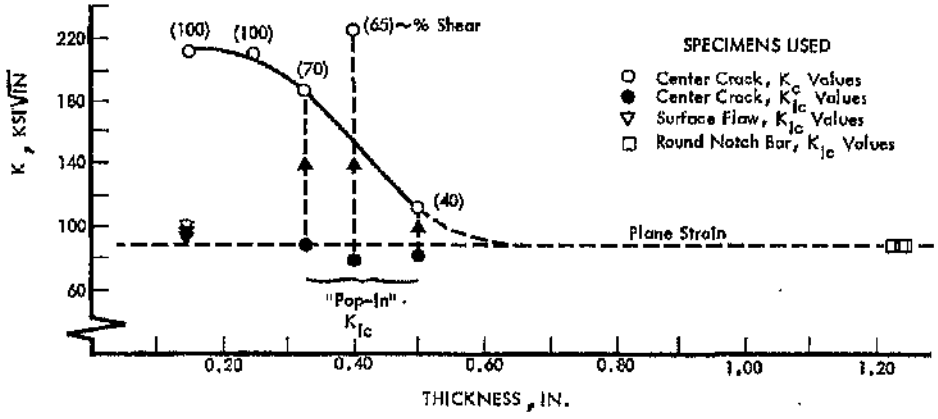


Figure 3.22: Thickness effect on toughness after Tiffany and Masters (1965). Single edge notch tension, surface flaw and round notch bar for 18% Nickel (300) steel.

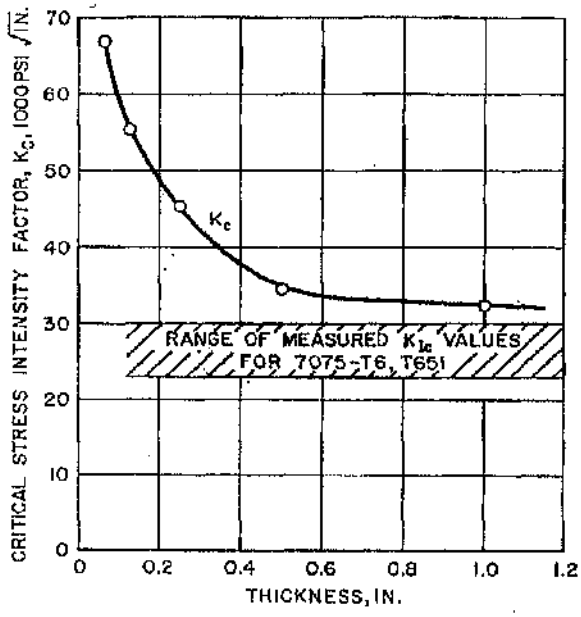


Figure 3.23: Thickness effect on toughness after Kaufmann and Hunsicker (1965). Single edge notched tension specimens of 7075-T6 Aluminium alloy.

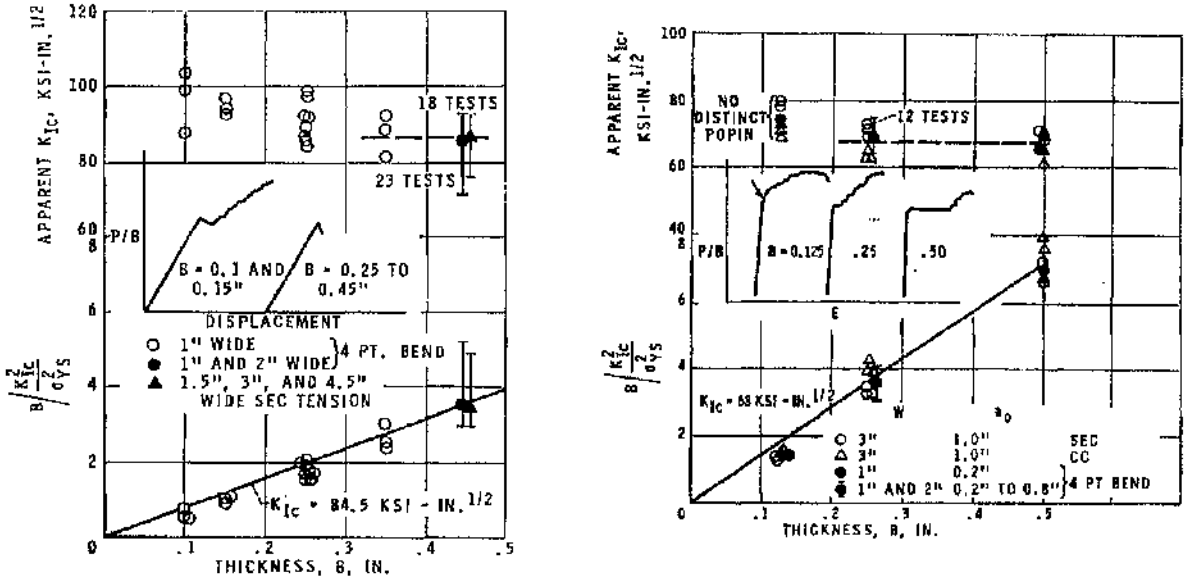


Figure 3.24: Thickness effect on toughness after Srawley and Brown (1967). 4 pt bend specimens in different yield stress (a) 242 ksi and (b) 259 ksi maraging steels.

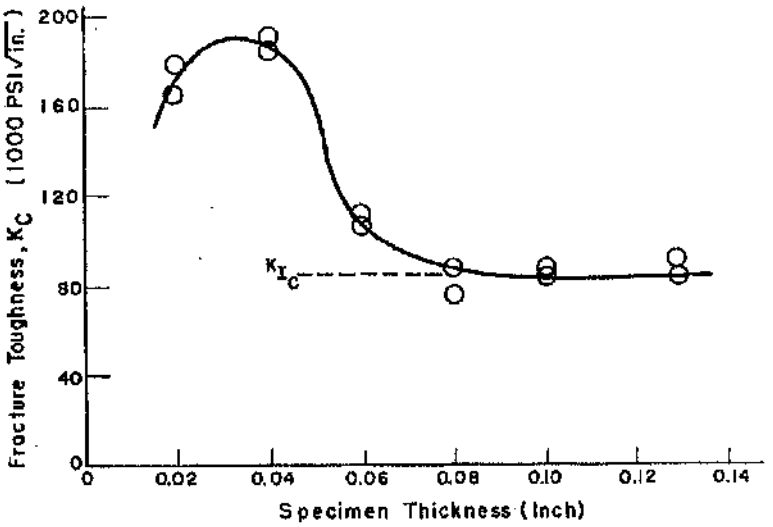


Figure 3.25: Thickness effect on toughness for H11 steel at 225 kpsi yield stress after unpublished work by Srawley shown in Brothers and Yukawa (1965).

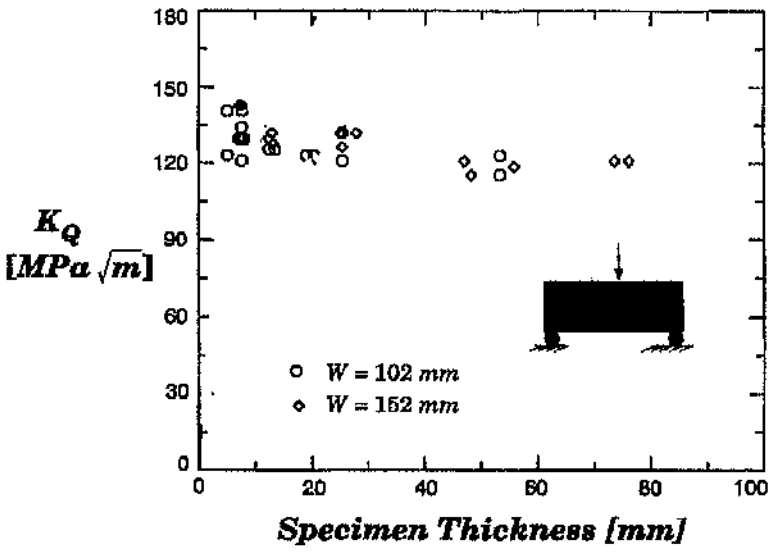


Figure 3.26: Thickness effect on toughness for 18 Ni maraging steel after Koppenhoefer et al. (1995) from Rolfe and Novack (1970).

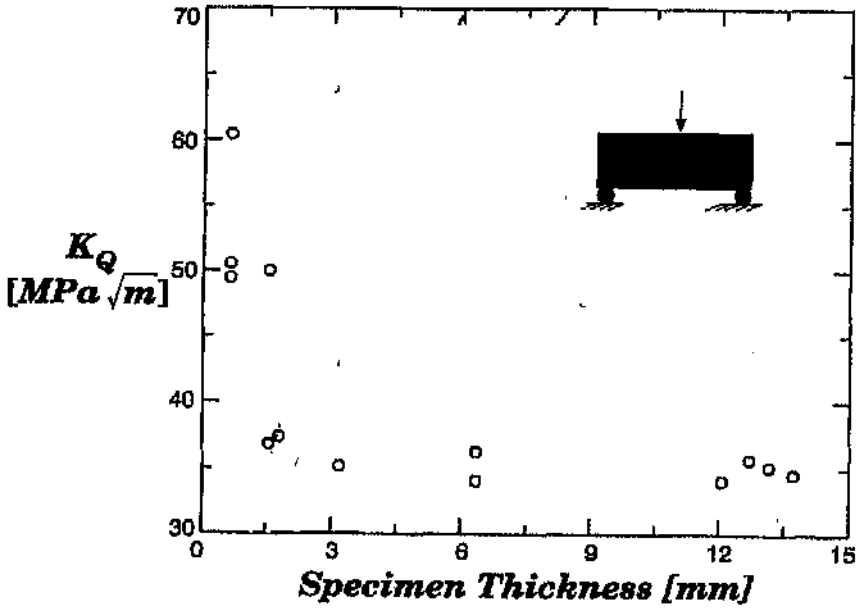


Figure 3.27: Thickness effect on toughness for Ti 6Al-6V-2Sn Titanium alloy after Koppenhoefer et al. (1995) from Jones and Brown (1970).

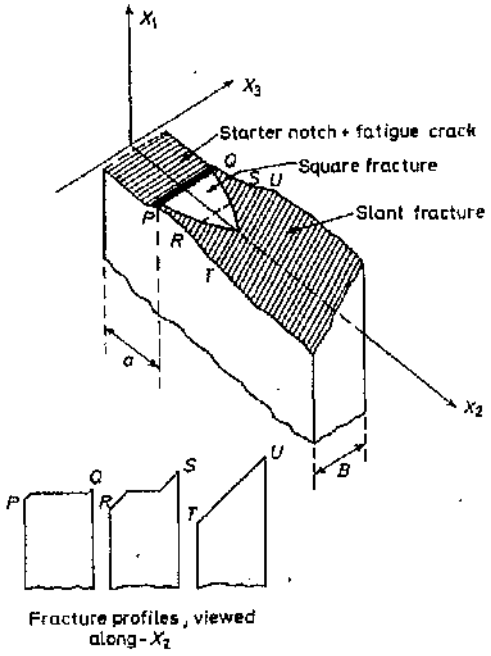


Figure 3.28: Fracture profile in the intermediate B range after Knott (1973).

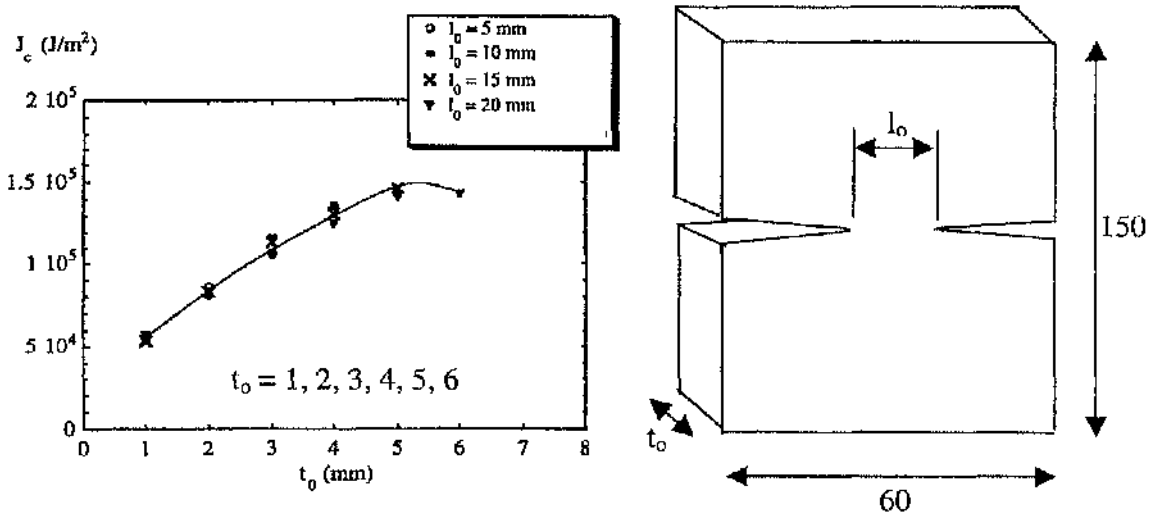


Figure 3.29: The effect of thickness on toughness in Double Edge Notch Tension 6082T0 Aluminium specimens after Pardoen (1999).

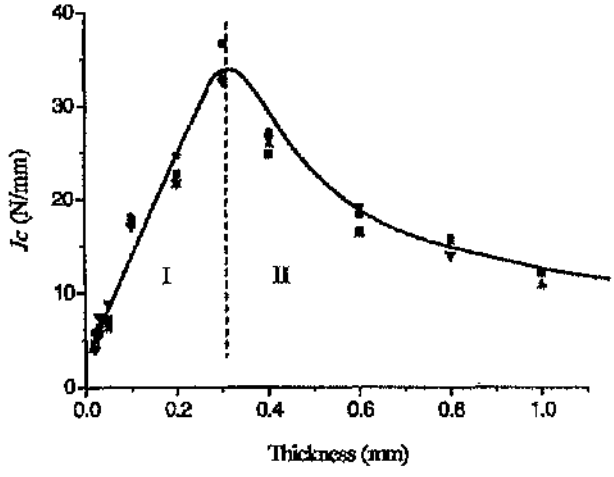


Figure 3.30: The effect of thickness on toughness in Double Edge Notch Tension copper foils after Wang et al. (2003).

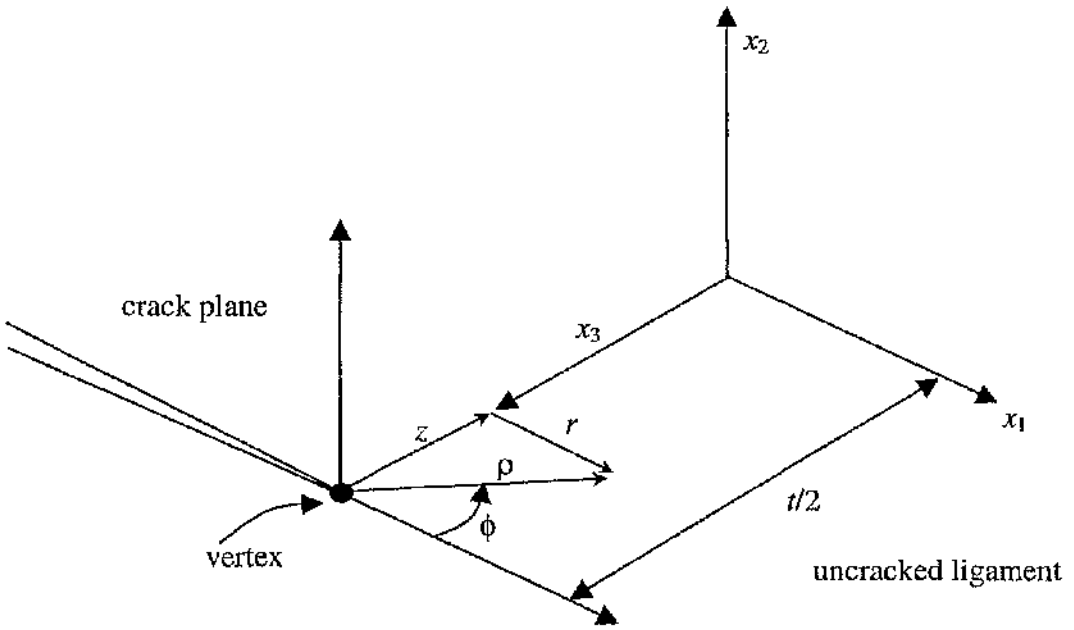


Figure 3.31: Corner singularity co-ordinate system.

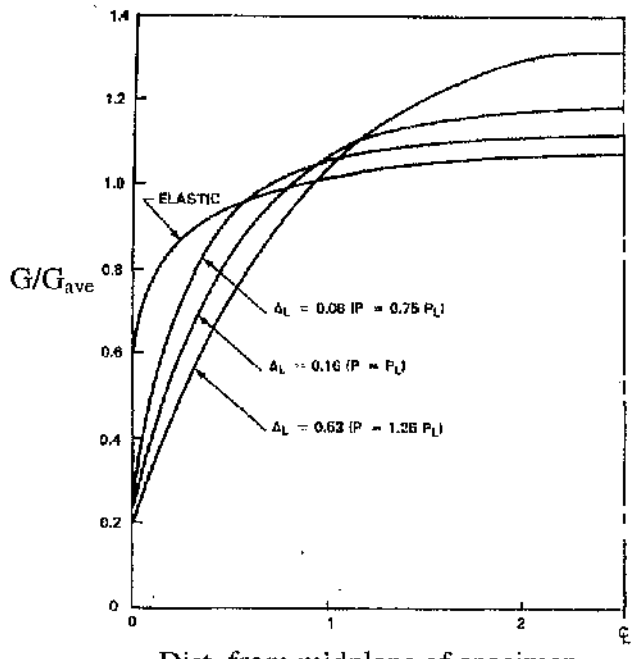


Figure 3.32: Variation of local energy release rate G along the crack front for compact tension specimen after deLorenzi and Shih (1983).

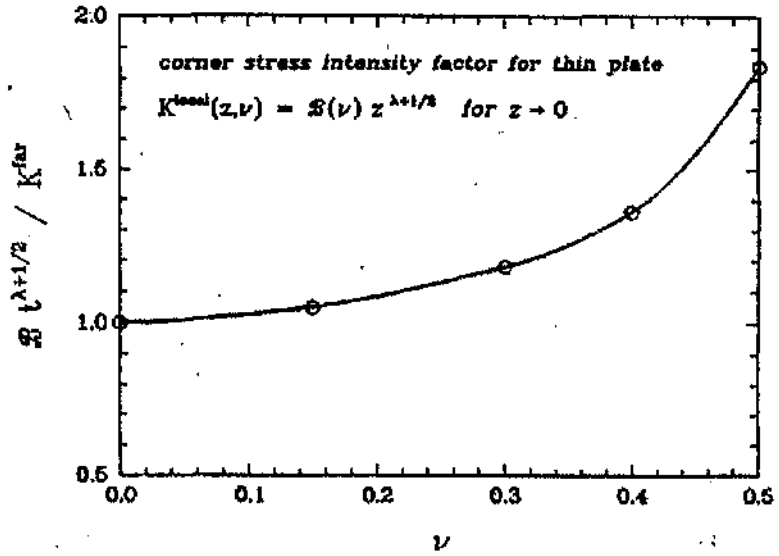


Figure 3.33: The corner stress intensity factor for a thin plate β normalised by $K_{far}$ as a function of Poisson's ratio ν after Nakamura and Parks (1988a).

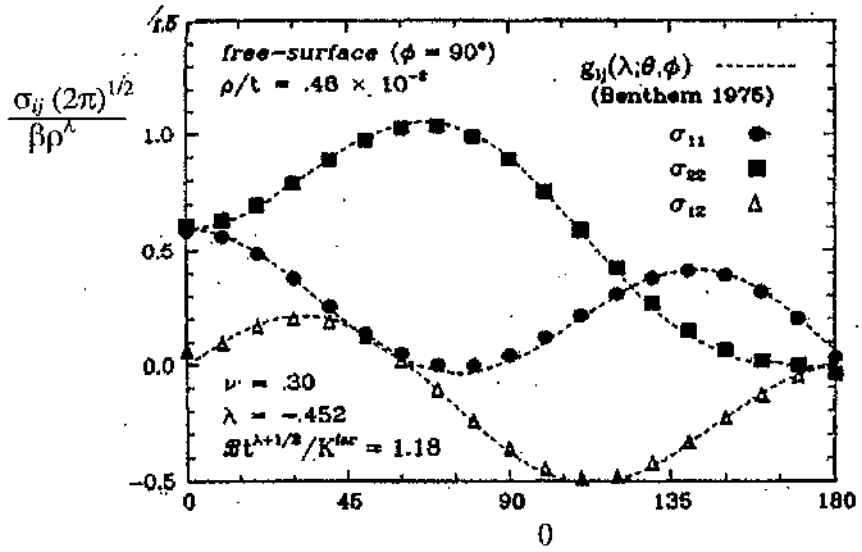


Figure 3.34: The asymptotic field of non-zero stress components normalised by the corner stress intensity factor β very near the intersection of a crack front and the free surface after Nakamura and Parks (1988a). Corresponding functions $g_{ij}$ after Benthem (1975) are shown with broken lines.

# Numerical Methods

This chapter describes the numerical methods used in the current work. These include boundary layer formulations and full-field SENB and CCP specimens in elastic-perfectly plastic conditions. Elastic solutions were compared against the three-dimensional boundary layer formulations of Nakamura and Parks (1988a). Three-dimensional elastic T-stresses have been extracted from the thin plate boundary layer formulation and full-field SENB and CCP solutions for thicknesses B/(W-a) = 1, 0.5 and 0.1 and a/W = 0.5.

## 4.1 Three-dimensional Boundary Layer Formulations.

A cracked geometry similar to that used by Nakamura and Parks (1988a) was adopted to study the three-dimensional stress field along the crack front using a boundary layer formulation method. A circular disk or cylinder was used to model the near tip region of a thin plate with thickness t, as shown in Figure 4.1. The geometry is defined by a system of right handed Cartesian axes $x_1$, $x_2$, $x_3$ centred at the crack-tip on the midplane of the plate ($x_3 = 0$) such that the crack front is located on the $x_3$-axis and the crack flank lies on the plane ($x_2 = 0$; $x_1 \leq 0$). A symmetric quarter of the circular disk (region $0 \leq \theta \leq \pi$, $0 \leq x_3/t \leq 0.5$) was modeled with finite elements, as the problem has reflective symmetry with respect to the midplane ($x_3 = 0$) and the crack plane ($x_2 = 0$). On planes perpendicular to the crack front ($x_1$, $x_2$), the element size was gradually increased with radial distance $r$ from the crack tip, while the angular span of each element was kept constant, $\Delta\theta = \pi/36$, throughout the mesh. An identical planar mesh was repeated along the $x_3$-axis from the symmetry plane ($x_3 = 0$) to the free surface ($x_3/t = 0.5$). To accommodate the variations of field quantities with respect to the $x_3$-axis, the thickness of successive element layers was gradually reduced toward the free surface.

### 4.1.1 Generation of Finite Element Mesh.

Initially, two-dimensional plane strain and plane stress boundary layer formulations models were created using PATRAN (2003) and analysed using ABAQUS (2003). A typical two-dimensional boundary layer formulation mesh is shown in Figure 4.2.

Three-dimensional boundary layer formulations meshes were developed from the two-dimensional meshes using Microsoft Excel. In order to facilitate systematic node and element numbering for the post processing, the numbering order of the two-dimensional mesh was repeated through the thickness by assigning an additive factor to the node numbers across the mesh:

$$\begin{aligned} &rstu_{2D} \quad 2D \text{ assigned numbering} \\ &a\,rstu_{3D} \quad 3D \text{ designated numbering} \end{aligned} \tag{4.1}$$

where $r$, $s$, $t$, $u$ are integers from 0 – 9, $a$ is a numeric system that refers to the layers which constitute the three-dimensional mesh defining the section through the thickness. The assigned numbering refers to the numbering created from Patran (2003) while designated numbering refers to nodal and elemental numbering created in Microsoft Excel spreadsheet.

In contrast to the boundary layer formulations models used by Nakamura and Parks (1990), all the crack-tips were modelled by 19 coincident but independent nodes. It was found that the scheme proposed by Nakamura and Parks (1990) which used a crack tip notch in the outer-model significantly altered the displacement field near the crack tip and elevated the crack tip stresses in the tip-model. Substructured models with notches did not recover the remotely applied elastic plane stress field. When the outer and intermediate meshes had coincident but independent crack tip nodes, the normalised opening stress converged to the plane stress solution at r/t > 1.5 as shown in Figure 4.9 in accord with the results of Nakamura and Parks' (1988a) elastic solution. It may be speculated that the notch in

Nakamura and Parks (1990) analyses was needed because the mesh at crack tip could not meet the necessary element aspect ratios.

To achieve a highly refined crack tip mesh with suitable element aspect ratio, three substructured finite element meshes were employed. The loading applied to the coarse mesh was used to drive an intermediate mesh which was used to drive a refined crack tip mesh. The three meshes are referred as the outer-mesh, the middle-mesh and the near tip-mesh respectively.

The finite element models are shown in Figure 4.3 (a), (b) and (c). The outer-mesh had a radius to thickness ratio, $r_{max}/t$ = 100 ($r_{max}$ = 50000, $t$ = 500), in which, one layer element modelled the entire disk in the quarter-half space. The outer-mesh consisted of 360 elements (18 circumferential x 20 radial in-plane elements) arranged in a single layer through the half thickness) using 800 nodes.

The middle-mesh had a radius to thickness ratio, $r_{max}/t$ = 18 ($r_{max}$ = 9000, $t$ = 500), in order to capture the transitional field variation between plane stress applied field in the outer-mesh to the plane stress state near the crack tip as the crack front in the tip-mesh was approached (Levy, Marcal and Rice (1971), Nakamura and Parks (1988a)). Five element layers were built up in the through thickness direction ($x_3$) with a thickness of (t = 50) for each layer. The middle-mesh consisted of 1350 elements (18 circumferential x 15 radial in-plane) defined by 1800 nodes.

The tip-mesh had a radius to thickness ratio, $r_{max}/t$ = 5 ($r_{max}$ = 2500, $t$ = 500). It is important to increase the density of the mesh near the crack tip because this determines the accuracy of the results. As the mesh must be able to analyse elastic-plastic contained yielding problems, the radius of the disk relative to the thickness was chosen so that the plastic zone remained well contained within the outer boundary. Sixteen element layers were build up in $x_3$ direction with thicknesses 20, 20, 20, 20, 20, 20, 20, 20, 20, 16, 16, 12, 10, 6, 5, 5 toward the free surface. The tip-mesh comprised of 7776 elements (18 circumferential x 27 radial in plane) arranged in 16 layers through the half thickness and 9520 nodes. The radial

extent of the outer boundary was approximately 2500 or $5t$, while the crack-tip elements had a radial extent of 2 or $0.004t$. The thickness of the element adjoining the free surface was 5 or $0.01t$.

To analyse crack tip stress and strain fields within the small-scale yielding, the tip-mesh must have radius greater than r/t = 10 to ensure numerical stability at the point of nodal interpolation in substructuring. A second crack tip mesh was setup to allow plasticity to extend to r/t = 10 while allowing the interpolation of nodal variables in an elastic domain near to the plastic small-scale yielding boundary. The second tip-mesh consisted of thirteen element layers build up in $x_3$ direction with relative thicknesses 20, 20, 20, 20, 20, 20, 20, 20, 20, 20, 18, 16, 16 toward the free surface.

All the meshes (out-mesh; middle-mesh; near tip-mesh) were built from 8 noded trilinear hexahedron isoparametric brick elements, using reduced integration and linear pressure interpolation (ABAQUS (2003) element type C3D8RH). The 8 noded trilinear hexahedron elements were collapsed at the crack tip to give four coincident but independent nodes as shown in Figure 4.4 by the element denoted by *B*. Elements elsewhere in the mesh follow the structure represented by element *A*.

### 4.2 Three-dimensional Full-field SENB and CCP models

The ability of boundary layer formulations to model crack tip plasticity is limited by the requirement that the plastic zone must be confined within one-tenth of the radius of the outer boundary, Rice (1973). In order to carry out elastic-plastic analysis beyond small scale yielding and into full plasticity, full-field solutions of standard plane strain fracture toughness specimens have been developed. Single edge notched specimens in three point bending (SENB) and centre crack tension panels (CCP) were built using the boundary layer formulation node and element scheme. The full-field models are shown in Figure 4.5 which defines the notation used in the present work. For the SENB and CCP specimens, the crack lengths are $a$ and $2a$ and the widths are $W$ and $2W$ respectively while the thickness is $B$. It should be pointed out that the thickness is also referred as $t$. The half

length of the specimen $L$ was 3000. To consider the effect of thickness, three values of B/(W-a) were considered: B/(W-a) = 1, 0.5 and 0.1. The geometry B/(W-a) = 1, a/W = 0.5 corresponds to the standard plane strain fracture toughness test specimen.

Figure 4.6 illustrates the three-dimensional full-field finite element meshes. The nodal and elemental configurations in SENB and CCP models are similar but differ in the boundary conditions applied. The radial extent in the domain used for data analysis was 250 or $0.5t$, the crack-tip element had a radial extent of 2.0 or $0.004t$, and the thickness of the element adjoining the free surface was 5 or $0.010t$ for B/(W-a) = 1, 4; $0.016t$ for B/(W-a) = 0.5, and 2 or $0.040t$ for B/(W-a) = 0.1.

Each element layer through the thickness, comprised of 850 elements. The element layers were stacked according to the total thickness required and the ability to control the aspect ratio to provide a gradual reduction of element thickness from the midplane towards the free surface plane. At the crack tip, there were 19 coincident but independent nodes.

For the thickest model {B/(W-a) = 1}, 20 element layers were build up in the $x_3$ direction with layer x thickness setup (13 x 16, 1x 12, 3 x 10, 1 x 6, 2 x 5) from the midplane to the free surface. For the medium thickness model {B/(W-a) = 0.5}, 18 element layers were build in the $x_3$ direction with layer x thickness setup (12 x 8, 1 x 6, 3 x 5, 2 x 4). For the thin model {B/(W-a) = 0.1}, 9 element layers were built in in the $x_3$ direction using layer x thickness setup (1 x 4, 5 x 3, 3 x 2).

### 4.3 Loading Conditions

In the three-dimensional thin plate boundary layer formulations, an elastic plane stress field was applied on the nodes of the outer perimeter of the outer model shown in Figure 4.3(a). The in-plane displacement $u_1$ and $u_2$ are given by equation (2.73) while the displacement in the out-of-plane $u_3$ direction was left to develop freely. With or without the application of the remote out-of-plane displacement, $u_3$, the crack tip stress field can

develop a similar out-of-plane local kinematic at crack tip. Similar observations have been made by Kim et al. (2001).

The outer-mesh was used to drive the middle-mesh shown in Figure 4.3(b) through nodal interpolation of the displacement of the nodes at the perimeter of the middle-mesh boundary. The computed nodal displacement of the near tip-mesh boundary shown in Figure 4.3(c) was driven by displacements interpolated from the middle-mesh. The near tip-mesh was used to obtain accurate solutions near the crack front and at the intersection of the crack front with the free surface. Nodal interpolation was achieved through the ABAQUS (2003) submodeling analysis card.

For the full-field model, loading was applied by line displacements $u_1$ across the thickness of a three-point-bending specimen. In the CCP models, a uniform tensile displacement $u_2$ was applied normal to the crack flank on the outer surface of the model.

### 4.4 Computational Procedure

The numerical method employed in the present analyses is the finite element method. In linear and nonlinear analysis, the code initially discretised the problem and then linearised the governing equations so that non-linear problems are solved incrementally as a sequence of linear problems. Typical elastic-plastic analyses used about a thousand increments to generate the complete response. Numerical results were generated using a Dell Precision 450 series workstation with Intel Xeon processor 3.06 GHz with CPU processing speed of 512 KB integrated level 2 cache. The central processing unit is equipped with system memory of 2 Gbyte which operates at 266 MHz. A disk space of at least 100 Gbyte is required to store the processed data. Typically a 9000 element boundary layer formulation model or a 16000 elements full-field model required 5 to 7 hours of clock time.

Under the near incompressible conditions associated with plastic flow, the use of reduced integration hybrid elements, combined with a Poisson's ratio with a small departure from perfect incompressibility, $\nu = 0.49$, helped to avoid mesh locking problems. Analysis was

based on infinitesimal strain theory using incremental plasticity and the modified B-bar method discussed in Nakamura et al. (1986) to stabilise the model against spurious pressure modes. In ABAQUS, the stabilisation procedure was carried out using a "*S*tabilise*" card employing a weighting factor of .0001 together with the "*Static*" analysis card. This method was employed for all geometries and material responses to obtain consistent results.

### 4.5 Material Response

The elastic-perfectly plastic material response, was based on uniaxial idealisation of the form:

$$\sigma = E\sigma \qquad \sigma \le \sigma_o \tag{4.2}$$

$$\sigma = \sigma_o \qquad \sigma \ge \sigma_o \tag{4.3}$$

Here $\sigma$ is the uni-axial stress, $\sigma_o$ is the yield stress, $\varepsilon$ is strain and $E$ is Young's modulus. For purely elastic analyses, equation (4.2) is applicable while both equations (4.2 - 4.3) are applicable for an elastic-perfectly plastic material response as shown in Figure 4.7. The material was homogenous isotropic with a Poisson's ratio of 0.49 giving a nearly incompressible response. A Poisson's ratio 0.3 was also used for the purpose of comparing solutions to those available in the literature.

The uni-axial stress-strain relations were generalised for multi-axial stress states of stress using the Mises yield criterion with an associated flow rule and incremental plasticity within a framework of small displacement deformation theory. Numerical calculations were performed with Young's modulus, $\sigma_o/\varepsilon_o = E$, of 200 GPa and yield stress, $\sigma_o$, of 200 MPa, although non-dimensional results are always presented to allow general applicability of the results.

## 4.6 Benchmarking of Three-Dimensional Models

Two-dimensional elastic solutions are widely available and have been extensively applied in engineering applications. In contrast, three-dimensional crack analyses are complex and difficult. To ensure the three-dimensional solutions are credible, the results of three-dimensional elastic analyses are now compared with well established three-dimensional analyses and two-dimensional plane strain solutions.

### 4.6.1 Boundary Layer Formulations

The three-dimensional boundary layer formulations crack tip models have been developed with the purpose of analysing elastic-plastic solutions. Before directly embarking on elastic-plastic solutions, it is important to verify that the model can produce results in linear elastic cases. Well established results in three-dimensional thin plate boundary layer formulations have been given by Nakamura and Parks (1988a).

The comparison was initially carried out by analysing the opening stress as a function of distance ahead of the crack front at the midplane, and at the free surface, as shown in Figure 4.8 for Poisson's ratio 0.49. Similar plots from Nakamura and Parks (1988a) are shown in Figure 4.9. The midplane and the free surface values in the three-dimensional boundary layer models agree within 2 percent of Nakamura and Parks's (1988a) results. Another benchmarking comparison was made on the asymptotic stress very near the crack front. Figures 4.10 and 4.11 show the asymptotic stress field for Poisson's ratio 0.3 and 0.49 while the Nakamura and Parks (1988a) data are shown in Figure 4.12. The asymptotic stress fields are compared with the angular distributions of stress for a mode I given in equation (2.72). For both Poisson's ratios, the asymptotic fields behave identically to the two-dimensional solution as well as the three-dimensional solution of Nakamura and Parks (1988a).

Nakamura and Parks (1992) gave the biaxiality parameter in a thin plate boundary layer formulation for various Poisson's ratio as shown in Figure 3.1. The effect of the three-

dimensional T-stress for $\nu = 0.3$ and 0.49 are shown in Figure 4.13. The current solutions correlate well with those of Nakamura and Parks (1988a) for both Poisson's ratios.

It has been demonstrated that the substructured three-dimensional models can be used to analyse the three-dimensional crack tip stress and strain fields under largely incompressible response. This is important to ensure the model will be able to analyse incompressible plastic flow. The benchmarking results for boundary layer formulation are summarised in Table 4.2.

### 4.6.2 Full-Field Solutions

The three-dimensional full-field SENB and CCP solutions have been benchmarked using the stress intensity factor, K, the biaxiality function, $\beta$, and the T-stress concentration factor, $T/\sigma_{app}$.

In three-dimensional fields, the local J or K varies along the crack front. However, a local plane strain condition has been shown to be approached on the midplane ($x_3/t = 0$). Therefore the calculation at the midplane for SENB and CCP models have been benchmarked against the two-dimensional plane strain solution. The benchmarking is carried out by comparing the calculated shape functions, $f$ (a/W), to shape function published in standard stress intensity factor handbooks. Using Tada et al. (1985), the non-dimensional shape function for single edge notch bend (SENB) specimens is given in equation (2.75) while the shape function for centre crack panel (CCP) as a function of a/W is given in Table 2.1. The shape functions, $f$(a/W), for a/W = 0.5 are 1.46 and 1.18 for SENB and CCP specimens.

To calculate the shape function from the three-dimensional models, the stress intensity factor in terms of the J-integral can be changed to represent the stress intensity factor, K in plane strain using:

$$K = \sqrt{\frac{E\,J}{(1-\nu^2)}} \tag{4.4}$$

The shape function $f(a/W)$ is related to the stress intensity factor, K, as given in equation (2.74). The applied stress, $\sigma_{app}$, for SENB geometries can be determined through bending moment following Lianis and Ford (1958):

$$M = \frac{\sigma_{app} B(W-a)^2}{4} \tag{4.5}$$

where M is the bending moment, B is thickness of the plate, W is the ligament length and a is the crack length. The moment, M, is determined from the reaction force, RF, parallel to the crack flanks :

$$M = RF\frac{S}{2} \tag{4.6}$$

S is the span from load to crack flanks.

The applied stress in the three-dimensional CCP models can be determined from the remote reaction force from the three-dimensional model, RF :

$$\sigma_{app} = RF/WB \tag{4.7}$$

The applied load in the centre crack tension panel can be calculated from the applied stress, $\sigma_{app}$, per unit thickness is :

$$P = \sigma_{app} W \tag{4.8}$$

Shape functions from the three-dimensional models are shown to be 1.4 and 1.27 which are accurate to 4 percent. A similar observation was made for the CCP specimen where the shape function was accurate to 7 percent. However, benchmarking based on shape functions $f(a/W)$ is useful only when crack tip plasticity is negligible. In small scale yielding, crack tip plasticity is known to be affected by the T-stress and another benchmark used the biaxiality factors.

The biaxiality factors for plane strain SENB specimen given by Sham (1991) are tabulated in Tables 2.2. For a/W = 0.5, the biaxiality factor is 0.216. However, the T-stress in three-dimensional crack tip field is strongly affected by the Poisson's ratio and the thickness of the plate as discussed by Nakamura and Parks (1992). Therefore a plane strain biaxiality factor can be defined by taking accounts the effects of Poisson's ratio and thickness following equation (3.7). Using equation (3.7), the biaxiality factor for SENB becomes 0.341. The three-dimensional SENB model biaxiality function is 0.37 which demonstrate a correlation accurate to 8 percent.

The T-stress concentration factor, $T/\sigma_{app}$, can be obtained from the plane strain shape function of Sham (1991) by subtituting equation (2.74) into equation (2.144) to give:

$$\frac{T}{\sigma_{app}} = \beta f\left(\frac{a}{W}\right) \tag{4.9}$$

The plane strain SENB T-stress concentration factor is $T/\sigma_{app} = 0.497$. The calculated three-dimensional elastic SENB $T/\sigma_{app}$ is 0.52 which is accurate to 5 percent. The benchmark parameters for the full-field SENB specimens are tabulated in Tables 4.3.

As the SENB and the CCP finite element meshes are related, the same accuracy should be expected for both. These are reflected in the biaxiality functions and T-stress concentration factors as a function of thickness for different SENB and CCP specimens thickness as illustrated in Figures 4.14 to 4.17. The thickness effect indicates that the biaxiality function and the T-stress concentration factor approach the plane strain values as the thickness is

increased in both the SENB and CCP specimens. From a different perspective, the biaxiality factor and the stress concentration factor are inversely related to the thickness. This is due to the inherent positive T-stress in thin plates as observed by Nakamura and Parks (1992) and indicated by Sherry et al. (1995).

Although the T-stress is significantly affected by Poisson's ratio and the plate thickness, the shape function based on the stress intensity factor, K, correlates well with existing data. Therefore, it can be argued that the three-dimensional models produce acceptable results.

## 4.7 Conclusions

Three submodels were used to model a cracked thin plate using boundary layer formulations. To produce accurate crack tip kinematics, the submodels employ coincident and independent crack tip nodes in contrast to the Nakamura and Parks (1990) model which employed a notch in the outer-model. The advantage of the technique is the ability to simulate elastic and elastic-plastic analyses using the same model by changing the applied loads and material properties.

The benchmark calculations show that the three-dimensional models have been able to recover the behaviour of three-dimensional field in the way identified by Nakamura and Parks (1988a). The full-field solutions which used a similar crack tip mesh configuration to the boundary layer formulation have been shown to predict the two-dimensional plane strain parameters in an acceptable manner.

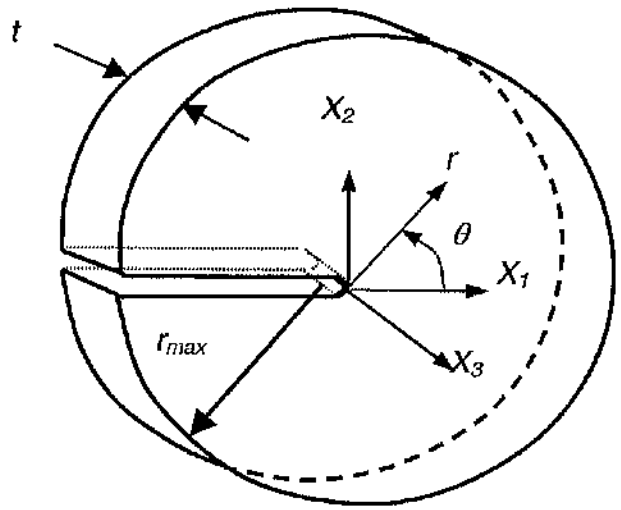


Figure 4.1: Circular disk representing a thin cracked plate.

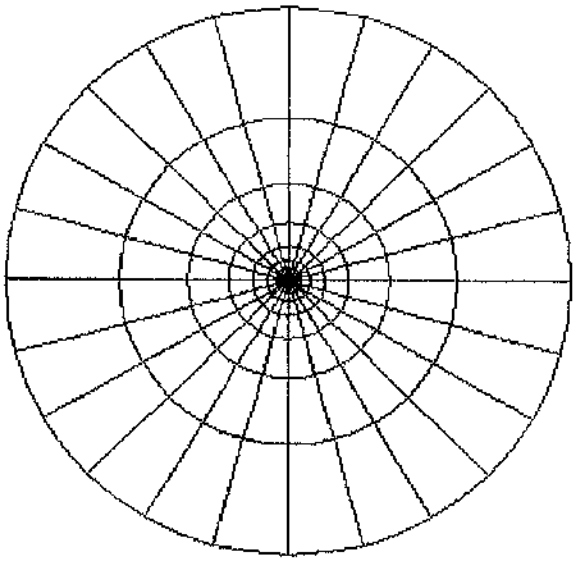

Figure 4.2: Typical two-dimensional boundary layer formulations mesh.

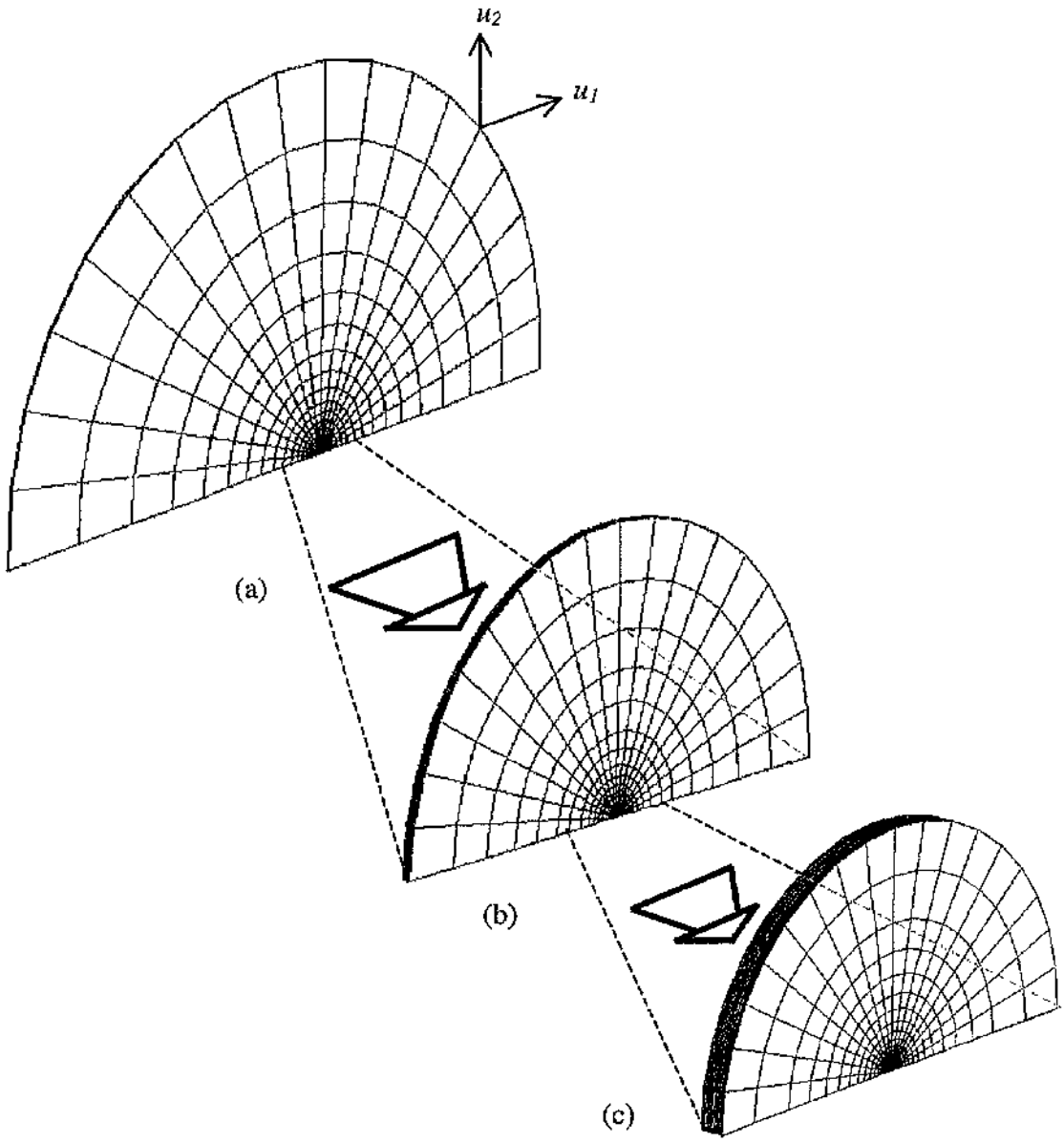


Figure 4.3: Boundary Layer Formulation model in quarter half space for (a) Outer-mesh, (b) Middle-mesh and (c) near Tip-mesh.

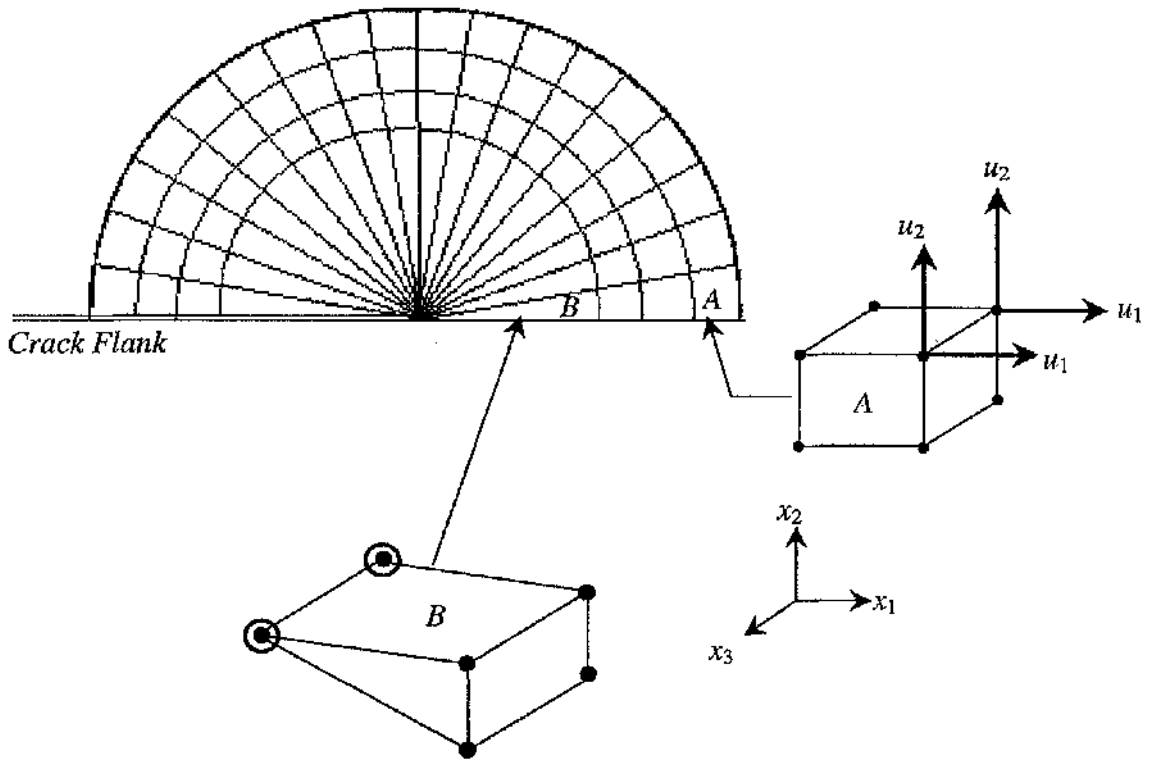


Figure 4.4: Boundary layer formulation finite element mesh, three-dimensional element and boundary conditions applied to the nodes.

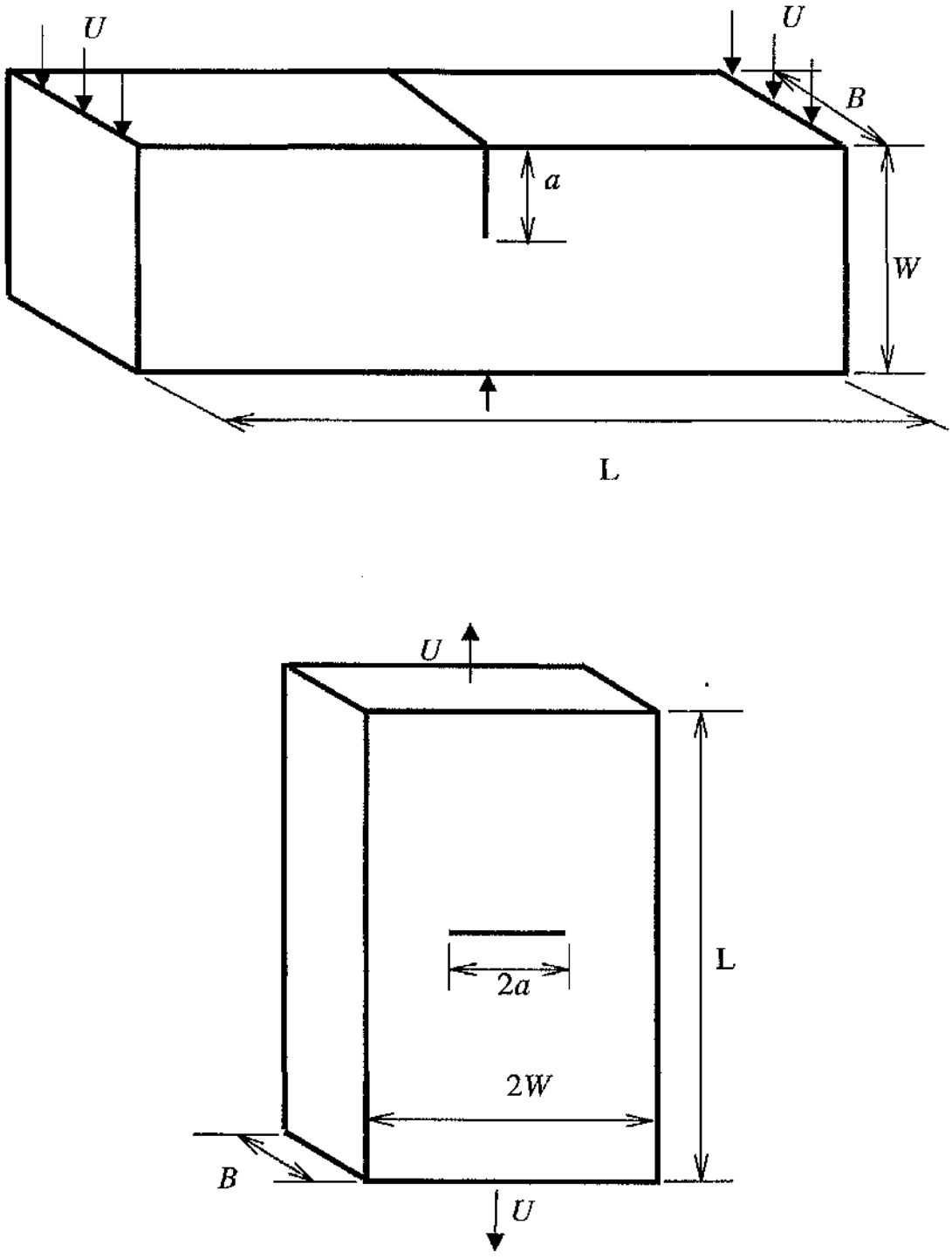


Figure 4.5: Geometry of the SENB and CCP specimens.

| | a | W | B | L |
|---|---|---|---|---|
| B/(w-a) = 1 | 500 | 1000 | 500 | 3000 |
| B/(W-a) = 0.5 | 500 | 1000 | 250 | 3000 |
| B/(W-a) = 0.1 | 500 | 1000 | 50 | 3000 |

Table 4.1: Dimensions of the SENB and CCP specimens.

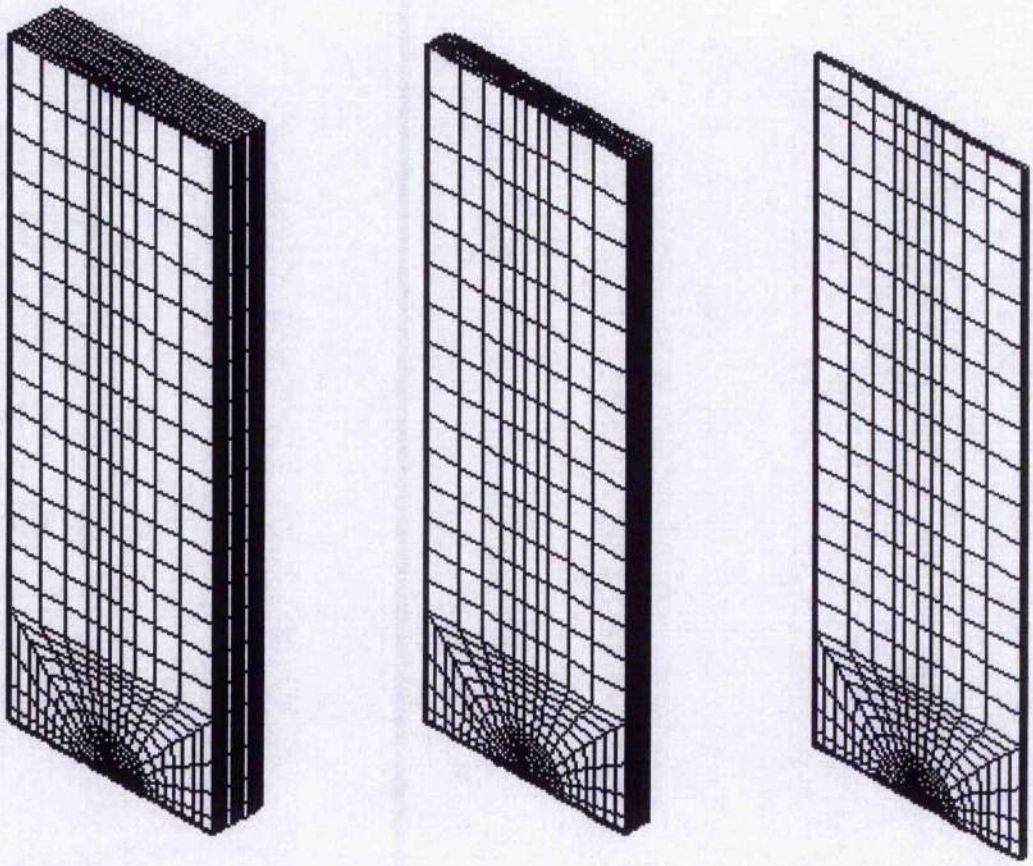

(a) B/W-a = 1 (b) B/W-a = 0.5 (c) B/W-a = 0.1

Figure 4.6: Three-dimensional full-field models.

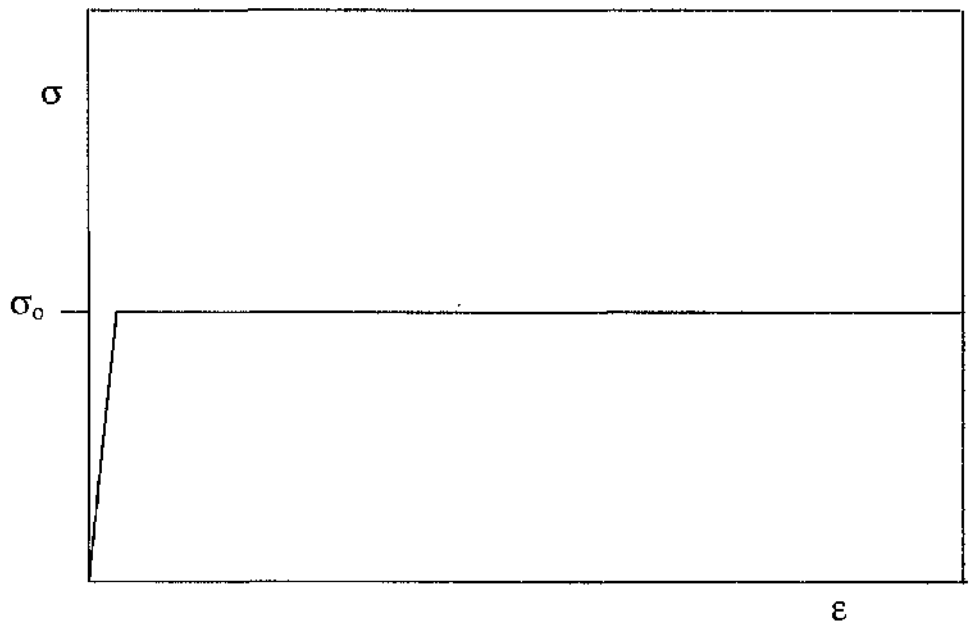


Figure 4.7: Stress-Strain curve for an elastic-perfectly plastic material.

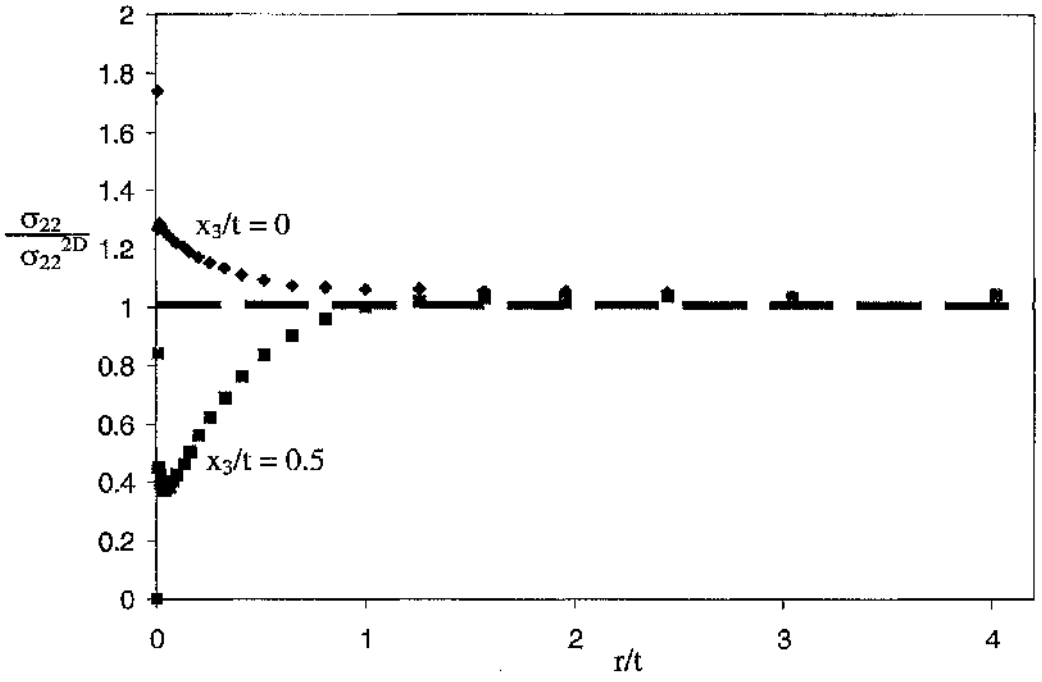


Figure 4.8: The opening stress ahead of the crack front at the midplane and the free surface for Poisson's ratio 0.49 normalised by the two-dimensional plane stress solution. The broken line indicates $\sigma_{22}/\sigma_{22}^{2D} = 1$.

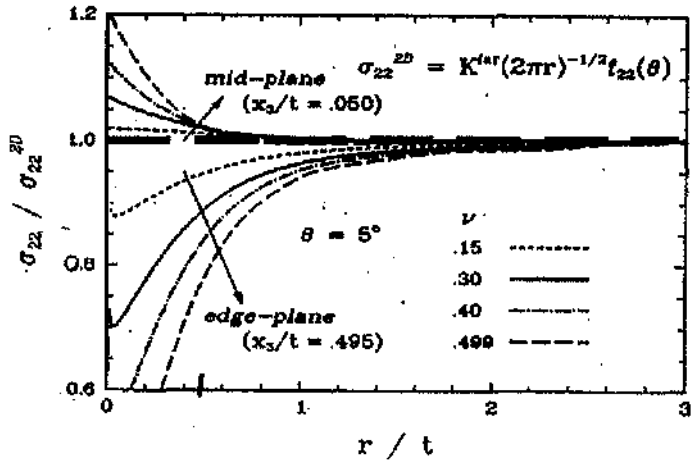


Figure 4.9: The opening stress ahead of the crack front at the midplane and the free surface for various Poisson's ratio after Nakamura and Parks (1988a). A broken line is drawn at $\sigma 22/\sigma_{22}^{2D}$ which indicate a constant value is reached for all Poisson's ratio at $r/t > 1.5$.

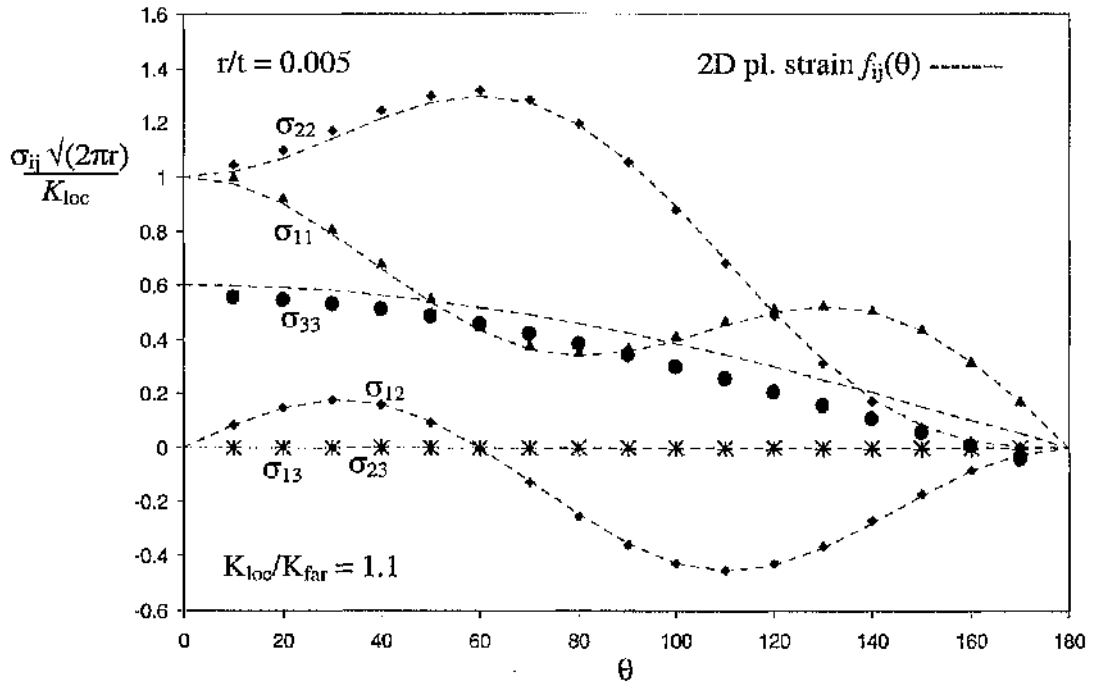


Figure 4.10: The asymptotic plane strain behaviour at the midplane $x_3/t = 0$ with Poisson's ratio = 0.30 compared to the two-dimensional plane strain solution.

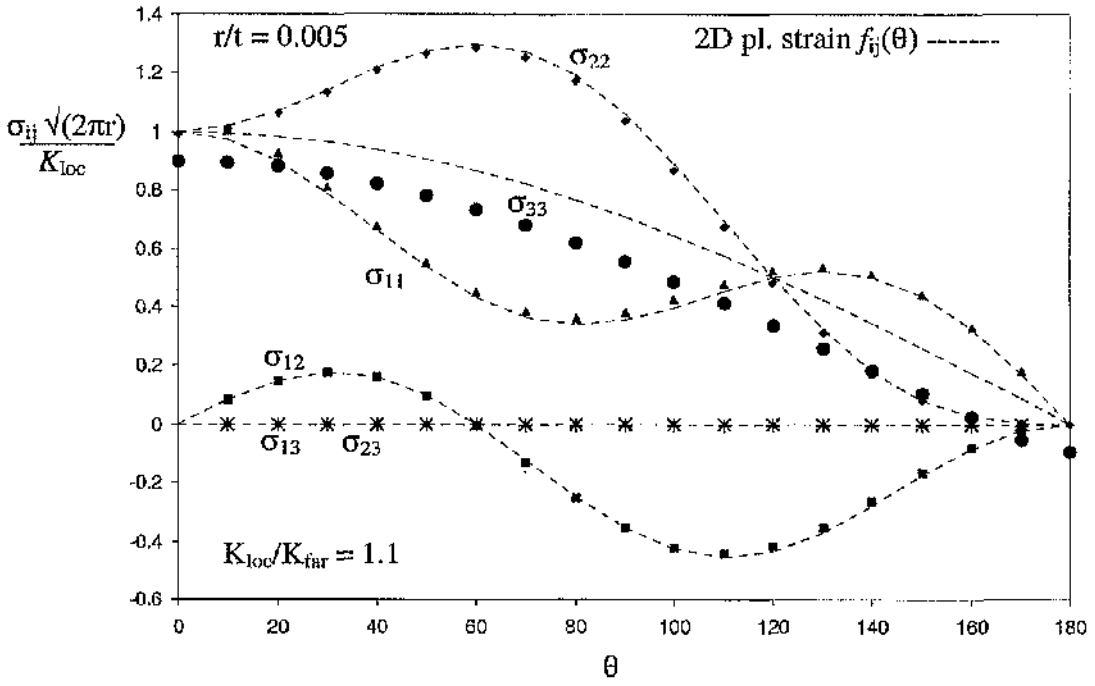


Figure 4.11: The asymptotic plane strain behaviour at the midplane $x_3/t = 0$ with Poisson's ratio = 0.49 compared to the two-dimensional plane strain solution.

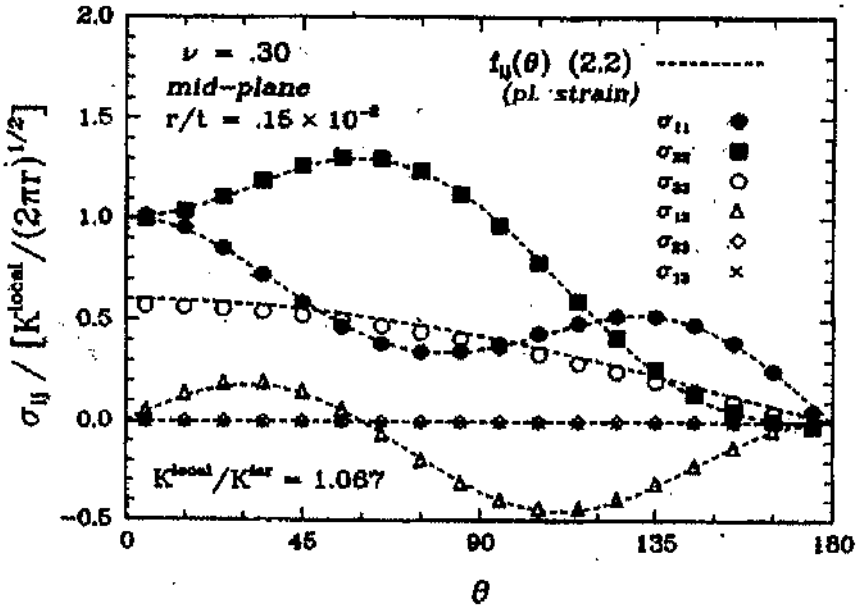


Figure 4.12: The asymptotic stress field for a thin plate boundary layer formulation at the midplane with Poisson's ratio, ν = 0.3 after Nakamura and Parks (1988a).

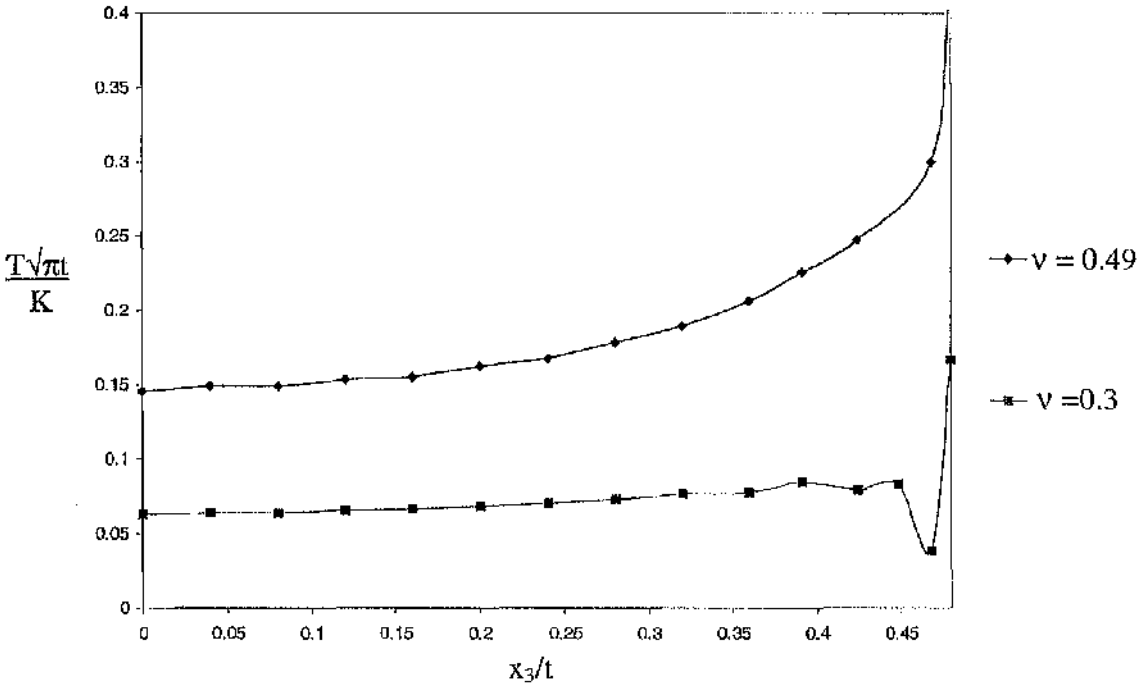


Figure 4.13: Variation of the biaxiality factor, β, along the crack front in a thin plate for Poisson's ratios, ν = 0.3 and 0.49.

| | Nakamura and Parks | 3-D BLF | Correlation |
|---|---|---|---|
| $\sigma_{22}/\sigma_{22}^{2D}$ at $r/t > 1.5^*$ | 1 | 1 | 1 |
| $\nu = 0.49$, $\beta$ $(x_3/t = 0)^\#$ | 0.14 | 0.14 | 1 |
| $\nu = 0.3$, $\beta$ $(x_3/t = 0)^\#$ | 0.05 | 0.05 | 1 |

Table 4.2: Three-dimensional thin plate boundary layer formulation elastic solution compared against Nakamura and Parks (1988a and 1992 solutions, which are represented as * and #).

| | 2-D Pl. Strain | SENB; B/(W-a) = 1 | Correlation |
|---|---|---|---|
| $f(a/W) = K/(\sigma_{app}\sqrt{(\pi\, a)})$ | 1.46 | 1.4 | 0.96 |
| $\beta = (T\sqrt{(\pi a)})/K$ | 0.341 | 0.37 | 0.92 |
| $T/\sigma_{app}$ | 0.497 | 0.52 | 0.95 |

Table 4.3: SENB elastic correlation for plane strain and three-dimensional models B/(W-a) = 1 with a/W = 0.5 at the midplane ($x_3/t = 0$).

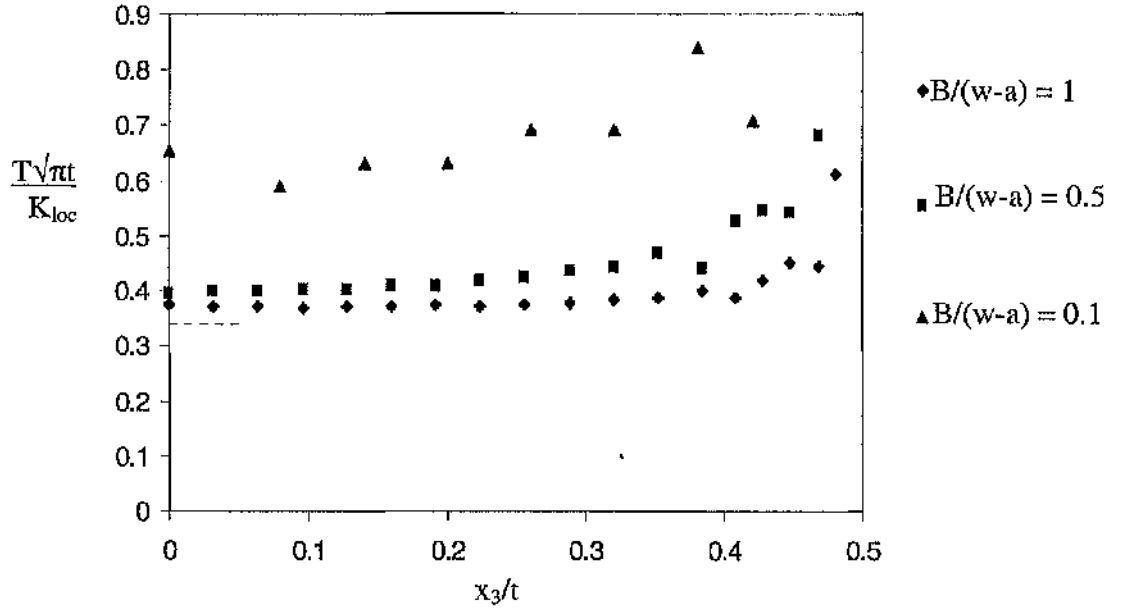


Figure 4.14: The variation of the biaxiality parameter, β, along the crack front in SENB specimen with thickness B/(W-a) = 1, 0.5 and 0.1. The broken line shows the plane strain biaxiality factor calculated using equation (3.7).

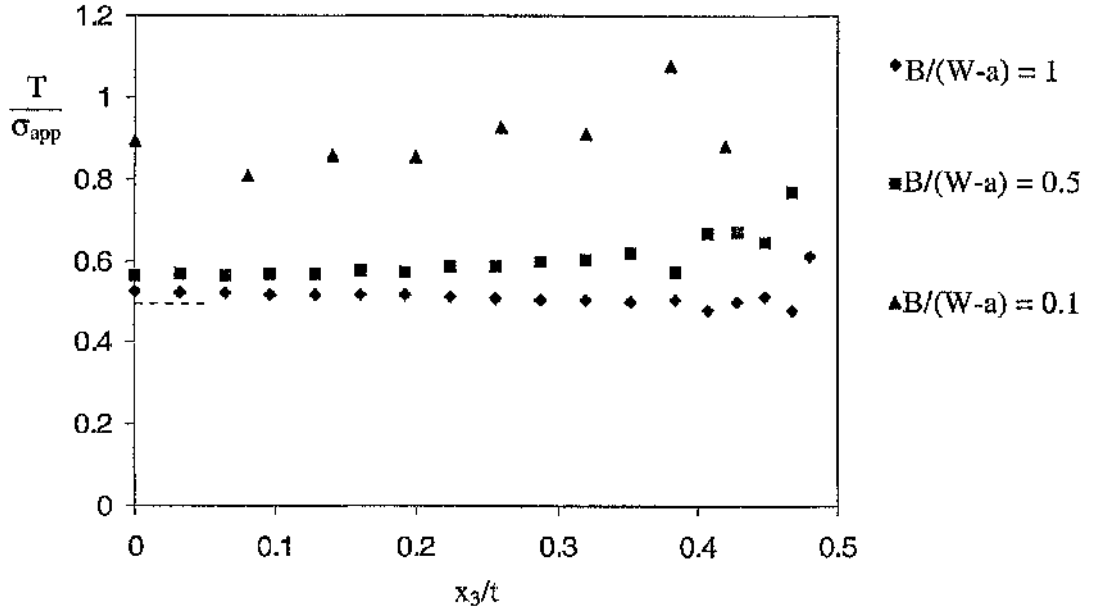


Figure 4.15: The variation of the stress concentration factor, $T/\sigma_{app}$, along the crack front in SENB specimen of thickness B/(W-a) = 1, 0.5 and 0.1. The broken line shows the plane strain $T/\sigma_{app}$ factor calculated using equation (4.11).

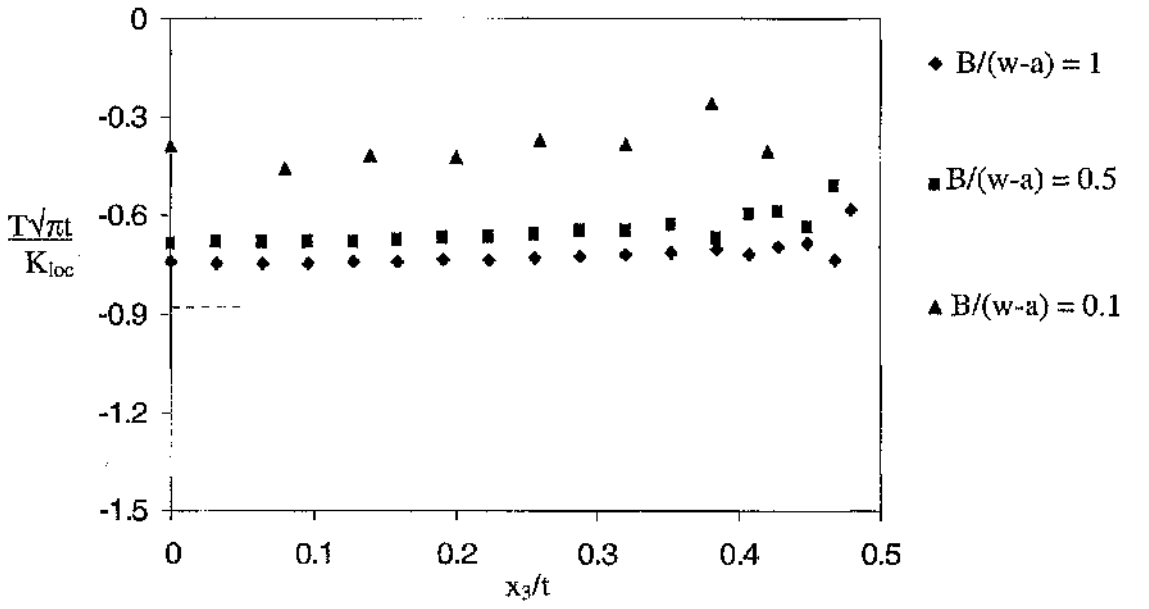


Figure 4.16: The variation of the biaxiality parameter, β, along the crack front in a CCP specimen of thicknesses B/(W-a) = 1, 0.5 and 0.1. Broken line shows the plane strain biaxiality factor from equation (3.7).

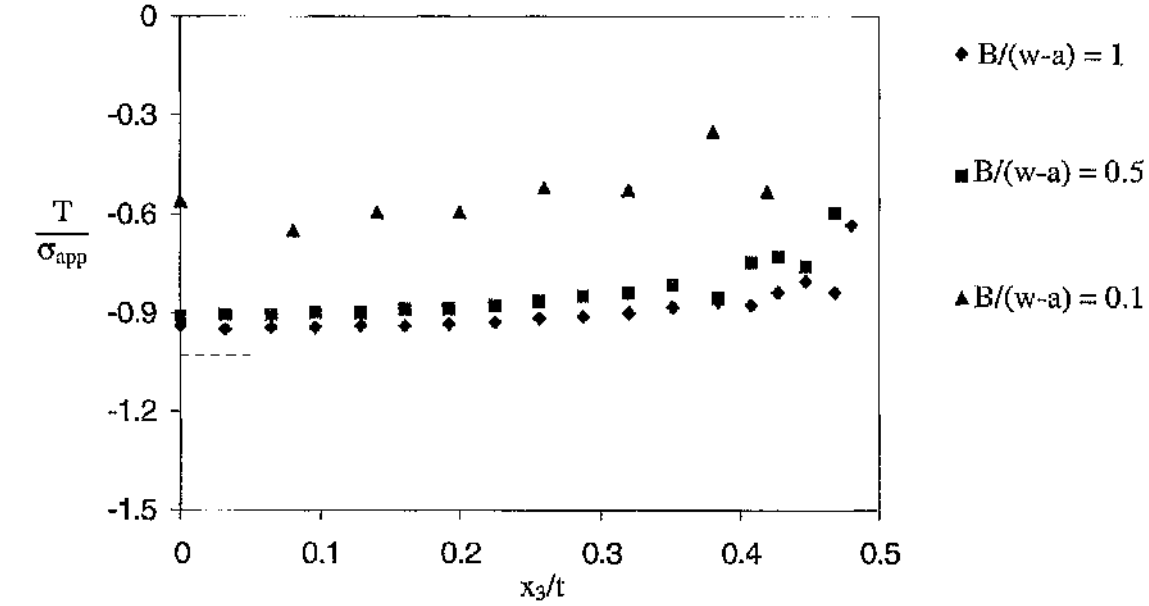


Figure 4.17: The variation of the stress concentration factor, $T/\sigma_{app}$, along the crack front in a CCP specimen of thicknesses B/(W-a) = 1, 0.5 and 0.1. Broken line shows the plane strain $T/\sigma_{app}$ factor from equation (4.11).

# Three-Dimensional Elastic-Plastic Fields

The structure of three-dimensional crack tip fields is a fundamental issue in fracture mechanics. Although a number of studies of three-dimensional elastic-plastic crack tip fields exist in the literature, conclusive results have been elusive due to problems with the numerical stability of three-dimensional numerical models and the interaction between in-plane and out-of-plane effects. In this chapter, the nature of the elastic-perfectly plastic mode I three-dimensional crack tip field has been studied systematically using boundary layer formulations. These solutions are complemented by full-field analyses of deeply cracked bend bar and centre crack panels in varying thicknesses (B/(W-a) = 1, 0.5 and 0.1) while maintaining the crack to ligament ratio at a/W = 0.5. The three dimensional fields are compared with the plane strain small scale yielding field, and the plane stress slip line fields as limiting two dimensional solutions. Within this context the analysis addresses evolution of crack tip fields from the centre of the plate (mid-plane) to the free surface, as well as the way in which the structure of the fields changes from small scale yielding to full plasticity. The analyses inevitably produce a large amount of fundamental data which is presented in this chapter. Subsequent chapters draw out systematic and unifying trends in the data leading finally to a simple constraint estimation scheme.

The results are presented in three sections. Section 5.1 discusses crack tip deformation and the development of plasticity at the crack tip. Section 5.2 initially describes the asymptotic field at the crack tip, ($r = 0$) and at $r = 2J/\sigma_o$. This section is sub-structured into sections which consider; boundary layer formulations; modified boundary layer formulations, deeply cracked bend bars, and finally centre cracked panels. Section 5.3 focuses on two important stress components which control fracture toughness: the mean or hydrostatic stress and the maximum principal stress. Interest is focused on the plane directly ahead of the crack ($\theta = 0^o$), and the way on which the stress field changes with distance. Section 5.4 discusses the proximity of the three dimensional fields to the plane strain and the plane stress fields using boundary layer formulations; deeply cracked bend bars and centre

cracked panels. Finally a systematic pattern of constraint loss in three-dimensional crack tip field emerges which is discussed in Chapters 6 and 7.

## 5.1 Crack Tip Deformation and Plasticity

In this section, the evolution of the plastic zone at the crack tip is described from small scale yielding to full plasticity. The shape of the plastic zone is compared with plastic zone shapes from two-dimensional plane strain and plane stress analyses.

### 5.1.1 Crack Tip Deformation

#### 5.1.1.1 Boundary Layer Formulations

An elastic-perfectly plastic analysis of the crack tip field in a thin plate has been carried out using three-dimensional boundary layer formulations. The model is shown in Figure 4.3 (a), (b) and (c). In contained yielding, the elastic field is driven by the stress intensity factor, K, which dominates the far field. This is related to the remote value of J, $J_{far}$, by the relationship:

$$J_{far} = \frac{K^2}{E} \tag{5.1}$$

The deformation level is quantified by a non-dimensional grouping, $\Omega_{far}$:

$$\Omega_{far} = \frac{J_{far}}{\sigma_o \varepsilon_o t} \tag{5.2}$$

where $J_{far}$ is the J-integral at the outer boundary determined from the applied stress intensity factor K using equation (5.1). As usual $\sigma_o$ is the yield stress, $\varepsilon_o$, the yield strain and t is the plate thickness. The data from three-dimensional boundary layer formulations are presented at deformation levels, $\Omega_{far}$ = 1, 3, 5, 8, 20. Although the remote deformation

is uniform, the intensity of deformation as quantified by the local values of the J-integral, $J_{loc}$ varies along the crack front. Local values of J were determined by the domain integral method as implemented in ABAQUS (2003). Path independence is maintained close to the crack tip, but at contours remote from the tip, J converges to the applied value of J. Following equation (5.2), the non-dimensional deformation can also be interpreted at a local level as $\Omega_{loc}$ when J is interpreted as the local J. Table 5.1 shows how far field deformation translate into local deformation levels along the crack front; at the mid-plane $x_3/t = 0$; the quarter plane $x_3/t = 0.25$; near the free surface $x_3/t = 0.49$ and at the free surface $x_3/t = 0.5$.

Figure 5.1 shows the variation of $J_{loc}$ normalised by the remotely applied J, $J_{far}$, along the crack front at five deformation levels, $\Omega_{far} = 1, 3, 5, 8, 20$. It shows that the local values of J are amplified over the remotely applied value of J near the mid-plane but attenuated near the free surface. At all deformation levels the local J profiles intersect at $x_3/t = 0.2$ and decrease as the free surface is approached.

### 5.1.1.2 Modified Boundary Layer Formulations

It is well known from two-dimensional plane strain analyses that the T-stress affects the shape of the plastic zone and the hydrostatic component. The effect of the T-stress has been studied in three dimensional fields at a deformation level $\Omega_{far} = 8$ by applying positive ($+0.5\sigma_o$) and negative ($-0.5\sigma_o$) T-stresses to the thin plate as a modified boundary layer formulation, in remote plane stress as given in equation (2.149). Table 5.2 shows the far-field deformation levels and the corresponding local values along the crack front at $x_3/t = 0, 0.25, 0.49$ and $0.5$.

Figure 5.2 shows the effect of changing the T-stress on the local J along the crack front. At the mid-plane ($x_3/t = 0$), the local values of J are amplified, while the $T_{app} = 0$ solution is similar to the $T_{app}/\sigma_o = 0.5$ solution. This is due to the fact that three-dimensional boundary layer formulations develop an inherently positive biaxiality even if no T-stress is applied

remotely. The normalised value of J does not change with deformation as the free surface is approached at $x_3/t \geq 0.2$.

### 5.1.1.3 Full-field Solutions.

To study the development of plasticity in finite specimens, two fracture mechanics specimens were examined from small scale yielding to full plasticity. To represent a highly constrained configuration, a deeply cracked single edge notch three-point-bending (SENB) specimen with an a/W ratio of 0.5 was chosen. To represent configurations which lose in–plane constraint a centre cracked tension panel (CCP) with an a/W ratio of 0.5 was chosen. The centre cracked panel has negative biaxiality as shown in Figure 4.16, in contrast to the positive biaxiality of the bend bar, which is shown in Figure 4.14.

The loading of the SENB and CCP specimens are shown schematically in Figure 4.5. For the three-point SENB specimen, a line displacement was applied across the thickness at distance L/W = 3 from the crack flanks. To study the loss of out-of-plane constraint, three different thicknesses were studied: B/(W-a) = 1, 0.5 and 0.1 where B, is the thickness, W is the width and a is the crack length, a/W = 0.5.

Initially, local plasticity developed at the crack tip. As the levels of loading are increased, a plastic hinge formed in the bend specimen which combined with local plasticity at the crack tip. In contrast, plasticity in the centre cracked tension panel (CCP) spread to the free surface in two bands inclined at 45 degrees to the tensile axis. The levels of deformation on both specimens is conveniently quantified by the non-dimensional grouping $\mu$:

$$\mu = \frac{c\,\sigma_o}{J} \tag{5.3}$$

where c = (W-a) is the uncracked ligament. When J is interpreted as the far field value $J_{far}$, $\mu$ represents the remote deformation. When J is interpreted as the local value at a particular section on the crack front, $J_{local}$, $\mu$ represent the local deformation on the crack tip. The

parameter $\mu$ is related to the J-dominance criterion for plane strain fields discussed by McMeeking and Parks (1979) and Shih and German (1981). To ensure the deformation levels in full-field solutions can be compared to boundary layer formulations, the deformation levels along the crack front has also been shown in terms of $\Omega_{loc}$. The deformation levels can also be described in terms of load over limit load or simply (M/Mo in bend bars or $P/P_o$ in centre cracked tension panels). Miller (1988) provides a comprehensive list of limit load calculations for structures containing defects. For SENB with a/W > 0.295, the limit moment, $M_o$, per unit thickness is given by:

$$M_o = \frac{1.15W^2\sigma_o}{4}\left(1.261\left(1-\frac{a}{W}\right)^2\right) \tag{5.4}$$

The applied moment, M can be calculated from equation (4.5). The CCP limit load, $P_o$, per unit thickness given by Miller (1988) is :

$$P_o = \frac{2\sigma_o}{\sqrt{3}}\left(\frac{W-a}{2}\right) \tag{5.5}$$

The applied load, P, can be calculated from equation (4.8). Tables 5.4 and 5.5 show the local values of J non-dimensionalised as $\Omega_{loc}$ and in terms of the non-dimensional local load $\mu$ at different sections through the thickness of both SENB and CCP geometries.

Figures 5.3(a), (b) and (c) show the local deformation levels ($c\sigma_o/J_{loc}$) in the three bend bars while Figures 5.4(a), (b) and (c) show the local deformation levels in the centre crack tension panels. In the bend bars, the deformation was applied until the limit of J-Dominance was approached on the mid-plane ($\mu$ = 25) McMeeking and Parks (1979) and Shih and German (1981). In the bend specimens, J-Dominance is limited by the global bending field which affects the in-plane constraint at the crack tip. In contrast, CCP geometries are not limited in this way and maintain two-parameter (J-Q/T) characterisation to higher deformation levels.

### 5.1.2 Crack Tip Plasticity

#### 5.1.2.1 Thin Plate Boundary Layer Formulations

The development of plasticity depends on the local variation in J and constraint along the crack front. The radius of plastic zone for deformation levels $J_{far}/\sigma_o\varepsilon_o t$ = 1, 3, 5, 8, 20 in the $\theta = 0^\circ$ direction are $r/t$ = 0.3, 1, 1.6, 2.5, 6 and are tabulated in Table 5.3. The plastic zone shape is shown non-dimensionalised by $t$ or by $J_{loc}/\sigma_o$ in Figures 5.5 (a), (b) and (c) and 5.6 (a), (b) and (c) at the mid-plane, the quarter plane and the free surface.

At low levels of deformation, the plastic zone on the free surface develops a shape similar to that exhibited by two-dimensional plane strain solutions. In contrast, the plastic zone shape at the mid-plane is initially similar to that which develops in plane stress. However, at higher deformation levels, a plane stress like plastic zone develops at all sections.

From a classical viewpoint, a plane strain shaped plastic zone might be expected at the mid-plane while the plane stress shape might be expected to develop on the free surface. However in three-dimensional solutions, this does not happen. The current observations can be explained by noting the variation of local J along the crack front. The local values of J are highest on the mid-plane offsetting constraint differences, while lower values of J develop on the free surface.

At the free surface, the three-dimensional plastic zone shape resembles the two-dimensional plane strain shape. This behaviour was also noted by Benthem (1977) who commented that the plastic zone shape estimated from linear elastic corner solutions closely resembled the plane strain plastic zone shape. As deformation increases, a plane stress shape plastic zone with a small elastic enclave develops near the crack front.

### 5.1.2.2 Modified Boundary Layer Formulations

The plastic zone shapes associated with applied T-stresses at a remote deformation level $\Omega_{far} = 8$ are shown in Figures 5.7 (a), (b) and (c) and 5.8 (a), (b) and (c) for the mid-plane, the quarterplane and the free surface for all three thicknesses.

At the mid-plane, the applied positive T-stress and zero applied T-stress formulations show a plastic zone which fully envelops the crack tip. While the negative applied T-stress allows an elastic wedge to form on the crack flanks. At the quarter-plane, the plastic zone fully envelops the crack tip for positive, negative and zero applied T-stresses. While at the free surface, plasticity does not encompass the crack tip, and elastic sectors appear on the crack flanks for all values of applied T-stress either positive, negative or zero. The maximum extent of plasticity for positive T-stresses increased to r/t = 2.6 directly ahead the crack, compared to r/t = 2.0 for $T_{app} = 0$.

### 5.1.2.3 Full-field Solutions.

The development of plasticity in full-field solutions can be discussed within the context of the slip line fields illustrated in Figures 2.24 and 2.25 for CCP and SENB. At low load levels, the plastic zone in all the SENB specimens develops a small scale yielding plane strain like shape for all sections through the thickness as shown in Figures 5.9-5.14 (a), (b) and (c) for the mid-plane, the quarterplane and the free surface.

As the load increases, two plastic zones develop, one at crack tip and one on the compression surface of the bend bar. The two zones grow and coalesce as the applied load increases. The development of the plastic zone in the thinnest bend specimen is similar to that in the boundary layer formulations. At low loads, the plastic zone shape is more similar to the plane strain shape at the free surface than at the mid-plane. At high deformation levels in all three thicknesses of the bend bar, the plastic zone shape approaches the slip line field of a deeply crack bend bar shown in Figure 2.25 as discussed by Ewing (1968) and Green (1953). As with the boundary layer formulations, an elastic

enclave develops on the free surface near the crack front as the deformation level increases.

Figures 5.15-5.20 show the development of plasticity for all the CCP specimens. At low load levels in the thickest CCP specimen, the plastic zones are similar to a plane strain plastic zone but the plastic lobes are inclined at 45 degrees in all sections. However, at comparable load levels, the plastic zone for the intermediate thickness B/(W-a) = 0.5 and the thin B/(W-a) = 0.1 CCP specimens resemble a plane stress plastic zone at all sections. As deformation increases, the plastic zones extend across the ligament as a 45 degrees shear bands in the way illustrated to Figure 2.24.

It is evident from three-dimensional crack tip analyses, that the development of plasticity changes from an almost geometry independent plane strain plastic shape at very small deformation levels to a geometry dependent field in full plasticity.

## 5.2 The Asymptotic Crack Tip Fields (r = 0)

Section 5.2 describes the asymptotic field at the crack tip (r = 0) as modelled by boundary layer formulations and full-field solutions. Initially the method by which the data was processed is described. This is followed by the results of three-dimensional boundary layer formulations at sections from the mid-plane to the free surface. A similar procedure is then followed for the full field solutions of bend bars with three different thicknesses. Finally the asymptotic stress field of centre cracked panels with three different thicknesses is described. Each sub-section presents the stresses at three representative sections: the mid-plane; the quarter plane and the free surface. This is followed by a detailed presentation of the development each of the stress components through the thickness of the plate.

### 5.2.1 Data Extraction Procedures

Three-dimensional crack tip fields have been analysed using boundary layer formulations and full-field SENB and CCP geometries using the commercial finite element software package ABAQUS v 6.3 (2003). Post-processing routines were written using Python code available in ABAQUS. The routine extracted the stresses and strains along radial lines at 10 degrees intervals around the crack tip and stored them in a report file (*.rpt).

The asymptotic crack tip stresses at each angle were obtained by extrapolating the data to the crack tip using Matlab v 5.3 (1998) programs which read the data from the report file and fitted a linear curve through nodal values. The asymptotic crack tip stresses were then written to an output file (*.out). Subsequently the data were structured and sorted through each element layer at each deformation level using Microsoft Excel. The specific sections in ($x_3$/t) and ($\pi$/t) along the crack front where the stress components are presented are given in Table 5.6

### 5.2.2 Boundary Layer Formulations

The asymptotic crack tip stresses in Cartesian and cylindrical co-coordinates are shown at the mid-plane; at the quarter plane; and at the free surface in Figures 5.21-5.26 at

deformation levels $\Omega_{far}$= 1, 3, 5, 8, 20. The plastic zone sizes for the corresponding levels of deformations are 0.1$t$, 0.6$t$, 1.2$t$, 2$t$ and 5.5$t$. In all the figures, the solid lines correspond to the plane strain small scale yielding solution (T = 0).

At the mid-plane, $x_3/t$ = 0 (Figures 5.21-5.22), the results clearly show that a fully constrained field is maintained at the crack tip even at the highest deformation level when the radius of the plastic zone is more than five times the plate thickness. At low deformation levels the stresses are close to the two-dimensional small scale yielding plane strain (T = 0) solution. Higher constraint levels than the small scale yielding solution develop with deformation because the three-dimensional boundary layer formulation possesses an inherently positive T-stress. In the angular range $-45° \leq \theta \leq 45°$, the in-plane stresses $\sigma_{11}$, $\sigma_{22}$, $\sigma_{12}$ are constant and independent of angular co-ordinate. Similarly in this sector the mean stress, $\sigma_m$, and the out of plane stress, $\sigma_{33}$, are also independent of angle as expected from a constant stress region sector in a plane strain field

Trailing the constant stress sector, the stresses in the angular range $45° \leq \theta \leq 135°$ correspond to the centred fan of the plane strain field. The hoop and the radial stress are closely similar and decrease linearly with angle, while the shear stress, $\sigma_{r\theta}$, is equal to the yield stress in shear, $\frac{\sigma_o}{\sqrt{3}}$.

At low levels of deformation elastic sectors appear on the crack flank as expected from the plane strain small scale yielding field discussed by Du and Hancock (1991). However at increased levels of deformation plasticity spreads to the crack flanks as a positive T-stress develops.

At the quarter plane, $x_3/t$ = 0.25 (Figure 5.23-5.24), there is a loss of constraint which causes the direct stresses on the leading sections ahead of the crack tip to decay with deformation. The constraint loss is an out-of-plane effect which is associated with the loss of plane strain, discussed in more detail in Chapter 6. Directly ahead of the crack, in the angular range $-45° \leq \theta \leq 45°$ a constant stress sector appears as shown by the Cartesian

stresses illustrated in Figure 5.24. In this sector, the mean stress is independent of angular co-ordinate but is less than the fully constrained value of $2.97\sigma_o$. On the mid-plane the out-of-plane shear stresses $\sigma_{13}$ and $\sigma_{23}$ are necessarily zero due to symmetry as shown in Figure 5.35 and 5.36. However these shear stresses are also low on the quarter plane and the stress state in the sector ahead of the crack is essentially generalised plane strain in which the out-of-plane strain may be non-zero, but $\sigma_{33}$ is a principal stress.

Trailing the constant stress sector a degenerate centre fan appears in the angular range $45° \le \theta \le 135°$. Here the hoop and the radial stresses are similar but not identical (as rigorously required by a plane strain centred fan). However both the radial and the hoop stress decrease linearly with angle although angular stress gradients $\frac{\partial \sigma_{rr}}{\partial \theta} = \frac{\partial \sigma_{\theta\theta}}{\partial \theta} = \frac{\partial \sigma_m}{\partial \theta} < -2k$ are less than that required by a plane strain field. Nevertheless the shear stress $\sigma_{r\theta}$ is independent of angle and is close to the yield stress in shear $\frac{\sigma_o}{\sqrt{3}}$ as required by plane strain centred fans.

Finally in the trailing sector on the crack flanks the direct stress $\sigma_{22}$ and shear stress $\sigma_{12}$ remain close to the plane strain values however the direct stress $\sigma_{11}$ differs from the plane strain field. The Mises stress shown in Figure 5.37 demonstrates that yielding occurs all around the crack tip.

The crack tip stresses at the free surface, $x_3/t = 0.5$ are shown in (Figure 5.25-5.26). The leading sector $-45° \le \theta \le 45°$, again comprises a constant stress regime in which the Cartesian stresses and the stress invariants are independent of angular co-ordinate $\theta$. The stress system in this sector is a simple state of uniaxial tension at the yield stress:

$$\sigma_{22} = \sigma_o;\ \sigma_{11} = \sigma_{12} = \sigma_{33} = \sigma_{13} = \sigma_{23} = 0;\ r \to 0,\ x_3 \to 0 \qquad (5.6)$$

Trailing the constant stress sector is a sector in the approximate range $45° \le \theta \le 135°$. The shear stress reduces from the plane strain value and the angular span of the constant shear stress region reduces to 60 to 80 degrees. However, unlike the related plane strain sector,

the radial stress is consistently greater than the hoop stress. In comparison with the mid-plane, the angular stress gradients $\frac{\partial \sigma_{rr}}{\partial \theta}$ and $\frac{\partial \sigma_{\theta\theta}}{\partial \theta}$ are very much less than the plane strain gradient of -2k. Finally on the crack flanks an elastic sector appears in the angular range $160^o \leq \theta \leq 180^o$, as shown in Figure 5.37.

The free surface field should be compared with the two dimensional plane stress field which is shown in Figure 2.18. The plane stress field features a curved fan sector ahead of the crack in which the streses change with angle as given by equations (2.114 – 2.116). In contrast, the free surface field exhibits a constant stress sector in which the Cartesian stresses and the stress invariants are independent of angle. In the plane stress field the curved fan is complemented by an elastic sector to the crack flanks in the range $0^o < \theta < 39.126^o$, Sham and Hancock (1999). However in the free surface field plasticity extends over the approximately range $0^o < \theta < 160^o$ as shown in Figure 5.37.

The development of the direct stresses, the in-plane shear and the out-of-plane shear stress, the mean stress and the Mises stress at sections tabulated in Table 5.6 are shown in Figures 5.27-5.37. The data are given in both cylindrical and Cartesian co-ordinates. In the leading sector ($0^o \leq \theta \leq 45^o$), the Cartesian stresses $\sigma_{11}$, $\sigma_{22}$, $\sigma_{12}$, $\sigma_m$ do not change with angle and can be regarded as comprising a family of constant stress sectors from the mid-plane to the free surface. This is most clearly seen in Figures 5.31 and 5.34 which show $\sigma_{22}$ and $\sigma_m$. In this family of fields, the mean stress changes systematically from the mid-plane to the free surface as shown in Figure 5.34. The change from the mid-plane to the free surface is accompanied by a change in strain state from plane strain to uniaxial tension. Thus the fields are rigorously not part of the plane strain family of J-Q/T fields which are deviatorically similar, but hydrostatically different, as these field differ hydrostatically, but also deviatorically. At the mid-plane the stress system corresponds to the fully constrained plane strain field which evolves to a state of simple uniaxial tension at the yield stress on the free surface.

In the sector from 45 to 135 degrees, the shear stress $\sigma_{r\theta}$ does not change with angle and is close to the yield stress in shear near the mid-plane. However the angular span of this sector becomes smaller toward the free surface and the shear stress eventually decays from the yield stress in shear as shown in Figure 5.29.

The out-of-plane shear $\sigma_{13}$ shown in Figure 5.35 is not completely non-zero around the crack tip in contrast to the $\sigma_{23}$ which can be regarded as being zero aound the crack tip as shown in Figure 5.36. Figure 5.35 shows that the out-of-plane shear stress, $\sigma_{13}$, at the mid-plane, is zero as indicated by the diamond markers and required by symmetry. The free surface field shows a near zero out-of-plane shear in front of the crack. Within the angular range of 45 to 135 degrees, out-of-plane shear, $\sigma_{13}$ is slightly negative. However, at the trailing sector, the out-of-plane stress, $\sigma_{13}$ approach zero to the crack flank.

### 5.2.3 Modified Boundary Layer Formulations

The effect of the T-stress is shown in Figures 5.38-5.43 for the mid-plane; the quarter plane and the free surface using cylindrical and Cartesian co-ordinate systems. A positive T-stress, $T_{app} = +0.5\sigma_o$ and a negative T-stress, $T_{app} = -0.5\sigma_o$ were applied at a level of deformation $\Omega_{far} = 8$. The effect of a negative T-stress is to decrease the direct stresses, ($\sigma_{\theta\theta}$, $\sigma_{rr}$) around the crack tip uniformly from the plane strain field at the mid-plane and quarter plane, while the shear stress $\sigma_{r\theta}$ remained unaffected as shown at the mid-plane and the quarter plane in Figure 5.38 and 5.40. In the mid-plane of the plate the effect of applied T-stresses is the same as that observed in two-dimensional plane strain solutions. Negative T-stresses reduce the mean stress, giving rise to a family of fields which are broadly deviatorically similar, but hydrostatically different.

However at the free surface and near the free surface the effect of the T-stress is distinctly different. At the free surface (Figures 5.42 and 5.43), the hoop stress directly ahead of the crack is unaffected by the applied positive and negative T-stress. However directly ahead of the crack the radial stress for an applied positive T-stress is nearly half the hoop stress which may suggest that the free surface field at this orientation approaches a plane stress

field when the T-stress is highly positive. However, this is only observed directly ahead of the crack tip ($\theta = 0^o$), while at the remaining angles the free surface field does not show any similarity to the plane stress field. A negative T-stress causes the radial stress on the free surface to drop to zero and leads to a state of pure tension directly ahead of the crack.

The development of the direct stresses, the in-plane shear and the out-of-plane shear stress, the mean stress and the Mises stress at the sections tabulated in Table 5.6 are shown in Figures 5.44-5.52 for positive and negative applied T-stresses. The direct stresses through the thickness increase or decrease by the same amount according to the applied T-stresses in the leading sectors ahead of the crack front. The in-plane shear stresses for applied positive and negative T-stress are largely unaffected within the angular range $0^o < \theta < 90^o$. However in the trailing sector $90^o < \theta < 180^o$, the effect of applied T-stress affects the fields, although the out-of-plane shear stresses are largely unaffected.

The Mises stress is given in Figure 5.52. The figure shows that negative T-stresses increase the angular span of elastic wedge from the crack flanks compared to the T= 0 field. In the positive T-stress field, plasticity completely envelops the crack tip from the mid-plane to the free surface.

### 5.2.4 SENB Solutions

This section describes the stress field which develops at the crack tip in deeply cracked three point bend bars of three different thicknesses, B/(W-a) = 1, 0.5 and 0.1 with a/W = 0.5.

#### 5.2.4.1 Thick Specimen (B/(W-a) = 1)

Initially the asymptotic stress field is shown at the mid-plane; the quarterplane; and the free surface of a thick SENB specimen, B(W-a) = 1. This is given from small scale yielding to the limit of J-Dominance on the mid-plane in Figures 5.53-5.58. For reference, the solid lines show the small scale yielding plane strain (T = 0) field. Figures 5.53 and 5.54 show

that at the mid-plane the asymptotic stresses are close but slightly higher than the plane strain (T = 0) values. The same effect can also be seen at the quarterplane (Figure 5.55 and 5.56) where the plane strain field is maintained around the crack tip at all angles.

As the free surface is approached (Figure 5.57 and 5.58), the stresses directly ahead of the crack drop to a field which is distinctly different to the plane stress field, but similar to that on the free surface of thin plate boundary layer formulations. Notably in the leading sector, there is a state of uniaxial tension ($\sigma_{\theta\theta} = \sigma_o$, $\sigma_{rr} = \sigma_{r\theta} = \sigma_{zz} = 0$). In contrast, the Sham and Hancock (1999) plane stress field features a bi-axial stress system in which :

$$\sigma_{\theta\theta} = 2\sigma_{rr}, \ \sigma_{r\theta} = \sigma_{zz} = 0 \tag{5.7}$$

The development of the direct stresses, the in-plane shear and the out-of-plane shear stresses, the mean stress and the Mises stress are shown in Figures 5.59-5.68. The direct stresses are maintained at a level close to the plane strain (T = 0) field from small scale yielding to full plasticity. While the constraint loss through the thickness at all sectors ($0^o < \theta < 180^o$) shows a similar pattern for all load levels. Within the sector $45^o \leq \theta \leq 135^o$, the angular stress gradients $\frac{\partial \sigma_{rr}}{\partial \theta}$ and $\frac{\partial \sigma_{\theta\theta}}{\partial \theta}$ reduce systematically from the mid-plane to the free surface.

The in-plane stresses (Figures 5.61 and 5.64) show that the stress field around the crack tip and through the thickness are similar to the plane strain (T = 0) field within the angular range $0^o < \theta < 90^o$. At angles approximately greater than 90 degrees, the in-plane shear stresses reduce through the thickness. The out-of-plane shear stresses (Figures 5.66 and 5.67) $\sigma_{13}$ and $\sigma_{23}$ show a similar behaviour to the boundary layer formulations.

The Mises stress as a function of angle from small scale yielding to full plasticity is shown in Figure 5.68. At the mid-plane, plasticity completely envelops the crack tip field even at low load levels. In contrast, an elastic sector can be seen to develop in sections close to the

free surface at very low load levels. However, at increased load levels, plasticity fully envelops the crack tip field at all sections.

### 5.2.4.2 Intermediate Thickness Specimen (B/(W-a) = 0.5)

The asymptotic stress fields in the intermediate thickness bend bar, B/(W-a) = 0.5 are shown in Figures 5.69-5.74 at the mid-plane; the quarter plane and the free surface using cylindrical and Cartesian co-ordinate system. At the mid-plane, the asymptotic stresses are close to the fully constrained plane strain (T = 0) field as on the mid-plane of the thick bend bar.

At the quarter plane, constraint is lost as shown in Figure 5.71 and 5.72. The constraint loss is evidenced by a drop in the direct stresses while the shear stresses remain unchanged. As in the boundary layer formulations, which show constraint loss with increase in deformation, constraint loss in SENB is caused by the global bending field which perturbs the local crack tip field with increasing levels of deformation.

At the free surface (Figure 5.73 and 5.74), an elastic-plastic corner field can be identified directly ahead of the crack. In this field, a uniaxial constant stress sector develops in the leading sector $-45^{\circ} \leq \theta \leq 45^{\circ}$ similar to that observed on the free surface of the boundary layer formulation.

The development of the direct stresses, the in-plane shear and the out-of-plane shear stress, the mean stress and the Mises stress are shown in Figures 5.75-5.84. In the intermediate thickness SENB specimen, the components of stress were similar to the thick SENB specimen. A reduction of fifty percent in the thickness while maintaining the in-plane dimensions does not affect constraint. To examine the effect of thickness on constraint, a much thinner specimen was generated, B/(W-a) = 0.1.

### 5.2.4.3 Thin Specimen (B/(W-a) = 0.1)

In the thinnest SENB specimen, B/(W-a) = 0.1, the asymptotic stress field at the mid-plane, the quarterplane and the free surface are shown in Figure 5.85-5.90. At the mid-plane (Figures 5.85 and 5.86), the stresses are close to the plane strain (T = 0) values within the leading sector $-45^{\circ} < \theta < 45^{\circ}$ at small levels of deformation. However, at deformation levels close to limit of plane strain J-Dominance (as measured at the mid-plane) constraint is lost at the mid-plane. The constraint loss is associated with a reduction in the direct stress while maintaining the shear stresses.

On the quarter plane, $x_3/t = 0.25$ (Figure 5.87-5.88), there is a loss of constraint which causes the direct stresses on the leading sections ahead of the crack tip to decay from the plane strain (T = 0) field. Directly ahead of the crack, in the angular range $-45^{\circ} \leq 0 \leq 45^{\circ}$ a constant stress sector appears as shown by the Cartesian stresses illustrated in Figure 5.88. In this sector, the mean stress is independent of angular co-ordinate but is less than the fully constrained value of $2.97\sigma_o$.

Trailing the constant stress sector a degenerate centre fan appears. In plane strain centred fans, the radial and hoop stress are equal to each other and reduce with angle. However in the thinnest SENB specimen, the hoop stress and the radial stress reduce but are not equal. The angular span of the fan-like feature reduces with deformation. At low levels of deformation it extends from 45 to 110 degrees while at high levels of deformation near the limit of plane strain J-Dominance the centred fan extends from 45 to 80 degrees. Nevertheless the shear stress $\sigma_{r\theta}$ is independent of angle and is equal to the yield stress in shear $\frac{\sigma_o}{\sqrt{3}}$ as required by plane strain centred fans. Finally in the trailing sector on the crack flanks, the direct stress $\sigma_{22}$ and shear stress $\sigma_{12}$ remain close to the plane strain (T = 0) values although the direct stress $\sigma_{11}$ falls.

On the free surface directly ahead of the crack tip, Figure 5.89-5.90, a corner field again develops. This is similar to that found in the modified boundary layer formulations with

positive T-stresses. As deformation increases, the radial stress at $\theta = 0^o$ tends to increase and approaches a plane stress field. This can be attributed to the inherently positive T-stress of very thin bend bars as shown in Figure 4.14. However, at all other angles, the free surface field differs significantly from the plane stress field.

The development of the direct stresses, the in-plane shear and the out-of-plane shear stress, the mean stress and the Mises stress at sections as tabulated in Table 5.6 are shown in Figures 5.91-5.100. In small scale yielding, the stress fields through the thickness behave in similar way to the thin plate boundary layer formulation. Within the forward sector $-45^o < \theta < 45^o$, the direct stresses show constraint loss but feature a constant stress sector. The sector outwith the $-45 < \theta < 45$ degrees shows a slightly different feature at deformation levels smaller than $c\sigma_o/J < 1284.3$. The out-of-plane shear stresses (Figure 5.98 and 5.99) are generally unaffected at all angles. The $\sigma_{23}$ shear component is close to zero at all angles through the thickness while the $\sigma_{13}$ shear component is finite and similar to the boundary layer formulations. The Mises stress shows a similar behaviour to thick and intermediate thickness SENB plates in which the sections near the free surface are elastic at low levels of deformation but are engulfed by plasticity as deformation develops.

### 5.2.5 CCP Solutions.

This section describes the stress field which develops at the crack tip in deeply cracked tension panels of three different thicknesses, by B/(W-a) = 1, 0.5 and 0.1. The important point to note about the CCP geometry is that it features a compressive T-stress which leads to a loss of in-plane constraint. Thus in full three-dimensional specimens, constraint loss arises from both in-plane and out-of-plane effects.

#### 5.2.5.1 Thick Specimen (B/(W-a) = 1)

Initially the asymptotic cylindrical and Cartesian stress field is shown at the mid-plane; the quarter plane; and the free surface of a thick specimen, B/(W-a) = 1 in Figures 5.101-

5.106. The figures show the asymptotic hoop, radial and shear stress at the mid-plane; the quarter plane; and the free surface at low levels of deformation to full plasticity.

At the mid-plane (Figures 5.101 and 5.102), the effect of in-plane constraint loss within the leading sector $-45^{\circ} < \theta < 45^{\circ}$ causes the direct stresses to fall from the fully constrained plane strain value. However the shear stresses remain similar to the plane strain shear stress within the same angle. In the sector $45^{\circ} < \theta < 135^{\circ}$, the effect of compressive T-stress inherent for CCP specimens causes a decrease in the angular span of the centred fan. This directly affects the angular extent of plasticity around the crack tip. An elastic field dominates trailing the angle $\theta \geq 135^{\circ}$ where the yield criteria is not satisfied.

At the quarter plane, constraint is lost due to both in-plane and out-of-plane effects as shown in the forward sector Figure 5.103 and 5.104. The constraint loss is evidenced by a drop in the direct stresses while the shear stress remain unchanged. The direct stresses in the sector $45^{\circ} < 0 < 135^{\circ}$ show a further decrease in the angular span of the centred fan when compared to the stress field on the mid-plane. The trailing sector is elastic similar to the trailing sector of the mid-plane.

Directly ahead of the crack on the free surface (Figure 5.105 and 5.106), an elastic-plastic corner field characterised by a uniaxial tension sector can be identified which is similar to the free surface of the boundary layer formulation and the SENB specimens.

The development of the direct stresses, the in-plane shear and the out-of-plane shear stress, the mean stress and the Mises stress are shown in Figures 5.107-5.116. In-plane effects cause the direct stresses to drop in response to the level of compressive T-stress. The direct stresses are then influenced by an out-of-plane effect similar to those observed in boundary layer formulation or the full-field SENB solutions. In all three configurations, the free surface field exhibits an elastic-plastic corner field.

The in-plane shear stresses are similar to the plane strain field within the plastic sectors, while the out-of-plane shear stresses are similar to the boundary layer formulation and the

full-field SENB solution. The Mises stress in Figure 5.116 shows that the elastic wedge on the mid-plane is bigger than at the free surface. Increase in deformation levels causes the span of the elastic wedge to reduce from the mid-plane to the free surface.

#### 5.2.5.2 Intermediate Thickness Specimen (B/(W-a) = 0.5)

The asymptotic stress field in the intermediate thickness CCP specimen, B/(W-a) = 0.5 are given in Figures 5.117-5.122 while the development of the direct stresses, the in-plane shear and the out-of-plane shear stress, the mean stress and the Mises stress are shown in Figures 5.123-5.132.

From these figures, it is clear that the stress fields are similar to the thick specimen. This is consistent with the level of T-stress which is close to the thick CCP specimen particularly at the mid-plane as shown in Figures 4.15 to 4.17. However as the free surface is approached the level of T-stress in the intermediate thickness specimen increases markedly. This causes the span of plasticity around the crack tip to increase toward the free surface as shown in the Mises stress in Figure 5.132.

#### 5.2.5.3 Thin Specimen (B/W-a) = 0.1)

A thin specimen, one-tenth of the thickness of the thickest specimen, was generated to examine out-of-plane effects in a very thin CCP specimen. The asymptotic stress fields are presented in Figures 5.133-5.138 while the development of the direct stresses, the in-plane shear and the out-of-plane shear stress, the mean stress and the Mises stress are shown in Figures 5.139-5.148.

At the mid-plane within the leading sector ($-45^\circ < \theta < 45^\circ$) as shown in Figures (5.133 and 5.134), the stress field features a constant stress sector in which the direct stresses are reduced because of the in-plane effect associated with a compressive T-stress. However the in-plane shear stresses are similar to the plane strain (T = 0) field in the leading sector as shown in Figures 5.141 and 5.145. The sector $45^\circ < \theta < 135^\circ$ shows that the direct stresses

reduced with angle. In the trailing sector, the yield criterion was not fulfilled leading to elastic sectors as shown by the Mises plot of Figure 5.148.

At the quarter plane (Figures 5.137 and 5.138), the stress field exhibits further constraint loss due to out-of-plane effects which occur at all angles. At the free surface, the forward sector exhibits a constant stress uniaxial tension field similar to the boundary layer formulation and the SENB specimens.

The out-of-plane effect in the thin specimen features a similar constraint loss as discussed in the thick and intermediate thickness CCP specimens. However, the Mises stress shown in Figure 5.148 indicates an increase in angle span of plasticity around the tip because thin CCP specimen have a less negative T-stress than thick specimens.

## 5.3 Stress Field Ahead of the Crack Front ($\theta = 0^o$)

### 5.3.1 The Mean Stress and the Maximum Principal Stress

In this part of chapter 5, attention is focused on two stress components which are particularly important in fracture mechanics: the hydrostatic stress or mean stress, $\sigma_m$, and the maximum tensile stress or the hoop stress, $\sigma_{\theta\theta}$, directly ahead of the crack

Fracture mechanisms can be broadly described as being ductile or brittle. In ductile failure, crack extension occurs by the nucleation, growth and coalescence of micro-voids which form at inclusions and second phase particles by interface decohesion or particle cracking. The voids grow by plastic strain and mean stress, and finally coalesce with the blunting crack tip. Rice and Tracey (1969) have given an analysis of the growth of a spherical hole in a perfectly plastic matrix in terms of rate of change of the mean hole radius R with plastic strain as:

$$\frac{1}{R}\frac{dR}{d\bar{\varepsilon}^p} = 0.28\exp\left(\frac{3\sigma_m}{2\bar{\sigma}}\right) \tag{5.8}$$

The void growth rate is markedly amplified by the mean stress or triaxiality $\sigma_m/\bar{\sigma}$, which is known to affect ductility as shown experimentally by Hancock and Mackenzie (1976).

In contrast, brittle failure occurs by the low energy separation of atomic planes through cleavage. This occurs when the maximum principal stress attains a critical value $\sigma_{\theta\theta} = \sigma_c$, over a characteristic micro-structural distance, $r = r_c$ (usually two grain diameters) for $\theta = 0^o$ as discussed by Ritchie, Knot and Rice (1973).

The maximum principal stress and the mean stress, $\sigma_m$, are thus important drivers for two mechanisms of crack extension. In this section, the stress state ahead of the crack front is investigated with particular reference to the mean stress and the hoop stress normalised by the yield stress, $\sigma_o$, while the radial distance ahead of the crack front, r, is non-dimensionalised by $J/\sigma_o$. The investigations attempt to show the transition from plane

strain to plane stress in the three-dimensional field ahead of the crack front, and to systematically examine the applicability of constraint based fracture mechanics to three-dimensional crack tip fields.

### 5.3.2 Boundary Layer Formulations

Figures 5.149-5.150 show the mean stress directly ahead of the crack while Figures 5.151-5.152 show the hoop stress. Data is presented between the crack tip and a distance r $=10J/\sigma_o$, on sections from the mid-plane to the free surface, and at deformation levels $\Omega_{far}$ = 3 and 8. At these deformation levels, the mean stress, $\sigma_m = 2.39\sigma_o$, and the hoop stress, $\sigma_{\theta\theta} = 2.97\sigma_o$ at the mid-plane crack tip correspond to a fully constrained field. At both levels of deformation, the hoop and the mean stress decrease with distance from the crack tip. The difference between the stresses on the mid-plane and that on any given section is almost distance independent (i.e. the stress profiles are broadly parallel). However an increase in deformation is shown to increase the stress gradient. Similar observations are presented for the hoop stress in Figure 5.151-5.152.

The effect of deformation on the mean and hoop stress on the mid-plane and free surface are shown in Figures 5.153 and 5.154. The mean and hoop stress become increasingly dependent on distance as the deformation level increases. At the crack tip, the mean and the hoop stress approach the limiting plane strain value at the mid-plane. However at the free surface, stress field can not be simply identified as being a plane stress field because the stresses attained in a perfect plane stress field ($\theta = 0^o$) are $\sigma_m = 0.577\sigma_o$, $\sigma_{00} = 1.15\sigma_o$.

To determine the location of the plane stress field, the hoop stress has been used as shown in Figure 5.155. This figure shows the hoop stress ahead of the crack front at r/t = 0.013 and 1 for various levels of deformation and on sections normal to the crack front. On the mid-plane, the hoop stress approaches the plane strain value of $2.97\sigma_o$. However at r/t = 1, the hoop stress on the mid-plane and on the free surface are both close to $\sigma_{\theta\theta} \approx 1.15\sigma_o$, indicating a plane stress-like field. Detailed insight into the hoop stress at $J_{far}/\sigma_o\varepsilon_o\, t = 8$ is

shown in Figure 5.156 in which the hoop stress reduces across the thickness until at a distance, r = t a plane stress field dominates across the full section.

### 5.3.3 SENB Stress Field

In this part of chapter 5, the hoop and mean stress in full-field SENB solutions are shown at the mid-plane and the free surface ahead of the crack front for a sequence of increasing levels of deformation and for three different thicknesses, B/(W-a) = 1, 0.5 and 0.1.

Figures 5.157-5.159 show the hoop stress at the mid-plane and at the free surface at increasing levels of deformation. In this series of figures, those denoted (a) describe the mid-plane. In all cases, the hoop stress at the crack tip on the mid-plane is close to the limiting value of $\sigma_m = 2.97\sigma_o$ for all thicknesses. Ahead of the crack front, this stress is maintained at a distance of $2J/\sigma_o$ in the two thicker specimens. However, in the thinnest specimens, the plane strain constraint hoop stress is lost immediately. At small distances from the crack tip, the hoop stress becomes distance dependent. For the thinnest specimen, the hoop stress eventually approaches $1.15\sigma_o$ at the free surface indicating a plane stress field at a distance $5J/\sigma_o$ when the deformation level, $\mu$, is greater than 82.4.

In the series of Figures 5.157-5.159, those denoted (b) describe the free surface. At the intersection of the free surface and the crack front, the hoop stress does not approach the plane stress field in any of the three geometries. In the thinnest specimen, a full plane stress field develops at distance of $30J/\sigma_o$. For the B/(W-a) = 1 and 0.5, the hoop stress show a stress field pattern that becomes independent of distance at $r = 30J/\sigma_o$, but not identical to the plane stress field.

Similar trends are shown for the mean stress at the mid-plane and the free surface in Figures 5.160-5.162. The plane strain level is achieved at the mid-plane for B/(W-a) = 1 at distances less than $2J/\sigma_o$. While a plane stress field develops at distance $r > 30J/\sigma_o$ in the thinnest SENB specimens.

The proximity to plane stress has been examined as a function of r/t in Figures 5.163 to 5.165. In these figures, the three-dimensional fields are examined on lines parallel to the crack front, and at an increasing distance r/t from the crack tip. Results are presented for all specimen thicknesses from low levels deformation to the limit of J-Dominance on the mid-plane ($\mu = (W\text{-}a)\sigma_o/J_{loc} \approx 25$). All the figures show a similar pattern, in which plane strain conditions are approached near the crack front at the mid-plane while plane stress conditions develop on the free surface but away from the corner intersection. At the crack tip on the free surface, the field is perturbed by the corner field.

### 5.3.4 CCP Stress Field

In the CCP solutions, the hoop and mean stress were determined as a function of distance from the crack tip, at the mid-plane and the free surface at a sequence of increasing levels of deformation and for three different thicknesses, B/(W-a) = 1, 0.5 and 0.1.

Figures 5.166-5.168 show the hoop stress as a function of distance, r, normalised by $J/\sigma_o$ ahead of the crack front on the mid-plane and the free surface. In the series of Figures 5.166-5.168, those denoted (a) describe the mid-plane. Significantly the hoop stress at the crack tip is less than the fully constrained plane strain field and the stress is dependent on distance from the crack tip. The first effect is due to in-plane constraint loss associated with the CCP geometries which feature a negative T-stress. In-plane constraint loss effects are recognised to be largely distance independent. Ahead of the crack front the stress approaches plane stress levels at distance remote from the crack tip. This is most clearly shown in the thinnest specimen B/(W-a) = 0.1 shown in Figure 5.168(a).

In the series of Figures 5.166-5.168, those denoted (b) represent the free surface, the field approaches the plane stress conditions at distance remote from the crack tip.

Similar trends at the mid-plane and at the free surface are shown in Figures 5.169-5.171 for the mean stress where (a) and (b) denote the mid-plane and the free surface field. A loss in the plane strain constraint is shown at the mid-plane for all thickness. On the mid-plane the

mean stress starts at a lower level because of in-plane constraint loss associated with a negative T-stress and additional out-of-plane constraint loss develops with increase in deformation. Increasing deformation causes the field to approach a plane stress field remote from the crack tip. Significantly, the mean stress is dependent on distance on the mid-plane and the free surface near to the crack tip.

At distances far from the crack front in the thinnest specimen B/(W-a) = 0.1, the mean stress approaches $0.577\sigma_o$ which corresponds to plane stress. However, remote from the tip, the mean stress at the mid-plane and the free surface approaches a plane stress field regardless of specimen thickness and levels of deformation.

When the distance, r, is normalised with $J/\sigma_o$, the physical location of stresses which are being measured move away from the crack tip with increasing levels of deformation. Consequently, in the subsequent figures, the occurrence of plane stress field has been analysed at a fixed distance r/t at increasing levels of deformation for all specimen thicknesses. Figures 5.172-5.174 show the hoop stress ahead of the crack front from small scale yielding to full plasticity in CCP specimens of different thicknesses. The figures show that plane strain conditions are lost at the mid-plane and with increasing distance from the crack front. At the free surface, the field is perturbed by the corner field which features a uniaxial tension field close to the crack front. In the thinnest CCP specimen, the plane stress field across the thickness is located at $r/t > 1$.

## 5.4 Proximity to Plane Strain and Plane Stress

Initially it is necessary to identify the way in which full three dimensional fields correspond to, or differ from, the two dimensional idealisations of plane strain and plane stress. The proximity to plane strain is easily assessed by a parameter derived from the requirement that the out of plane stress deviator is zero. Unfortunately, this does not distinguish between a plane stress field and a corner singularity, and a different parameter is introduced for this specific purpose.

### 5.4.1 Proximity to Plane Strain

#### 5.4.1.1 Boundary Layer Formulations

For an incompressible material ($\nu = 0.5$), plane strain conditions in the z direction require that the out-of-plane stress deviator $s_{zz}$ is zero and $\rho$ as given by equation (2.45) is 0.5.

In the three-dimensional boundary layer formulations, the proximity to plane strain has been examined at levels of deformation $\Omega_{far} = 1, 3, 5, 8$ and at a distance which is very close to the crack tip ($r/t = 0.013$) and at $r/t = 1$ as shown in Figure 5.175. On the mid-plane close to the crack tip, the parameter $\rho$ which measures the proximity to plane strain increases slightly with deformation but is largely uniform along the crack front until the free surface is approached, when plane strain constraint is necessarily lost. At a distance $r/t = 1$ from the crack tip, which is within the plastic zone at deformation levels $\Omega_{far} = 5, 8$, plane strain conditions are entirely lost, and $\rho = 0$.

The through thickness variation of $\rho$ is shown in Figure 5.176 for a deformation level $\Omega_{far} = 8$. At this level of deformation, $\rho$ is shown from $r/t = 0.013$ to $r/t = 1$. As the distance from the crack front increases, plane strain conditions are lost. At distances greater than one plate thickness, plane stress conditions occur and within $r/t < 1$ three-dimensional fields develop.

In Figure 5.177, the proximity to plane strain has been assessed at $\theta = 0^o$ within the plastic zone at levels of deformation $\Omega_{far}$ = 1, 3, 5, 8, and 20. On the mid-plane, plane strain is only approached very near the crack tip. Across the thickness, the tendency to plane strain reduces with distance from mid-plane.

### 5.4.1.2 Full-Field Solutions

In Figures 5.178-5.180, the proximity to plane strain along the crack front from the mid-plane to the free surface is given at fixed positions r/t = 0.015, 0.032 and 0.065 for the SENB specimens. The proximity to plane strain is dependent upon the thickness of the specimen and largely independent of deformation. On the mid-plane, plane strain is attained in the thickest specimen B/(W-a) = 1 and is maintained with deformation. At the free surface, plane strain conditions are lost sharply in thicker specimens but gradually reduce in the thinnest specimen. As the thickness is reduced, out-of-plane effects reduce the proximity to plane strain at the mid-plane. However, on the free surface $\rho = 0$ regardless of thickness.

Figures 5.187-5.189 show $\rho$ as a function of distance ahead of the crack front ($\theta = 0^o$) for the CCP geometries. The CCP specimens behave in a similar way to the bend bars in the sense that $\rho$ is affected by thickness but is independent of deformation. A distinct difference is the gradient of $\rho$ near the free surface in the thinnest specimen B/(W-a) = 0.1 compared with the intermediate and full thickness specimens.

The proximity to plane strain at increasing r/t parallel to the crack front is shown for SENB in Figures 5.181-5.183 and for CCP in Figures 5.190-5.192 respectively. The figures show that $\rho$ is highest near the mid-plane of the specimen and close to the crack tip. Constraint is entirely lost at (r/t > 1) for both SENB and CCP specimens.

Figures 5.184-5.186 and Figures 5.193-5.195 show $\rho$ for SENB and CCP specimens ahead of the crack at $\theta = 0^o$ from small scale yielding to full plasticity for plate thicknesses B/(W-a) = 1, 0.5 and 0.1. From the figures, the distance at which $\rho$ approaches zero increases

slightly with deformation for both SENB and CCP specimens. Comparing the SENB and the CCP specimens, there is a small difference in the transition near the free surface. For SENB, the stress drops to zero but increase slightly between $0.1 < r/t < 0.5$ and then approach to zero. While in CCP, the field drops slightly below zero at $r/t > 0.5$ and approaches zero with increase in distance.

### 5.4.2 Proximity to Plane Stress

The plane strain parameter, $\rho$, defined in equation (2.45) necessarily becomes zero at a free surface. At the free surface, the out-of-plane stresses vanish but in-plane components may exist. As a result, the parameter, $\rho$, cannot distinguish between plane stress and corner fields.

In elastic-perfectly plastic crack tip analyses in plane stress conditions, the slip lines comprise a non-orthogonal grid in which the direct stress across the lines is twice that along the lines. Consequently, the slip lines are lines of zero extension. From this argument, the proximity to plane stress can be assessed by a parameter $\lambda$ :

$$\frac{\sigma_{rr}}{\sigma_{\theta\theta} + \sigma_{zz}} = \lambda \tag{5.9}$$

For incompressible elastic-perfectly plastic plane stress conditions $\lambda = 0.5$. Significantly, the requirement of a traction free surface normal to the $z$ direction does not necessarily lead to $\lambda = 0.5$, allowing plane stress and corner fields to be distinguished.

#### 5.4.2.1 Boundary Layer Formulations

In Figure 5.196, $\lambda$ is plotted along the crack front at $r = 0$. On the mid-plane, $\lambda$ remains close to 0.4 for all levels of deformation until $x_3/t = 0.32$. Close proximity to plane stress occurs at $x_3/t = 0.465$ but plane stress conditions are lost at the free surface. At the intersection of the free surface and the crack front, a corner field develops. Figure 5.196,

shows that in the boundary layer formulation, the corner field dominates over the range $0 < z/t < 0.035$ (z is distance from the free surface) which is consistent with observations by Nakamura and Parks (1988a) that the elastic corner singularity field which dominates in a spherical zone of approximately 3 percent of the plate thickness from the intersection of the free surface and the crack front.

#### 5.4.2.2 Full-Field Solutions

The behaviour of the full-field solutions is similar to the boundary layer formulation. The proximity to plane stress at increasing levels of deformation is shown in Figures 5.197-5.199 for the SENB geometries and Figures 5.200-5.202 for the CCP geometrics. At the crack tip ($r = 0$), plane stress occurs at $x_3/t = 0.46$ for all specimen thicknesses. A domain dominated by the corner singularity field occurs independent of specimen thickness at about 3.5 percent of the plate thickness from the free surface.

## 5.5 Conclusions

Three-dimensional crack tip analyses indicate that the loss of out-of-plane constraint is associated with asymptotic fields which differ both hydrostatically and deviatorically while the stress ahead of the crack front is distance dependent. However, plane strain J-Q/T theory requires the stress fields to be deviatorically similar and differ only hydrostatically. J-Q/T theory also requires that within the microstructural-separation distance ahead of the crack front normally $2J/\sigma_o \leq r \leq 5J/\sigma_o$, the stress difference Q is distance independent. In three-dimensional crack tip fields, the two requirements are not met. This suggests that J-T/Q theory may not be applicable to three-dimensional crack problems which do not approximate to plane strain.

Rice (1974) indicated that a three-dimensional crack tip field should be bounded by a plane strain and plane stress fields. However, three-dimensional crack tip analyses do not show the plane stress bound conclusively. In the current work, the fields have been shown to be bounded by a plane strain field close to the crack tip at the mid-plane. However, at the free

surface, there are two distinct fields. At the intersection of the crack front and the free surface, a corner field occurs as identified by a uniaxial tensile field in the leading sector. A stress field similar to the plane stress field occurs at approximately $x_3 = 0.97t$. This crack tip corner field has been shown in boundary layer formulations and full-field SENB and CCP solutions independent of specimen thickness. An exact plane stress field through the thickness occurs for the thin specimens of boundary layer formulation, SENB and CCP at $r/t = 1$. In the thick and the intermediate thickness specimens of SENB and CCP, a nearly plane stress field occurs at $r/t = 1$. The departure from plane stress in the thicker specimens is associated with the gradient of out-of-plane stress.

In the three-dimensional boundary layer formulation analyses, the J-Integral varies along the crack front although a uniform stress intensity, $K_{far}$, is applied on the remote boundary of the mesh. At each section along the crack front, the contour integral has been shown to be path independent for contours with a small radius. However at large contours, the J-Integral reduces to the applied value of J known as $J_{far}$. Consequently in three-dimensional cases, the contour integral is ultimately path dependent.

The out-of-plane constraint loss has been shown to occur in a similar manner in SENB and boundary layer formulations. In CCP specimens, out-of-plane constraint loss is complicated by in-plane constraint loss associated with the geometry but still shows a similar decreasing trend across the thickness. In all specimens, the lower bound stress field approaches the plane stress field. The systematic development of out-of-plane constraint loss from a three-dimensional field at the crack tip and ahead of the crack front is discussed in detail in chapters 6 and 7.

| | Midplane $x_3/t=0$ | Quarterplane $x_3/t=0.25$ | Near Free surface* $x_3/t=0.49$ | Free Surface $x_3/t=0.5$ |
|---|---|---|---|---|
| Load ($\Omega_{far}$) = $J_{far}/\sigma_o\varepsilon_o t$ | $J_{loc}/\sigma_o\varepsilon_o t$ | $J_{loc}/\sigma_o\varepsilon_o t$ | $J_{loc}/\sigma_o\varepsilon_o t$ | $J_{loc}/\sigma_o\varepsilon_o t$ |
| 1 | 1.13 | 1.08 | 0.28 | 0.21 |
| 3 | 3.65 | 3.09 | 0.60 | 0.46 |
| 5 | 7.12 | 5.11 | 0.92 | 0.78 |
| 8 | 11.99 | 7.91 | 1.34 | 1.26 |
| 20 | 30.46 | 19.43 | 5.22 | 3.95 |

Table 5.1: Load levels along the crack front of three-dimensional boundary layer formulations. For load = 20, the near free surface data is located at $x_3/t = 0.47$.

| | Midplane $x_3/t=0$ | Quarterplane $x_3/t=0.25$ | Near Free surface $x_3/t=0.49$ | Free surface $x_3/t=0.5$ |
|---|---|---|---|---|
| $\Omega_{far}+T_{app}$ | $J_{loc}/\sigma_o\varepsilon_o t$ | $J_{loc}/\sigma_o\varepsilon_o t$ | $J_{loc}/\sigma_o\varepsilon_o t$ | $J_{loc}/\sigma_o\varepsilon_o t$ |
| $8+0\sigma_o$ | 11.99 | 7.91 | 1.34 | 1.26 |
| $8+0.5\sigma_o$ | 11.82 | 8.13 | 1.58 | 1.27 |
| $8-0.5\sigma_o$ | 10.28 | 8.07 | 1.57 | 1.64 |

Table 5.2: Load levels along the crack front of three-dimensional modified boundary layer formulations at a remote load 8 with positive and negative applied T-stress.

| Load ($\Omega_{far}$) = $J_{far}/\sigma_o\varepsilon_o t$ | Plastic zone r/t |
|---|---|
| 1 | 0.1 |
| 3 | 0.6 |
| 5 | 1.2 |
| 8 | 2 |
| 20 | 5.5 |

Table 5.3: The radius of the plastic zone at $\theta = 0^\circ$ for three-dimensional thin plate boundary layer formulations for a range of load levels.

(a)SENB B/(W-a) = 1

| | | Midplane $x_3/t$=0 | | Quarterplane $x_3/t$=0.25 | | Near Free Surface $x_3/t$=0.49 | | Free Surface $x_3/t$=0.5 | |
|---|---|---|---|---|---|---|---|---|---|
| $M/M_o$ | $r_p/t$ | $J_{loc}/\sigma_o\varepsilon_o t$ | $c\,\sigma_o/J_{loc}$ | $J_{loc}/\sigma_o\varepsilon_o t$ | $c\,\sigma_o/J_{loc}$ | $J_{loc}/\sigma_o\varepsilon_o t$ | $c\,\sigma_o/J_{loc}$ | $J_{loc}/\sigma_o\varepsilon_o t$ | $c\,\sigma_o/J_{loc}$ |
| 0.55 | 0.04 | 0.62 | 1615.5 | 0.56 | 1759.4 | 0.16 | 5994.3 | 0.12 | 8393.1 |
| 0.956 | 0.3 | 4.90 | 204.1 | 4.3 | 232.2 | 0.55 | 1786.5 | 0.56 | 1768.6 |
| 0.971 | 1 | 10.9 | 92 | 9.04 | 110.5 | 1.13 | 879 | 1.22 | 817.1 |
| 0.977 | 1 | 17.4 | 57.4 | 13.8 | 72.1 | 1.8 | 546.8 | 1.92 | 519.8 |
| 0.98 | 1 | 23.9 | 41.7 | 18.7 | 53.5 | 2.6 | 389.3 | 2.63 | 380 |
| 0.985 | 1 | 34.0 | 29.3 | 26.2 | 38.2 | 3.7 | 268.6 | 3.6 | 272 |

(b)SENB B/(W-a) = 0.5

| | | Midplane $x_3/t$=0 | | Quarterplane $x_3/t$=0.25 | | Near Free Surface $x_3/t$=0.49 | | Free Surface $x_3/t$=0.5 | |
|---|---|---|---|---|---|---|---|---|---|
| $M/M_o$ | $r_p/t$ | $J_{loc}/\sigma_o\varepsilon_o t$ | $c\,\sigma_o/J_{loc}$ | $J_{loc}/\sigma_o\varepsilon_o t$ | $c\,\sigma_o/J_{loc}$ | $J_{loc}/\sigma_o\varepsilon_o t$ | $c\,\sigma_o/J_{loc}$ | $J_{loc}/\sigma_o\varepsilon_o t$ | $c\,\sigma_o/J_{loc}$ |
| 0.268 | 0.15 | 0.61 | 1634.3 | 0.57 | 1737.4 | 0.18 | 5499.4 | 0.13 | 7545.4 |
| 0.436 | 0.75 | 5.6 | 178.6 | 3.9 | 256.2 | 0.72 | 1392.6 | 0.65 | 1520 |
| 0.443 | 2 | 12.2 | 82.2 | 7.7 | 129.2 | 1.3 | 765.5 | 1.33 | 749.8 |
| 0.445 | 2 | 18.8 | 52.9 | 11.6 | 85.7 | 1.9 | 505.5 | 2.03 | 492.3 |
| 0.447 | 2 | 25.7 | 38.9 | 15.6 | 63.8 | 2.7 | 368.7 | 2.73 | 366.2 |
| 0.45 | 2 | 35.9 | 27.7 | 21.7 | 45.9 | 3.87 | 258.2 | 3.73 | 267.9 |

(c) SENB B/(W-a) = 0.1

| | | Midplane $x_3/t$=0 | | Quarterplane $x_3/t$=0.25 | | Near Free Surface $x_3/t$=0.42 | | Free Surface $x_3/t$=0.5 | |
|---|---|---|---|---|---|---|---|---|---|
| $M/M_o$ | $r_p/t$ | $J_{loc}/\sigma_o\varepsilon_o t$ | $c\,\sigma_o/J_{loc}$ | $J_{loc}/\sigma_o\varepsilon_o t$ | $c\,\sigma_o/J_{loc}$ | $J_{loc}/\sigma_o\varepsilon_o t$ | $c\,\sigma_o/J_{loc}$ | $J_{loc}/\sigma_o\varepsilon_o t$ | $c\,\sigma_o/J_{loc}$ |
| 0.034 | 0.5 | 0.24 | 4178.5 | 0.22 | 4583.4 | 0.14 | 6987.5 | 0.07 | 13893 |
| 0.054 | 1.2 | 0.77 | 1284.3 | 0.53 | 1851.9 | 0.31 | 3215.8 | 0.16 | 6081.9 |
| 0.088 | 3.5 | 6.15 | 162.5 | 3.58 | 279.3 | 1.73 | 577.4 | 0.92 | 1084.8 |
| 0.096 | 3.7 | 12.1 | 82.4 | 7.24 | 138 | 3.5 | 284.4 | 1.62 | 617 |
| 0.103 | 10 | 17.7 | 56.2 | 10.9 | 91.6 | 5.4 | 184.4 | 2.32 | 430.8 |
| 0.109 | 10 | 23.3 | 42.8 | 14.6 | 68.4 | 7.4 | 134.2 | 3.02 | 331.3 |
| 0.119 | 10 | 31.6 | 31.6 | 20.3 | 49.2 | 10.6 | 94.1 | 3.98 | 251.2 |

Table 5.4: SENB full-field specimens characterised in terms of local load level along the crack front, $J_{loc}/\sigma_o\varepsilon_o t$ and J-Dominance parameter, $c\,\sigma_o/J_{loc}$ for (a) B/W-a = 1 (b) 0.5 and (c) 0.1. The limit load is given in terms of as $M/M_o$ where $M_o$ is limit load in three-point-bend and M is bend load as given in equations (4.4) and (4.5).

(a) CCP B/(W-a) = 1

| | | Midplane $x_3/t=0$ | | Quarterplane $x_3/t=0.25$ | | Near Free Surface $x_3/t=0.49$ | | Free Surface $x_3/t=0.5$ | |
|---|---|---|---|---|---|---|---|---|---|
| $P/P_o$ | $r_p/t$ | $J_{loc}/\sigma_o\varepsilon_o t$ | $c\,\sigma_o/J_{loc}$ | $J_{loc}/\sigma_o\varepsilon_o t$ | $c\,\sigma_o/J_{loc}$ | $J_{loc}/\sigma_o\varepsilon_o t$ | $c\,\sigma_o/J_{loc}$ | $J_{loc}/\sigma_o\varepsilon_o t$ | $c\,\sigma_o/J_{loc}$ |
| 0.005 | 0.25 | 0.85 | 1170.6 | 0.84 | 1188.1 | 0.26 | 3803.9 | 0.22 | 4414.7 |
| 0.734 | 0.8 | 1.9 | 512.9 | 1.8 | 557.9 | 0.56 | 1779.8 | 0.515 | 1939.6 |
| 0.912 | 1 | 6.9 | 144.6 | 5.9 | 169.6 | 2.1 | 476.6 | 1.89 | 529.3 |
| 0.938 | 1 | 18.3 | 54.8 | 15.1 | 66.1 | 5.4 | 184.2 | 4.9 | 202.1 |
| 0.953 | 1 | 35.4 | 28.2 | 29.3 | 34.1 | 9.4 | 95.1 | 9.4 | 105.9 |
| 0.985 | 1 | 57.4 | 17.4 | 47.9 | 20.8 | 16.8 | 59.6 | 14.9 | 66.8 |

(b) CCP B/(W-a) = 0.5

| | | Midplane $x_3/t=0$ | | Quarterplane $x_3/t=0.25$ | | Near Free Surface $x_3/t=0.49$ | | Free Surface $x_3/t=0.5$ | |
|---|---|---|---|---|---|---|---|---|---|
| $P/P_o$ | $r_p/t$ | $J_{loc}/\sigma_o\varepsilon_o t$ | $c\,\sigma_o/J_{loc}$ | $J_{loc}/\sigma_o\varepsilon_o t$ | $c\,\sigma_o/J_{loc}$ | $J_{loc}/\sigma_o\varepsilon_o t$ | $c\,\sigma_o/J_{loc}$ | $J_{loc}/\sigma_o\varepsilon_o t$ | $c\,\sigma_o/J_{loc}$ |
| 0.729 | 0.56 | 0.95 | 1049.7 | 0.88 | 1139.8 | 0.27 | 3746.5 | 0.23 | 4314.3 |
| 0.897 | 1.4 | 2.2 | 453.3 | 1.87 | 534.4 | 0.62 | 1614.7 | 0.55 | 1825.6 |
| 0.917 | 2 | 7.4 | 134.7 | 6.1 | 164.7 | 2.2 | 450 | 1.9 | 525 |
| 0.922 | 2 | 19.1 | 52.3 | 15.4 | 64.7 | 5.8 | 172.5 | 4.94 | 202.4 |
| 0.926 | 2 | 36.1 | 27.7 | 29.3 | 34.1 | 10.6 | 94.3 | 9.34 | 107.1 |
| 0.931 | 2 | 58.9 | 17.2 | 47.7 | 20.9 | 16.9 | 59.2 | 14.6 | 68.5 |

(c) CCP B/(W-a) = 0.1

| | | Midplane $x_3/t=0$ | | Quarterplane $x_3/t=0.25$ | | Near Free Surface $x_3/t=0.42$ | | Free Surface $x_3/t=0.5$ | |
|---|---|---|---|---|---|---|---|---|---|
| $P/P_o$ | $r_p/t$ | $J_{loc}/\sigma_o\varepsilon_o t$ | $c\,\sigma_o/J_{loc}$ | $J_{loc}/\sigma_o\varepsilon_o t$ | $c\,\sigma_o/J_{loc}$ | $J_{loc}/\sigma_o\varepsilon_o t$ | $c\,\sigma_o/J_{loc}$ | $J_{loc}/\sigma_o\varepsilon_o t$ | $c\,\sigma_o/J_{loc}$ |
| 0.724 | 3 | 1.2 | 834.7 | 0.89 | 1124.4 | 0.48 | 2060.6 | 0.3 | 3330.2 |
| 0.876 | 7.5 | 2.5 | 400 | 1.9 | 523.8 | 1.1 | 939.1 | 0.63 | 1568.5 |
| 0.887 | 9.8 | 8 | 125.4 | 6.24 | 160.4 | 3.7 | 272.4 | 1.89 | 526.8 |
| 0.892 | 10 | 19.2 | 52.7 | 15.3 | 65.4 | 9.6 | 107.8 | 4.84 | 206.6 |
| 0.898 | 10 | 35.4 | 28.3 | 28.5 | 35.1 | 17.8 | 56.1 | 9.05 | 110.5 |
| 0.904 | 10 | 56.9 | 17.5 | 46.0 | 21.7 | 28.9 | 34.5 | 13.8 | 72.1 |

Table 5.5: CCP full-field specimens characterised in terms of load level along the crack front for $J_{loc}/\sigma_o\varepsilon_o t$ and J-Dominance parameter, $c\,\sigma_o/J_{loc}$. The limit load is given in terms of as $P/P_o$ where $P_o$ is limit load in centre crack tension panel and P is bend load as given in equations (4.7) and (4.9).

| | | | | SENB and CCP | | | | | |
|---|---|---|---|---|---|---|---|---|---|
| BLF/MBLF | | BLF* | | B/(W-a) = 1 | | B/(W-a) = 0.5 | | B/(W-a) = 0.1 | |
| $x_3/t$ | z/t | $x_3/t$ | z/t | $x_3/t$ | z/t | $x_3/t$ | z/t | $x_3/t$ | z/t |
| 0 | 0.5 | 0 | 0.5 | 0 | 0.5 | 0 | 0.5 | 0 | 0.5 |
| 0.04 | 0.46 | 0.04 | 0.46 | 0.032 | 0.468 | 0.032 | 0.032 | 0.08 | 0.42 |
| 0.08 | 0.42 | 0.08 | 0.42 | 0.064 | 0.436 | 0.064 | 0.064 | 0.14 | 0.36 |
| 0.12 | 0.38 | 0.12 | 0.38 | 0.096 | 0.404 | 0.096 | 0.096 | 0.2 | 0.3 |
| 0.16 | 0.34 | 0.16 | 0.34 | 0.128 | 0.372 | 0.128 | 0.372 | 0.25 | 0.25 |
| 0.2 | 0.3 | 0.2 | 0.3 | 0.16 | 0.34 | 0.16 | 0.34 | 0.32 | 0.18 |
| 0.25 | 0.25 | 0.25 | 0.25 | 0.192 | 0.308 | 0.192 | 0.308 | 0.38 | 0.12 |
| 0.28 | 0.22 | 0.28 | 0.22 | 0.224 | 0.276 | 0.224 | 0.276 | 0.42 | 0.08 |
| 0.32 | 0.18 | 0.32 | 0.18 | 0.25 | 0.25 | 0.25 | 0.25 | 0.47 | 0.03 |
| 0.36 | 0.14 | 0.36 | 0.14 | 0.288 | 0.212 | 0.288 | 0.212 | 0.5 | 0 |
| 0.39 | 0.11 | 0.4 | 0.1 | 0.32 | 0.18 | 0.32 | 0.18 | | |
| 0.42 | 0.08 | 0.436 | 0.064 | 0.352 | 0.148 | 0.352 | 0.148 | | |
| 0.45 | 0.05 | 0.47 | 0.033 | 0.384 | 0.116 | 0.384 | 0.116 | | |
| 0.46 | 0.04 | 0.5 | 0 | 0.408 | 0.092 | 0.408 | 0.092 | | |
| 0.48 | 0.02 | | | 0.428 | 0.072 | 0.428 | 0.072 | | |
| 0.49 | 0.01 | | | 0.448 | 0.052 | 0.448 | 0.052 | | |
| 0.5 | 0 | | | 0.468 | 0.032 | 0.468 | 0.032 | | |
| | | | | 0.48 | 0.02 | 0.49 | 0.01 | | |
| | | | | 0.49 | 0.01 | 0.5 | 0 | | |
| | | | | 0.5 | 0 | | | | |

Legends

a) BLF = Boundary Layer Formulations, MBLF = Modified Boundary Layer Formulations.

b) BLF*: Only in tip-mesh for $\Omega_{far} = 20$.

c) t and B are interchangeably use to represent the thickness.

d) The sections $(x_3/t) = 0$, 0.25 and 0.5 represent the midplane, the quarterplane and the free surface.

e) $x_3/t$ is referenced from the midplane while z/t is referenced from the free surface.

Table 5.6: The sections of the three-dimensional specimens $(x_3/t)$ and (z/t) at which data are extracted.

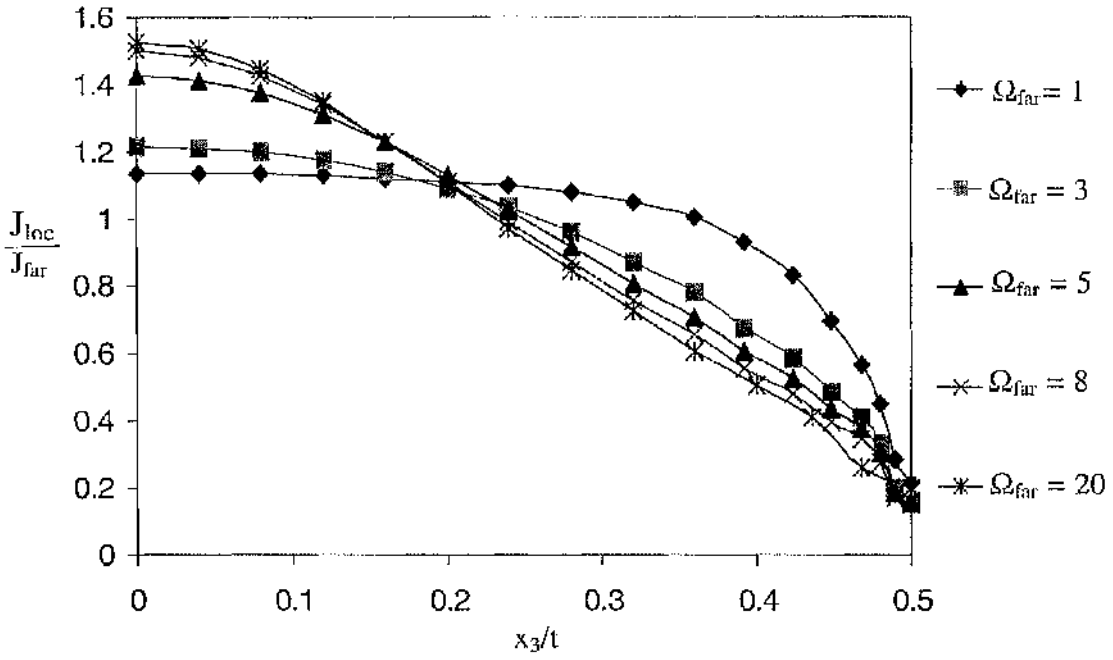


Figure 5.1: The variation of the local J along the crack front for load levels, $\Omega_{far}$ = 1, 3, 5, 8, 20.

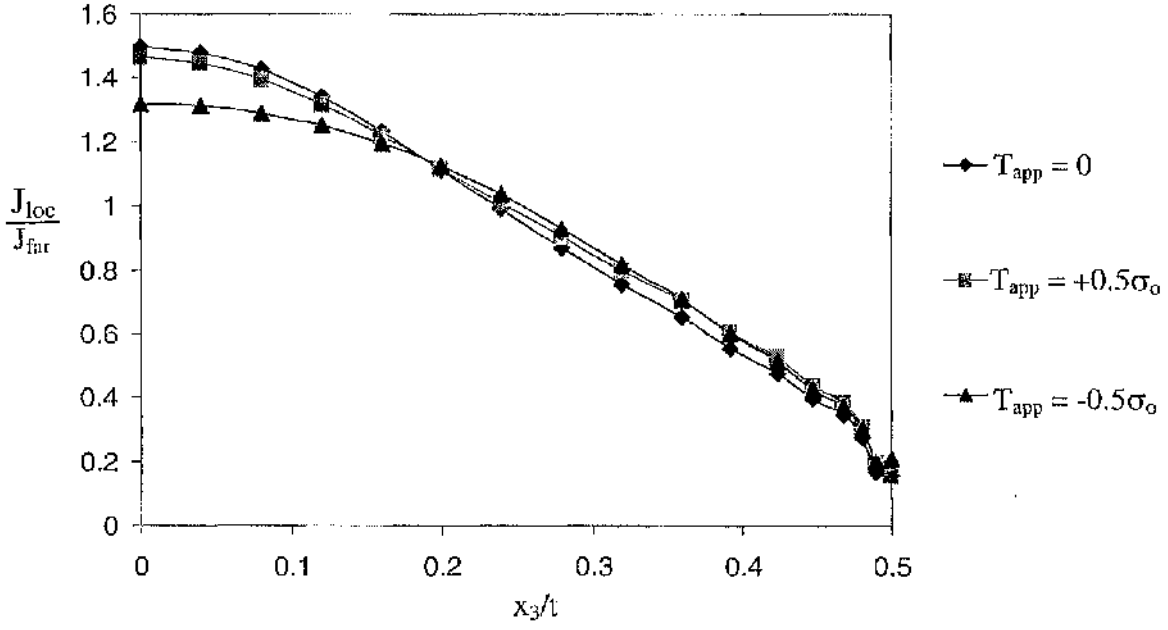


Figure 5.2: The variation of the local J along the crack front at a remote load levels $\Omega_{far}$ = 8 showing the effect of $T_{app}$.

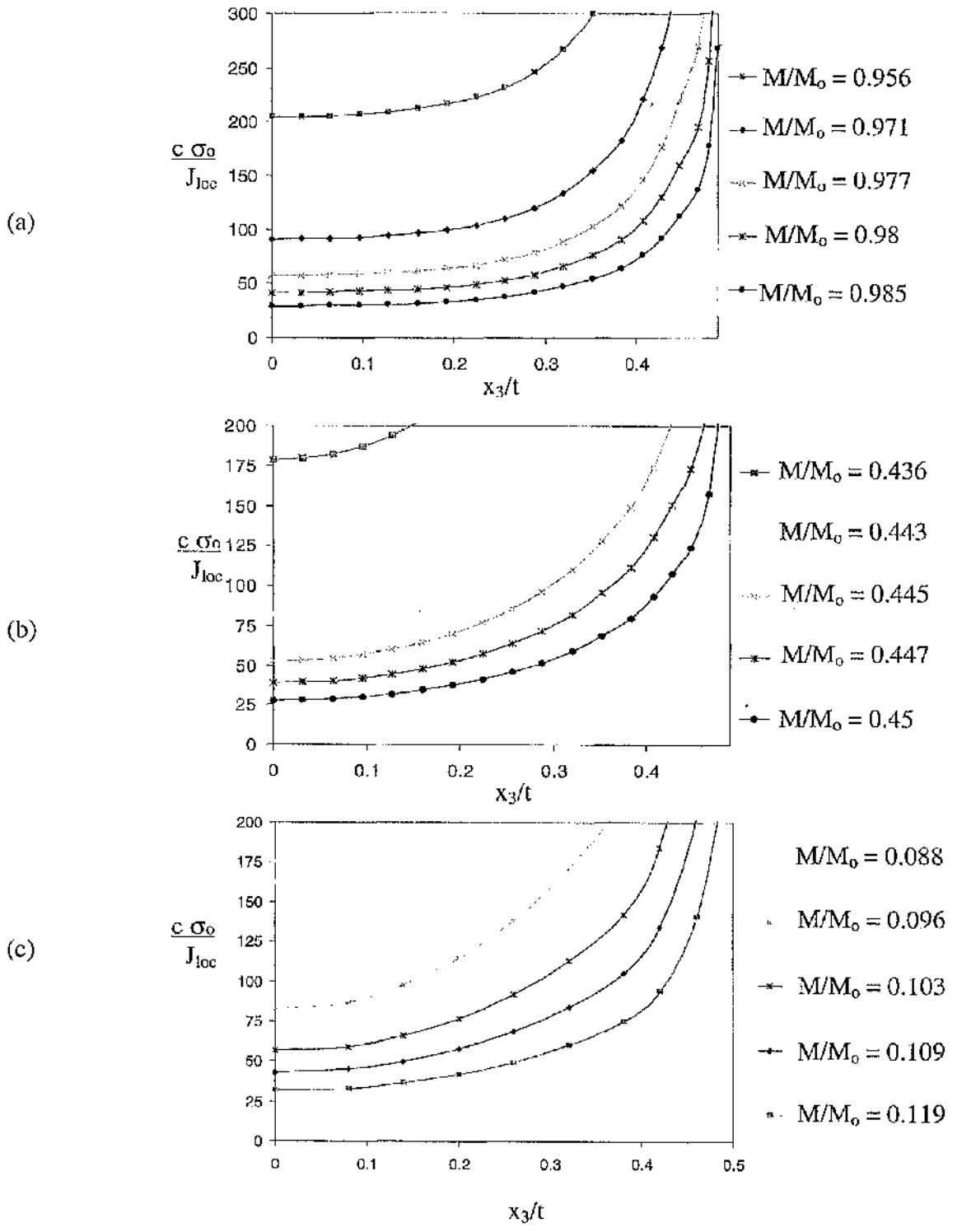


Figure 5.3: The local loading parameter ($c\sigma_o/J_{loc}$) along the crack front of SENB specimens (a) B/(W-a) = 1, (b) B/(W-a) = 0.5, (c) B/(W-a) = 0.1 at load levels characterised by the radius of plasticity at the midplane $x_3/t = 0$.

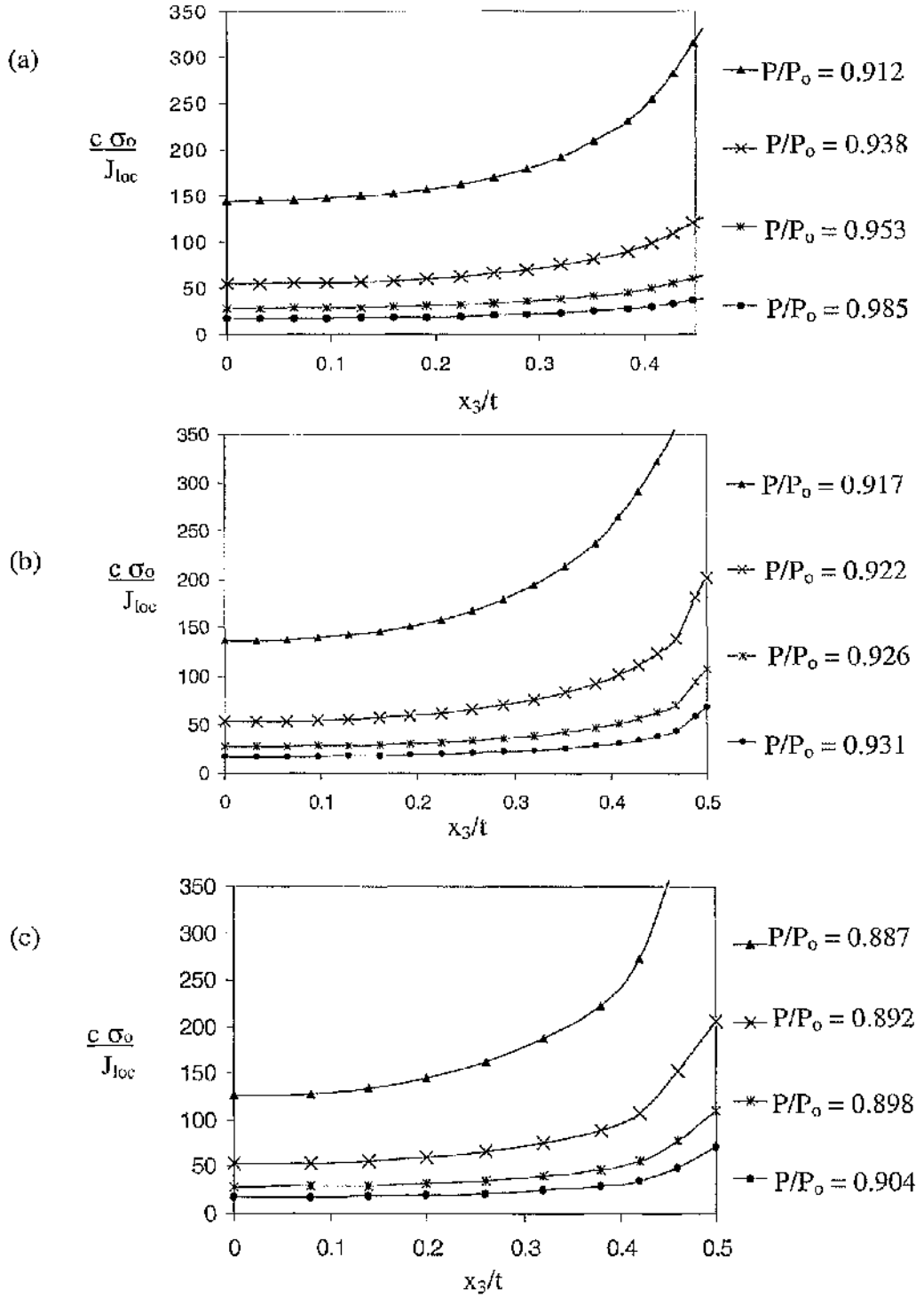


Figure 5.4: The local loading parameter ($c\sigma_o/J_{loc}$) along the crack front of CCP specimens (a) B/(W-a) = 1, (b) B/(W-a) = 0.5, (c) B/(W-a) = 0.1 at load levels identified by the radius of plasticity at the midplane $x_3/t = 0$.

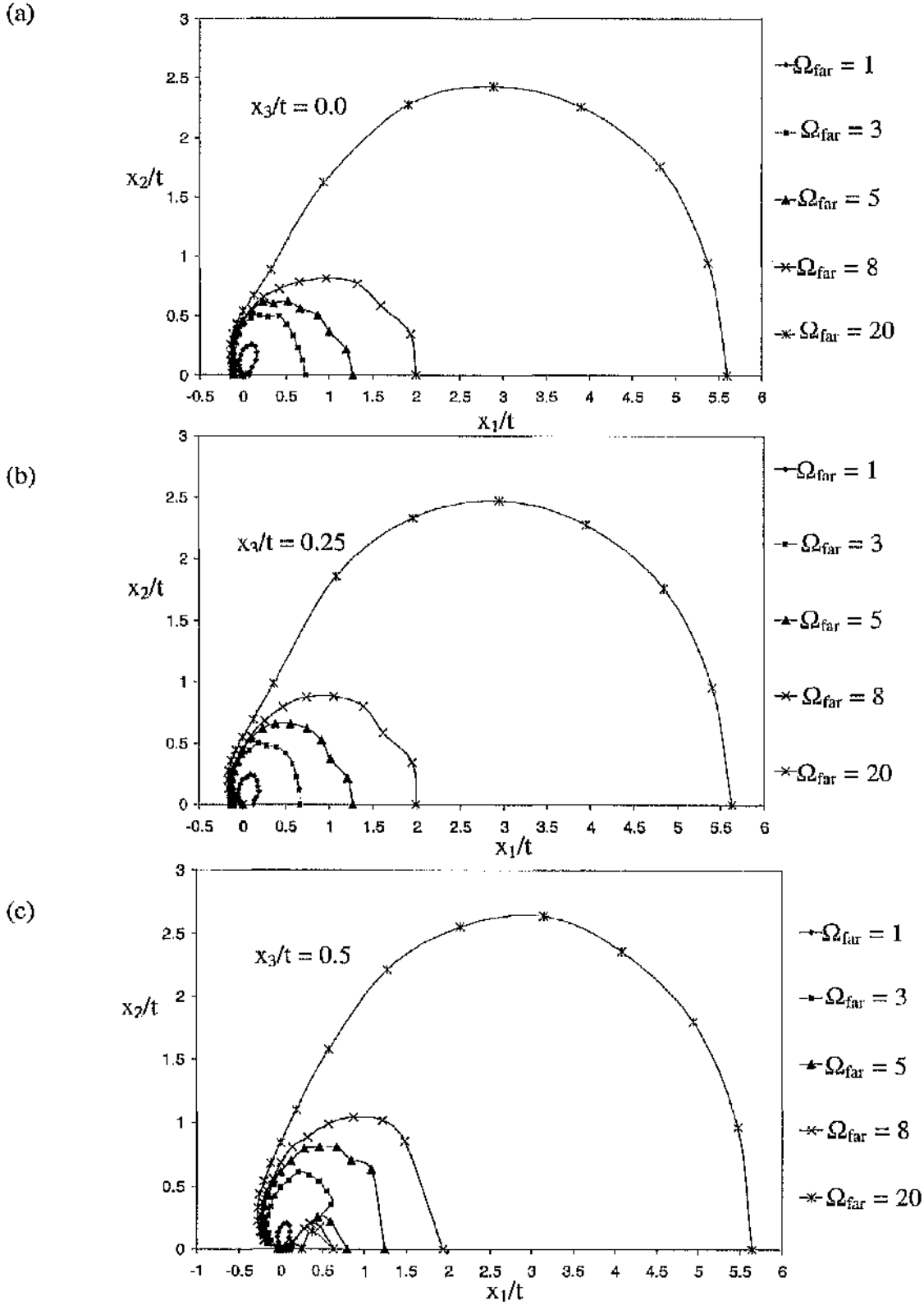


Figure 5.5: The plastic zone determined in a non-hardening boundary layer formulations for $\Omega_{far} = 1, 3, 5, 8, 20$ at (a) the midplane, (b) the quarterplane and (c) the free surface non-dimensionalised by t.

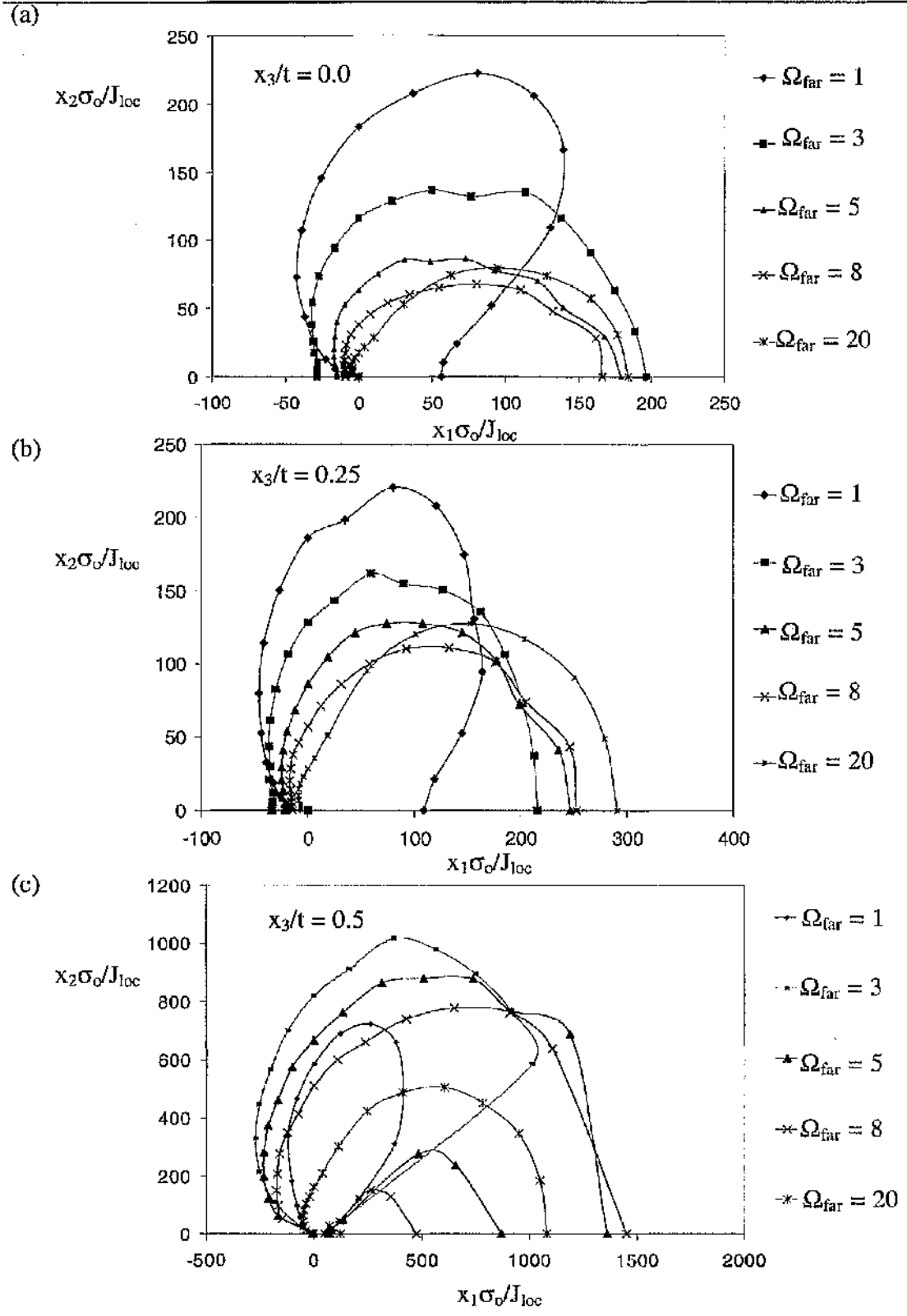


Figure 5.6: The plastic zone determined in a non-hardening boundary layer formulation for $\Omega_{far} = 1, 3, 5, 8, 20$ at (a) the midplane, (b) the quarterplane and (c) the free surface non-dimensionalised $J_{loc}/\sigma_o$.

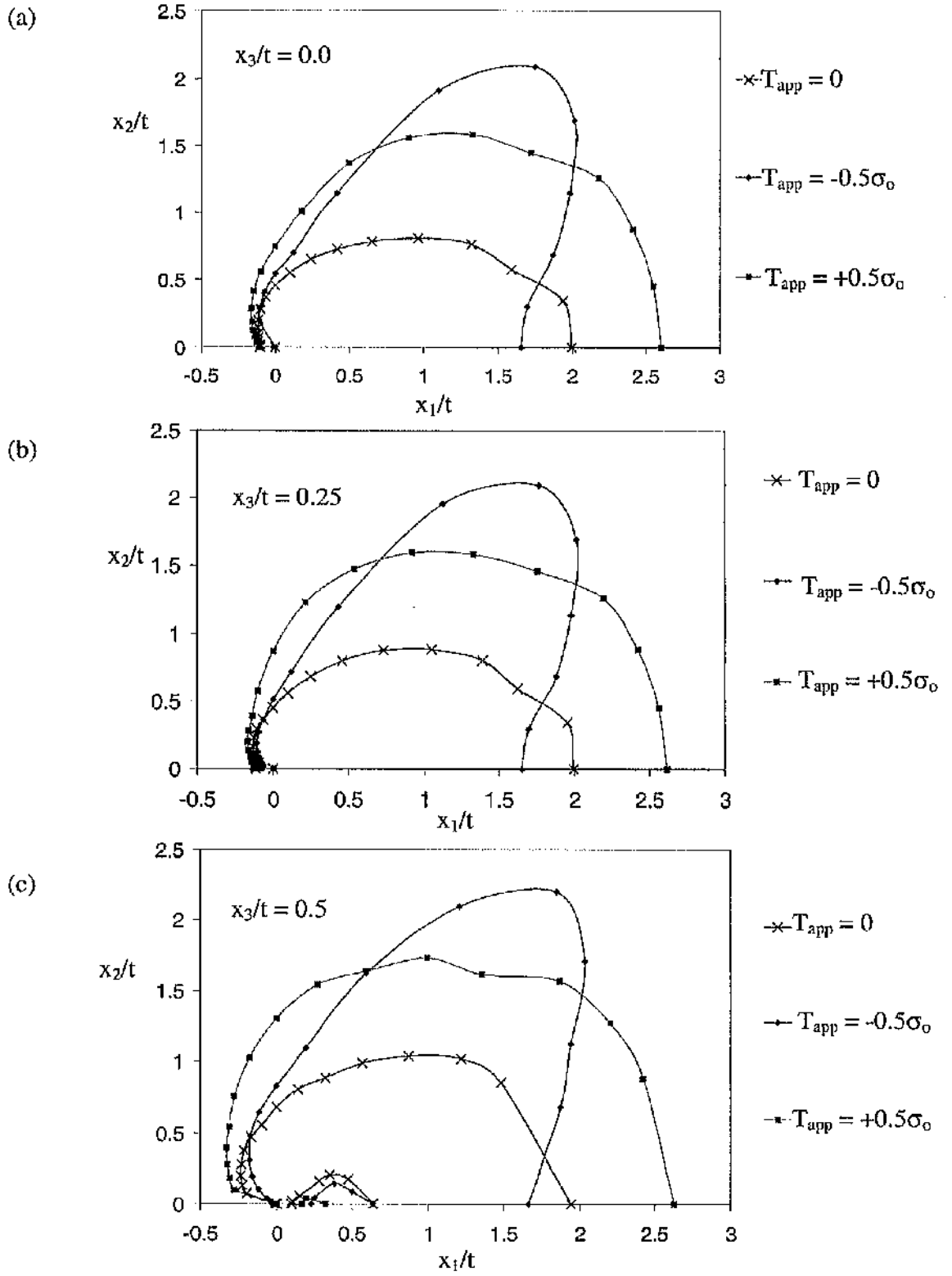


Figure 5.7: The plastic zone determined in a non-hardening boundary layer formulation for $\Omega_{far} = 8$ for (a) the midplane, (b) the quarter plane and (c) the free surface non-dimensionalised by t at different $T_{app}$.

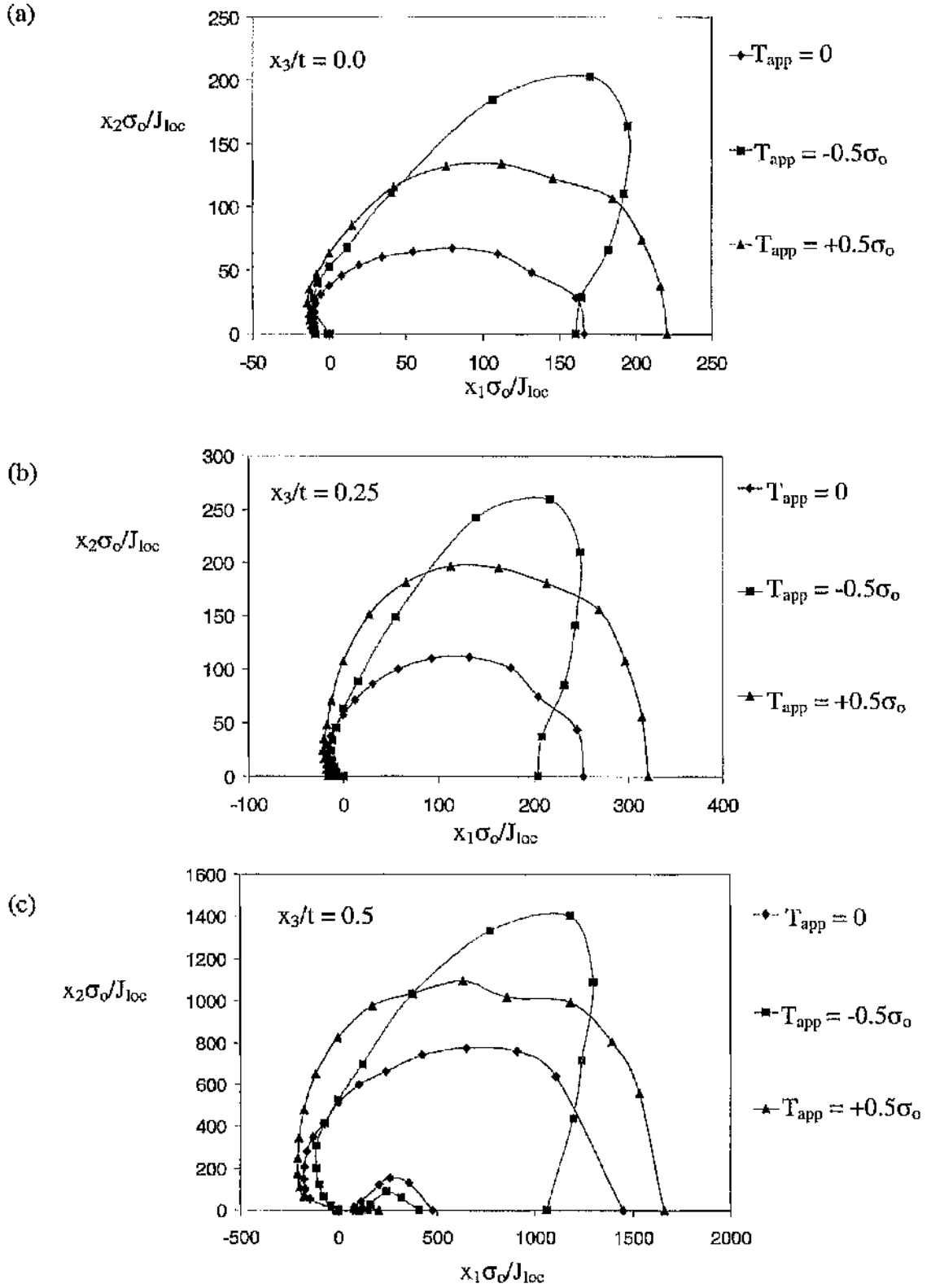


Figure 5.8: The plastic zone determined in a non-hardening boundary layer formulations for $\Omega_{far} = 8$ at (a) the midplane, (b) the quarter plane and (c) the free surface non-dimensionalised by $J_{loc}/\sigma_o$ at different $T_{app}$.

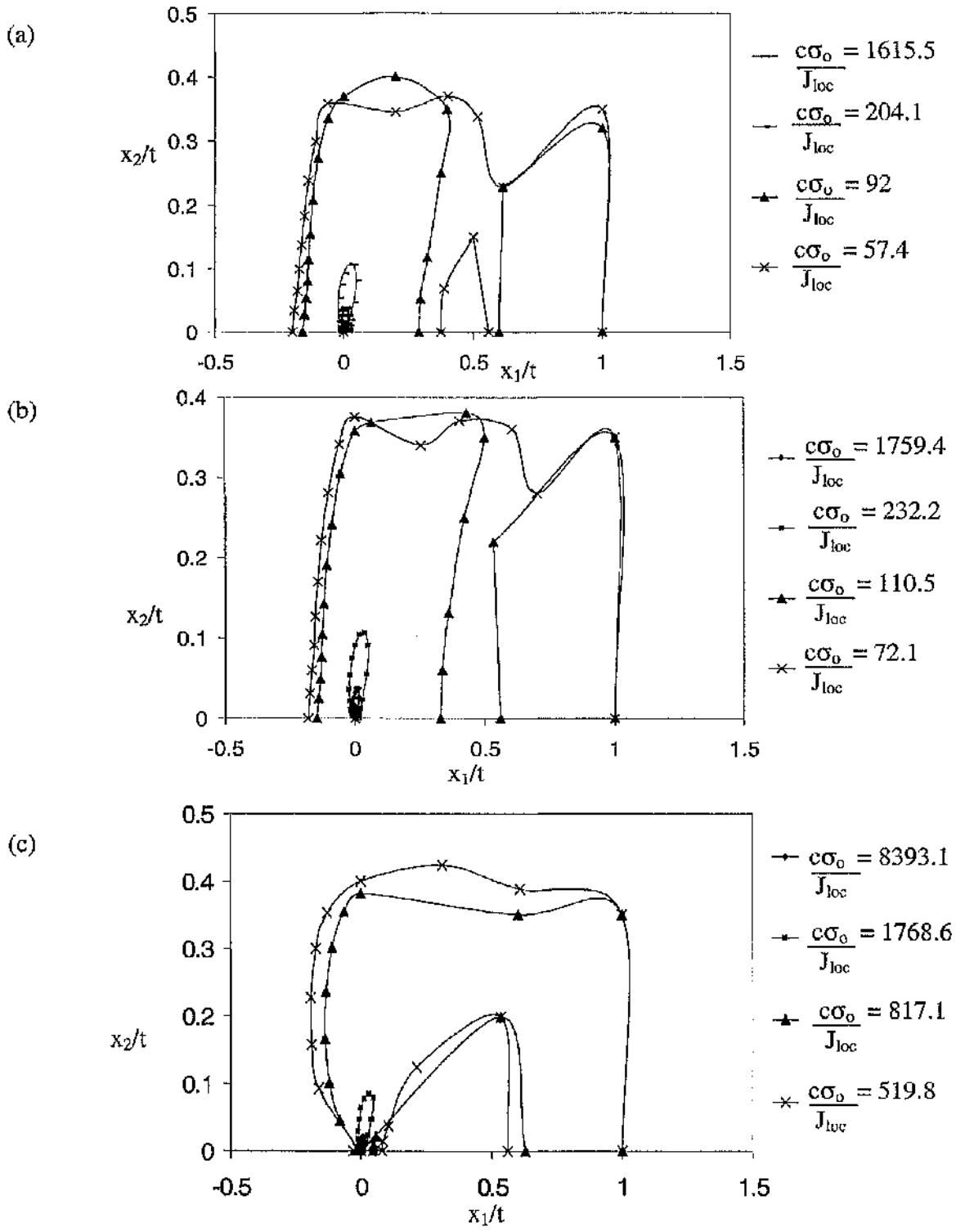


Figure 5.9: The plastic zone for a non-hardening SENB B/(W-a) = 1 at (a) the midplane, (b) the quarter plane and (c) the free surface non-dimensionalised t.

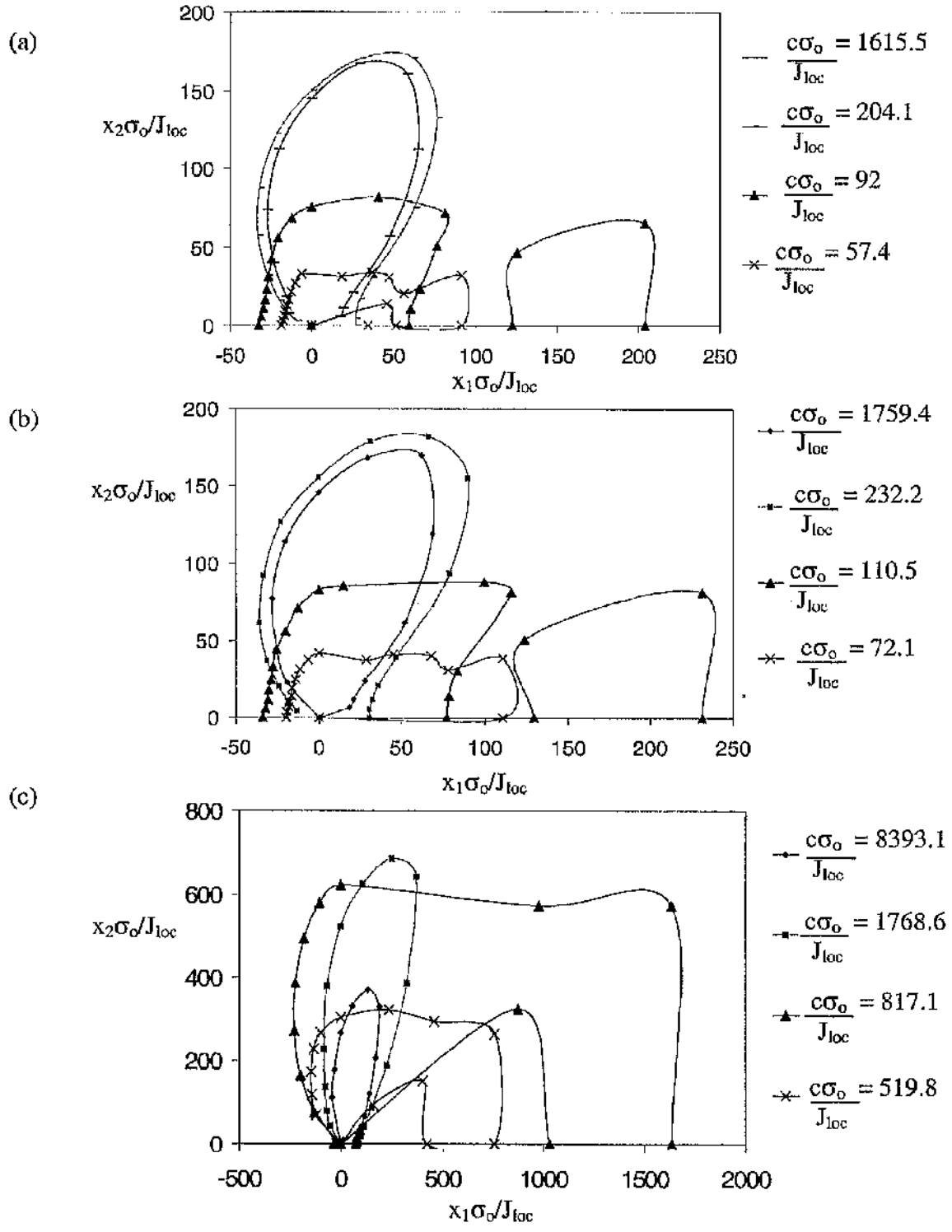


Figure 5.10: The plastic zone for a non-hardening SENB B/(W-a) = 1 at (a) the midplane, (b) the quarter plane and (c) the free surface non-dimensionalised by $J_{loc}/\sigma_o$.

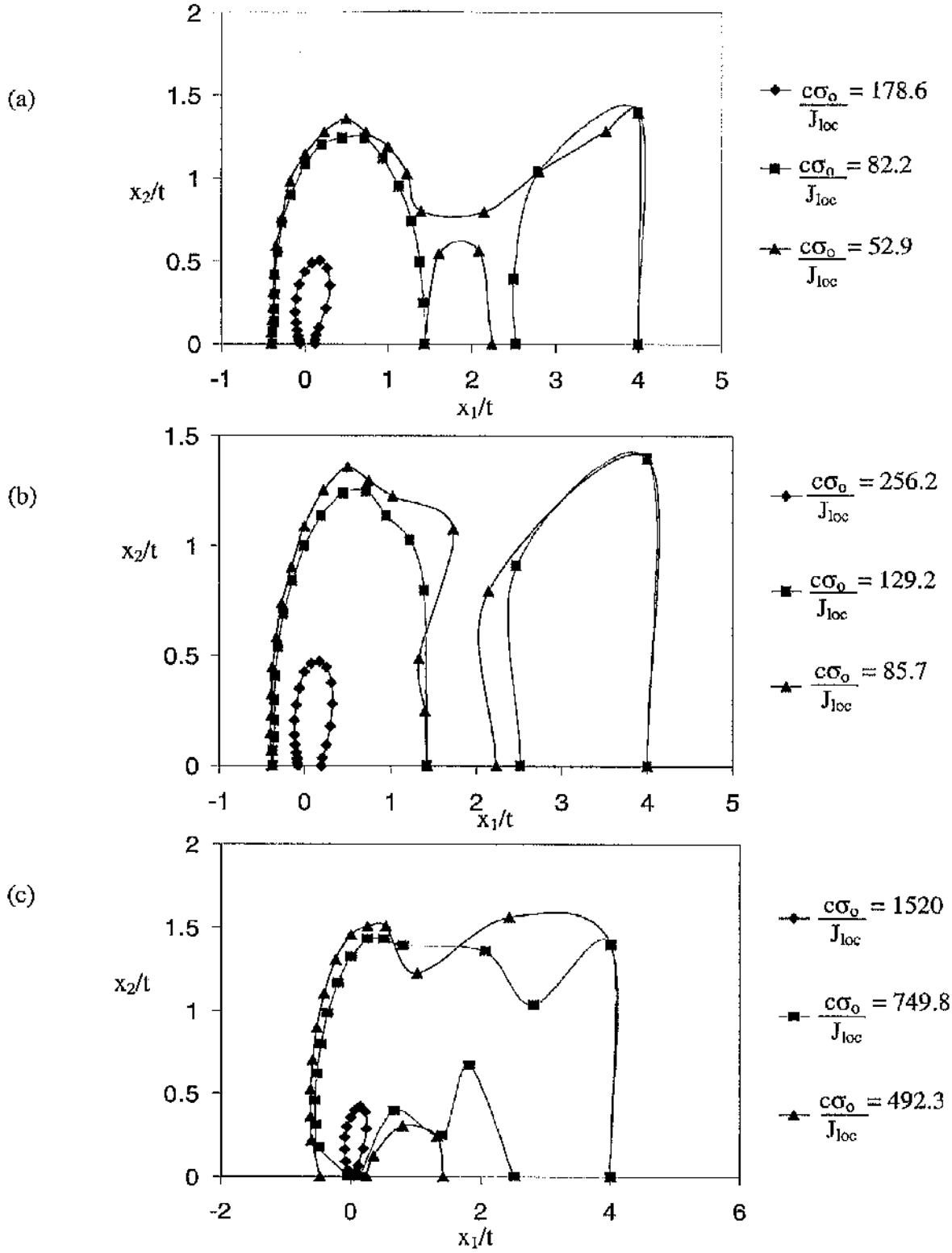


Figure 5.11: The plastic zone for a non-hardening SENB B/(W-a) = 0.5 at (a) the midplane, (b) the quarterplane and (c) the free surface non-dimensionalised t.

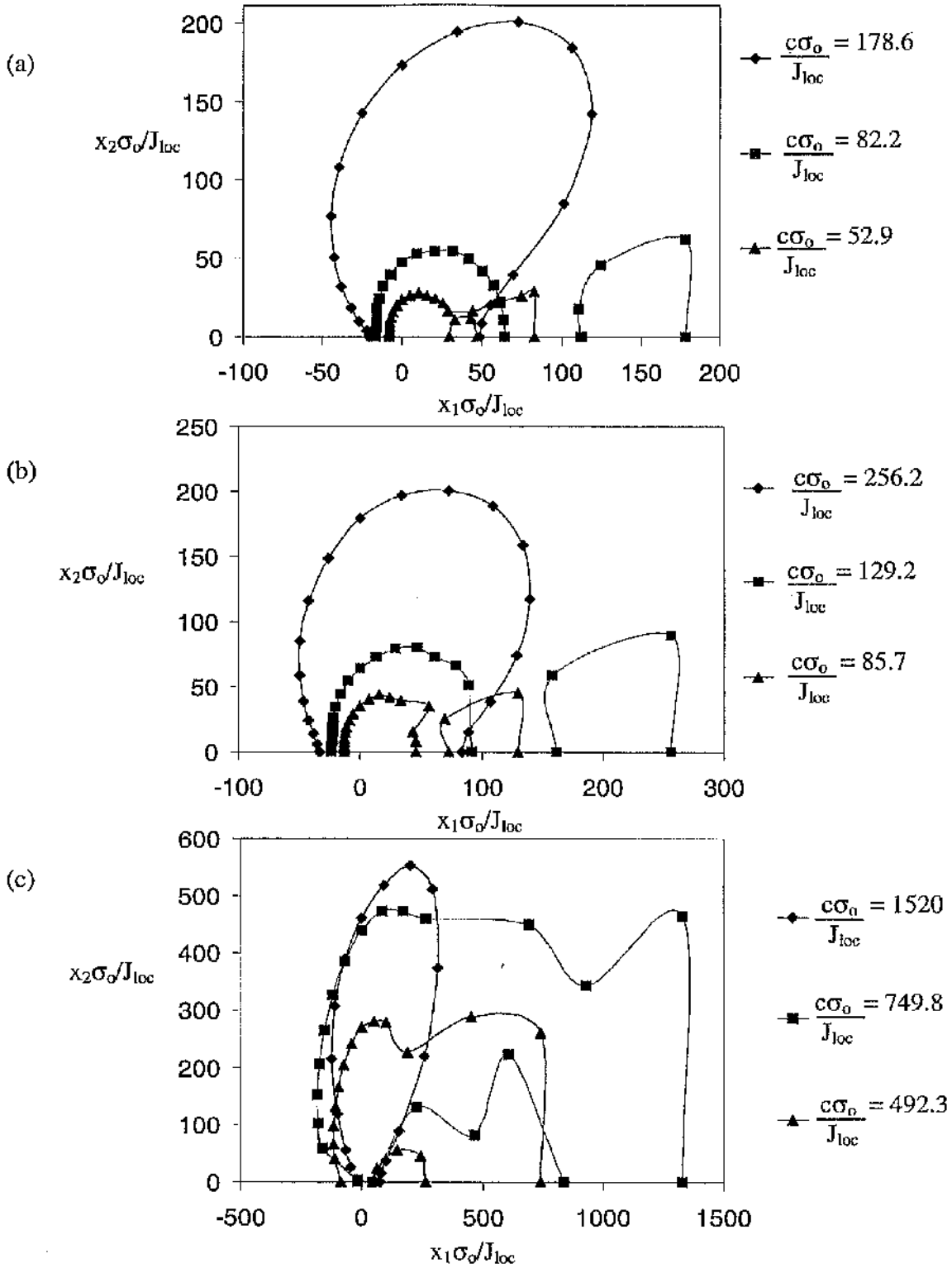


Figure 5.12: The plastic zone for non-hardening SENB B/(W-a) = 0.5 at (a) the midplane, (b) the quarter plane and (c) the free surface non-dimensionalised by $J_{loc}/\sigma_o$.

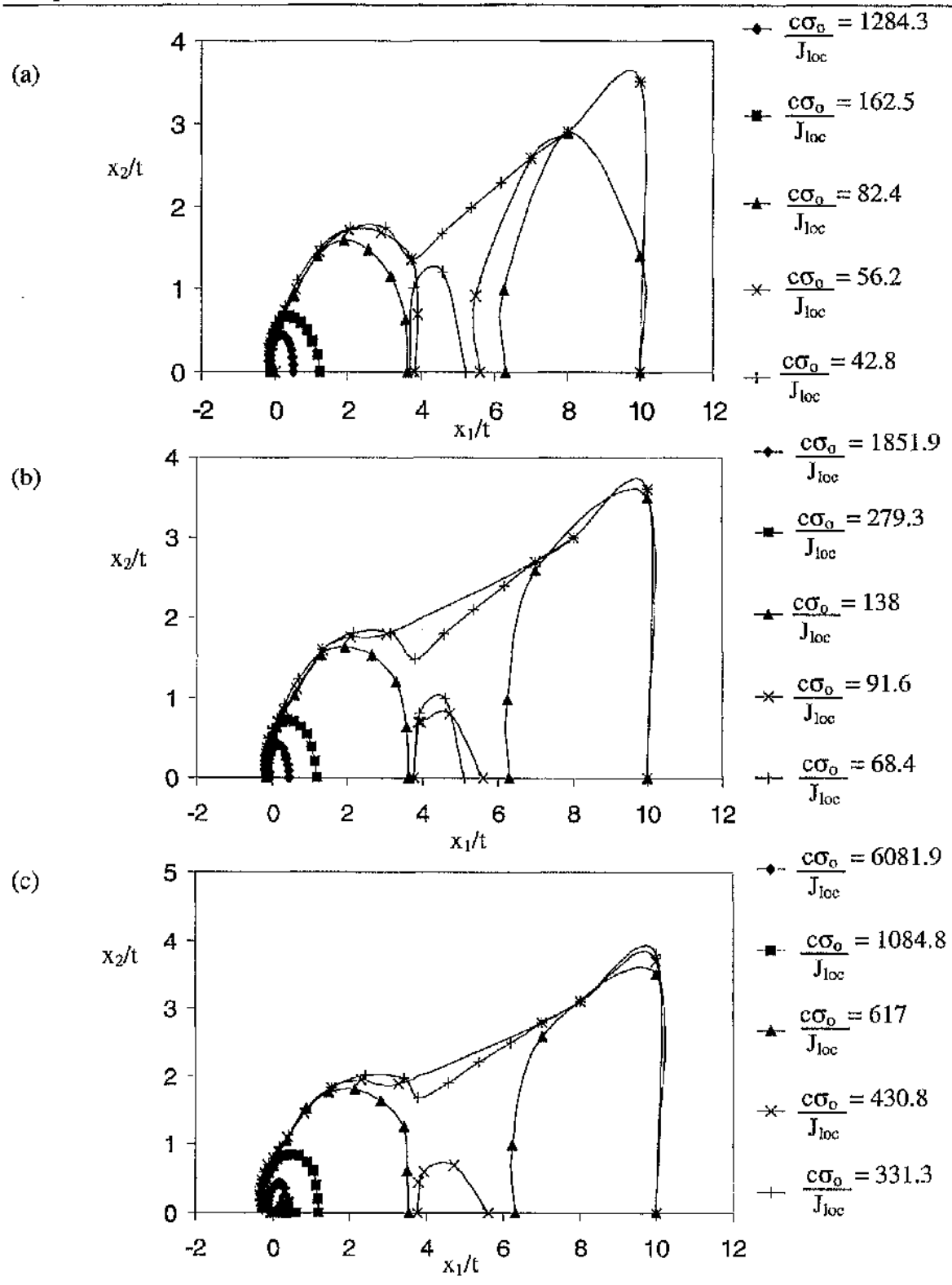


Figure 5.13: The plastic zone for a non-hardening SENB B/(W-a) = 0.1 at (a) the midplane, (b) the quarterplane and (c) the free surface non-dimensionalised t.

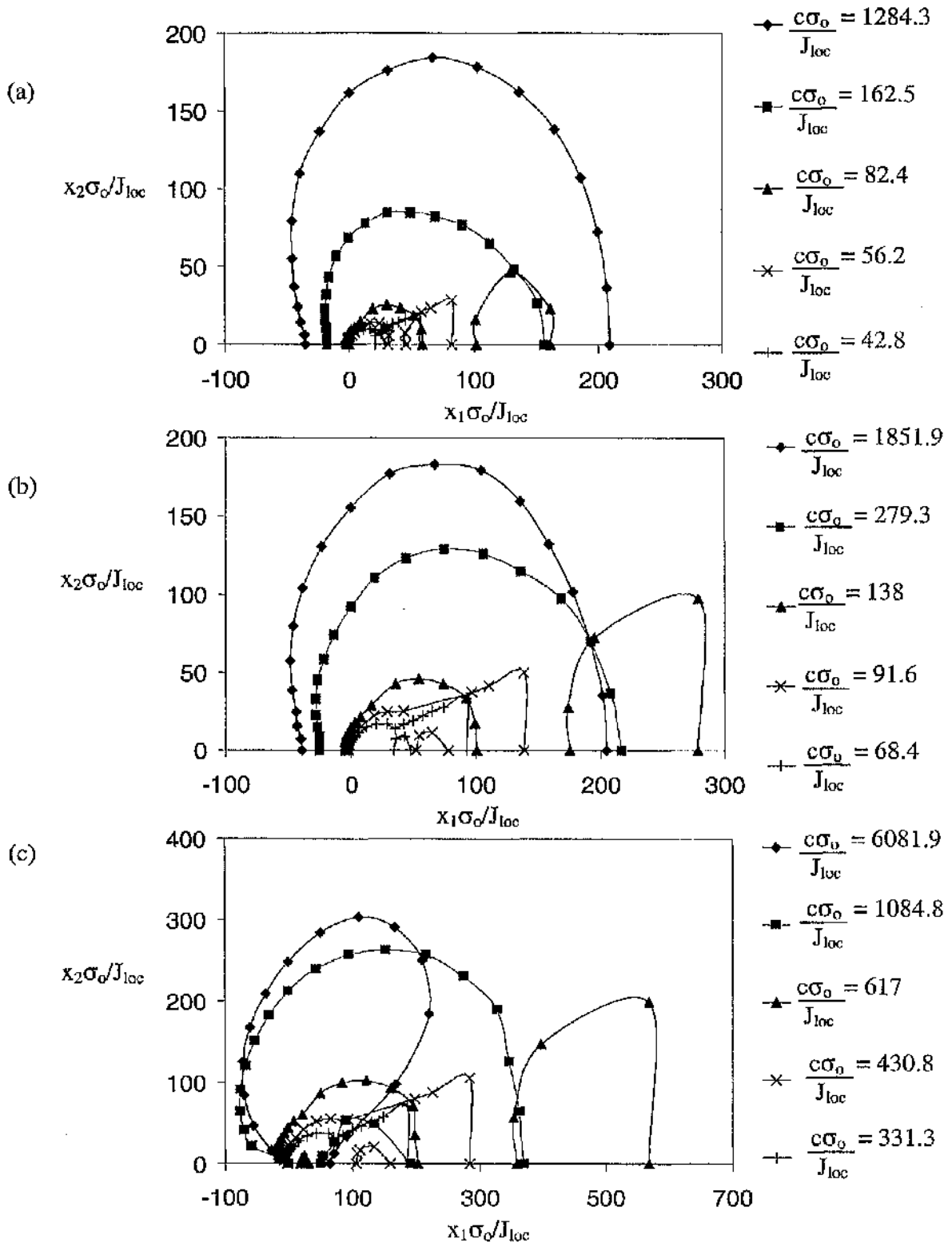


Figure 5.14: The plastic zone for a non-hardening SENB B/(W-a) = 0.1 at (a) the midplane, (b) the quarterplane and (c) the free surface non-dimensionalised $J_{loc}/\sigma_o$.

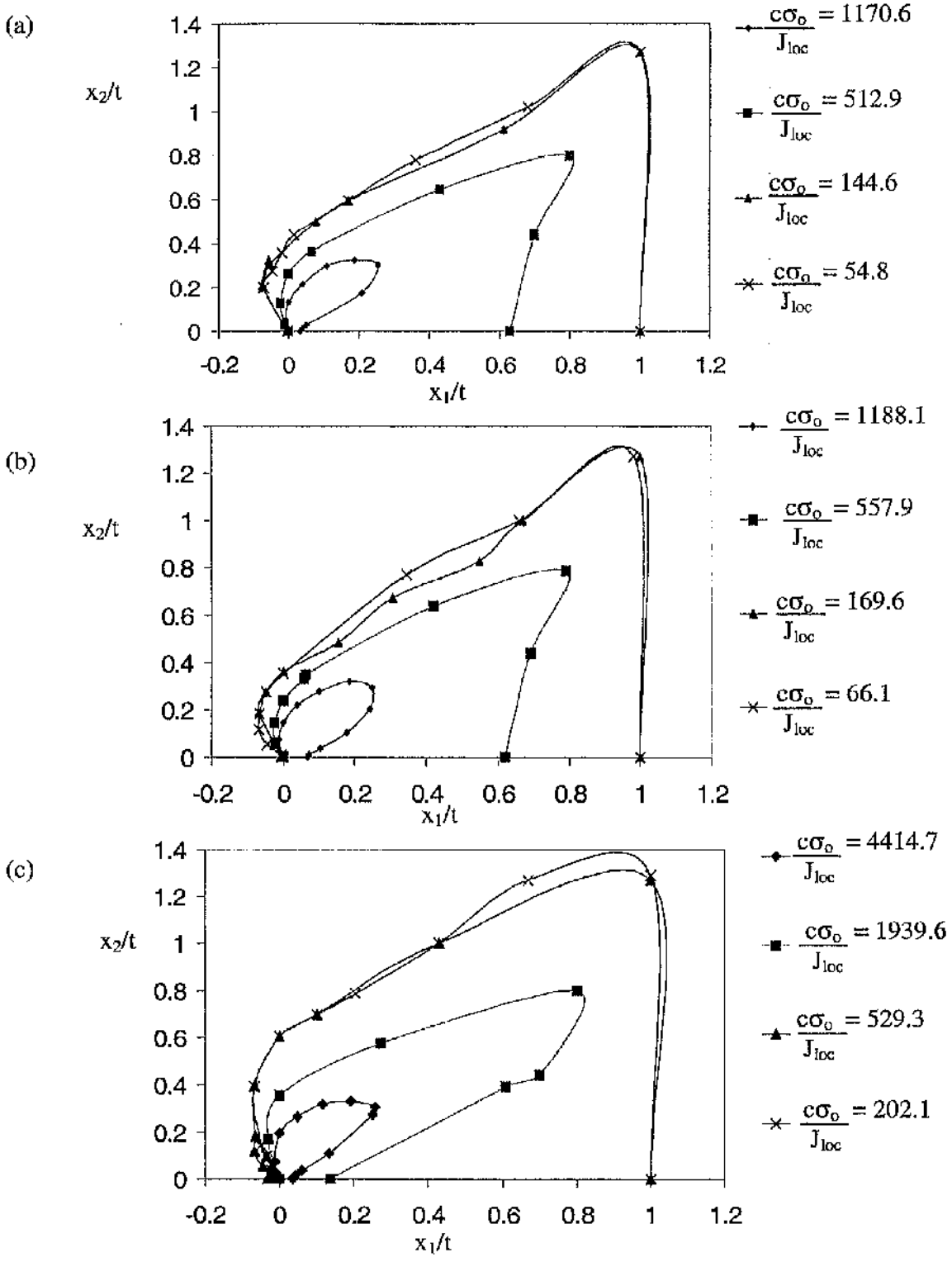


Figure 5.15: The plastic zone for a non-hardening CCP specimen B/(W-a) = 1 at (a) the midplane, (b) the quarterplane and (c) the free surface non-dimensionalised by t.

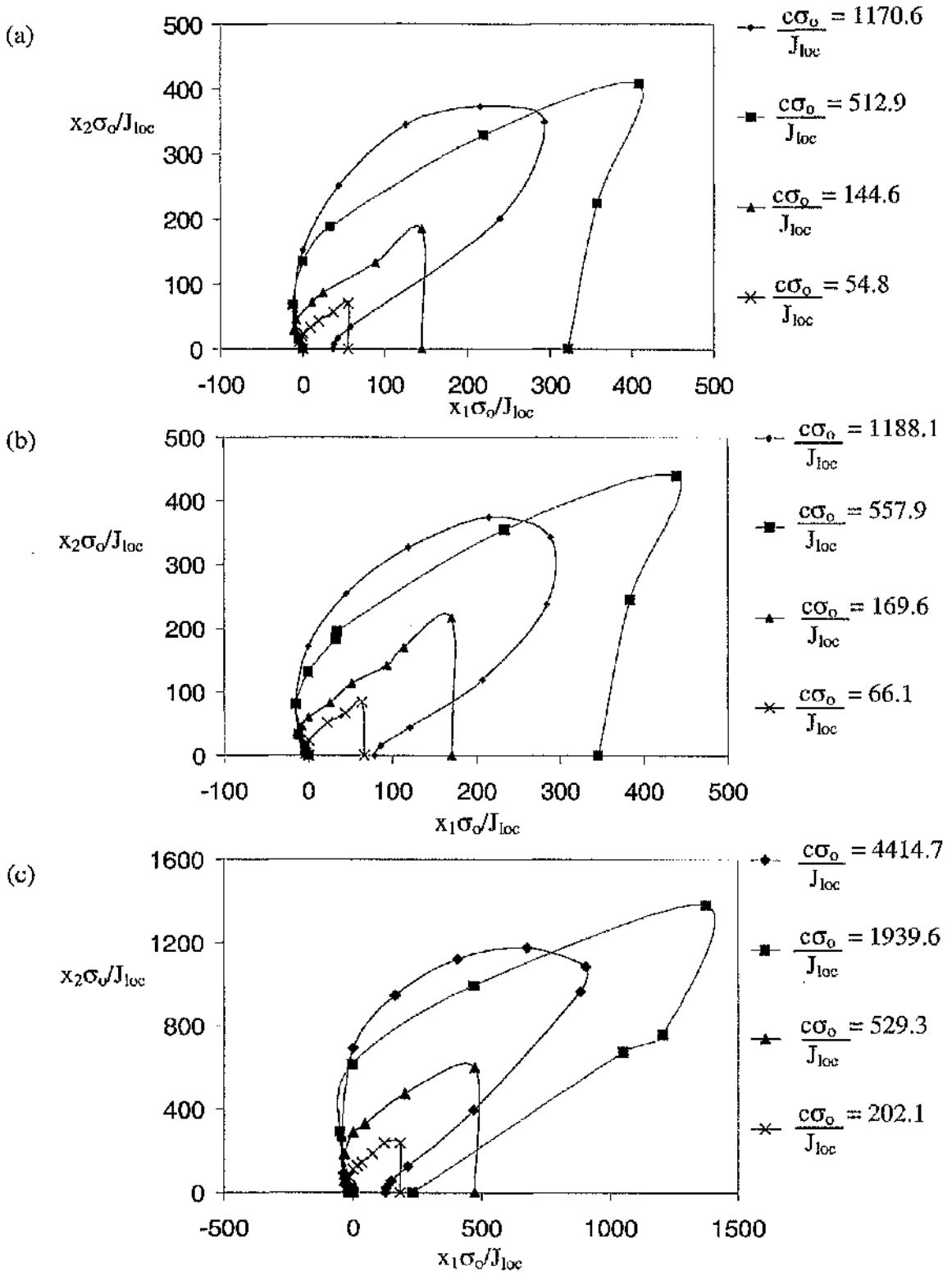


Figure 5.16: The plastic zone for a non-hardening CCP specimen B/(W-a) = 1 at (a) the midplane, (b) the quarter plane and (c) the free surface non-dimensionalised by $J_{loc}/\sigma_o$.

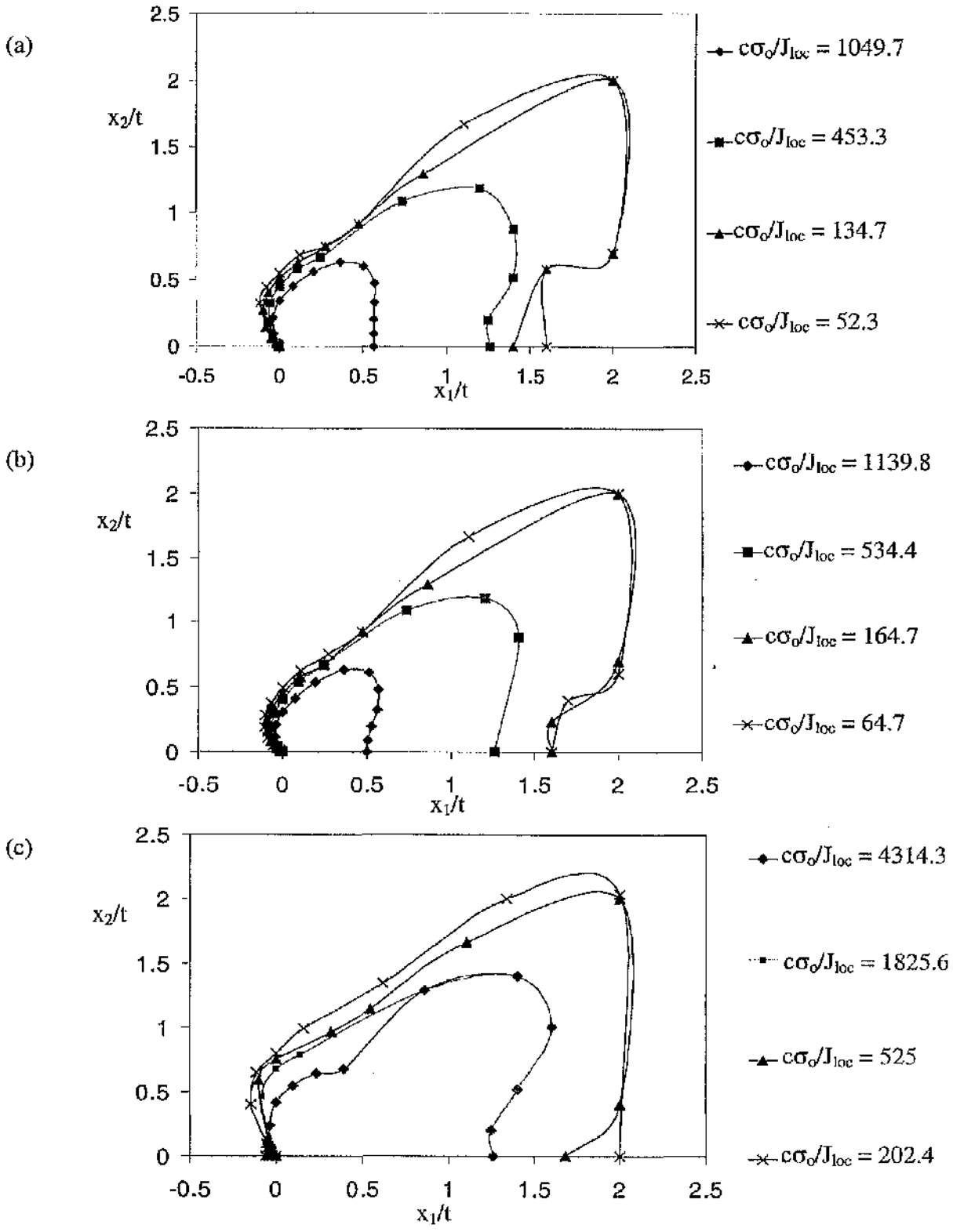


Figure 5.17: The plastic zone for a non-hardening CCP specimen B/(W-a) = 0.5 at (a) the midplane, (b) the quarter plane and (c) the free surface non-dimensionalised by t.

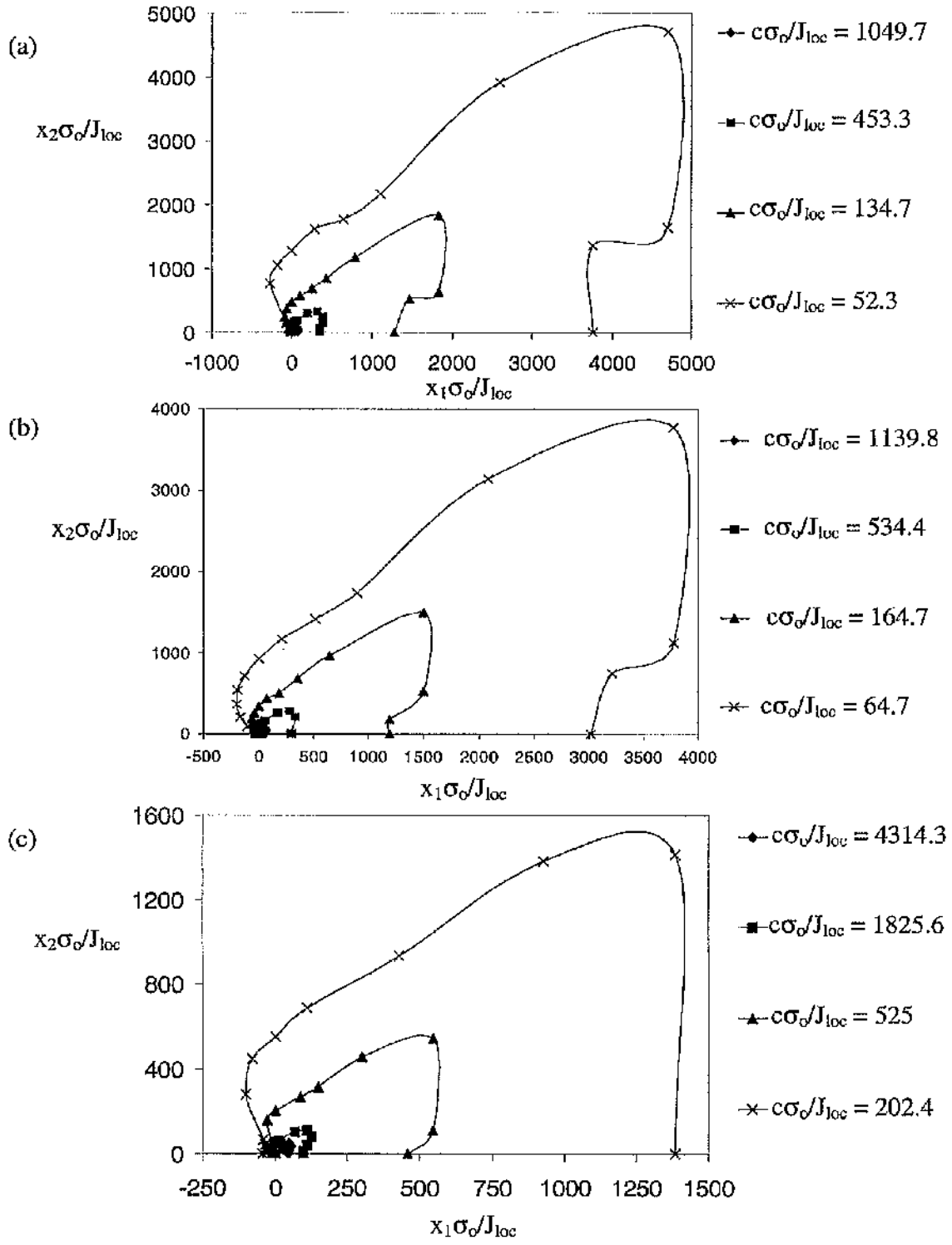


Figure 5.18: The plastic zone for a non-hardening CCP specimen B/(W-a)=0.5 at (a) the midplane, (b) the quarterplane and (c) the free surface non-dimensionalised $J_{loc}/\sigma_o$.

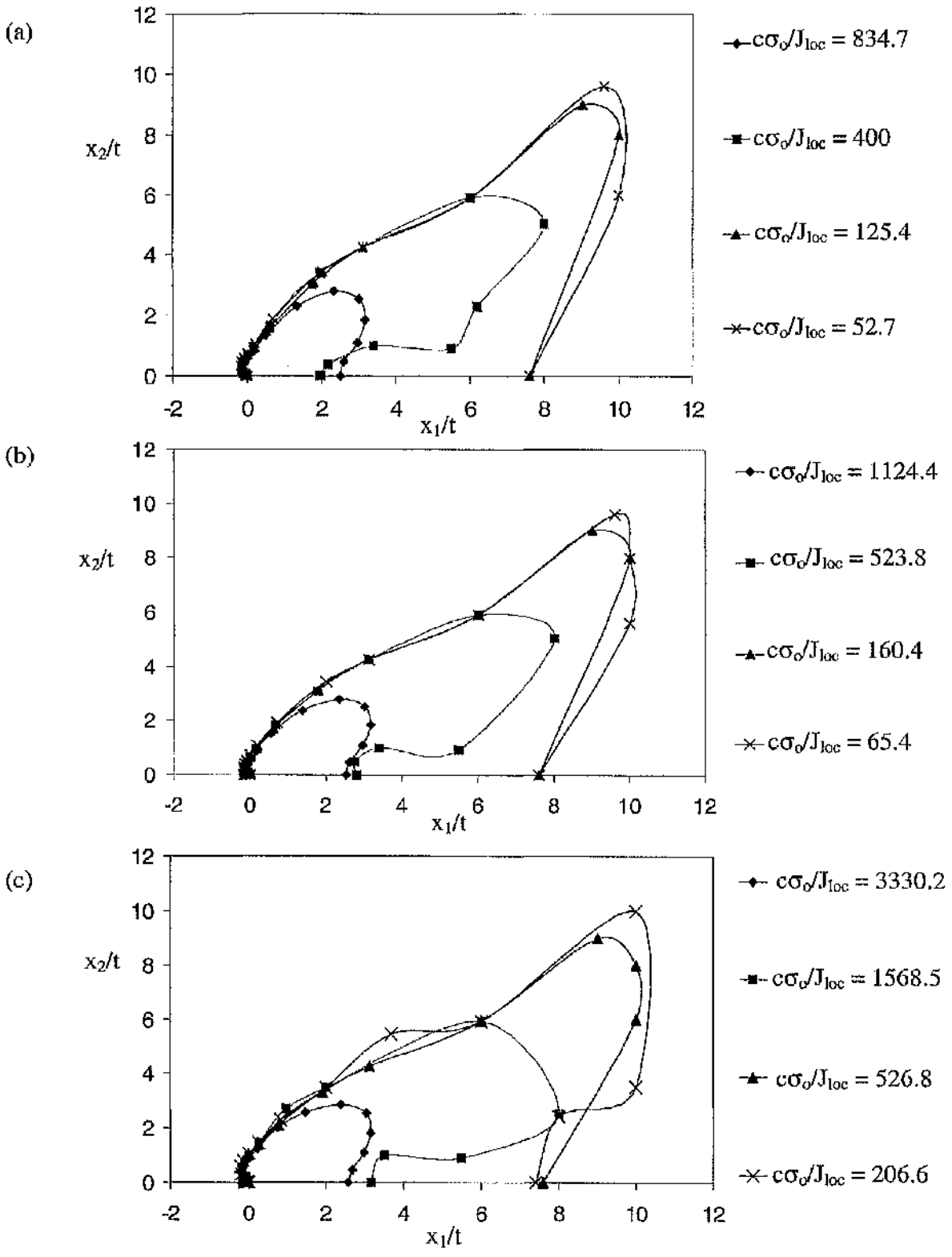


Figure 5.19: The plastic zone for a non-hardening CCP specimen B/(W-a) = 0.1 at (a) the midplane, (b) the quarter plane and (c) the free surface non-dimensionalised by t.

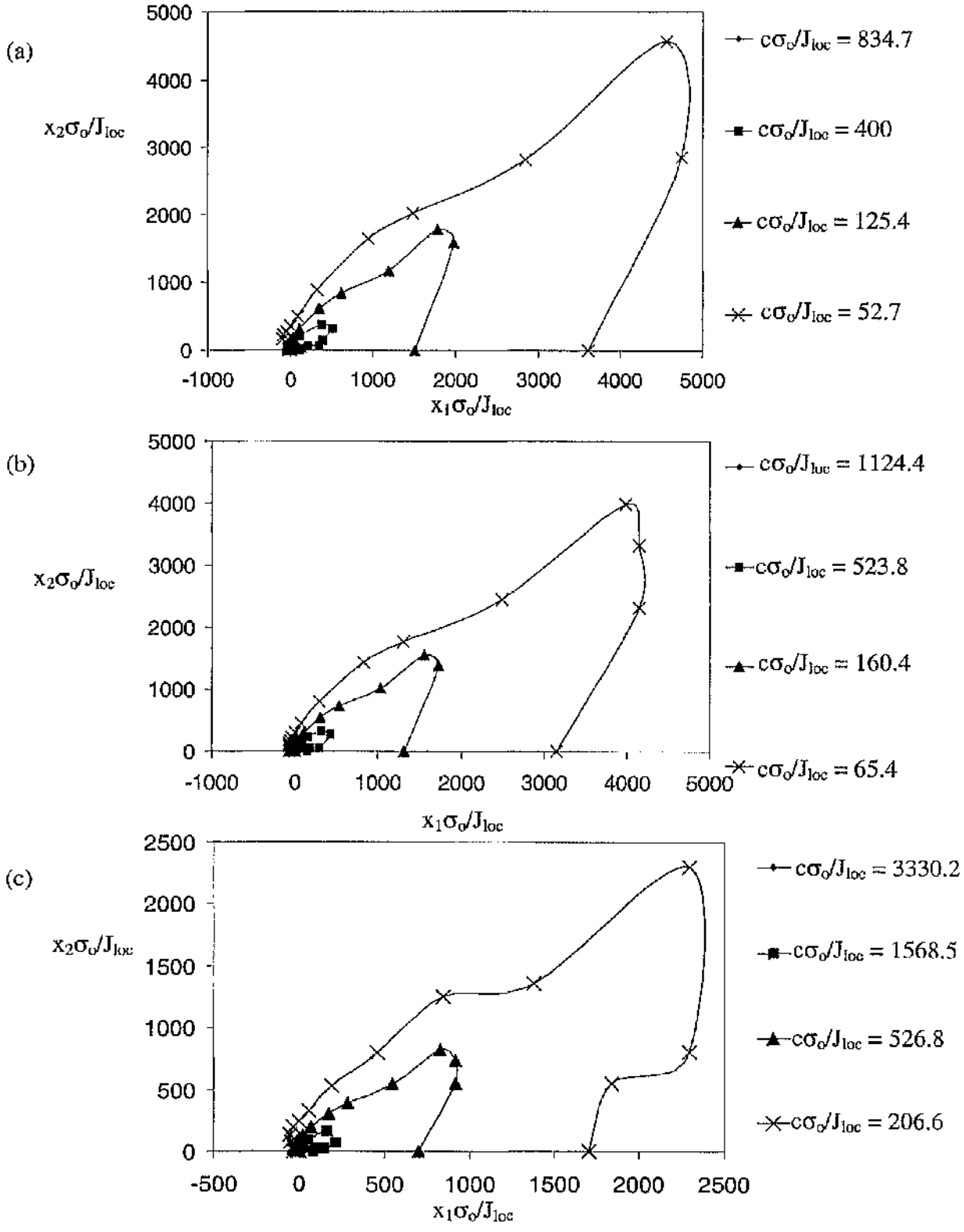


Figure 5.20: The plastic zone for a non-hardening CCP specimen B/(W-a) = 0.1 at (a) the midplane, (b) the quarterplane and (c) the free surface non-dimensionalised $J_{loc}/\sigma_o$.

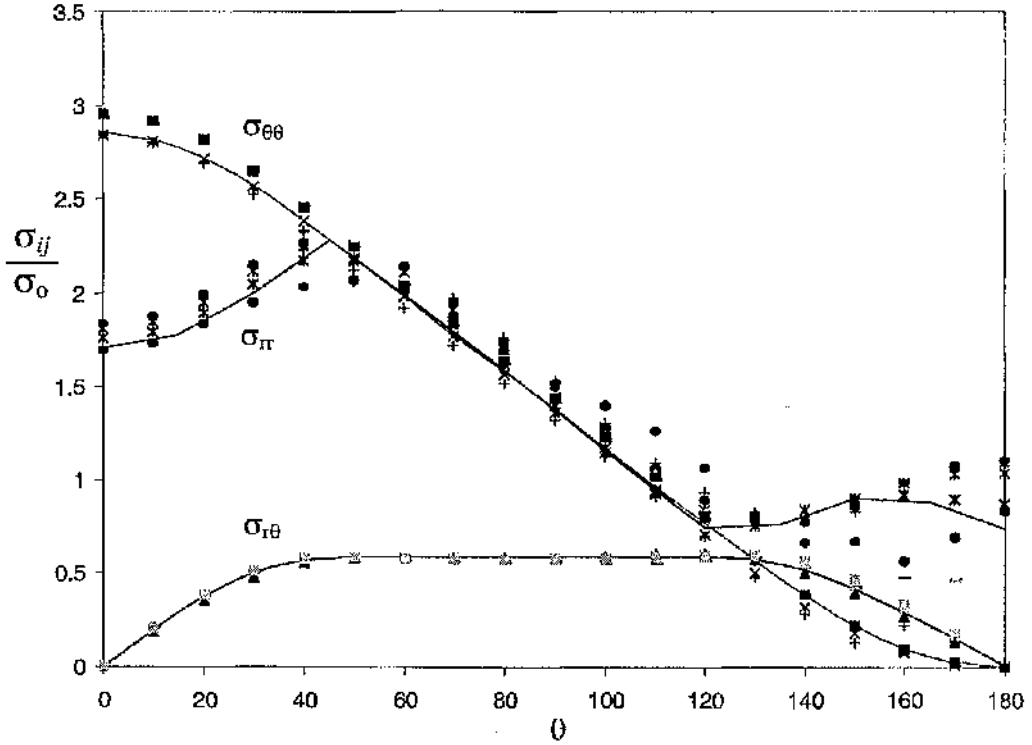


Figure 5.21: The boundary layer formulation asymptotic polar stresses for $\Omega_{far}$ = 1, 3, 5, 8, 20 at the midplane $x_3/t = 0$. The solid lines represent the two-dimensional plane strain solution.

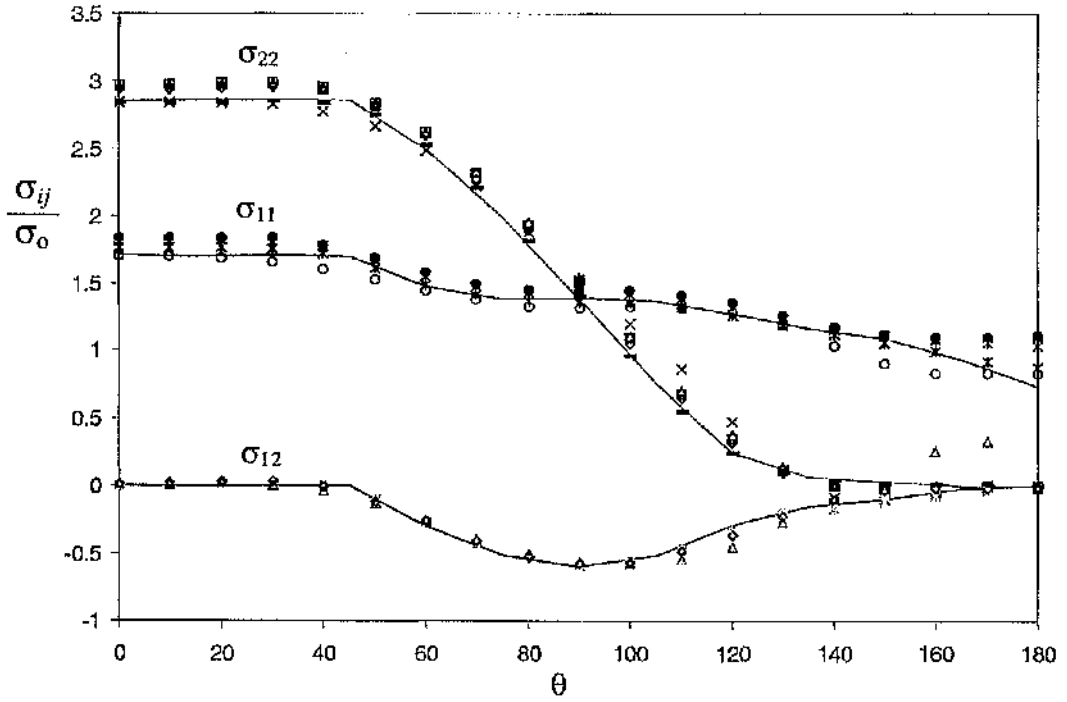


Figure 5.22: The boundary layer formulation asymptotic Cartesian stresses for $\Omega_{far}$ = 1, 3, 5, 8, 20 at the midplane $x_3/t = 0$. The solid lines represent the two-dimensional plane strain solution.

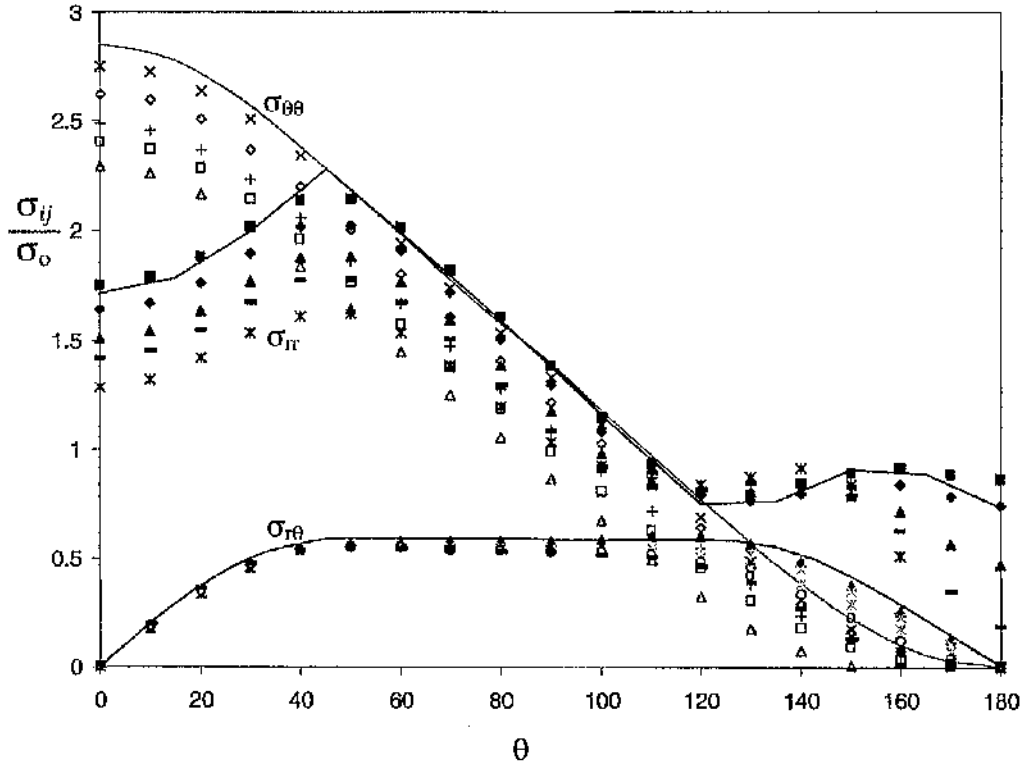


Figure 5.23: The boundary layer formulation asymptotic polar stresses for $\Omega_{far}$ = 1, 3, 5, 8, 20 at the quarterplane $x_3/t$ = 0.24. The solid lines represent the two-dimensional plane strain solution.

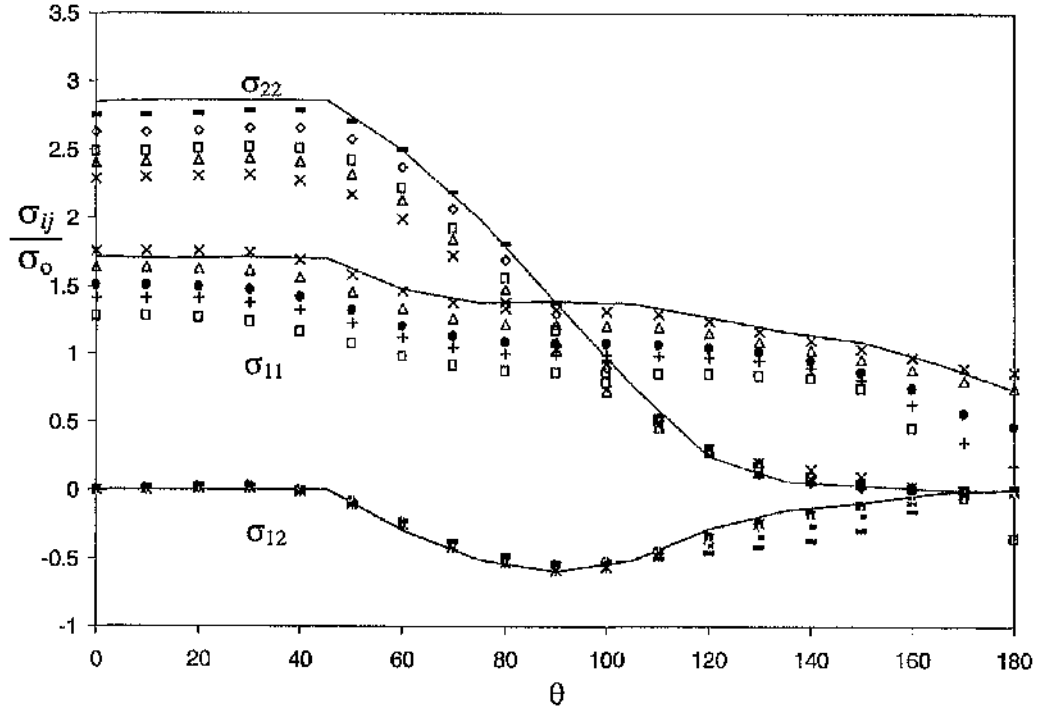


Figure 5.24: The boundary layer formulation asymptotic Cartesian stresses for $\Omega_{far}$ = 1, 3, 5, 8, 20 at the quarterplane $x_3/t$ = 0.24. The solid lines represent the two-dimensional plane strain solution.

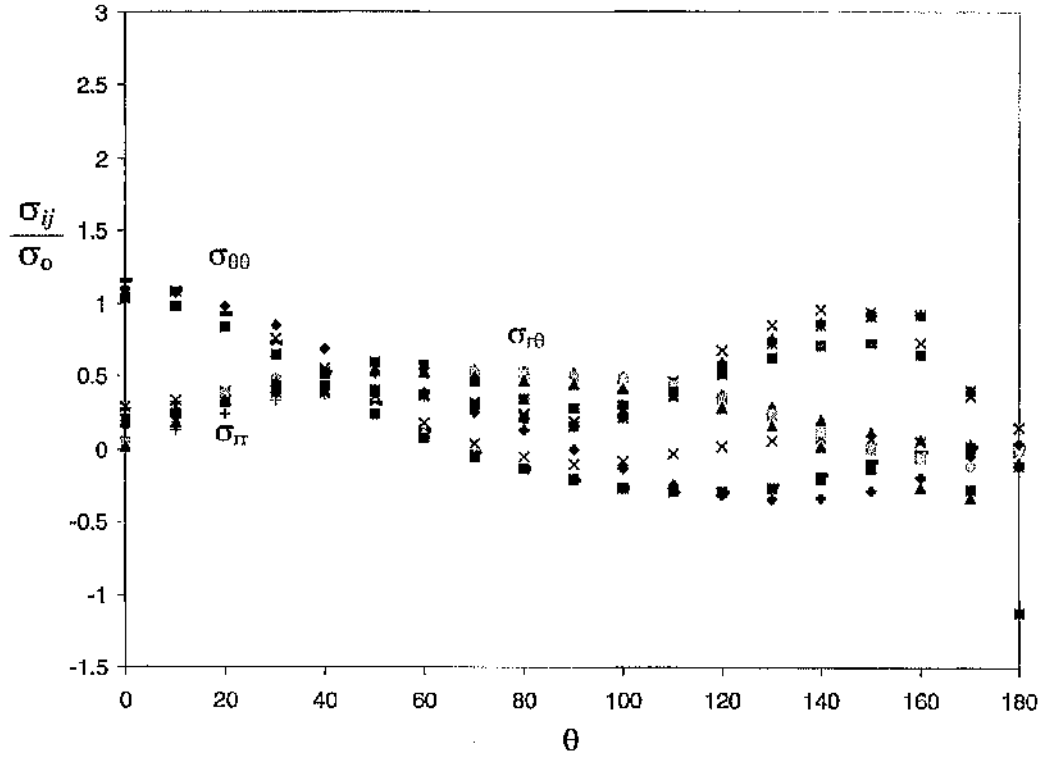


Figure 5.25: The boundary layer formulation asymptotic polar stresses for $\Omega_{far} = 1, 3, 5, 8, 20$ at the free surface $x_3/t = 0.5$.

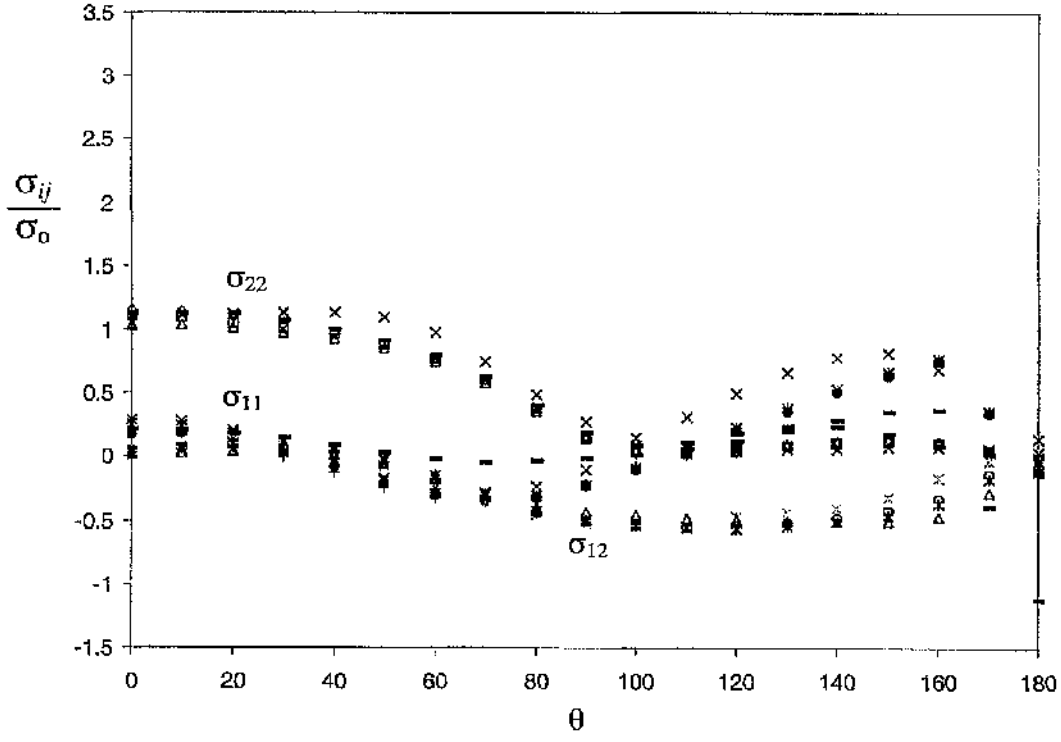


Figure 5.26: The boundary layer formulation asymptotic Cartesian stresses for $\Omega_{far} = 1, 3, 5, 8, 20$ at the free surface $x_3/t = 0.5$.

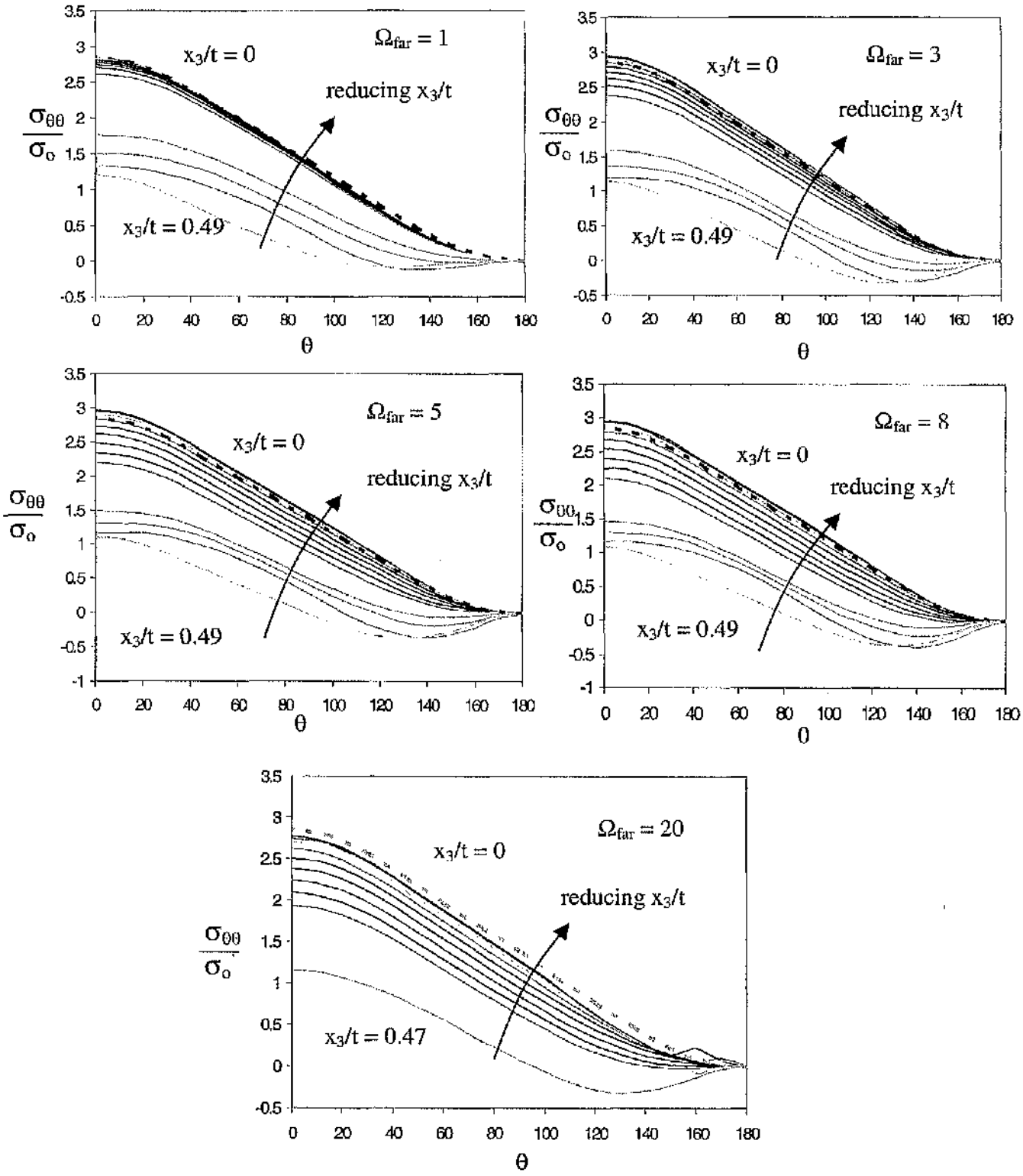


Figure 5.27: The hoop stress $\sigma_{\theta\theta}$ at load levels $J_{far}/\sigma_o\varepsilon_o t$ = 1, 3, 5, 8, 20 through the thickness, $T_{app}$ = 0. The broken line determined from a boundary layer formulation indicates the two-dimensional plane strain field for $\sigma_{\theta\theta}$.

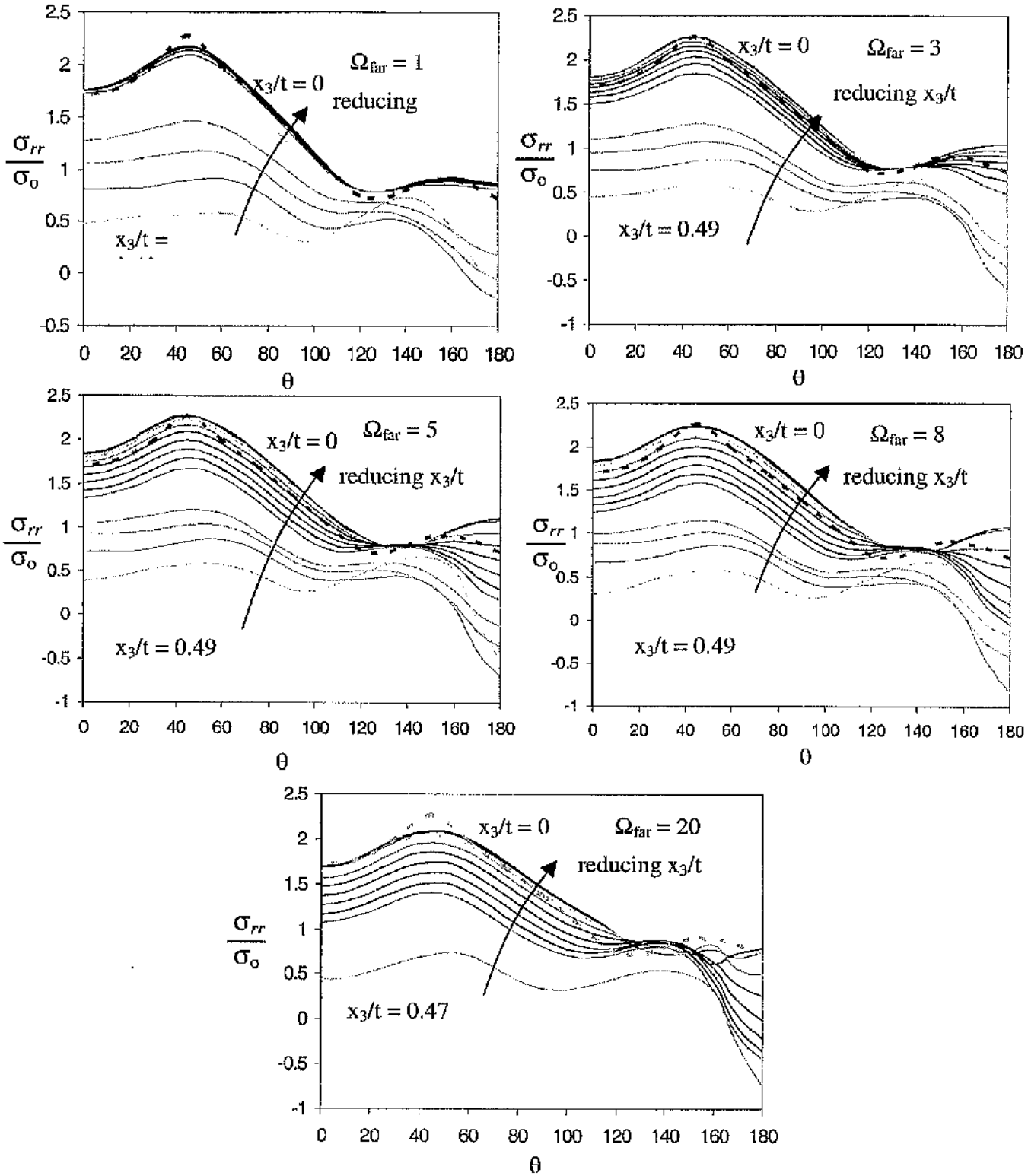


Figure 5.28: The radial stress $\sigma_{rr}$ at load levels $J_{far}/\sigma_o\varepsilon_o t$ = 1, 3, 5, 8, 20 through the thickness, $T_{app} = 0$. The broken line determined in a boundary layer formulation indicates the two-dimensional plane strain field for $\sigma_{rr}$.

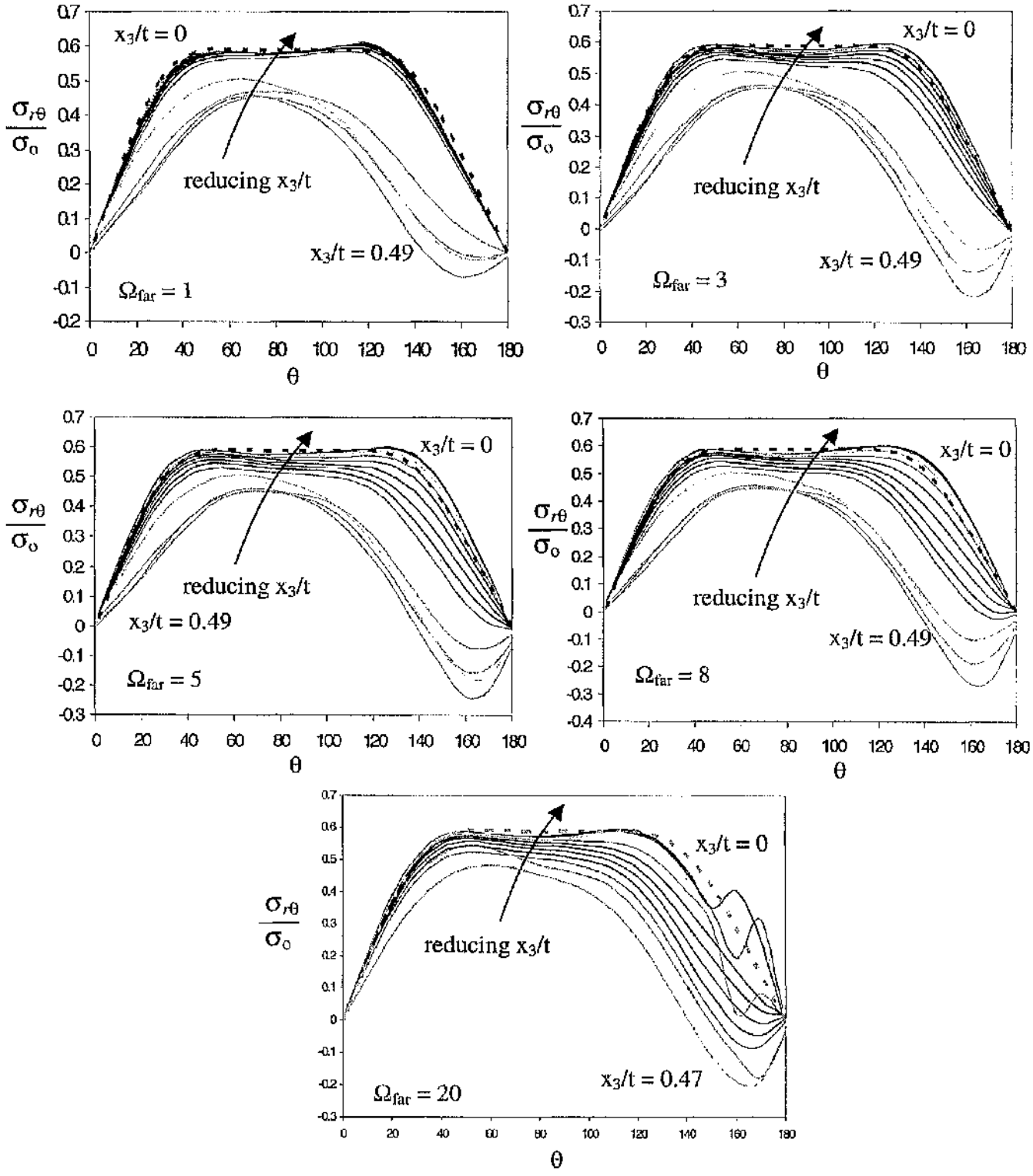


Figure 5.29: The shear stress $\sigma_{r\theta}$ at load levels $J_{far}/\sigma_o\varepsilon_o t$ = 1, 3, 5, 8, 20 through the thickness, $T_{app} = 0$. The broken line determined in a boundary layer formulation indicates the two-dimensional plane strain field for $\sigma_{r\theta}$.

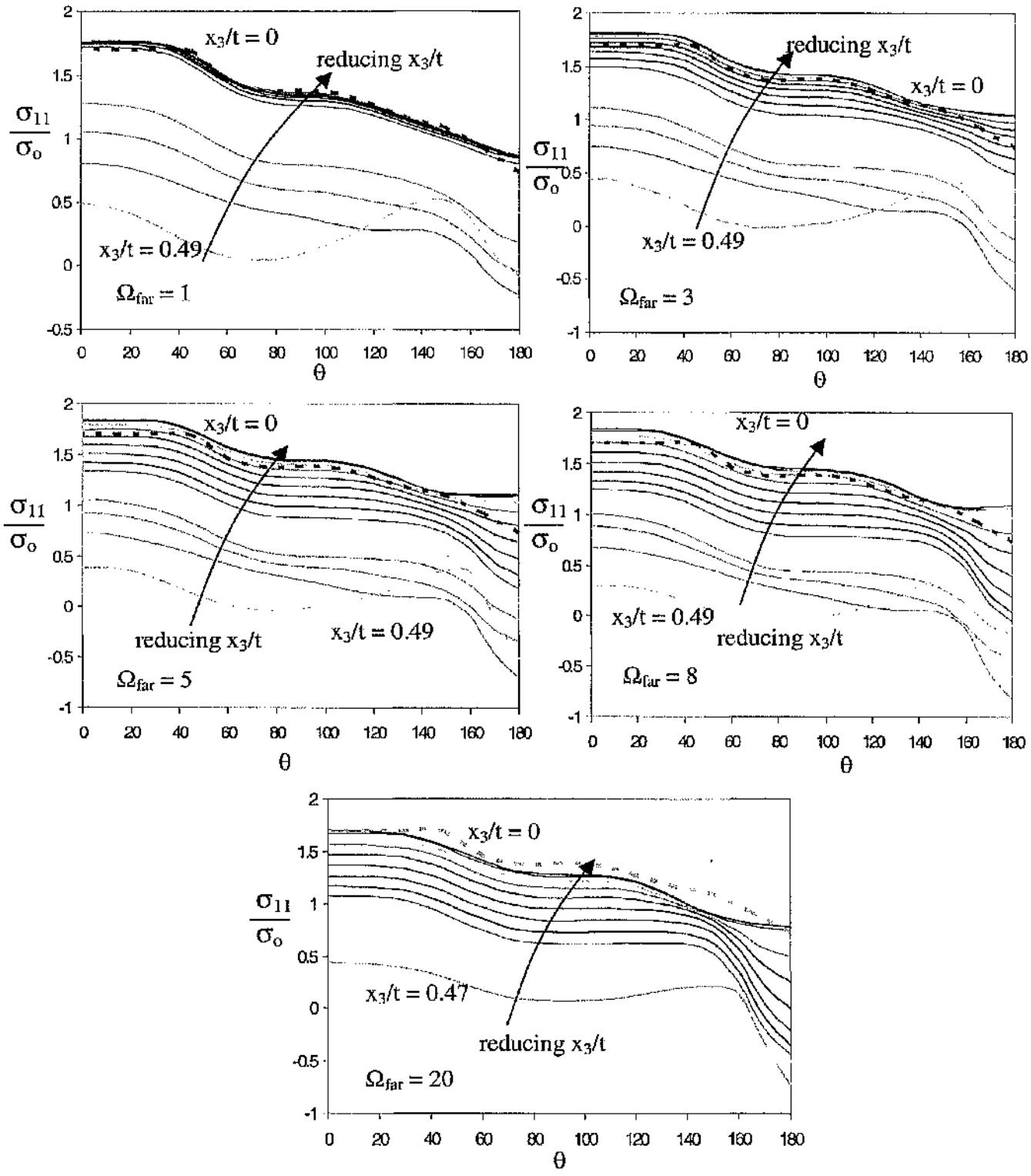


Figure 5.30: The direct stress $\sigma_{11}$ at load levels $J_{far}/\sigma_o\varepsilon_o t$ = 1, 3, 5, 8, 20 through the thickness, $T_{app} = 0$. The broken line determined in a boundary layer formulation indicates the two-dimensional plane strain field for $\sigma_{11}$.

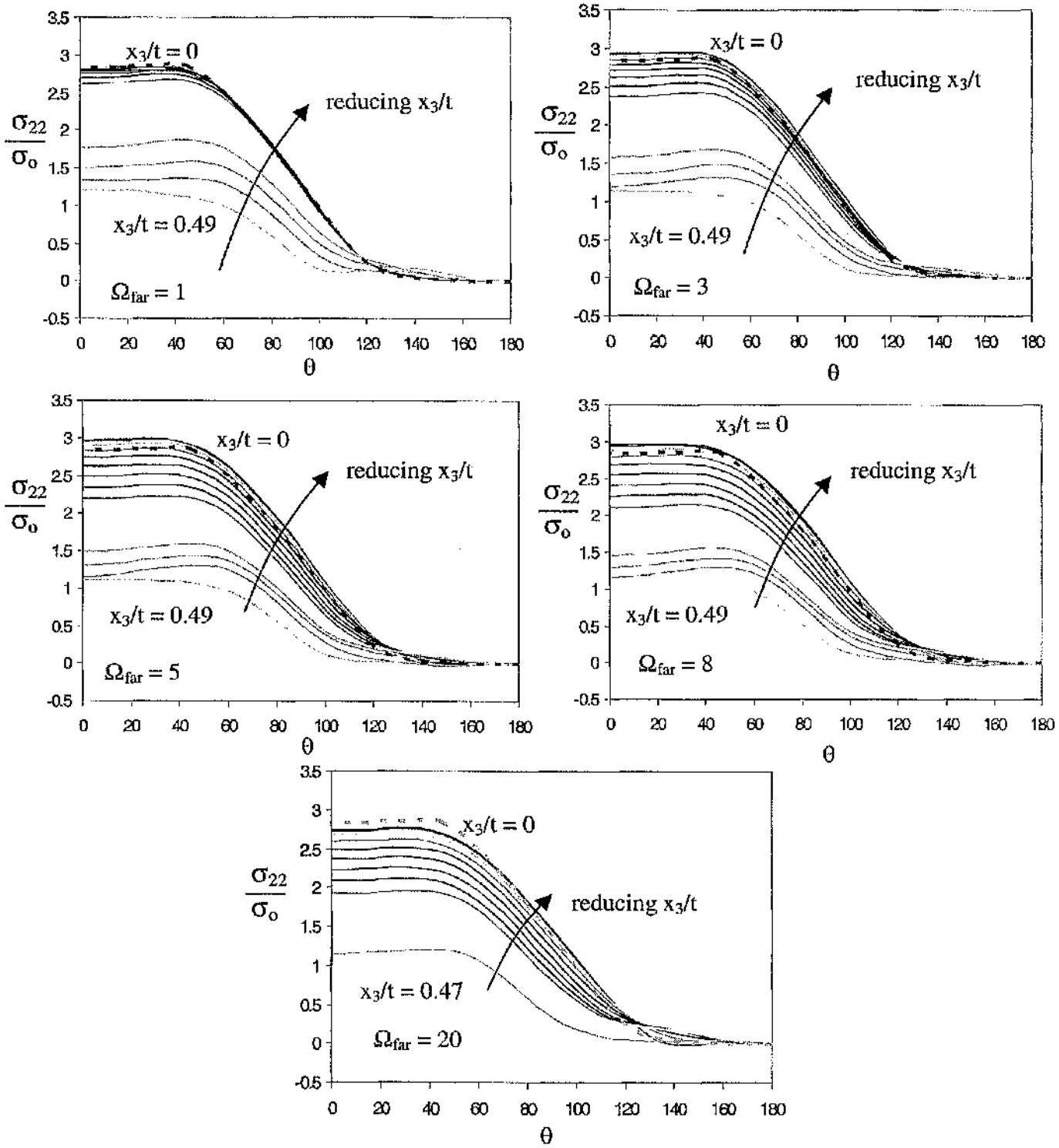


Figure 5.31: The direct stress $\sigma_{22}$ at load levels $J_{far}/\sigma_o\varepsilon_o t$ = 1, 3, 5, 8, 20 through the thickness, $T_{app} = 0$. The broken line determined in a boundary layer formulation indicates the two-dimensional plane strain field for $\sigma_{22}$.

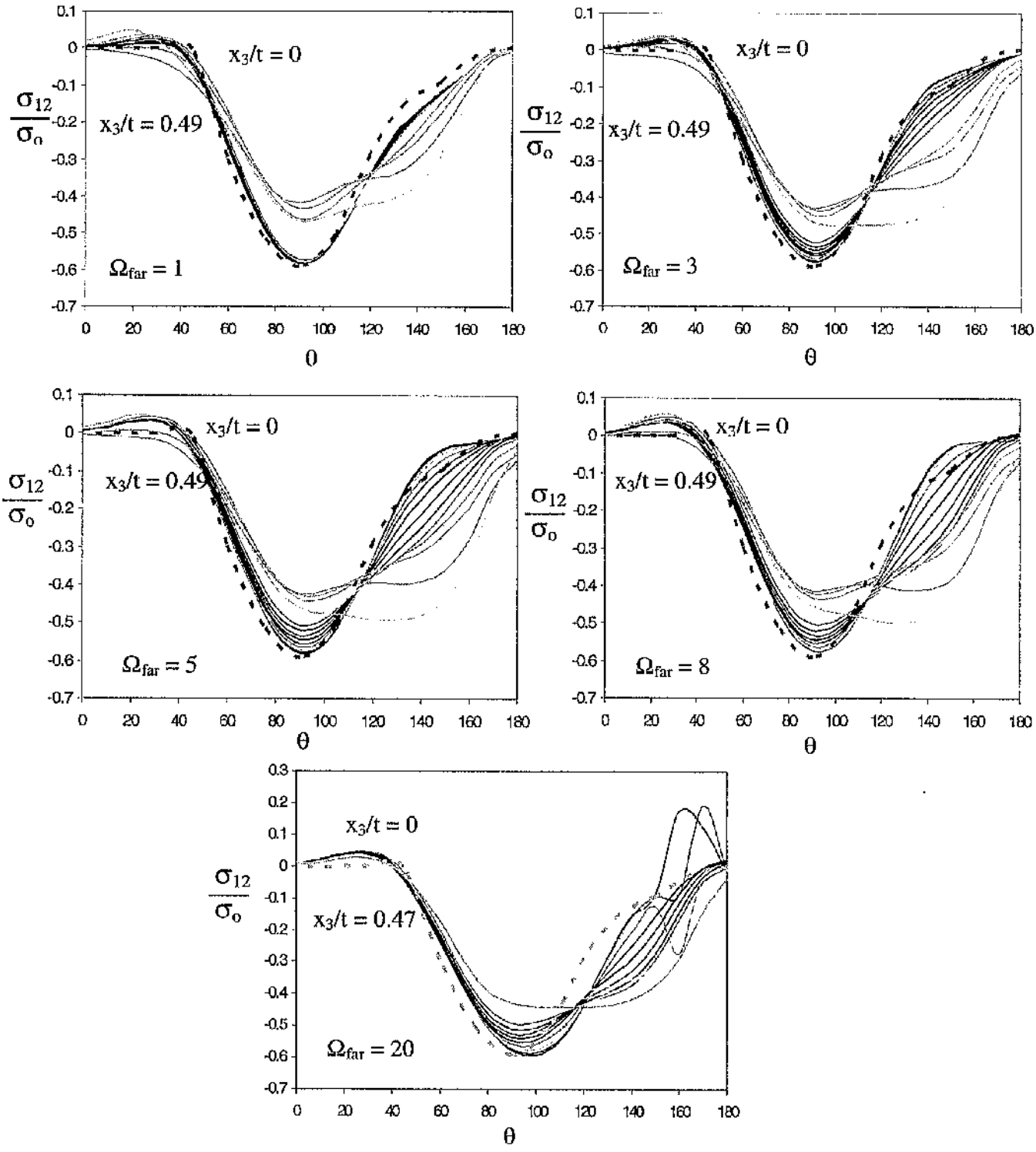


Figure 5.32: The shear stress $\sigma_{12}$ at load levels $J_{far}/\sigma_o\varepsilon_o t$ = 1, 3, 5, 8, 20 through the thickness, $T_{app} = 0$. The broken line determined in a boundary layer formulation indicates the two-dimensional plane strain field for $\sigma_{12}$.

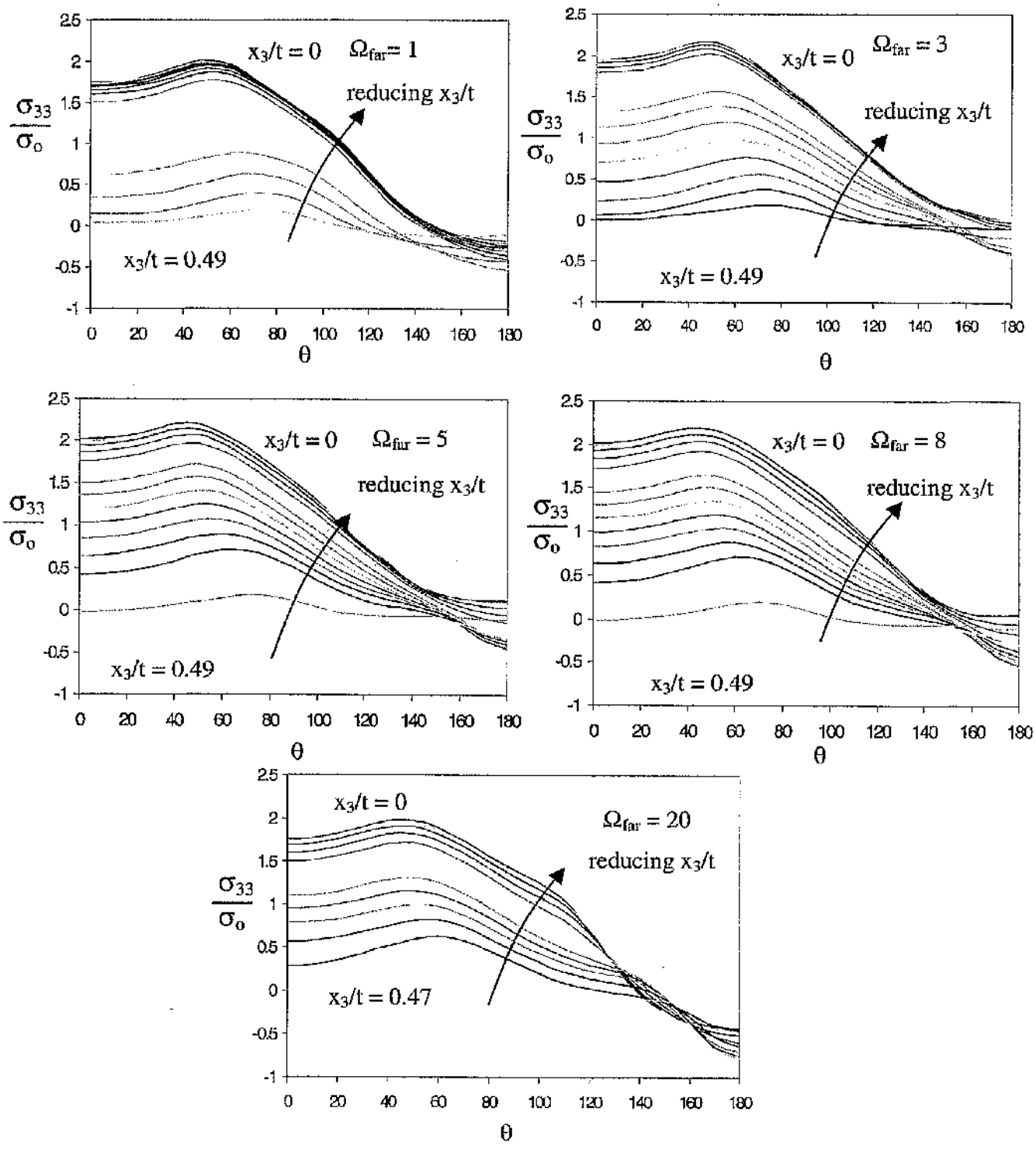


Figure 5.33: The direct stress $\sigma_{33}$ at load levels $J_{far}/\sigma_o\varepsilon_o t$ = 1, 3, 5, 8, 20 through the thickness, $T_{app} = 0$.

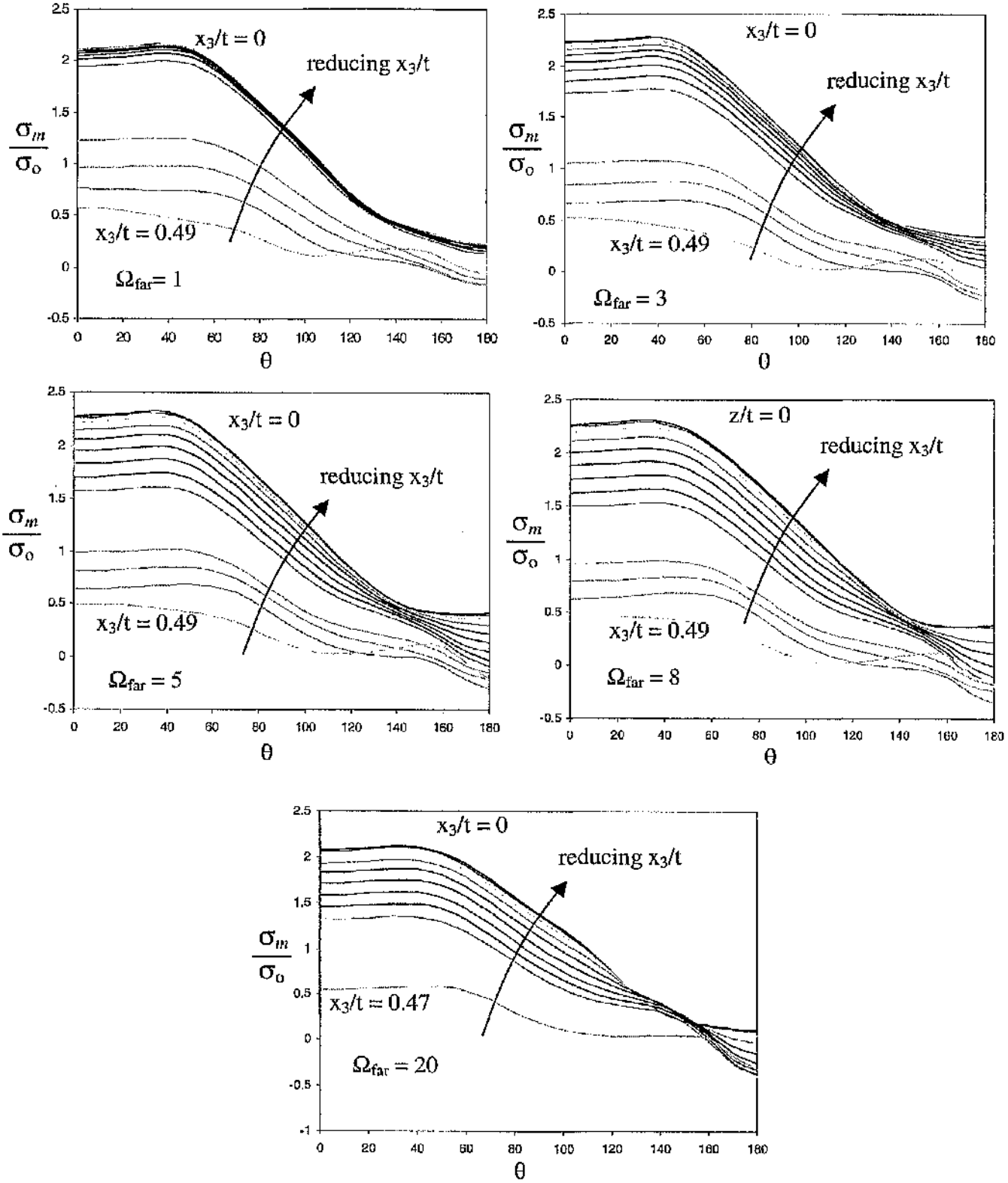


Figure 5.34: The mean stress $\sigma_m$ at load levels $J_{far}/\sigma_o\varepsilon_o t$ = 1, 3, 5, 8, 20 through the thickness, $T_{app} = 0$.

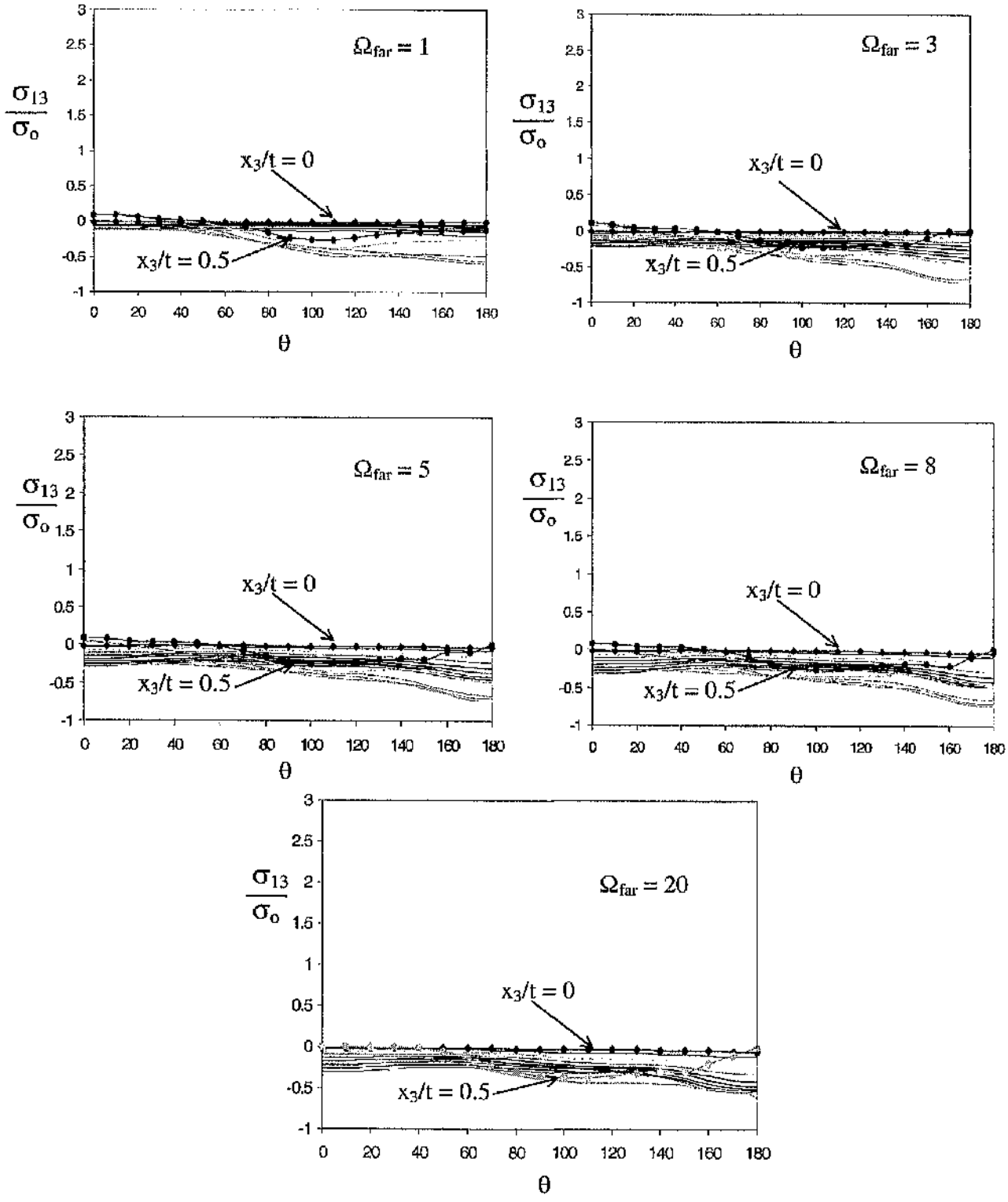


Figure 5.35: The out-of-plane stress $\sigma_{13}$ at load levels $J_{far}/\sigma_o\varepsilon_o t = 1, 3, 5, 8, 20$ through the thickness, $T_{app} = 0$. The diamond markers show the stress at the midplane while the circular markers show the stress at the free surface.

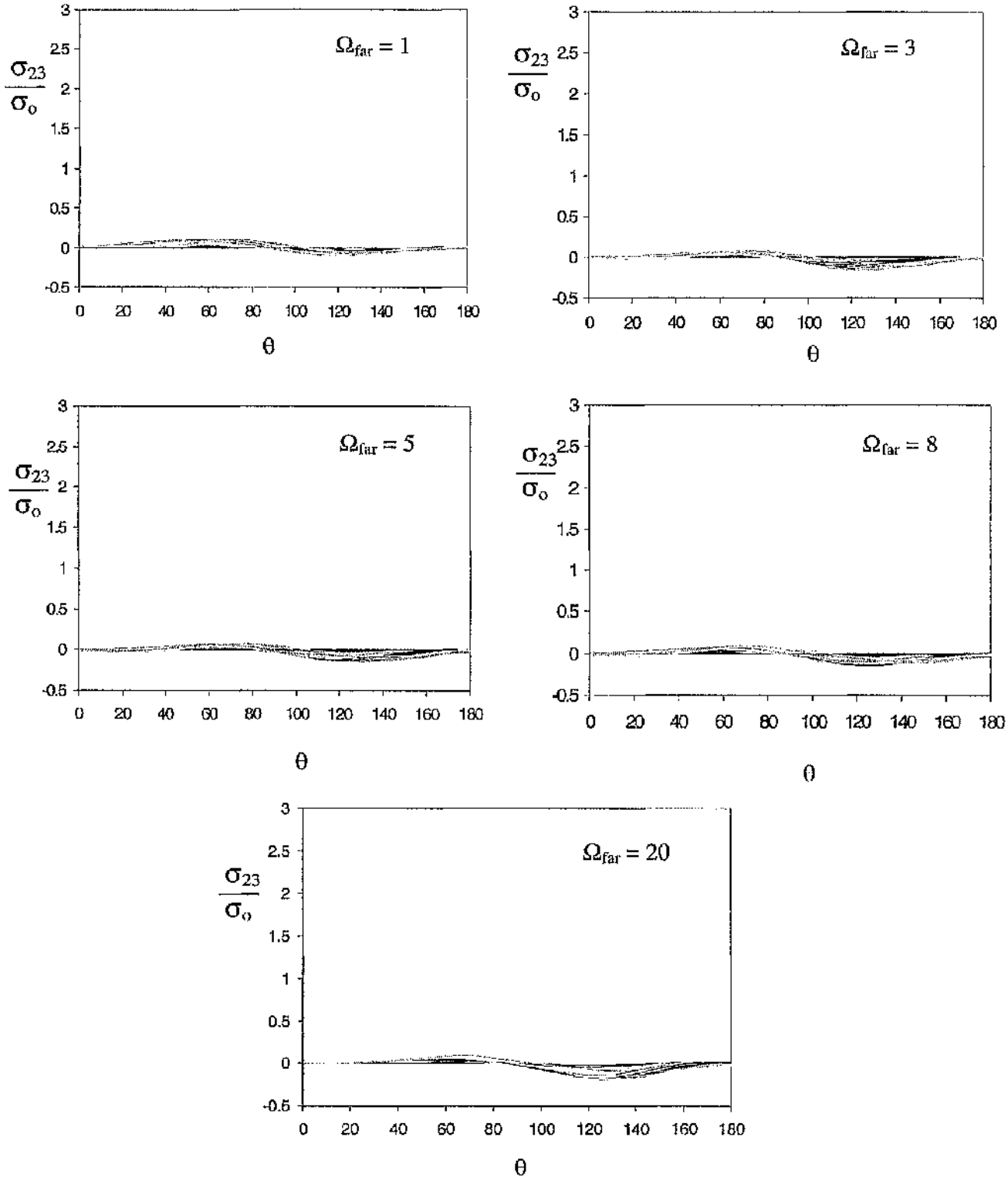


Figure 5.36: The out-of-plane stress $\sigma_{23}$ at load levels $J_{far}/\sigma_o\varepsilon_o t = 1, 3, 5, 8, 20$ through the thickness, $T_{app} = 0$.

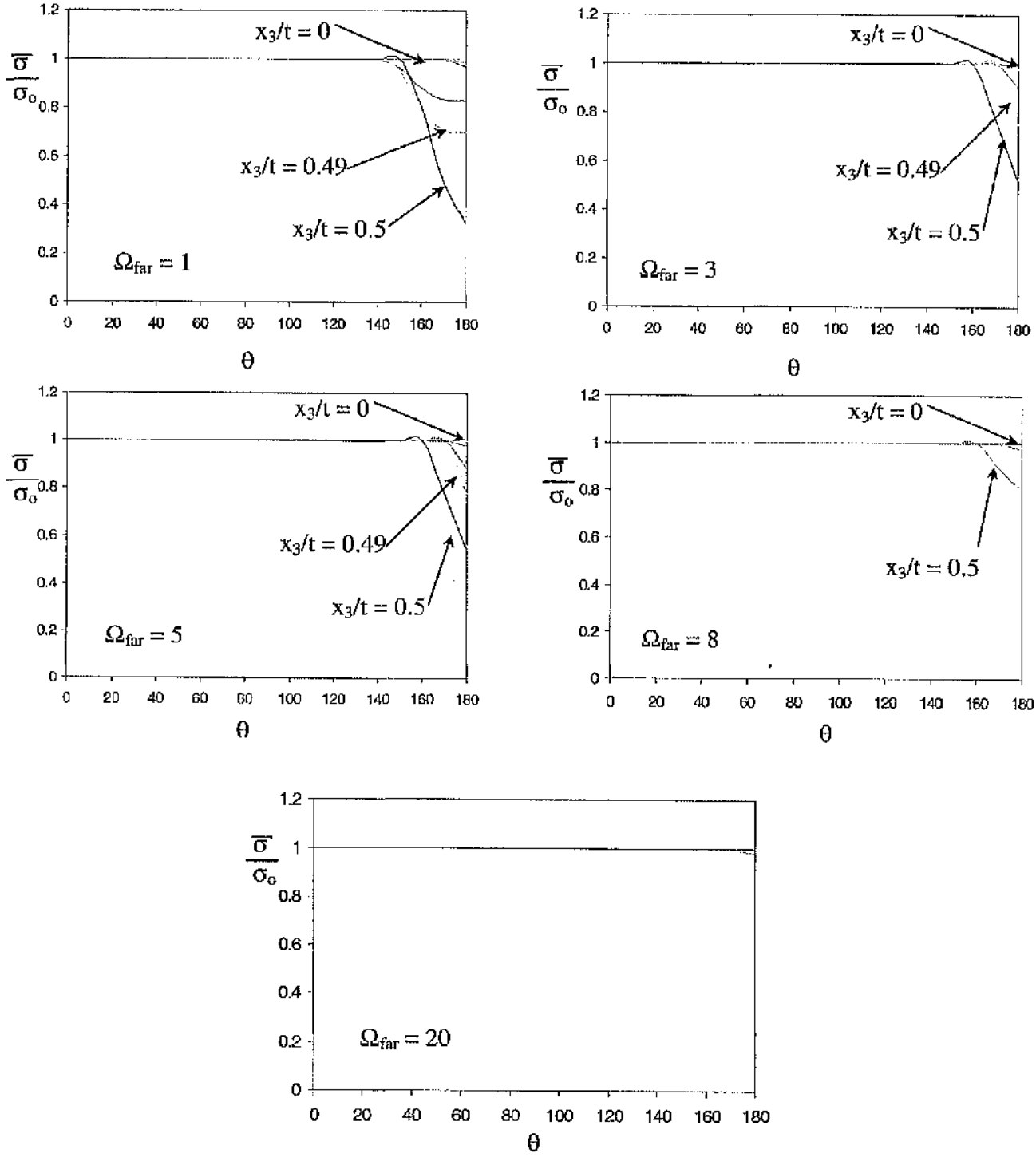


Figure 5.37: The Mises stress $\bar{\sigma}/\sigma_o$ at load levels $J_{far}/\sigma_o\varepsilon_o t$ = 1, 3, 5, 8, 20 through the thickness, $T_{app} = 0$.

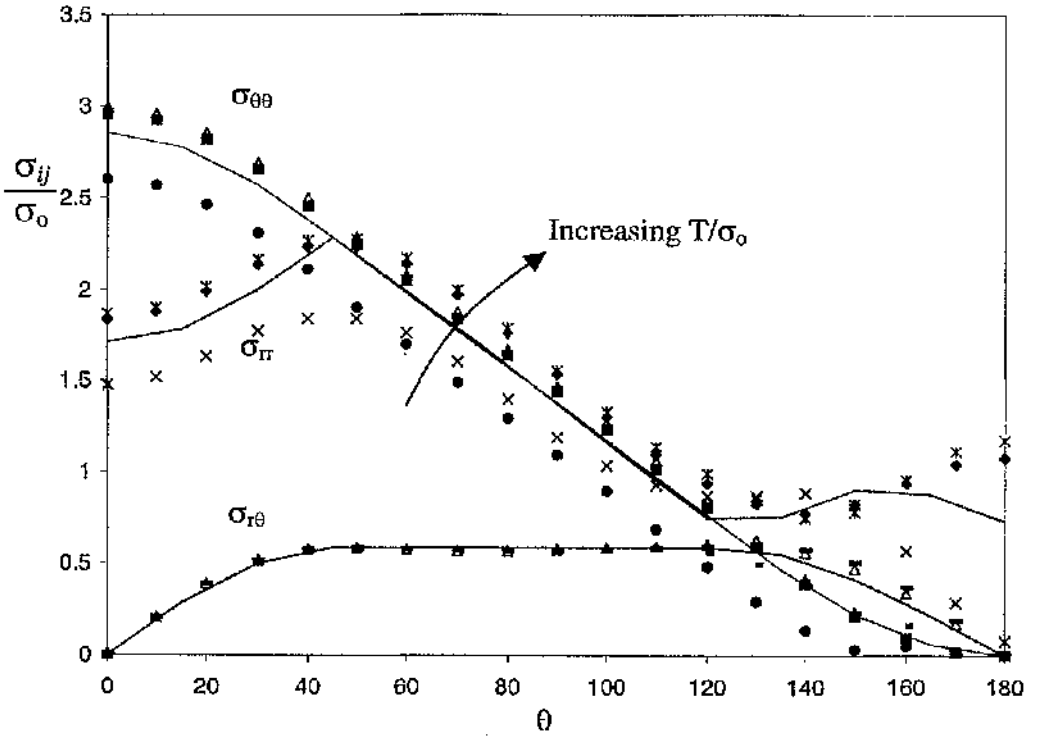


Figure 5.38: The modified boundary layer formulation asymptotic polar stresses for $\Omega_{far}$ = 8 with $T_{app}$ 0, $-0.5\sigma_o$ and $+0.5\sigma_o$ at the midplane $x_3/t = 0$. The solid lines represent the two-dimensional plane strain solution (T = 0).

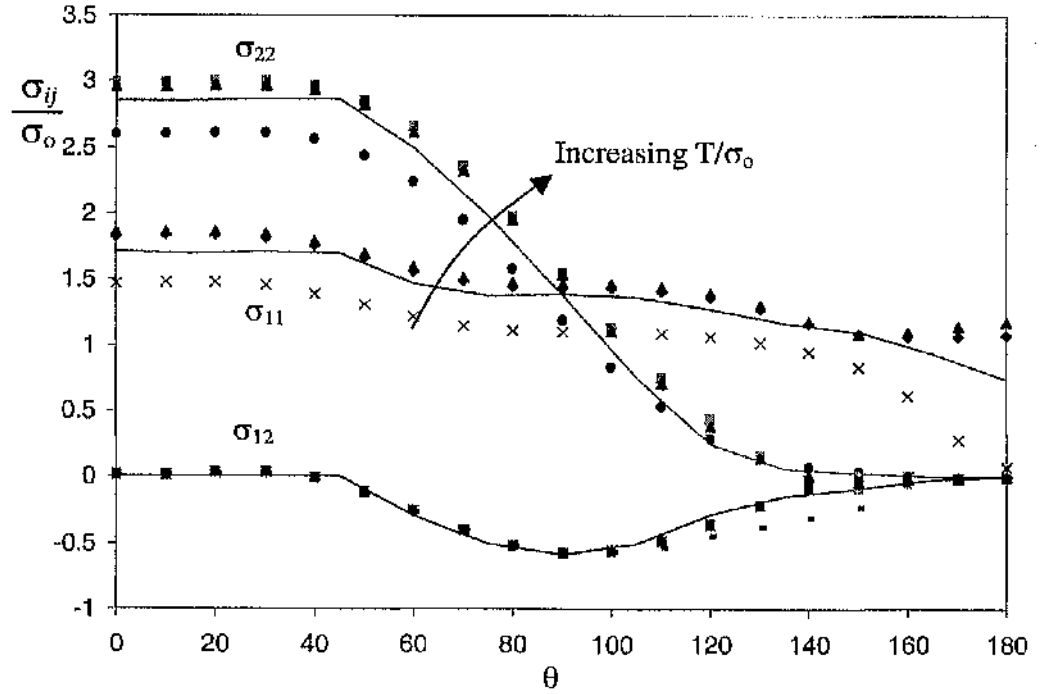


Figure 5.39: The modified boundary layer formulation asymptotic Cartesian stresses for $\Omega_{far}$ = 8 with $T_{app}$ 0, $-0.5\sigma_o$ and $+0.5\sigma_o$ at the midplane $x_3/t = 0$. The solid lines represent the two-dimensional plane strain solution (T = 0).

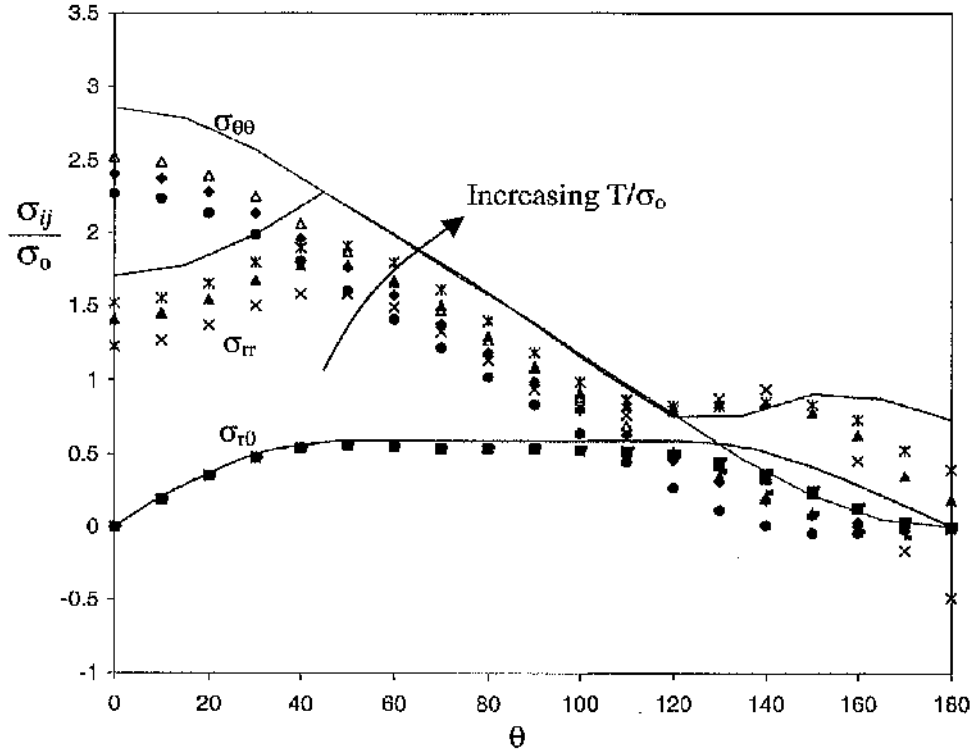


Figure 5.40: The modified boundary layer formulation asymptotic polar stresses for the load level $\Omega_{far} = 8$ with $T_{app}$ 0, $-0.5\sigma_o$ and $+0.5\sigma_o$ at the quarterplane $x_3/t = 0.24$. The solid lines represent the two-dimensional plane strain solution ($T = 0$).

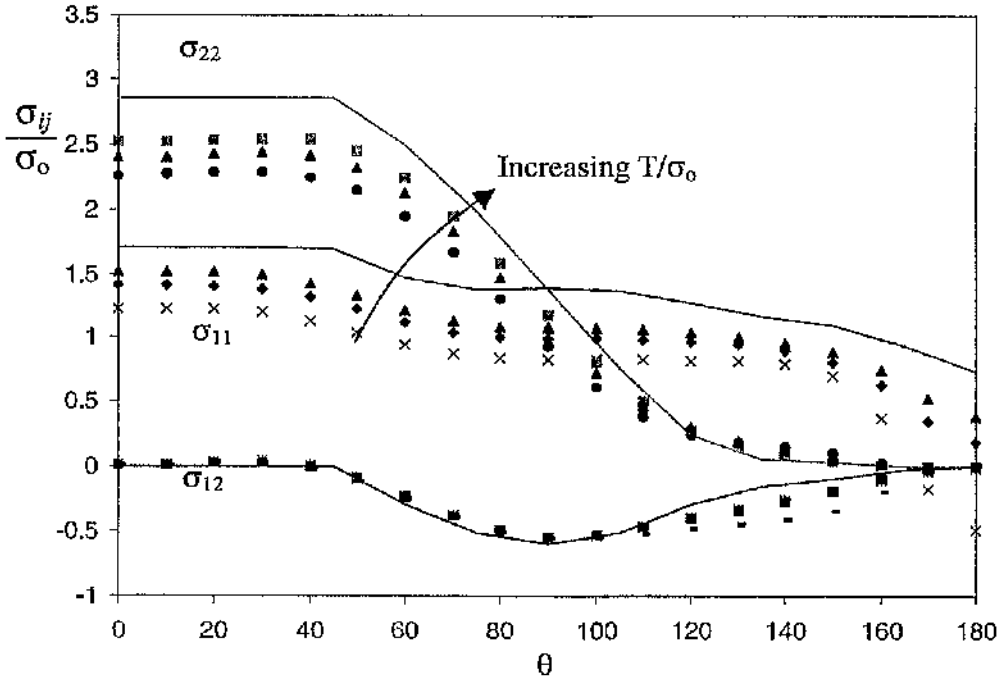


Figure 5.41: The modified boundary layer formulation asymptotic Cartesian stresses for the load level $\Omega_{far} = 8$ with $T_{app}$ 0, $-0.5\sigma_o$ and $+0.5\sigma_o$ at the quarterplane $x_3/t = 0.24$. The solid lines represent the two-dimensional plane strain solution ($T = 0$).

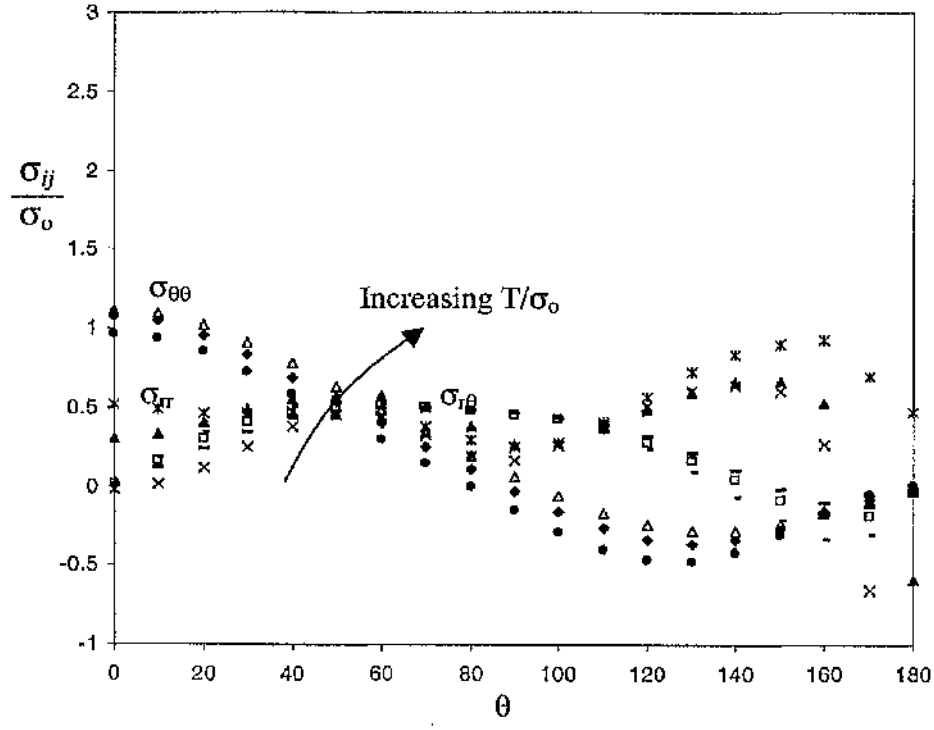


Figure 5.42: The modified boundary layer formulation asymptotic polar stresses for $\Omega_{far}$ = 8 with $T_{app}$ 0, -0.5$\sigma_o$ and +0.5$\sigma_o$ at free surface $x_3/t = 0.5$.

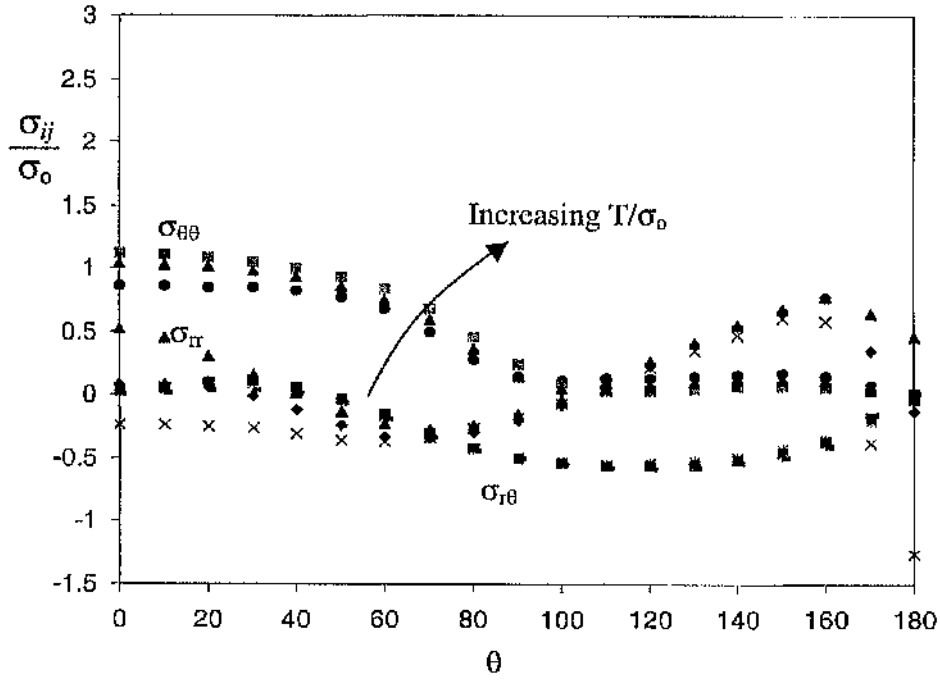


Figure 5.43: The modified boundary layer formulation asymptotic Cartesian stresses for $\Omega_{far}$ = 8 with $T_{app}$ 0, -0.5$\sigma_o$ and +0.5$\sigma_o$ at free surface $x_3/t = 0.5$.

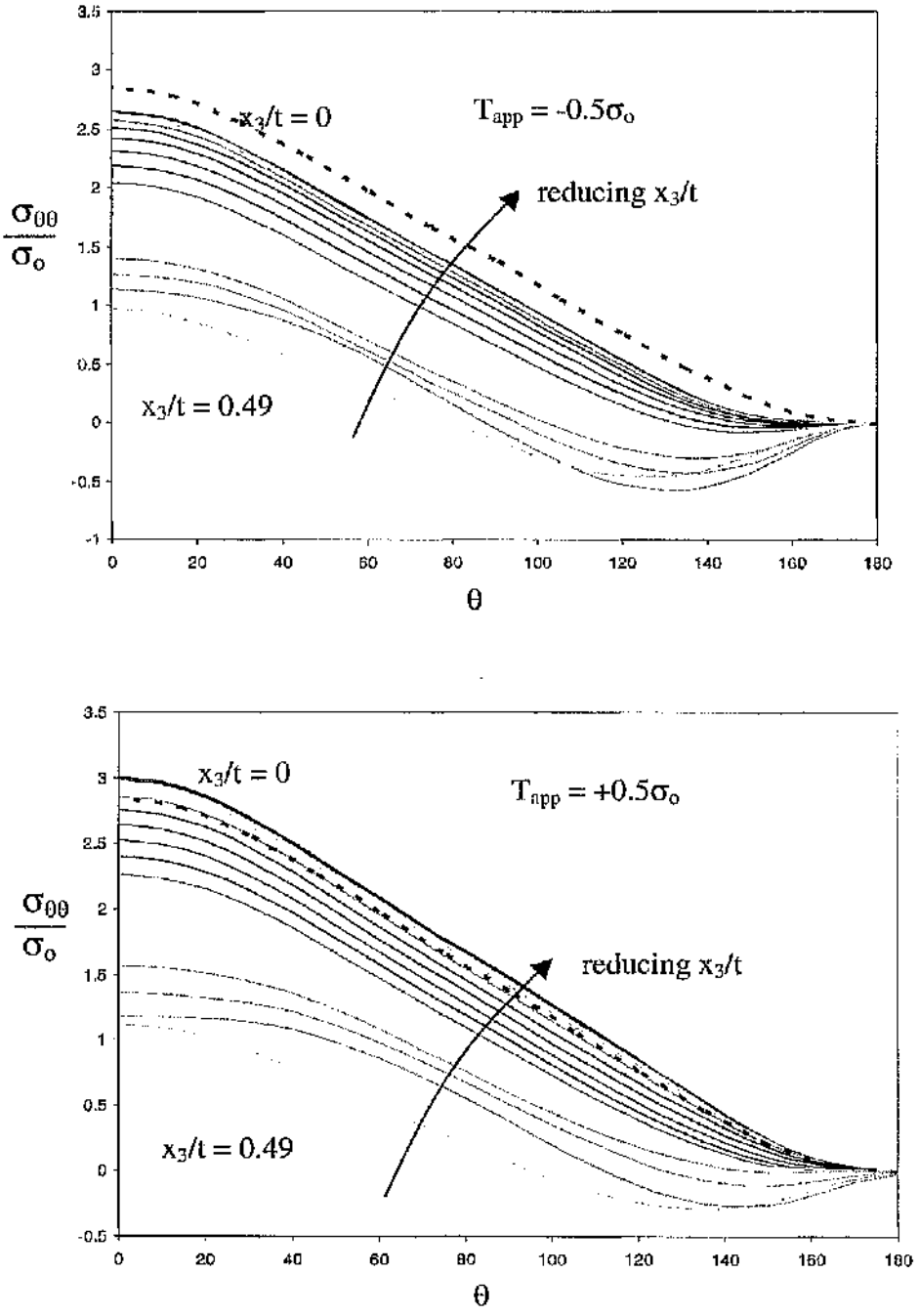


Figure 5.44: The hoop stress $\sigma_{\theta\theta}$ at a load level $J_{far}/\sigma_o\varepsilon_o t = 8$ through the thickness, $T_{app} =$ -0.5 and +0.5. The broken line determined in a boundary layer formulation indicates the two-dimensional plane strain field for $\sigma_{\theta\theta}$.

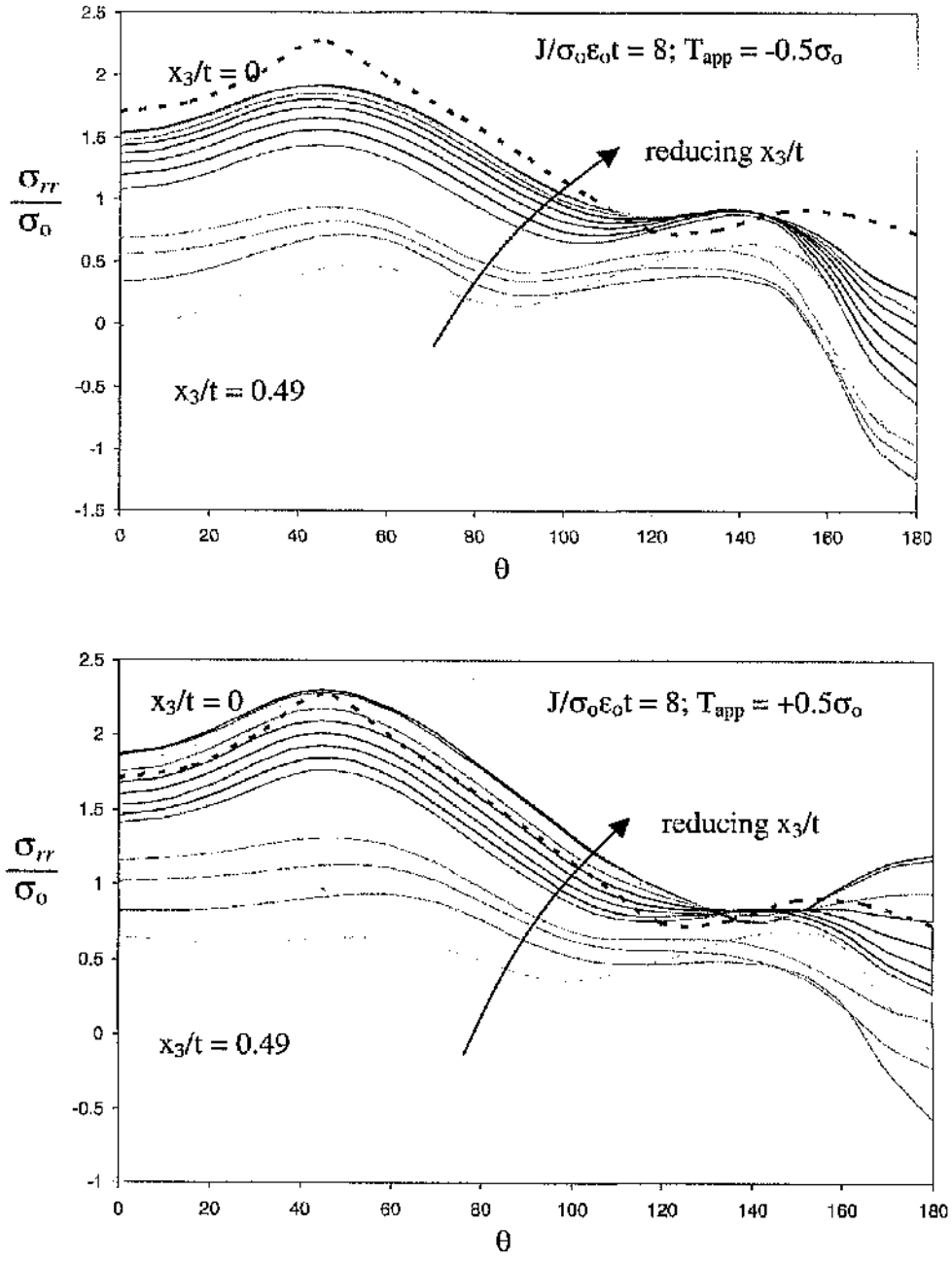


Figure 5.45: The radial stress $\sigma_{rr}$ at a load level $J_{far}/\sigma_o\varepsilon_o t = 8$ through the thickness, $T_{app} = -0.5$ and $+0.5$. The broken line determined in a boundary layer formulation indicates the two-dimensional plane strain field for $\sigma_{rr}$.

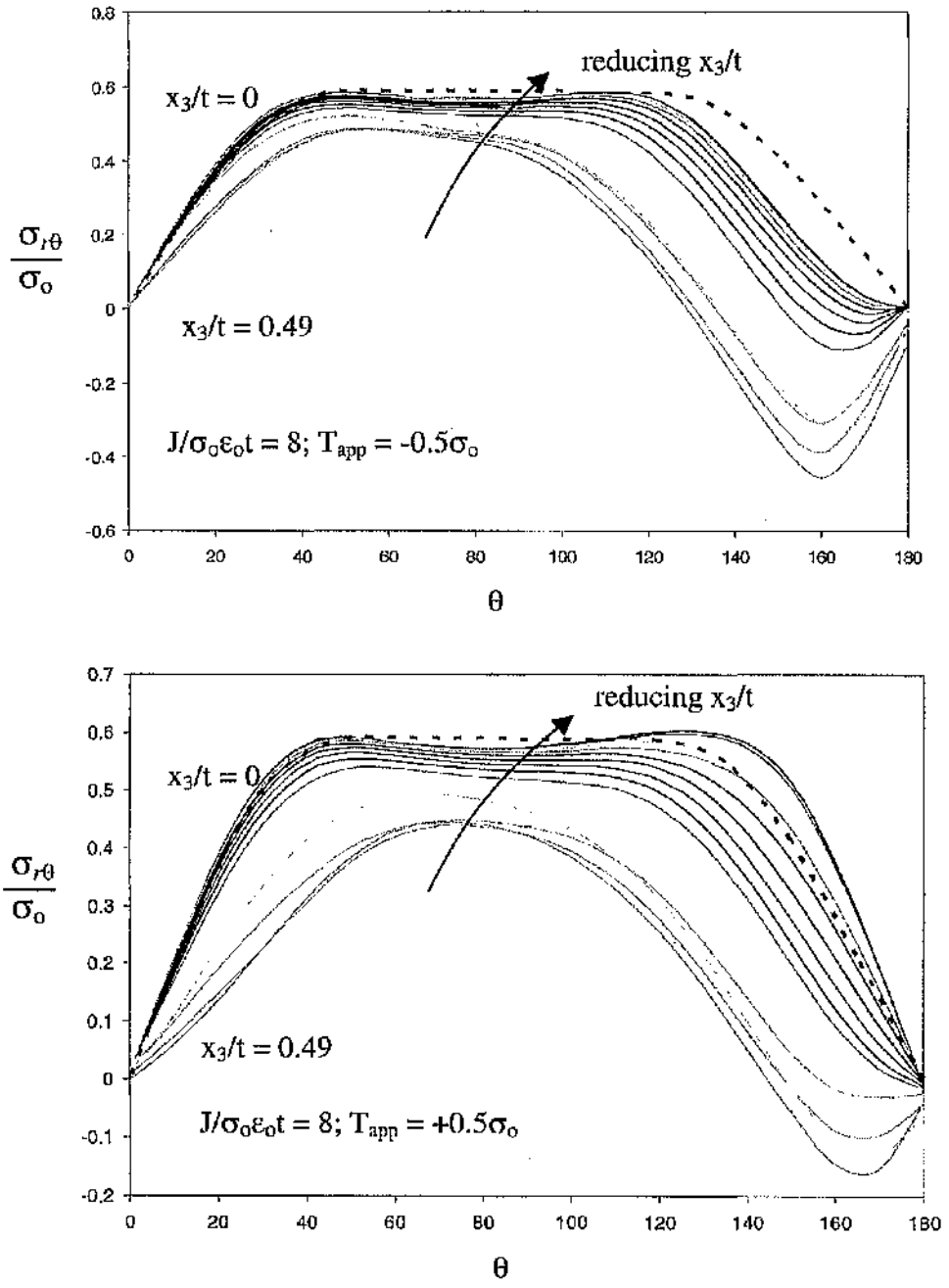


Figure 5.46: The shear stress $\sigma_{r\theta}$ at a load level $J_{far}/\sigma_o\varepsilon_o t = 8$ through the thickness, $T_{app}$ = -0.5 and +0.5. The broken line determined in a boundary layer formulation indicates the two-dimensional plane strain field for $\sigma_{r\theta}$.

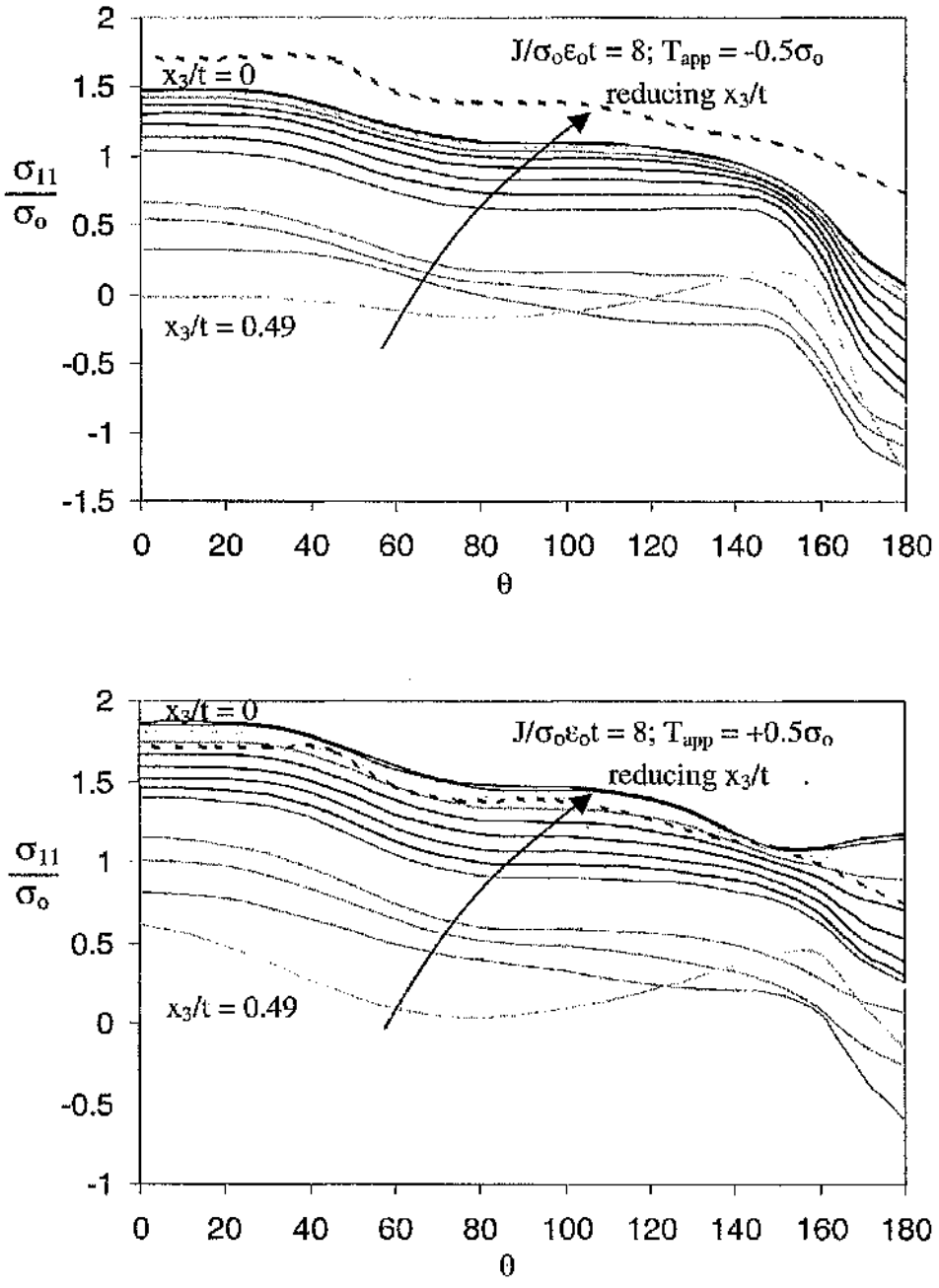


Figure 5.47: The direct stress $\sigma_{11}$ at a load level $J_{far}/\sigma_o\varepsilon_o t = 8$ through the thickness, $T_{app}$ = -0.5 and +0.5. The broken line determined in a boundary layer formulation indicates the two-dimensional plane strain field for $\sigma_{11}$.

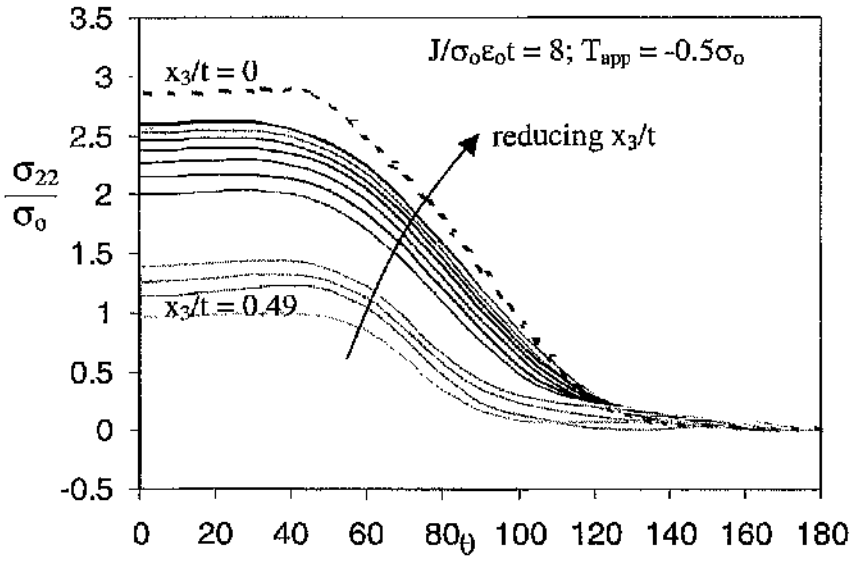


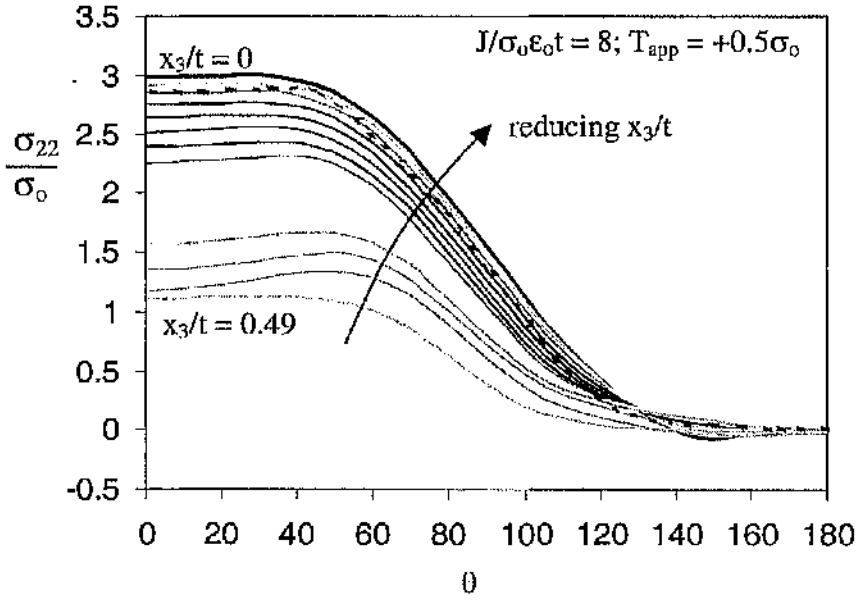


Figure 5.48: The direct stress $\sigma_{22}$ at a load level $J_{far}/\sigma_o\varepsilon_o t = 8$ through the thickness, $T_{app}$ = -0.5 and +0.5. The broken line determined in a boundary layer formulation indicates the two-dimensional plane strain field for $\sigma_{22}$.

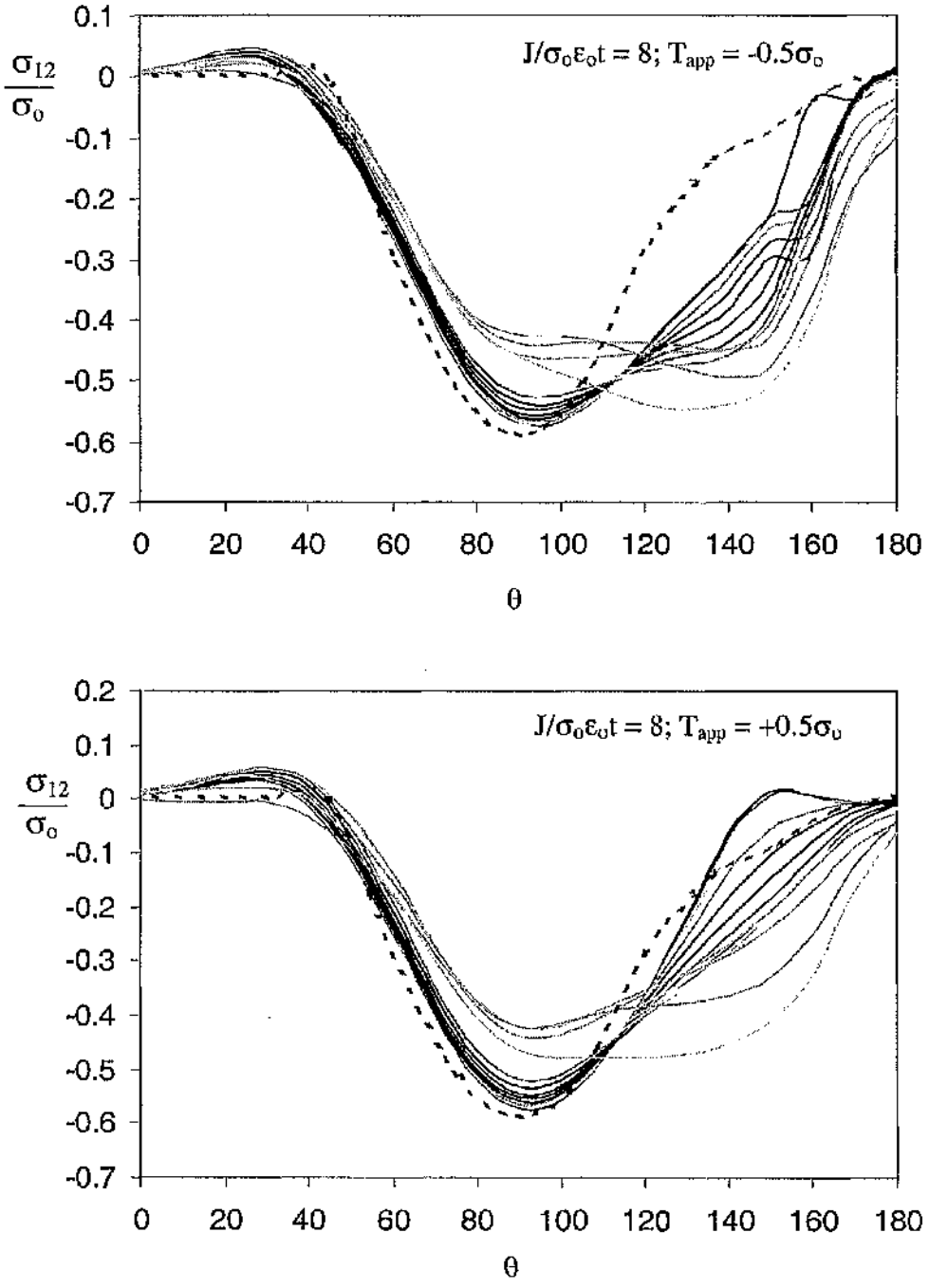


Figure 5.49: The shear stress $\sigma_{12}$ at a load level $J_{far}/\sigma_o\varepsilon_o t = 8$ through the thickness, $T_{app}$ = -0.5 and +0.5. The broken line determined in a boundary layer formulation indicates the two-dimensional plane strain field for $\sigma_{12}$.

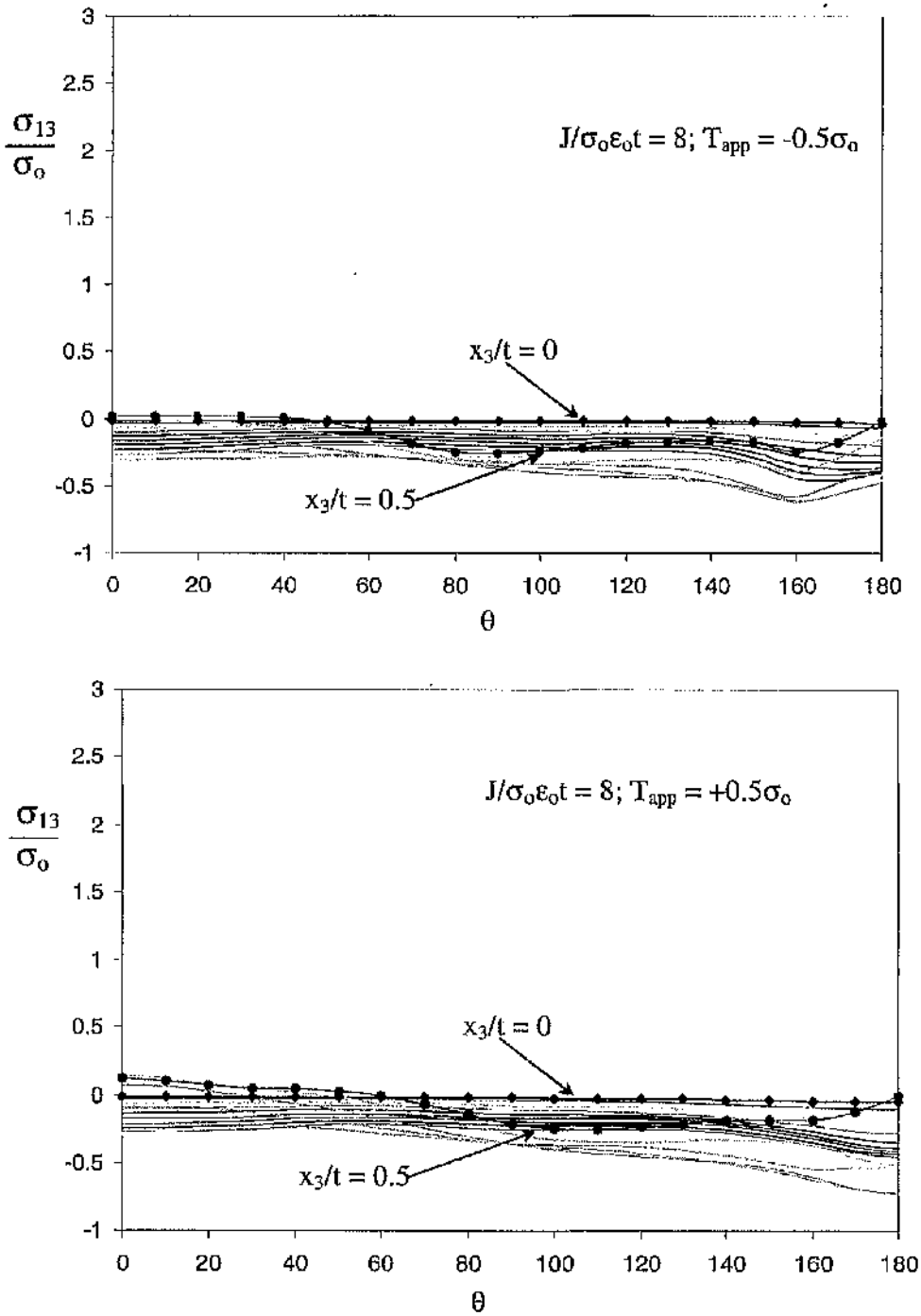


Figure 5.50: The out-of-plane stress $\sigma_{13}$ at a load level $J_{far}/\sigma_o\varepsilon_o t = 8$ through the thickness, $T_{app}$ = -0.5 and +0.5. The diamond markers show the midplane stress and the circular markers show the free surface stress.

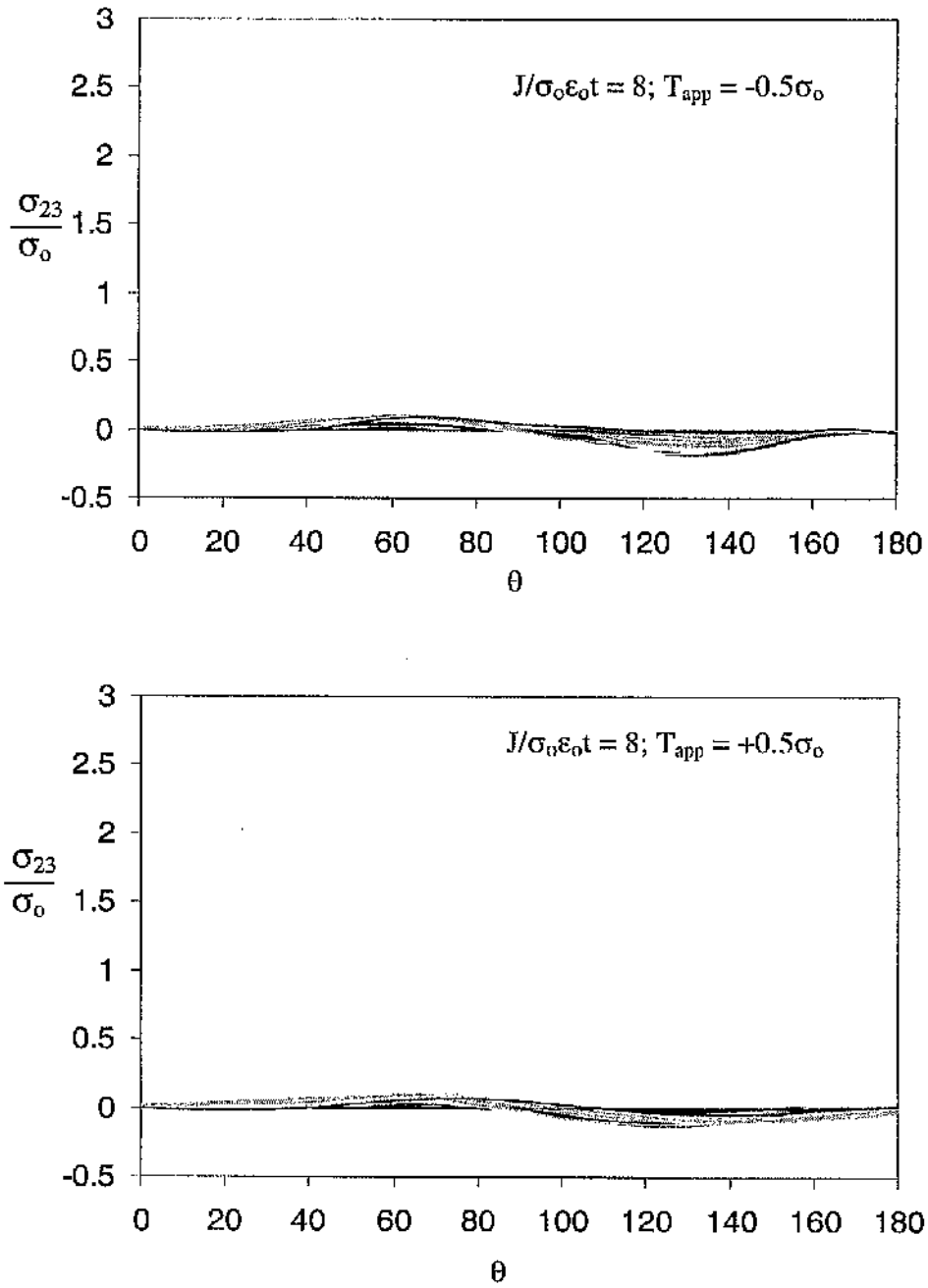


Figure 5.51: The out-of-plane stress $\sigma_{23}$ at a load level $J_{fat}/\sigma_o\varepsilon_o t = 8$ through the thickness, $T_{app} = -0.5$ and $+0.5$.

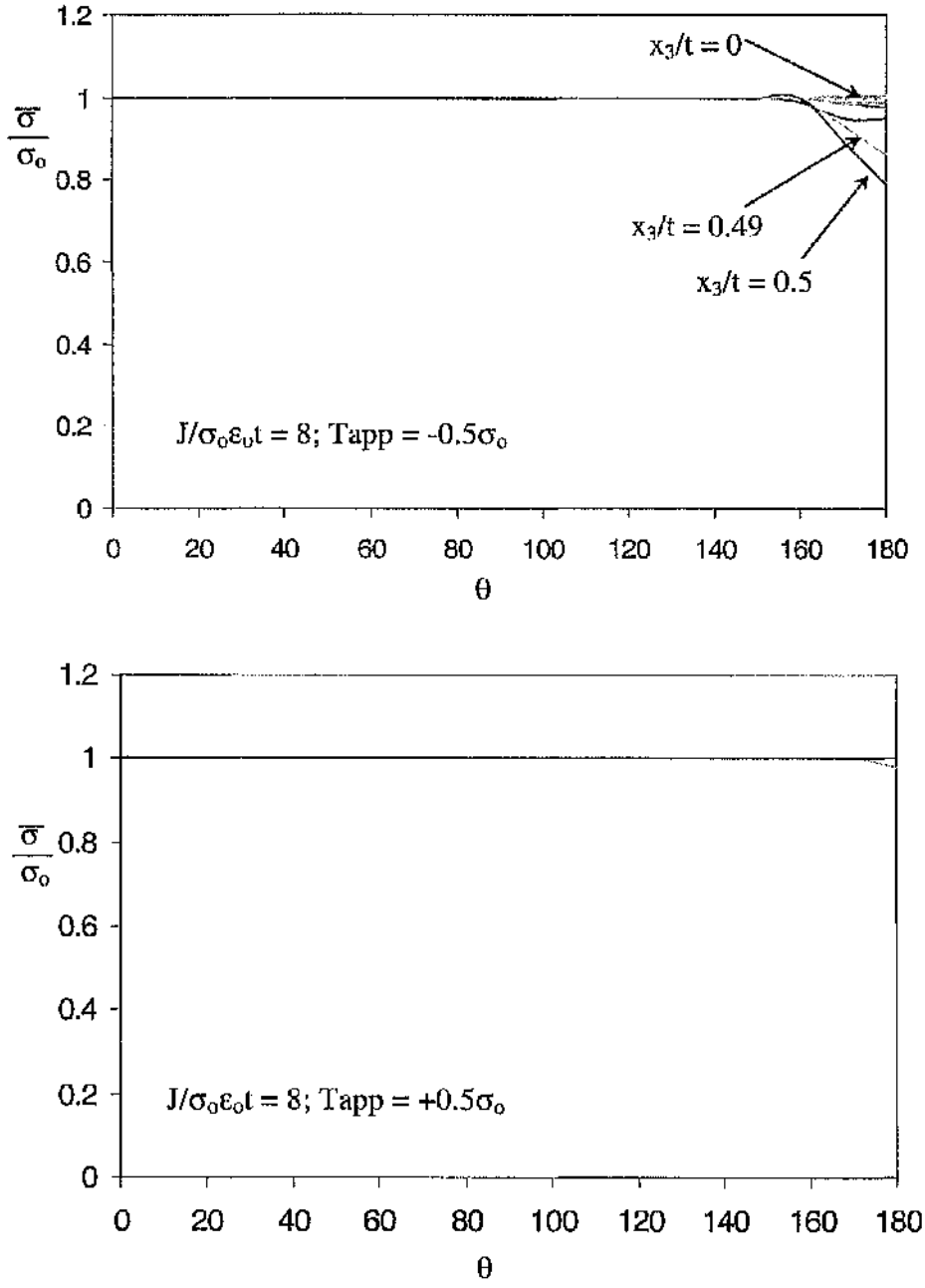


Figure 5.52: The Mises stress $\overline{\sigma}$ at a load level $J_{far}/\sigma_o\varepsilon_o t = 8$ through the thickness, $T_{app}$ = -0.5 and +0.5.

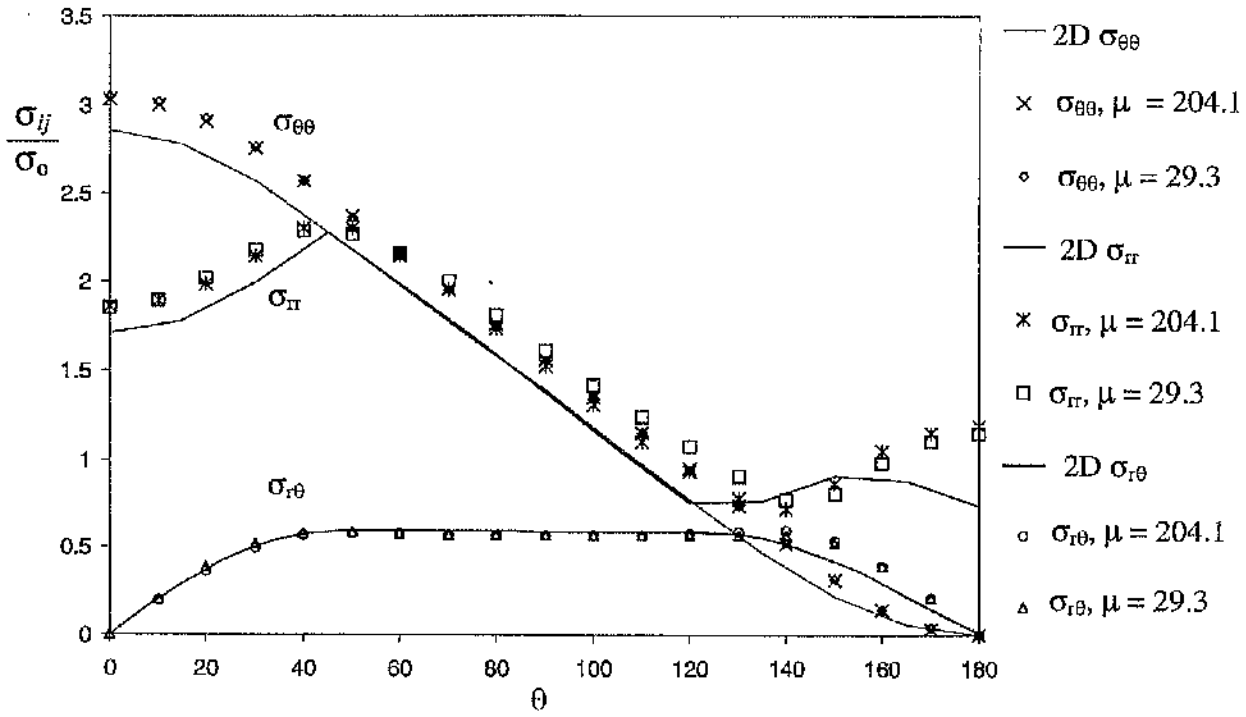


Figure 5.53: The asymptotic cylindrical stresses at the midplane for a SENB specimen B/(W-a) = 1 compared with a two-dimensional plane strain field.

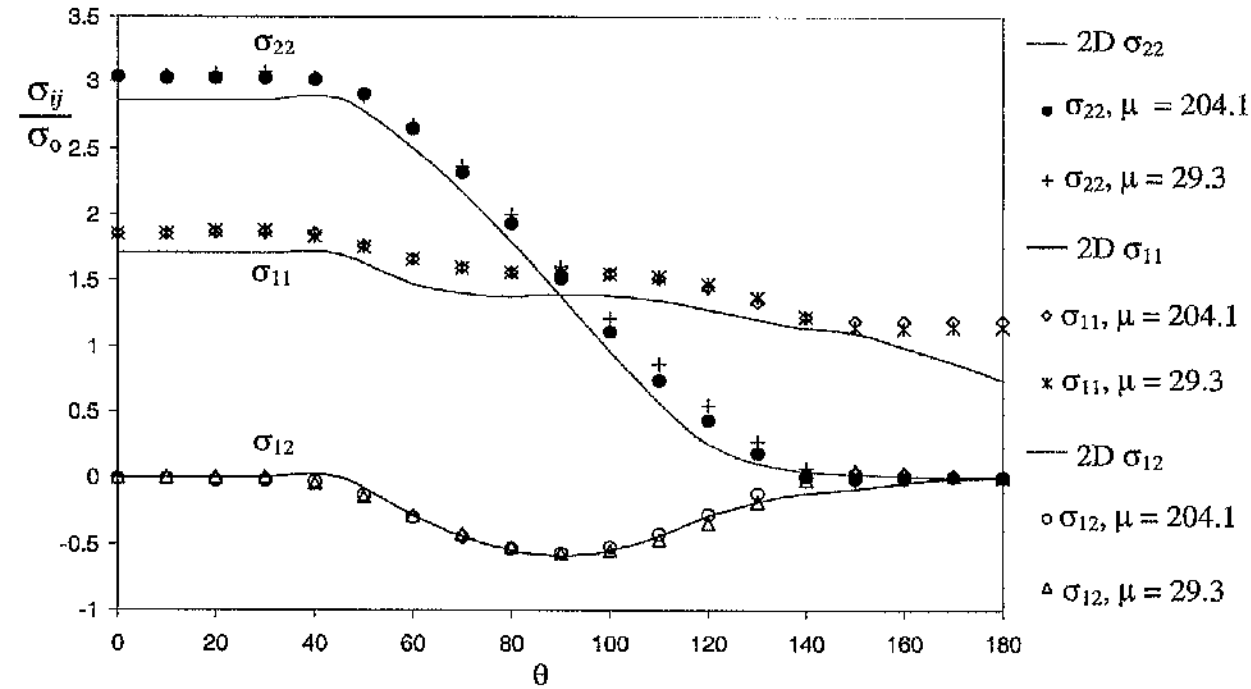


Figure 5.54: The asymptotic Cartesian stresses at the midplane for a SENB specimen B/(W-a) = 1 compared with a two-dimensional plane strain field.

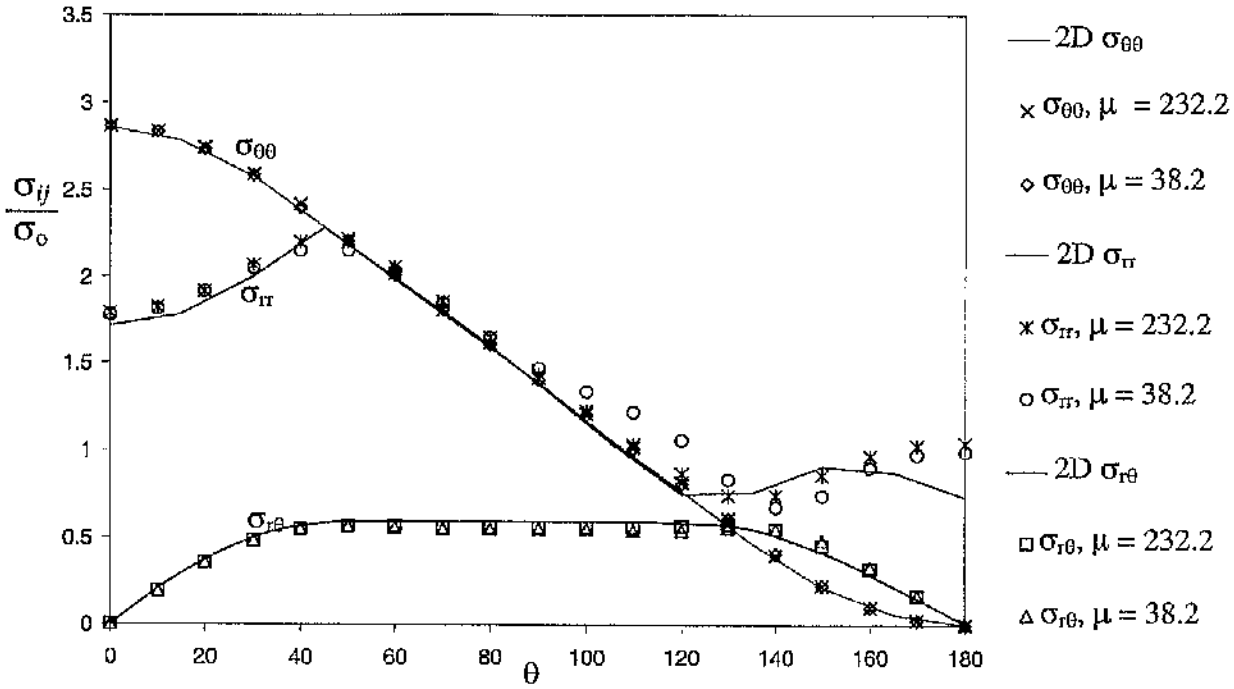


Figure 5.55: The asymptotic cylindrical stresses at the quarterplane for a SENB specimen B/(W-a) = 1 compared with a two-dimensional plane strain field.

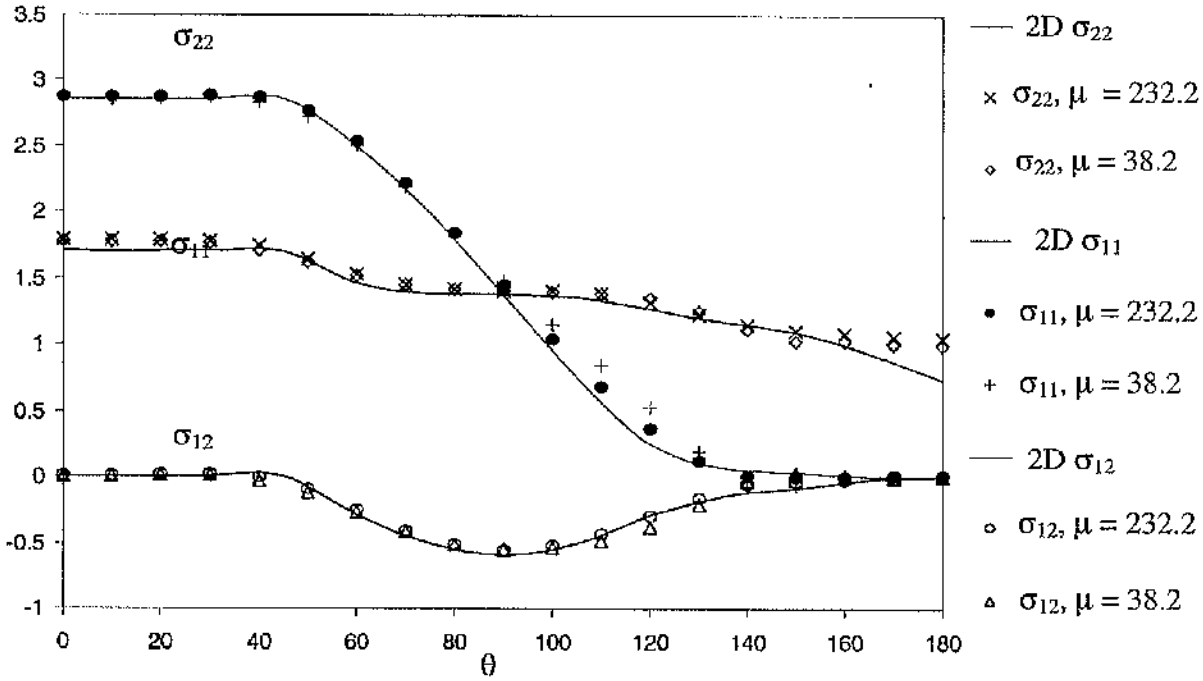


Figure 5.56: The asymptotic Cartesian stresses at the quarterplane for a SENB specimen B/(W-a) = 1 compared with a two-dimensional plane strain field.

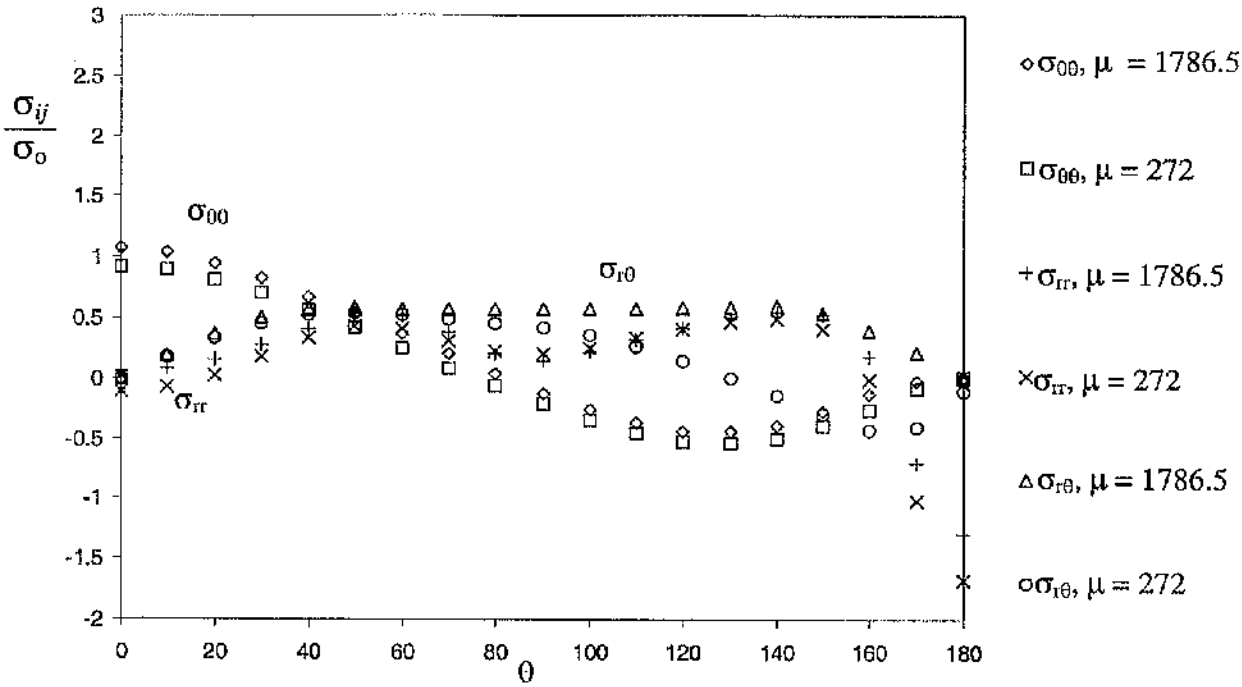


Figure 5.57: The asymptotic polar stresses at the free surface for a SENB specimen B/(W-a) = 1.

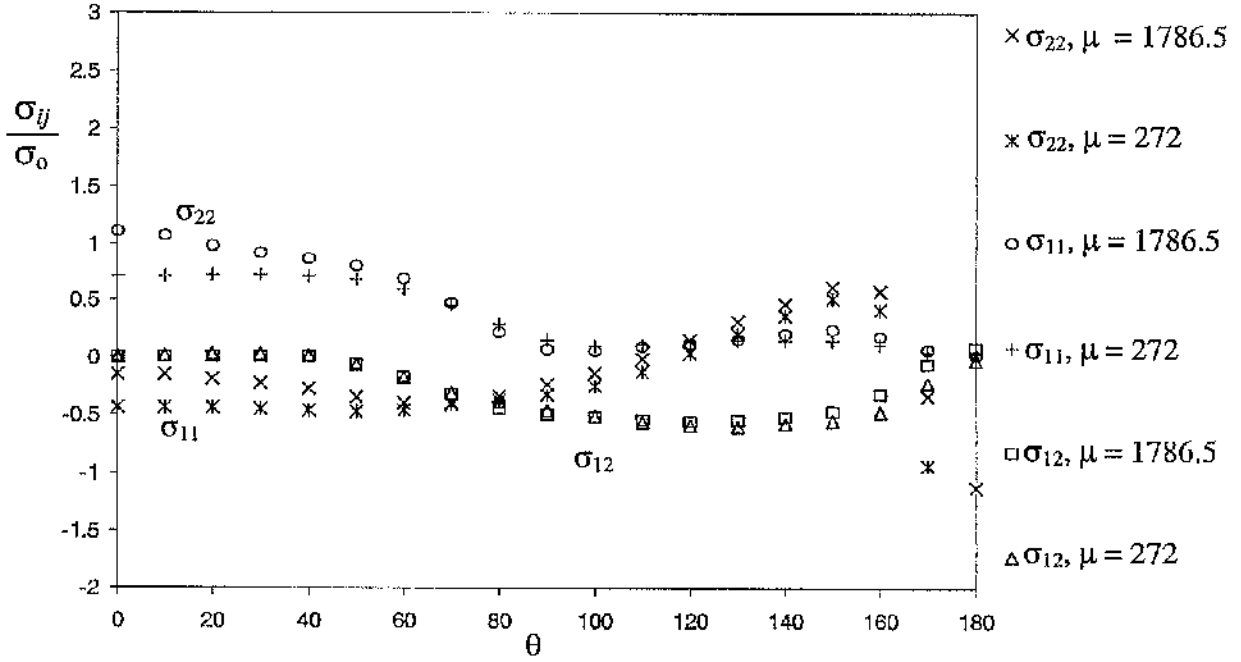


Figure 5.58: The asymptotic Cartesian stresses at the free surface for a SENB specimen B/(W-a) = 1.

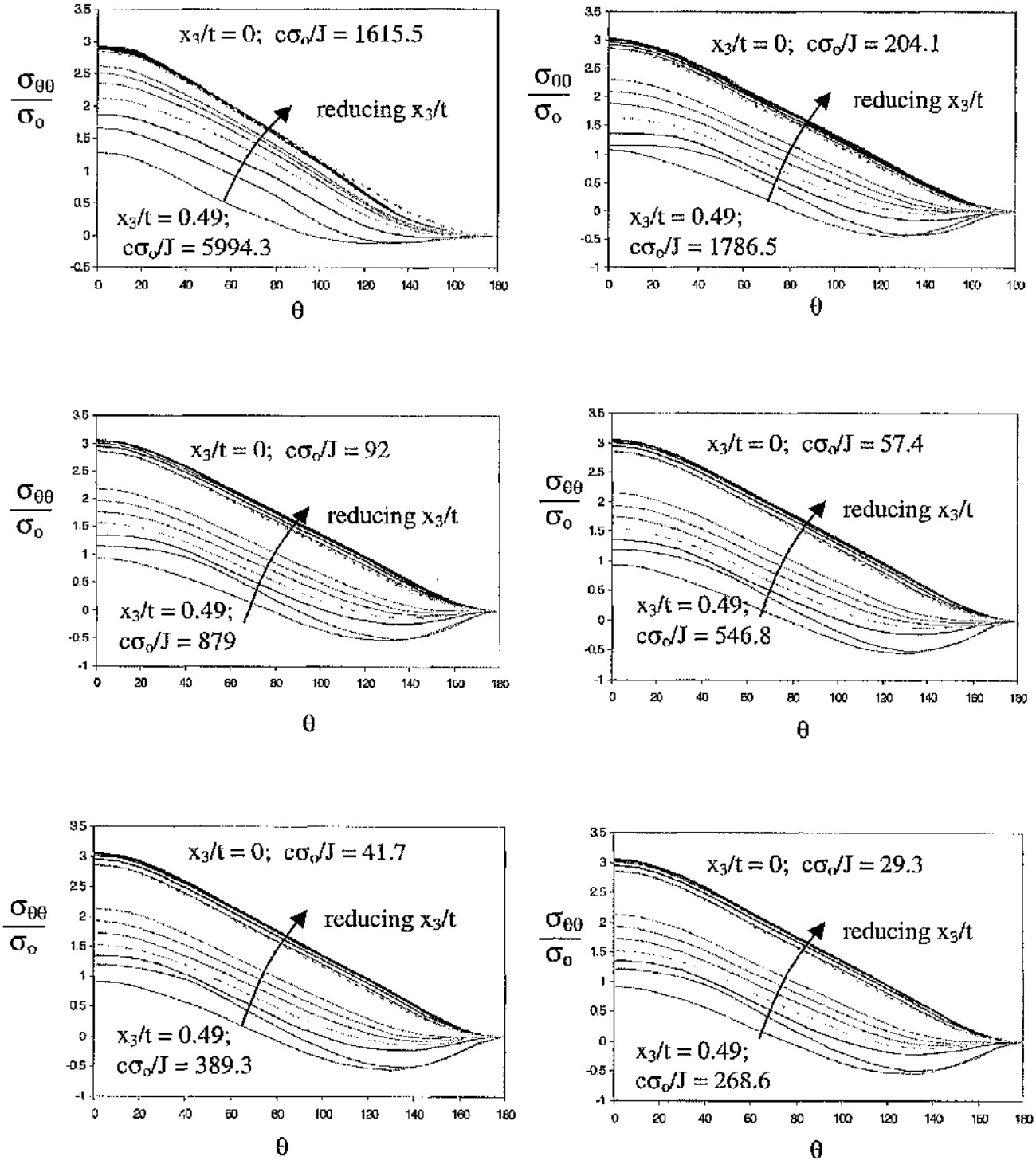


Figure 5.59: The hoop stress $\sigma_{\theta\theta}$ for SENB B/(W-a) = 1 through the thickness, $T_{app} = 0$. The broken line determined in a boundary layer formulation indicates the two-dimensional plane strain field for $\sigma_{\theta\theta}$.

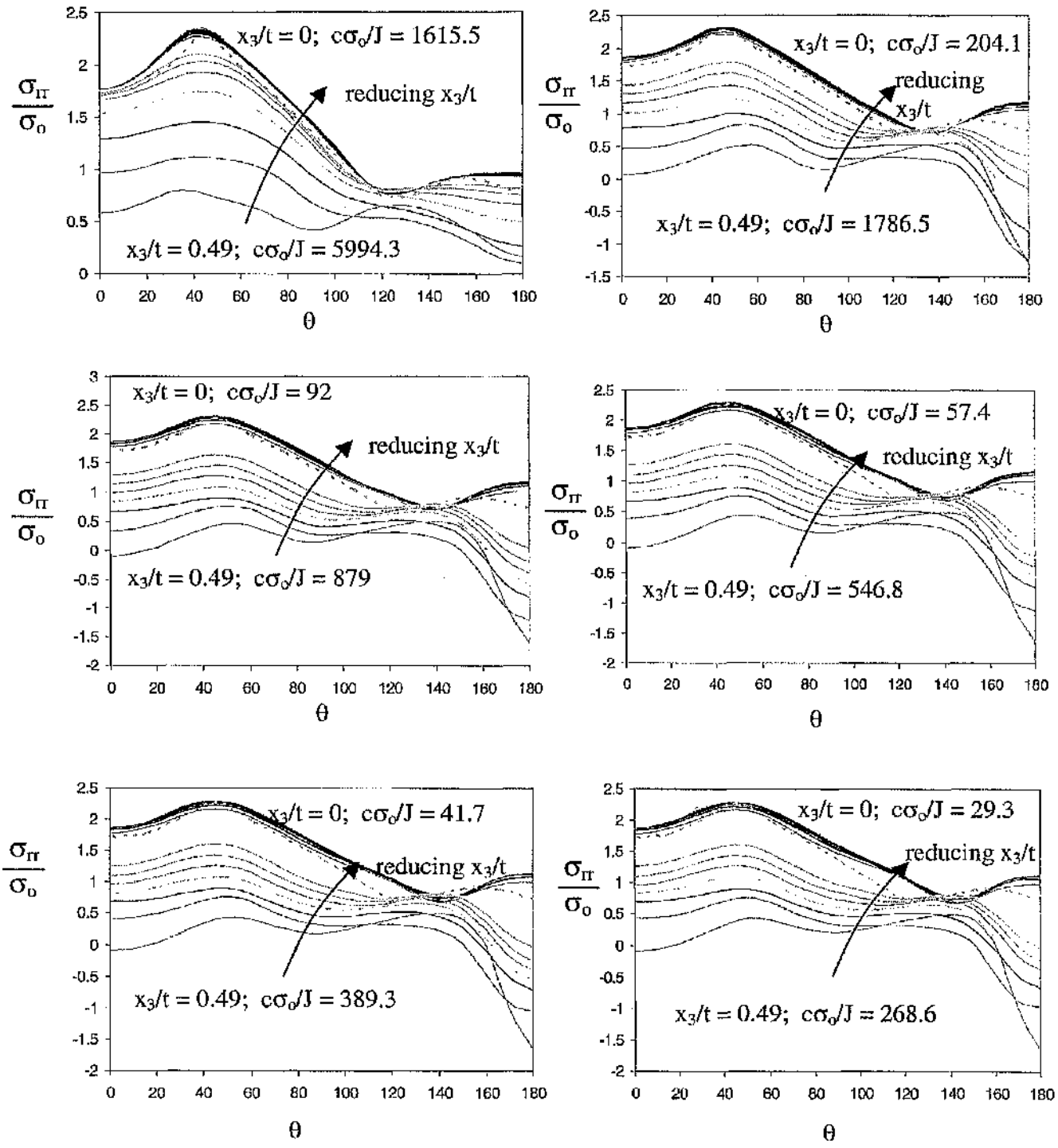


Figure 5.60: The stress $\sigma_{rr}$ for SENB B/(W-a) = 1 through thickness, $T_{app} = 0$. The broken line determined in a boundary layer formulations indicates the two-dimensional plane strain field for $\sigma_{rr}$.

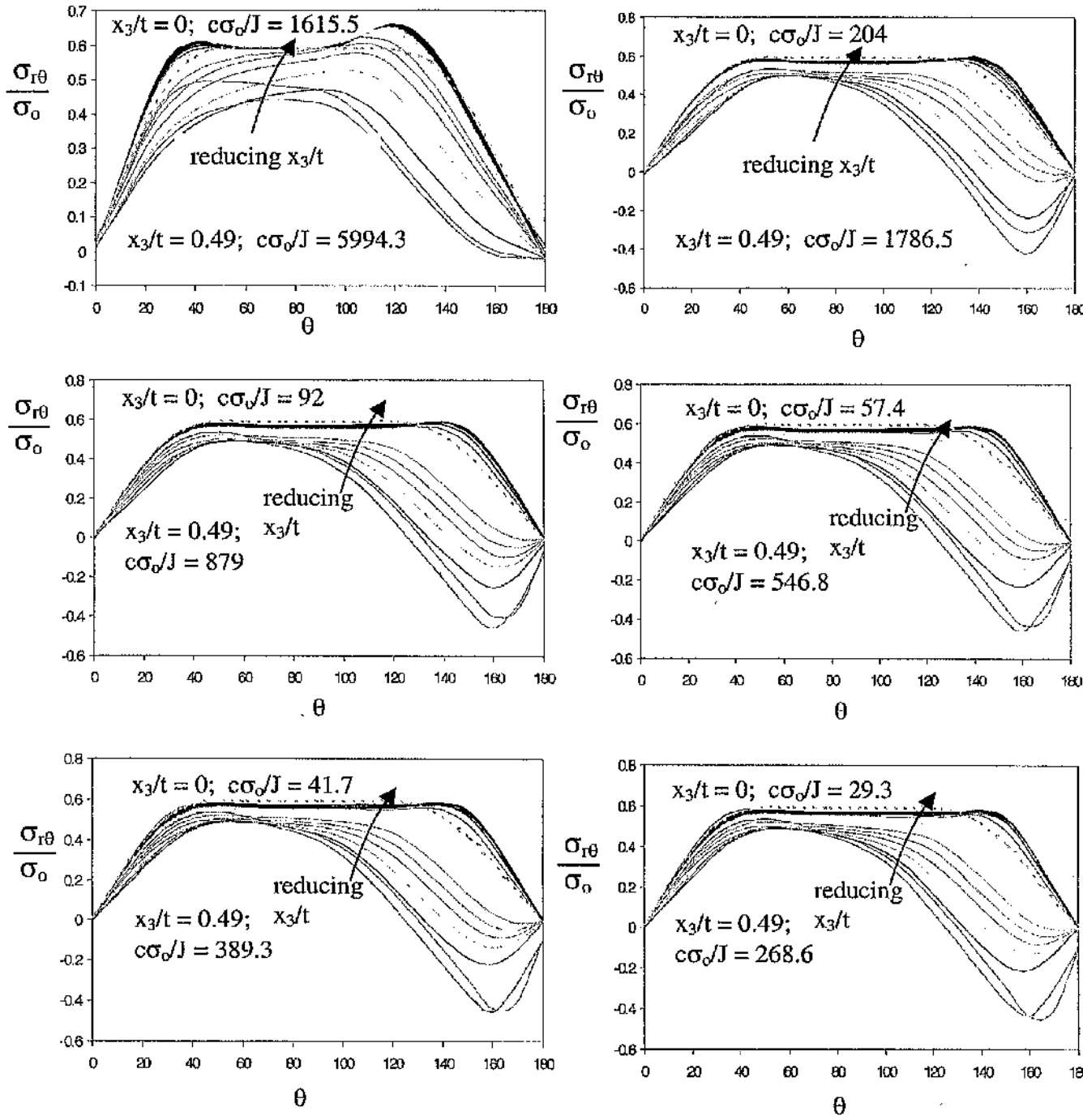


Figure 5.61: The shear stress $\sigma_{r\theta}$ for SENB B/(W-a) = 1 through thickness, $T_{app} = 0$. The broken line determined in a boundary layer formulation indicates the two-dimensional plane strain field for $\sigma_{r\theta}$.

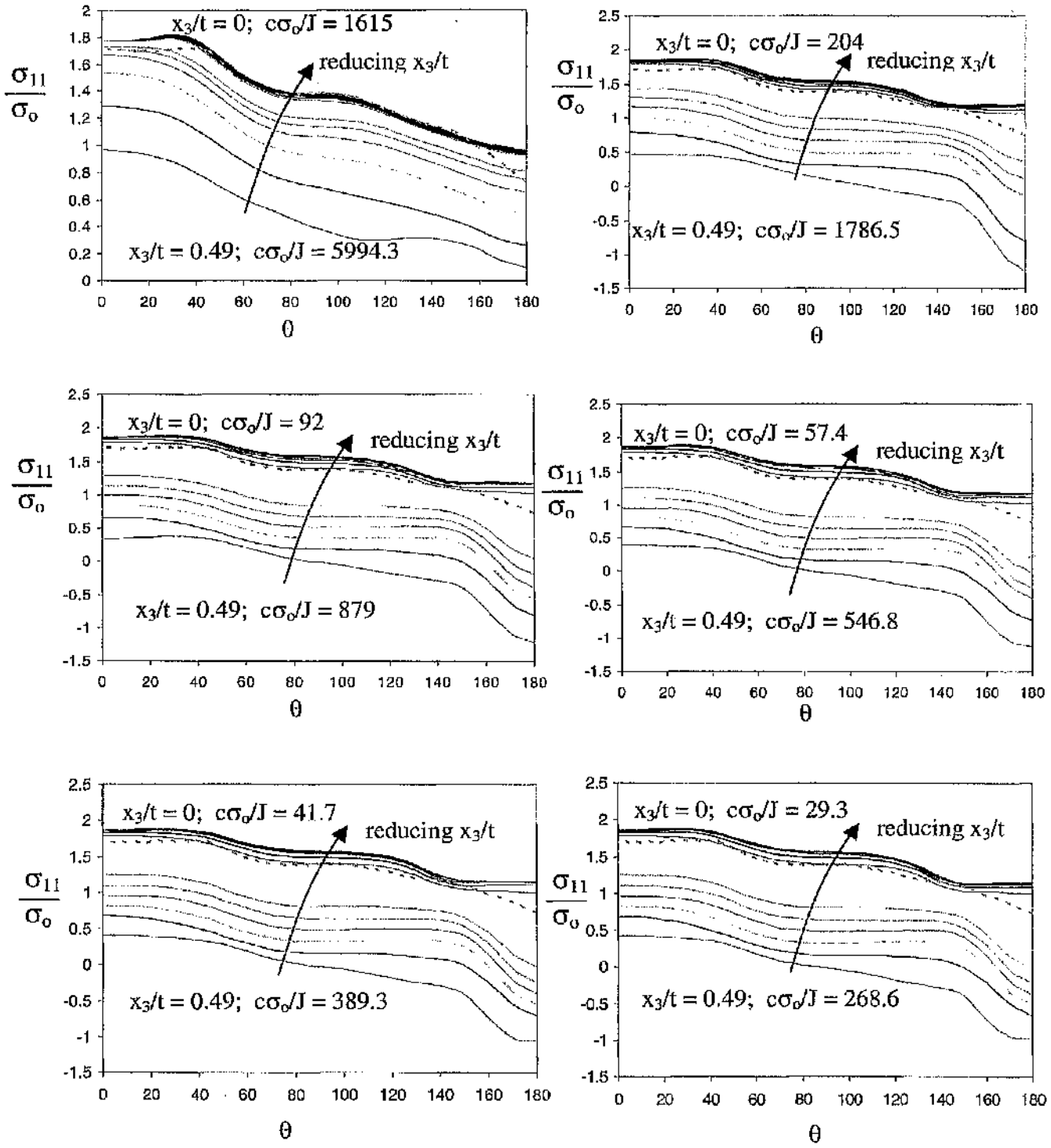


Figure 5.62: The direct stress $\sigma_{11}$ for SENB B/(W-a) = 1 through the thickness, $T_{app} = 0$. The broken line determined from a boundary layer formulation indicates the two-dimensional plane strain for $\sigma_{11}$.

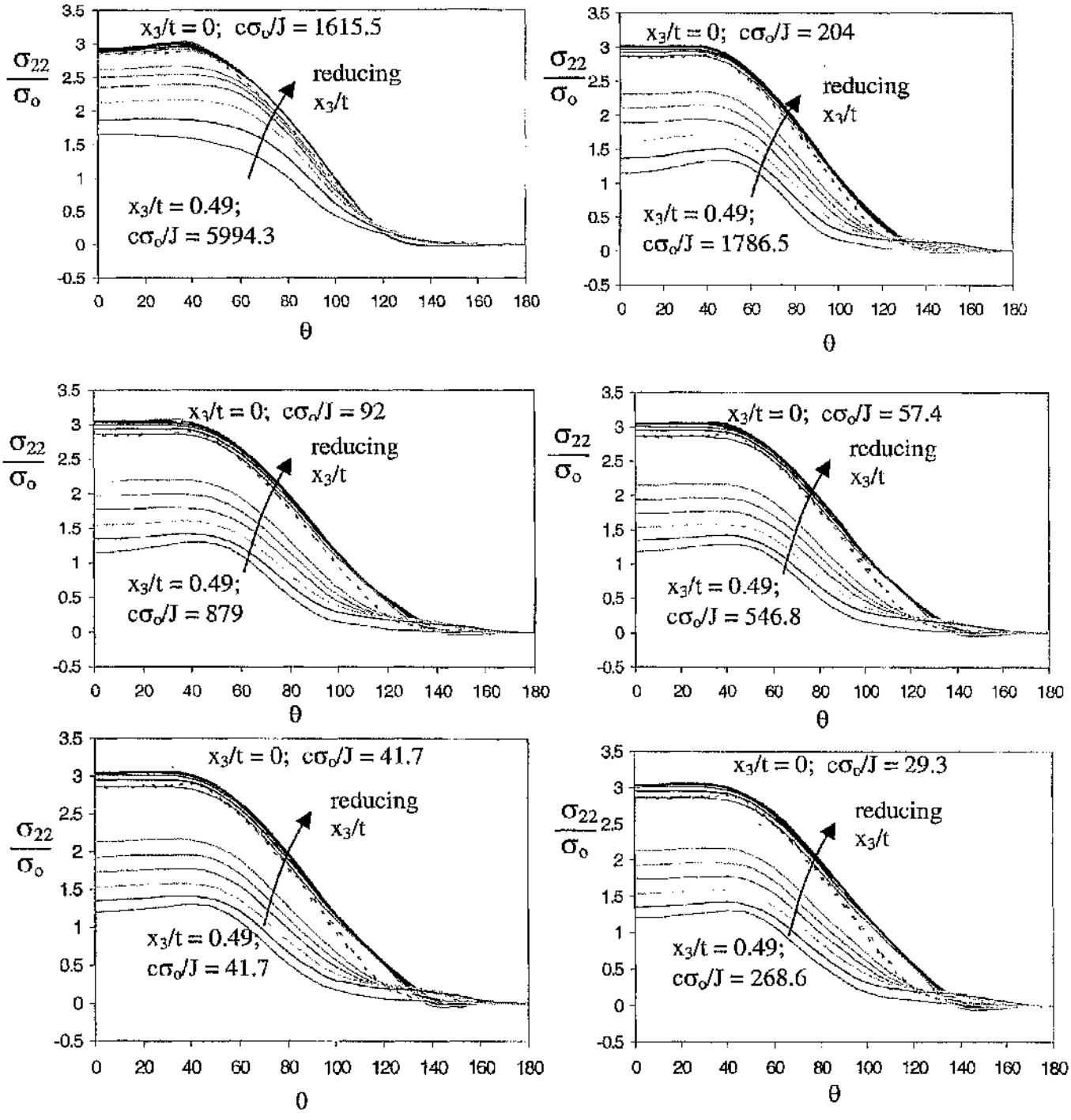


Figure 5.63: The direct stress $\sigma_{22}$ for SENB B/(W-a) = 1 through the thickness, $T_{app} = 0$. The broken line determined in a boundary layer formulation indicates the two-dimensional plane strain field for $\sigma_{22}$.

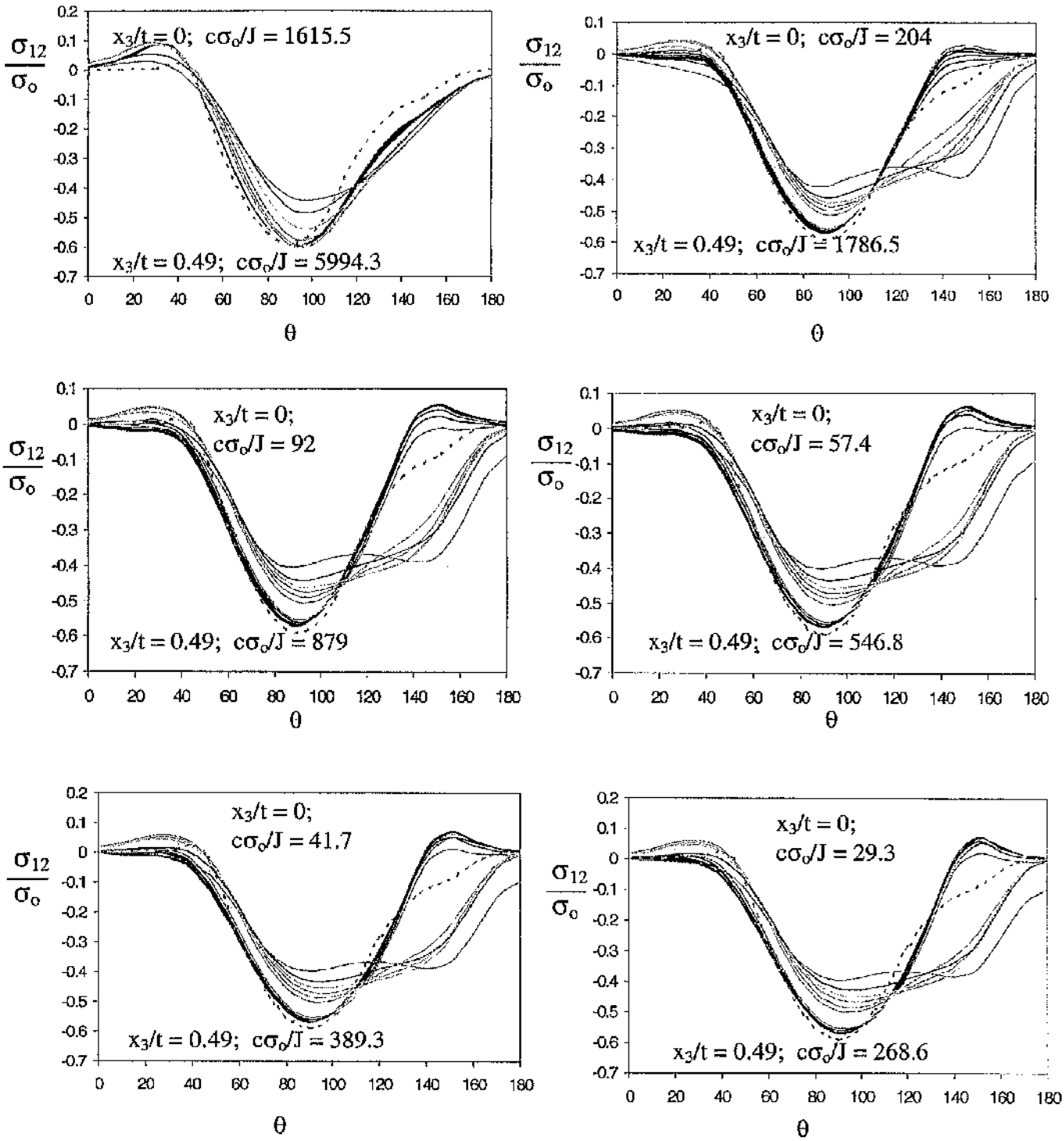


Figure 5.64: The shear stress $\sigma_{12}$ for SENB B/(W-a) = 1 through the thickness, $T_{app} = 0$. The broken line determined in a boundary layer formulation indicates the two-dimensional plane strain field for $\sigma_{12}$.

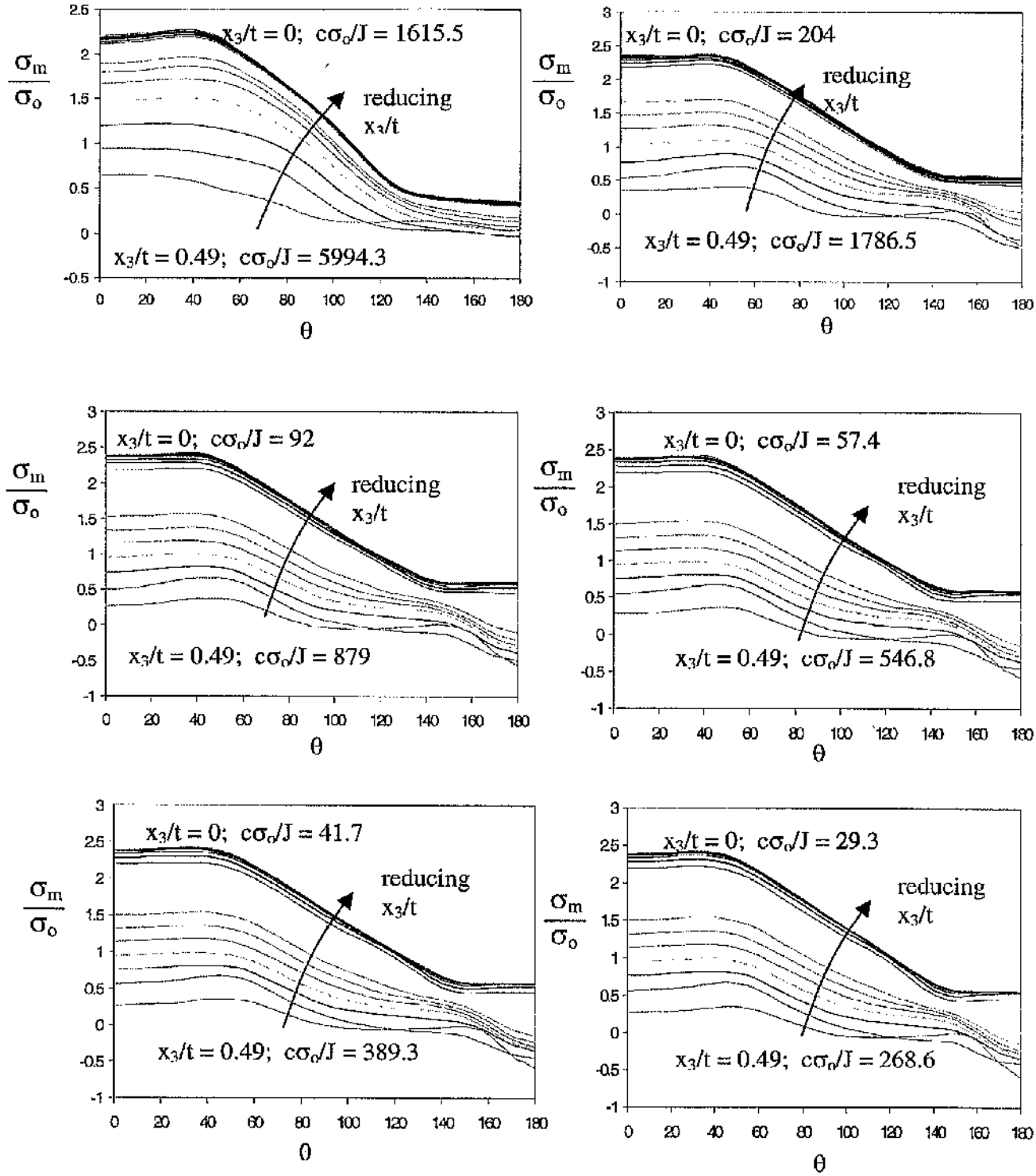


Figure 5.65: The mean stress $\sigma_m$ for SENB B/(W-a) = 1 through thickness, $T_{app} = 0$. The broken line determined in a boundary layer formulation indicates the two-dimensional plane strain field for $\sigma_m$.

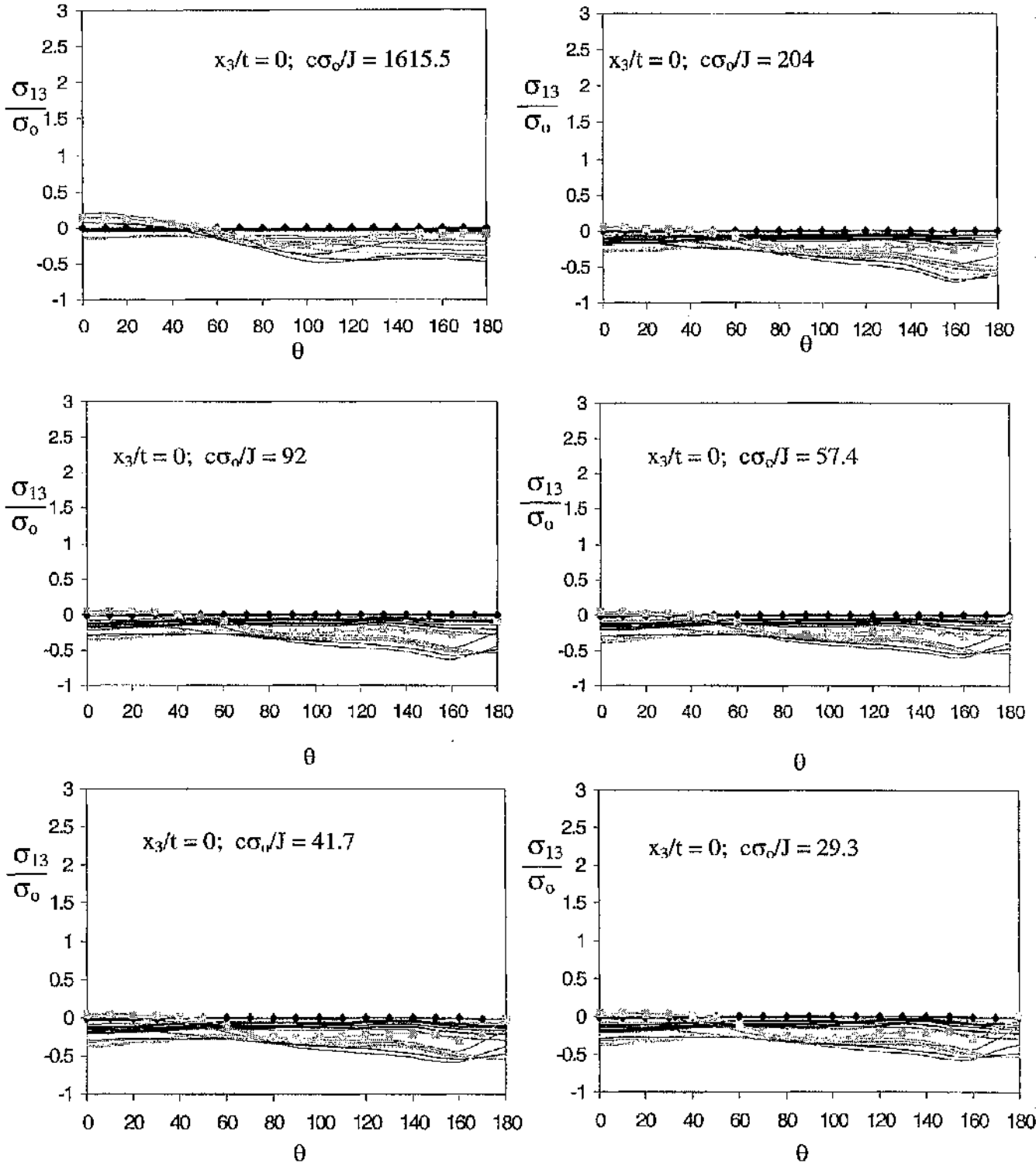


Figure 5.66: The shear stress $\sigma_{13}$ for SENB B/(W-a) = 1 through the thickness, $T_{app} = 0$. The diamond markers and the circular markers indicate the midplane and the free surface.

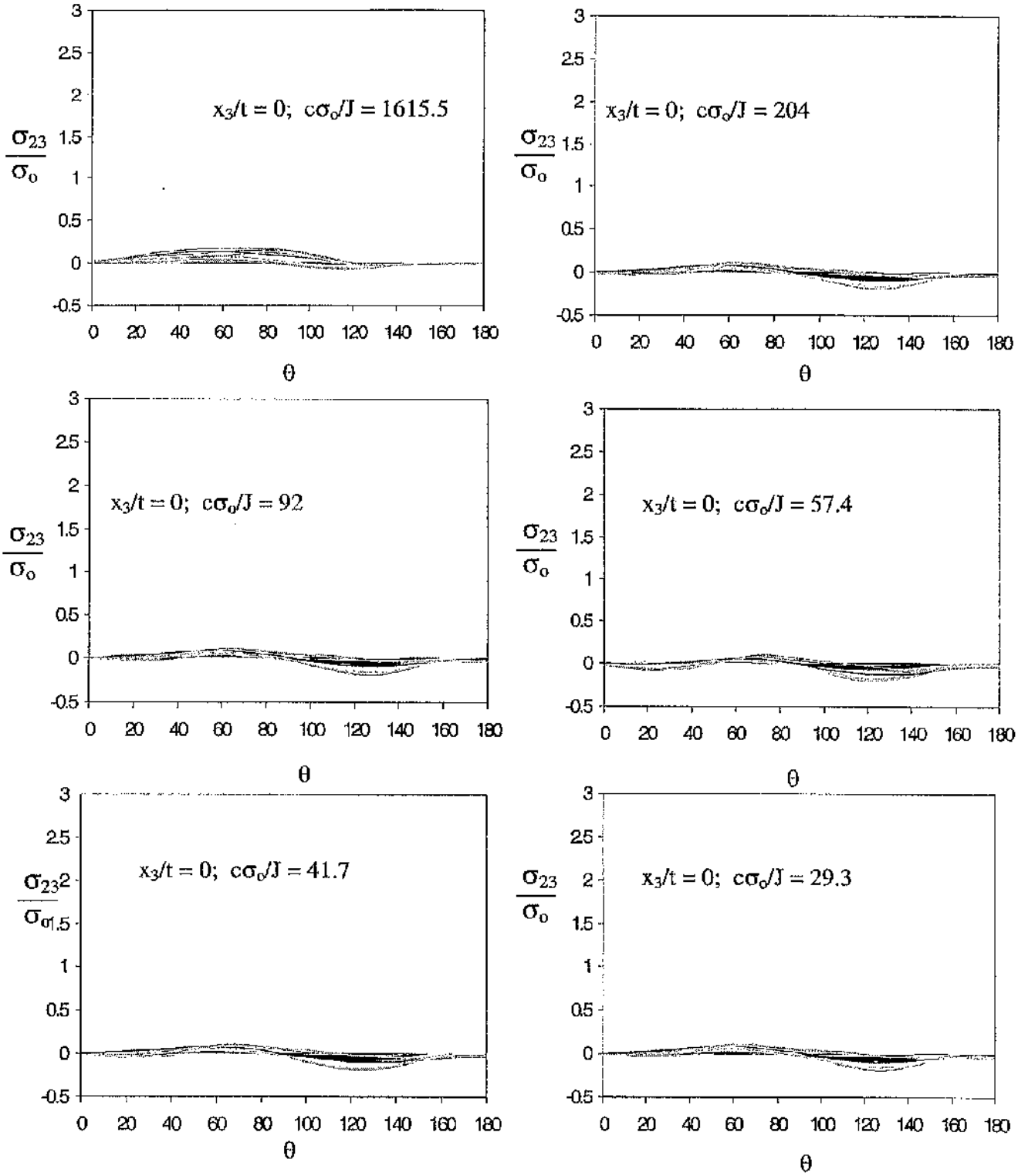


Figure 5.67: The shear stress $\sigma_{23}$ for SENB B/(W-a) =1 through thickness, $T_{app} = 0$.

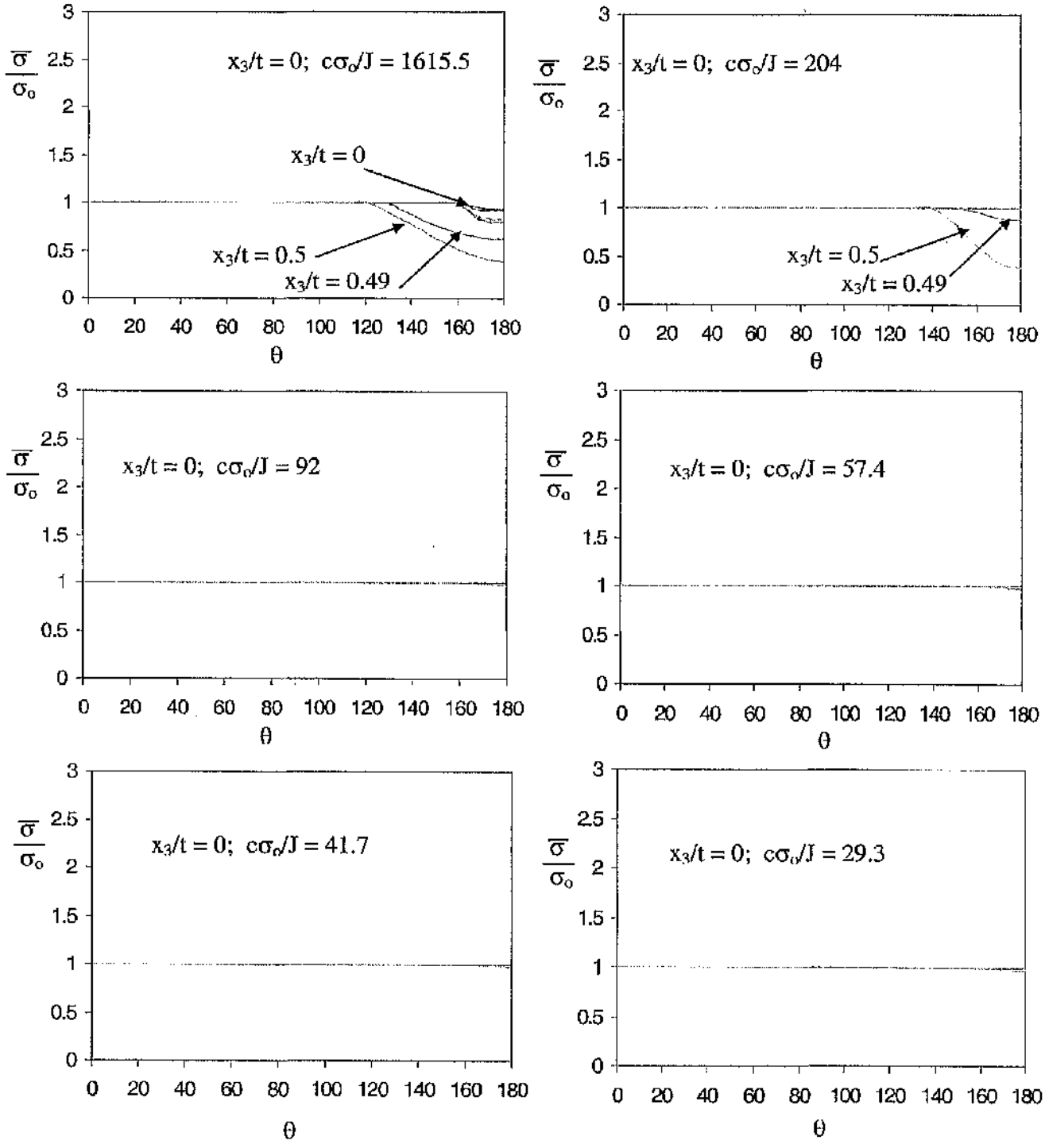


Figure 5.68: The Mises stress $\bar{\sigma}/\sigma_o$ for SENB B/(W-a) =1 through the thickness, $T_{app} = 0$.

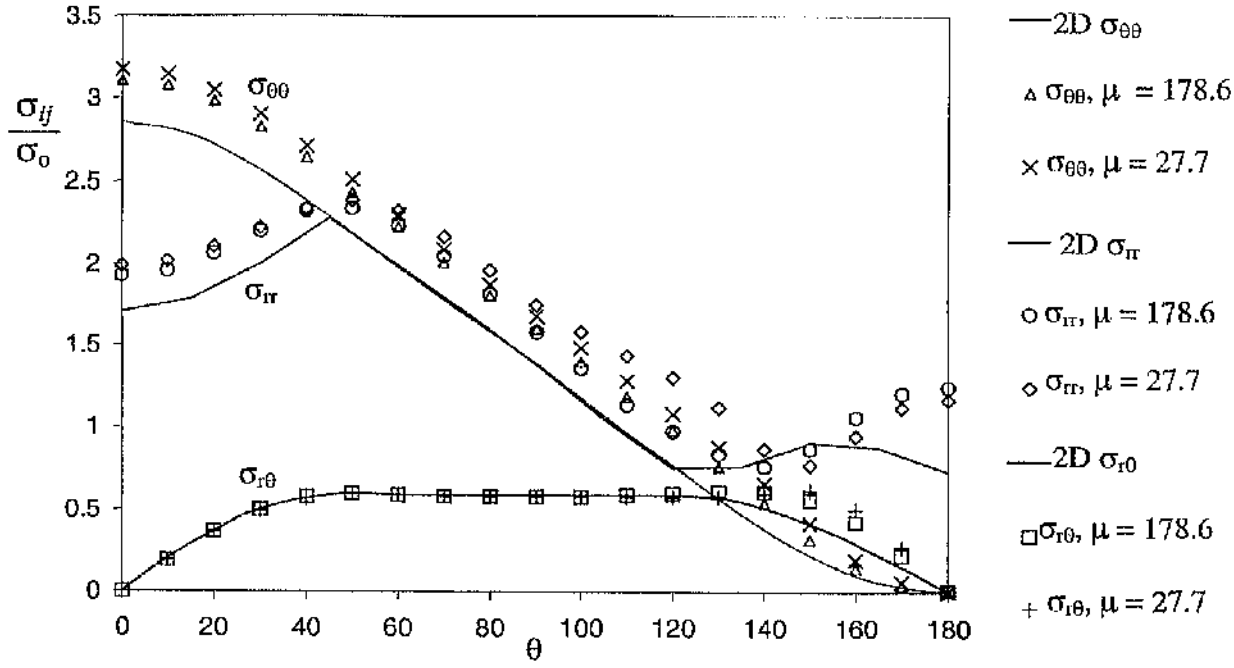


Figure 5.69: The asymptotic cylindrical stresses at the midplane for a SENB specimen B/(W-a) = 0.5 compared with a two-dimensional plane strain field.

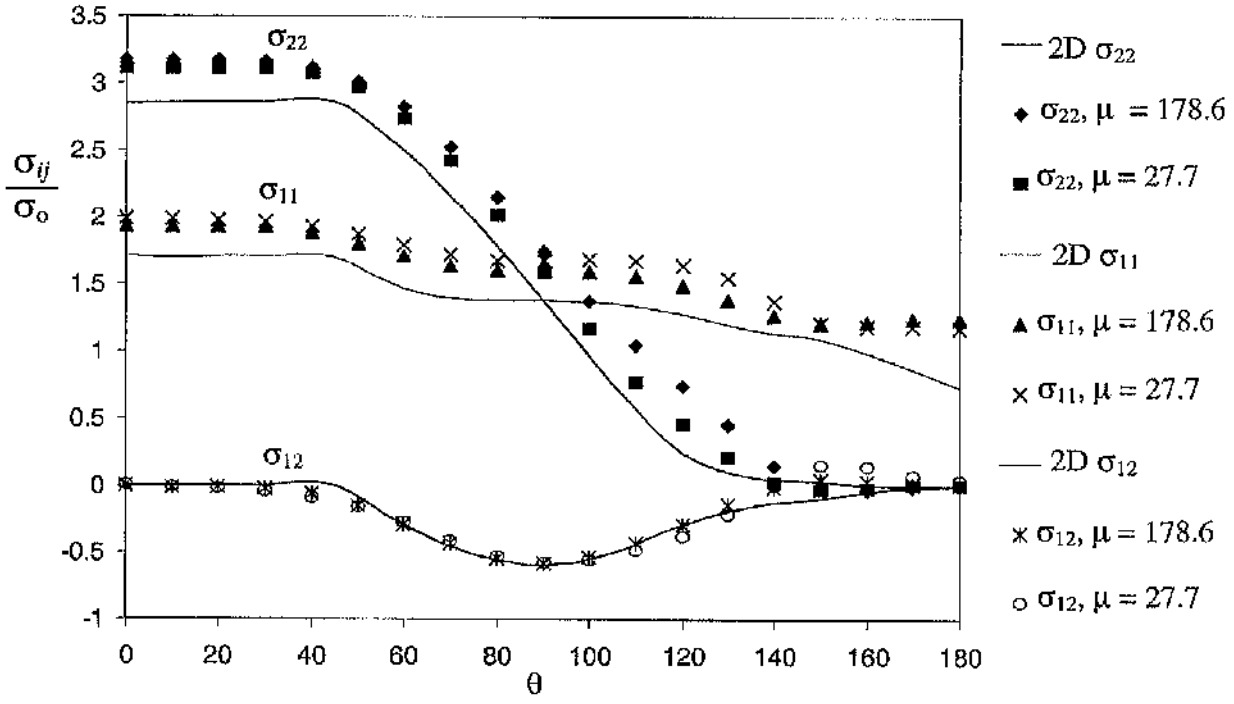


Figure 5.70: The asymptotic Cartesian stresses at the midplane for a SENB specimen B/(W-a) = 0.5 compared with the two-dimensional plane strain field.

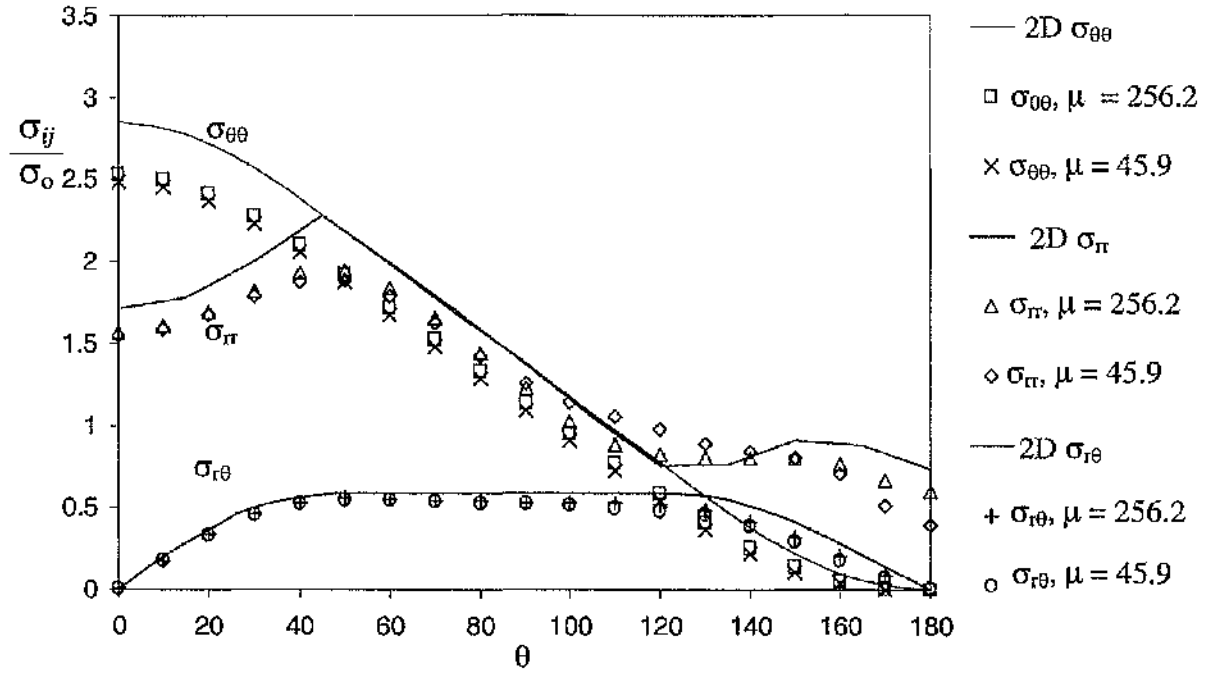


Figure 5.71: The asymptotic cylindrical stresses at the quarterplane for a SENB specimen B/(W-a) = 0.5 compared with the two-dimensional plane strain field.

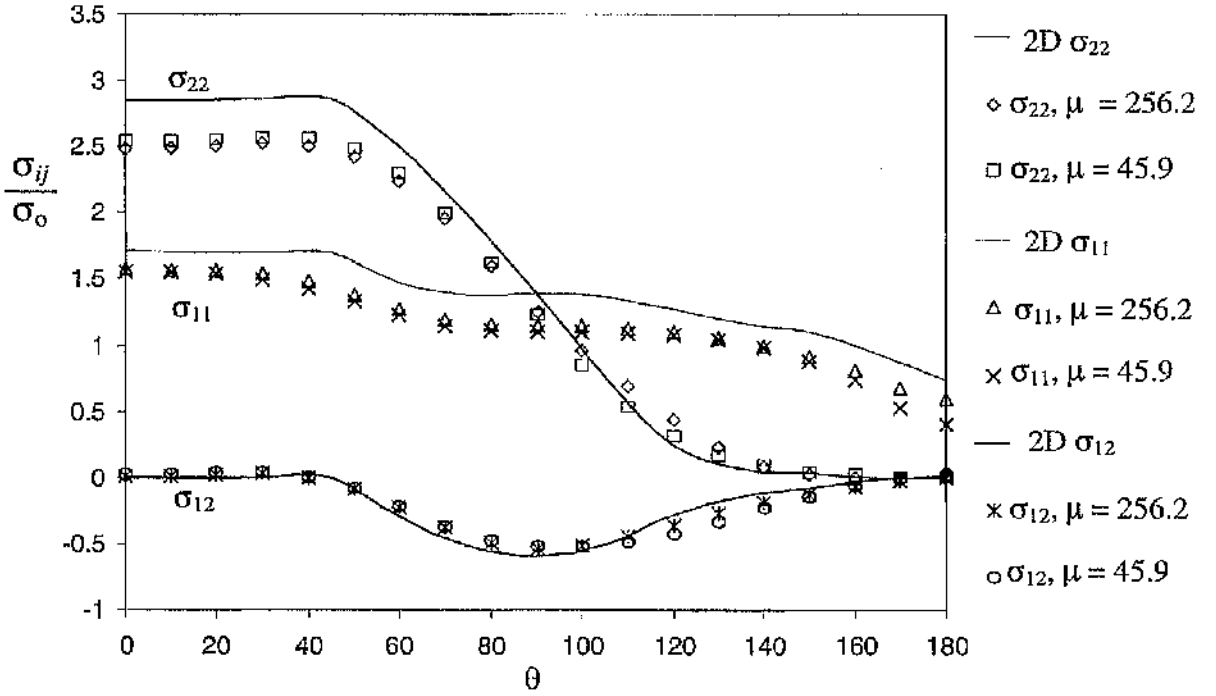


Figure 5.72: The asymptotic Cartesian stresses at the quarterplane for a SENB specimen B/(W-a) = 0.5 compared with the two-dimensional plane field.

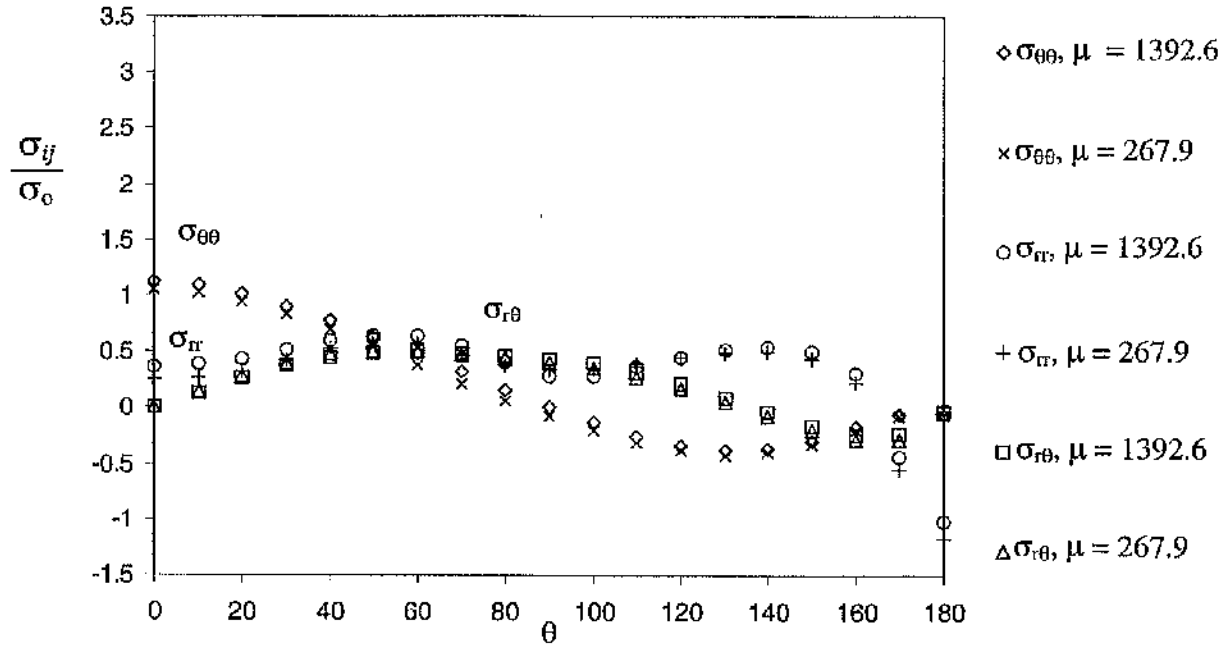


Figure 5.73: The asymptotic cylindrical stresses at the free surface for a SENB specimen B/(W-a) = 0.5.

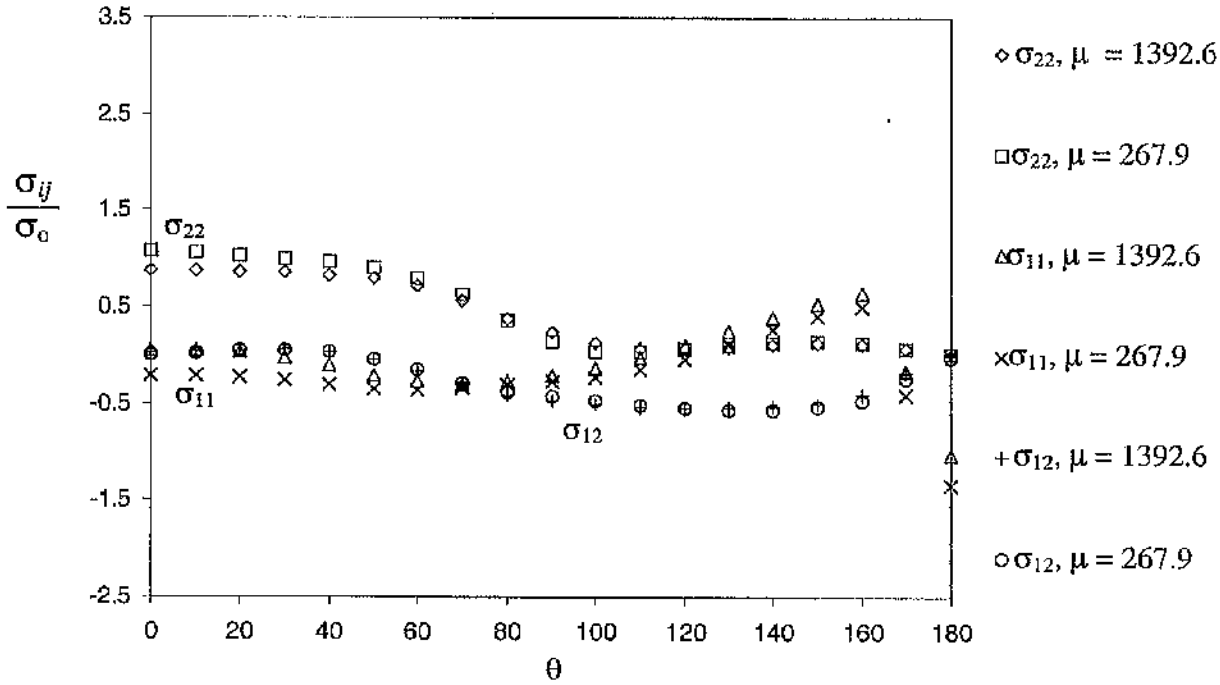


Figure 5.74: The asymptotic Cartesian stresses at the free surface for a SENB specimen B/(W-a) = 0.5.

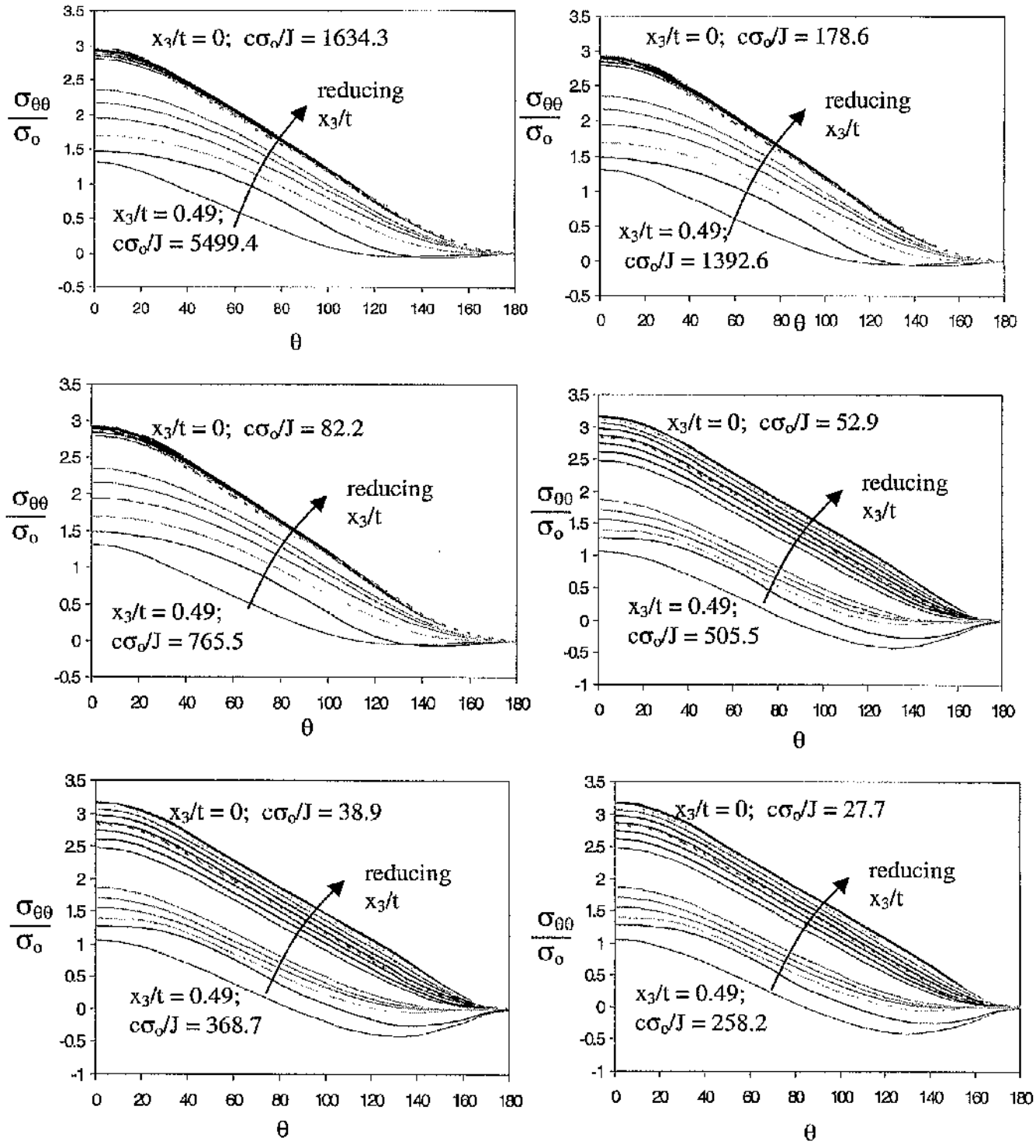


Figure 5.75: The hoop stress $\sigma_{\theta\theta}$ for SENB B/(W-a) = 0.5 through the thickness. The broken line determined in a boundary layer formulation indicates the two-dimensional plane strain field for $\sigma_{\theta\theta}$.

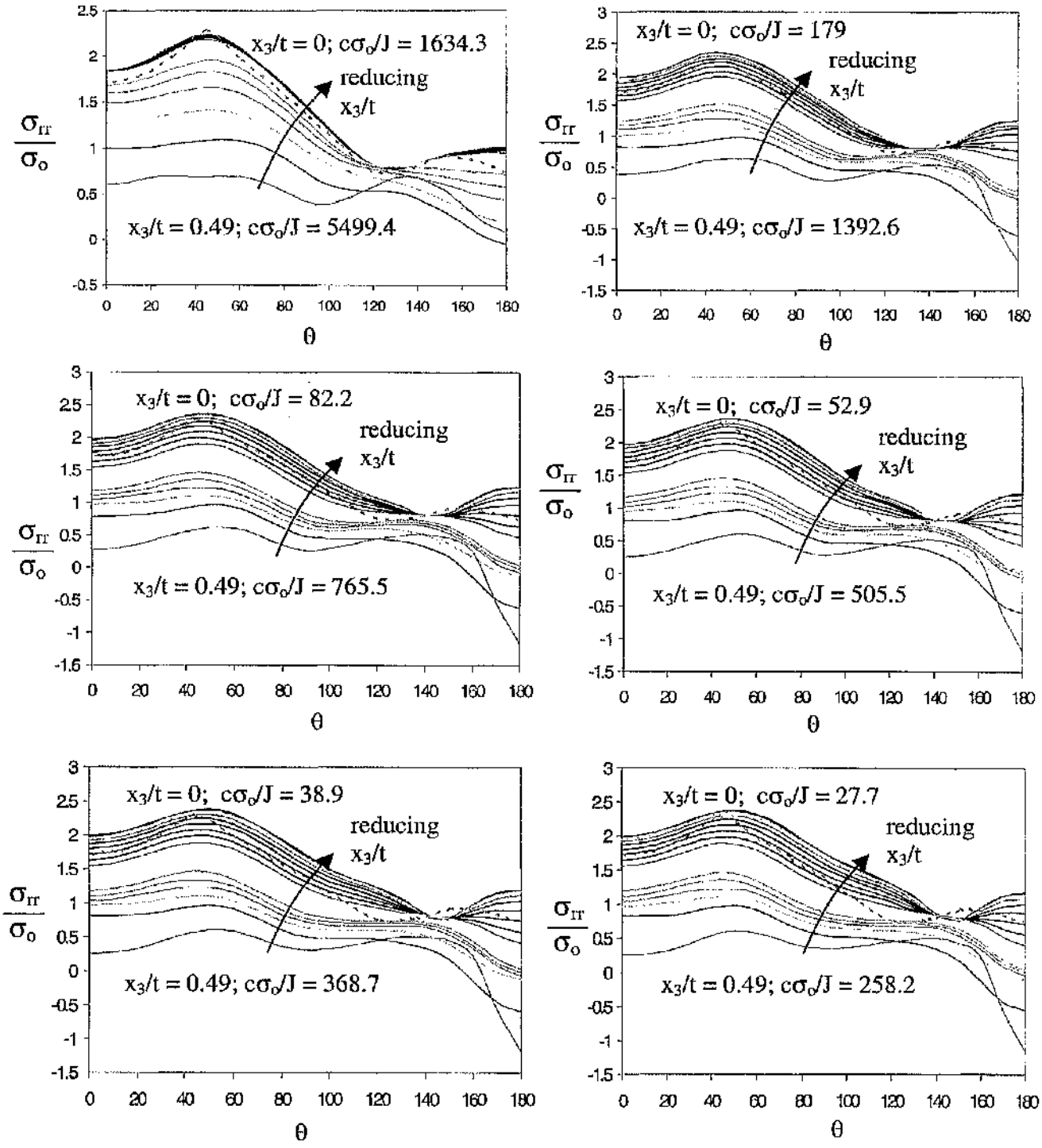


Figure 5.76: The radial stress $\sigma_{rr}$ for SENB B/(W-a) = 0.5 through the thickness. The broken line determined in a boundary layer formulation indicates a two-dimensional plane strain field for $\sigma_{rr}$.

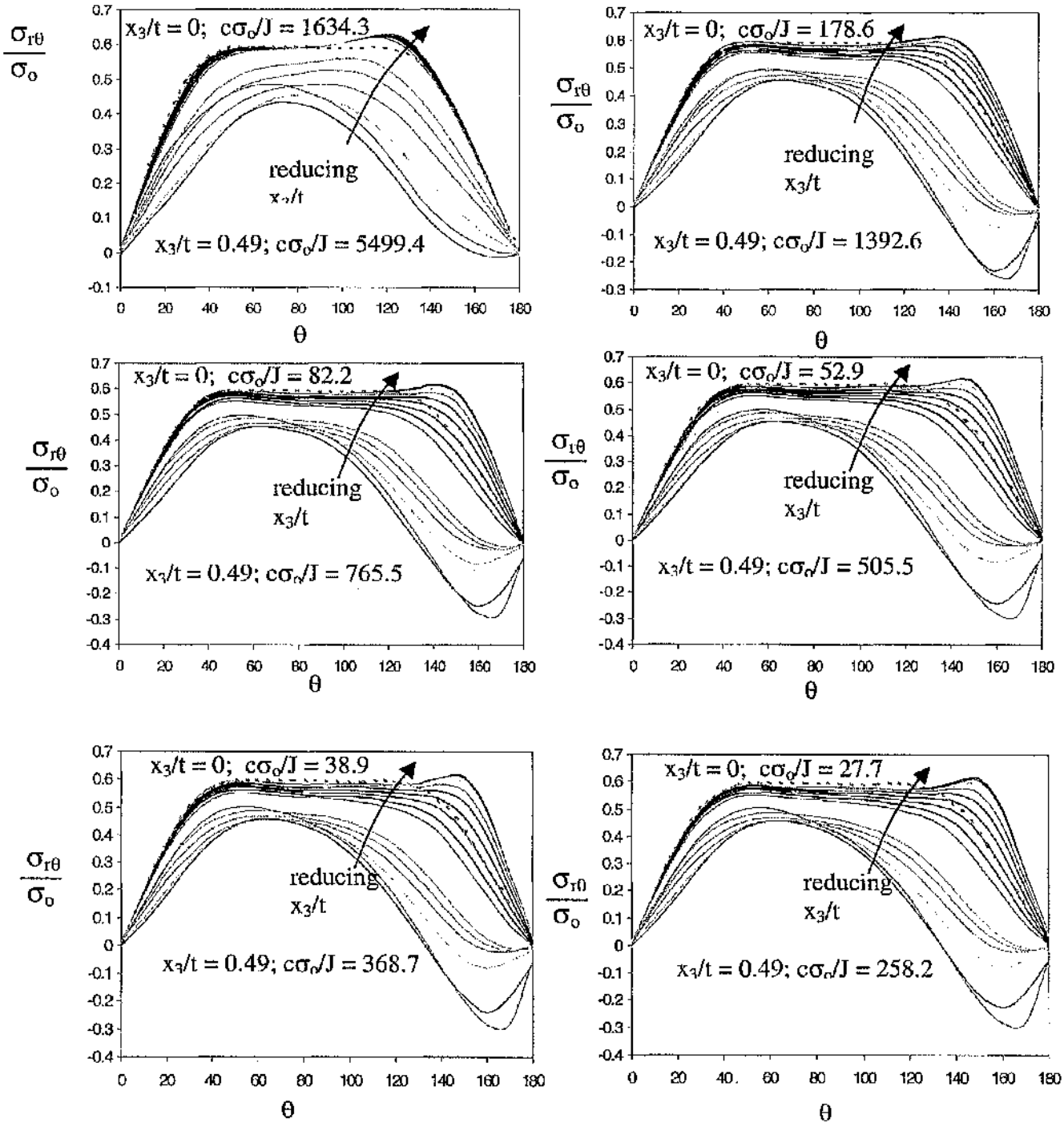


Figure 5.77: The shear stress $\sigma_{r\theta}$ for SENB B/(W-a) = 0.5 through the thickness. The broken line determined in a boundary layer formulation indicates a two-dimensional plane strain field for $\sigma_{r\theta}$.

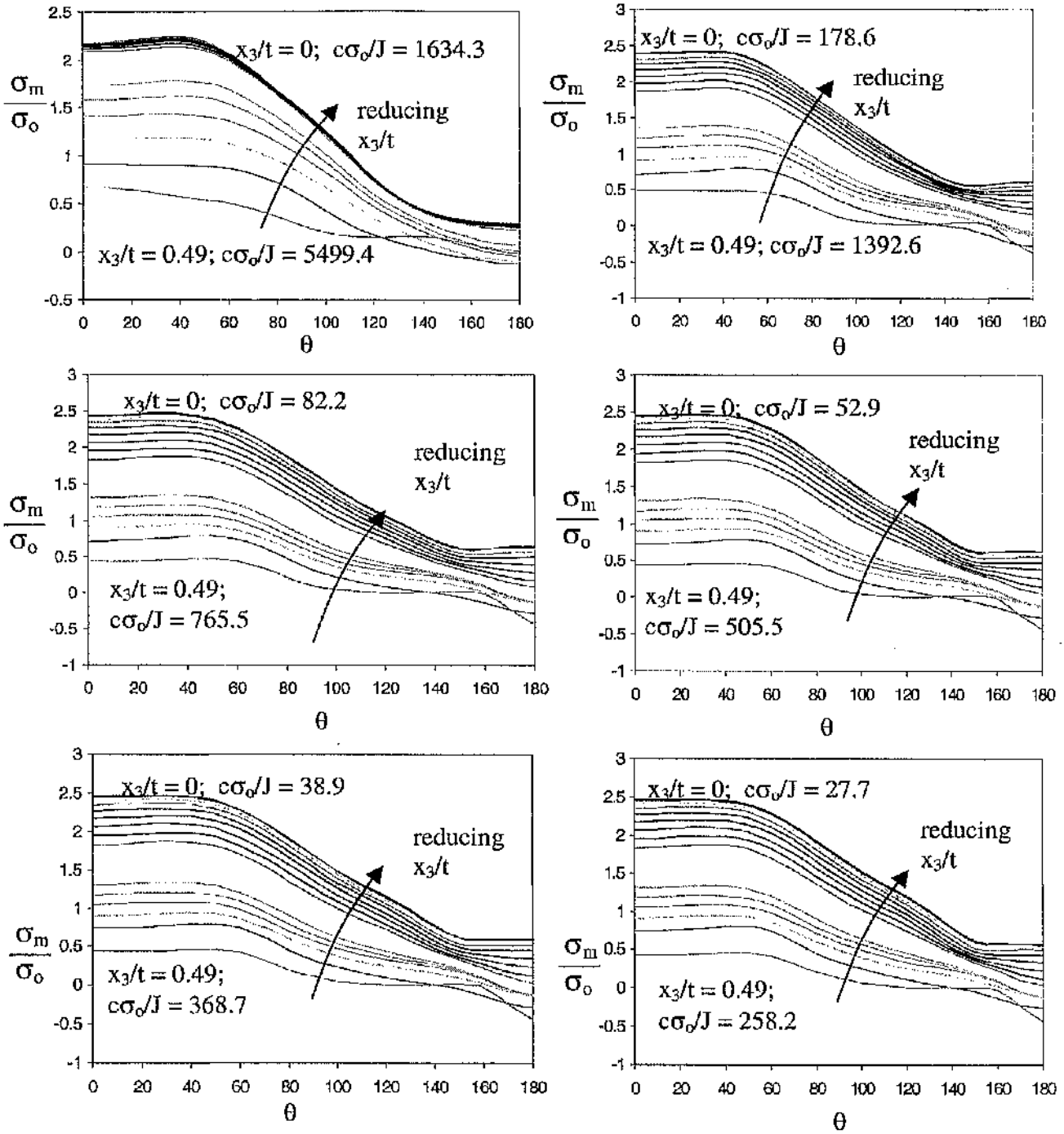


Figure 5.78: The mean stress $\sigma_m$ for SENB B/(W-a) = 0.5 through the thickness. The broken line determined in a boundary layer formulation indicates a two-dimensional plane strain field for $\sigma_m$.

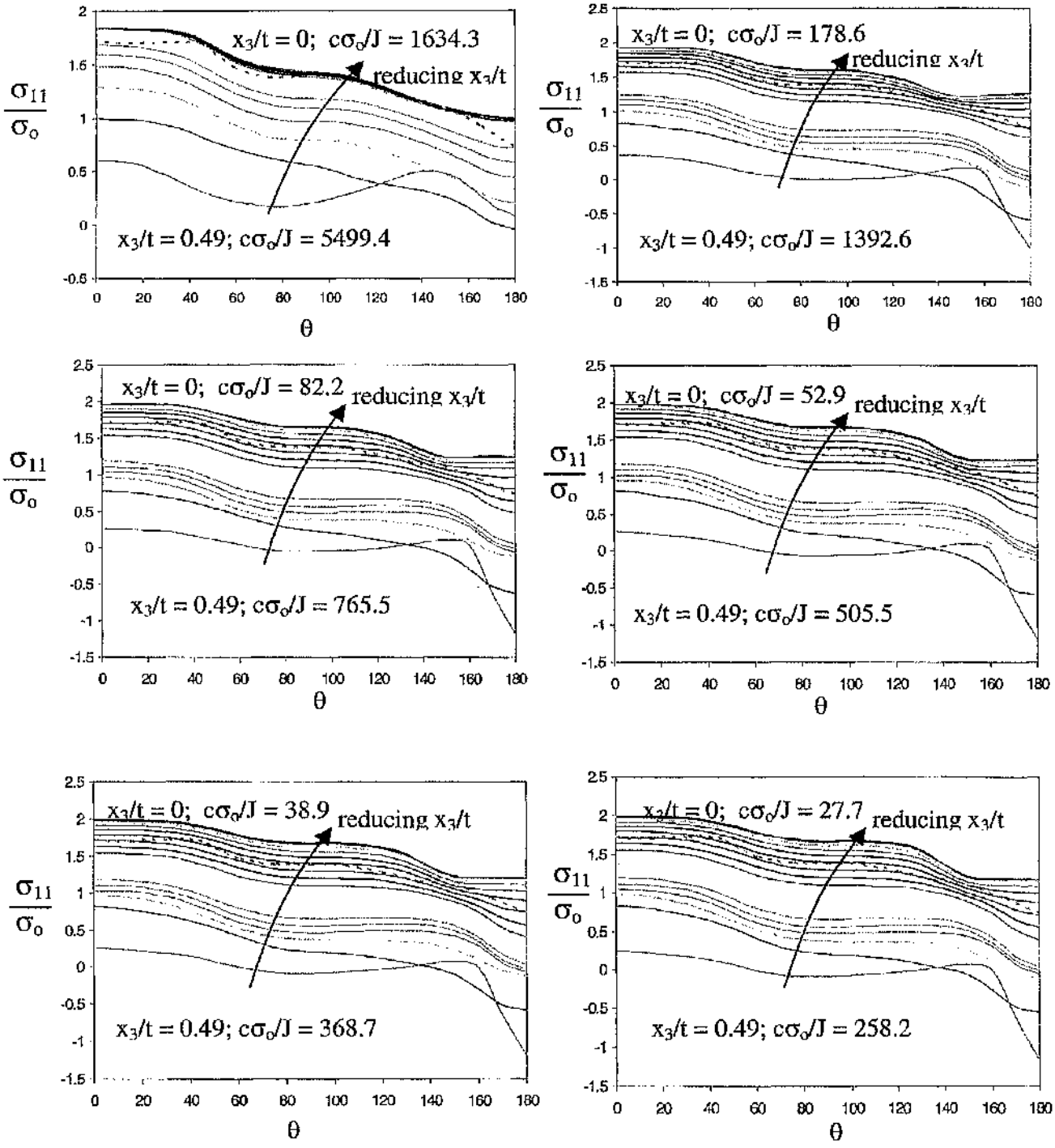


Figure 5.79: The direct stress $\sigma_{11}$ for SENB B/(W-a) = 0.5 through the thickness. The broken line determined in a boundary layer formulation indicates a two-dimensional plane strain field for $\sigma_{11}$.

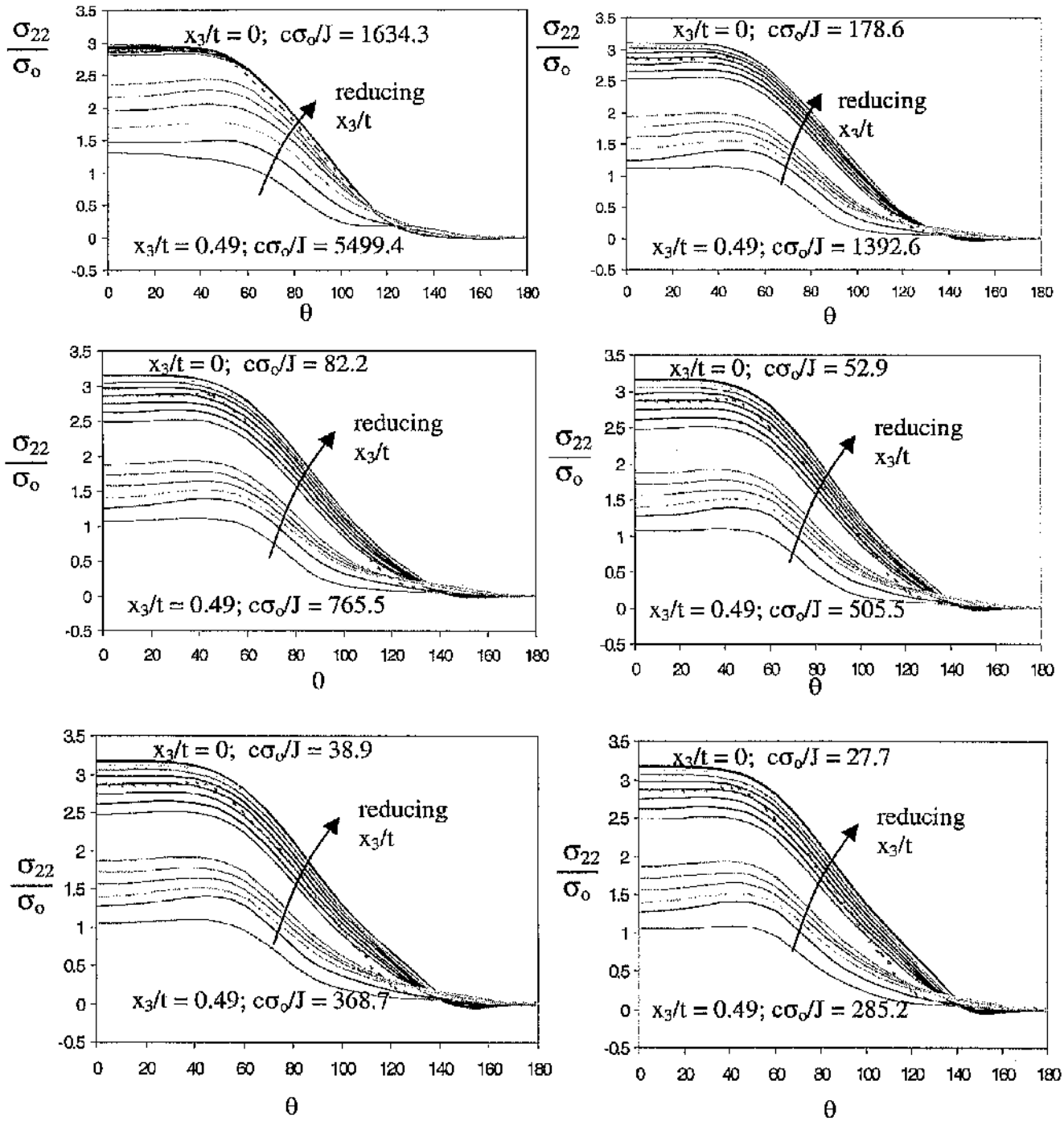


Figure 5.80: The direct stress $\sigma_{22}$ for SENB B/(W-a) = 0.5 through the thickness. The broken line determined in a boundary layer formulation indicates a two-dimensional plane strain field for $\sigma_{22}$.

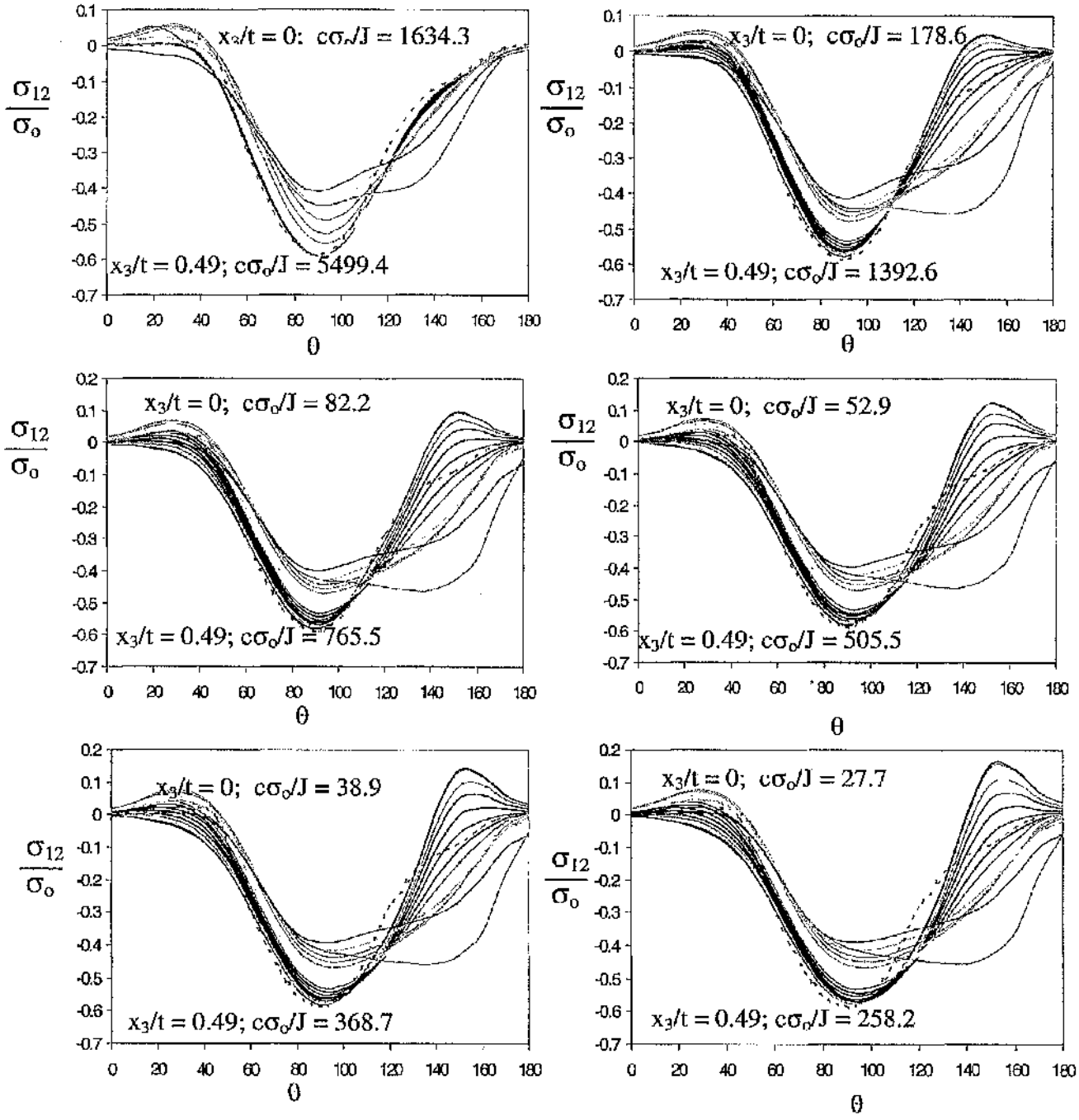


Figure 5.81: The shear stress $\sigma_{12}$ for SENB B/(W-a) = 0.5 through the thickness. The broken line determined in a boundary layer formulation indicates a two-dimensional plane strain for $\sigma_{12}$.

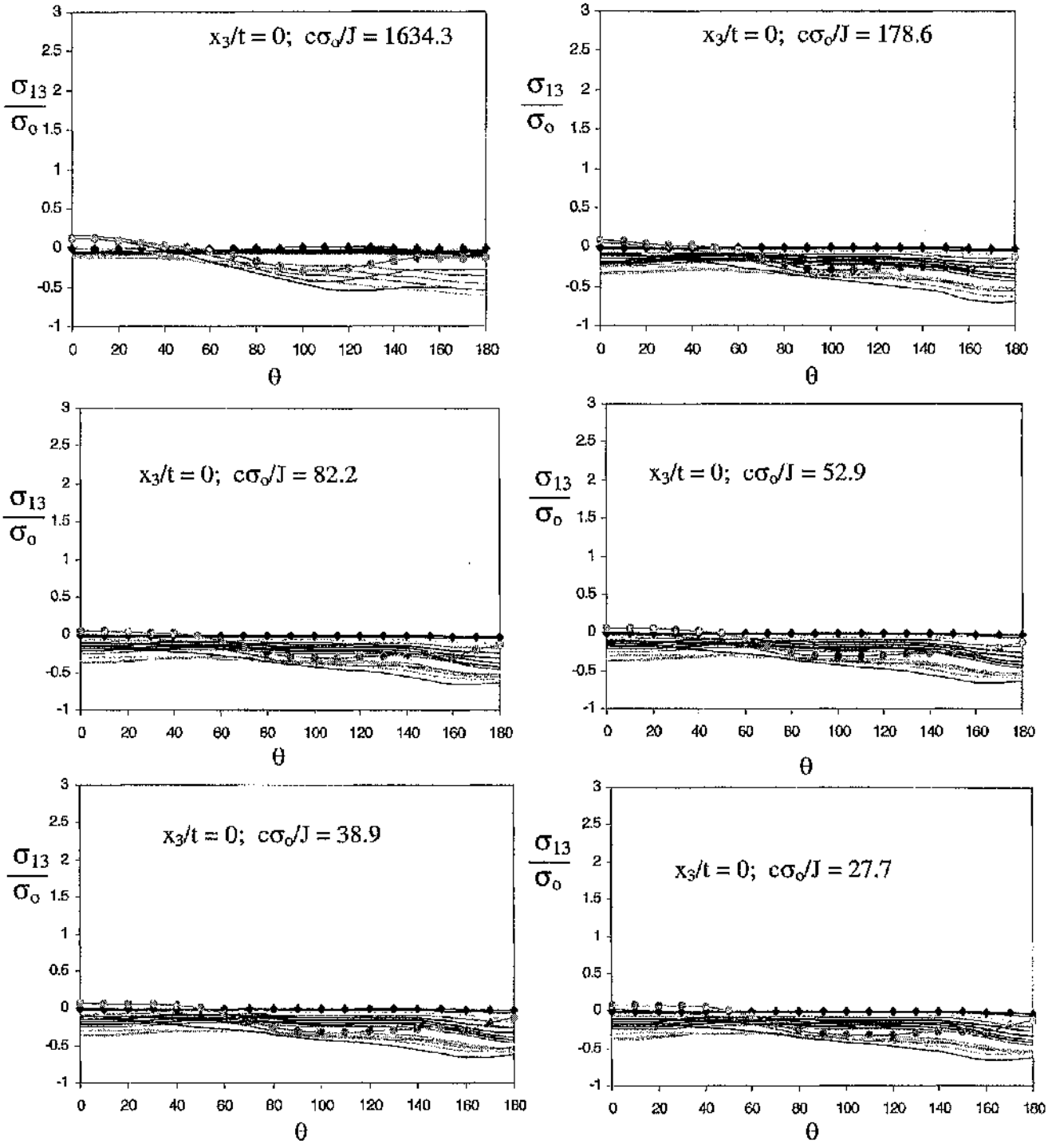


Figure 5.82: The shear stress $\sigma_{13}$ for SENB B/(W-a) = 0.5 through the thickness. The diamond and circular markers indicate the midplane and the free surface.

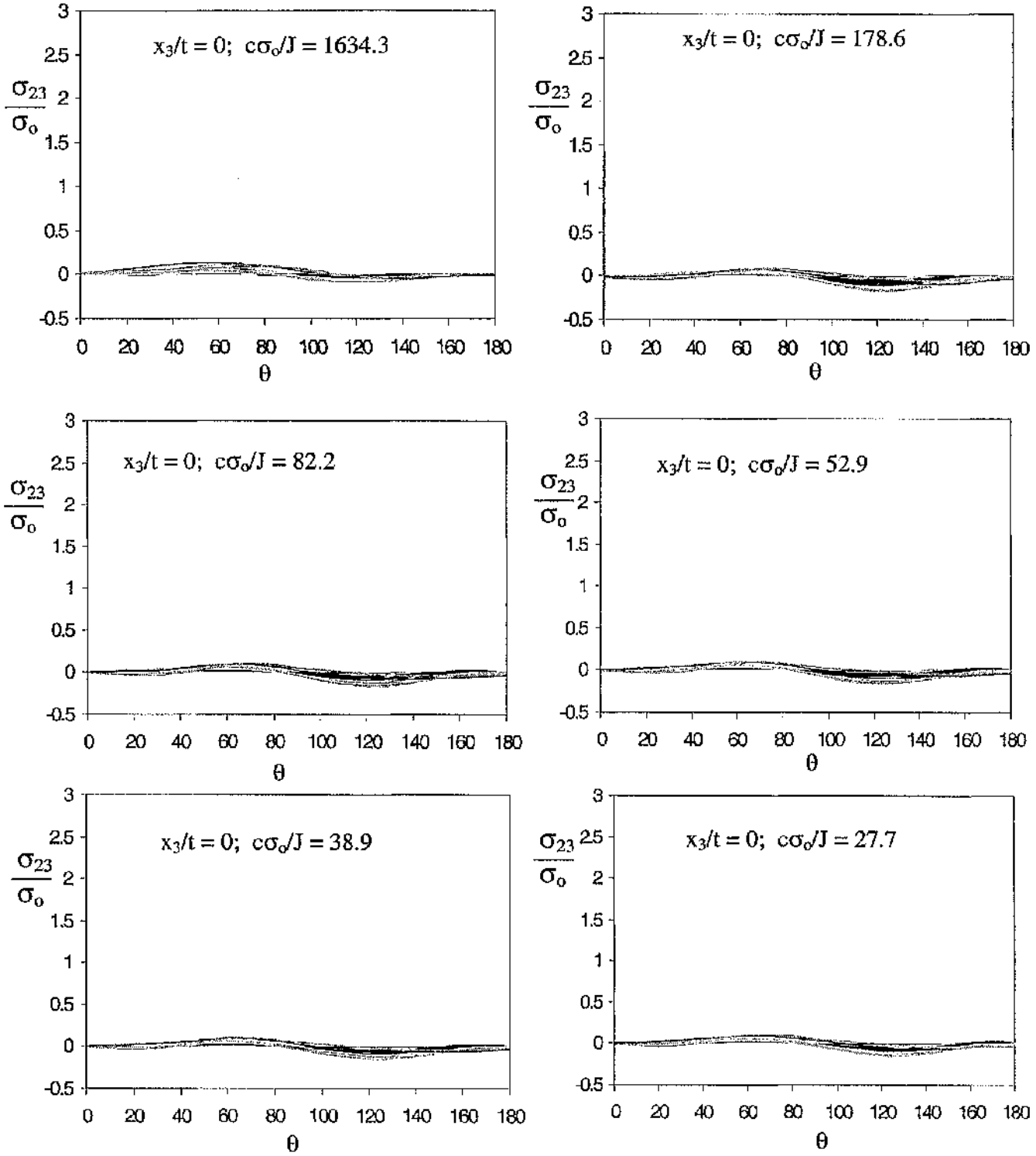


Figure 5.83: The shear stress $\sigma_{23}$ for SENB B/(W-a) = 0.5 through the thickness.

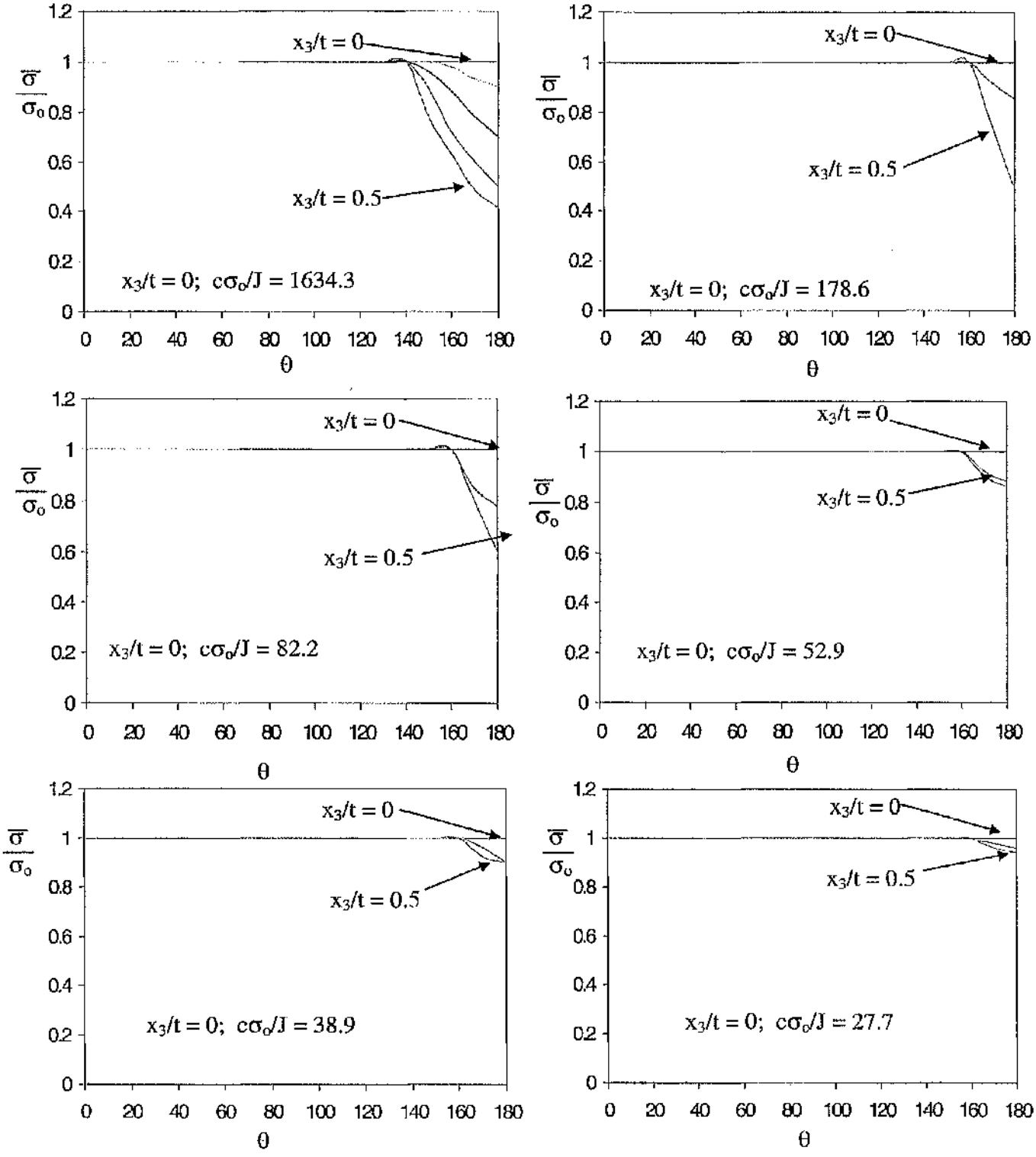


Figure 5.84: The Mises stress $\bar{\sigma}/\sigma_o$ for SENB B/(W-a) = 0.5 through the thickness.

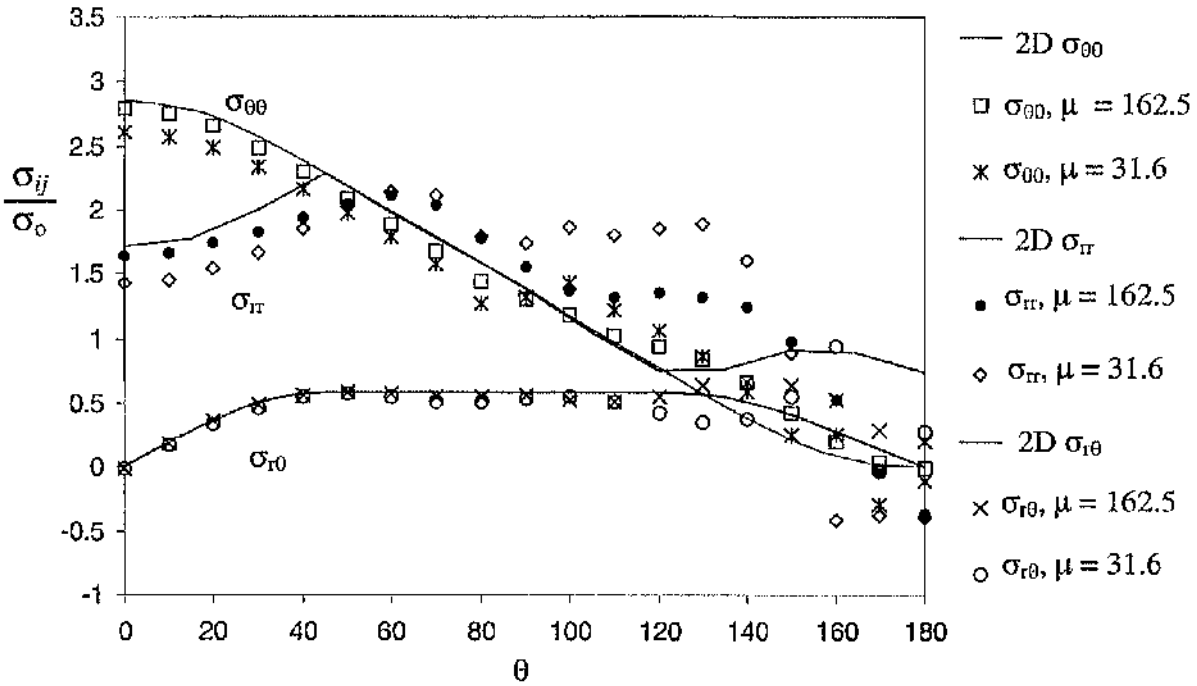


Figure 5.85: The asymptotic cylindrical stresses at the midplane for a SENB specimen B/(W-a) = 0.1 compared with the two-dimensional plane strain field.

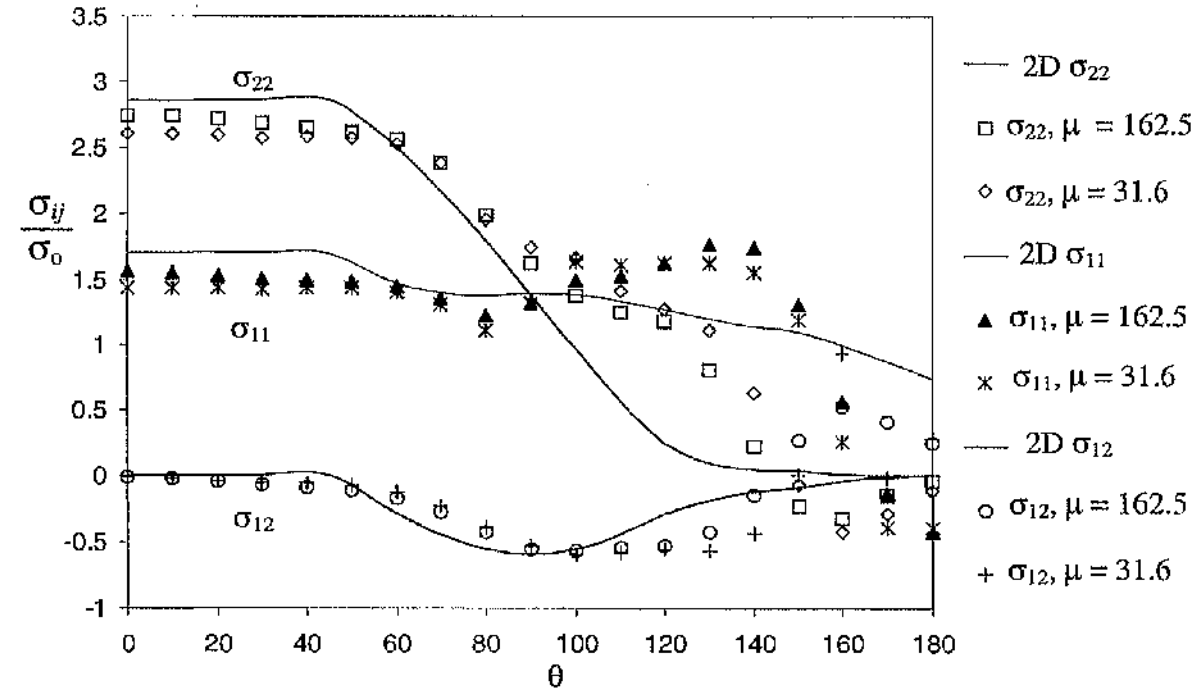


Figure 5.86: The asymptotic Cartesian stresses at the midplane for a SENB specimen B/(W-a) = 0.1 compared with the two-dimensional plane strain field.

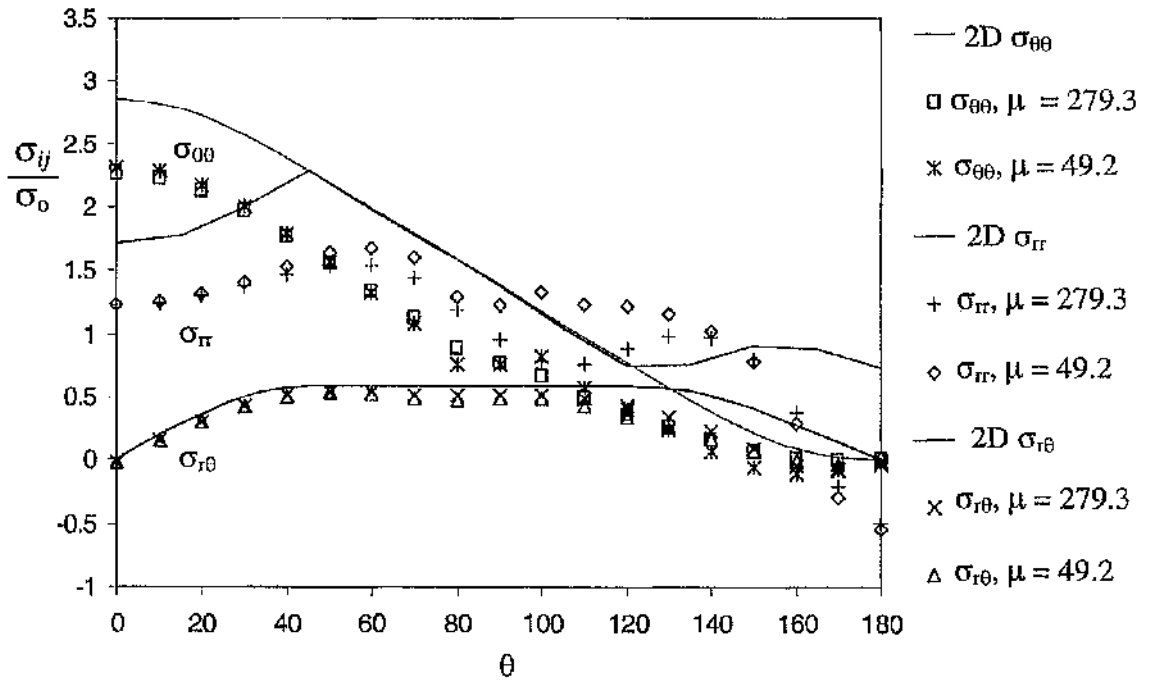


Figure 5.87: The asymptotic cylindrical stresses at the quarterplane for a SENB specimen B/(W-a) = 0.1 compared with the two-dimensional plane strain field.

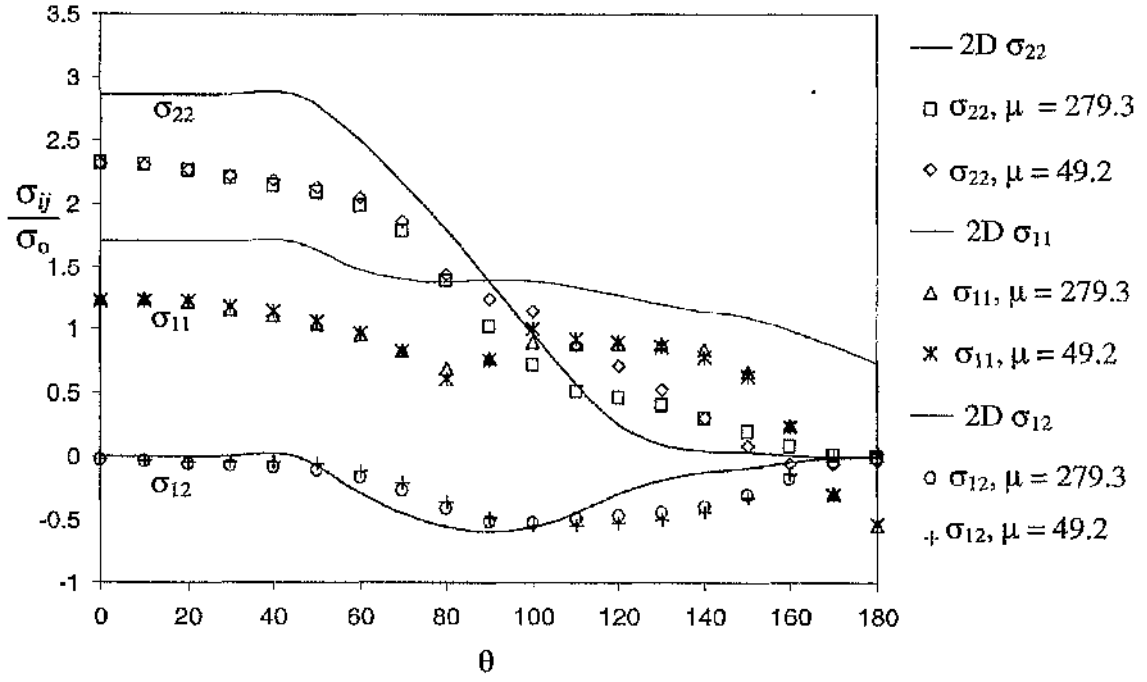


Figure 5.88: The asymptotic Cartesian stresses at the quarterplane for a SENB specimen B/(W-a) = 0.1 compared with the two-dimensional plane strain field.

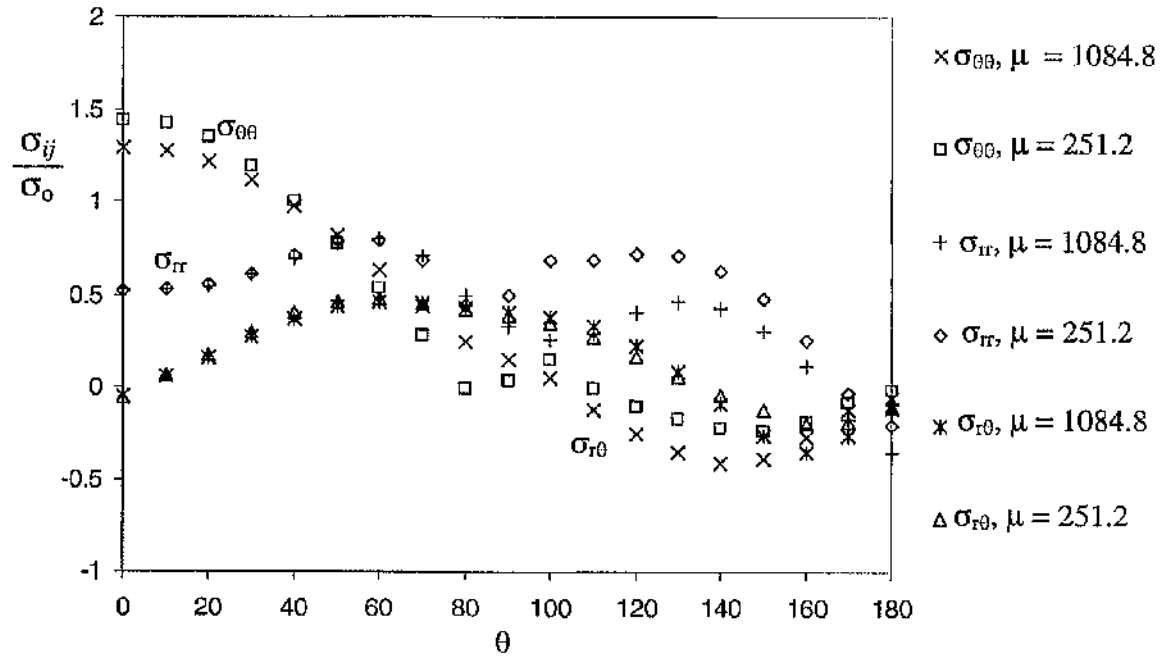


Figure 5.89: The asymptotic cylindrical stresses at the free surface for SENB B/(W-a) = 0.1.

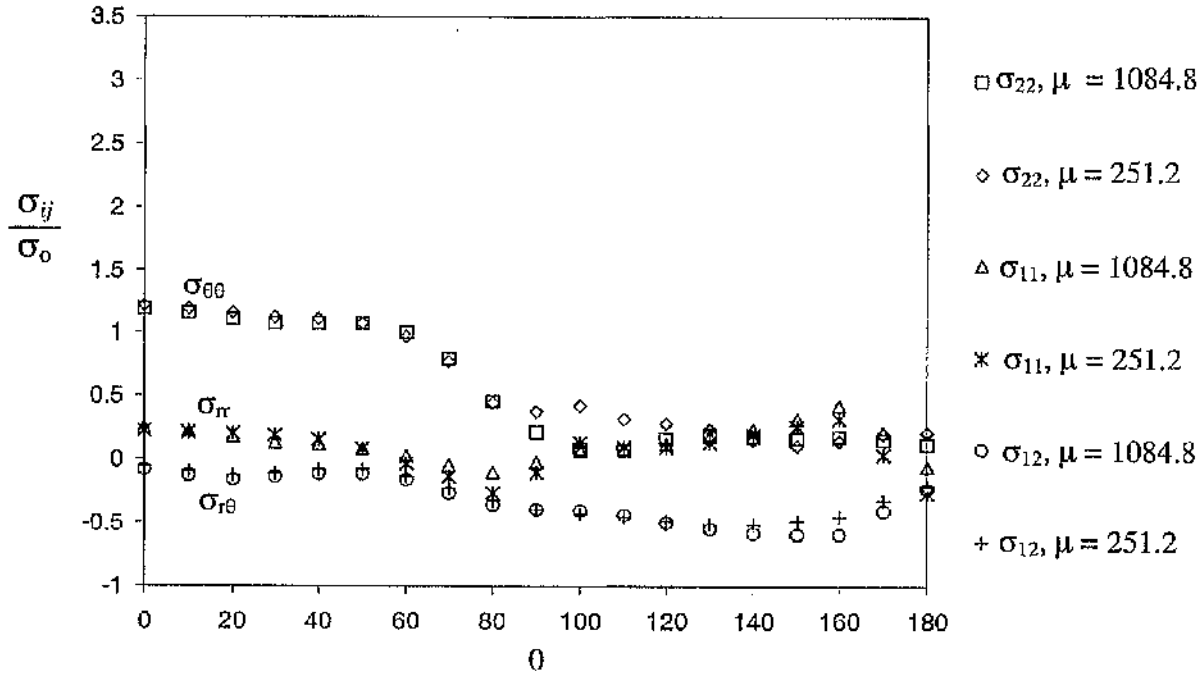


Figure 5.90: The asymptotic Cartesian stresses at the free surface for SENB B/(W-a) = 0.1.

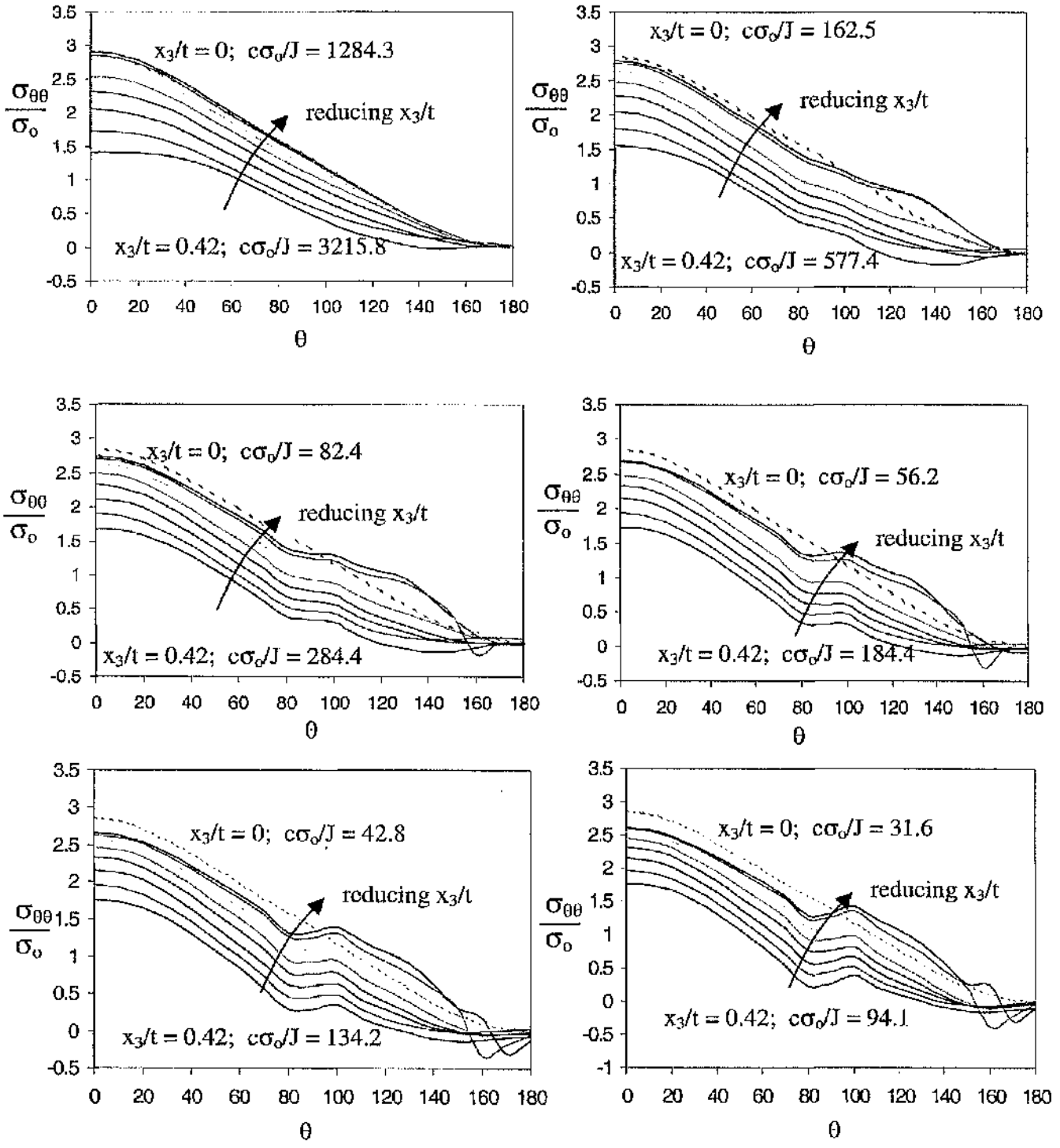


Figure 5.91: The hoop stress $\sigma_{\theta\theta}$ for SENB B/(W-a) = 0.1 through the thickness. The broken line determined in a boundary layer formulation indicates the two-dimensional plane strain field for $\sigma_{\theta\theta}$.

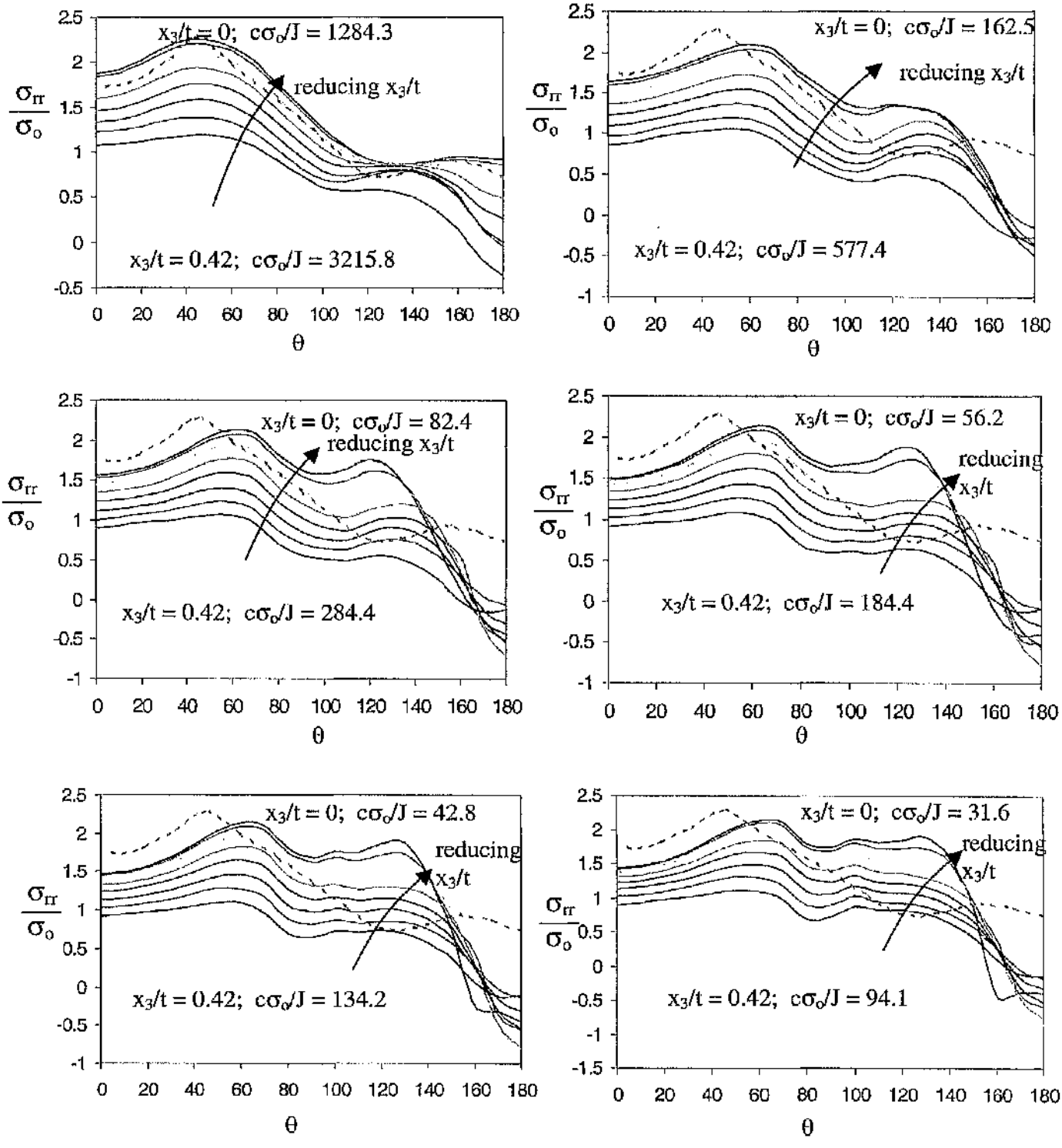


Figure 5.92: The radial stress $\sigma_{rr}$ for SENB B/(W-a) = 0.1 through the thickness. The broken line determined in a boundary layer formulation indicates the two-dimensional plane strain field for $\sigma_{rr}$.

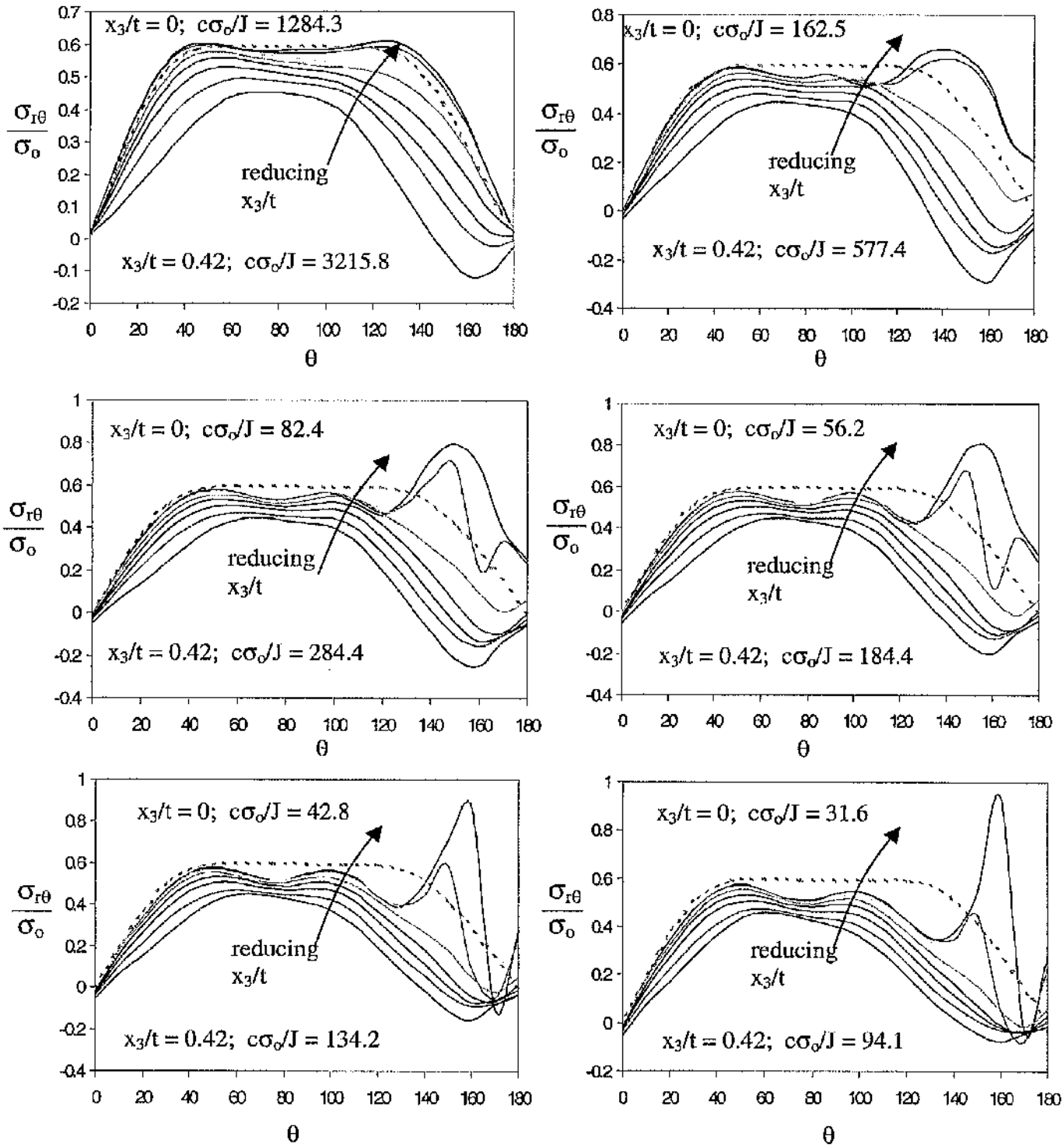


Figure 5.93: The shear stress $\sigma_{r\theta}$ for SENB B/(W-a) = 0.1 through the thickness. The broken line determined in a boundary layer formulation indicates the two-dimensional plane strain field for $\sigma_{r\theta}$.

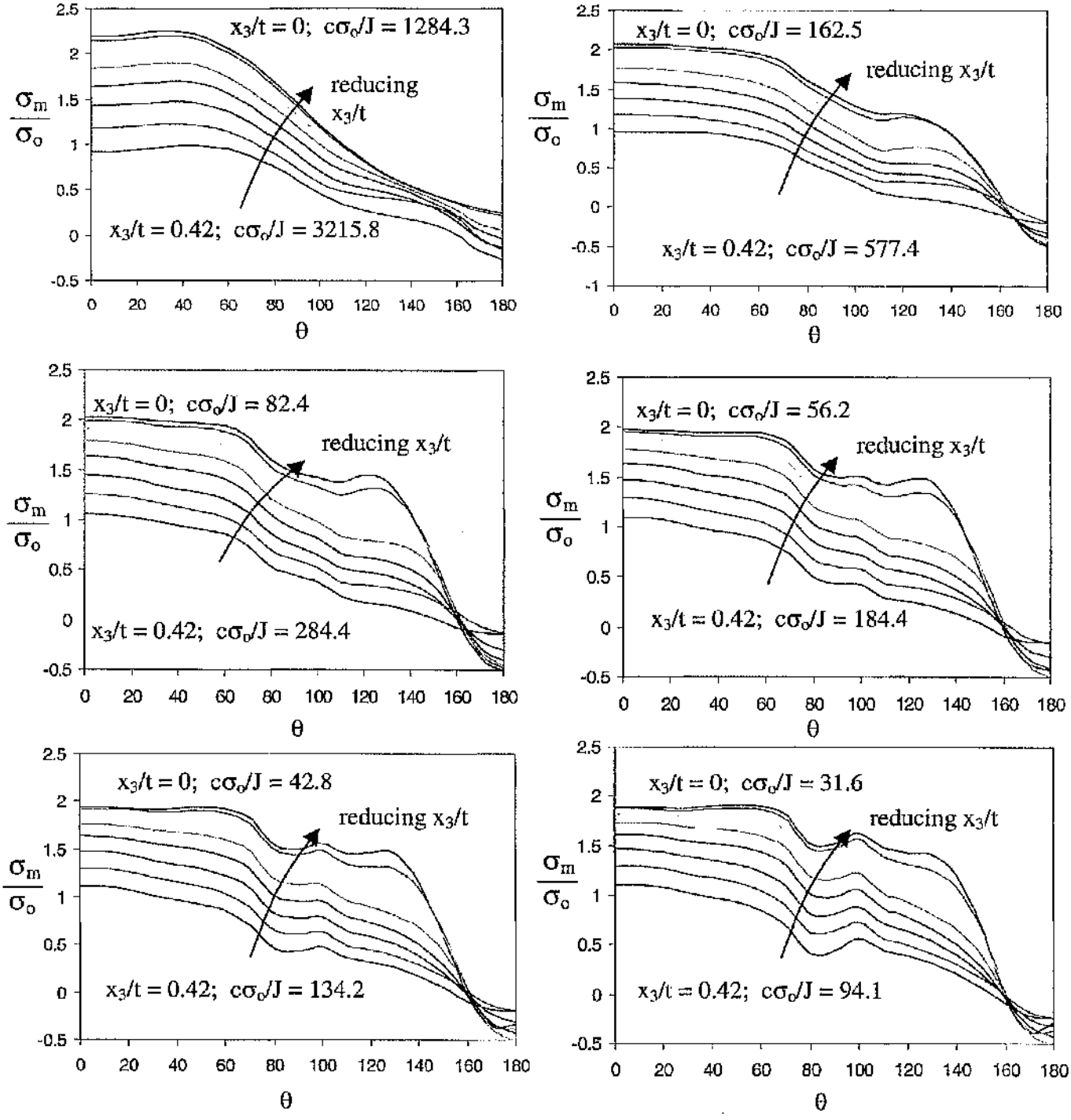


Figure 5.94: The mean stress $\sigma_m$ for SENB B/(W-a) = 0.1 through the thickness. The broken line determined in a boundary layer formulation indicates the two-dimensional plane strain field for $\sigma_m$.

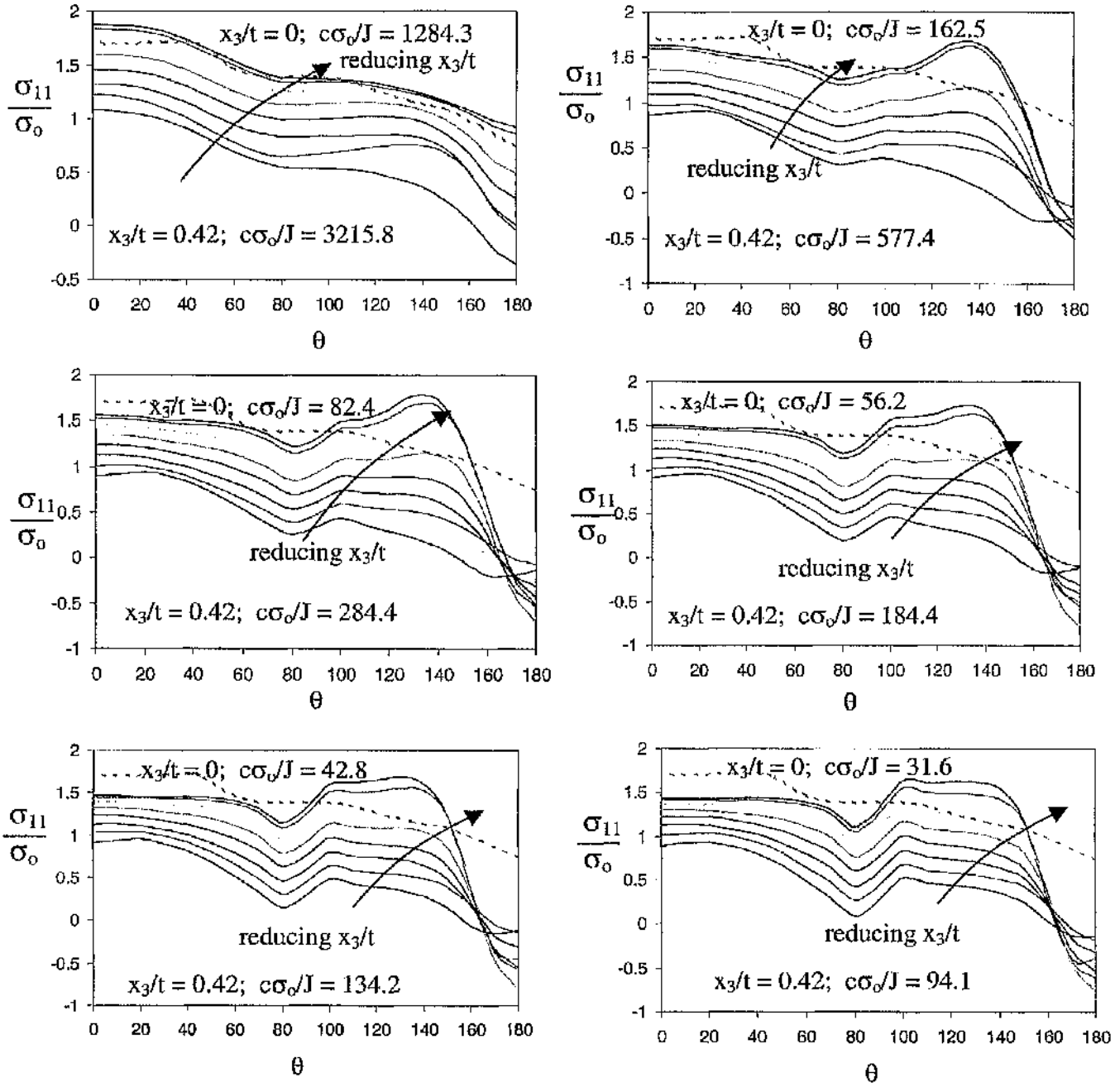


Figure 5.95: The direct stress $\sigma_{11}$ for SENB B/(W-a) = 0.1 through the thickness. The broken line determined in a boundary layer formulation indicates the two-dimensional plane strain field for $\sigma_{11}$.

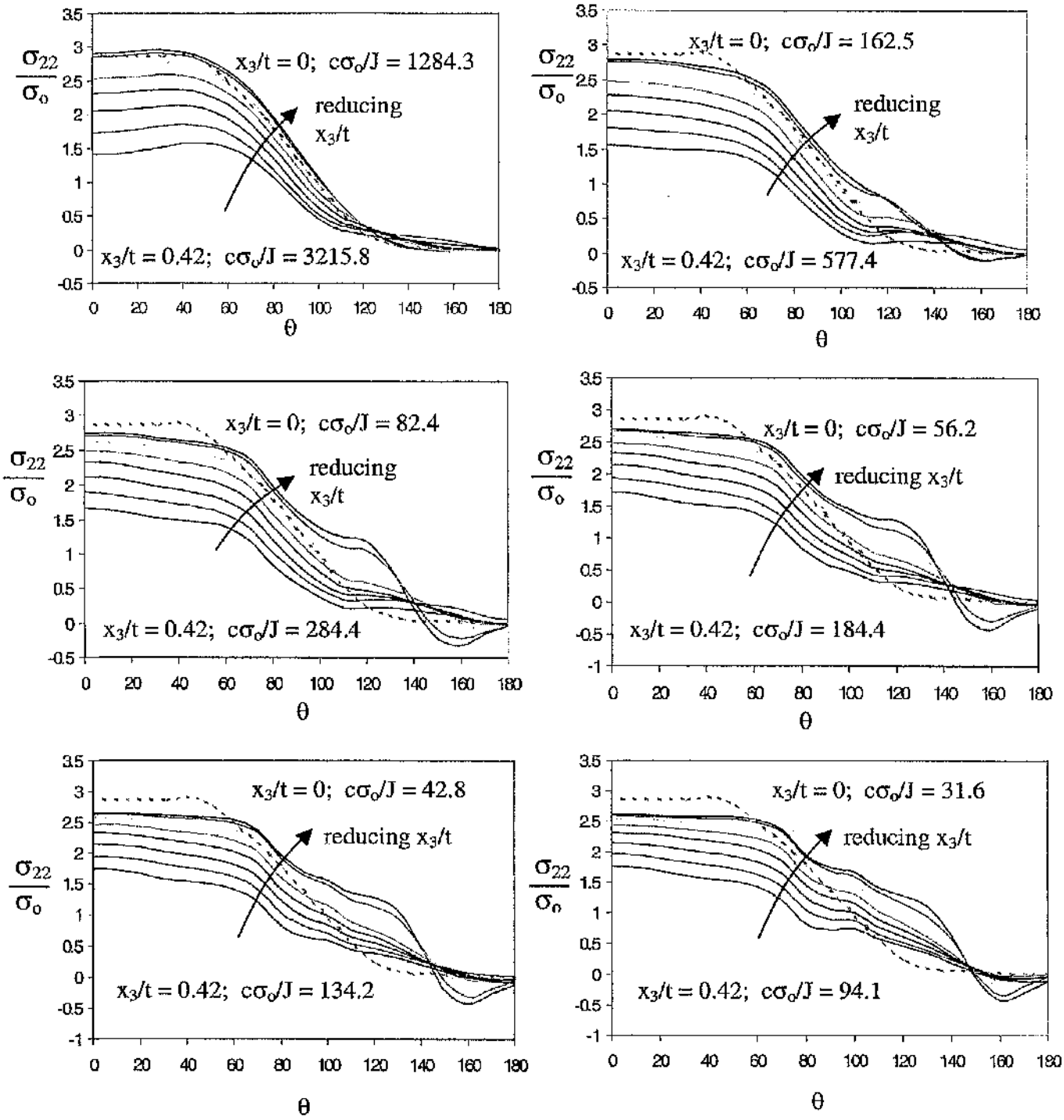


Figure 5.96: The direct stress $\sigma_{22}$ for SENB B/(W-a) = 0.1 through the thickness. The broken line determined in a boundary layer formulation indicates the two-dimensional plane strain field for $\sigma_{22}$.

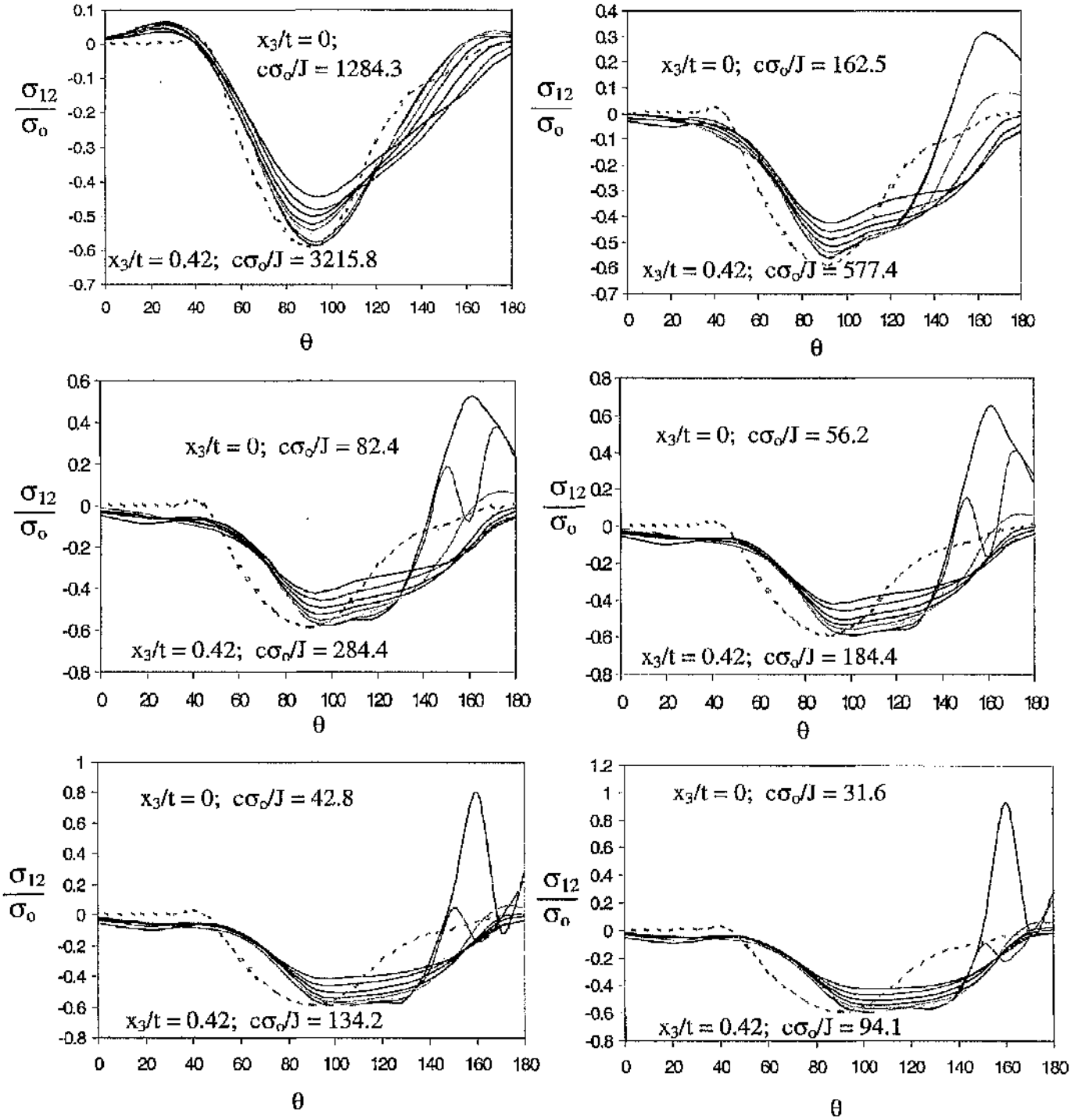


Figure 5.97: The shear stress $\sigma_{12}$ for SENB B/(W-a) = 0.1 through the thickness. The broken line determined in a boundary layer formulation indicates the two-dimensional plane strain field for $\sigma_{12}$.

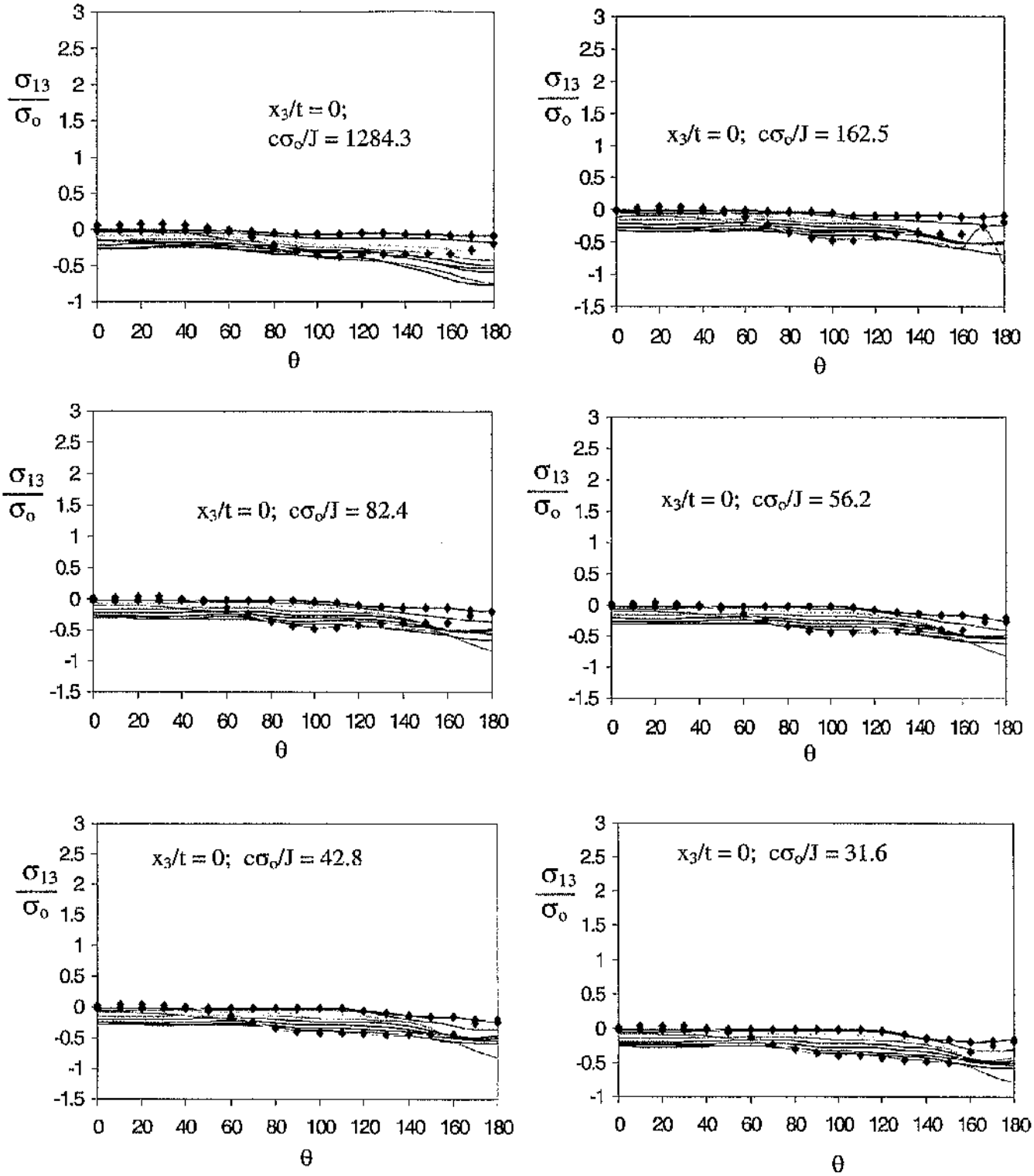


Figure 5.98: The shear stress $\sigma_{13}$ for SENB B/(W-a) = 0.1 through the thickness. The diamond and circular markers indicate the midplane and the free surface field.

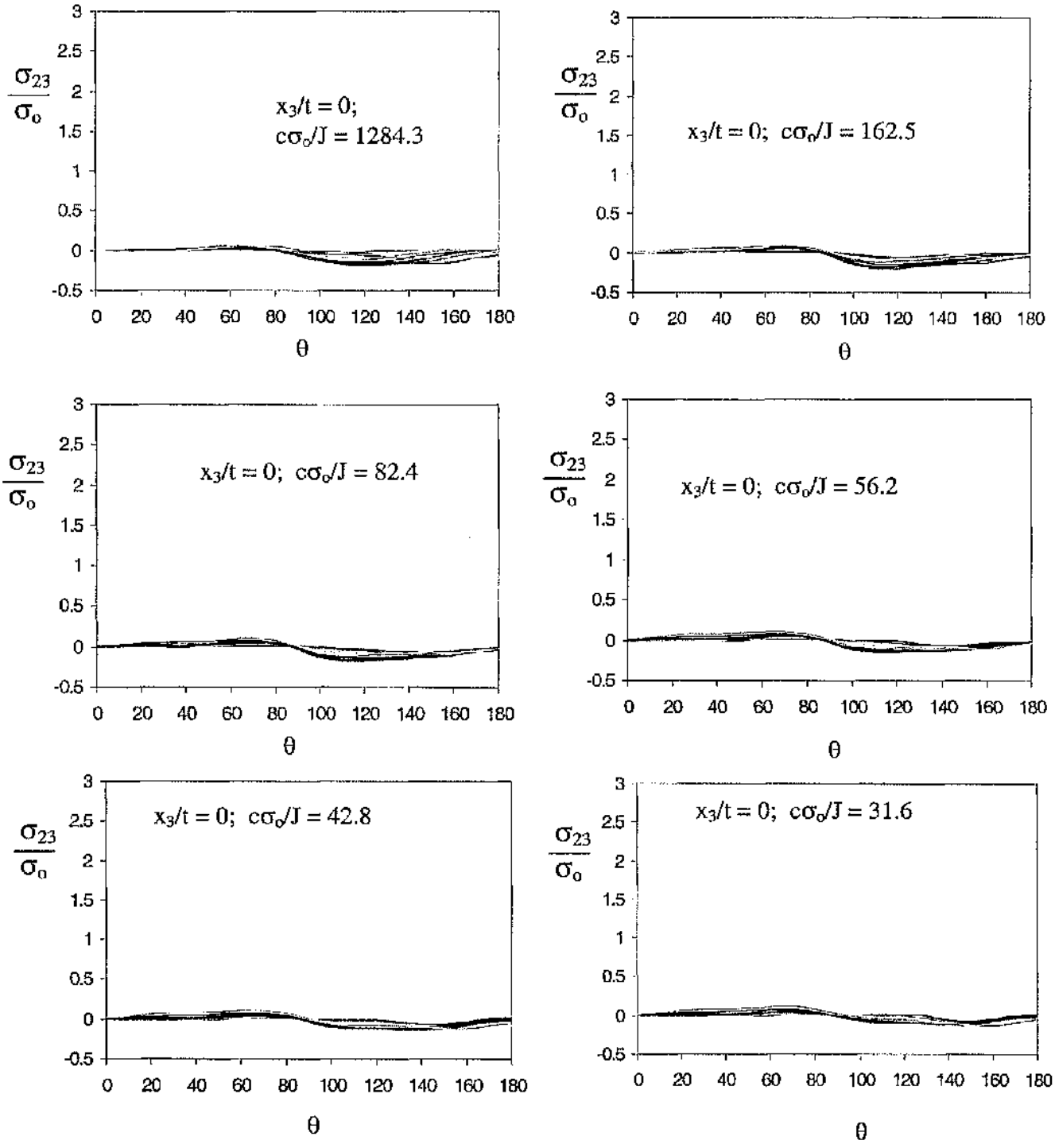


Figure 5.99: The shear stress $\sigma_{23}$ for SENB B/(W-a) = 0.1 through the thickness.

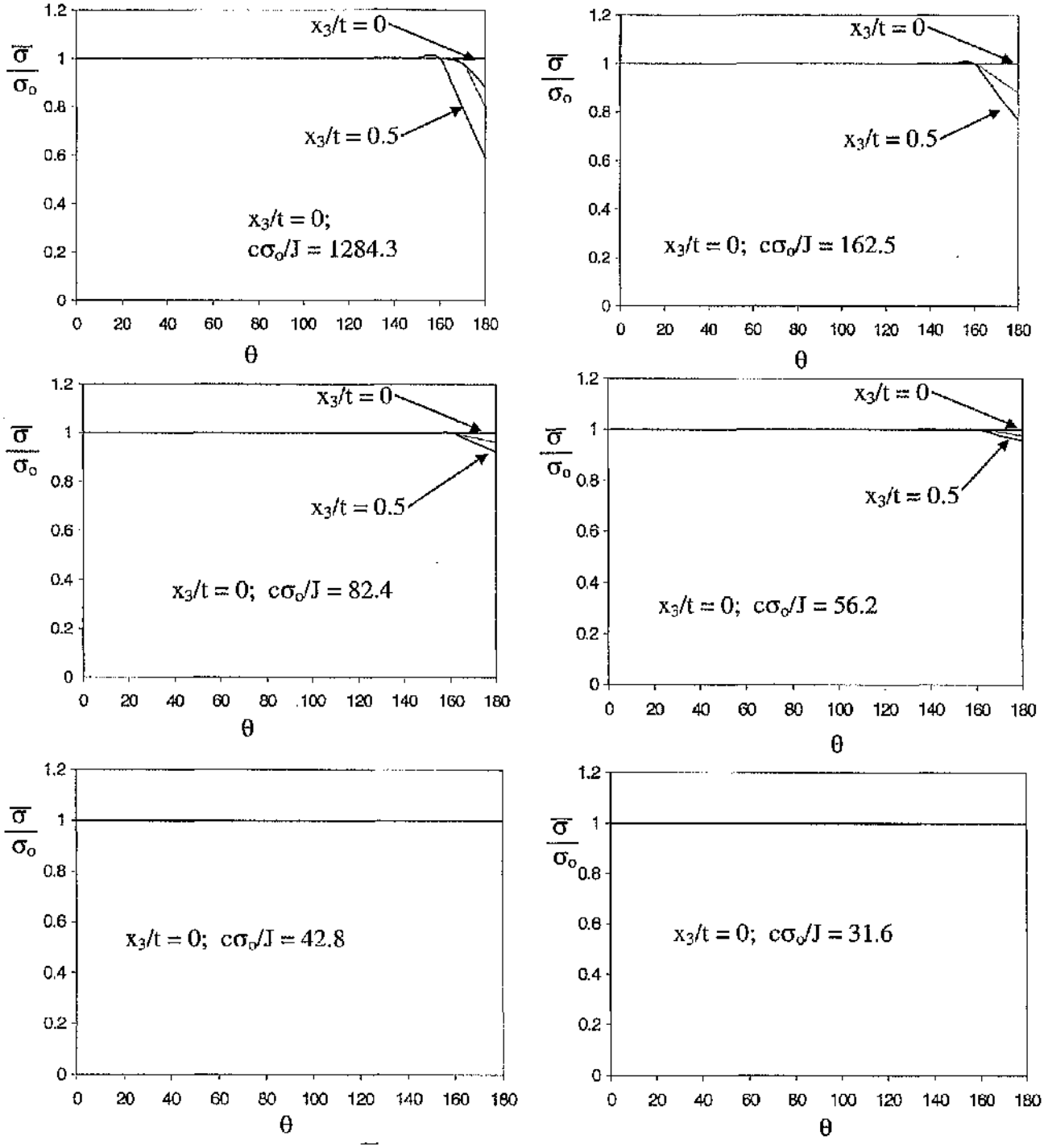


Figure 5.100: The Mises stress $\bar{\sigma}/\sigma_o$ for SENB B/(W-a) = 0.1 through the thickness.

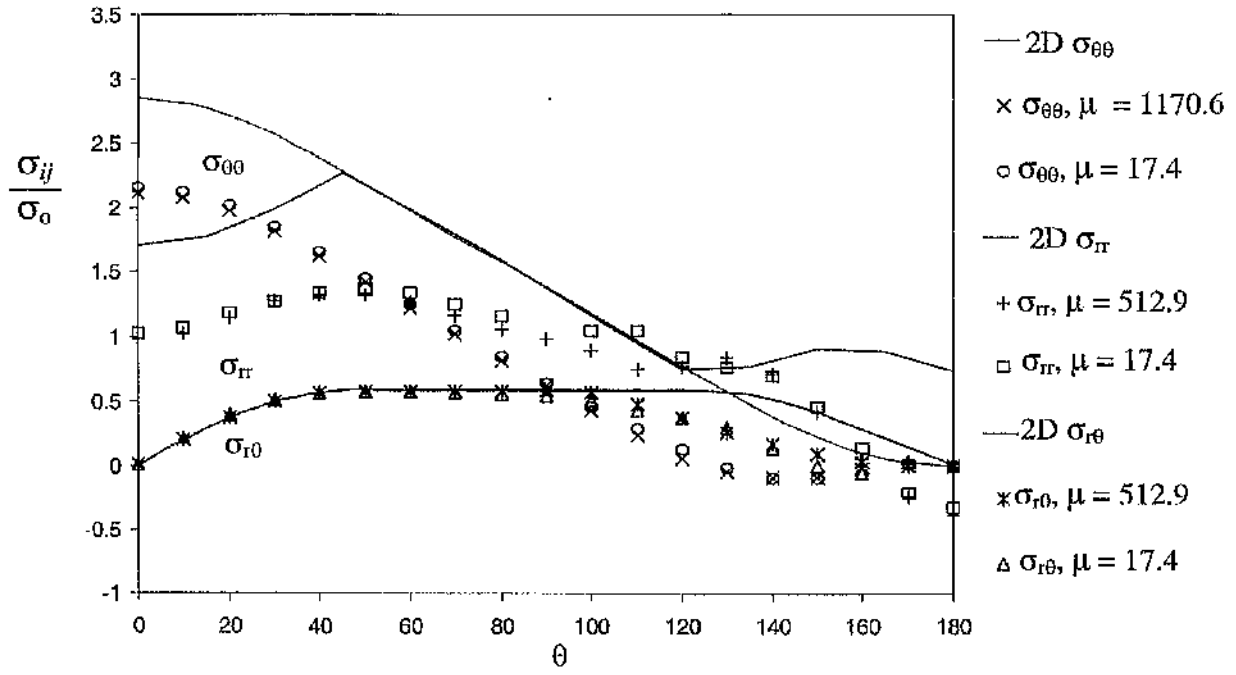


Figure 5.101: The asymptotic cylindrical stresses at the midplane for a CCP specimen B/(W-a) = 1 compared with the two-dimensional plane strain field.

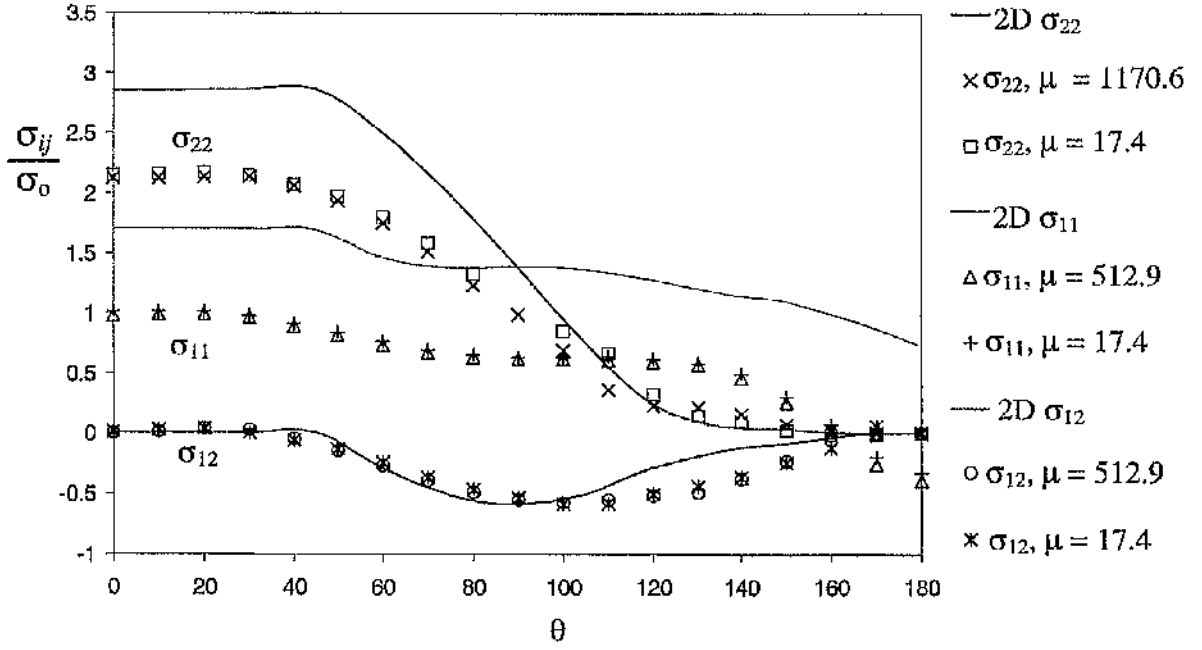


Figure 5.102: The asymptotic Cartesian stresses at the midplane for a CCP specimen B/(W-a) = 1 compared with the two-dimensional plane strain field.

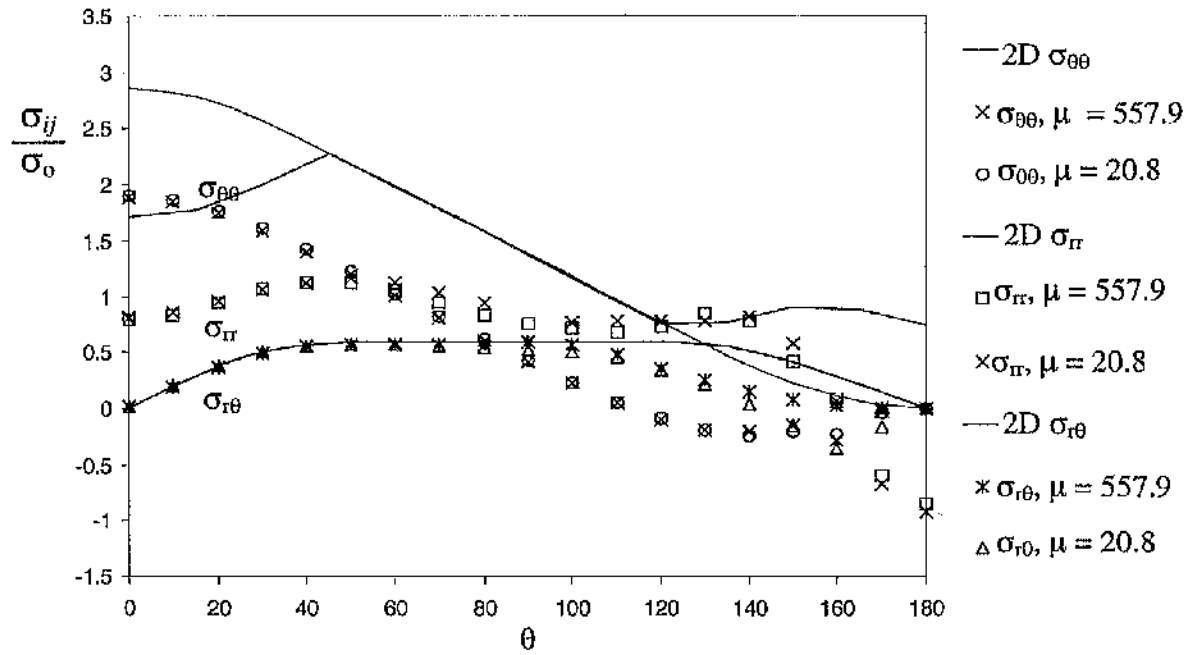


Figure 5.103: The asymptotic cylindrical stresses at the quarterplane for a CCP specimen B/(W-a) = 1 compared with the two-dimensional plane strain field.

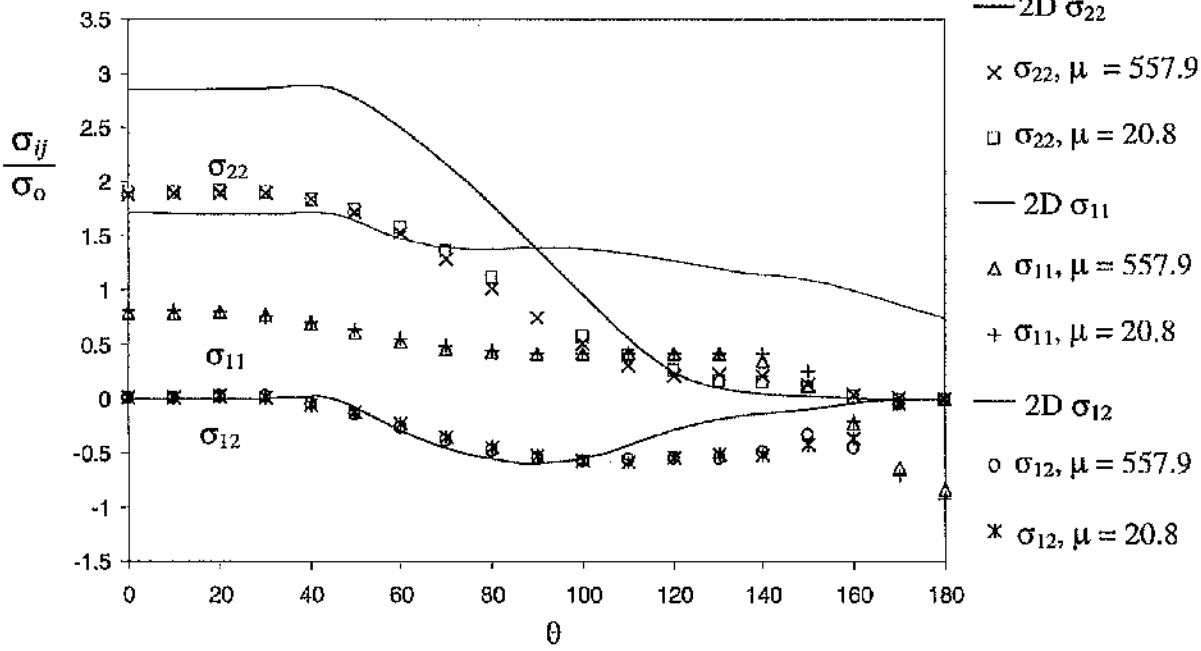


Figure 5.104: The asymptotic Cartesian stresses at the quarterplane for a CCP specimen B/(W-a) = 1 compared with the two-dimensional plane strain field.

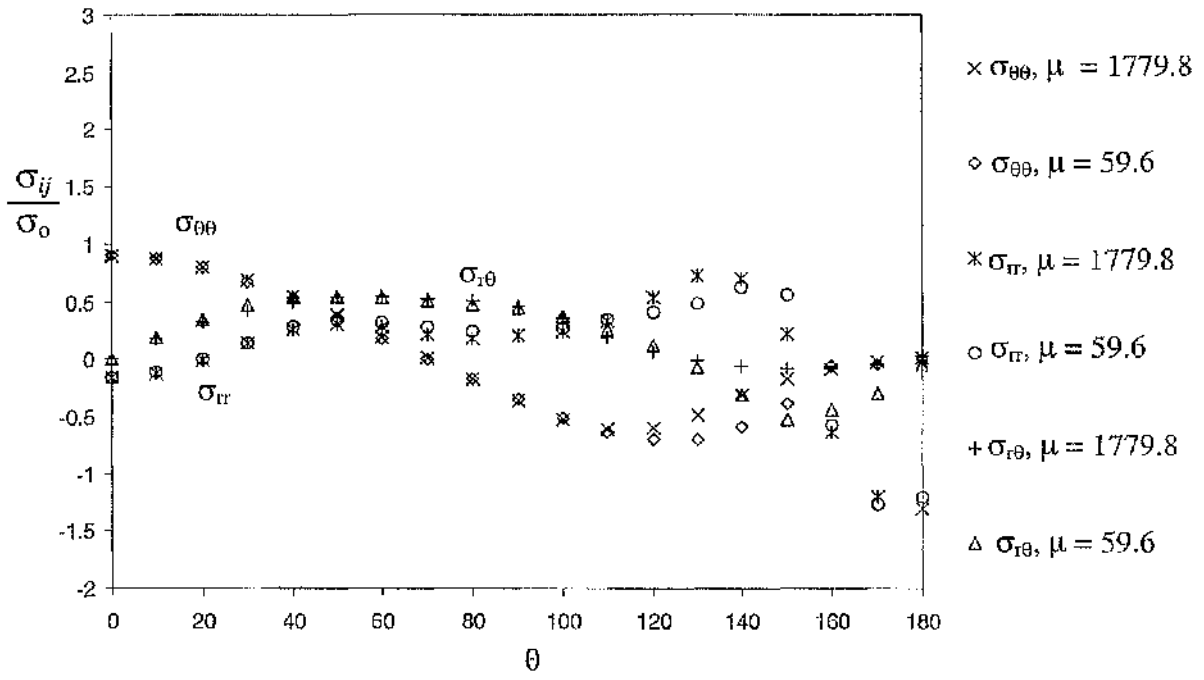


Figure 5.105: The asymptotic cylindrical stresses at the free surface for a CCP specimen B/(W-a) = 1.

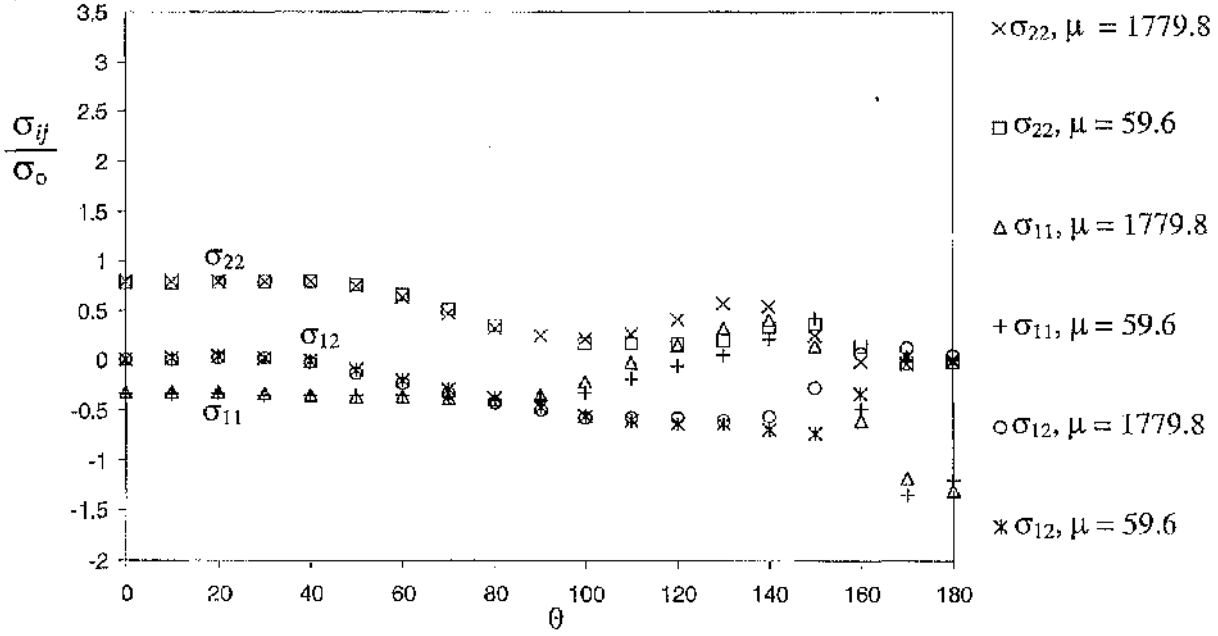


Figure 5.106: The asymptotic Cartesian stresses at the free surface for a CCP specimen B/(W-a) = 1.

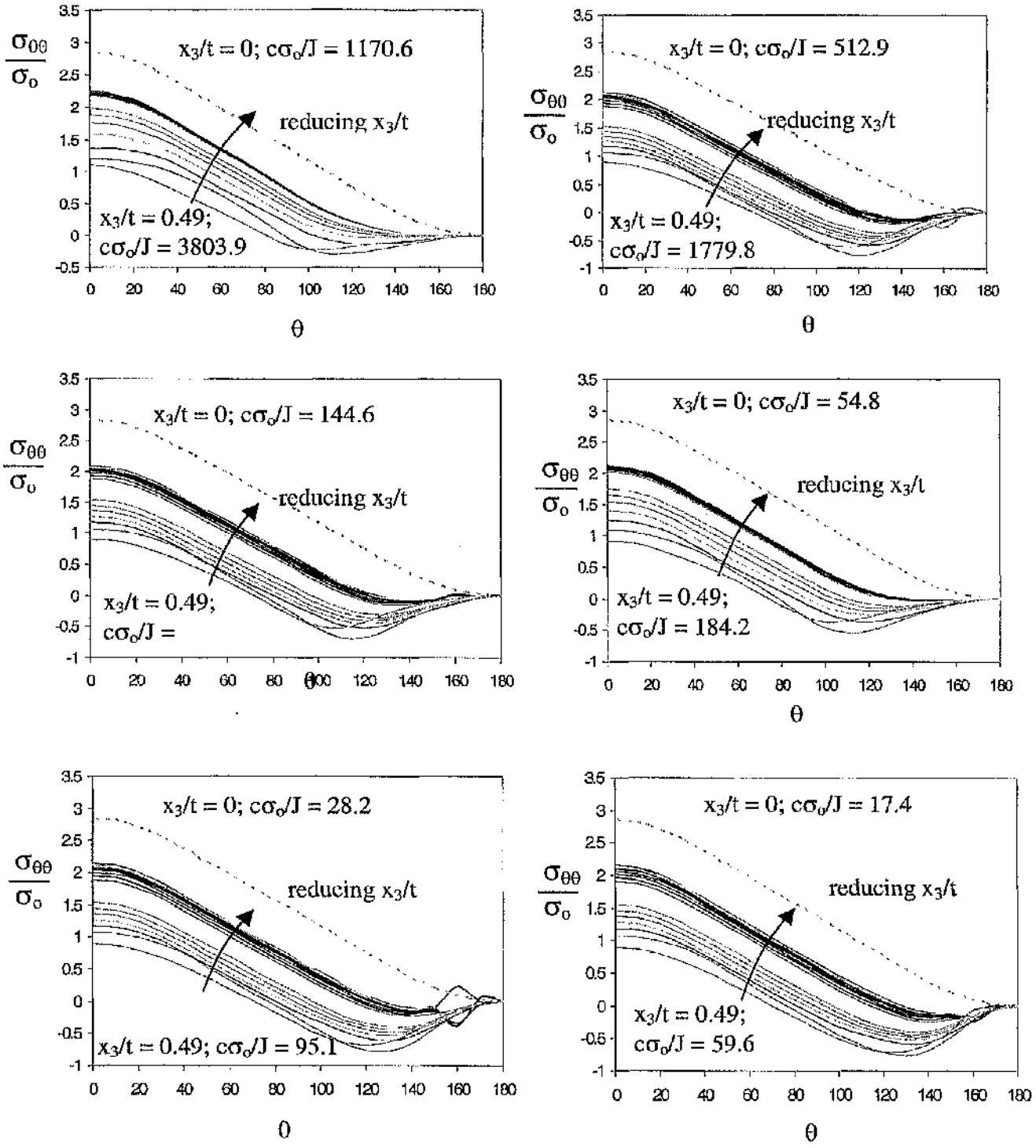


Figure 5.107: The hoop stress $\sigma_{\theta\theta}$ for a CCP specimen B/(W-a) = 1 through the thickness. The broken line determined in a boundary layer formulation indicates the two-dimensional plane strain field for $\sigma_{\theta\theta}$.

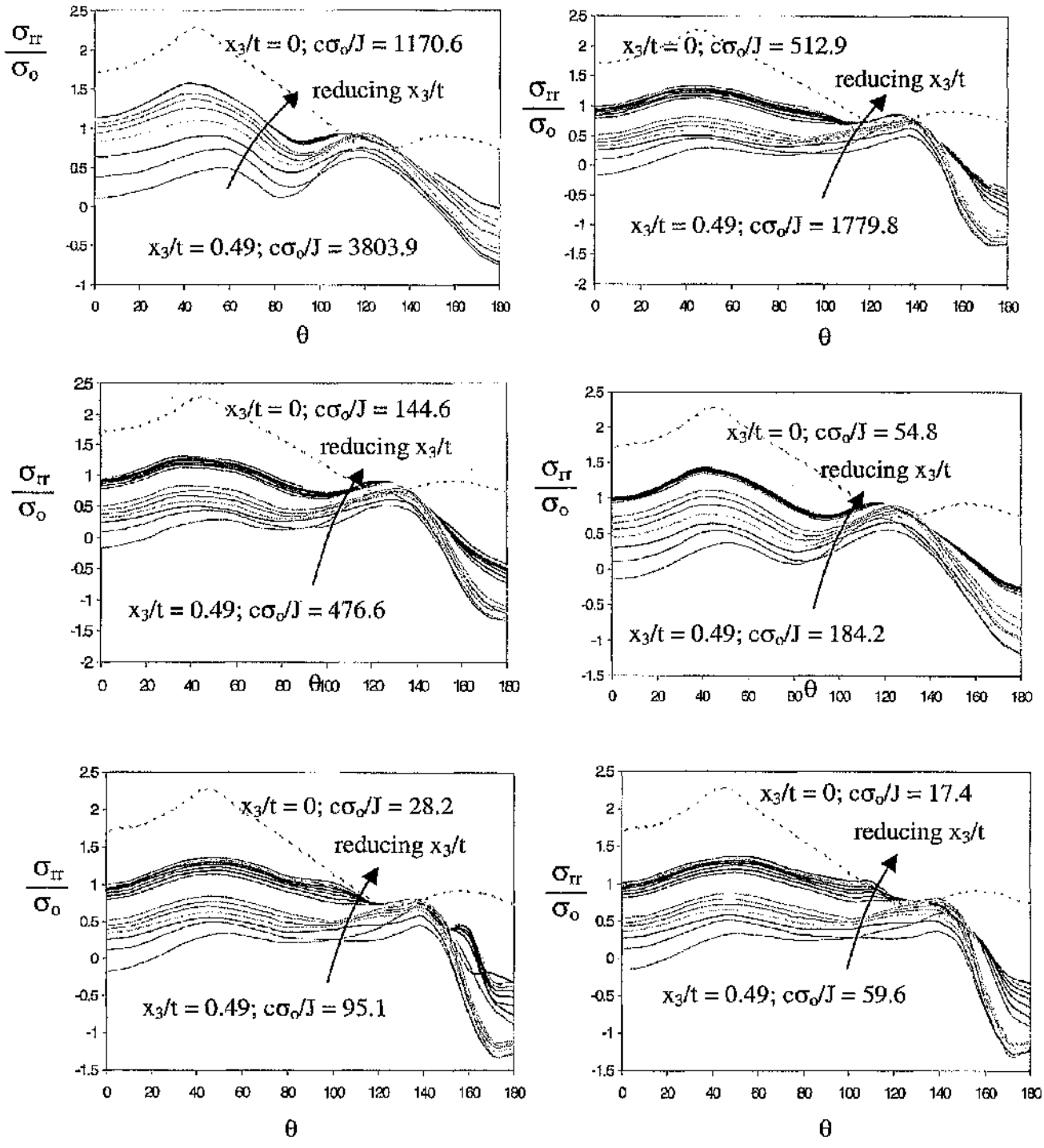


Figure 5.108: The radial stress $\sigma_{rr}$ for a CCP specimen B/(W-a) = 1 through the thickness. The broken line determined in a boundary layer formulation indicates the two-dimensional plane strain field for $\sigma_{rr}$.

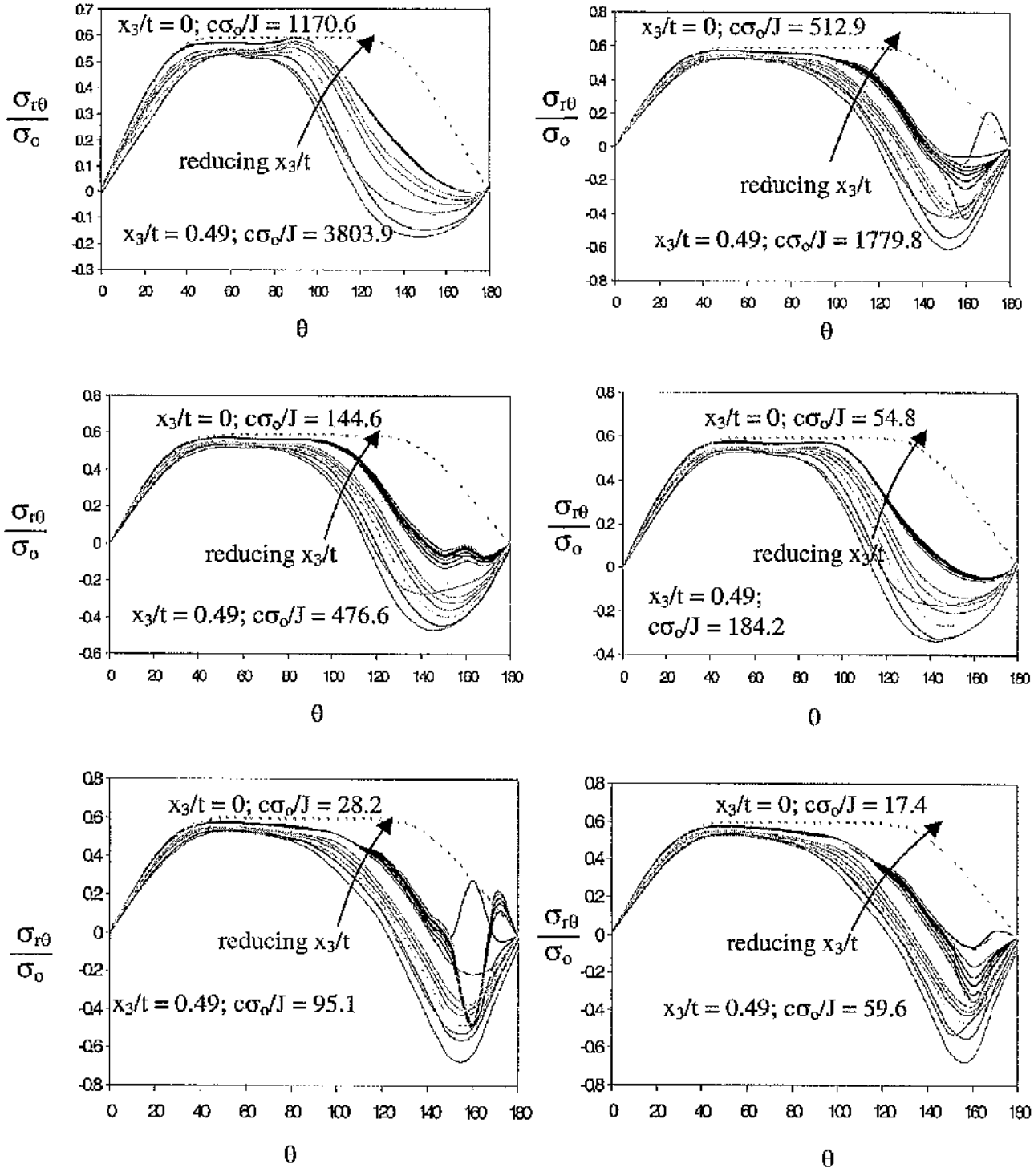


Figure 5.109: The shear stress $\sigma_{r\theta}$ for a CCP specimen B/(W-a) = 1 through the thickness. The broken line determined in a boundary layer formulation indicates the two-dimensional plane strain field for $\sigma_{r\theta}$.

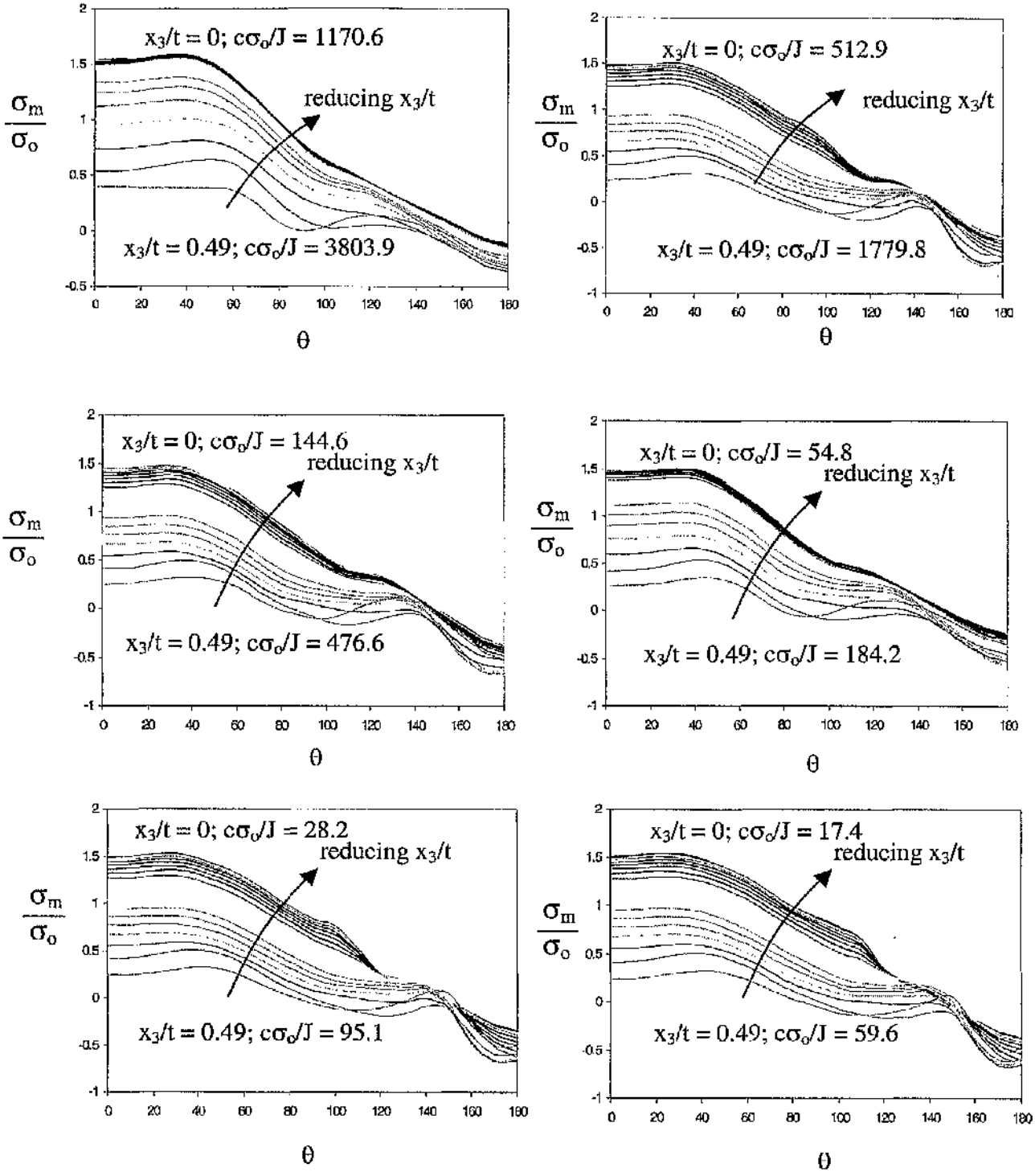


Figure 5.110: The mean stress $\sigma_m$ for a CCP specimen B/(W-a) = 1 through the thickness. The broken line determined in a boundary layer formulation indicates the two-dimensional plane strain field for $\sigma_m$.

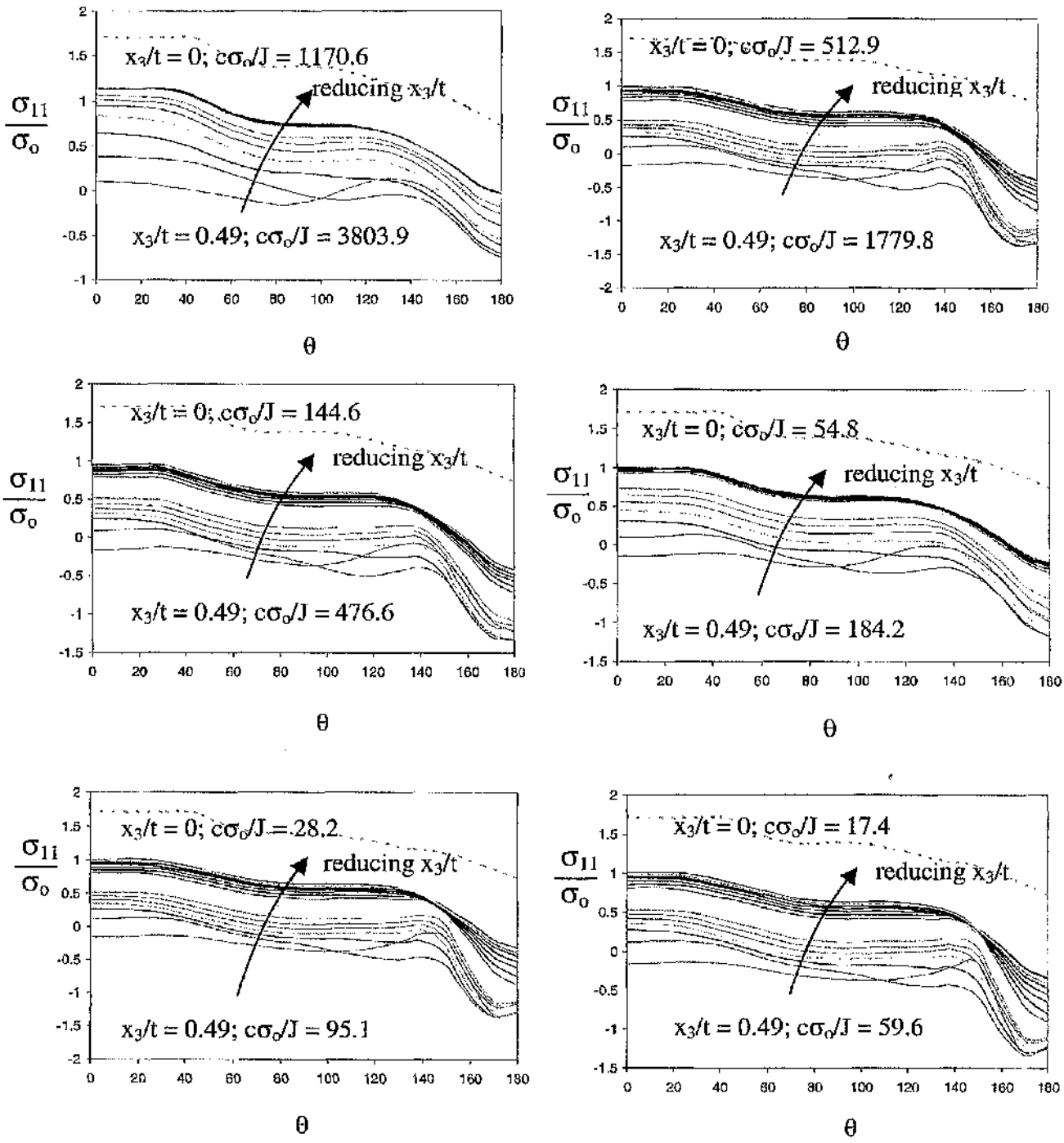


Figure 5.111: The direct stress $\sigma_{11}$ for a CCP specimen B/(W-a) = 1 through the thickness. The broken line determined in a boundary layer formulation indicates the two-dimensional plane strain field for $\sigma_{11}$.

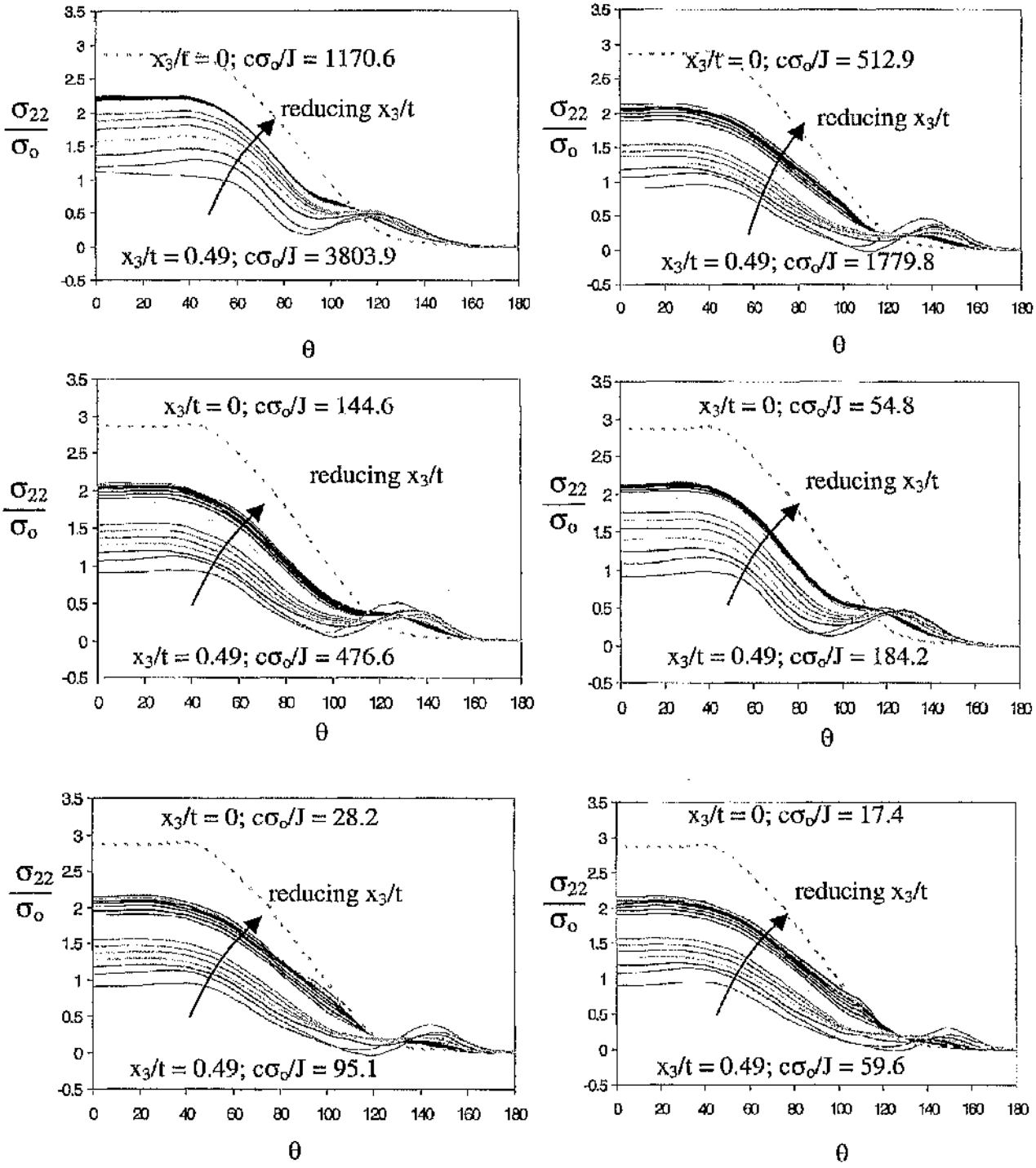


Figure 5.112: The direct stress $\sigma_{22}$ for a CCP specimen B/(W-a) = 1 through the thickness. The broken line determined in a boundary layer formulation indicates the two-dimensional plane strain field for $\sigma_{22}$.

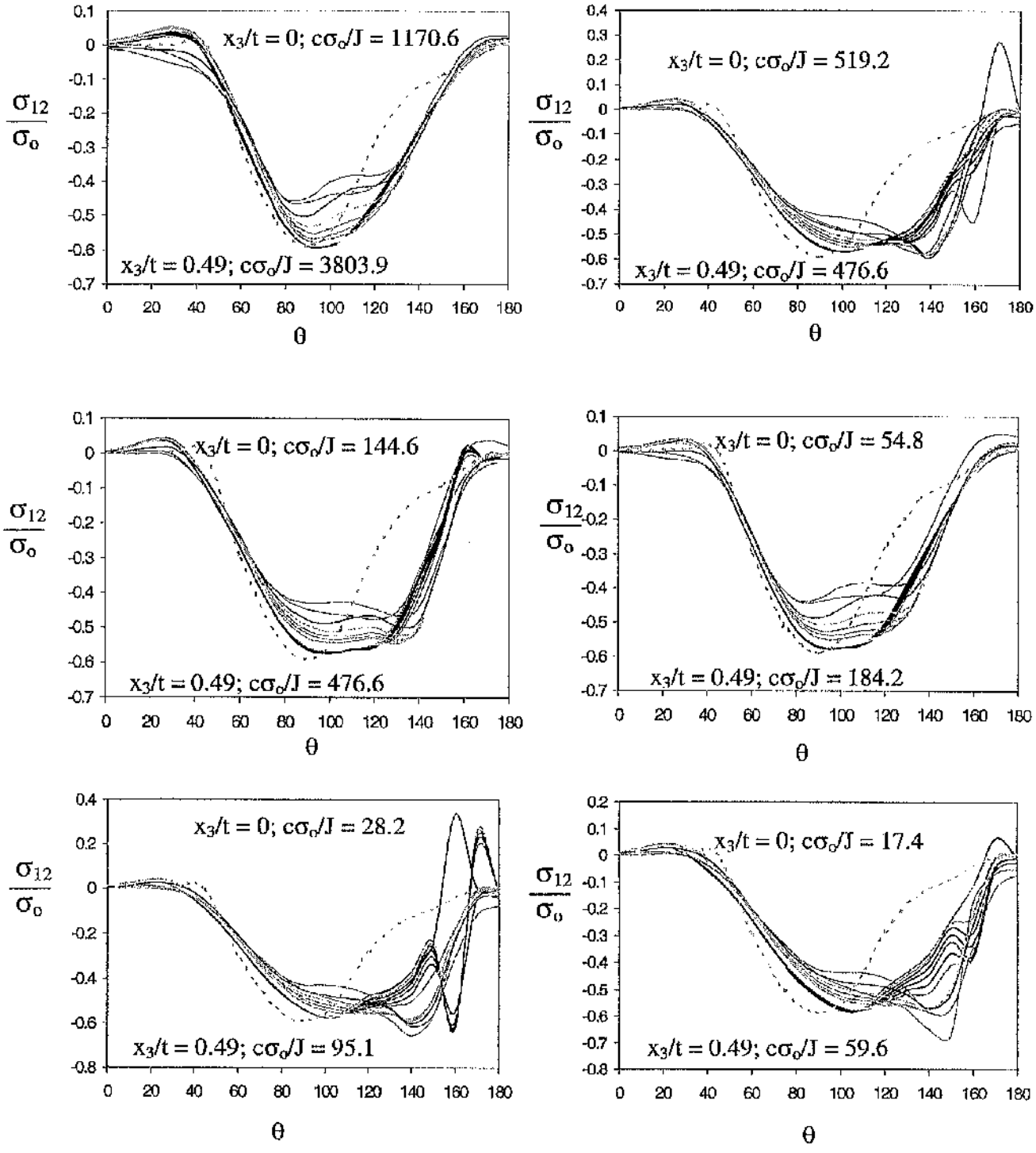


Figure 5.113: The shear stress $\sigma_{12}$ for a CCP specimen B/(W-a) = 1 through the thickness. The broken line determined in a boundary layer formulation indicates the two-dimensional plane strain field for $\sigma_{12}$.

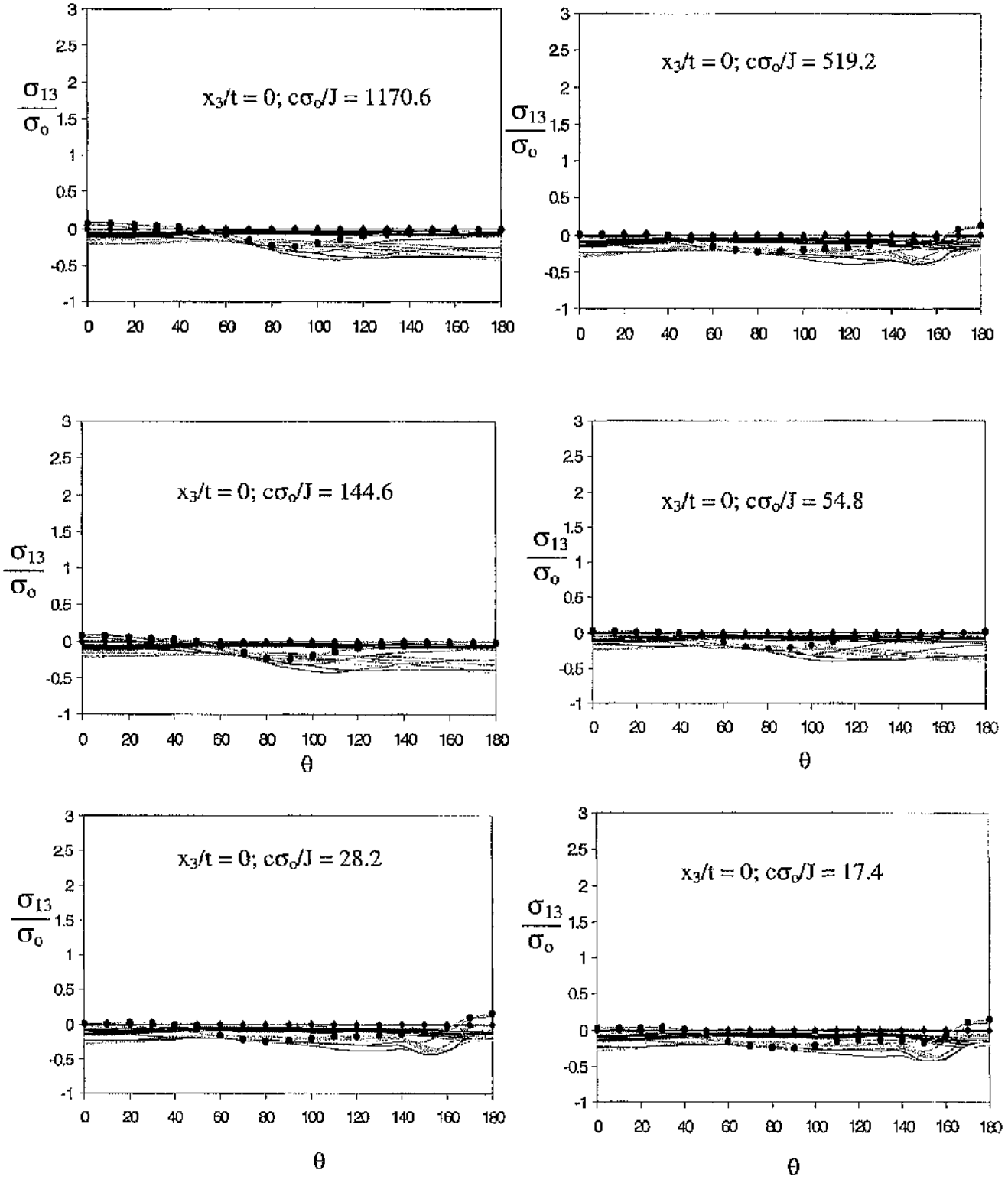


Figure 5.114: The shear stress $\sigma_{13}$ for a CCP specimen B/(W-a) = 1 through the thickness. The diamond and circular markers indicate the midplane and the free surface field.

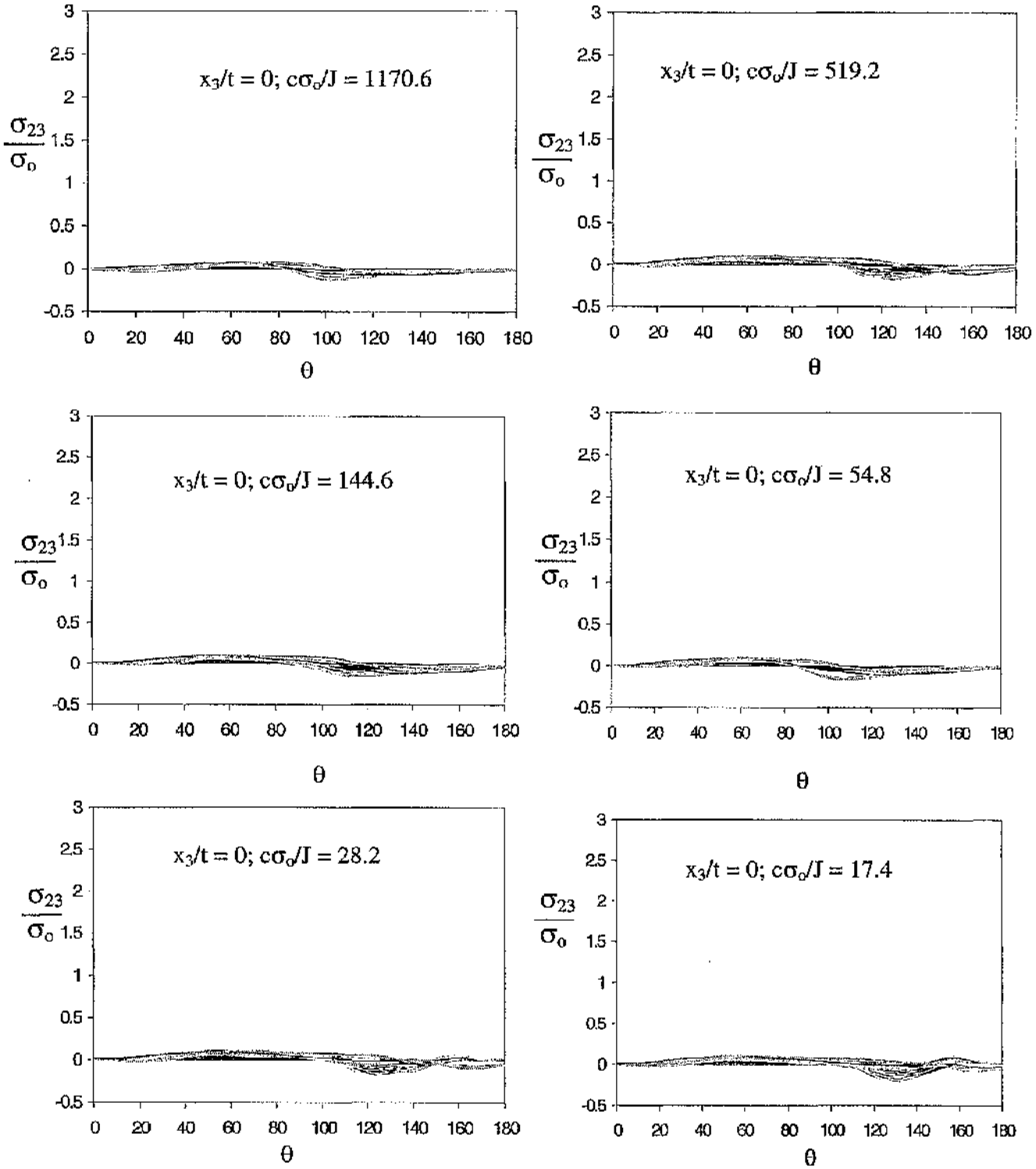


Figure 5.115: The shear stress $\sigma_{23}$ for a CCP specimen B/(W-a) = 1 through the thickness.

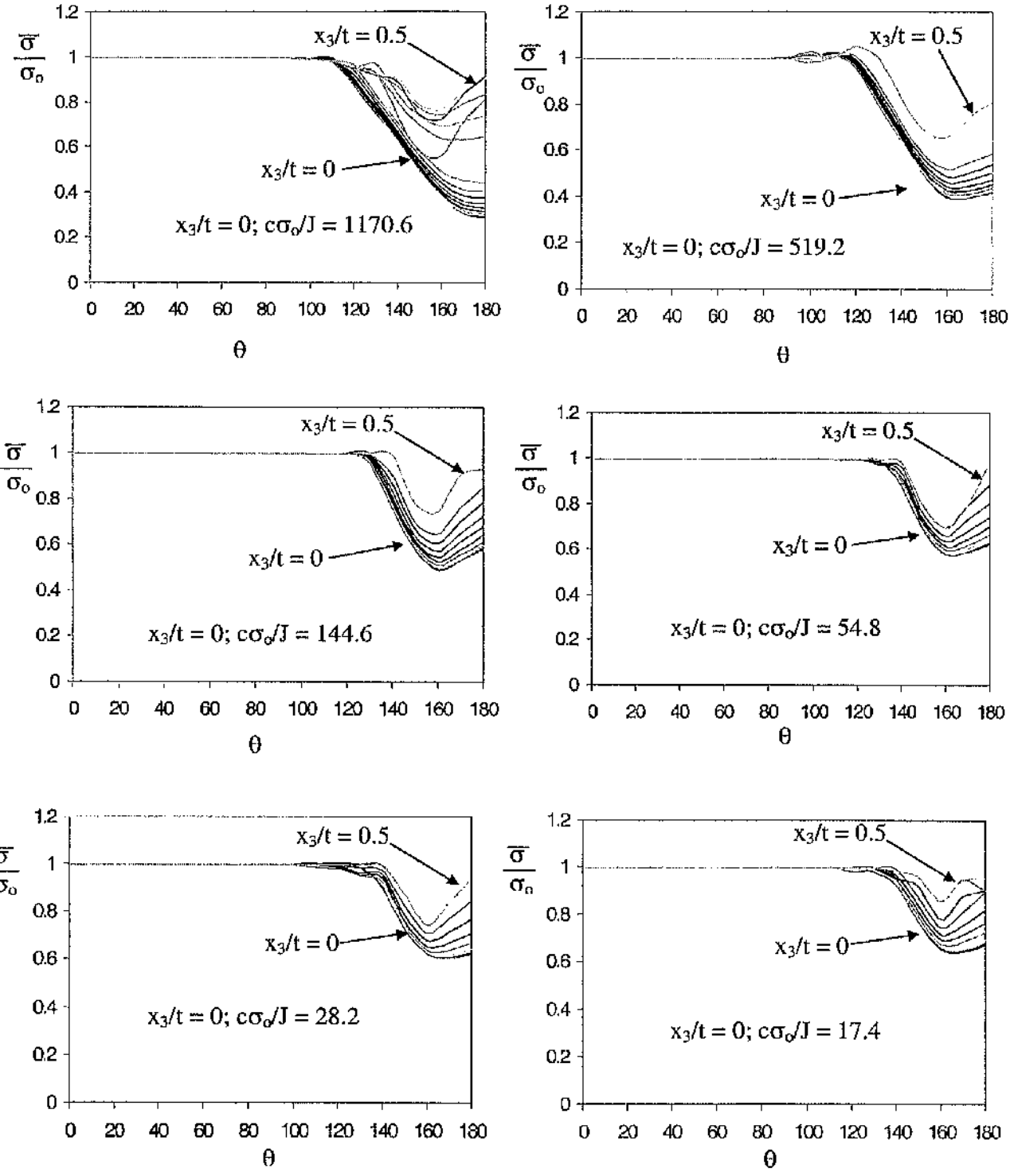


Figure 5.116: The Mises stress $\bar{\sigma}/\sigma_o$ for a CCP specimen B/(W-a) = 1 through the thickness.

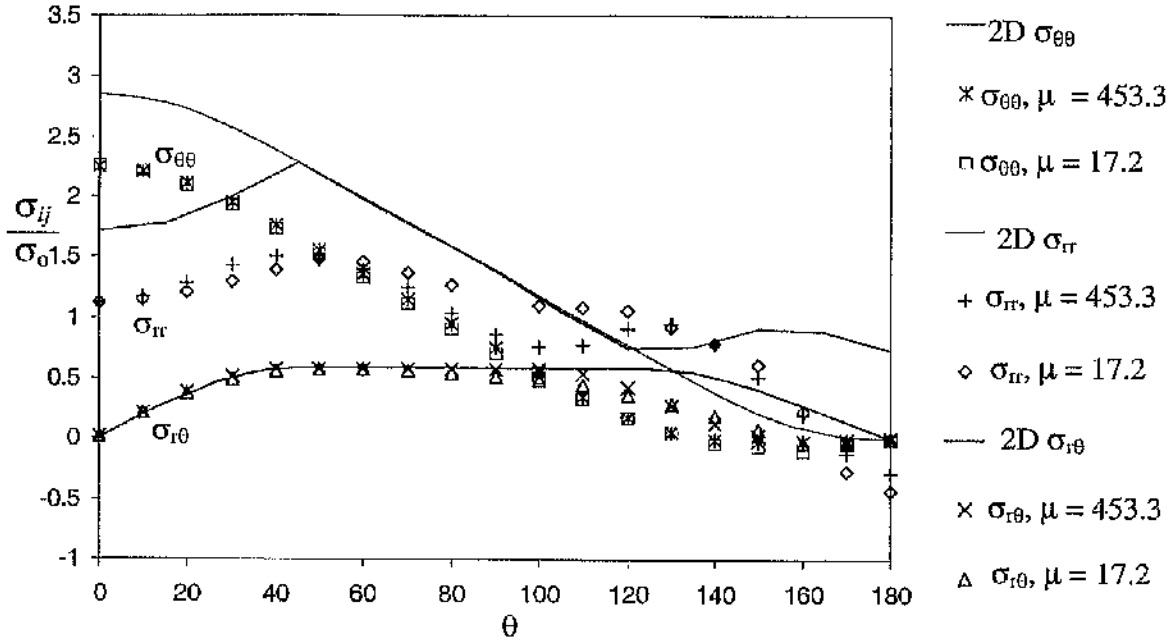


Figure 5.117: The asymptotic cylindrical stresses at the midplane for a CCP specimen B/(W-a) = 0.5 compared with the two-dimensional plane strain field.

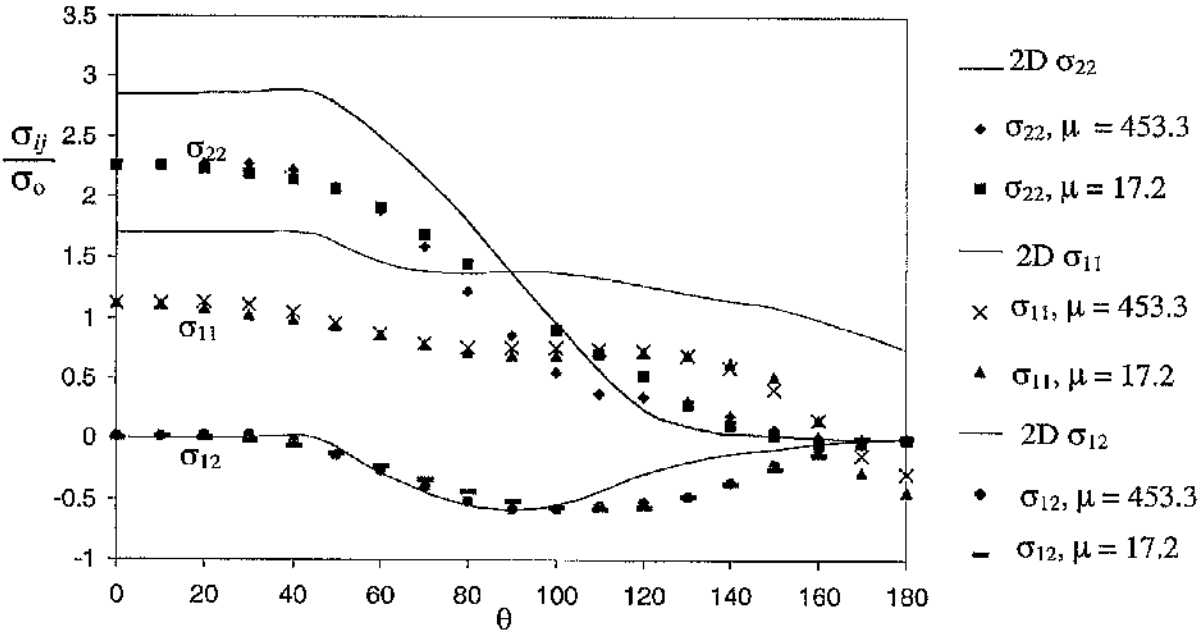


Figure 5.118: The asymptotic Cartesian stresses at the midplane for a CCP specimen B/(W-a) = 0.5 compared with the two-dimensional plane strain field.

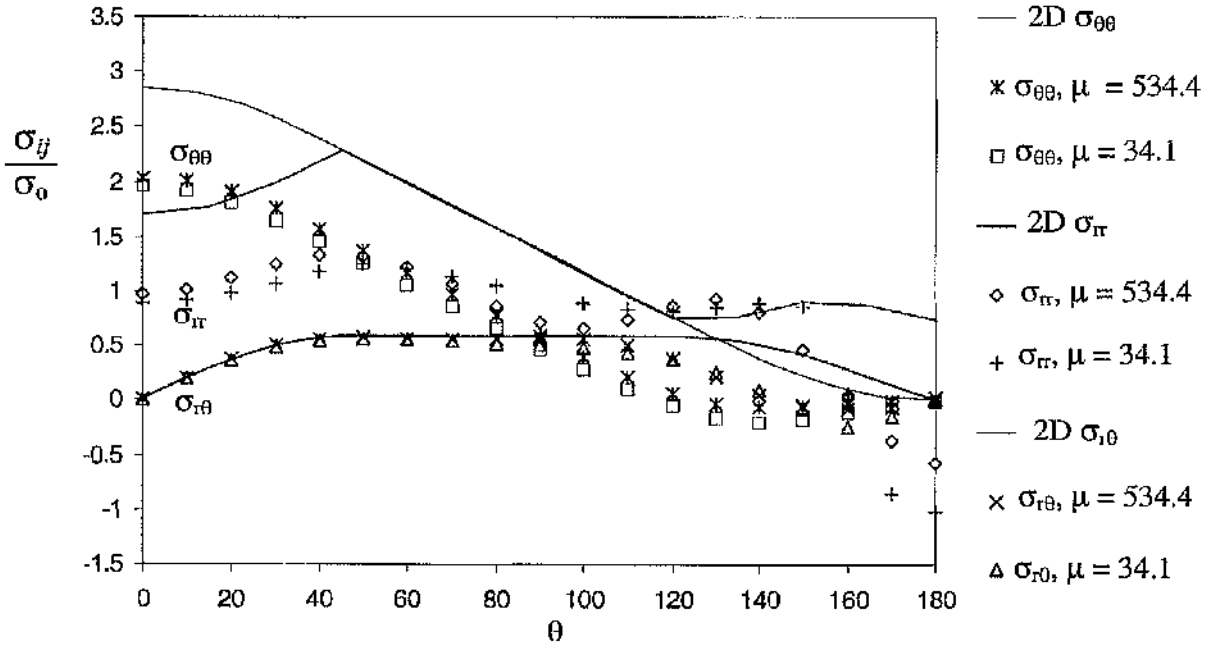


Figure 5.119: The asymptotic cylindrical stresses at the quarterplane for a CCP specimen B/(W-a) = 0.5 compared with the two-dimensional plane strain field.

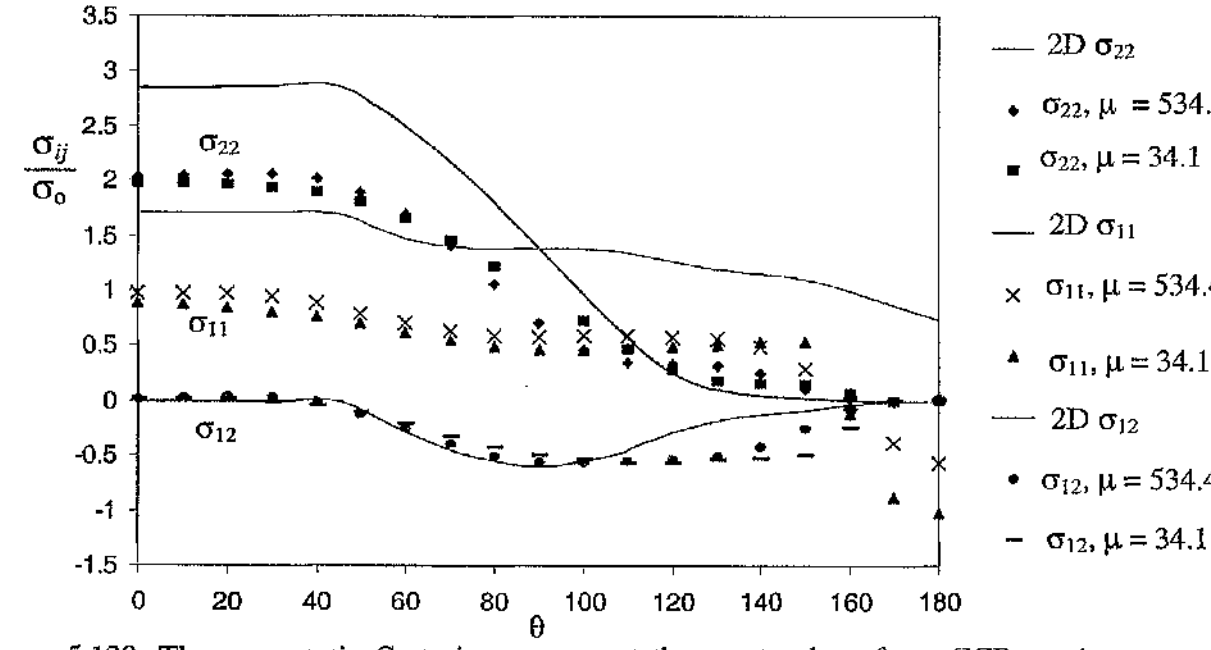


Figure 5.120: The asymptotic Cartesian stresses at the quarterplane for a CCP specimen B/(W-a) = 0.5 compared with the two-dimensional plane strain field.

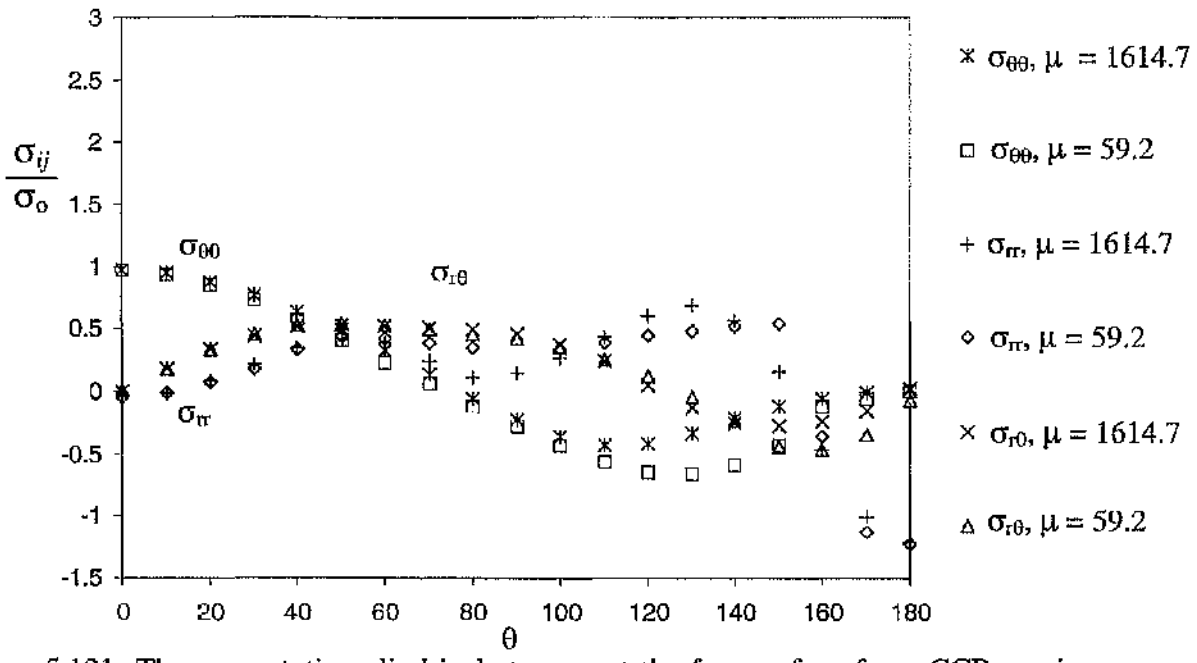


Figure 5.121: The asymptotic cylindrical stresses at the free surface for a CCP specimen B/(W-a) = 0.5 compared with the two-dimensional plane strain field.

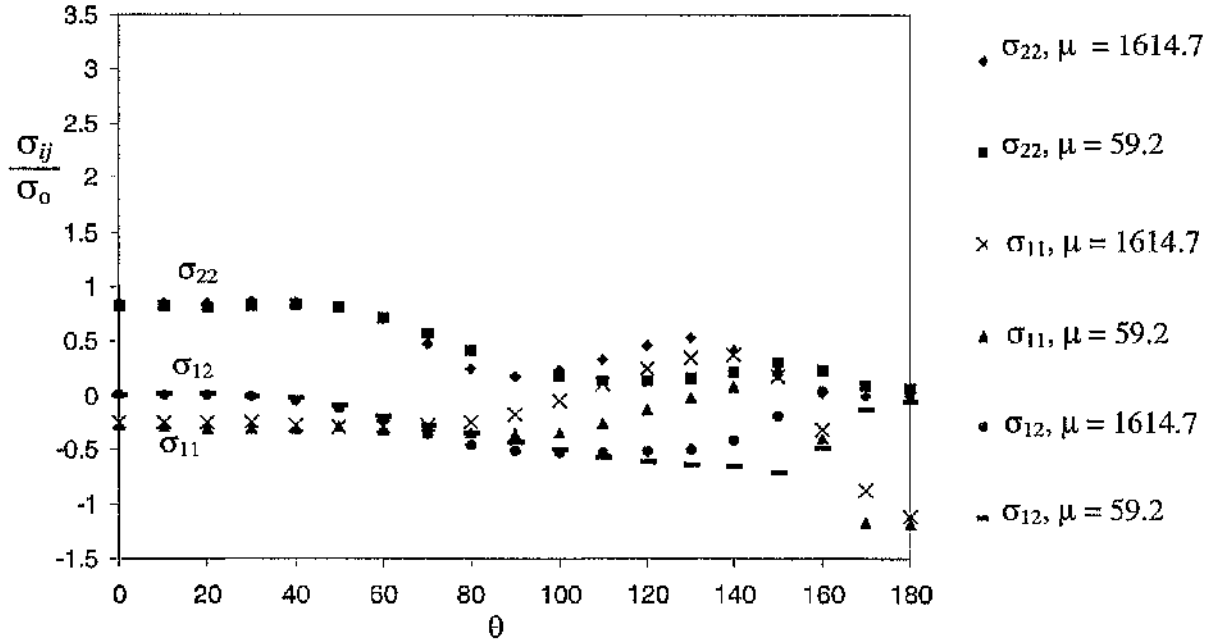


Figure 5.122: The asymptotic Cartesian stresses at the free surface for a CCP specimen B/(W-a)=0.5 compared with the two-dimensional plane strain field.

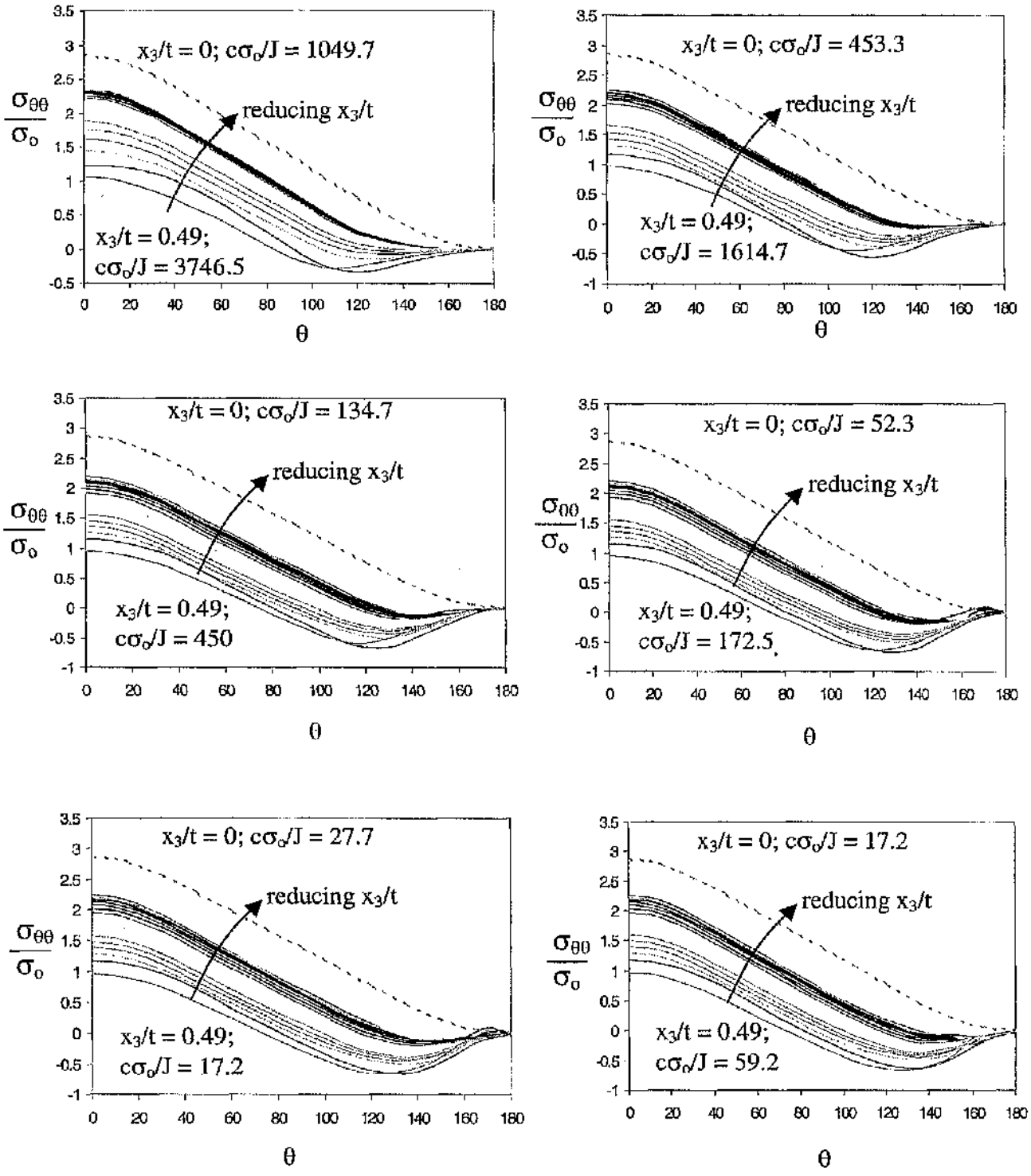


Figure 5.123: The hoop stress $\sigma_{\theta\theta}$ for a CCP specimen B/(W-a) = 0.5 through the thickness. The broken line determined in a boundary layer formulation indicates the two-dimensional plane strain field for $\sigma_{\theta\theta}$.

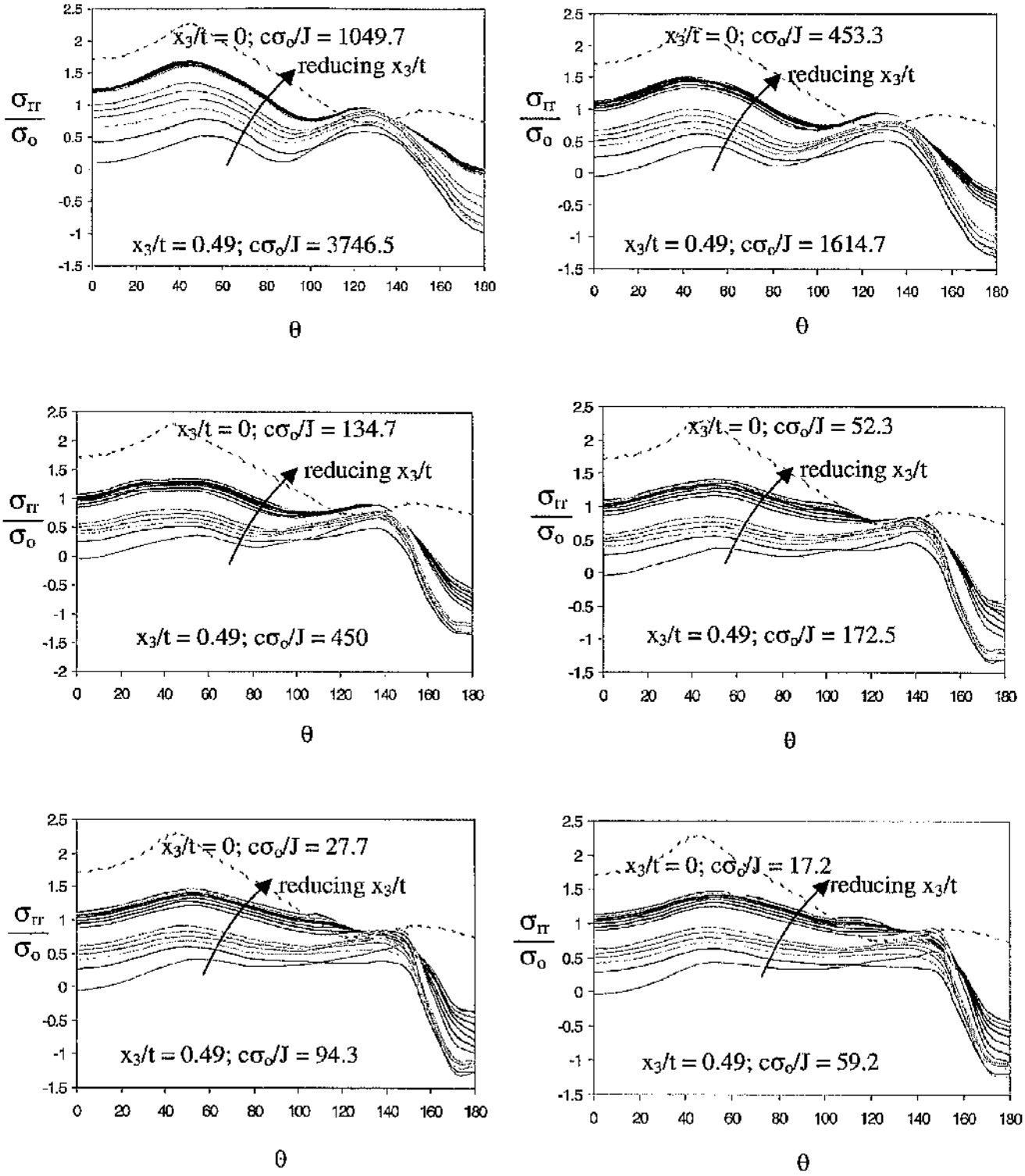


Figure 5.124: The radial stress $\sigma_{rr}$ for a CCP specimen B/(W-a) = 0.5 through the thickness. The broken line determined in a boundary layer formulation indicates the two-dimensional plane strain field for $\sigma_{rr}$.

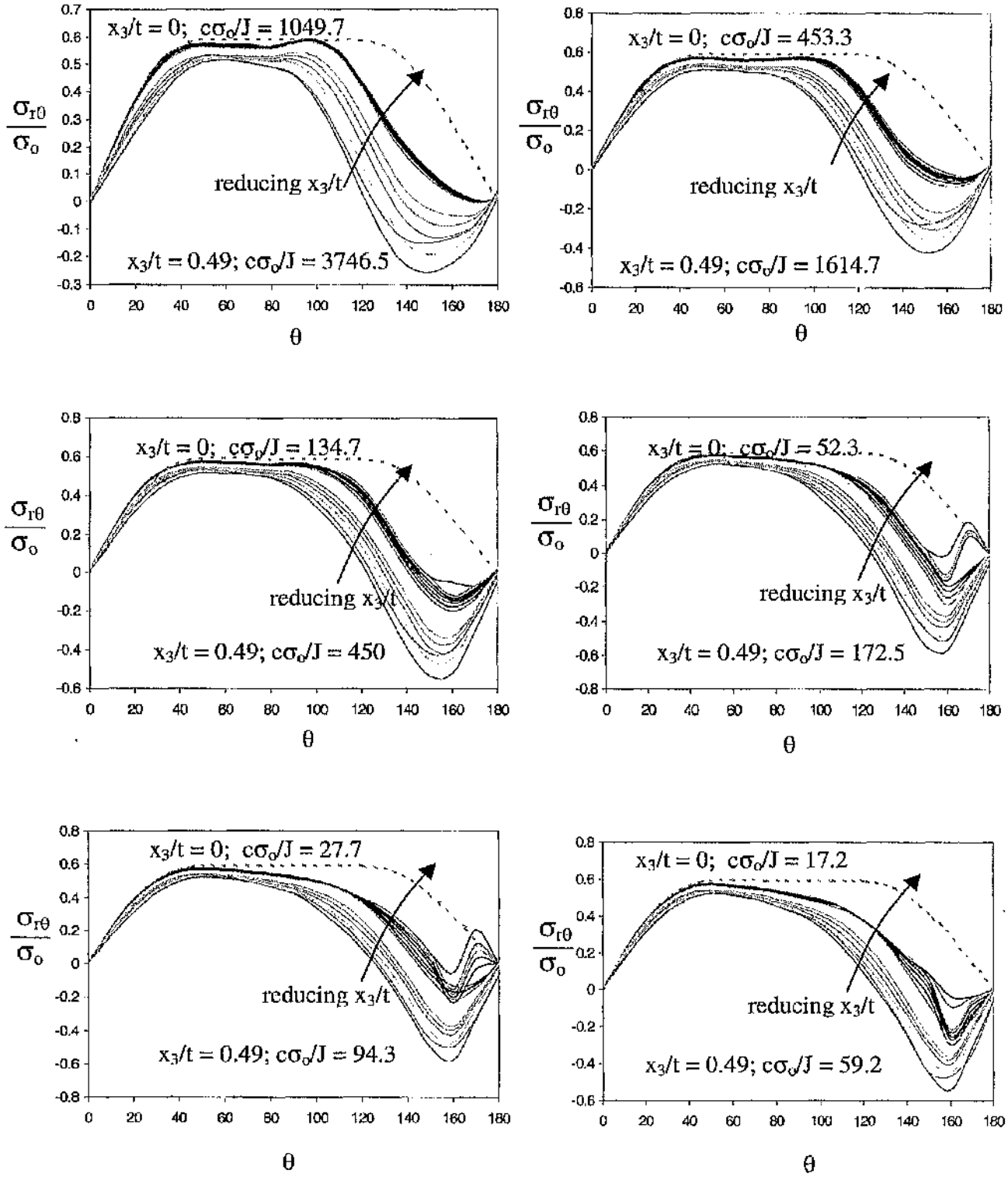


Figure 5.125: The shear stress $\sigma_{r\theta}$ for a CCP specimen B/(W-a) = 0.5 through the thickness. The broken line determined in a boundary layer formulation indicates the two-dimensional plane strain field for $\sigma_{r\theta}$.

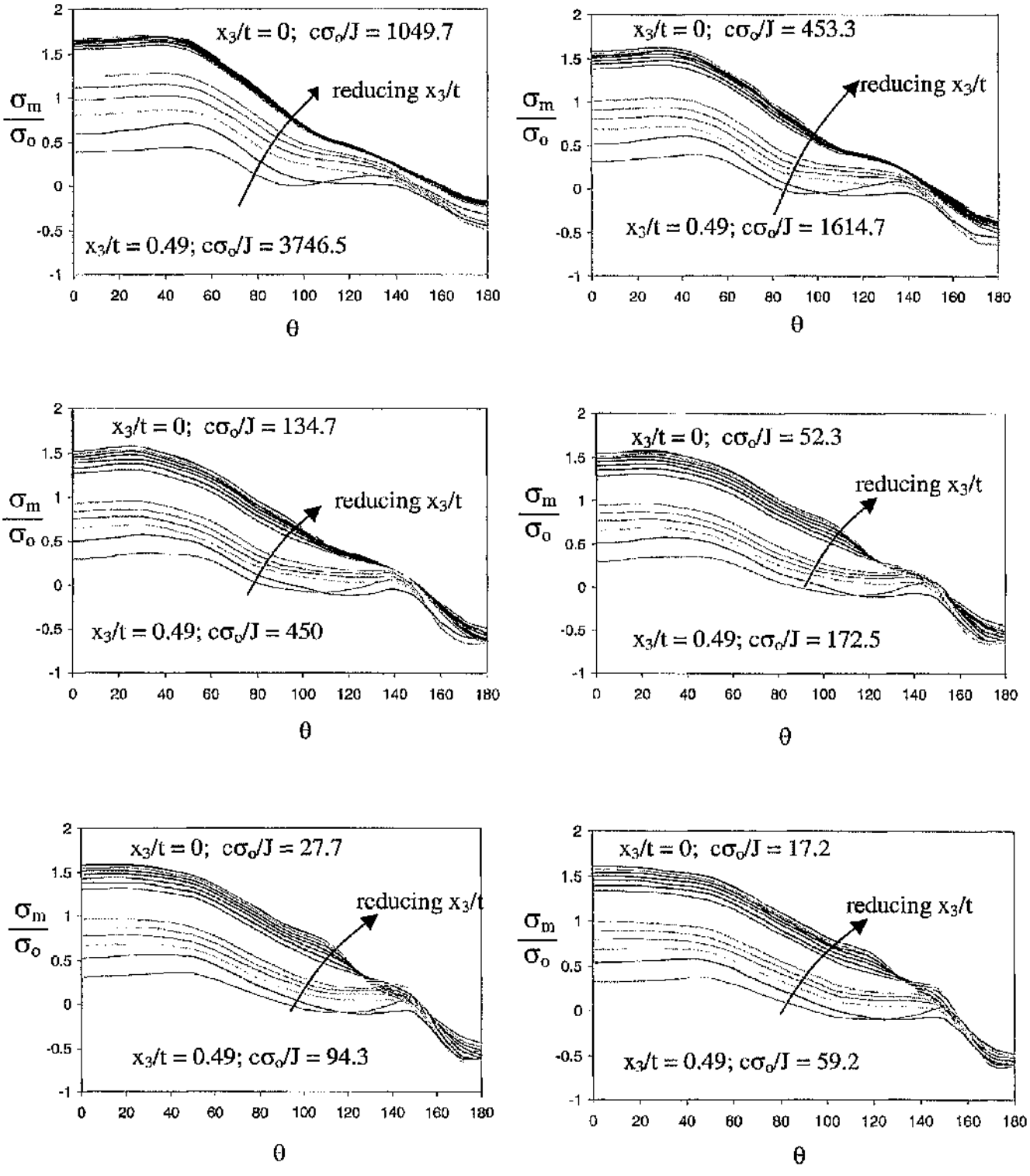


Figure 5.126: The mean stress $\sigma_m$ for a CCP specimen B/(W-a) = 0.5 through the thickness. The broken line determined in a boundary layer formulation indicates the two-dimensional plane strain field for $\sigma_m$.

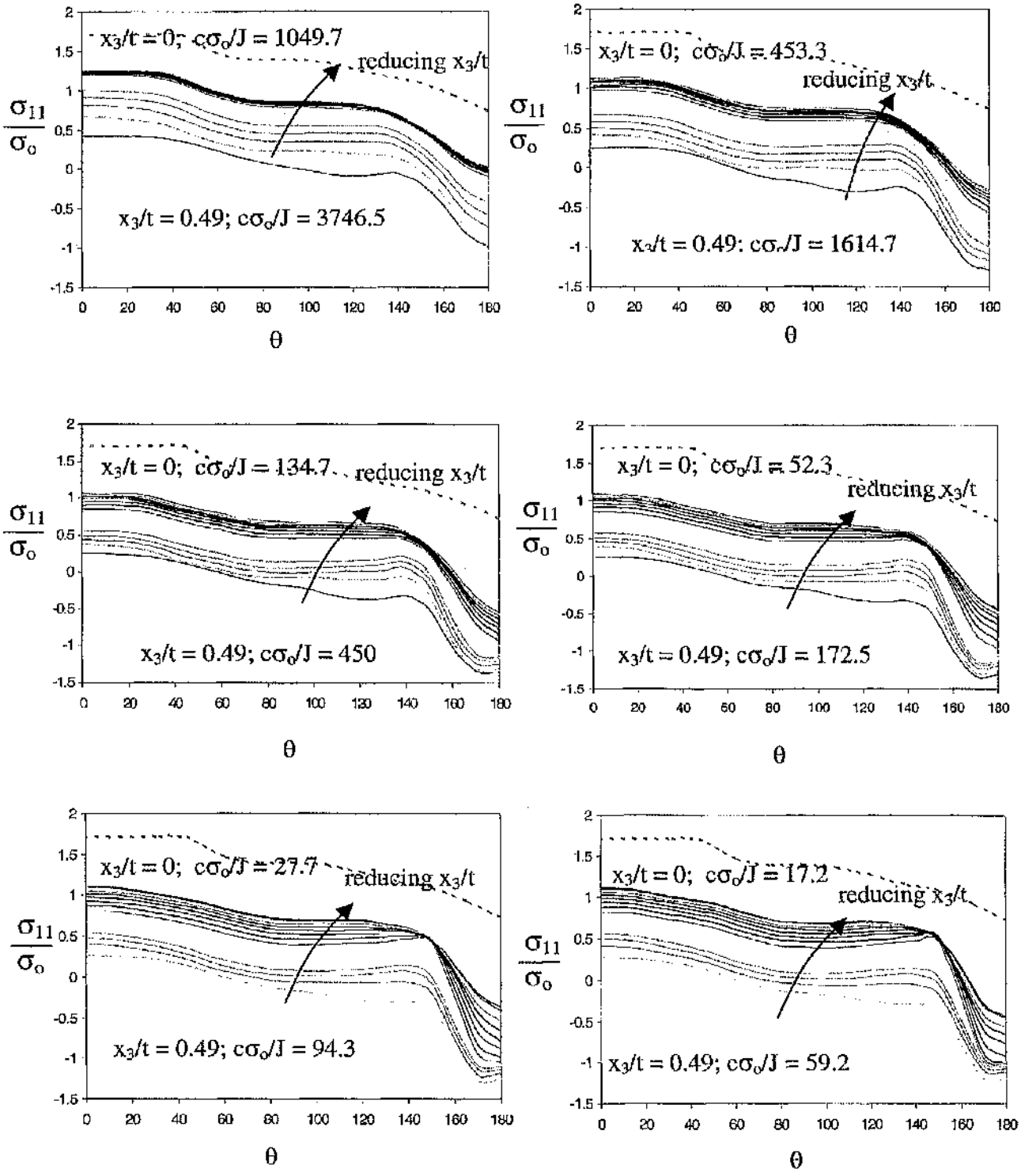


Figure 5.127: The direct stress $\sigma_{11}$ for a CCP specimen B/(W-a) = 0.5 through the thickness. The broken line determined in a boundary layer formulation indicates the two-dimensional plane strain field for $\sigma_{11}$.

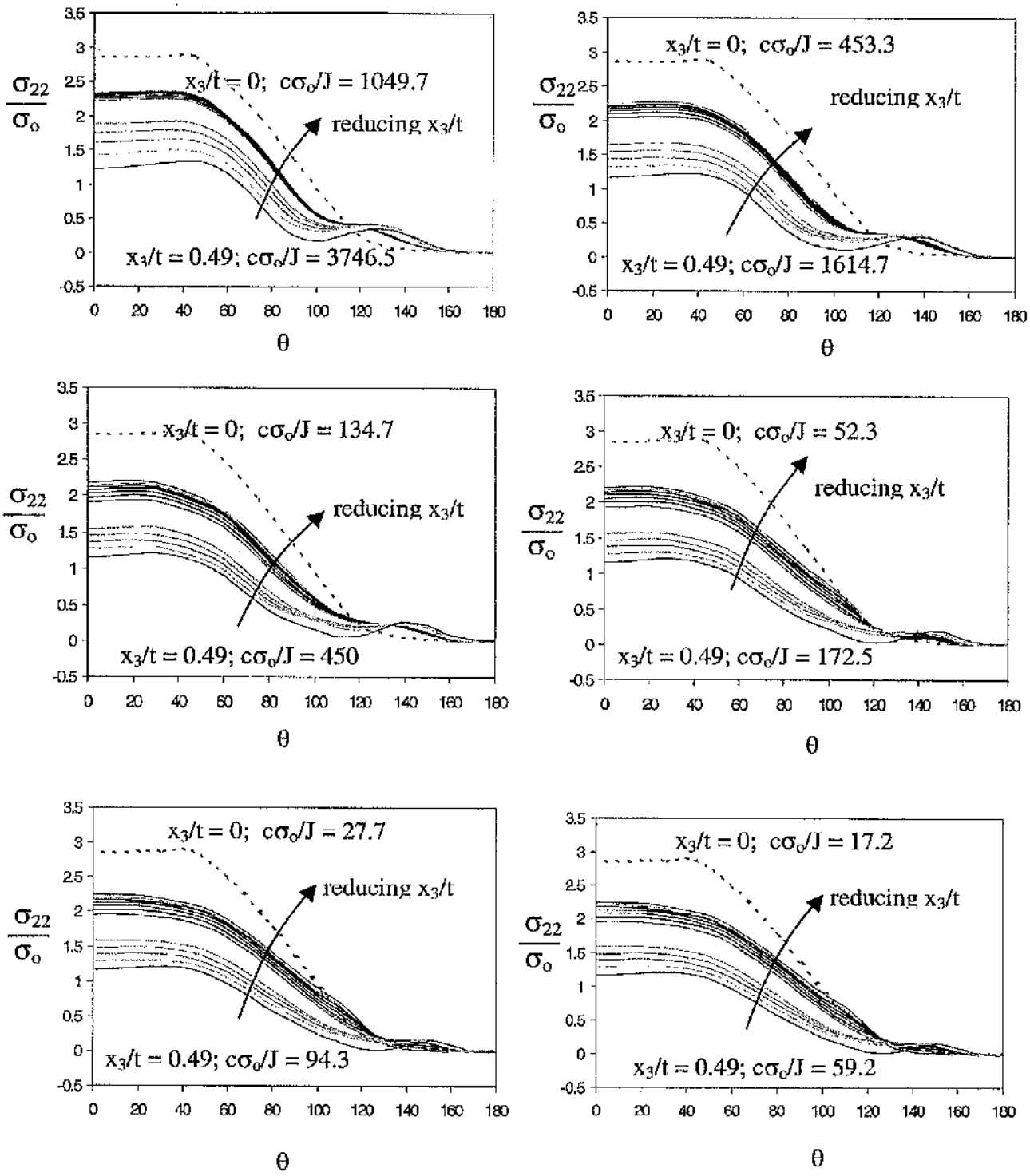


Figure 5.128: The direct stress $\sigma_{22}$ for a CCP specimen B/(W-a) = 0.5 through the thickness. The broken line determined in a boundary layer formulation indicates the two-dimensional plane strain field for $\sigma_{22}$.

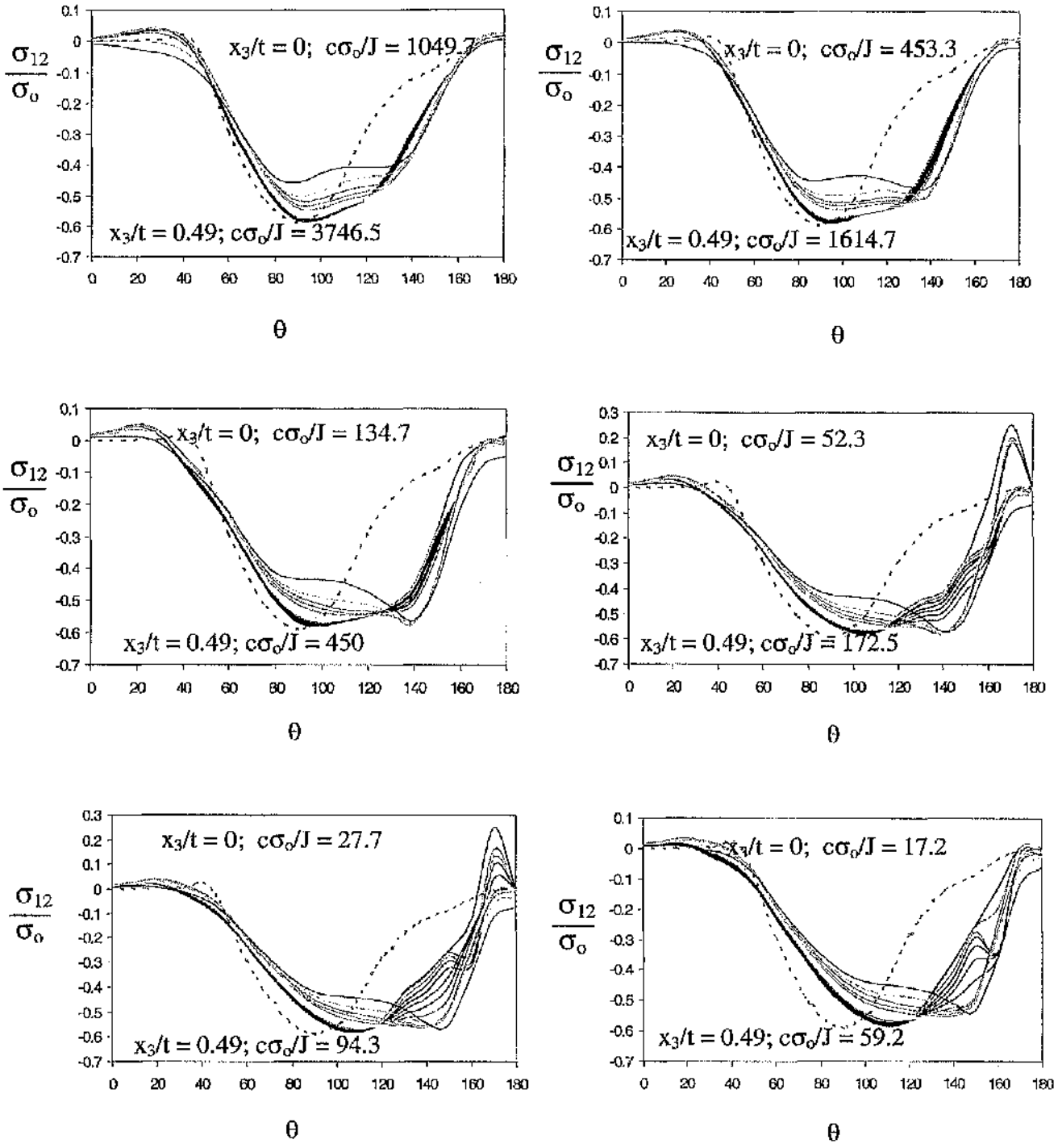


Figure 5.129: The shear stress $\sigma_{12}$ for a CCP specimen B/(W-a) = 0.5 through the thickness. The broken line determined in a boundary layer formulation indicates the two-dimensional plane strain field for $\sigma_{12}$.

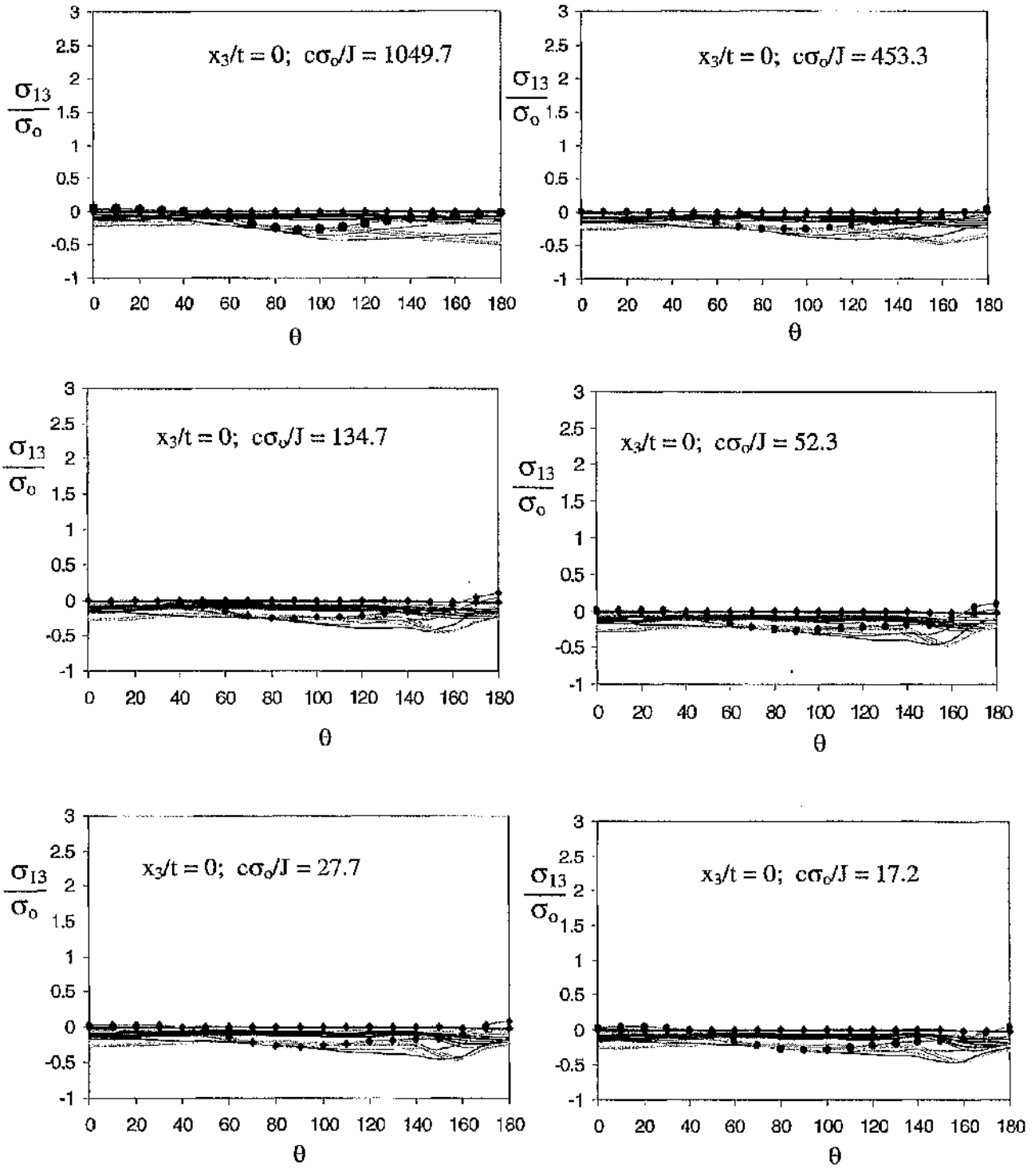


Figure 5.130: The shear stress $\sigma_{13}$ for a CCP specimen B/(W-a) = 0.5 through the thickness. The diamond and circular markers indicate the midplane and the free surface fields.

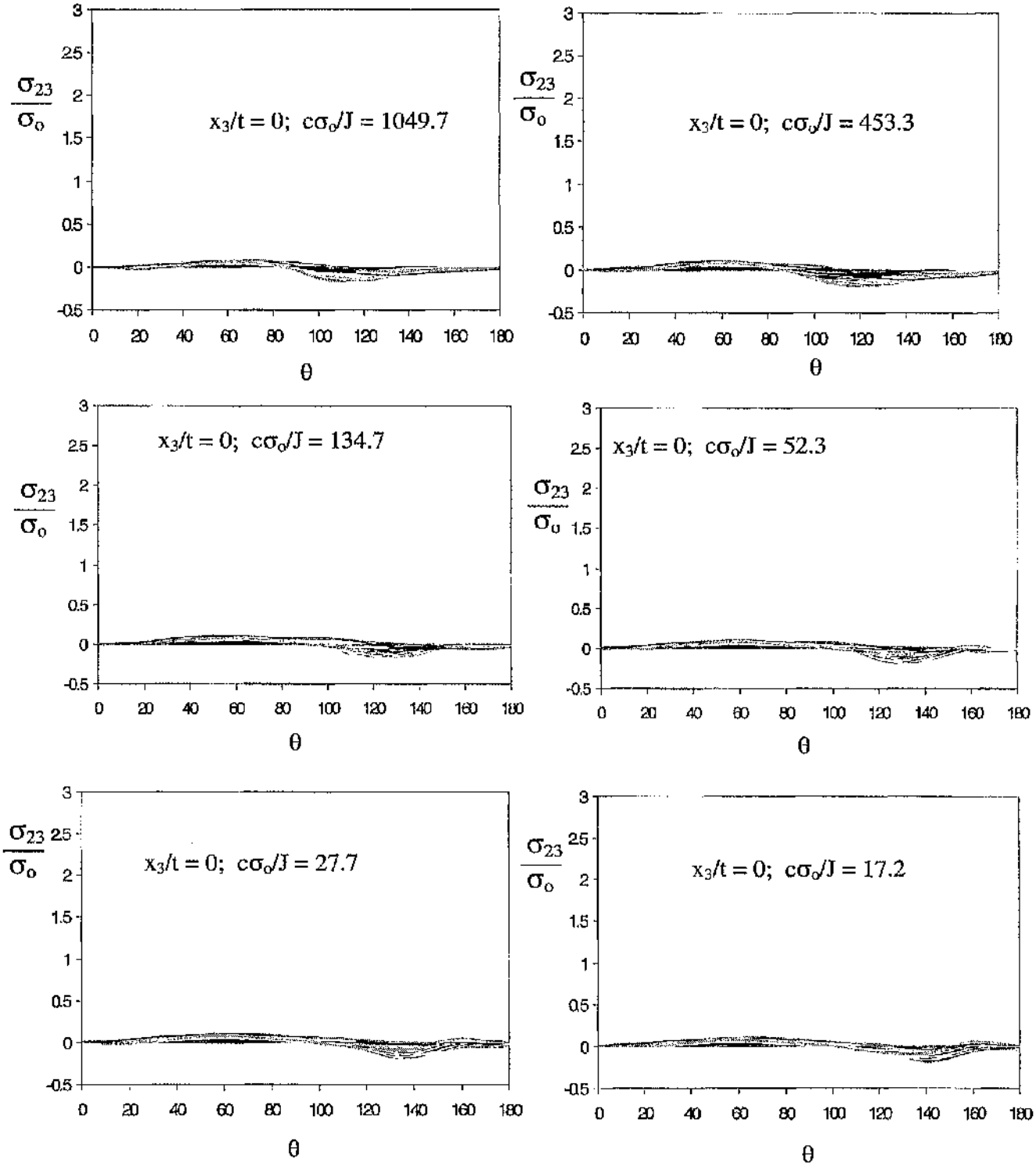


Figure 5.131: The shear stress $\sigma_{23}$ for a CCP specimen B/(W-a) = 0.5 through the thickness.

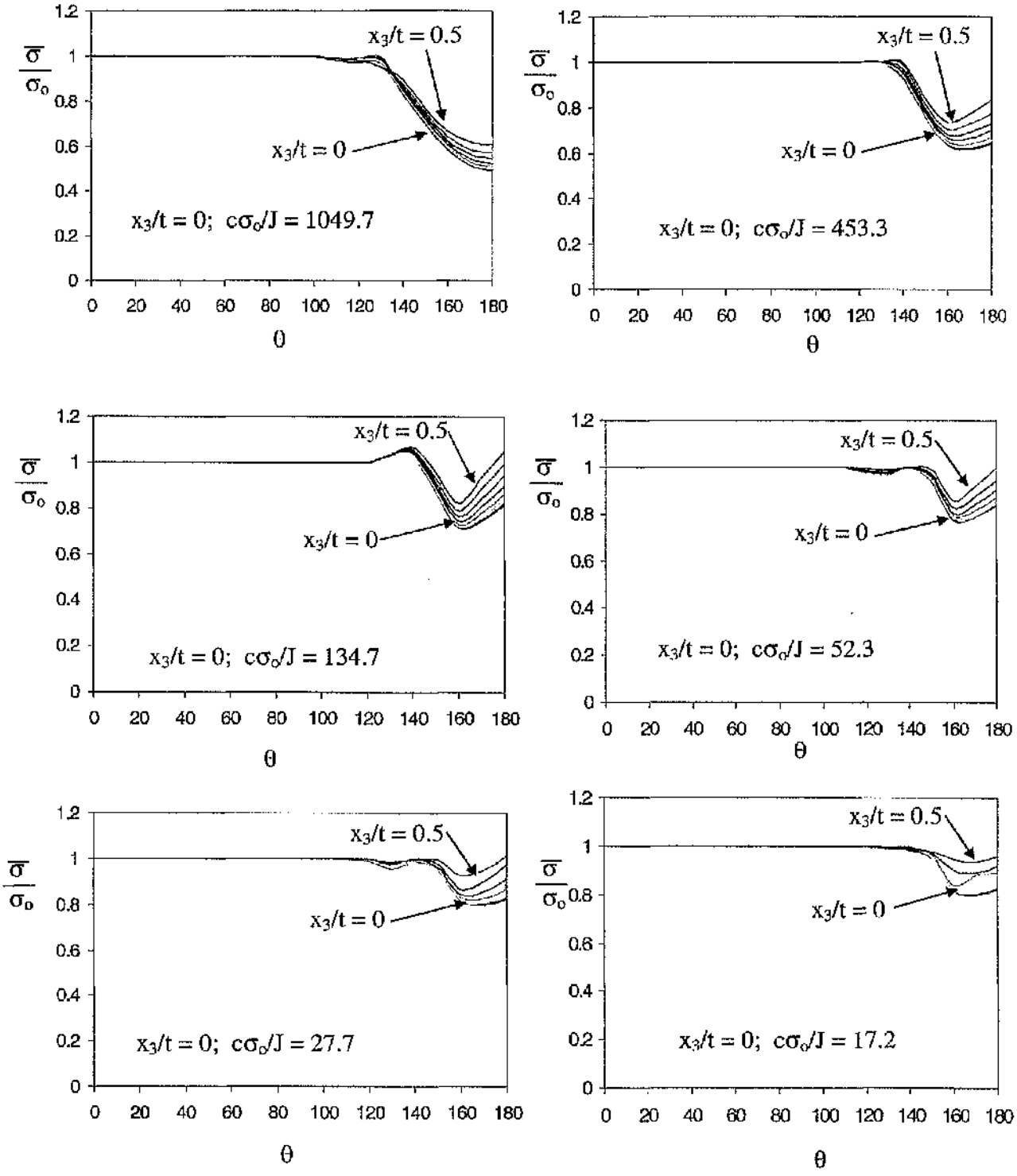


Figure 5.132: The Mises stress $\bar{\sigma}/\sigma_o$ for a CCP specimen B/(W-a) = 0.5 through the thickness.

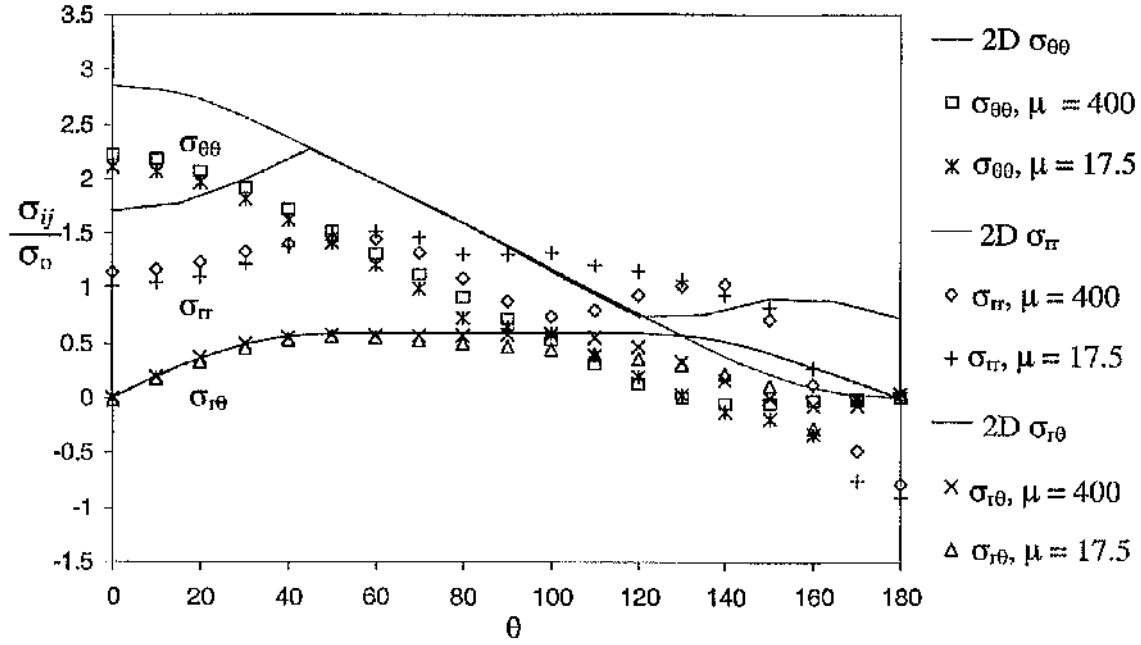


Figure 5.133: The asymptotic cylindrical stresses at the midplane for a CCP specimen B/(W-a) = 0.1 compared with the two-dimensional plane strain field.

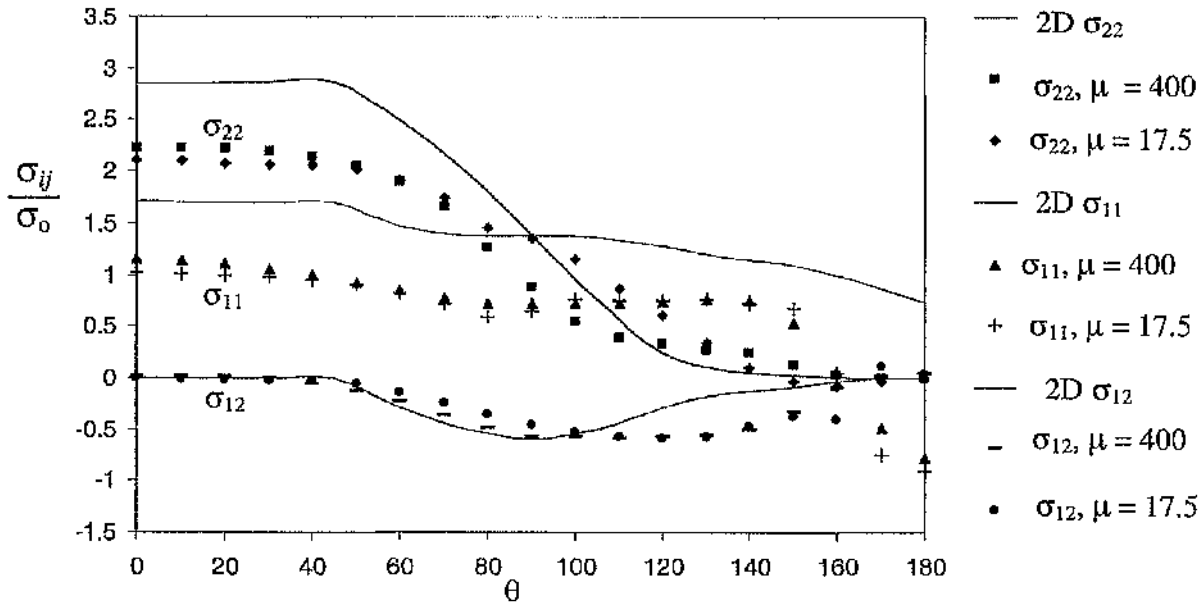


Figure 5.134: The asymptotic Cartesian stresses at the midplane for a CCP specimen B/(W-a) = 0.1 compared with the two-dimensional plane strain field.

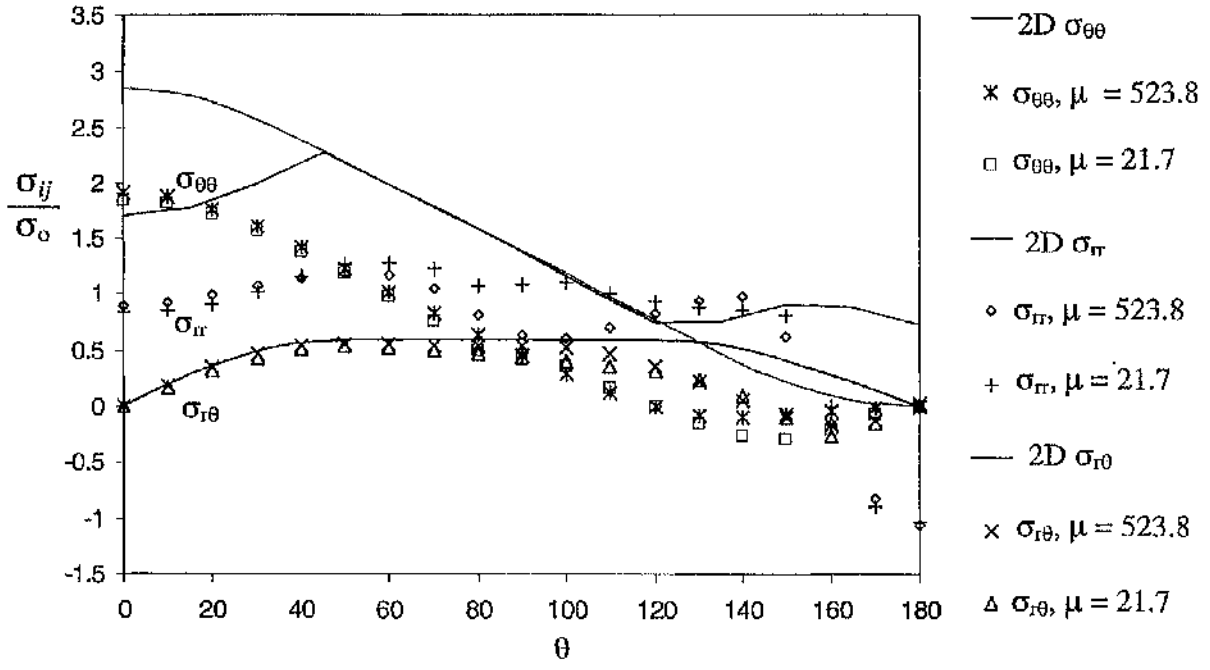


Figure 5.135: The asymptotic cylindrical stresses at the quarterplane for a CCP specimen B/(W-a) = 0.1 compared with the two-dimensional plane strain field.

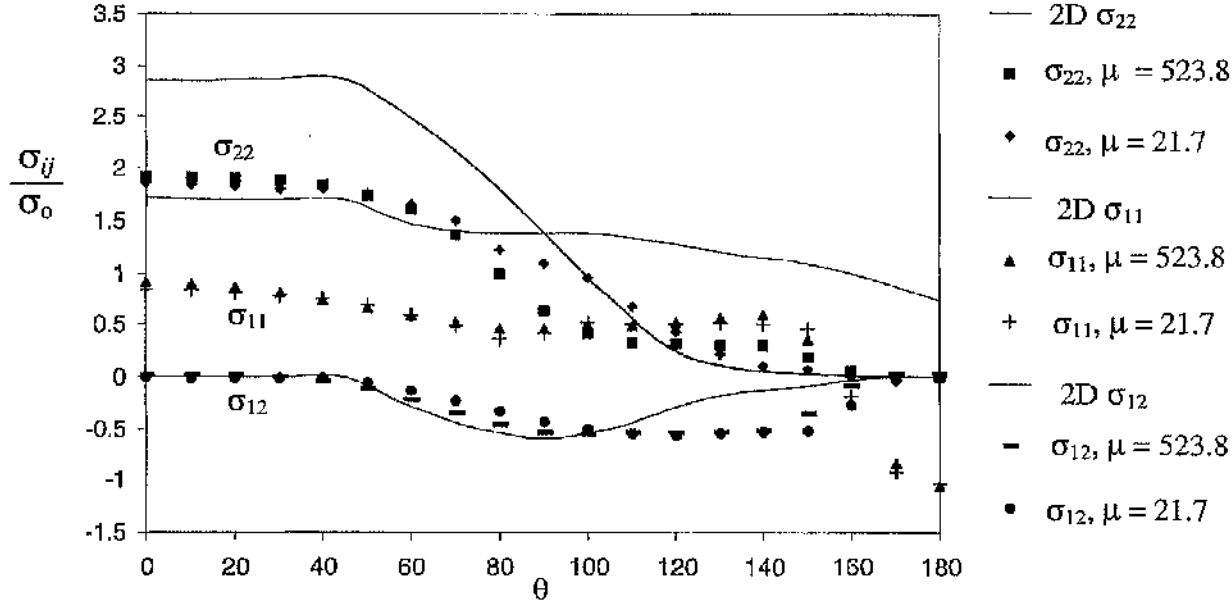


Figure 5.136: The asymptotic Cartesian stresses at the quarterplane for a CCP specimen B/(W-a) = 0.1 compared with the two-dimensional plane strain field.

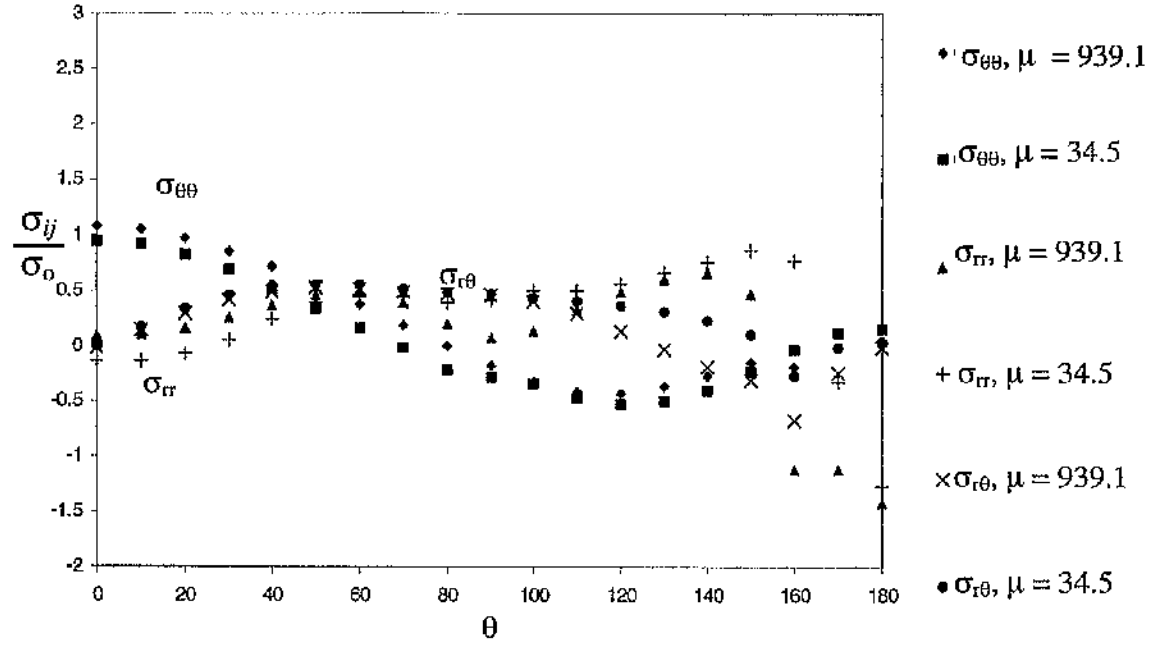


Figure 5.137: The asymptotic cylindrical stresses at the free surface for a CCP specimen B/(W-a) = 0.1.

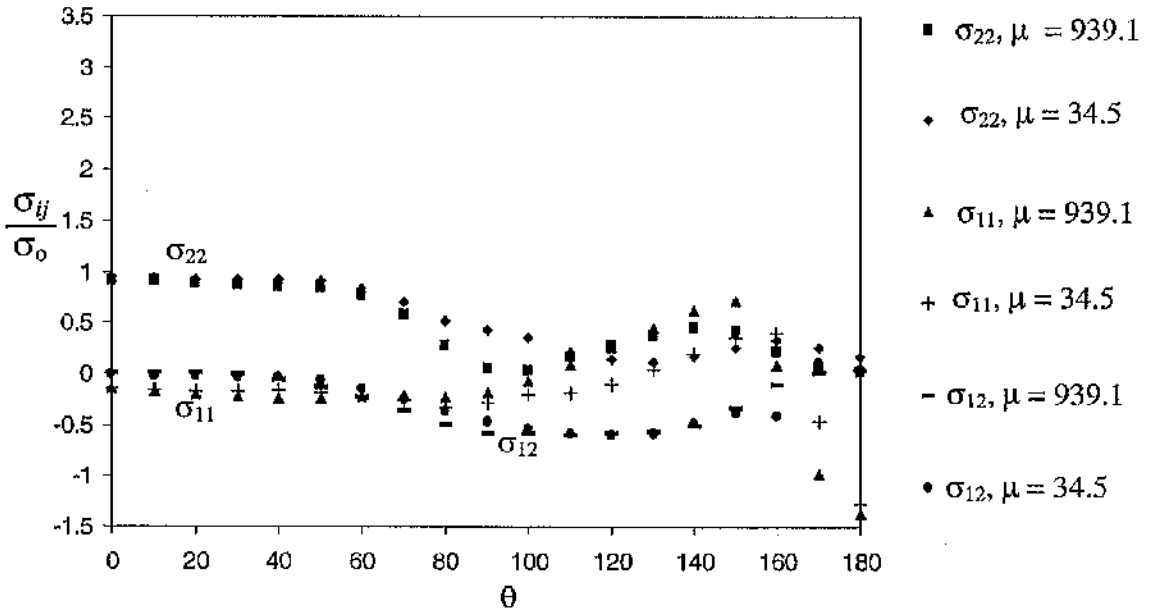


Figure 5.138: The asymptotic Cartesian stresses at the free surface for a CCP specimen B/(W-a) = 0.1.

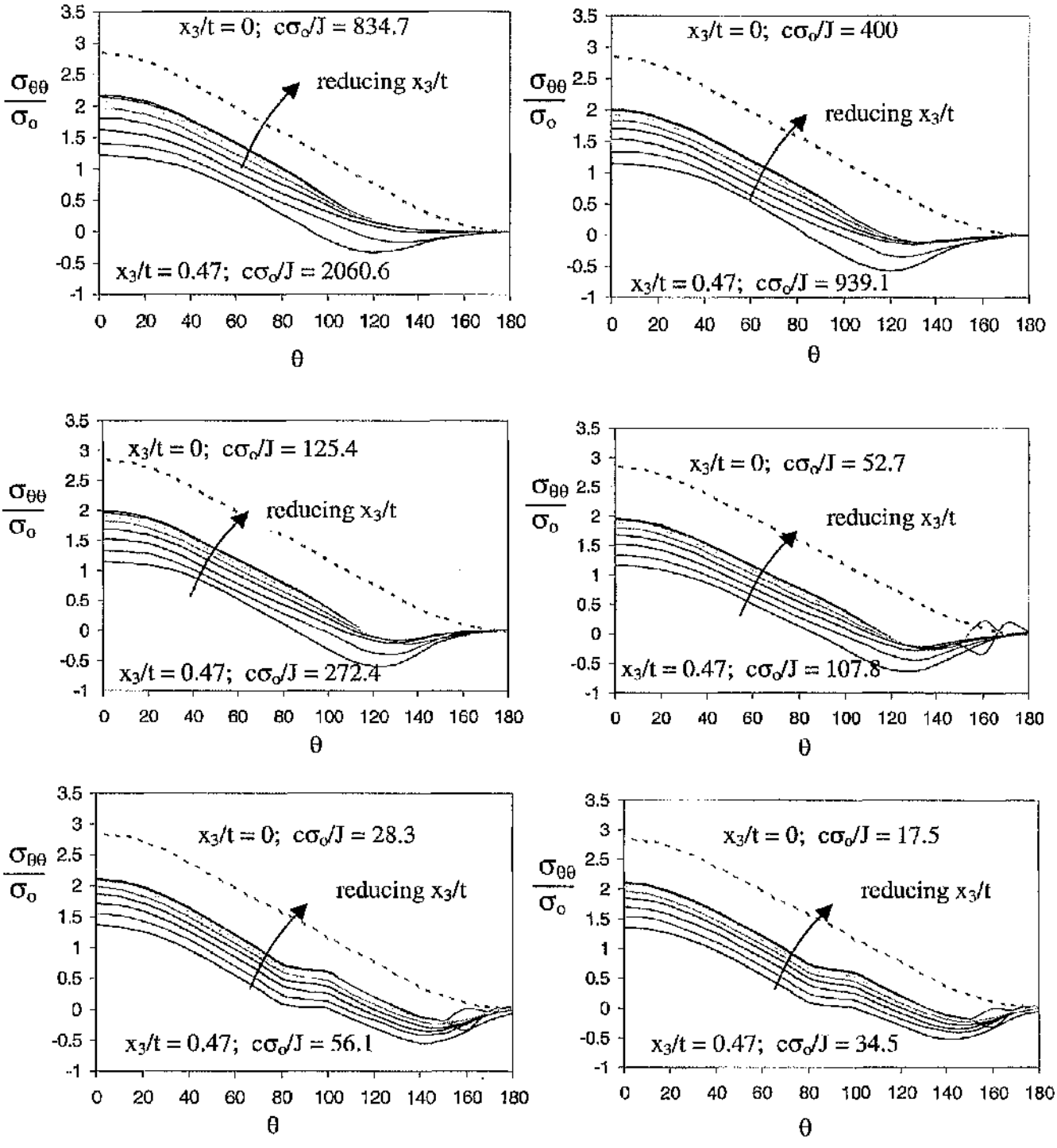


Figure 5.139: The hoop stress $\sigma_{\theta\theta}$ for a CCP specimen B/(W-a) = 0.1 through the thickness. The broken line determined in a boundary layer formulation indicates the two-dimensional plane strain field for $\sigma_{\theta\theta}$.

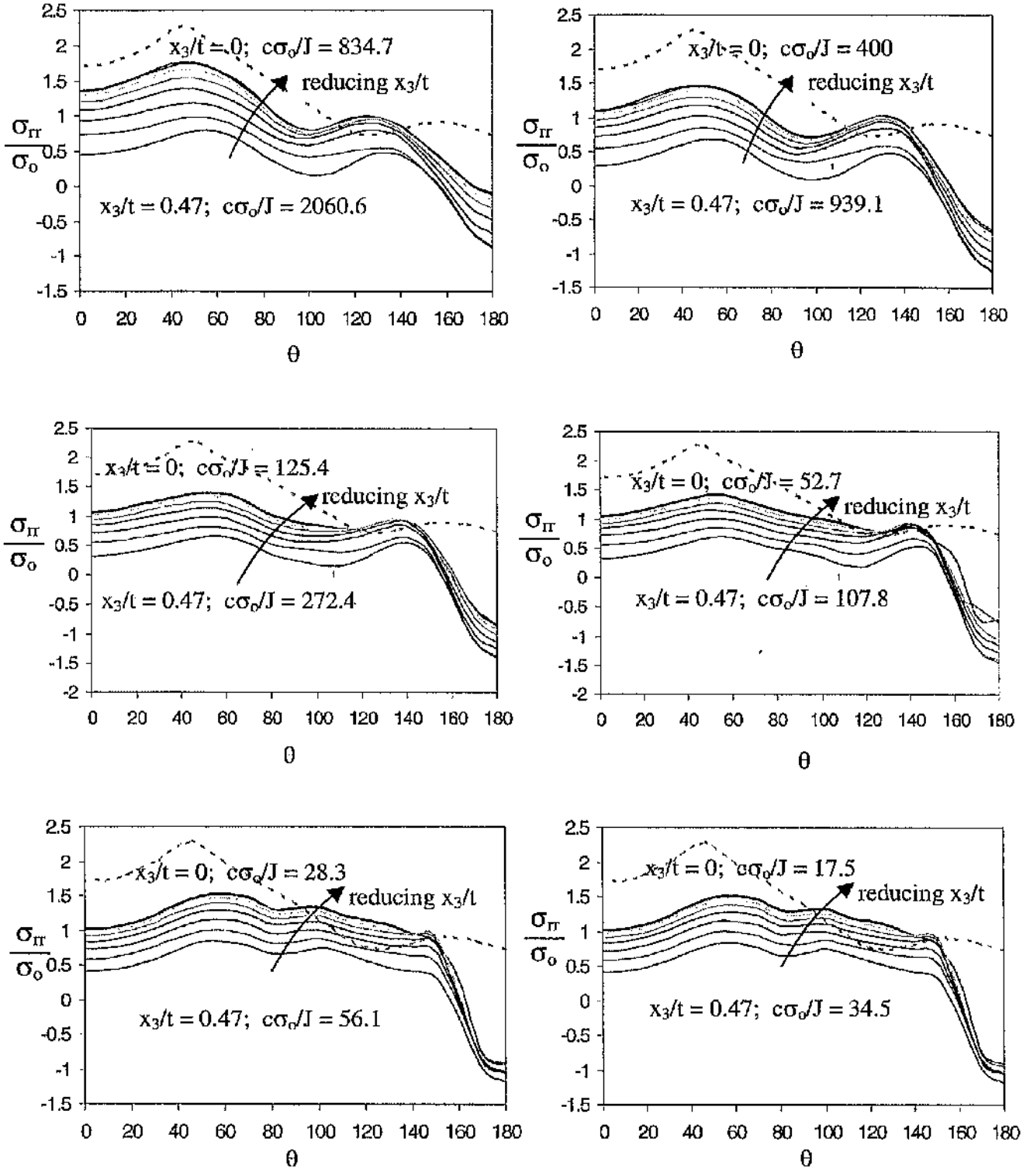


Figure 5.140: The radial stress $\sigma_{rr}$ for a CCP specimen B/(W-a) = 0.1 through the thickness. The broken line determined in a boundary layer formulation indicates the two-dimensional plane strain field for $\sigma_{rr}$.

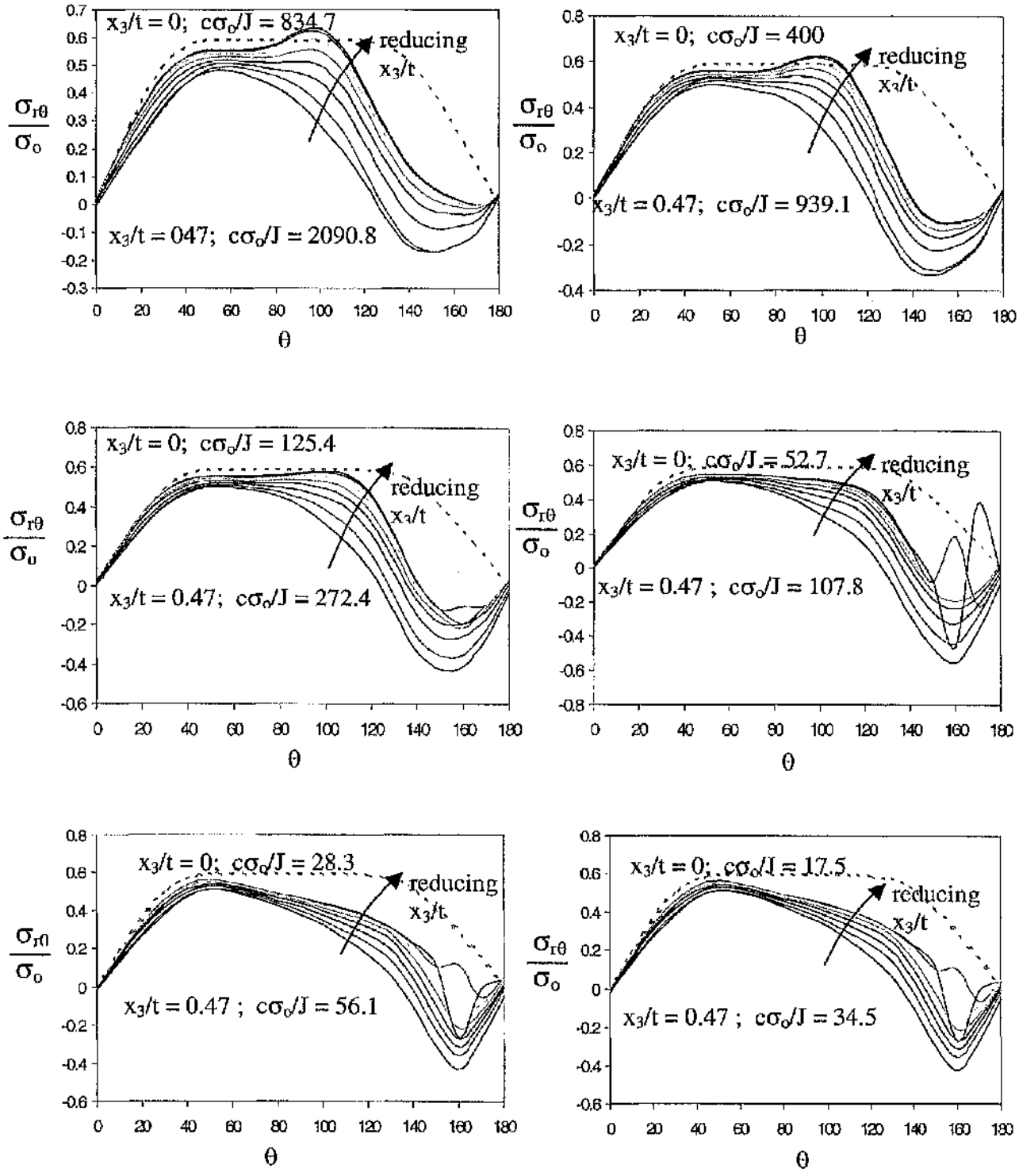


Figure 5.141: The shear stress $\sigma_{r\theta}$ for a CCP specimen B/(W-a) = 0.1 through the thickness. The broken line determined in a boundary layer formulation indicates the two-dimensional plane strain field for $\sigma_{r\theta}$.

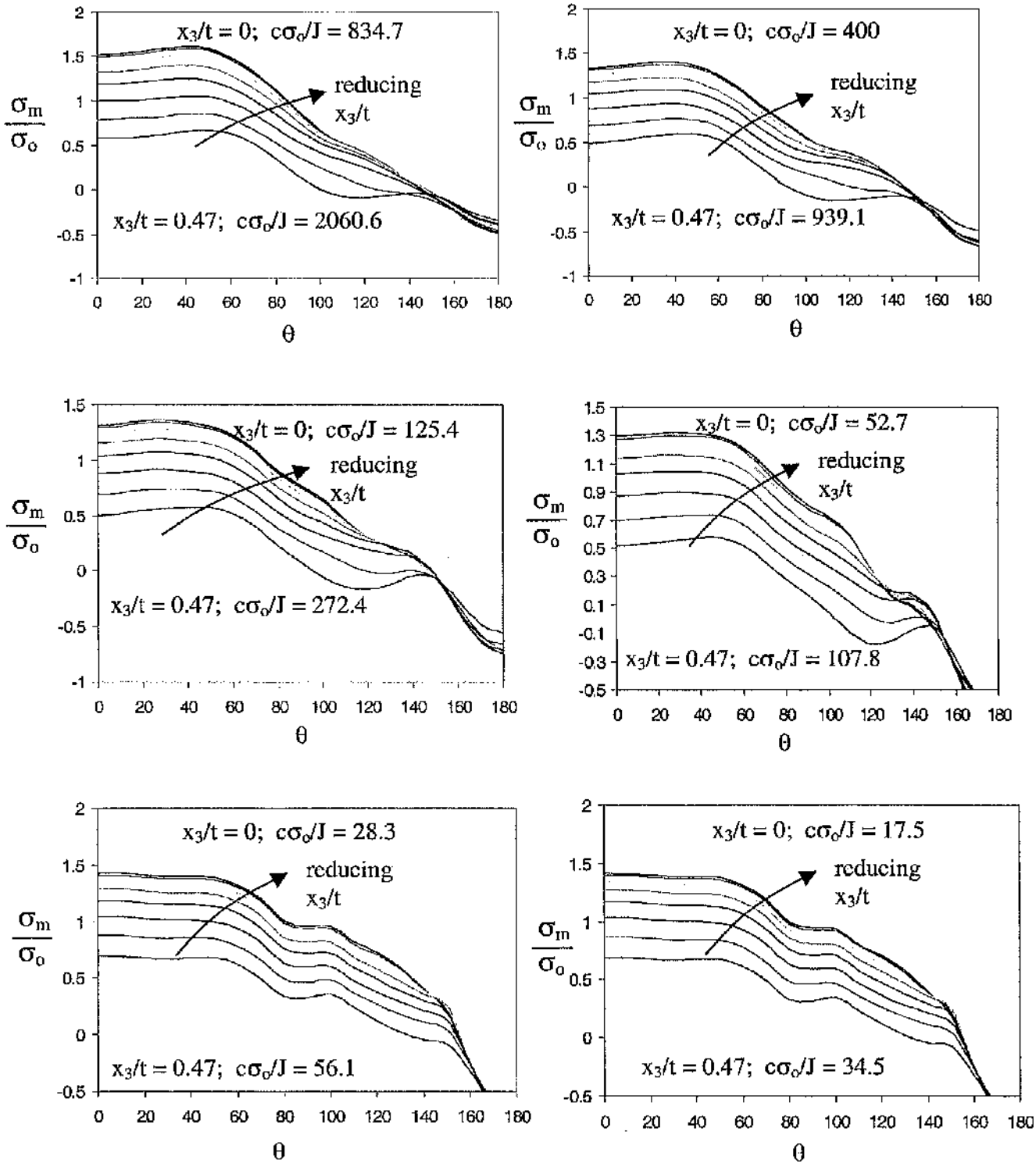


Figure 5.142: The mean stress $\sigma_m$ for a CCP specimen B/(W-a) = 0.1 through the thickness. The broken line determined in a boundary layer formulation indicates the two-dimensional plane strain field for $\sigma_m$.

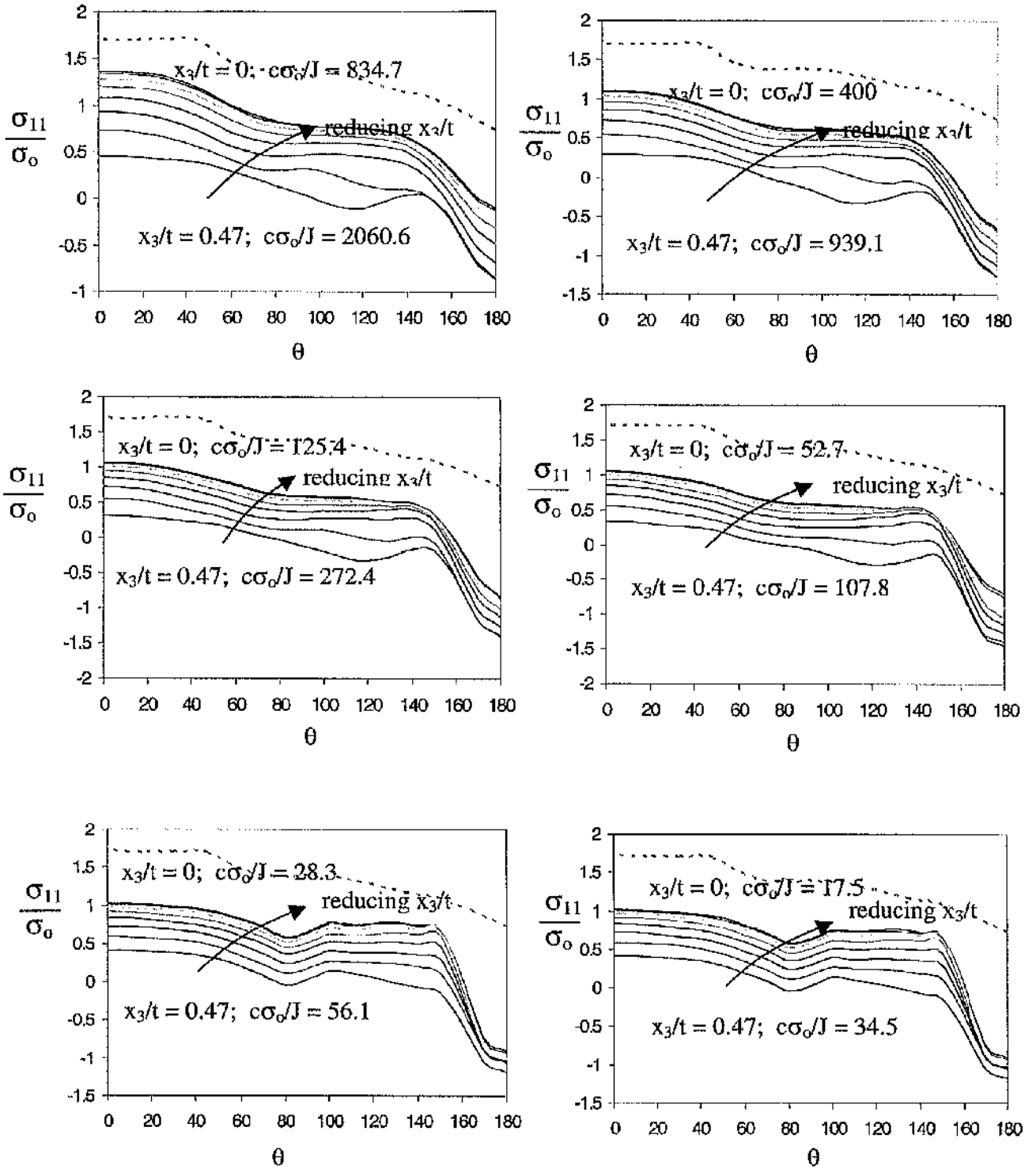


Figure 5.143: The direct stress $\sigma_{11}$ for a CCP specimen B/(W-a) = 0.1 through the thickness. The broken line determined in a boundary layer formulation indicates the two-dimensional plane strain field for $\sigma_{11}$.

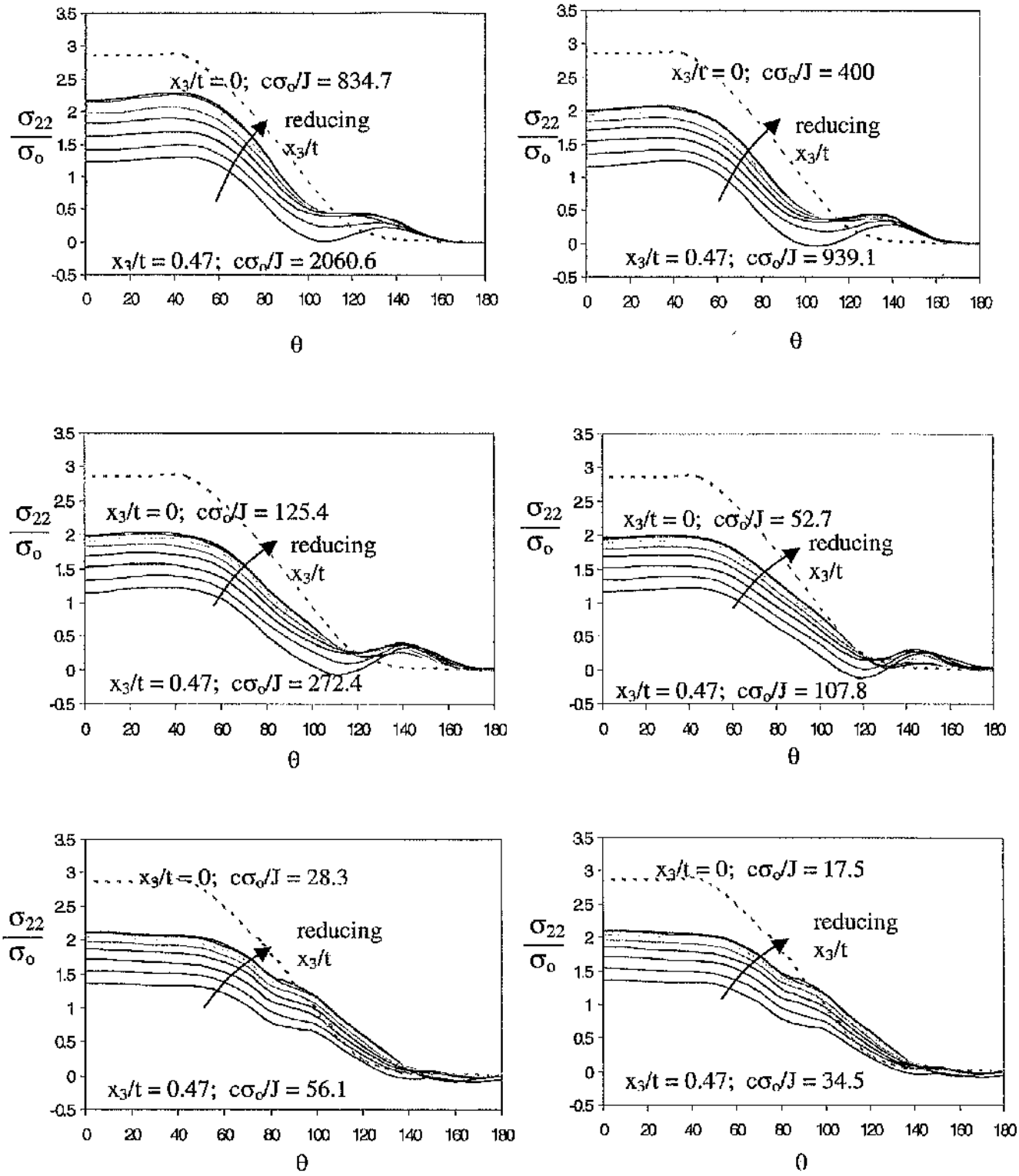


Figure 5.144: The direct stress $\sigma_{22}$ for a CCP specimen B/(W-a) = 0.1 through the thickness. The broken line determined in a boundary layer formulation indicates the two-dimensional plane strain field for $\sigma_{22}$.

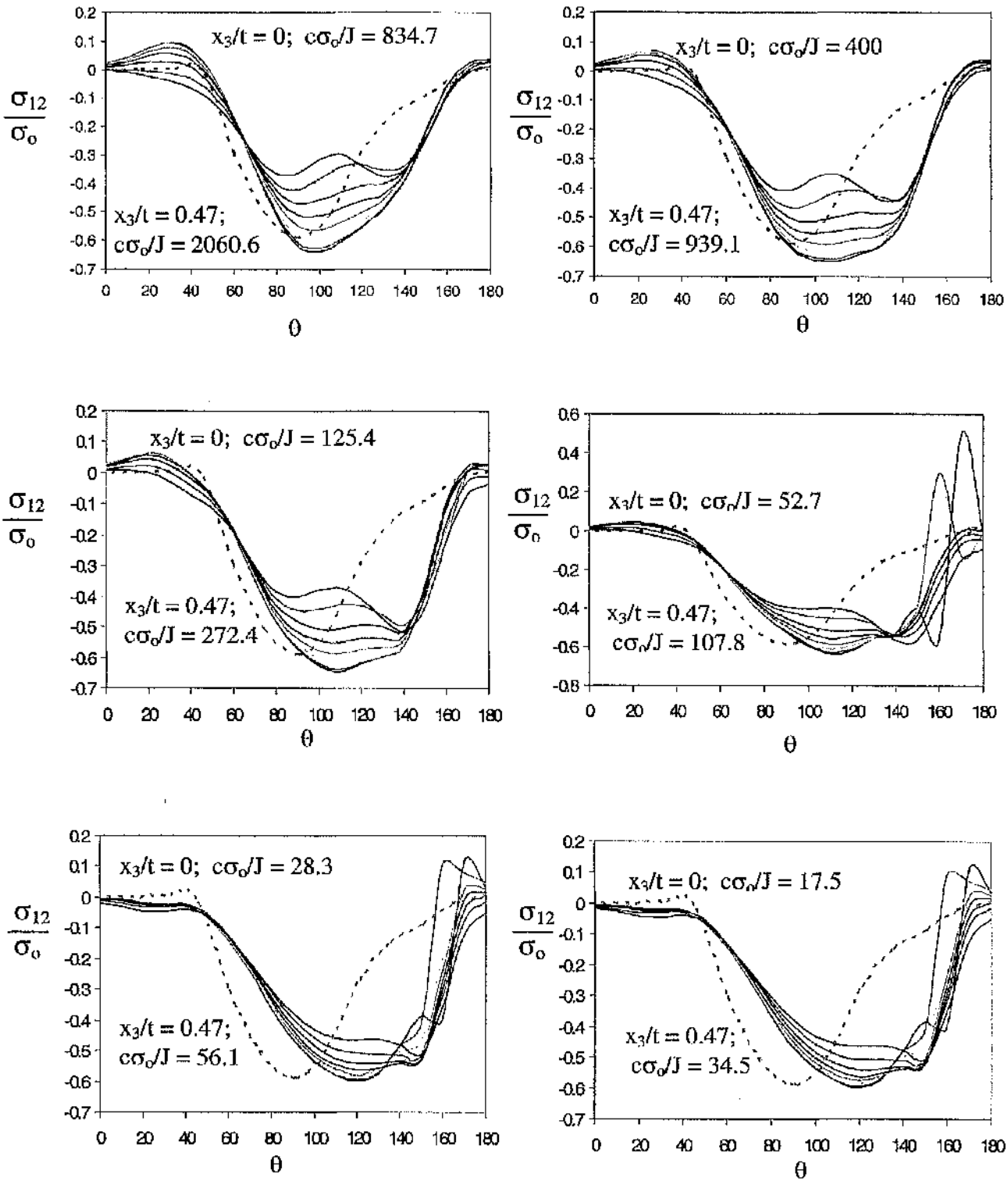


Figure 5.145: The shear stress $\sigma_{12}$ for a CCP specimen B/(W-a) = 0.1 through the thickness. The broken line determined in a boundary layer formulation indicates the two-dimensional plane strain field for $\sigma_{12}$.

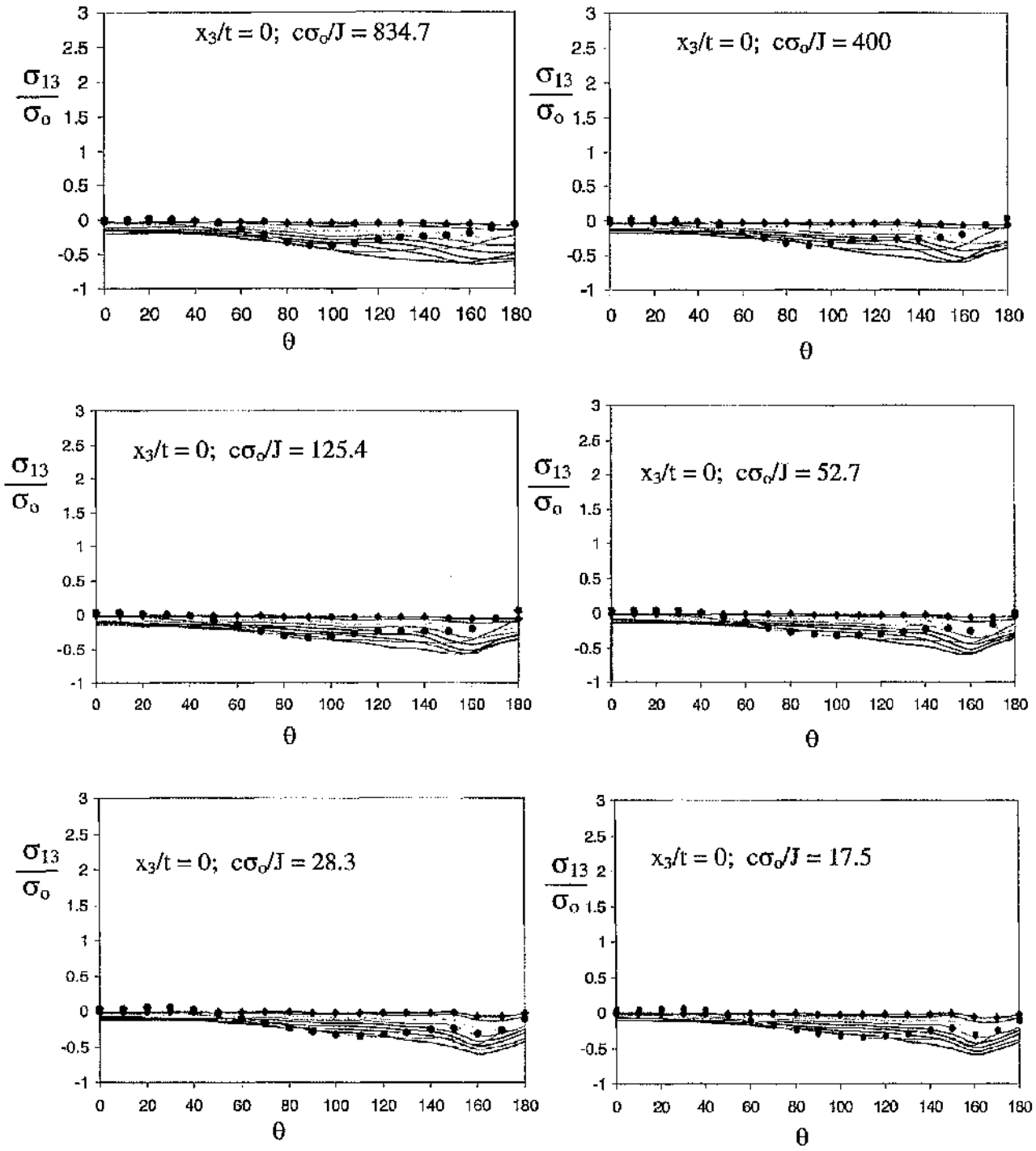


Figure 5.146: The shear stress $\sigma_{13}$ for a CCP specimen B/(W-a) = 0.1 through the thickness. The diamond and round markers indicate the midplane and the free surface fields.

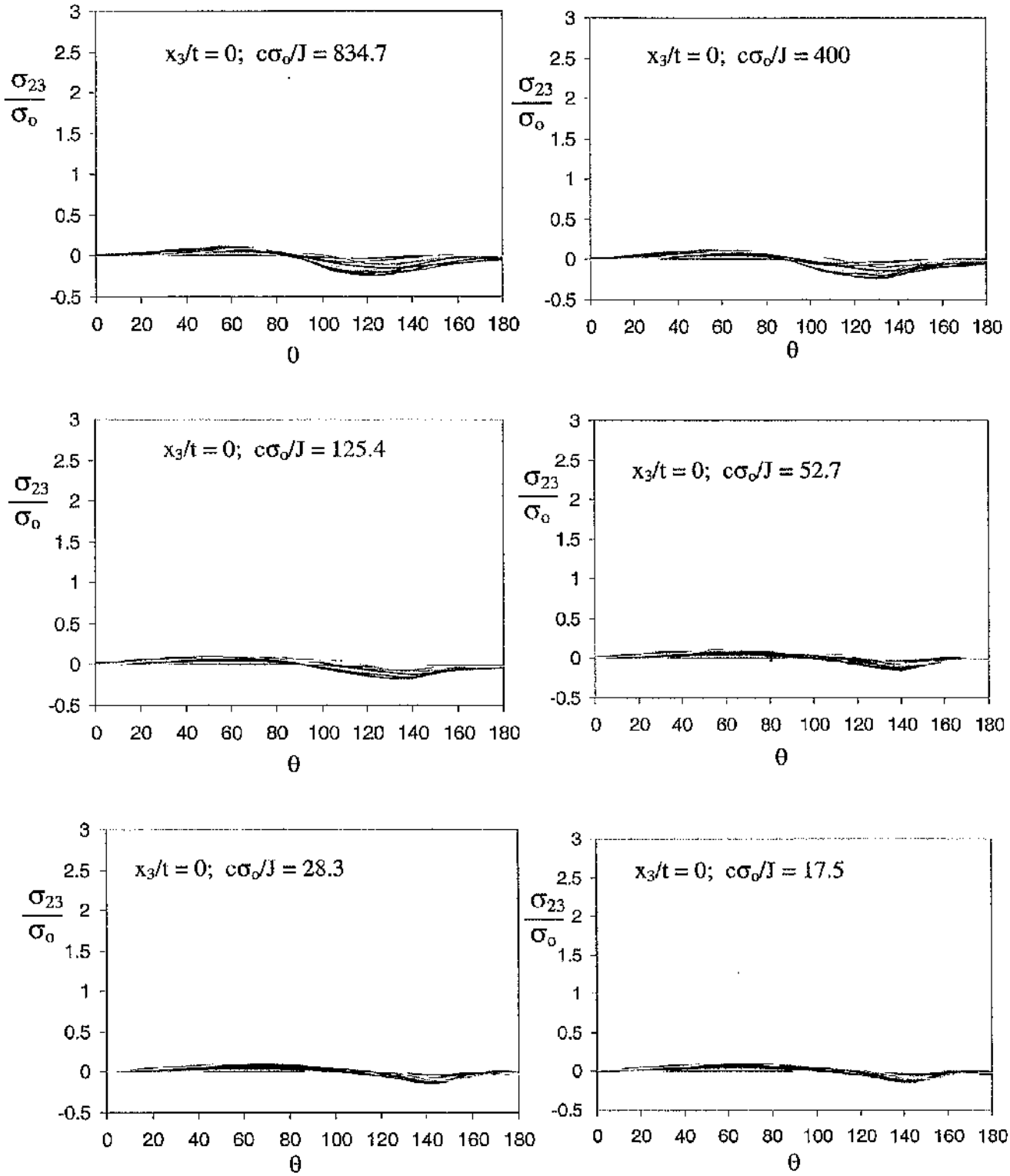


Figure 5.147: The shear stress $\sigma_{23}$ for a CCP specimen B/(W-a) = 0.1 through the thickness.

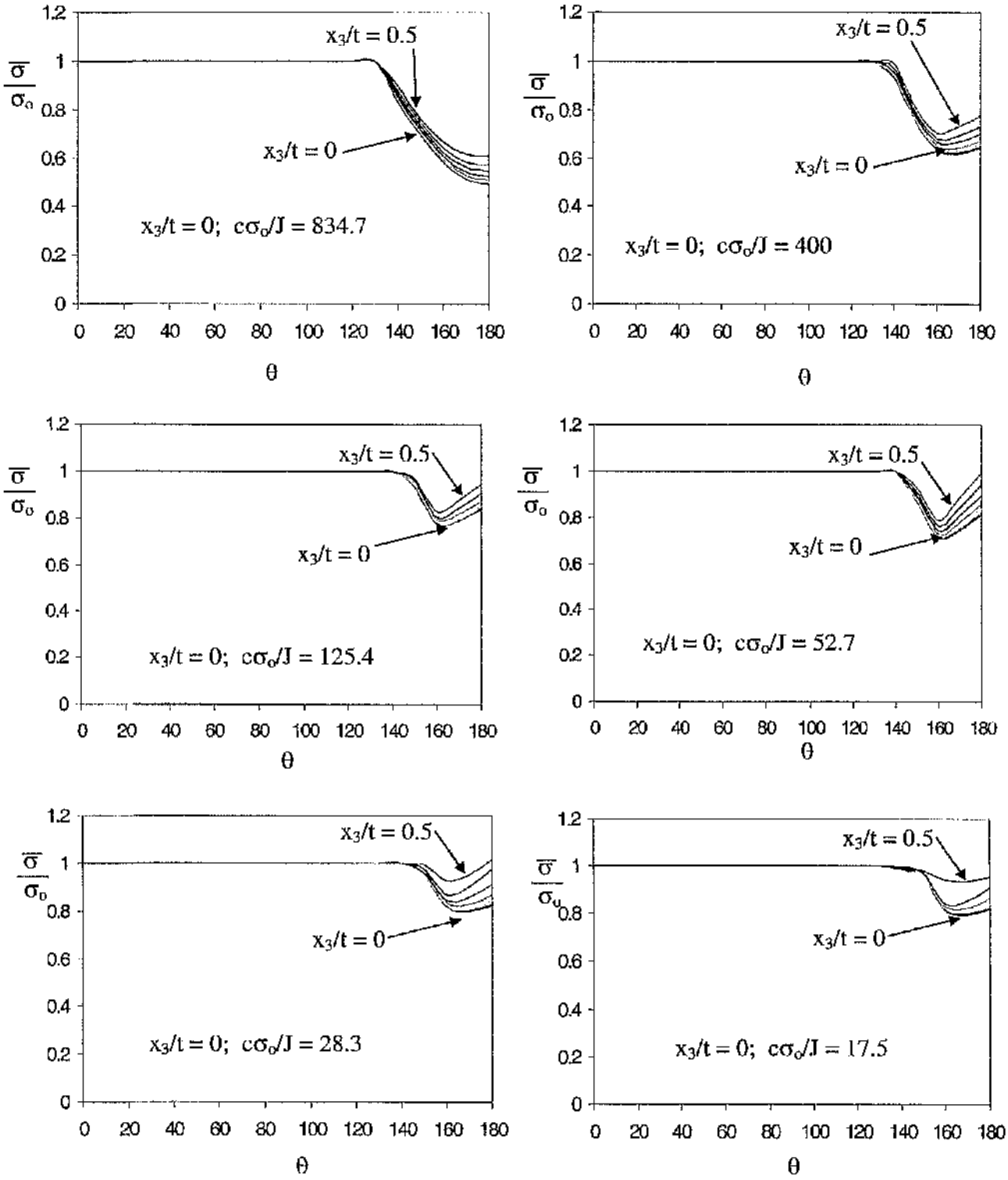


Figure 5.148: The Mises stress $\overline{\sigma}/\sigma_o$ for a CCP specimen B/(W-a) = 0.1 through the thickness.

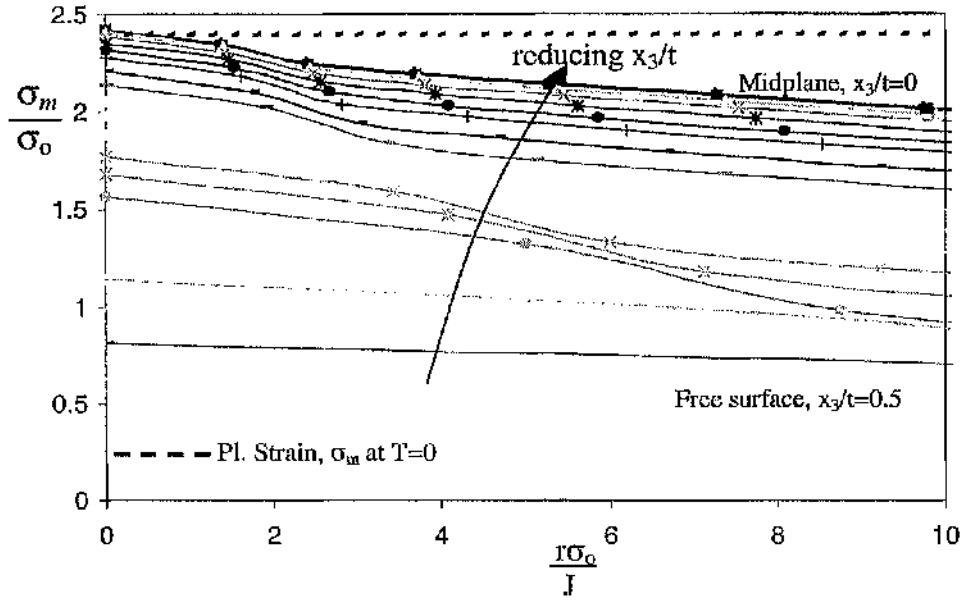


Figure 5.149: The mean stress ahead crack front from midplane to free surface at load $\Omega_{far}$ = 3 between $r\sigma_o/J = 0$ and 10 using a boundary layer formulation.

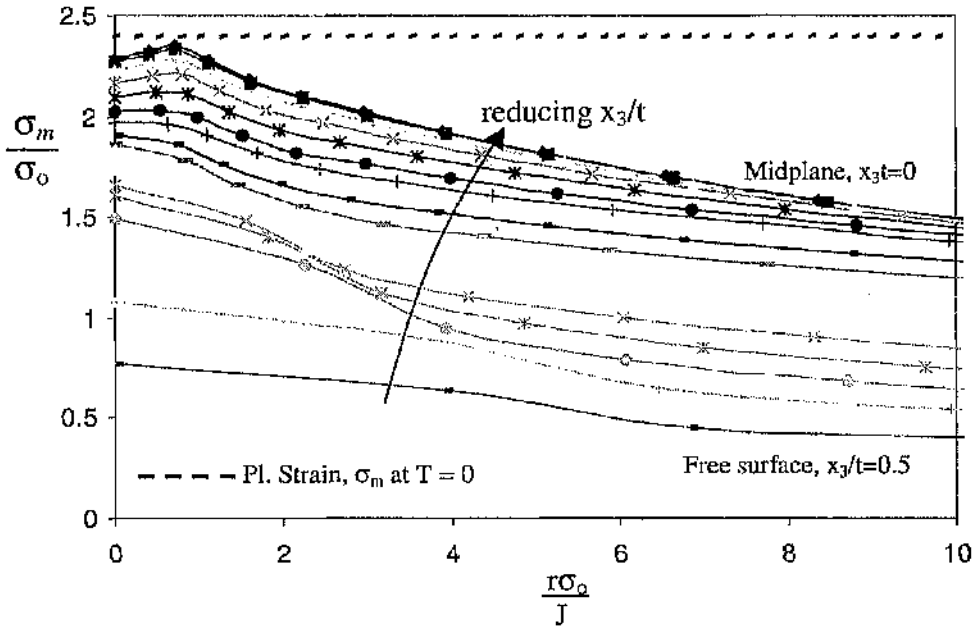


Figure 5.150: The mean stress ahead crack front from midplane to free surface at load $\Omega_{far}$ = 8 between $r\sigma_o/J = 0$ and 10 using a boundary layer formulation.

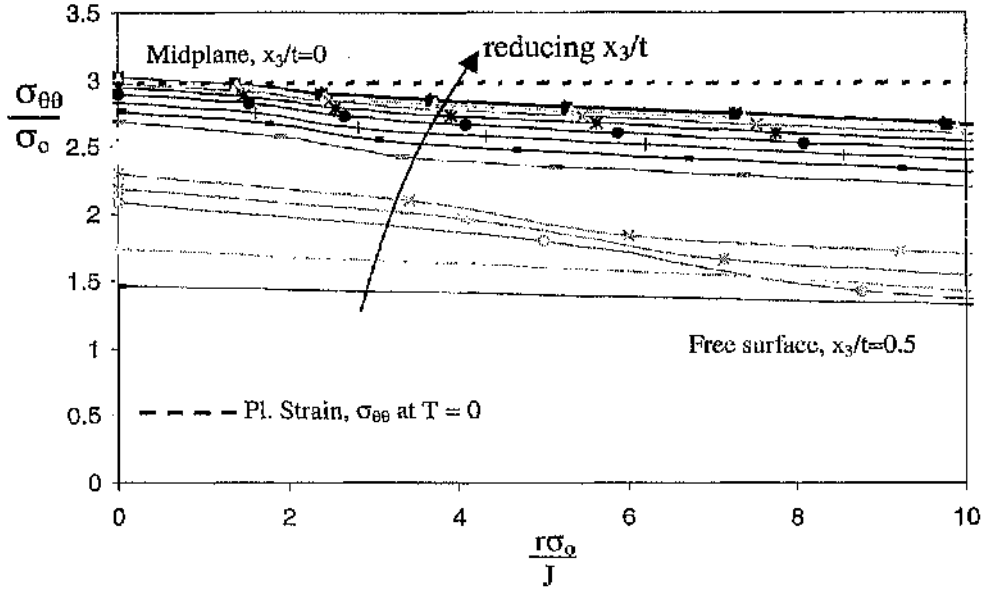


Figure 5.151: The hoop stress ahead crack front from midplane to free surface at load $\Omega_{far}$ = 3 between $r\sigma_o/J = 0$ and 10 using a boundary layer formulation.

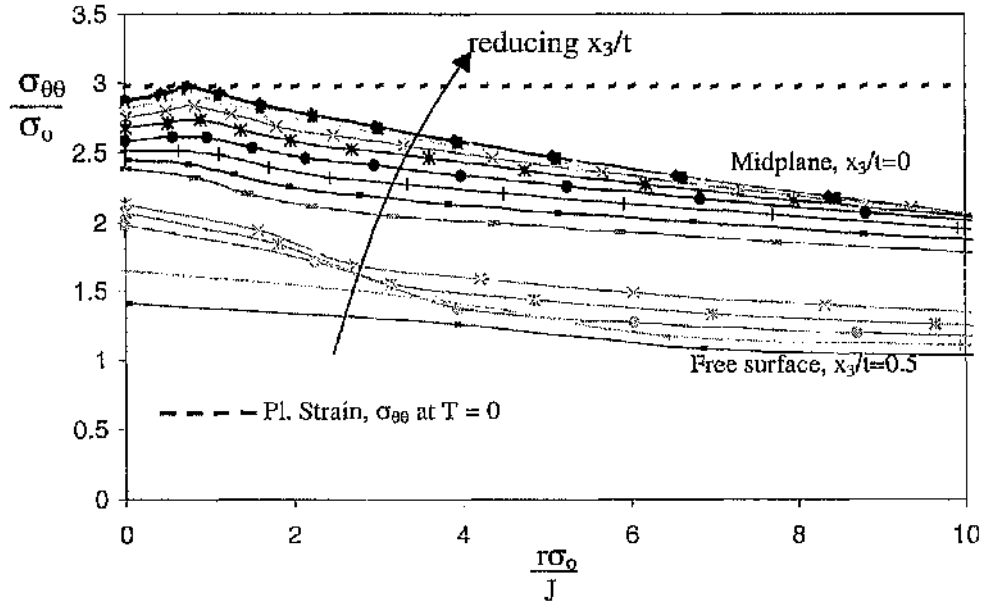


Figure 5.152: The hoop stress ahead crack front from midplane to free surface at load $\Omega_{far}$ = 8 between $r\sigma_o/J = 0$ and 10 using a boundary layer formulation.

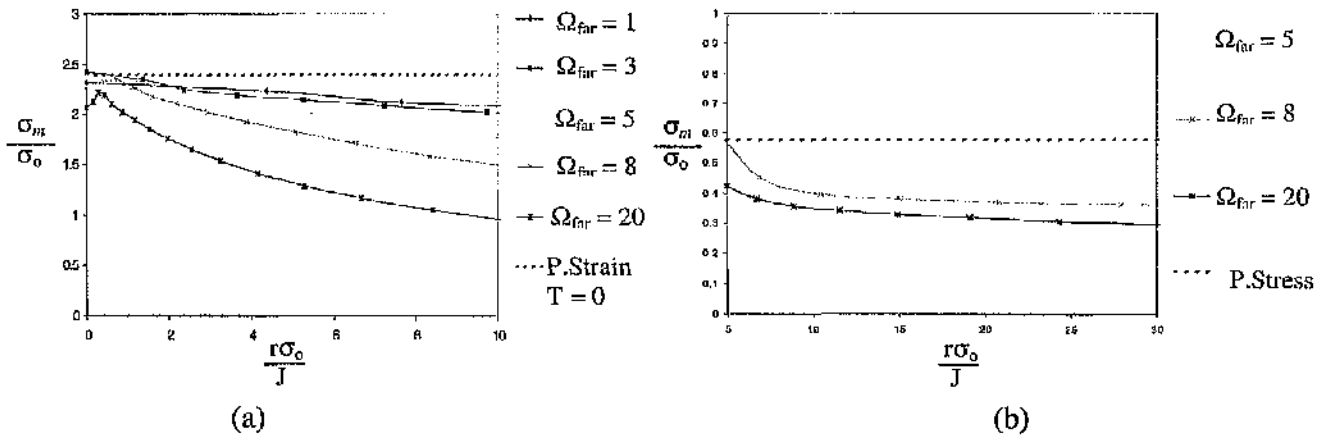


Figure 5.153: The mean stress at (a) midplane and (b) free surface for load $\Omega_{far}$ = 1, 3, 5, 8, 20 for boundary layer formulation. Broken lines indicate two-dimensional plane strain in (a) and plane stress in (b).

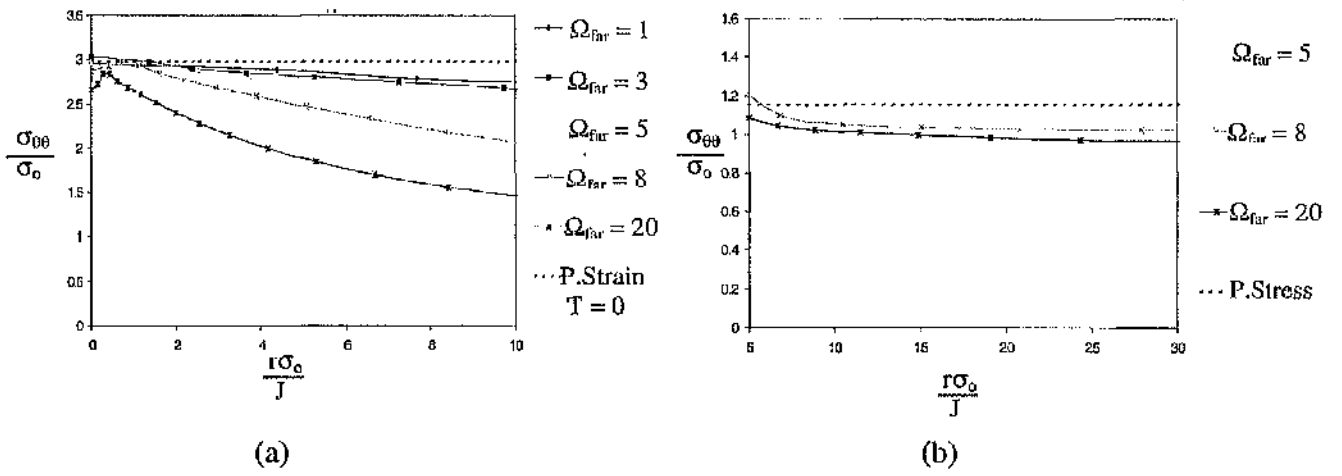


Figure 5.154: The hoop stress at (a) midplane and (b) free surface for load $\Omega_{far}$ = 1, 3, 5, 8, 20 for boundary layer formulation. Broken lines indicate two-dimensional plane strain in (a) and plane stress in (b).

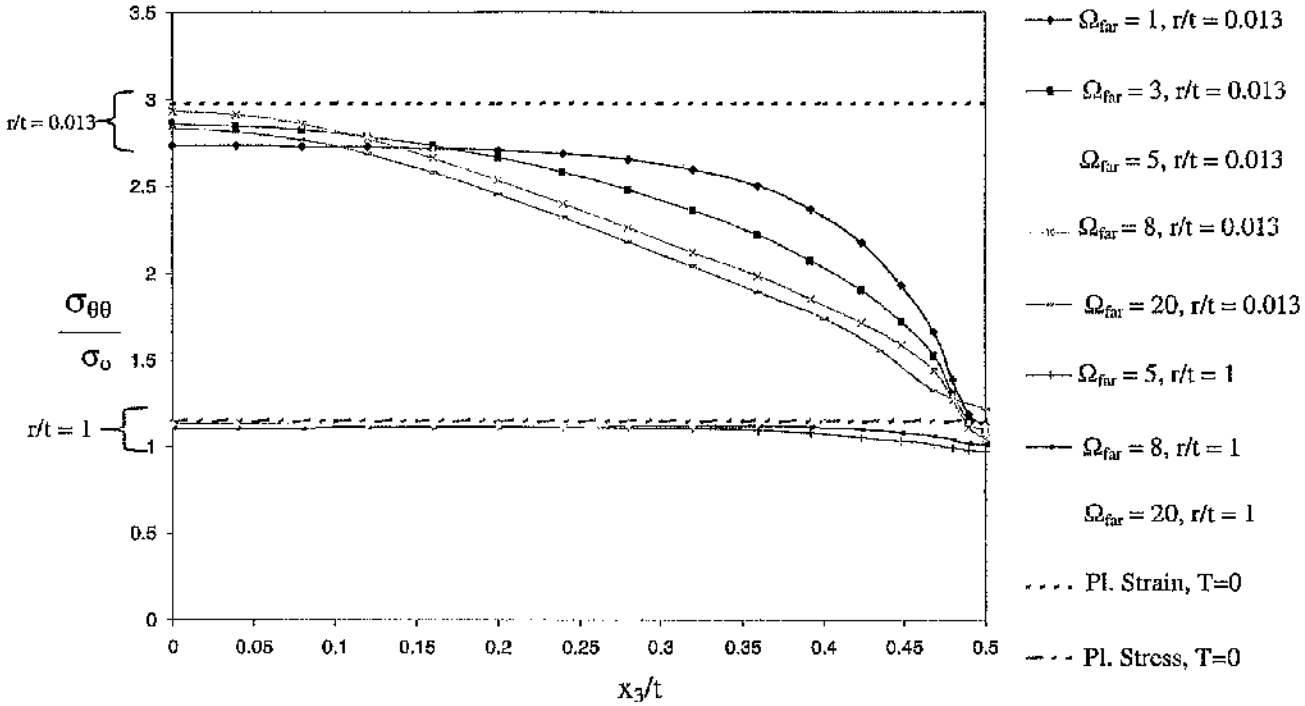


Figure 5.155: Comparison of hoop stress ahead crack front $\theta = 0^\circ$ at radial distance r/t = 0.013 for load level $\Omega_{far}$ 1, 3, 5, 8, 20 and r/t = 1 for load level $\Omega_{far}$ 5, 8, 20 using boundary layer formulation. The broken lines indicate a two-dimensional plane strain and plane stress.

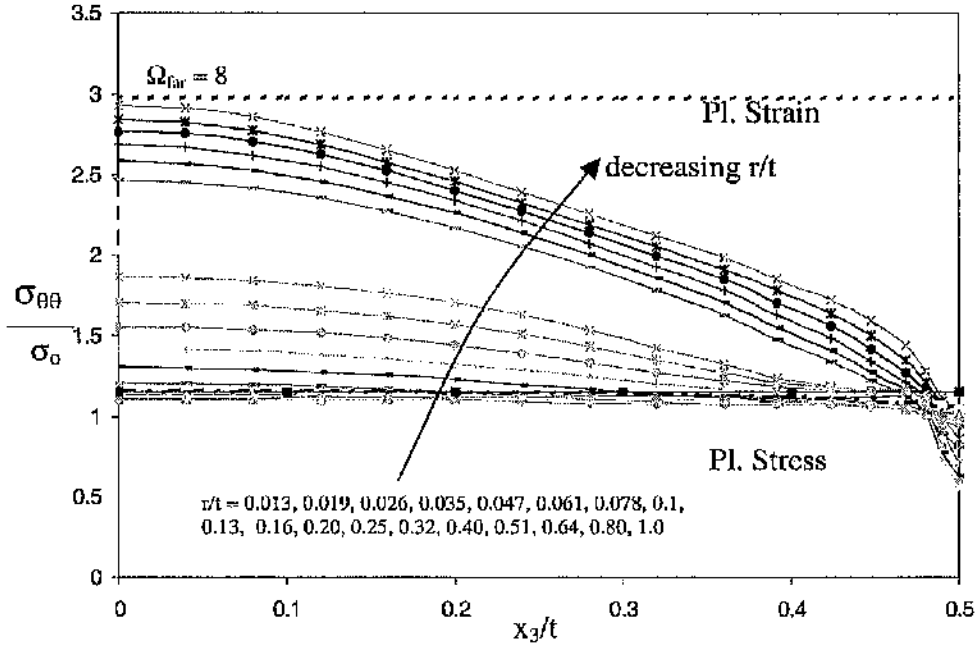


Figure 5.156: Through thickness variation of opening stress/hoop stress ahead crack front $\theta = 0^\circ$ at various radial distances for load level $\Omega_{far} = 8$ using boundary layer formulation. Broken lines indicate two-dimensional plane strain and plane stress.

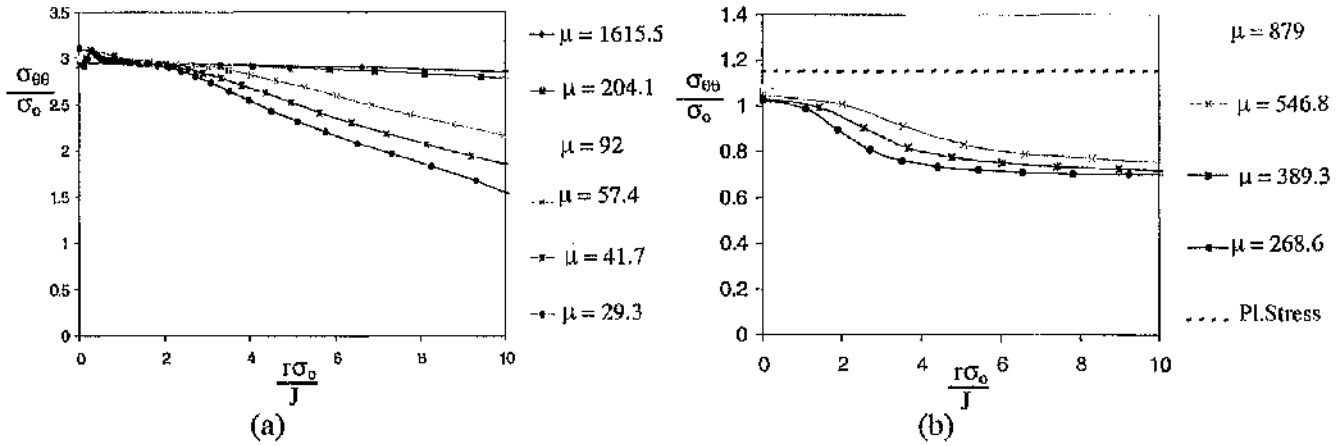


(a) (b)

Figure 5.157: The hoop stress ahead crack front from at (a) the midplane and (b) the free surface for SENB B/(W-a) = 1.

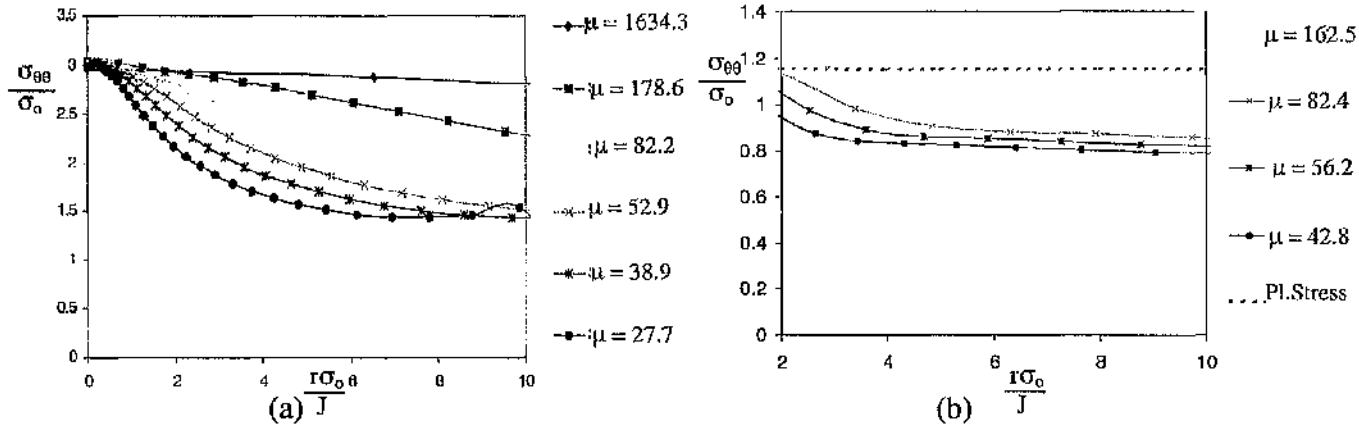


(a) (b)

Figure 5.158: The hoop stress ahead crack front from at (a) the midplane and (b) the free surface for SENB B/(W-a) = 0.5.

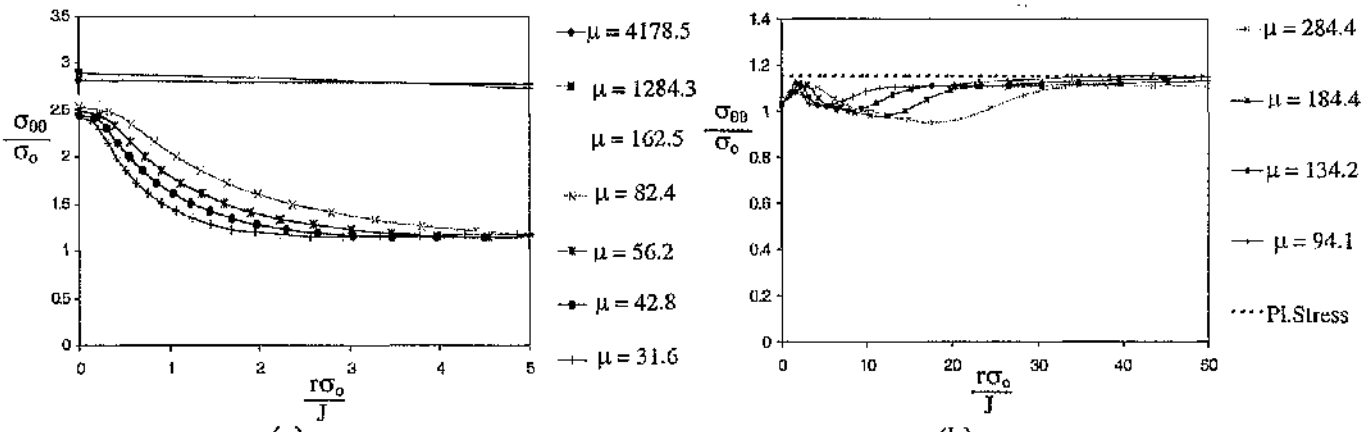


(a) (b)

Figure 5.159: The hoop stress ahead crack front from at (a) the midplane and (b) the free surface for SENB B/(W-a) = 0.1.

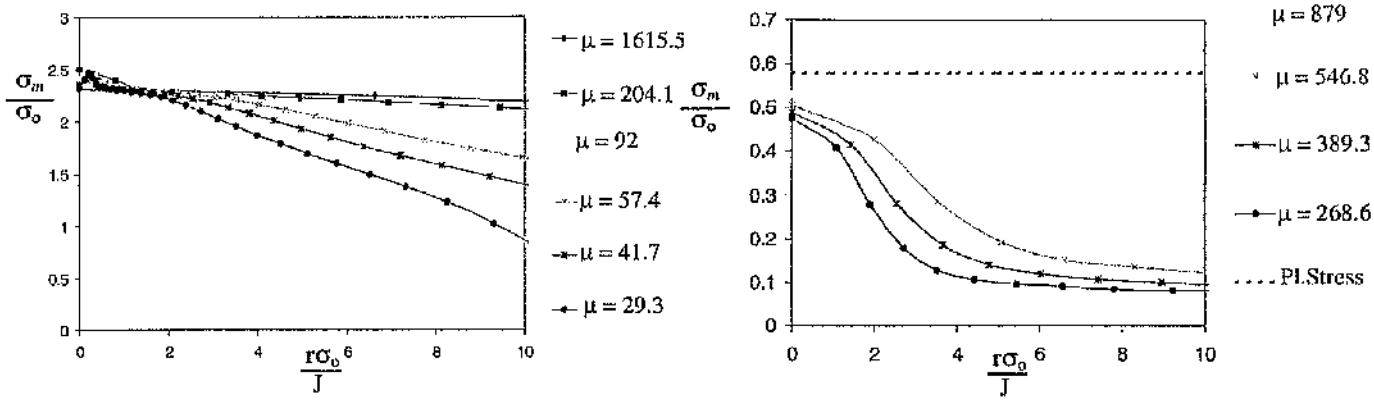


(a) (b)

Figure 5.160: The mean stress ahead crack front for SENB B/(W-a) = 1, at (a) the midplane and (b) the free surface at increasing load levels.

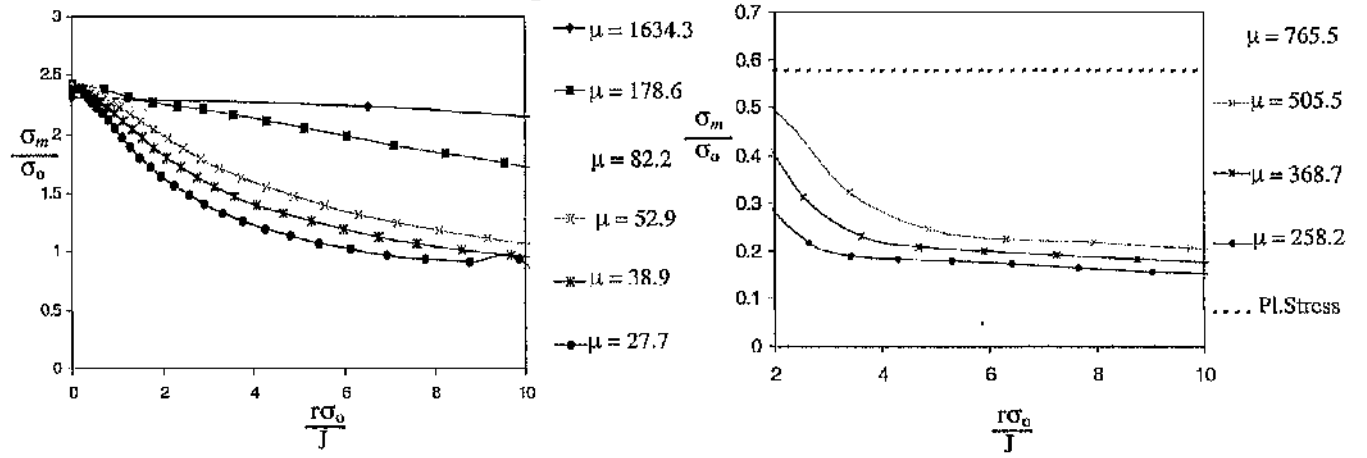


(a) (b)

Figure 5.161: The mean stress ahead crack front for SENB B/(W-a) = 0.5, at (a) the midplane and (b) the free surface at increasing load levels.

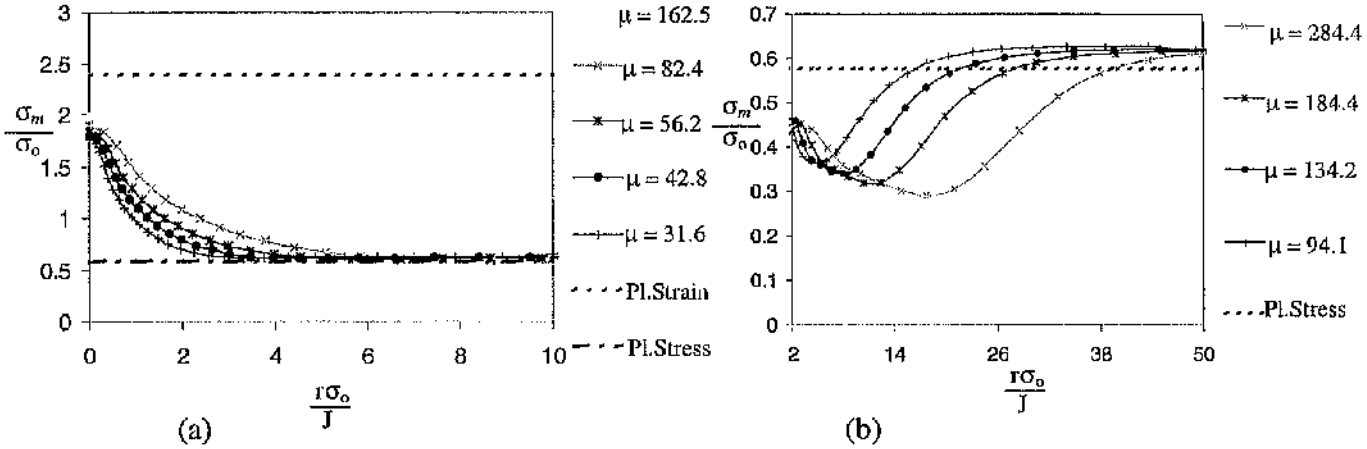


(a) (b)

Figure 5.162: The mean stress ahead crack front for SENB B/(W-a) = 0.1, at (a) the midplane and (b) the free surface at increasing load levels.

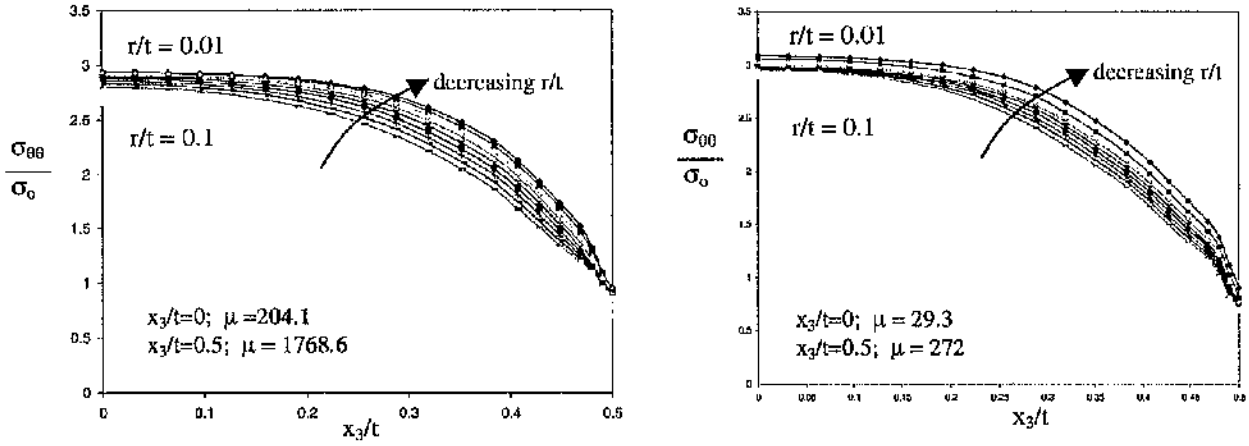


(a) (b)

Figure 5.163: The hoop stress ahead crack front at $\theta = 0^o$ at load (a) small scale yielding and (b) full plasticity for SENB B/(W-a) = 1.

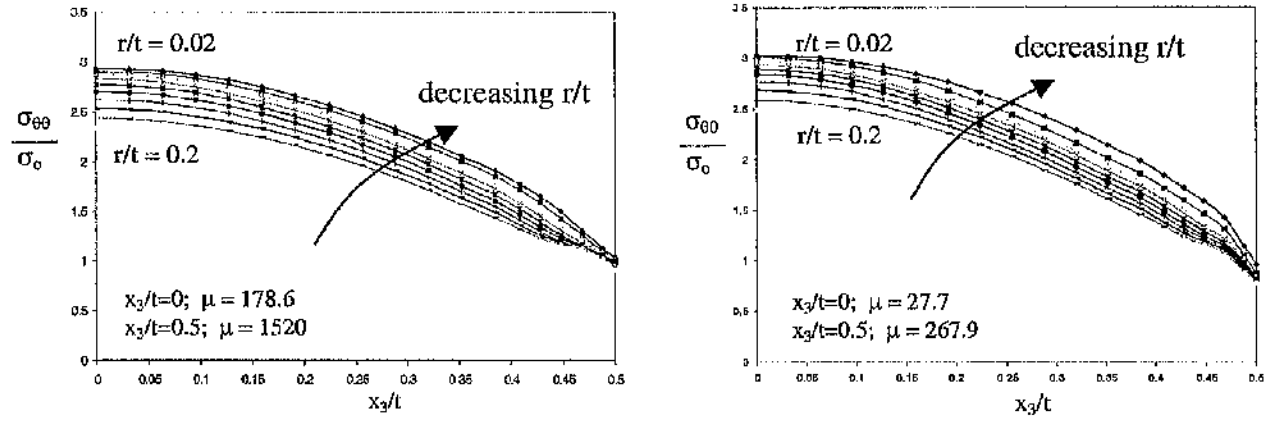


(a) (b)

Figure 5.164: The hoop stress ahead crack front at $\theta = 0^o$ at load (a) small scale yielding and (b) full plasticity for SENB B/(W-a) = 0.5.

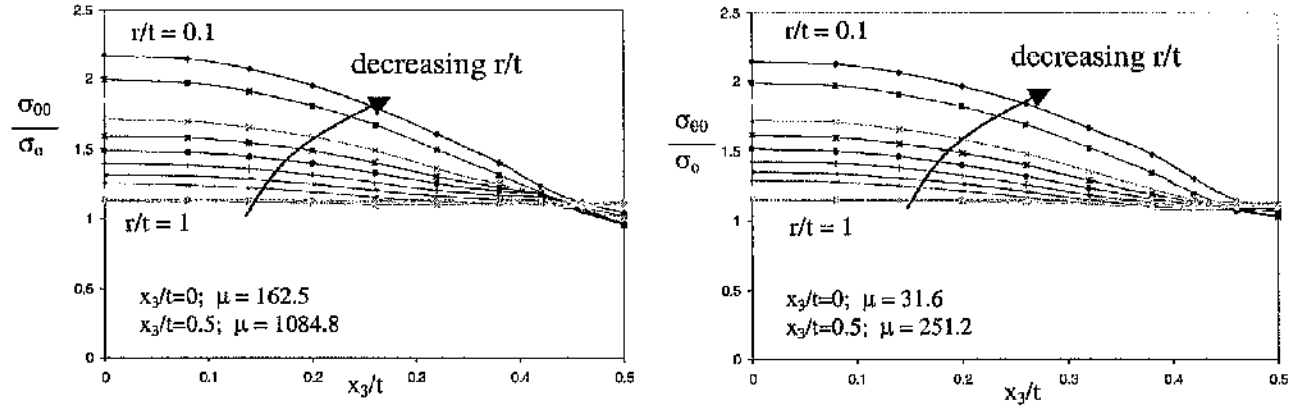


(a) (b)

Figure 5.165: The hoop stress ahead crack front at $\theta = 0^o$ at load (a) small scale yielding and (b) full plasticity for SENB B/(W-a) = 0.1.

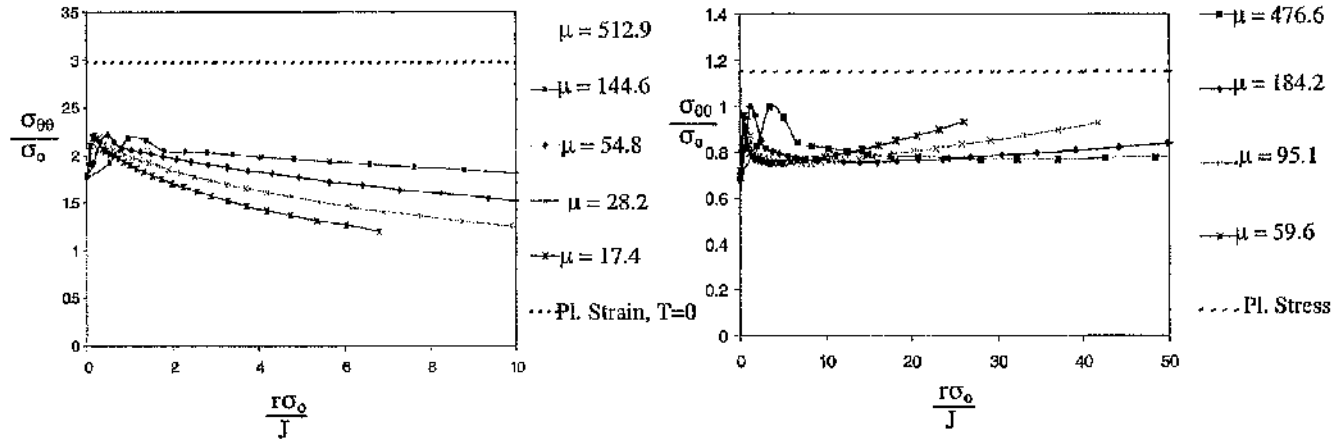


(a) (b)

Figure 5.166: The hoop stress ahead the crack front at (a) the midplane and (b) the free surface at increasing load levels for a CCP specimen B/(W-a) = 1.

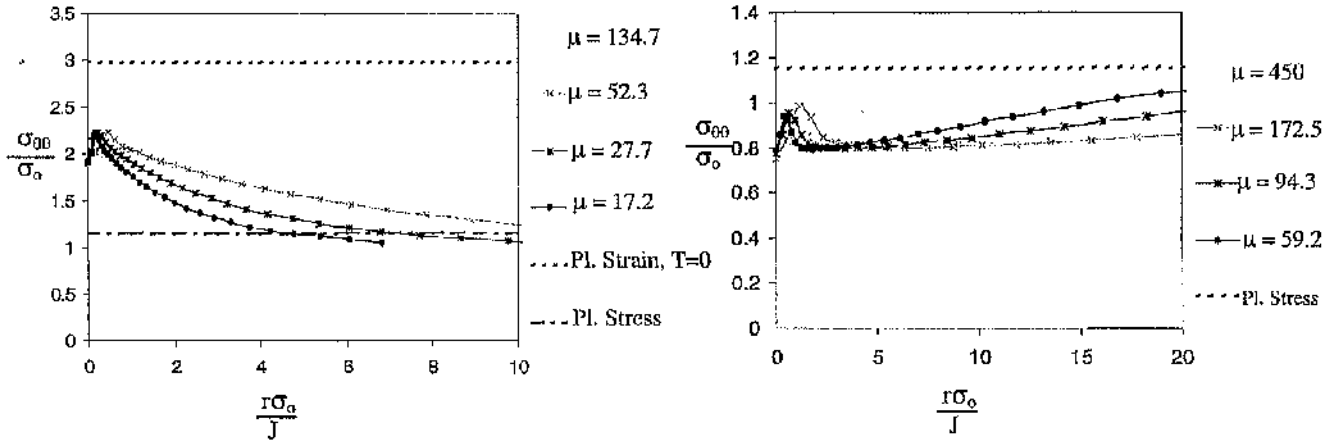


(a) (b)

Figure 5.167: The hoop stress ahead the crack front at (a) the midplane and (b) the free surface at increasing load levels for a CCP specimen B/(W-a) = 0.5.

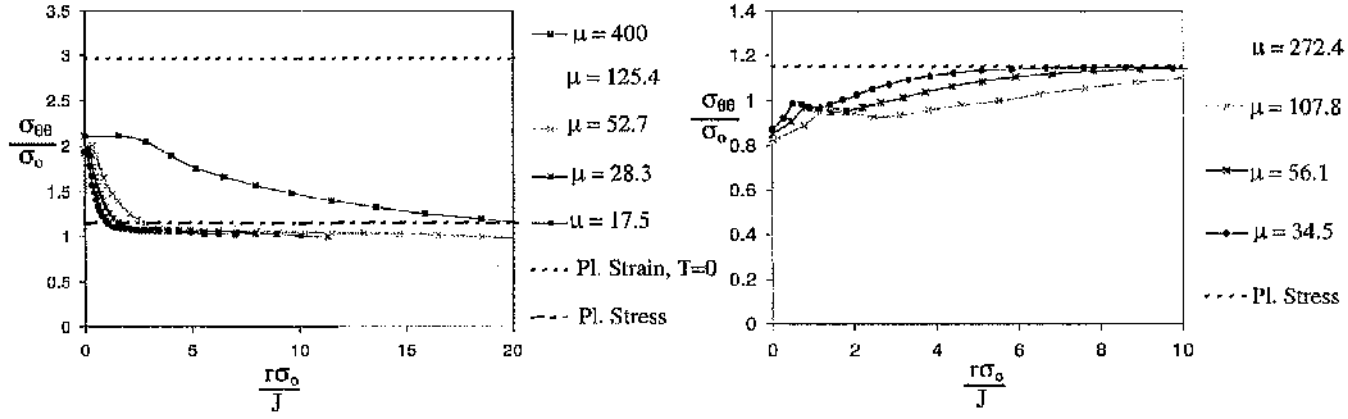


(a) (b)

Figure 5.168: The hoop stress ahead the crack front at (a) the midplane and (b) the free surface at increasing load levels for a CCP specimen B/(W-a) = 0.1.

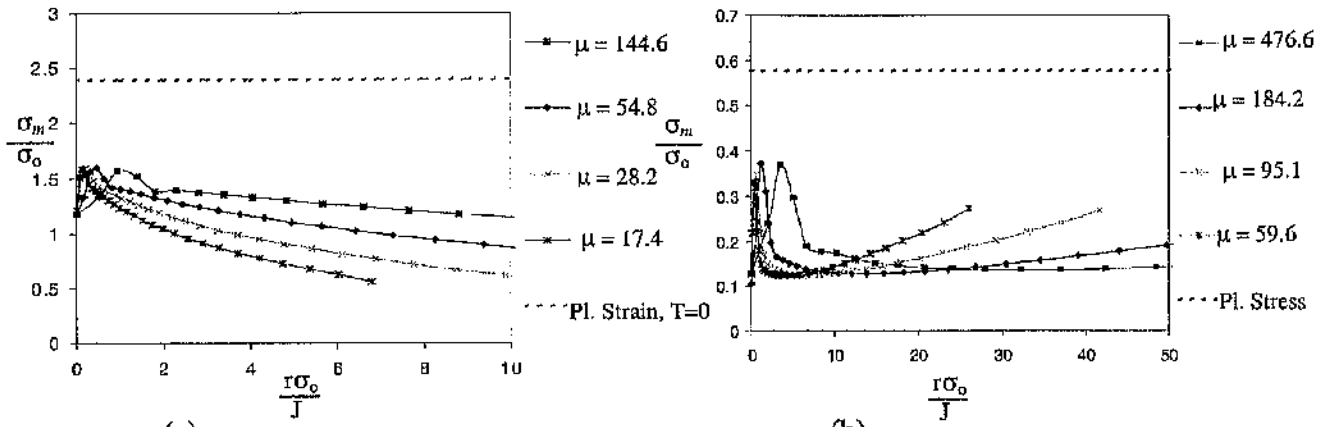


Figure 5.169: The mean stress ahead the crack front at (a) the midplane and (b) the free surface at increasing load levels for a CCP specimen B/(W-a) = 1.

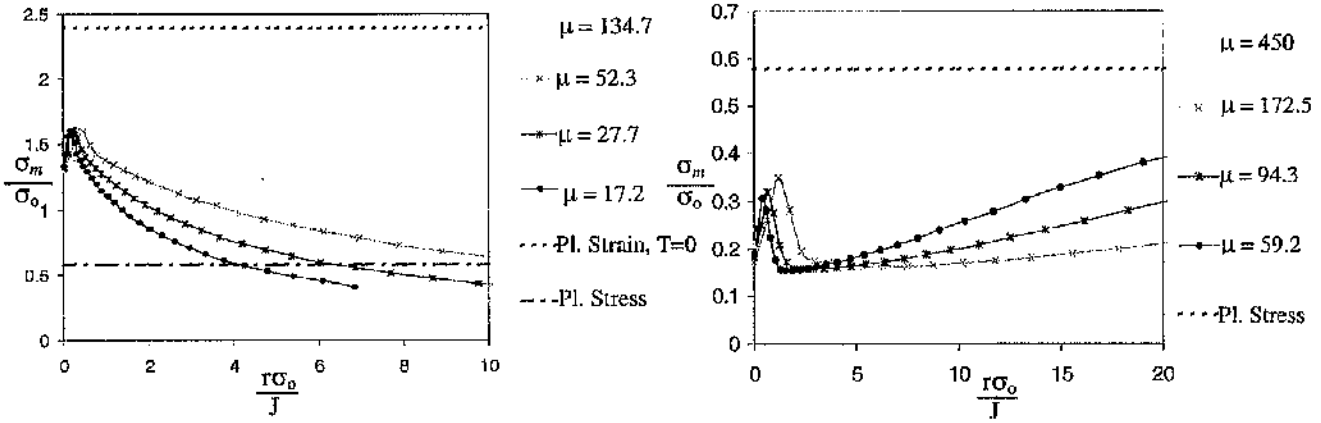


Figure 5.170: The mean stress ahead the crack front at (a) the midplane and (b) the free surface at increasing load levels for a CCP specimen B/(W-a) = 0.5.

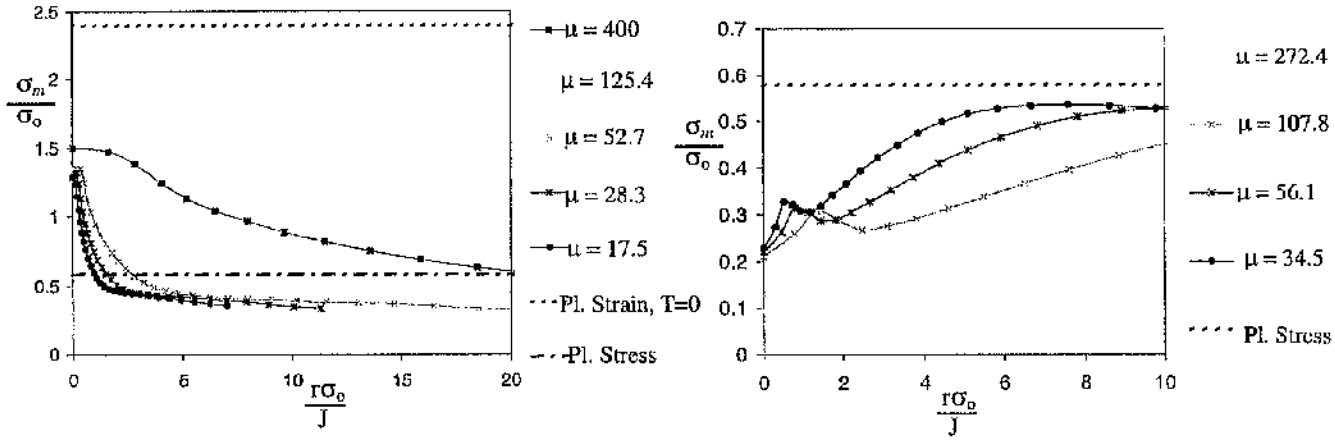


Figure 5.171: The mean stress ahead the crack front at (a) the midplane and (b) the free surface at increasing load levels for a CCP specimen B/(W-a) = 0.1.

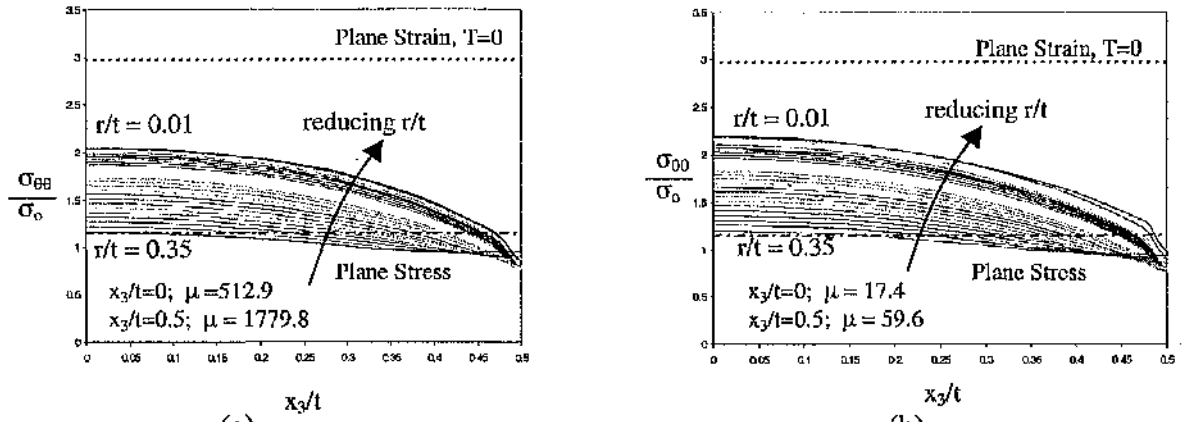


Figure 5.172: The hoop stress along the crack front at r/t = 0.01 to 0.35 at (a) small scale yielding to (b) full plasticity for a CCP specimen B/(W-a) = 1.

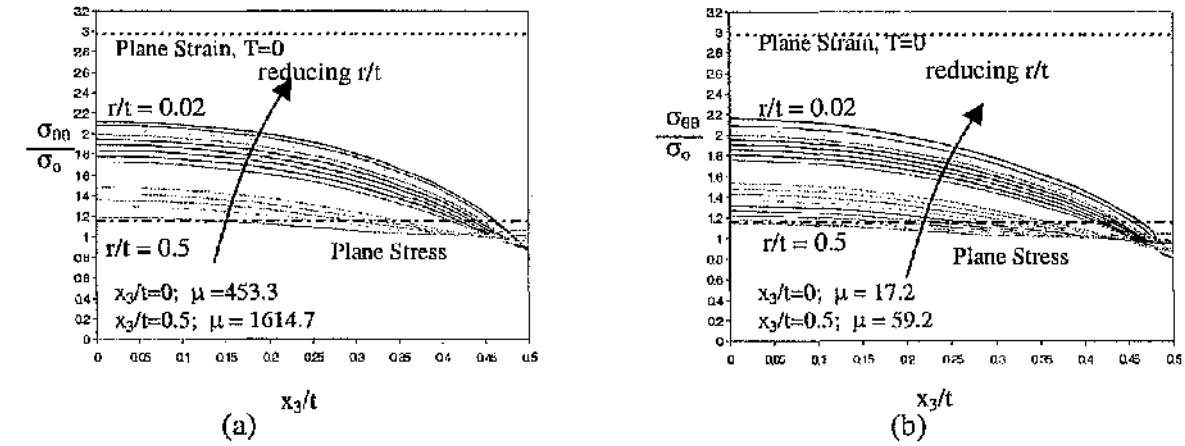


Figure 5.173: The hoop stress along the crack front at r/t = 0.02 to 0.5 at (a) small scale yielding to (b) full plasticity for a CCP specimen B/(W-a) = 0.5.

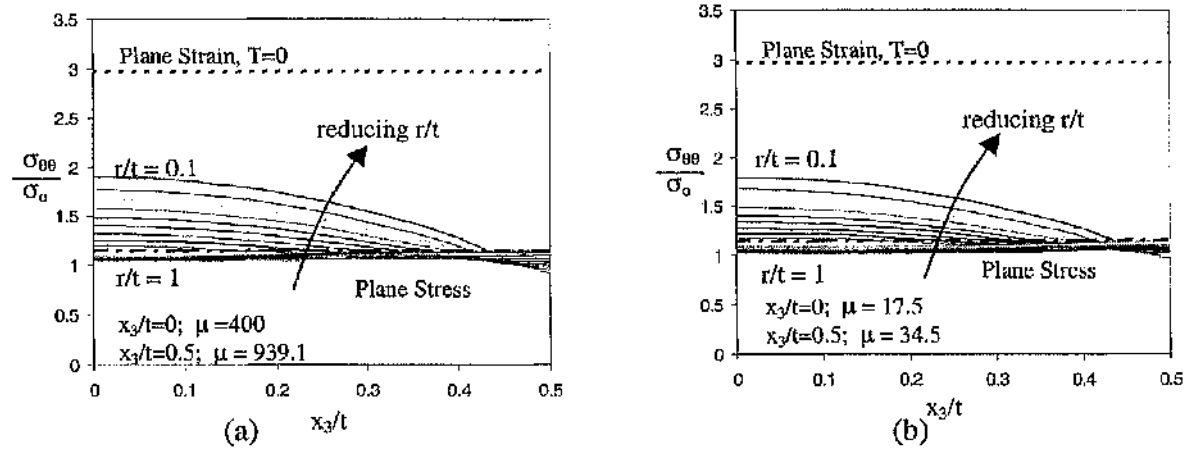


Figure 5.174: The hoop stress along the crack front at r/t = 0.1 to 1 at (a) small scale yielding to (b) full plasticity for a CCP specimen B/(W-a) = 0.1.

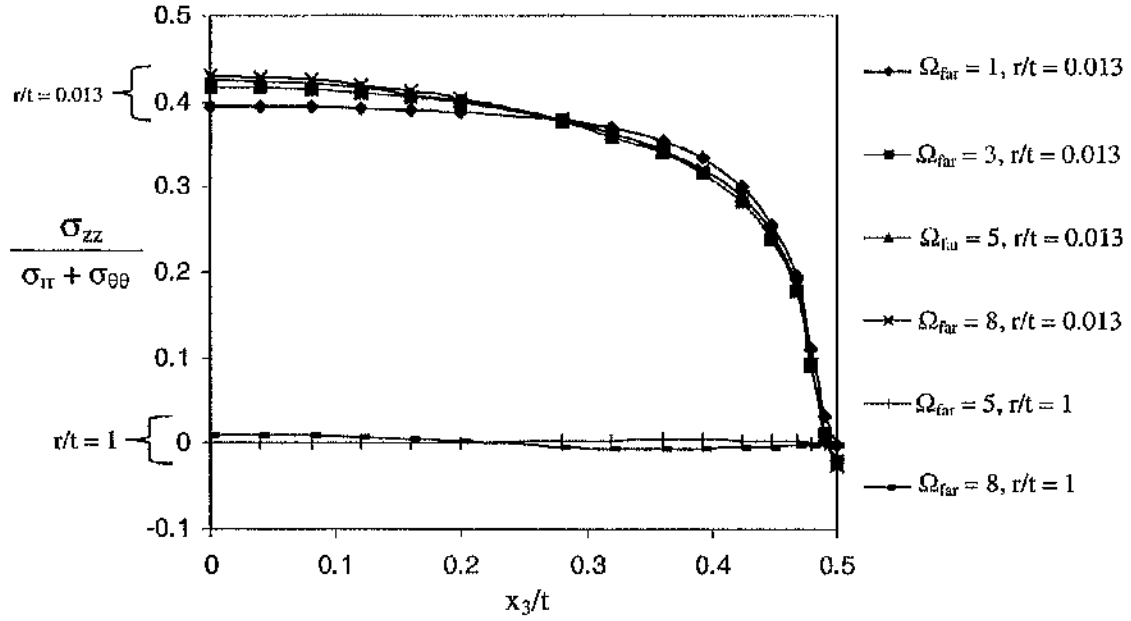


Figure 5.175: Comparison of the level of plane strain ahead of the crack front at radial distance r/t = 0.013 at load levels 1, 3, 5, 8 and at distance r/t = 1 at load levels $\Omega_{far}$ = 5, 8 for boundary layer formulations.

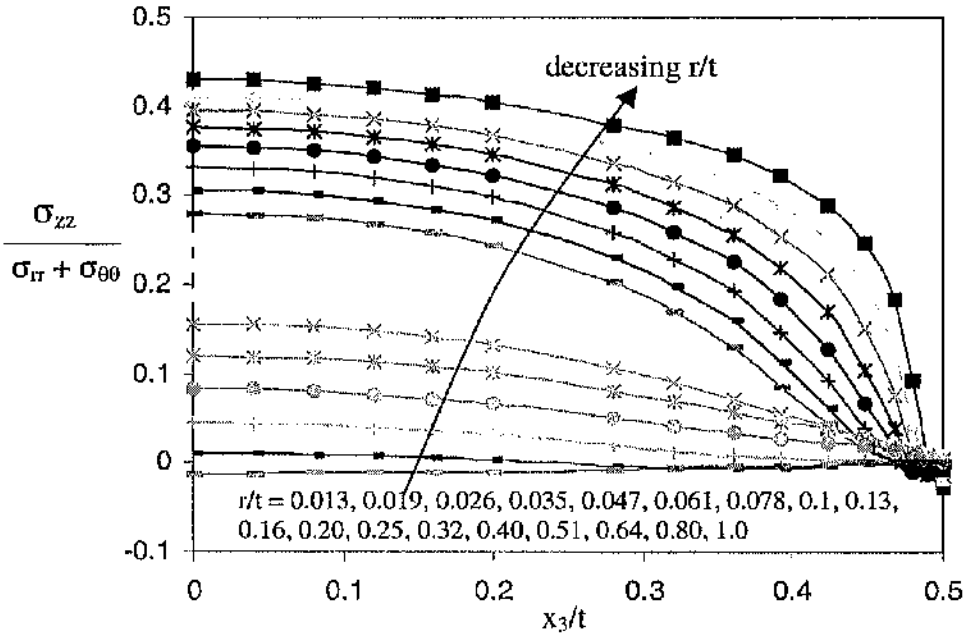


Figure 5.176: Through thickness variation of the level of plane strain ahead of the crack front $\theta = 0^{\circ}$ at various radial distances for load level $\Omega_{far}$ = 8 for boundary layer formulations.

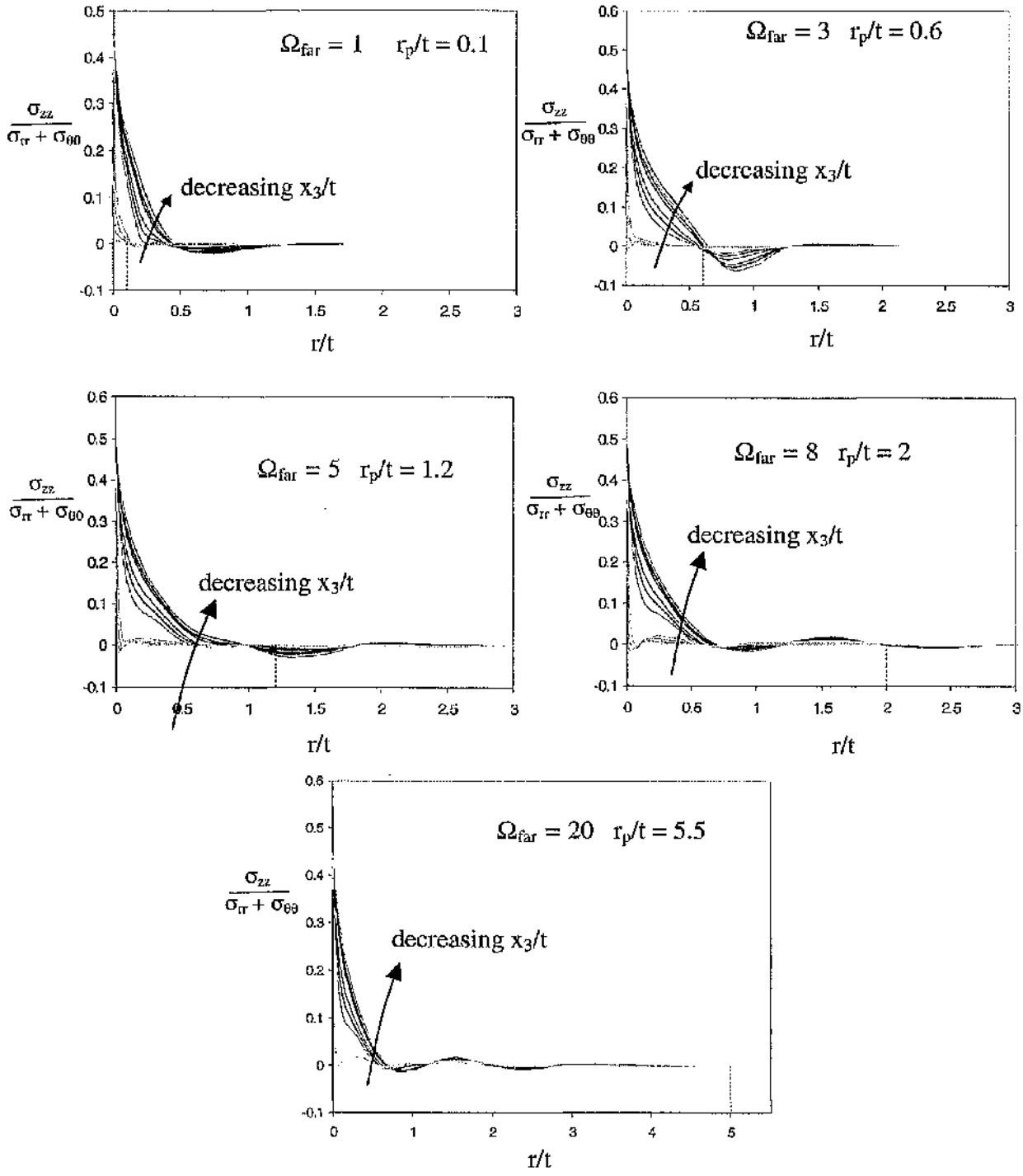


Figure 5.177: In-plane degree of plane strain at $\theta = 0°$ within the plastic zone radius for load 1, 3, 5, 8, 20 through the thickness. Broken line corresponds to the plastic zone ahead of the crack.

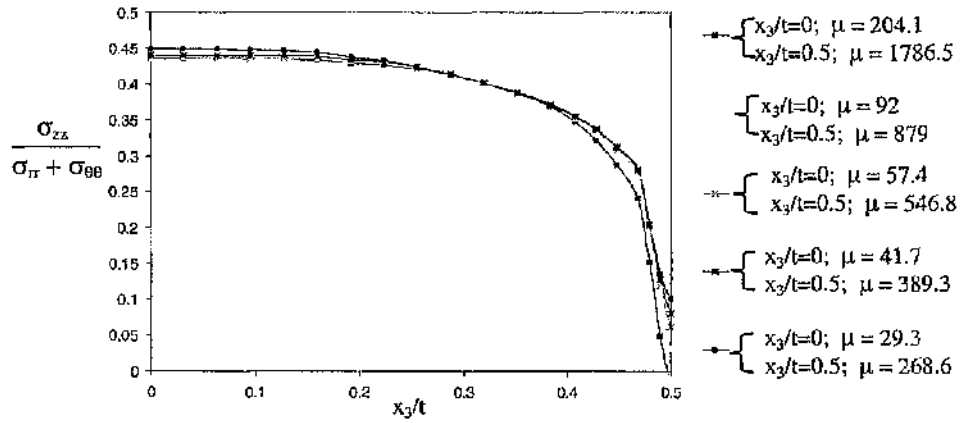


Figure 5.178: The degree of plane strain in SENB specimens (B/W-a = 1) along the crack front at r/t = 0.009 at increasing load levels.

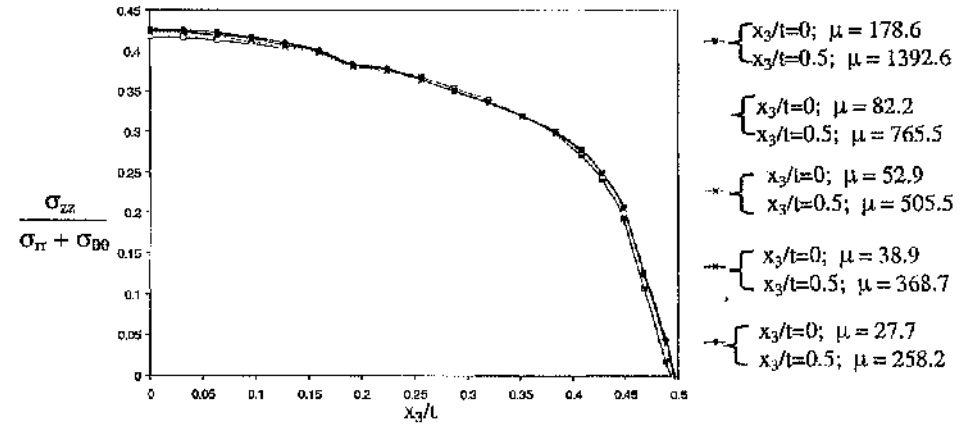


Figure 5.179: The degree of plane strain in SENB specimens (B/(W-a) = 0.5) along the crack front at r/t = 0.009 at various load levels.

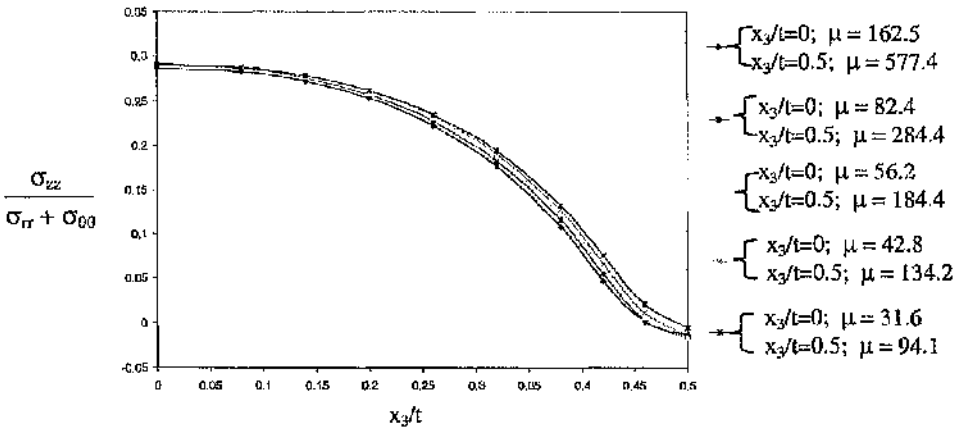


Figure 5.180: The degree of plane strain in SENB specimens (B/W-a = 0.1) along the crack front at r/t = 0.009 at various load levels.

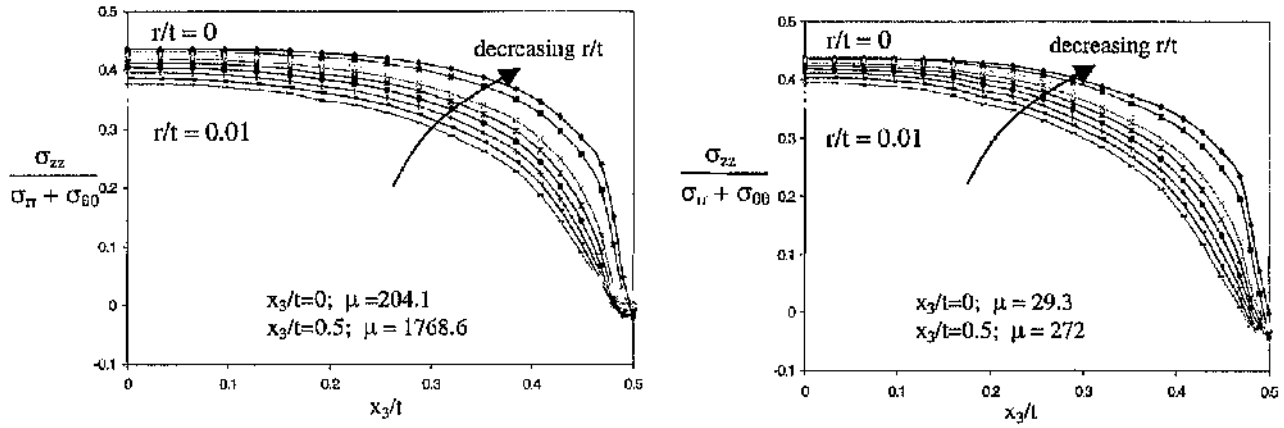


(a) (b)

Figure 5.181: The degree of plane strain in SENB specimens along the crack front at θ = 0° in (a) small scale yielding and (b) full plasticity for B/(W-a) = 1.

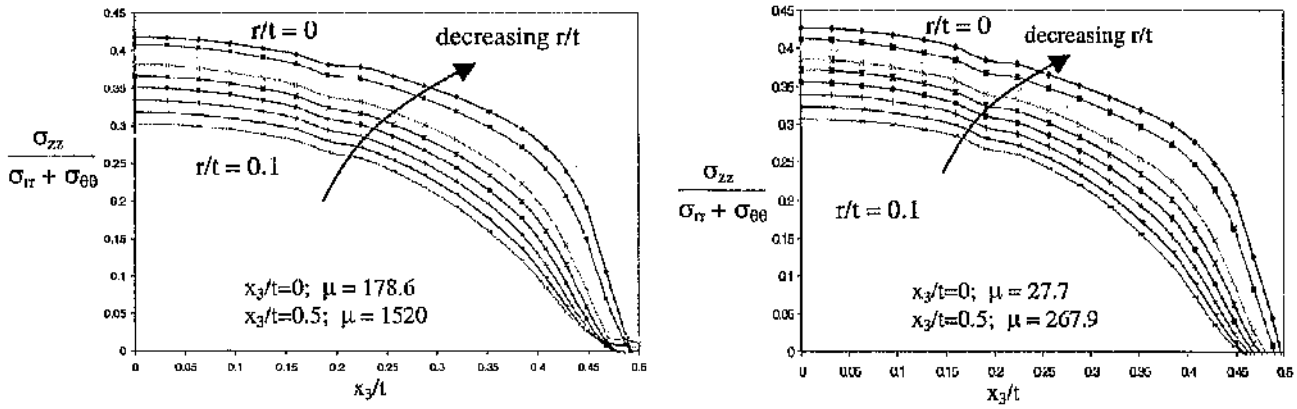


(a) (b)

Figure 5.182: The degree of plane strain in SENB specimens along the crack front at θ = 0° in (a) small scale yielding and (b) full plasticity for B/(W-a) = 0.5.

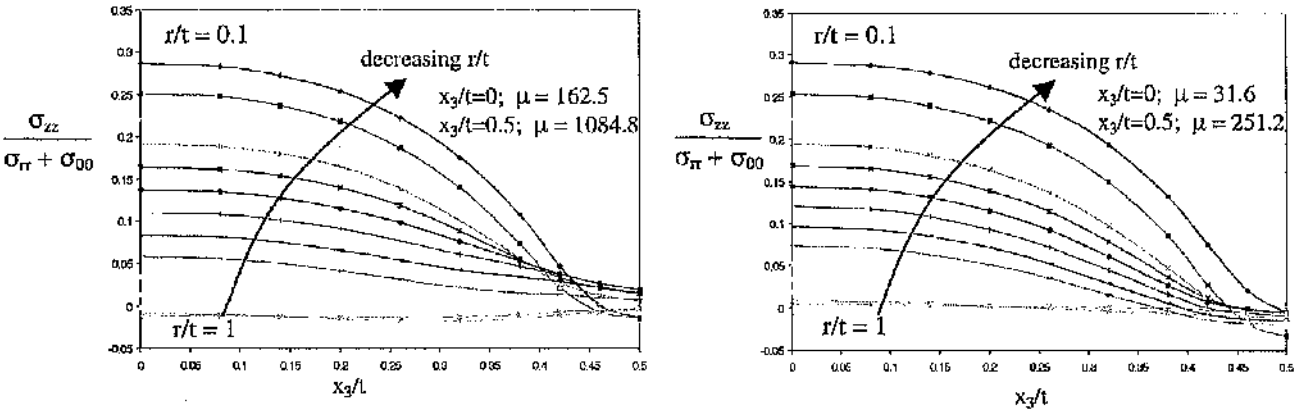


(a) (b)

Figure 5.183: The degree of plane strain in SENB specimens along the crack front at θ = 0° in (a) small scale yielding and (b) full plasticity for B/(W-a) = 0.1.

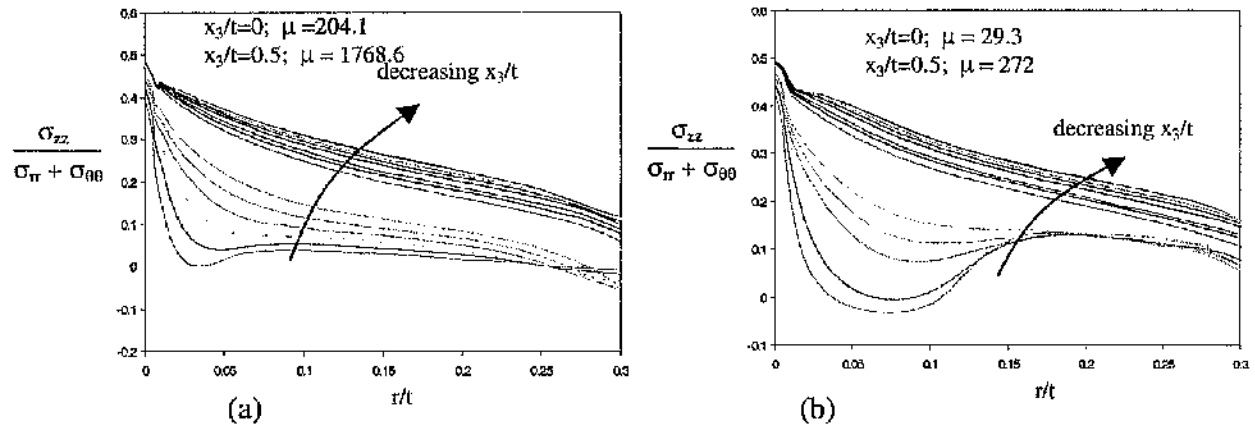


Figure 5.184: The degree of plane strain in SENB specimens ahead of the crack front at $\theta = 0^\circ$ in (a) small scale yielding and (b) full plasticity for B/(W-a) =1.

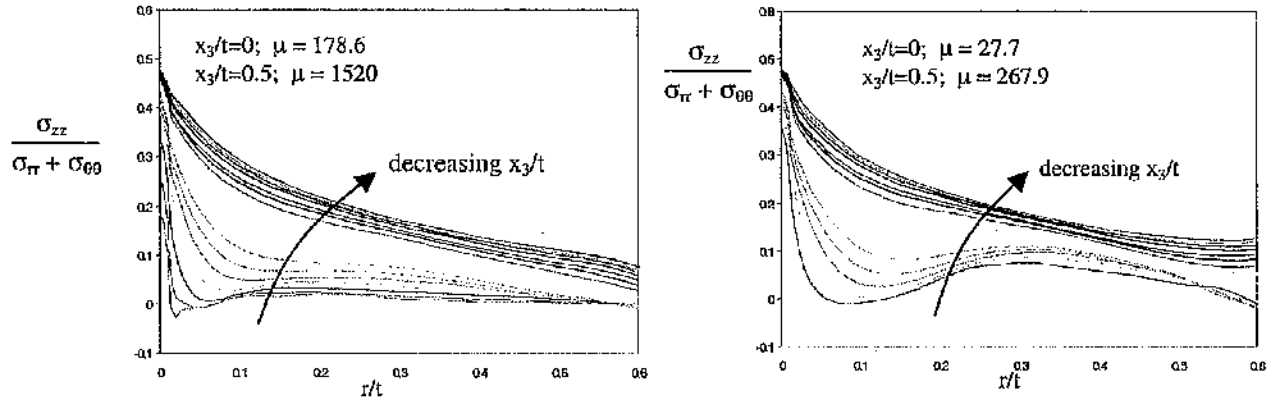


Figure 5.185: The degree of plane strain in SENB specimens ahead of the crack front at $\theta = 0^\circ$ in (a) small scale yielding and (b) full plasticity for B/(W-a) = 0.5.

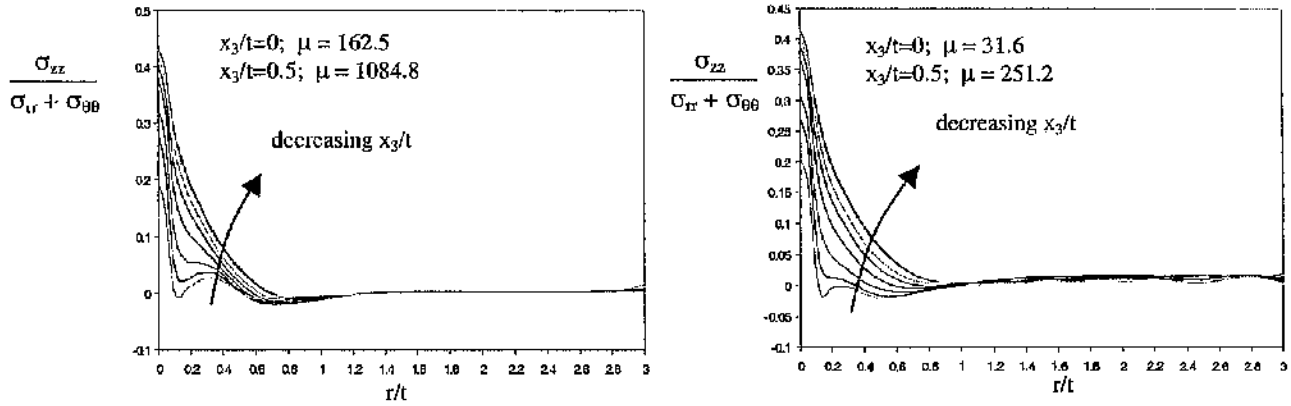


Figure 5.186: The degree of plane strain in SENB specimens ahead of the crack front at $\theta = 0^\circ$ in (a) small scale yielding and (b) full plasticity for B/(W-a) = 0.1.

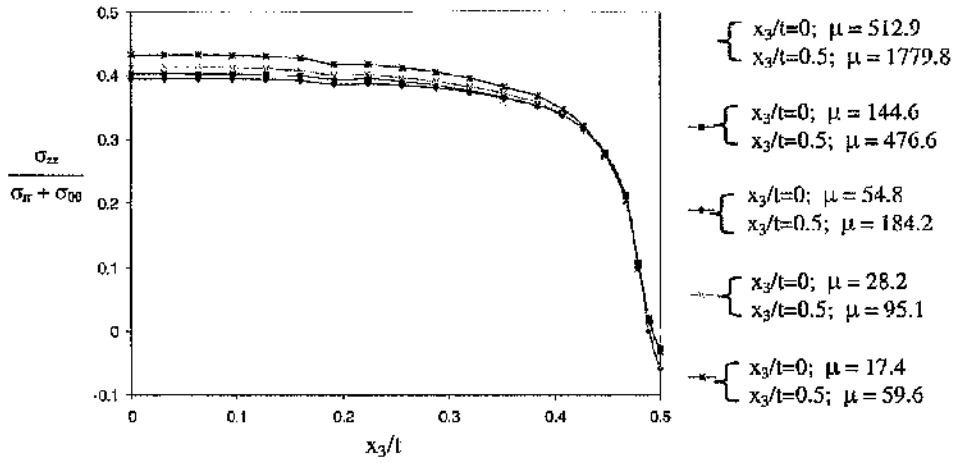


Figure 5.187: The degree of plane strain in CCP specimens (B/W-a = 1) along the crack front at increasing load levels at r/t = 0.015.

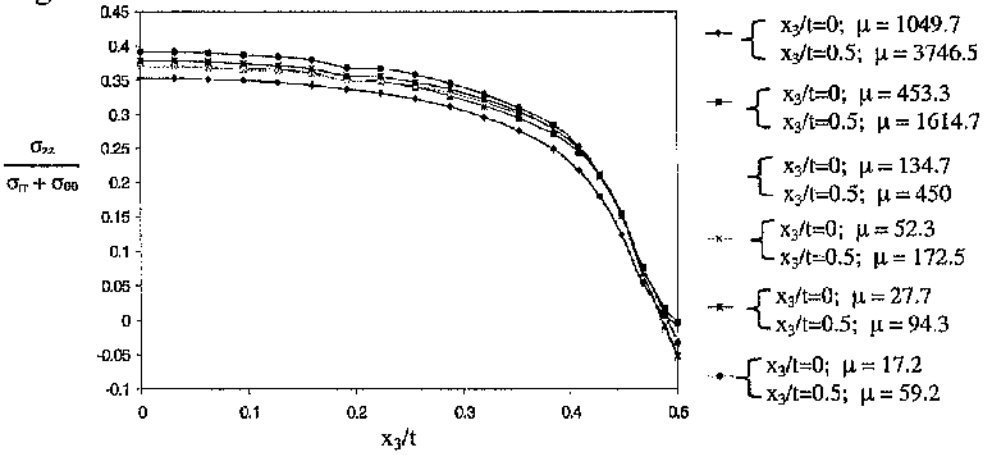


Figure 5.188: The degree of plane strain in CCP specimens (B/W-a = 0.5) along the crack front at increasing load levels at r/t = 0.032.

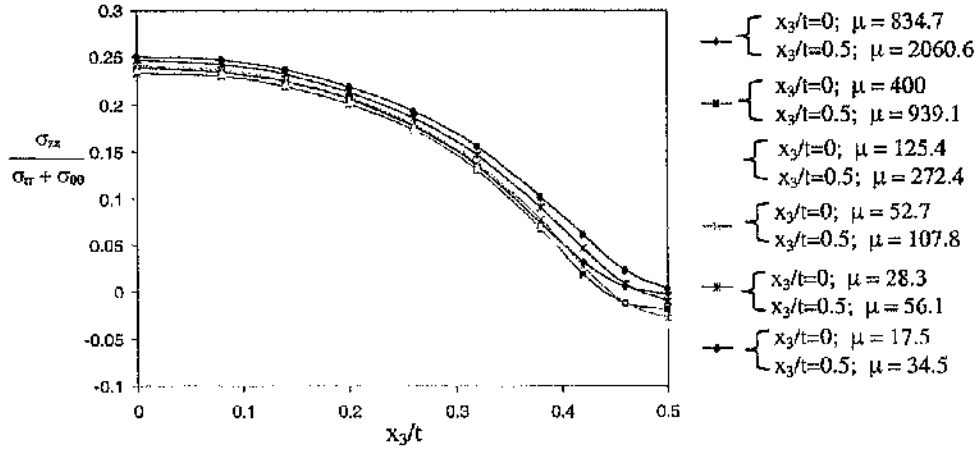


Figure 5.189: The degree of plane strain in CCP specimens (B/W-a = 0.1) along the crack front at increasing load levels at r/t = 0.065.

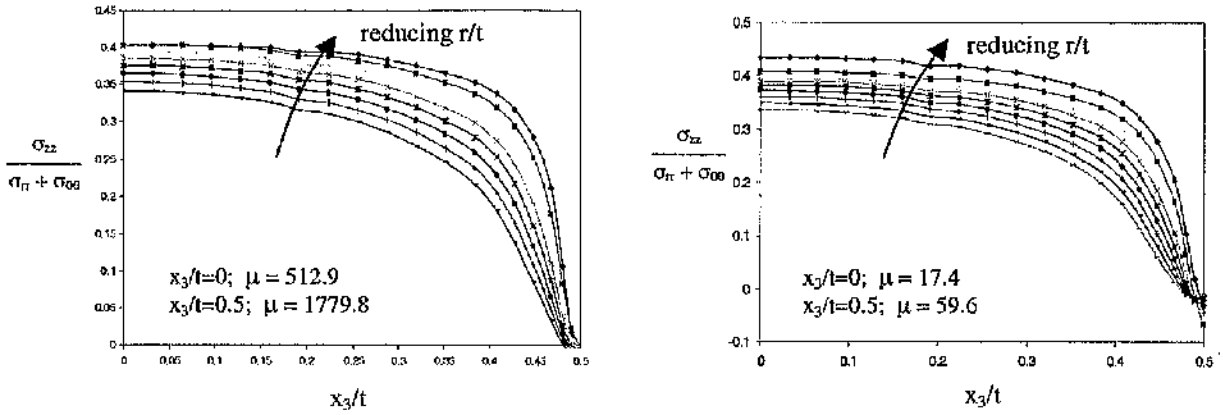


(a) (b)

Figure 5.190: The degree of plane strain along the crack front at increasing r/t for a CCP specimen B/(W-a) = 1.

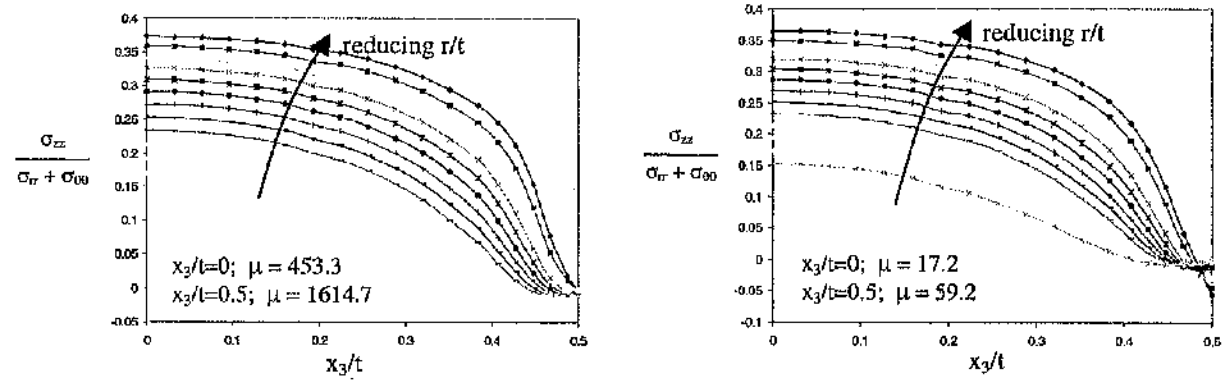


(a) (b)

Figure 5.191: The degree of plane strain along the crack front at increasing r/t for a CCP specimen B/(W-a) = 0.5.

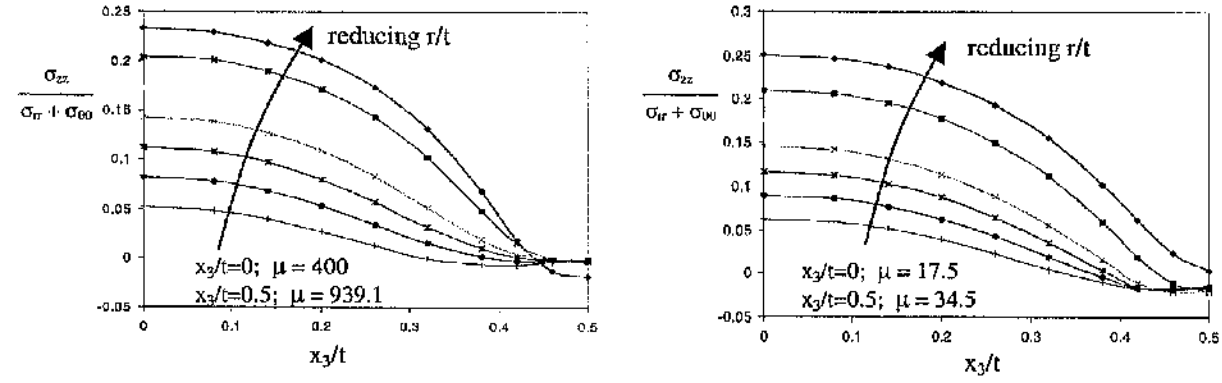


(a) (b)

Figure 5.192: The degree of plane strain along the crack front at increasing r/t for a CCP specimen B/(W-a) = 0.1.

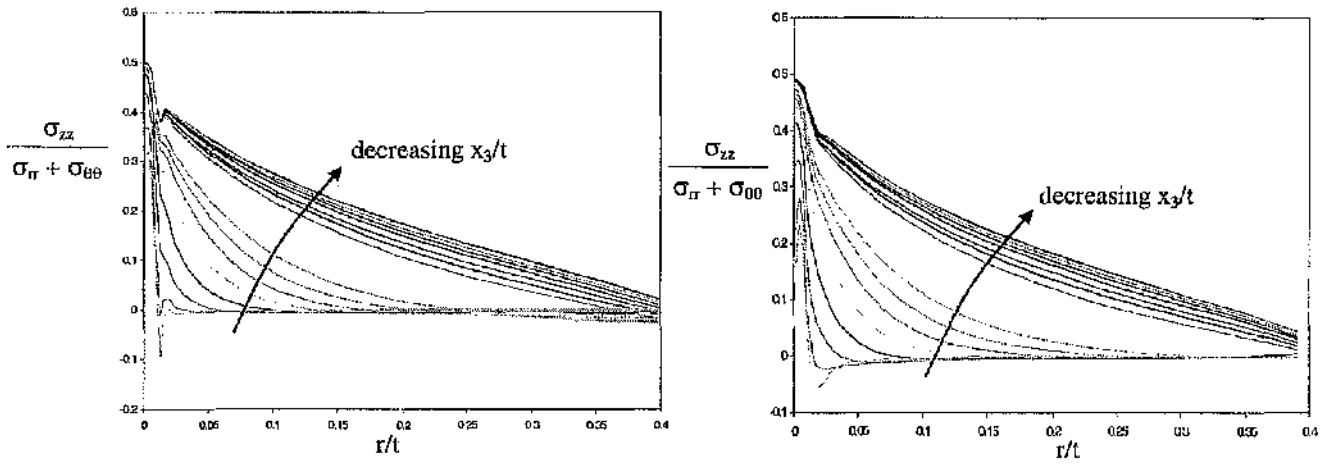


(a) (b)

Figure 5.193: The degree of plane strain ahead of the crack front at small scale yielding to full plasticity in CCP specimens B/(W-a) = 1.

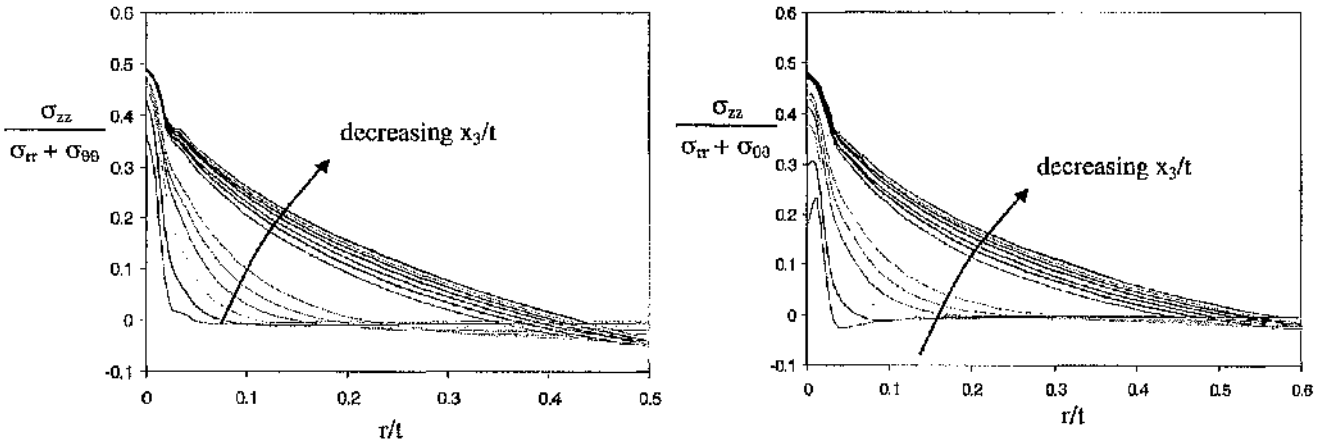


(a) (b)

Figure 5.194: The degree of plane strain ahead of the crack front at small scale yielding to full plasticity in CCP specimens B/(W-a) = 0.5.

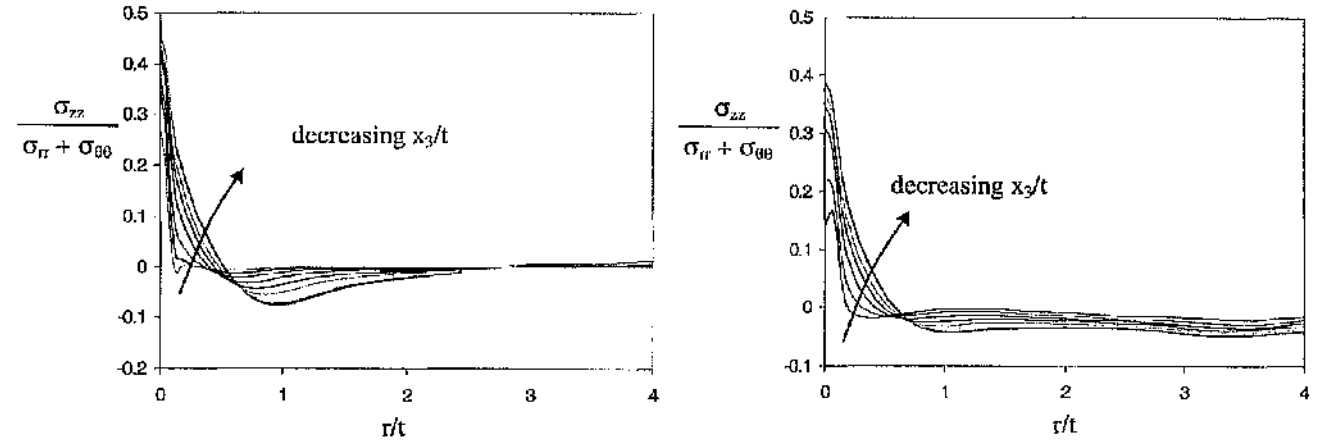


(a) (b)

Figure 5.195: The degree of plane strain ahead of the crack front at small scale yielding to full plasticity in CCP specimens B/(W-a) = 0.1.

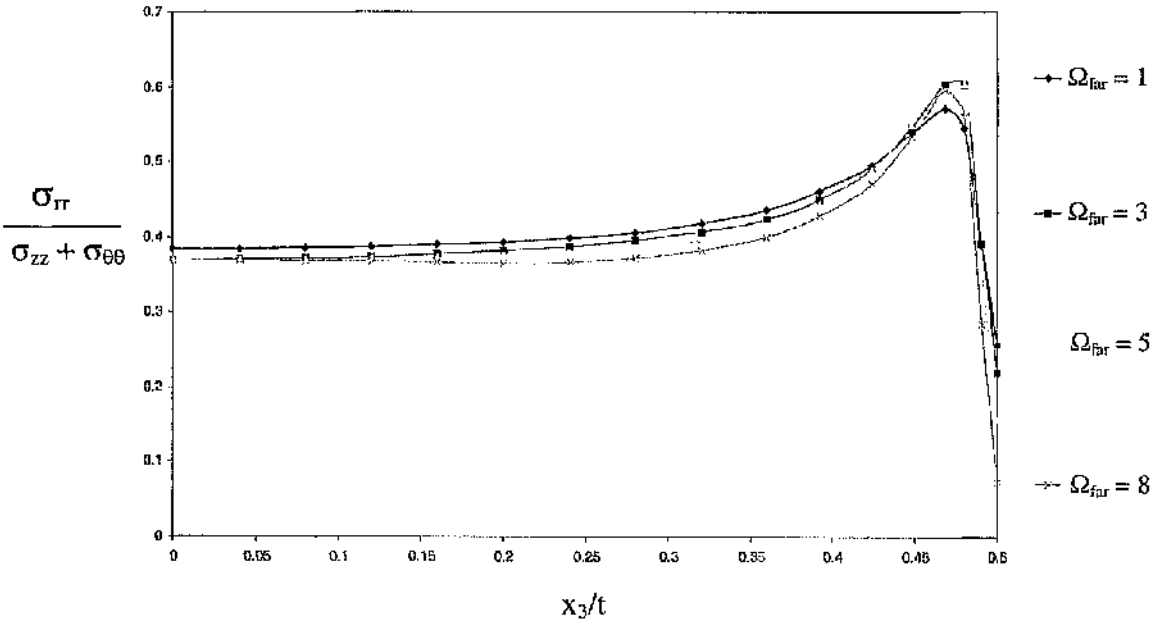


Figure 5.196: Proximity to plane stress along the crack front at r = 0 at increasing deformation levels for a boundary layer formulation.

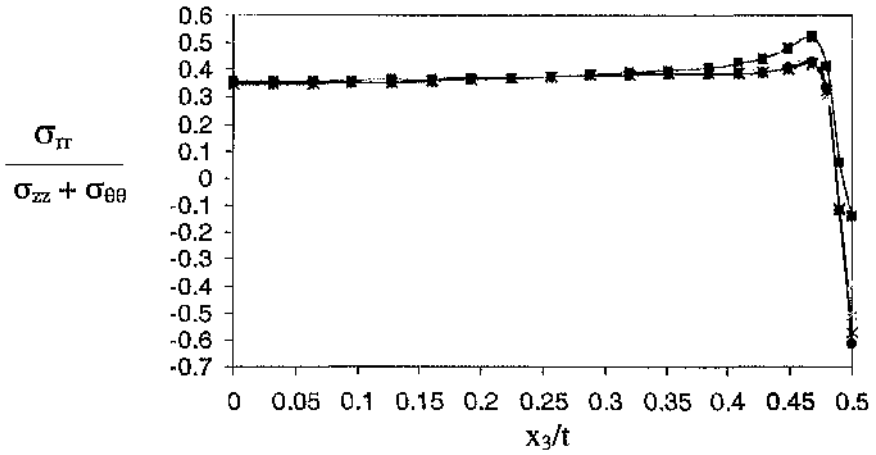


Figure 5.197: Proximity to plane stress at r = 0 in SENB, B/(W-a) = 1 along the crack front at different deformation levels.

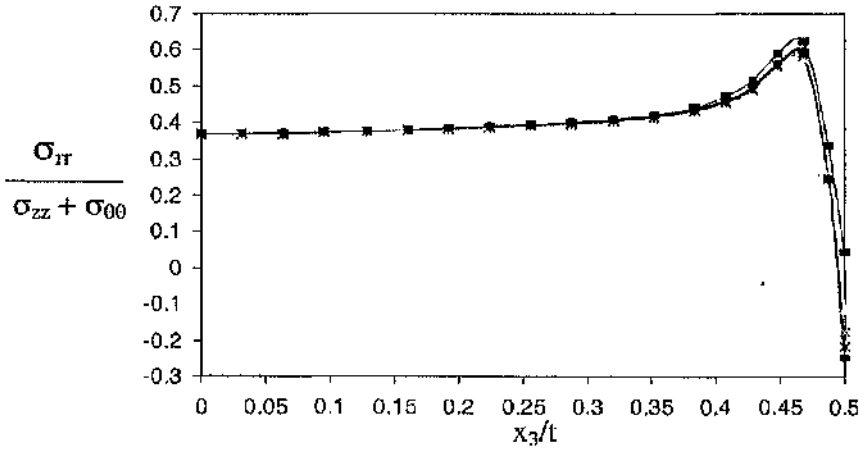


Figure 5.198: Proximity to plane stress at r = 0 in SENB, B/(W-a) = 0.5 along the crack front at different deformation levels.

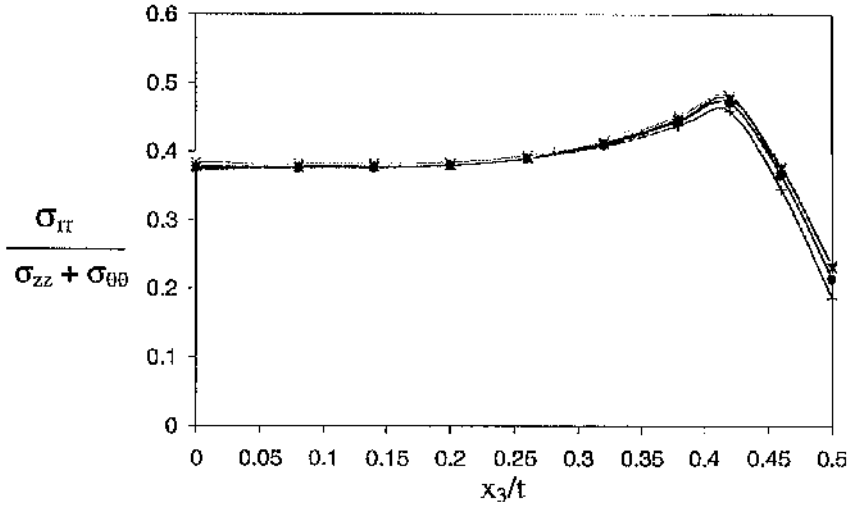


Figure 5.199: Proximity to plane stress at r = 0 in SENB, B/(W-a) = 0.1 along the crack front at different deformation levels.

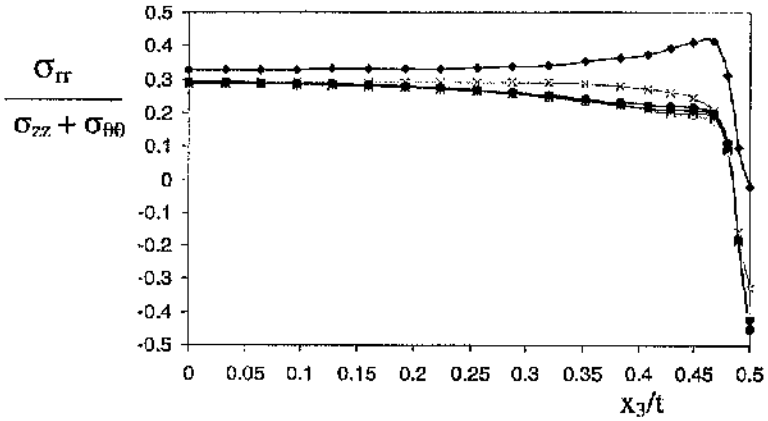


Figure 5.200: Proximity to plane stress in CCP, B/(W-a) = 1 along the crack front at r = 0 at increasing deformation levels.

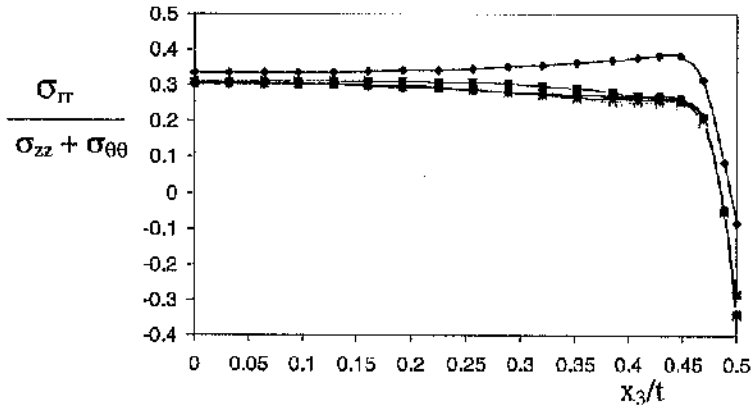


Figure 5.201: Proximity to plane stress in CCP, B/(W-a) = 0.5 along the crack front at r = 0 at increasing deformation levels.

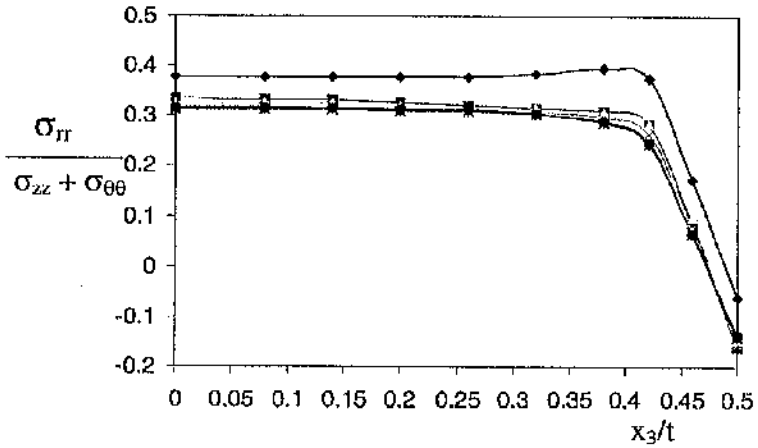


Figure 5.202: Proximity to plane stress in CCP, B/(W-a) = 0.1 along the crack front at r = 0 at increasing deformation levels.

# Out-of-Plane Constraint Effects Quantified by a Plane Strain Parameter

The quantification of constraint loss is a central objective of three-dimensional crack tip analyses. Chapter 5 presented the basic data from which systematic trends must be extracted. Chapter 6 starts this process. Constraint loss through the thickness, and as a function of distance from the crack tip is related to a parameter which measures the proximity to plane strain. A similar approach is taken to identifying the zone in which plane stress dominates.

## 6.1 Out-of-Plane Constraint Loss at the Crack Tip (r = 0)

### 6.1.1 Boundary Layer Formulations and Single Edge Notched Bend Bars

Fracture processes usually initiate in the leading sector ahead of the crack tip. It has already been shown that in three-dimensional fields that this is a constant stress sector. Two important stress components; the maximum hoop stress ($\sigma_{\theta\theta}$) and the mean stress ($\sigma_m$) have been used to quantify out-of-plane constraint loss.

The hoop and the mean stress determined from boundary layer formulations are given as a function of the plane strain parameter, $\rho$, defined in equation (2.45) in Figures 6.1 and 6.2 for deformation levels $\Omega_{far} = 3, 5, 8$. The constraint loss exhibits a unique behaviour which can be expressed by a single curve which is bounded by plane strain conditions at the midplane. Near the free surface, the field approaches a plane stress field or a corner singularity field which cannot be distinguished by $\rho$. Figures 6.3 and 6.4 show the hoop and the mean stress as a function of $\rho$ for both boundary layer formulations and full-field SENB solutions. The deformation levels in the full-field solutions ranged from small plasticity to fully plastic. Figures 6.3 and 6.4 show that the out-of-plane constraint loss at the crack tip in boundary layer formulations and full-field solutions fall on a single unified locus.

### 6.1.2 Centre Crack Tension Panels

In CCP specimens, constraint loss is more complex because constraint is lost due to in-plane and out-of-plane effects. To quantify the out-of-plane constraint loss, it is initially necessary to quantify in-plane constraint loss. An in-plane constraint estimation scheme for a family of crack tip stress field based on the T-stress was proposed by Betegón and Hancock (1991). Karstensen (1996) extended the range of the estimation scheme from $-1 < T/\sigma_o < 1$ and proposed values for the two constants, $A_n$ and $B_n$ tabulated in Table 6.1. The T-stress is related to the applied stress, $\sigma_{app}$, through:

$$T = \tau\sigma_{app} \tag{6.1}$$

where $T/\sigma_{app}$ is known as the T-stress concentration factor. The applied load, P, from equation (4.8) normalised by the limit load, $P_o$, from equations (5.5) can be expressed in terms of the applied stress, $\sigma_{app}$, normalised by the yield stress, $\sigma_o$ :

$$\frac{P}{P_o} = \frac{\sigma_{app}}{\sigma_o}\frac{\sqrt{3}}{2}\left(\frac{1}{1-a/W}\right) \tag{6.2}$$

If $a/W = 0.5$, $P/P_o$ reduces to:

$$\frac{P}{P_o} = \sqrt{3}\frac{\sigma_{app}}{\sigma_o} \tag{6.3}$$

Putting equation (6.3) into (6.1) gives:

$$\frac{T}{\sigma_o} = \frac{\tau}{\sqrt{3}}\frac{P}{P_o} \tag{6.4}$$

In-plane constraint loss for three-dimensional CCP specimens can be estimated starting with a two-dimensional plane strain constraint assessment scheme from the modified boundary layer formulation. The Q term is given in equation (2.150). For a non-hardening response, $A_n$ and $B_n$ are 0.83 and –0.88. The Q values associated with in-plane constraint loss in the CCP specimens can be calculated at all loads. Specifically for thicknesses B/(W-a) = 1, 0.5 and 0.1, Q was determined to be -0.70, -0.68 and -0.38 at limit load. The mean and the hoop stress are then given by :

$$\frac{\sigma_{(\theta\theta;m)}}{\sigma_o} = \frac{\sigma^{SSY}_{(\theta\theta;m)}}{\sigma_o} + Q \tag{6.5}$$

The hoop and the mean stresses in CCP specimens at limit load are tabulated in Table 6.2.

Figures 6.5(a) to (f) show the constraint level as a function of the plane strain parameter for all the centre cracked panels. In each plot, constraint loss has been shown at limit load. The in-plane constraint loss for each configuration is indicated with broken lines. From the figures, it is clear that the out-of-plane effect causes an additional constraint loss in all the CCP specimens. As a first hypothesis it is appropriate to consider constraint loss due to in-plane and out-of-plane effects to be additive.

Figures 6.6 and 6.7 show the hoop and the mean stresses as a function of the plane strain parameter for all thicknesses of CCP specimens. This data is compared with the boundary layer formulations at deformation levels $\Omega_{loc}$ = 7.12 and 12. If the in-plane and out-of-plane effects are regarded as being additive, the boundary layer formulations show greater levels of out-of-plane constraint loss than the CCP specimens but both configurations approach the corner singularity field at the free surface. Different thickness CCP specimens do not exhibit a unique relation between out-of-plane constraint loss in contrast to the SENB specimens due to the different levels of in-plane constraint loss which is indexed by T. The highest out-of-plane constraint loss occurs in the thickest CCP specimen. As the CCP specimen thickness is reduced, the out-of-plane constraint loss approaches the boundary layer formulation data.

The mean and the hoop stress constraint loss at the crack tip in boundary layer formulations and full-field SENB and CCP specimens can be expressed as a simple polynomial expression :

$$\frac{\sigma_{(m;\theta\theta)}}{\sigma_o} = A_n \rho^n + \cdots + A_{n+1}\rho^n \qquad (6.6)$$

where $A_n$, $A_{n+1}$ are the constants determined by a curve fitting and ρ is the plane strain parameter.

The hoop and the mean stress out-of-plane constraint loss in the boundary layer formulations and the SENB specimens in Figures 6.1-6.2 and Figures 6.3-6.4 can be fitted using a quadratic polynomial curve and the associated constants $A_n$ tabulated in Table 6.3.

The hoop and the mean stress in the CCP specimens shown in Figure 6.6-6.7 can be fitted using a cubic polynomial curve using the constants tabulated in Table 6.4.

## 6.2 Out-of-Plane Constraint Loss Ahead of the Crack Front ($r = 2J/\sigma_o$)

The distance $2J/\sigma_o$ is important in fracture analyses because it is a distance where the small strain theory converges to large strain analyses. On this basis, out-of-plane effects are now examined at distance $2J/\sigma_o$.

### 6.2.1 Boundary Layer Formulation and Single Edge Notched Bend Bars

Out-of-plane effects at increasing levels of deformation have been examined using the mean and the hoop stress as a function of the plane strain parameter at a distance of $r = 2J/\sigma_o$ along the crack front. The objective is to develop an understanding on out-of-plane constraint loss over distances from the crack tip involved in the physics of failure.

Boundary layer formulations and the SENB solutions are discussed together because both develop positive T-stresses.

Figures 6.8 and 6.9 show the mean and the hoop stress as a function of the plane strain parameter in boundary layer formulations at a distance of $r = 2J/\sigma_o$ and at deformation levels, $\Omega_{far} = 1, 3, 5, 8$ and 20. At small levels of deformation ($\Omega_{far} = 1, 3, 5$), constraint loss fall on a single curve from the midplane to the free surface at increasing deformation. However as the deformation levels increase ($\Omega_{far} = 8, 20$), constraint loss is load dependent.

Figures 6.10 (a) to (c) and 6.11 (a) to (c) show the mean stress as a function of the plane strain parameter at increasing levels of deformation in the SENB specimens. Constraint reduces with deformation along the crack front and approaches the plane stress field on the free surface.

It is important to highlight that measurement of deformation using J cause the physical location of stresses to move away from the crack tip. As constraint is lost with distance from the crack tip, this causes constraint loss when measured at $r = 2J/\sigma_o$ shows a decaying trend.

However at low levels of deformation, the constraint loss for SENB solutions and the boundary layer formulations are similar as demonstrated in Figures 6.12 and 6.13. When the levels of deformation is small, essentially the measured J can be regarded as near the crack tip, therefore constraint loss through the thickness can be united into a single relationship.

Even though analyses of constraint loss in the same specimen thickness at increasing level of deformation show an independent decreasing pattern, constraint loss in different specimen thicknesses at the same section ($x_3/t$) regardless of thickness can be united into a single relationship. Constraint loss at the same section ($x_3/t$) as a function of the plane strain parameter are shown in Figures 6.14 (a) to (f) and 6.15 (a) to (f).

### 6.2.2 Centre Cracked Tension Panels

Initially, constraint loss at $r = 2J/\sigma_o$ is shown as a function of the plane strain parameter at increasing levels of deformation as illustrated in Figures 6.16 (a) to (c) and 6.17 (a) to (c) for the mean and the hoop stress. Increasing deformation causes constraint loss in all three thicknesses as shown in Figures 6.16 (a) and (b). However, as with the SENB specimens, the constraint loss is dependent on the levels of deformation due to the physical point at which stresses are measured changes because of deformation measured by J.

Figures 6.18 (a) to (f) and 6.19 (a) to (f) show the mean and the hoop stress for CCP specimen for different thicknesses at the same section ($x_3/t$) as a function of the plane strain parameter. First, in-plane constraint loss causes the crack tip stress field to drop from the limiting plane strain field, and then the out-of-plane constraint loss starts from the inherent in-plane constraint loss associated with the negative Q. For different specimen thicknesses but at identical sections ($x_3/t$), the out-of-plane constraint is lost in a similar way. The out-of-plane constraint loss at similar sections ($x_3/t$) of CCP specimens of different thicknesses exhibit similar behaviour.

## 6.3 Conclusions

At the crack tip, the out-of-plane constraint loss has a unique relation to $\rho$ which is independent of levels of deformation. This relation is bounded by the plane strain and the plane stress or corner fields. In the CCP specimens, the out-of-plane constraint loss is bounded by a geometry dependent constraint loss at the midplane while the free surface field is similar to that of the boundary layer formulation and the SENB specimens. The loss of constraint in the CCP specimens arises from in-plane effects which can be identified from a constraint estimation scheme combined with out-of-plane effects.

Out-of-plane constraint loss is dependent on the level of deformation at $r = 2J/\sigma_o$. The measurement of deformation by J essentially moves away from the crack tip and cause the

independent loss of constraint with increase in deformation. However, constraint loss in different thickness specimens at the same section ($x_3/t$) can be united into a single relationship.

There is a significant difference between the behaviour at a fixed physical location (the crack tip) and a moving location (at $r = 2J/\sigma_0$). If the level of deformation is small compared to limit load, constraint loss can be united into a single curve for boundary layer formulation and SENB at the crack tip and at $r = 2J/\sigma_0$. The constraint loss at the limit load in SENB specimens is still unique when measured at the crack tip. However, at $r = 2J/\sigma_0$ the physical measured distances are dynamic with increase in deformation and causes measurement of constraint at different position. This cause constraint cannot be unified on a single relationship. Similar behaviours are observed in the CCP specimens. Although there are differences in the pattern of constraint loss at $r = 2J/\sigma_0$, the loss of constraint in different thicknesses full-field solutions can be united at the same sections ($x_3/t$).

Although the plane strain parameter can quantify out-of-plane constraint loss, the analyses can not be directly applied unless $\rho$ and the development of constraint loss can be expressed simply in terms of geometry and deformation level. This is now addressed in chapter 7.

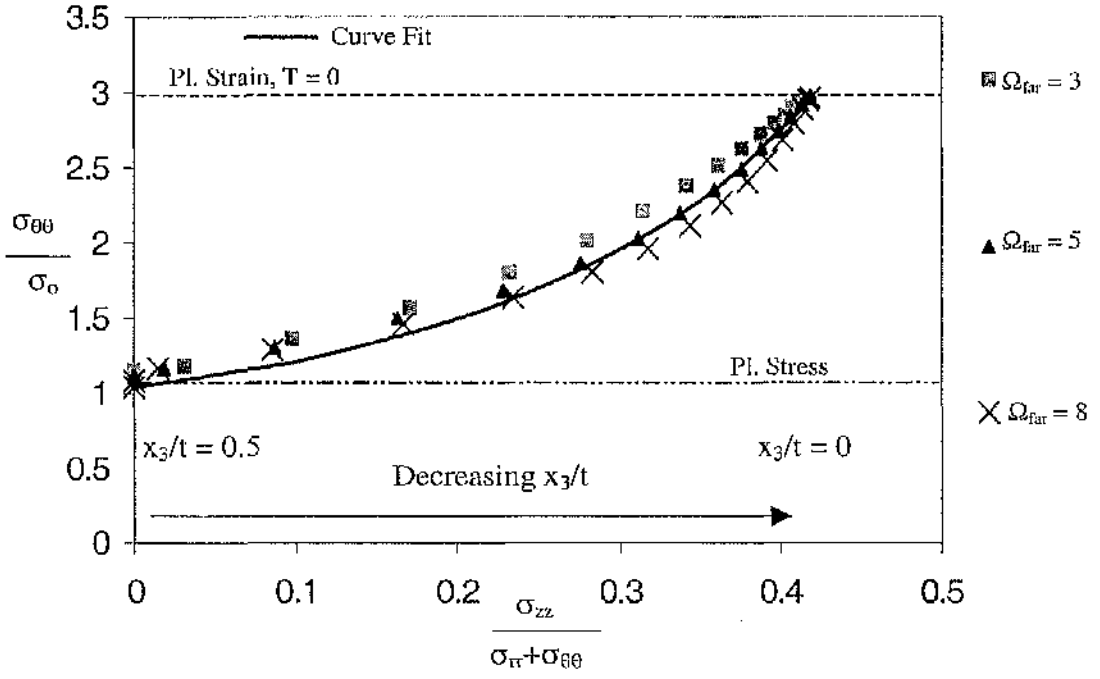


Figure 6.1: The hoop stress in a boundary layer formulation as a function of the plane strain parameter, ρ, at the crack tip.

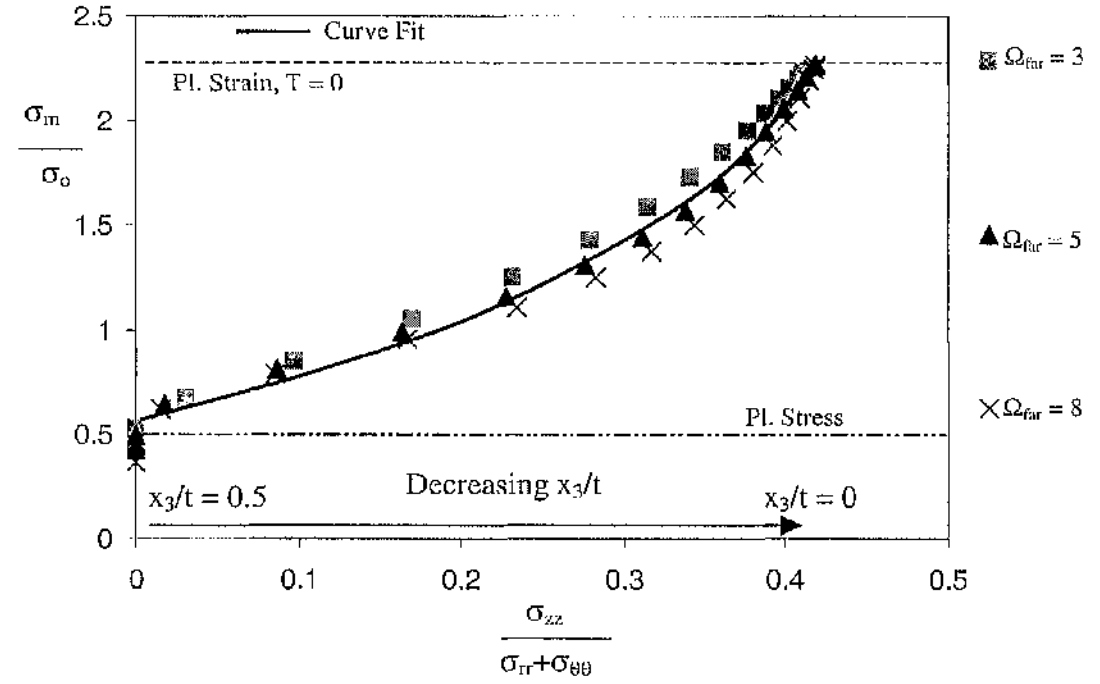


Figure 6.2: The mean stress in a boundary layer formulation as a function of the plane strain parameter, ρ, at the crack tip.

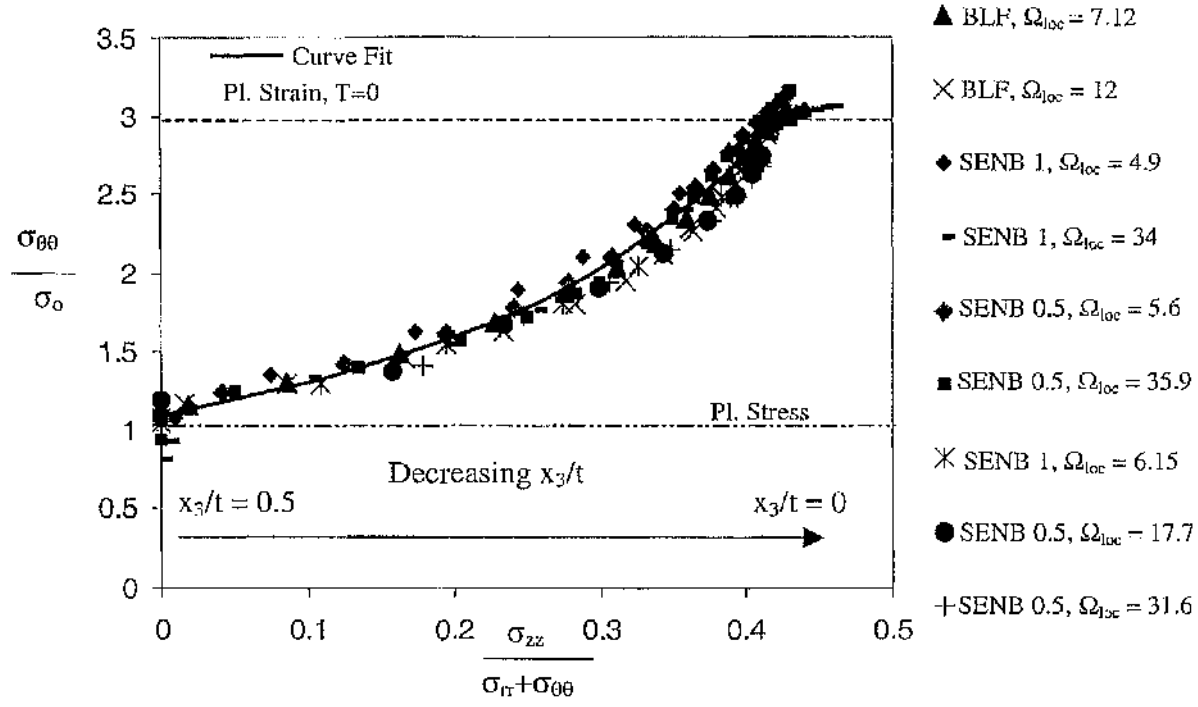


Figure 6.3: The hoop stress as a function of the plane strain parameter, ρ, for boundary layer formulations and SENB specimens B/(W-a) = 1, 0.5 and 0.1. The load levels are shown at the midplane.

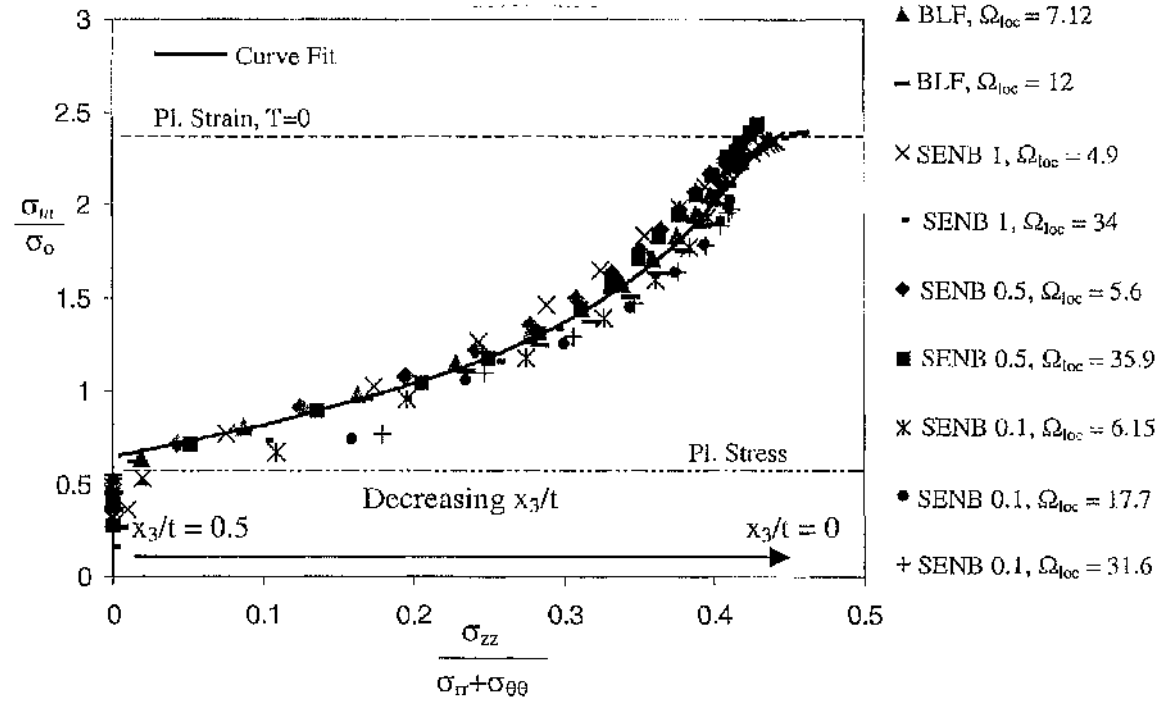


Figure 6.4: The mean stress as a function of the plane strain parameter, ρ, for boundary layer formulations and SENB specimens B/(W-a) = 1, 0.5 and 0.1. The load levels are shown at the midplane.

| n | $A_n$ | $B_n$ |
|---|---|---|
| 3 | 0.21 | -0.08 |
| 6 | 0.48 | -0.25 |
| 13 | 0.64 | -0.4 |
| ∞ | 0.83 | -0.88 |

Table 6.1: Curve fitting constants for a modified boundary layer formulation after Karstensen (1996).

| B/(W-a) | $T/\sigma_{app}$ | $T/\sigma_o$ | Q | $\sigma_{\theta\theta}^{ip}$ | $\sigma_m^{ip}$ |
|---|---|---|---|---|---|
| 1 | -0.94 | -0.54 | -0.70 | 2.27 | 1.69 |
| 0.5 | -0.92 | -0.53 | -0.68 | 2.29 | 1.71 |
| 0.1 | -0.6 | -0.34 | -0.38 | 2.59 | 2.01 |

Table 6.2: The mean and the hoop stress estimated due to in-plane constraint loss from equation (6.5) using three-dimensional CCP specimens limit load values.

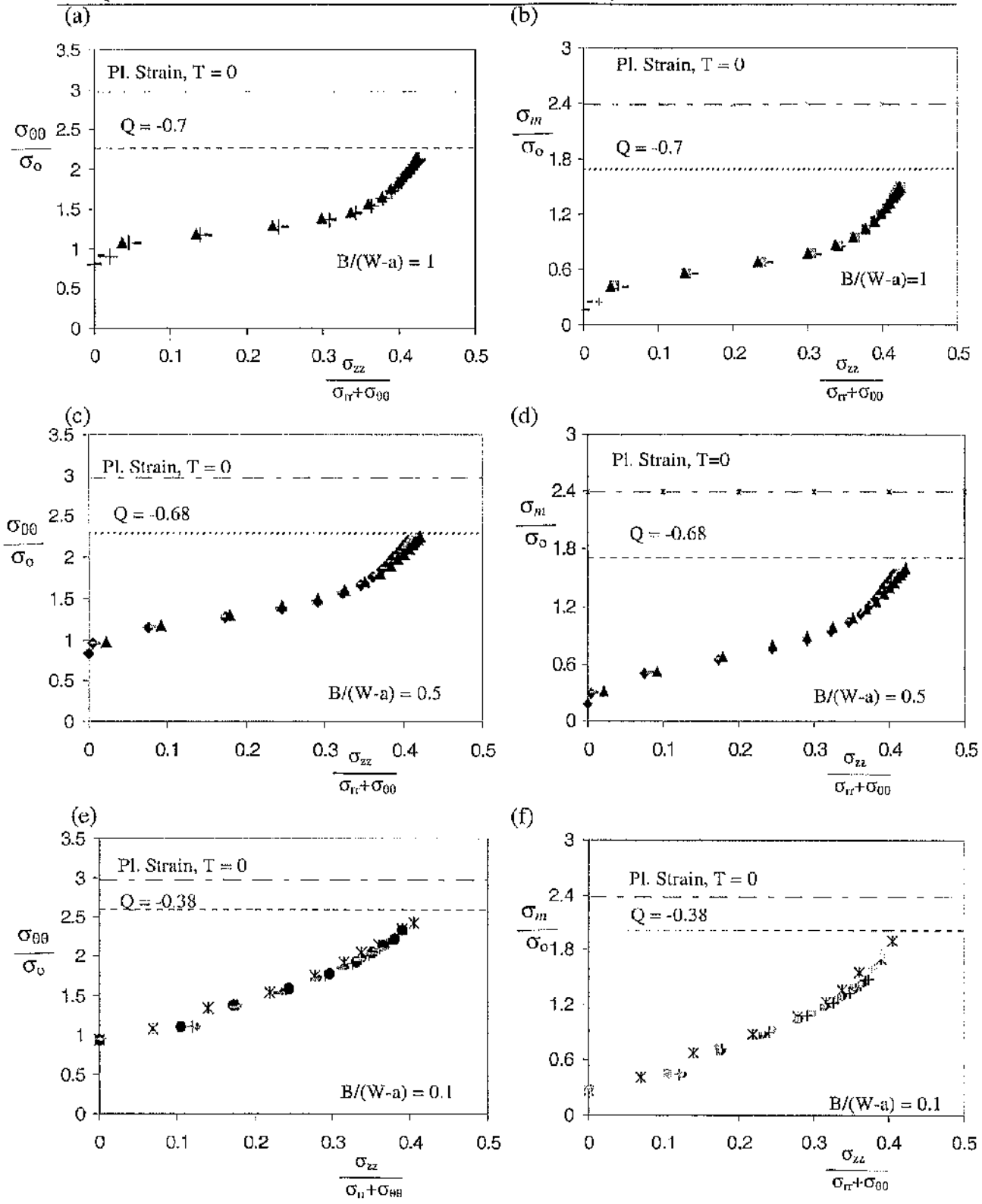


Figure 6.5: The hoop and the mean stress along the crack front for CCP specimens B/(W-a) = 1, 0.5 and 0.1 at limit load as a function of the plane strain parameter, ρ.

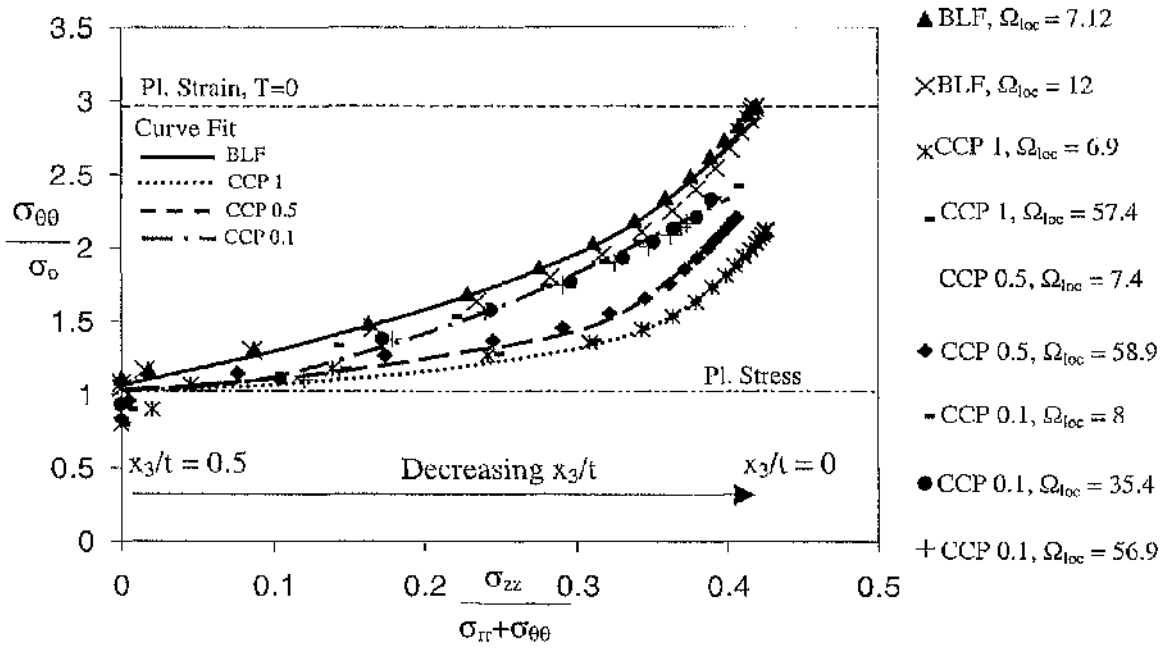


Figure 6.6: The hoop stress at the crack tip parameterised through the plane strain parameter, ρ, comparing boundary layer formulations and CCP specimens, B/(W-a) = 1, 0.5 and 0.1. The load levels are shown at the midplane.

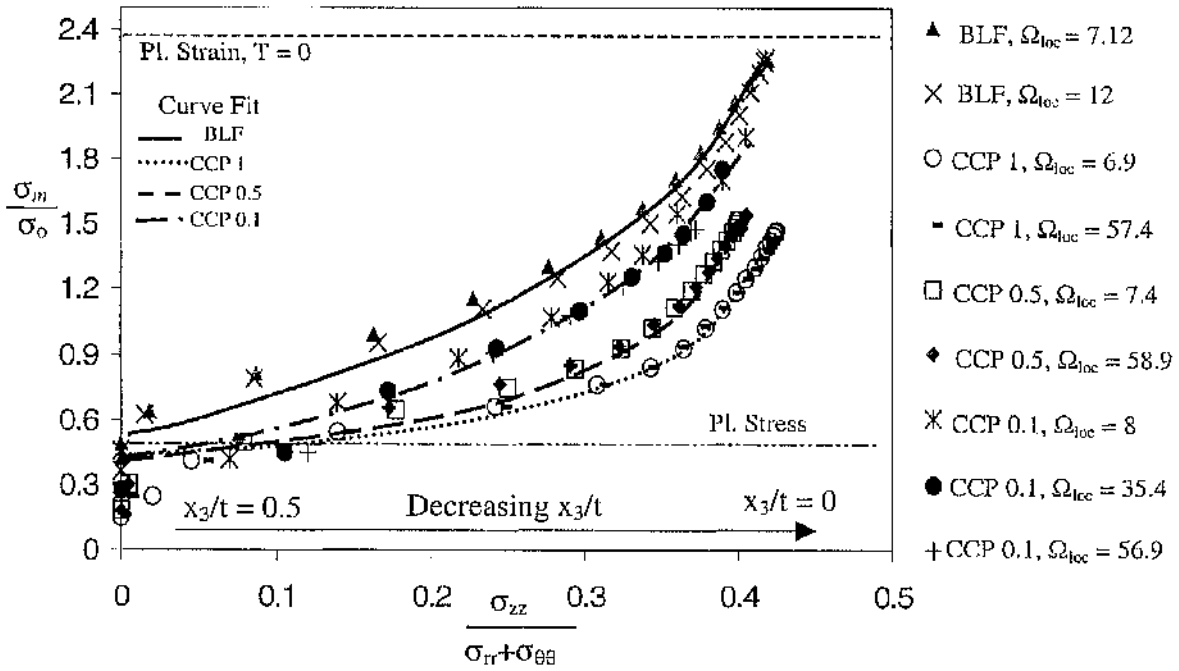


Figure 6.7: The mean stress at the crack tip parameterised through the plane strain parameter, ρ, comparing boundary layer formulations with CCP specimens, B/(W-a) = 1, 0.5 and 0.1. The load levels are shown at the midplane.

| | $\sigma_m$ | $\sigma_{\theta\theta}$ |
|---|---|---|
| $A_1$ | 0.577 | 1.15 |
| $A_2$ | 0.66 | -0.2 |
| $A_3$ | 7.7 | 10.5 |

Table 6.3: The hoop and the mean stress curve fitting constants $A_1$, $A_2$ and $A_3$ values for boundary layer formulations of Figures 6.1 and 6.2 and SENB curves of Figures 6.4 and 6.5 as related through the general equation 6.1.

| | $\sigma_m$ | | | $\sigma_{\theta\theta}$ | | |
|---|---|---|---|---|---|---|
| | G =1 | G = 0.5 | G = 0.1 | G = 1 | G = 0.5 | G = 0.1 |
| $A_1$ | 0.577 | 0.577 | 0.577 | 1.15 | 1.15 | 1.15 |
| $A_2$ | -0.79 | 0.37 | -2.39 | 0.77 | 1.64 | -1.2 |
| $A_3$ | -1.78 | -6.24 | 19.6 | -10.53 | -13.63 | 14.3 |
| $A_4$ | 19.6 | 27.2 | -17.8 | 32.6 | 39.1 | -9.78 |

Table 6.4: The hoop and the mean stress curve fitting constants $A_1$, $A_2$, $A_3$ and $A_4$ values for CCP of Figures 6.6 and 6.7 as related through equation 6.1. G is the thickness to ligament ratio B/(W-a).

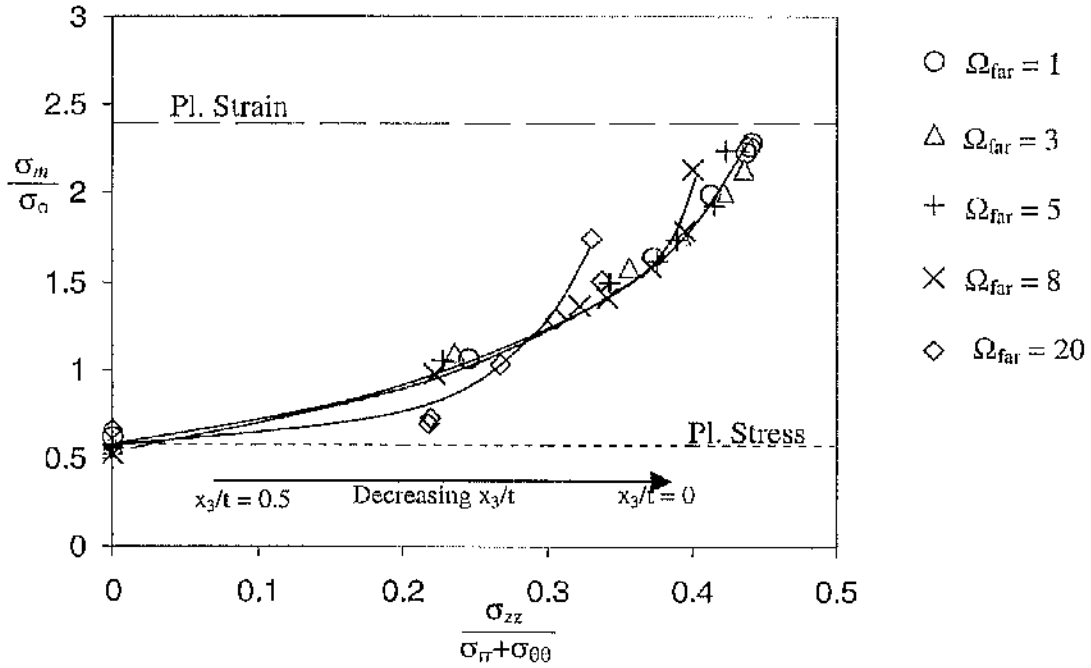


Figure 6.8: The mean stress as a function of the plane strain parameter, ρ, at $r = 2J/\sigma_o$ for boundary layer formulations.

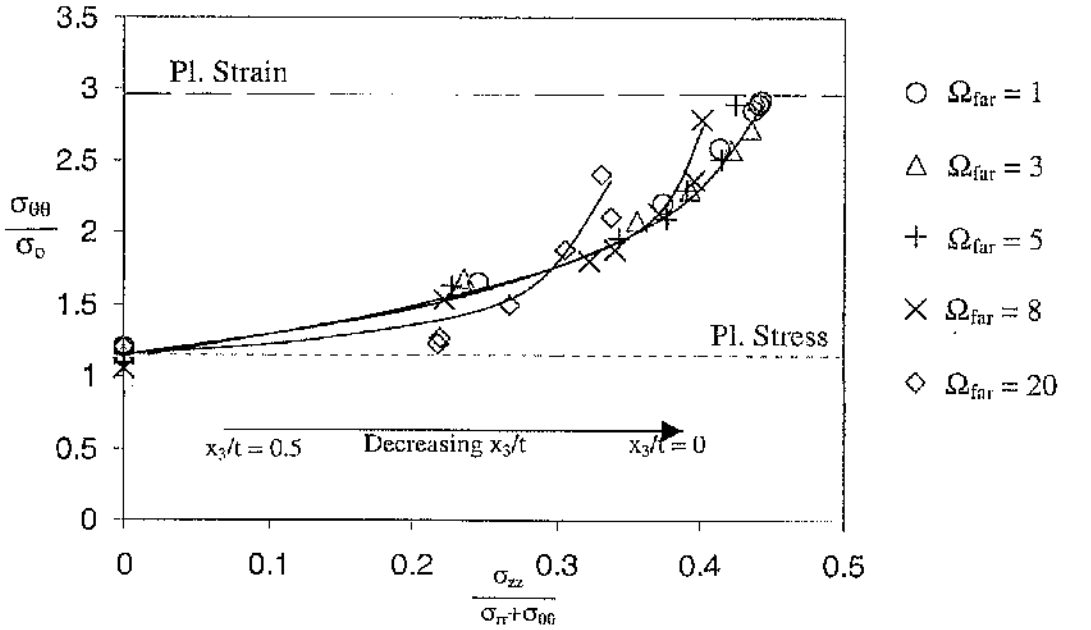


Figure 6.9: The hoop stress as a function of the plane strain parameter, ρ, at $r = 2J/\sigma_o$ for boundary layer formulations.

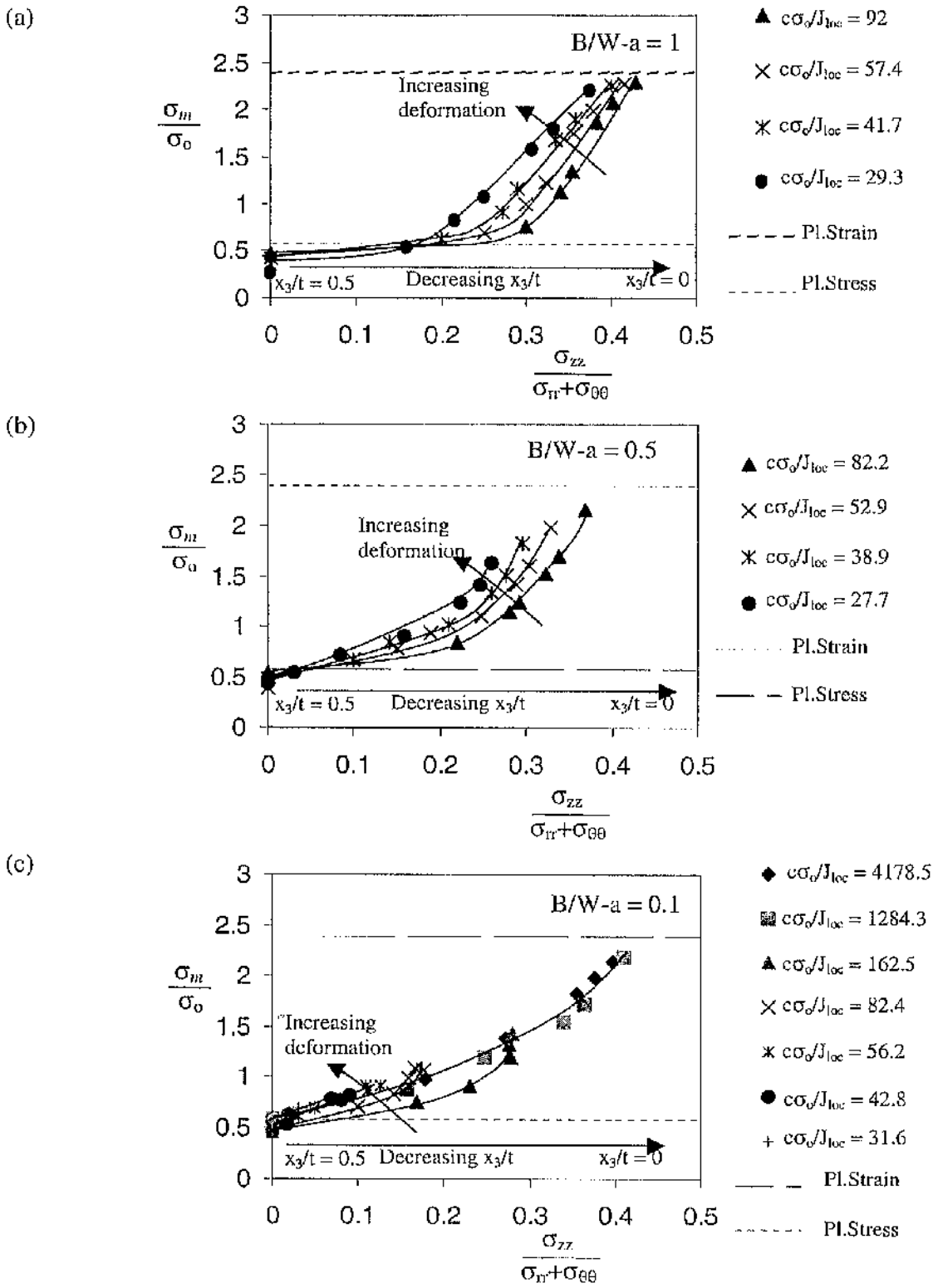


Figure 6.10: The mean stress as a function of the plane strain parameter, ρ, at $r = 2J/\sigma_o$ for SENB specimens B/(W-a) = 1, 0.1 and 0.5. The load levels are the midplane values.

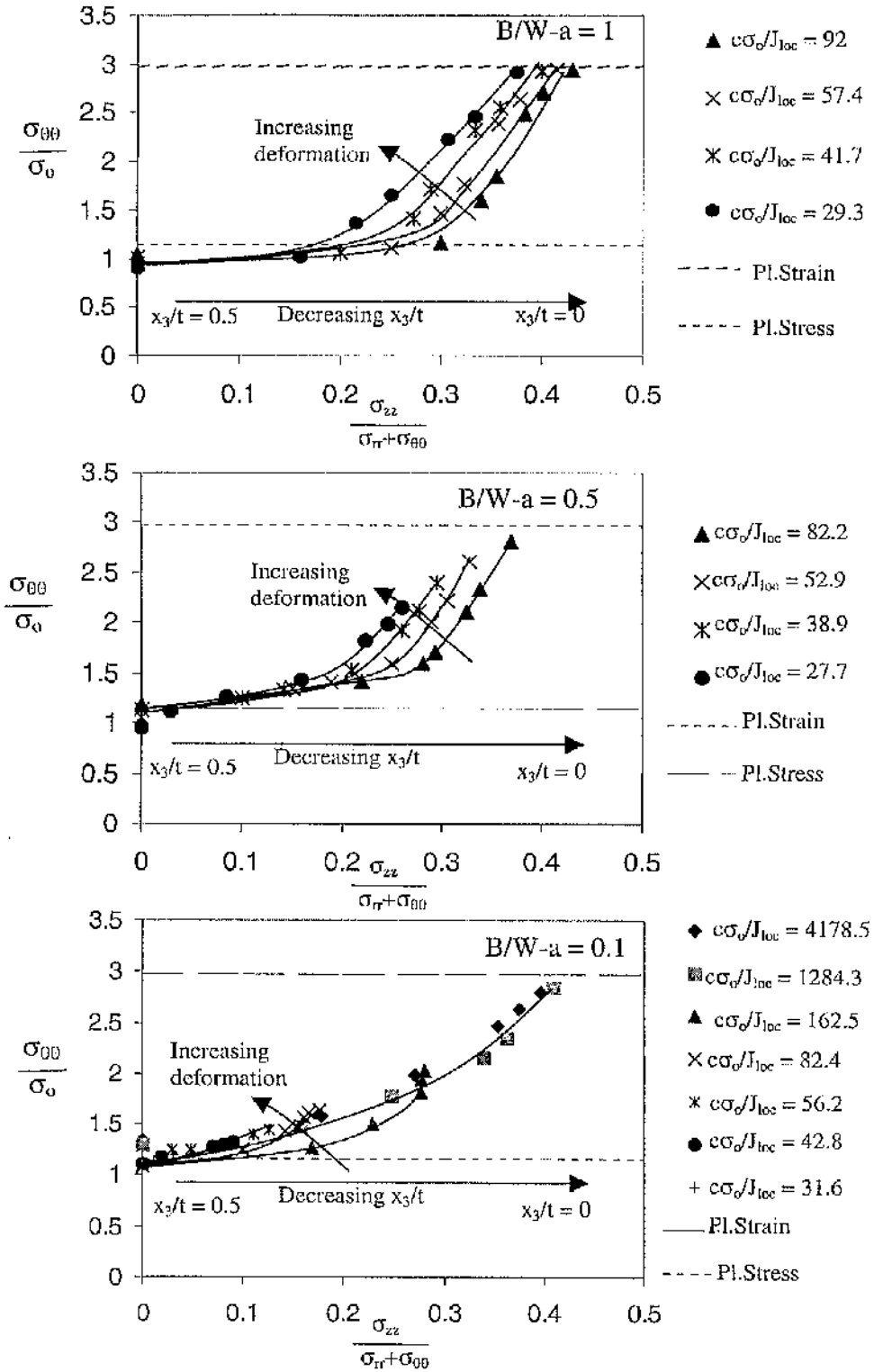


Figure 6.11: The hoop stress as a function of the plane strain parameter at r = $2J/\sigma_o$ for SENB specimens B/(W-a) = 1, 0.1 and 0.5. The load levels are the midplane values.

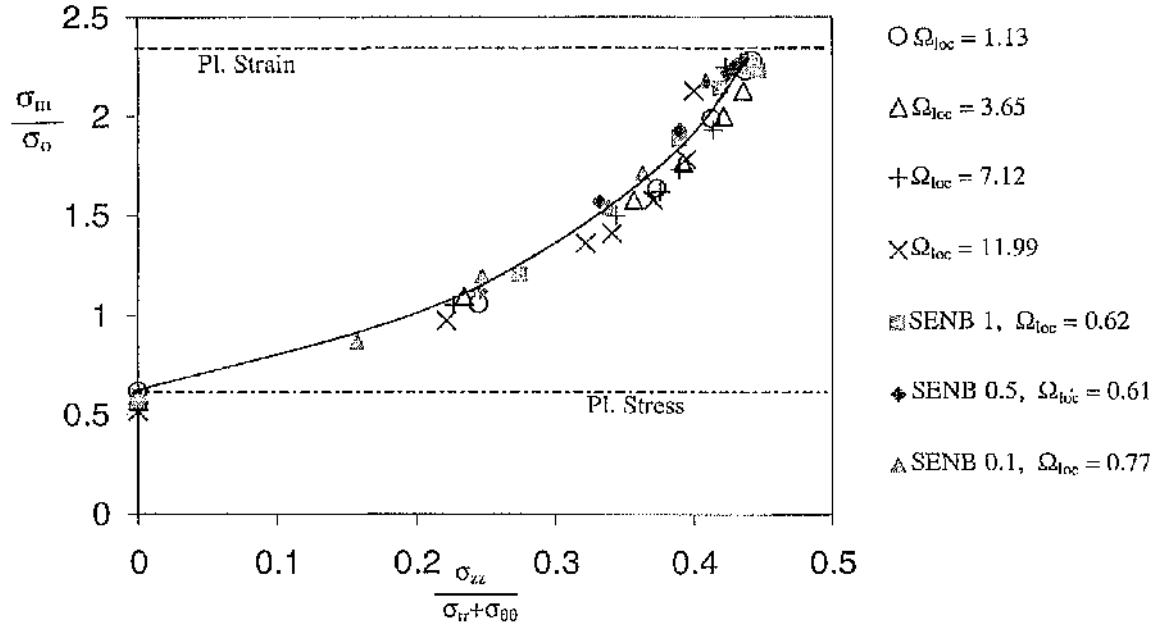


Figure 6.12: The mean stress in boundary layer formulation and SENB specimens as a function ρ at low load levels at $r = 2J/\sigma_o$.

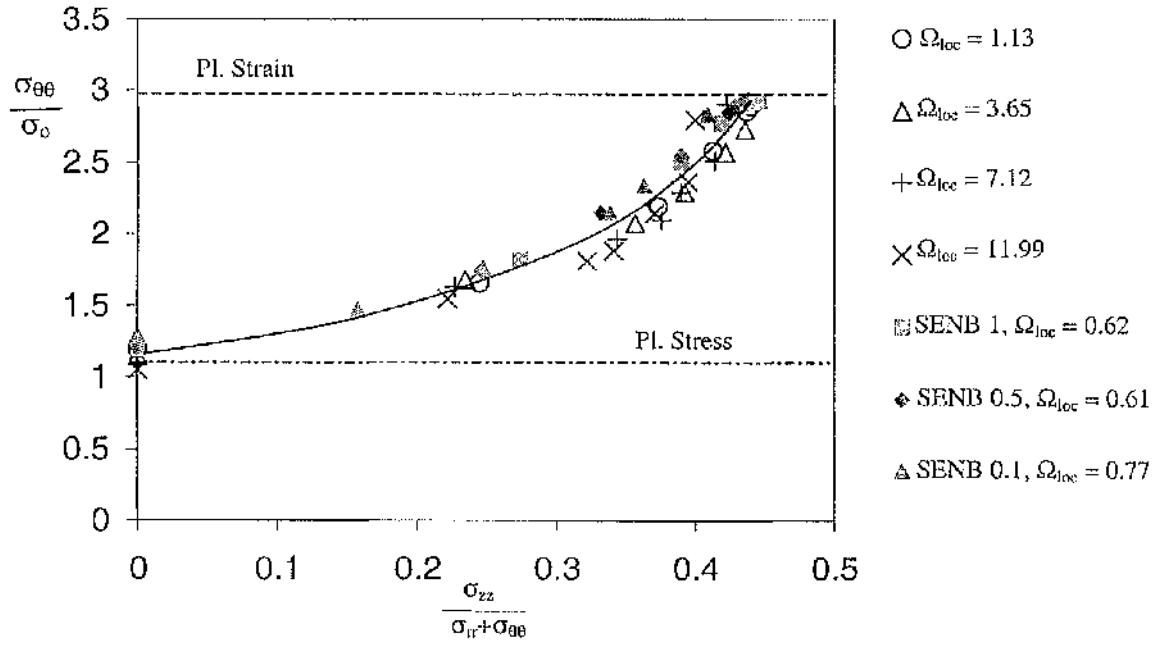


Figure 6.13: The hoop stress in boundary layer formulation and SENB as a function of ρ specimens at low load levels at $r = 2J/\sigma_o$.

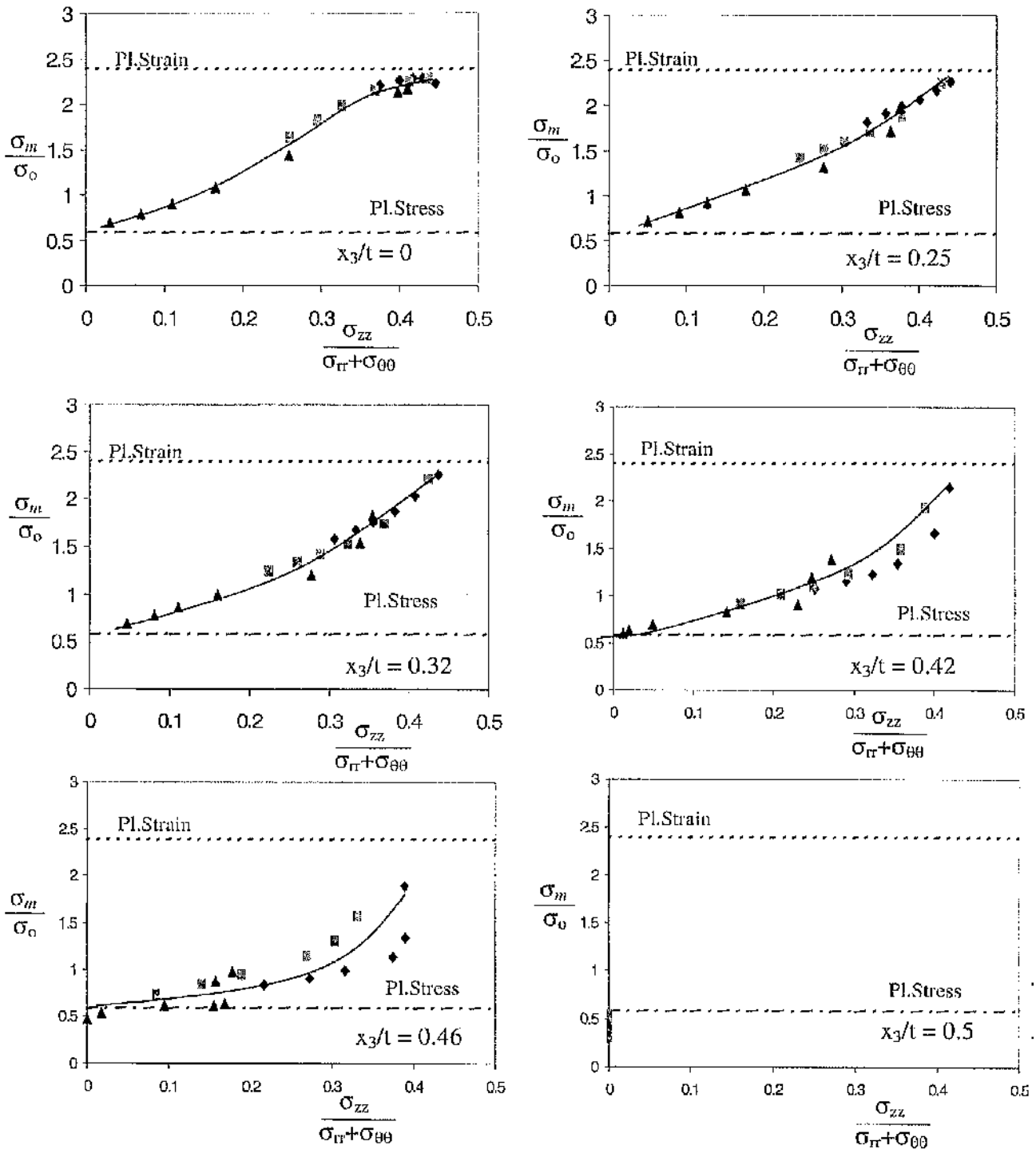


Figure 6.14: The mean stress as a function of the plane strain parameter at different sections ($x_3/t$) across the thickness for SENB specimens at $r = 2J/\sigma_o$. The diamond, square and triangular markers represent the thick, intermediate thickness and thin specimens.

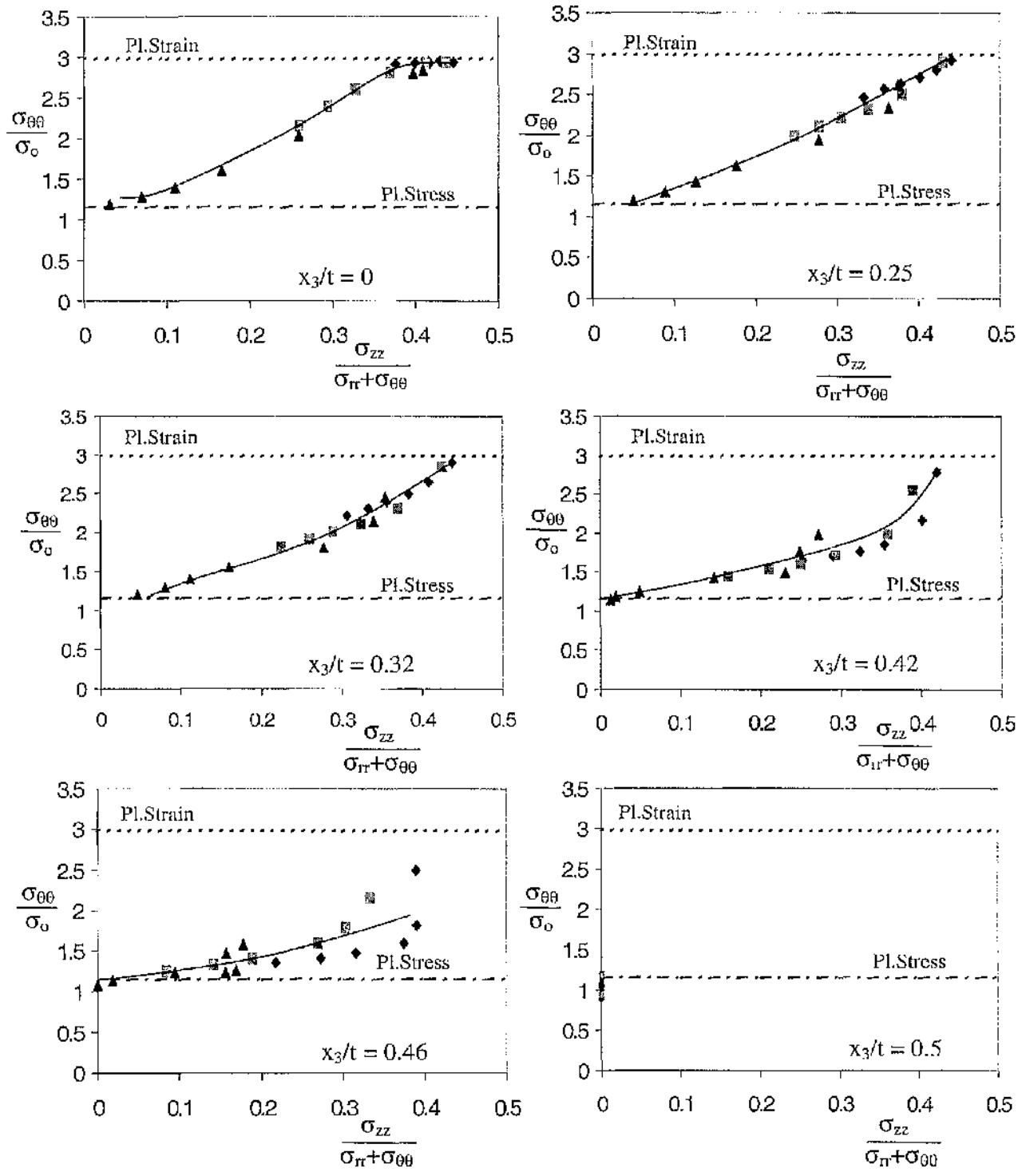


Figure 6.15: The hoop stress as a function of the plane strain parameter at different sections ($x_3/t$) across the thickness for SENB specimens at $r = 2J/\sigma_o$. The diamond, square and triangular markers represent the thick, intermediate thickness and thin specimens.

(a)

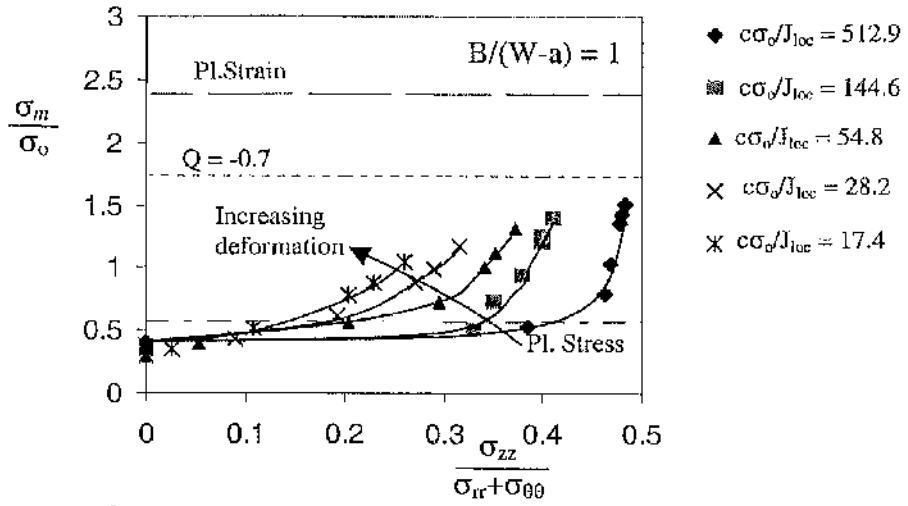


(b)

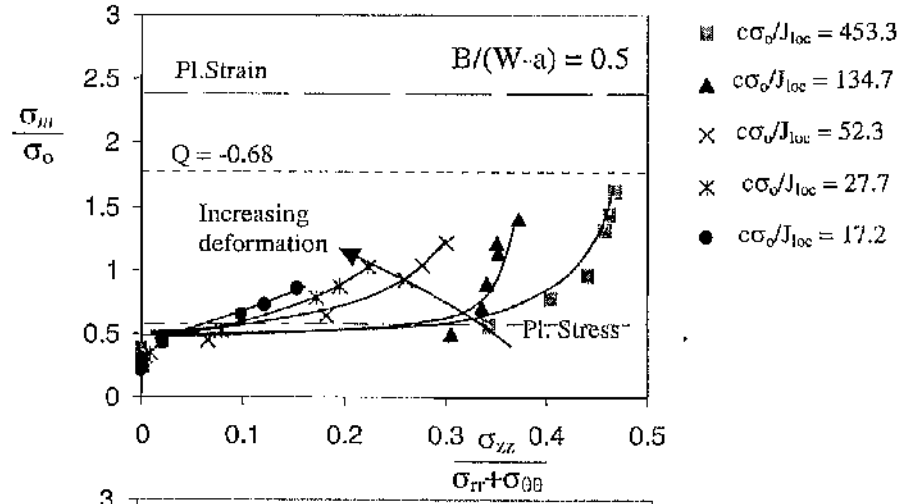


(c)

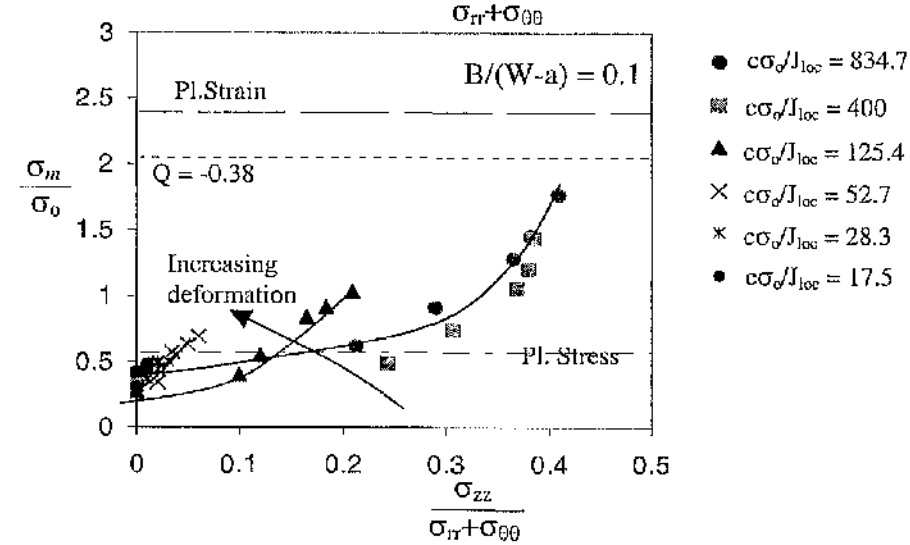


Figure 6.16: The mean stress as a function of the plane strain parameter at $r = 2J/\sigma_o$ at limit load in CCP specimens B/(W-a) = 1, 0.5 and 0.1. The load levels are the midplane values.

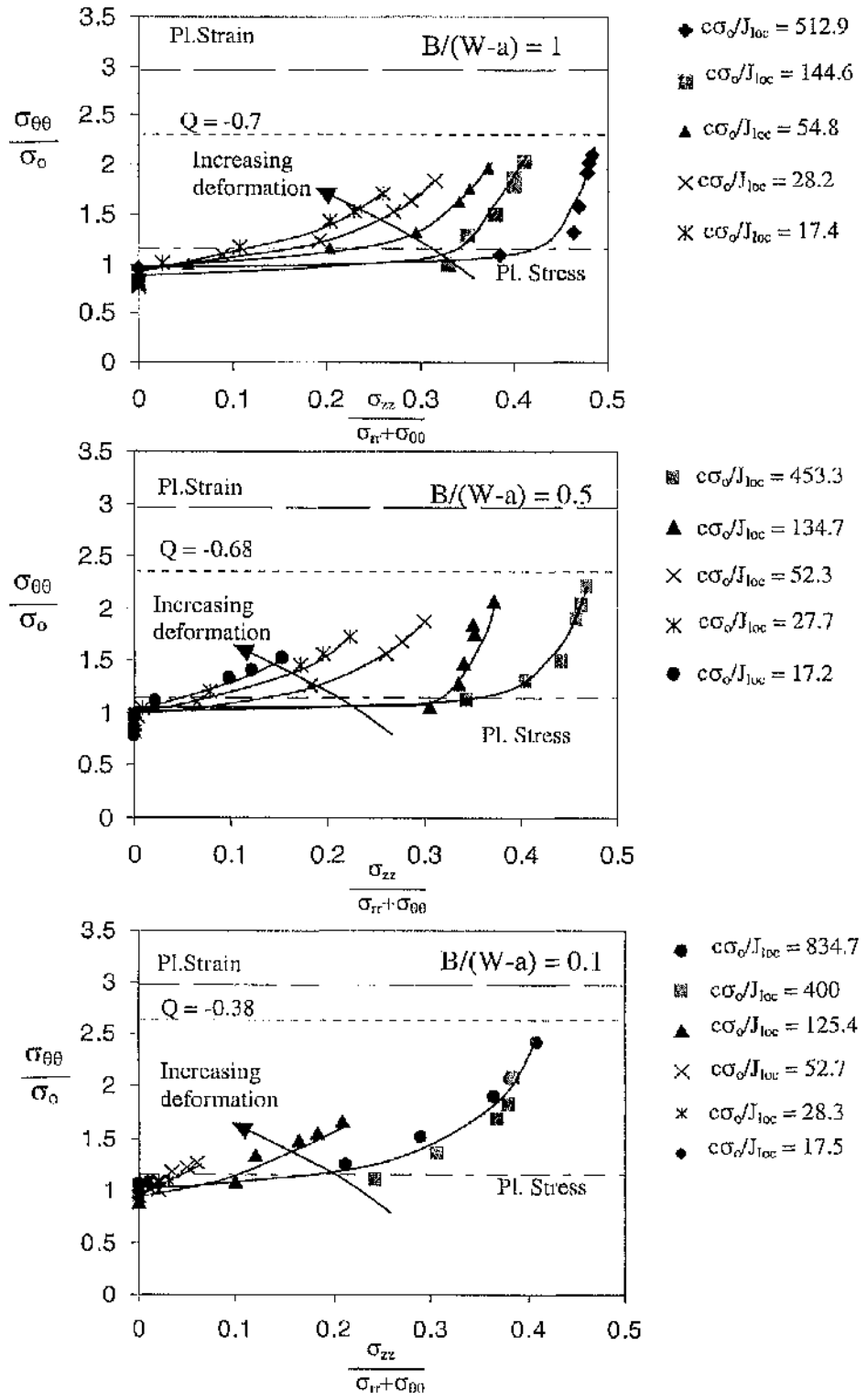


Figure 6.17: The mean stress as a function of the plane strain parameter at $r = 2J/\sigma_o$ at limit load in CCP specimens B/(W-a) = 1, 0.5 and 0.1. The load levels are midplane values.

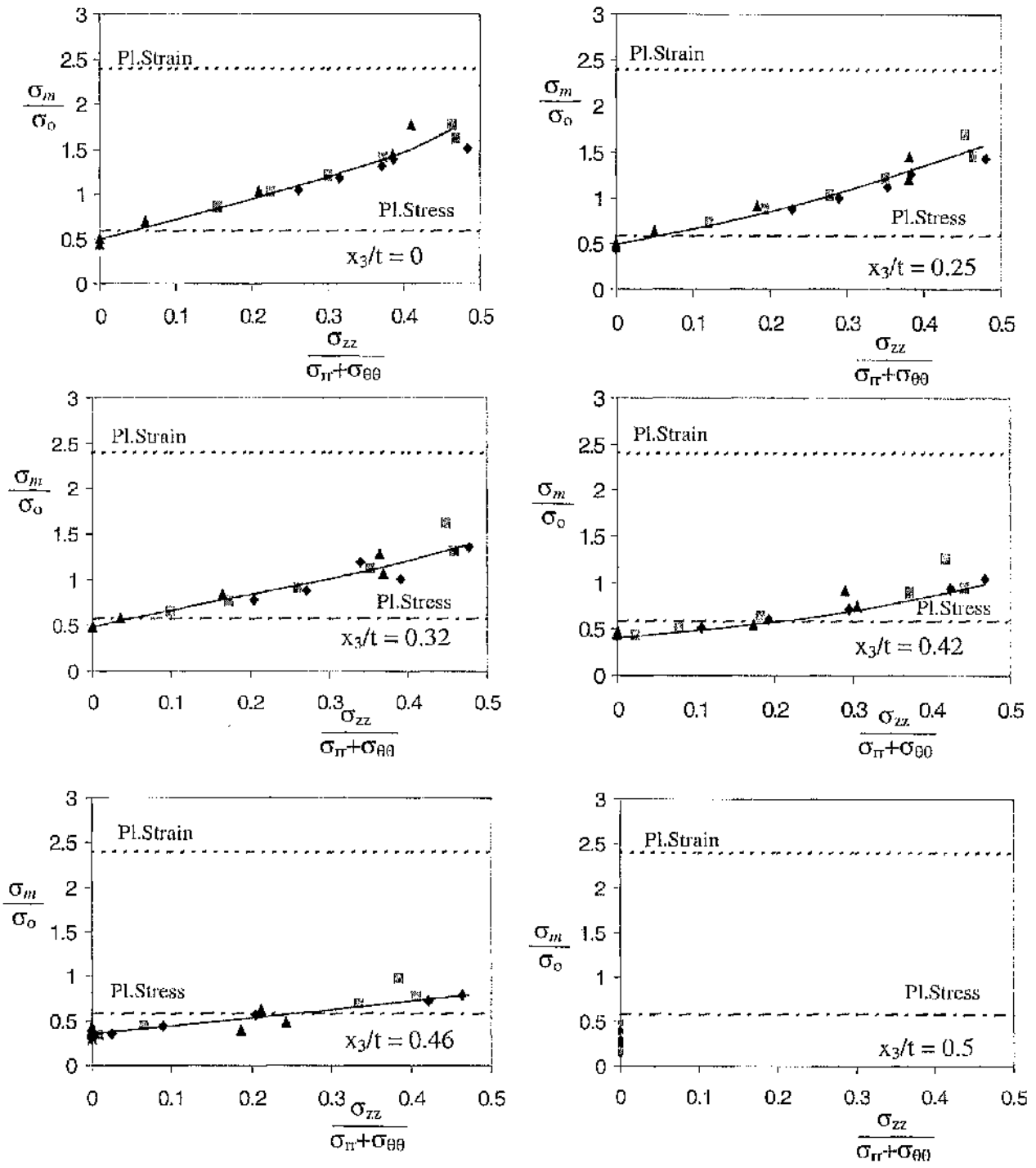


Figure 6.18: The mean stress as a function of the plane strain parameter at different sections ($x_3/t$) across the thickness at limit load for CCP specimens at $r = 2J/\sigma_o$. The diamond, square and triangular markers represent the thick, intermediate thickness and thin specimens.

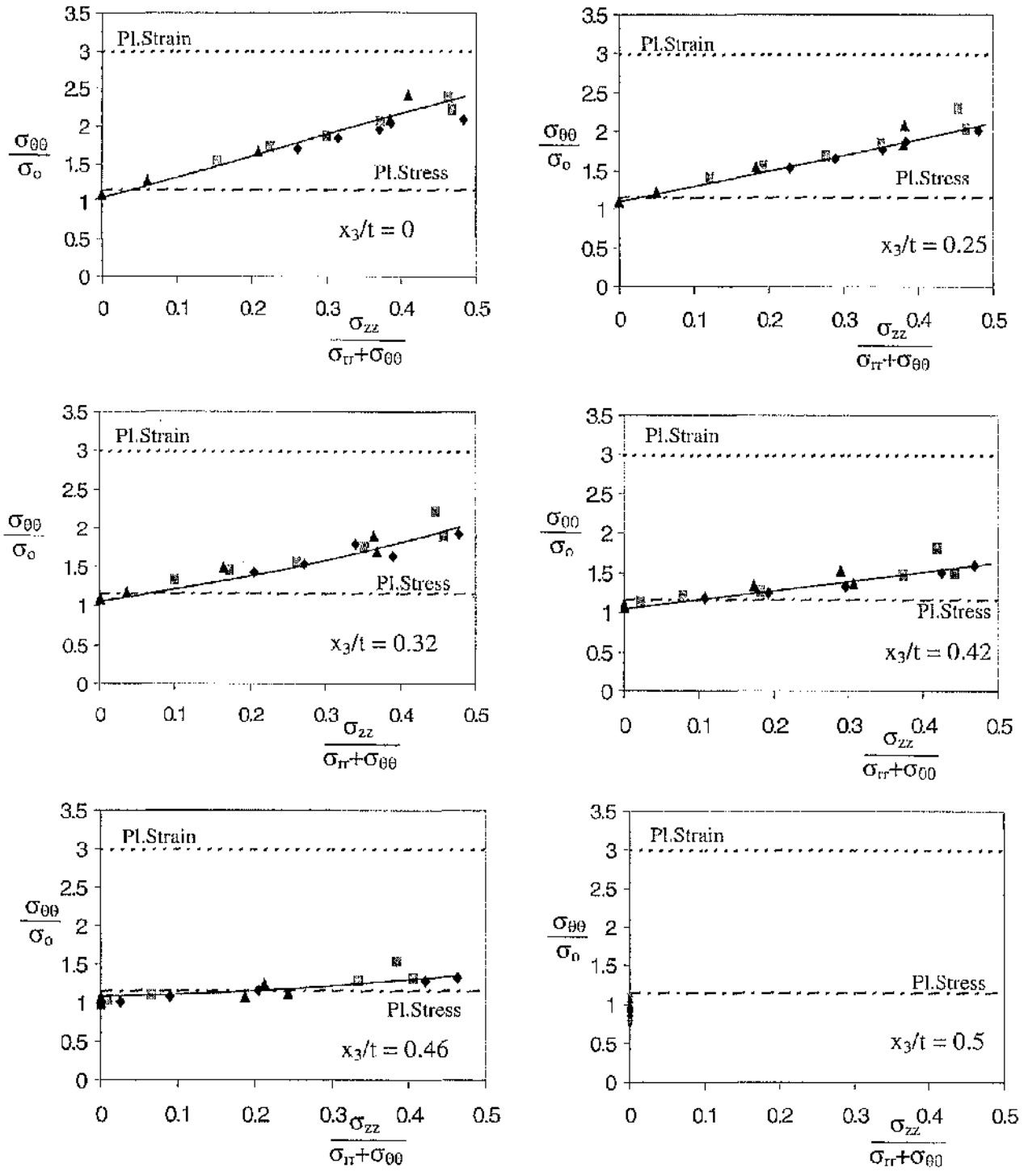


Figure 6.19: The hoop stress as a function of the plane strain parameter at different sections ($x_3/t$) across the thickness at limit load for CCP specimens at $r = 2J/\sigma_o$. The diamond, square and triangular markers represent the thick, intermediate thickness and thin specimens.

# Out-of-Plane Constraint Loss

Conservative approaches to defect assessment are based on the toughness in plane strain conditions. Unlike two-dimensional solutions, the structure of three dimensional crack tip fields has proved to be elusive. A systematic investigation of constraint loss in three-dimensional cracked problems has been a central focus in this thesis. Chapter 7 starts by considering a dimensional analysis of the problem. This leads to hypotheses about parameters which can quantify out-of-plane constraint loss as a function of deformation. These hypotheses are tested against the current numerical data.

## 7.1 A Dimensional Analysis

In order to consider the structure of three-dimensional elastic-plastic crack tip fields, it is appropriate to start by considering the dimensional nature of the problem, with the knowledge that continuum mechanics problems are inherently non-dimensional. Initially consider a two-dimensional (plane stress or plane strain) asymptotic crack tip field, possibly modelled by a two-dimensional boundary layer formulation as illustrated schematically in Figure 7.1(a). The local stresses at a point defined by co-ordinates (r, θ) are naturally normalised by the yield stress in tension, $(\sigma_{ij}/\sigma_o)$. The co-ordinates involve one length scale, r. The only other parameter in the problem which has the dimensions of length is the loading parameter $J/\sigma_o$. Physically $J/\sigma_o$ can be regarded as being proportional to the crack tip opening displacement, or equivalently the radius of the plastic zone. As a result, when the stress normalised by the yield stress are expressed as a function of $r\sigma_o/J$, the stresses are self similar. A specific and important case arises at the crack tip ($r = 0$) when there are no length dimensions in the problem, and for a perfectly plastic material the crack tip stress system is simply defined as $(\sigma_{ij}/\sigma_o)$ independent of applied load as measured by $(J/\sigma_o)$.

Now consider a semi-infinite three-dimensional boundary layer formulation, as illustrated schematically in Figure 7.1(b). As usual the crack flanks lie on $\theta = \pm \pi$, and a free surface exists at $z = 0$. The co-ordinates of an arbitrary point $(z, r, \theta)$ now involve two length scales. However at the crack tip ($r = 0$), there is only one co-ordinate in the problem, z. This can only be non-dimensionalised by $J/\sigma_o$. The appropriate parameter is thus $z\sigma_o/J$. It is worth noting that highly constrained (near plane strain) fields would be expected to occur remote from a free surface ($z \rightarrow \infty$), and at small deformation levels ($J \rightarrow 0$), while constraint is expected to be lost near a free surface, and at large deformation levels ($z \rightarrow 0$, $J \rightarrow \infty$). The parameter $z\sigma_o/J$ thus has the correct form to unify these effects.

Ahead of the crack there are three length parameters $(z, r, J/\sigma_o)$ which can not be uniquely arranged by purely dimensional arguments. However on a plane normal to the crack front, defined by $z\sigma_o/J$, the non-dimensionalised distance must at least incorporate $r\sigma_o/J$.

In a full three-dimensional problem Figure 7.1(c), such as a thin plate full-field solutions, the co-ordinates are still involve two physical length scales (z, r), while two additional length scales are introduced by the plate thickness, t, and the loading parameter $J/\sigma_o$. Consider the stress profile on two plates of different thickness within contained yielding. The stress profiles ahead of the crack, must involve the loading parameter $J/\sigma_o$, allowing distances to be expressed as $r\sigma_o/J$. A scaling argument suggests that at sections defined by z/t the stress profiles should be identical at the same applied load, $J/t\sigma_o$. However, the profiles are expected to change with both (z/t) and loading. Insight into the way that this change for specimens of different thickness may be obtained by recalling that in the semi-infinite problem the stress fields at the tip are expected to be unified by $z\sigma_o/J$. This parameter is investigated as a way of unifying out of plane constraint effects in boundary layer formulations and full-field solutions of different thicknesses.

## 7.2 Out-of-Plane Constraint Loss at the Crack Tip ( r = 0, θ = 0°)

### 7.2.1 Boundary Layer Formulations

To quantify out-of-plane constraint loss, attention is again focused on the mean stress and the hoop stress in the leading sector ahead of the crack tip. Figures 7.2 and 7.3 show the mean stress, $\sigma_m$, and the hoop stress, $\sigma_{\theta\theta}$, as a function of the deformation parameter ($J_{loc}/z\sigma_o$) from the midplane to a plane close to the free surface at the crack tip using a boundary layer formulation. The deformation levels applied in the boundary layer formulation ranged through $\Omega_{far}$ = 1, 3, 5, 8 and 20. On the midplane (z/t = 0.5), the mean stress and the hoop stress maintain stress levels close to the fully constrained plane strain values from small to moderate load levels ($\Omega_{far}$ = 1 to 8). However, at the maximum load ($\Omega_{far}$ = 20), constraint is lost. Across the plate thickness, constraint loss increases from the midplane to the free surface while an increase in load causes a drop in constraint at each section (z/t). At sections near the free surface, the constraint level approaches that associated with a plane stress field, but at the intersection of the crack front and the free surface, the field is perturbed by a corner field which features a uniaxial tension sector directly ahead of the crack.

### 7.2.2 SENB Specimens

In the SENB specimens, the mean stress and the hoop stress are shown as a function of deformation in Figure 7.4 (a) to (f) and Figure 7.5 (a) to (f). The order of the figures correspond to the order of the sections along the crack front; from z/t = 0.5 to 0.04. The stresses are represented by square, triangular and circular markers for the thick, intermediate thickness, and thin bend specimens. The important result is that identical constraint loss occurs at the corresponding sections (z/t) of different thickness specimens when deformation is parameterised by $J_{loc}/z\sigma_o$. As a result, the mean and the hoop stress at a given same section (z/t) in different thickness specimens can be unified as illustrated in Figures 7.4 and 7.5. The maximum deformation level in this data set, approaches the limit

of plane strain J-dominance of $25J_{loc}/\sigma_o$ in bending at the midplane. The thin specimen exhibited the highest $J_{loc}/z\sigma_o$ before the limit of plane strain J-dominance was reached at the midplane.

A compilation of all the out-of-plane constraint loss data at different sections of SENB specimens is shown in Figures 7.6 and 7.7. The figures, show that the stresses at the crack tip eventually approaches a steady state for each section for deformation levels $J_{loc}/z\sigma_o \geq 0.05$, which corresponds to limit load. At limit load the deformation becomes constant, and the stress distribution at the crack tip and all other fixed distances must also therefore become steady state.

### 7.2.3 CCP Specimens

In the CCP specimens, constraint is lost due to both in-plane and out-of-plane effects. The in-plane effect can be estimated using the load combined with the appropriate T-stress concentration factor, $T/\sigma_{app}$, for the geometry, and then using modified boundary layer formulation calculations to connect $T/\sigma_o$ to the level of constraint loss, Q. The in-plane constraint loss at limit load, calculated by this method is shown in Table 6.2. The table gives the level of the mean and the hoop stress for all thicknesses of CCP specimens. It is clear that constraint loss before limit load is largely attributable to the in-plane effect, while the out–of-plane effect dominates beyond limit load.

Figures 7.8 (a) to (f) and 7.9 (a) to (f) illustrate the mean stress and the hoop stress for CCP specimens at different sections (z/t) for three different thicknesses. Constraint loss in thick, intermediate thickness and thin CCP specimens is represented by the square, triangular and circular markers. Both figures show that the out-of-plane constraint loss is identical at the same section (z/t) of different thickness specimens when deformation is parameterised by $J_{loc}/z\sigma_o$.

The data presented in Figures 7.8 (a) to (f) and 7.9 (a) to (f) are plotted in Figures 7.10 and 7.11 to show the constraint loss as a function of $J_{loc}/z\sigma_o$ at all sections along the crack

front. Constraint loss increases with distance from the midplane to the free surface. The mean and the hoop stress fall as out-of-plane constraint is lost with increasing levels of deformation at limit load, $J_{lo}/z\sigma_o > 0.05$. At limit load, the deformation and the corresponding stress distribution become stationary.

Consequently, the constraint loss at the crack tip in both SENB and CCP specimens approaches a steady state in full plasticity. Therefore at limit load, the mean and the hoop stress along the crack front at the crack tip (r = 0) can be simplified as shown in Figures 7.12 and 7.13. These figures show that independent of thickness and at limit load, the out-of-plane constraint loss at the crack tip can be represented by single relationships from the midplane to the free surface. In the SENB specimens there is no in-plane constraint loss, unlike the CCP geometry, which allows the constraint loss to be split into in-plane and out-of plane components. The out-of-plane constraint loss in CCP specimen qualitatively follows a similar pattern to the SENB specimens but at a lower level due to in-plane constraint loss. At the free surface, the constraint level for SENB and CCP specimens both reduce to that of a corner field. The boundary layer formulation data is also similar to the SENB results. This demonstrates that, for positive T-stress configurations, the out-of-plane constraint loss at the crack tip (r = 0) for the mean and the hoop stress can be generally represented by the SENB curves for loads $J_{lo}/z\sigma_o \geq 0.05$.

## 7.3 Out-of-Plane Constraint Loss ($r = 2J/\sigma_o$, $\theta = 0^o$)

### 7.3.1 Boundary Layer Formulations

Out-of-plane constraint loss as a function of deformation and thickness is now examined at distance $r = 2J/\sigma_o$ from the crack tip. Figures 7.14 and 7.15 show the mean and hoop stress as a function of deformation in a boundary layer formulation. Both figures show that the constraint is lost with increasing deformation at all sections through the thickness. For all sections, the stress start at the fully constrained plane strain level and decays with increasing deformation. The loss of constraint is highest on planes close to the free surface. At the same applied load, the constraint loss at the crack tip (r = 0) is less than that at r =

$2J_{loc}/\sigma_o$, which is consistent with the observation that constraint loss increases both with distance from the tip and deformation.

### 7.3.2 SENB Specimens

The mean and the hoop stress at $r = 2J/\sigma_o$, at different sections (z/t) along the crack front of SENB specimens are shown in Figures 7.16 (a) to (f) and 7.17 (a) to (f). The data from thick, intermediate thickness and thin SENB specimens are represented by square, triangular and plus markers repectively. The plots show that the stresses at the same section (z/t) of different thickness specimens are unified when deformation is quantified by $J_{loc}/z\sigma_o$. However, unlike the behaviour at the crack tip, constraint continues to be lost at all deformation levels in contrast to the behaviour at the crack tip which reach a steady state at limit load. It is important to realise that the distance $r = 2J/\sigma_o$ is not constant but increases with deformation. Although the applied load and the stress distribution which equilibrates with it are expected to be stationary at limit load, the distance $2J/\sigma_o$ continues to sample the stress at increasing distances from the crack tip, even at limit load. As a result the stress at $2J/\sigma_o$ does not reach a steady state at limit load.

Figures 7.18 and 7.19 show compilations of the out-of-plane constraint loss for different sections (z/t) from the data presented in Figures 7.16 (a) to (f) and 7.17 (a) to (f). An increase in deformation causes significant loss of constraint across the crack front. The trends show that the constraint loss at all sections approaches the plane stress field at high deformation levels.

### 7.3.3 CCP Specimens

The constraint loss in CCP specimens at $r = 2J/\sigma_o$ is shown in Figures 7.20 (a) to (f) and 7.21 (a) to (f) as a function of $J_{loc}/z\sigma_o$. Initially, constraint is lost due to the in-plane effect, followed by out-of-plane constraint loss. For a given section (z/t), the out-of-plane constraint loss in all the CCP specimens can be unified by using the parameter $J_{loc}/z\sigma_o$.

Figures 7.22 and 7.23 show compilations of the out-of-plane constraint loss plots from Figures 7.20 (a) to (f) and 7.21 (a) to (f) for the mean and the hoop stress. The value of the mean and the hoop stress attributable to in-plane constraint loss in CCP specimens has been calculated at limit load using $T/\sigma_o$. Although the in-plane constraint loss for different thicknesses varies slightly with $T/\sigma_o$ given in Table 6.2, the stress field for different thicknesses converge to a unified curve. The mean and hoop stress at limit load for Q = -0.7 occurs on the midplane at approximately $1.69\sigma_o$ and $2.27\sigma_o$. However as the load is increased, out-of-plane effects cause a rapid loss of constraint and the stresses approach the plane stress field at deformation levels of the order $J_{loc}/z\sigma_o = 0.5$ when they approach a steady state. Conversely at $r = 2J/\sigma_o$, plane stress conditions occur on the centre plane for plates thinner than $4J_{loc}/\sigma_o$ which is approximately 4 crack tip opening displacements ($4\delta$). At the free surface, the corner field affects the constraint at low load levels when the field exhibits a uniaxial tension sector ahead of the crack. However, as the load increases, the field approach the plane stress field.

In both SENB and CCP specimens, the pattern of out-of-plane constraint loss is similar at the crack tip and at $r = 2J/\sigma_o$ at low loads, but differs at high levels of deformation. At $J_{loc}/z\sigma_o < 0.05$, constraint loss at the crack tip and $r = 2J/\sigma_o$ depends on the section (z/t). At $J_{loc}/z\sigma_o > 0.05$, the constraint loss at the crack tip become steady state for each section (z/t). However, at $r = 2J/\sigma_o$ and at high deformation levels, a steady state is only finally reached when a uniform state of plane stress is approached at deformation level $J_{loc}/z\sigma_o \geq 0.5$.

### 7.4 The Proximity to Plane Strain with Deformation

In chapter 6, out-of-plane constraint loss was shown to correlate with the plane strain parameter, $\rho$. In this section, the plane strain loss has been coupled with the deformation parameter ($J_{loc}/z\sigma_o$) in an attempt to unify out-of-plane constraint loss.

### 7.4.1 Plane Strain Loss at the Crack Tip (r =0)

Figure 7.24 shows the plane strain parameter as a function of deformation in a boundary layer formulation. The plane strain conditions are lost with increasing distance from the midplane. However at a given section (z/t), the plane strain parameter at the crack tip approaches steady state.

Figures 7.25 (a) to (f) and 7.26 (a) to (f) show the plane strain parameter for SENB and CCP specimens as a function of $J_{loc}/z\sigma_o$ at five sections across the crack front in different thicknesses. The proximity to plane strain for thick, intermediate thickness and thin specimens of different thickness fall on a single curve for a given section (z/t).

Compilations of $\rho$ as a function of $J_{loc}/z\sigma_o$ in SENB and CCP specimens for different section (z/t) are shown in Figures 7.27 and 7.28. Proximity to plane strain is lost along the crack front as shown in different sections. However, the proximity to plane strain at similar sections (z/t) exhibits a similar behaviour with deformation, and does not show significant differences between specimens with different levels of in-plane constraint.

### 7.4.2 Plane Strain Loss Ahead of the Crack Front ($r = 2J/\sigma_o$)

The loss of plane strain as a function of $J_{loc}/z\sigma_o$ at $2J/\sigma_o$ in a boundary layer formulation is shown in Figure 7.29. Unlike the trend at the crack tip, which exhibits a loss of plane strain before becoming constant at each section (z/t). The plane strain loss at $2J/\sigma_o$ reduces continuously on a unified locus as the deformation level increases at all sections (z/t).

The plane strain parameter as a function of deformation for SENB and CCP specimens at a distance of $r = 2J/\sigma_o$ at various sections (z/t) of different thickness specimens are shown in Figures 7.30 (a) to (f) and 7.31 (a) to (f). Plane strain conditions are lost at all sections as deformation increases, but approach a steady state as the plane stress field is approached.

Figures 7.32 and 7.33 show the plane strain parameter as a function of $J_{loc}/z\sigma_o$ at all sections of the SENB and CCP specimens. Plane strain conditions are lost from the midplane to the free surface as the load level increases and can be unified into a single locus.

At the crack tip, the plane strain parameter, $\rho$, approaches a constant value at limit load at each section across the crack front. However, when the $\rho$ is measured at $r = 2J/\sigma_o$, it continues to fall with deformation at all sections and approaches the plane stress field.

### 7.5 Unification of Out-of-Plane Constraint Loss

In previous sections, the deformation parameter $J/z\sigma_o$ has been used to demonstrate a systematic pattern of out-of-plane constraint loss. However a useful and simple interpretation of out-of-plane constraint loss requires the unification of constraint loss for all sections (z/t). A three-dimensional deformation parameter is proposed which is modified from equation (7.2) :

$$\frac{J_{loc}}{z\sigma_o}\frac{t}{z} \tag{7.4}$$

Figures 7.34 and 7.35 illustrate the mean and the hoop stress as a function of $J_{loc}t/z^2\sigma_o$ at the crack tip for boundary layer formulations. The out-of-plane constraint loss at all sections (z/t) and at all deformation levels can be unified into a single curve.

Figures 7.36 (a) and (b) and 7.37 (a) and (b) show the mean and the hoop stress as a function of the deformation parameter $J_{loc}t/z^2\sigma_o$ for the SENB and CCP specimens. In full field solutions of SENB and CCP specimens, limit load can be reached, and this allows the stresses at the crack tip to reach a steady state. In contrast, boundary layer formulation can never reach limit load conditions because it has no physical geometry. To relate constraint loss in SENB and CCP specimens to the boundary layer formulation at the crack tip, constraint loss can be discussed at low loads and at the limit load. At low loads, constraint

loss as a function of $J_{loc}t/z^2\sigma_o$ across the thickness exhibits a single unified trend shown by the boundary layer formulations. At limit load, constraint loss at the crack tip reaches a steady state as shown in Figures 7.12 and 7.13.

At a distance of $2J/\sigma_o$ ahead of the crack tip, remarkably, constraint loss can be unified onto a single curve at different sections (z/t) for all geometries and load levels. This behaviour is shown for the boundary layer formulation and full-field SENB and CCP specimens as demonstrated in Figures 7.38 (a) and (b), 7.39 (a) and (b), 7.40 (a) and (b), which allows the deformation parameter $J_{loc}t/z^2\sigma_o$ to systematize the constraint loss at different section (z/t) by a single unified curve.

## 7.6 Conclusions

Constraint loss in three-dimensional problems has been evaluated at the crack tip (r = 0) and at a distance of $r = 2J/\sigma_o$. The out-of-plane constraint loss in boundary layer formulations, SENB and CCP specimens exhibit a similar pattern at $r = 2J/\sigma_o$. Constraint is lost with an increase in deformation particularly in sections near the free surface. Constraint loss allows the stress field to approach the plane stress level at all sections at deformation of the order of $J/z\sigma_o \geq 0.5$. Constraint loss at different sections (z/t) can be united as a function of $J_{loc}t/z^2\sigma_o$, so that :

$$\sigma_{(m,\theta\theta)} = f\left(\frac{J_{loc}t}{z^2\sigma_o}\right) \tag{7.5}$$

At the crack tip the pattern of constraint loss is different from that at $r = 2J/\sigma_o$. For geometries which exhibit positive T-stresses, the constraint loss is identical to three-dimensional non-hardening boundary layer formulation. However SENB specimens differ from the boundary layer formulation at the crack tip at high deformation levels. Fundamentally, boundary layer formulation has no physical dimensions and never reaches limit load in contrast to the SENB and CCP configurations. In non-hardening plasticity, the

stresses reach a steady state at limit load which implies that the constraint at a fixed physical distance will reach a steady state. At the crack tip, at limit load, constraint loss has a single profile across the crack front. However, at low levels of deformation, constraint loss for SENB and boundary layer formulation is similar.

Constraint loss is dependent on distance from the tip. The out-of-plane constraint loss at the crack tip is always less than at $r = 2J/\sigma_0$. Consequently the distance $r = 2J/\sigma_0$ can be used as a conservative reference field to estimate constraint levels associated with real cracks and defects. A failure assessment scheme is now discussed in chapter 8.

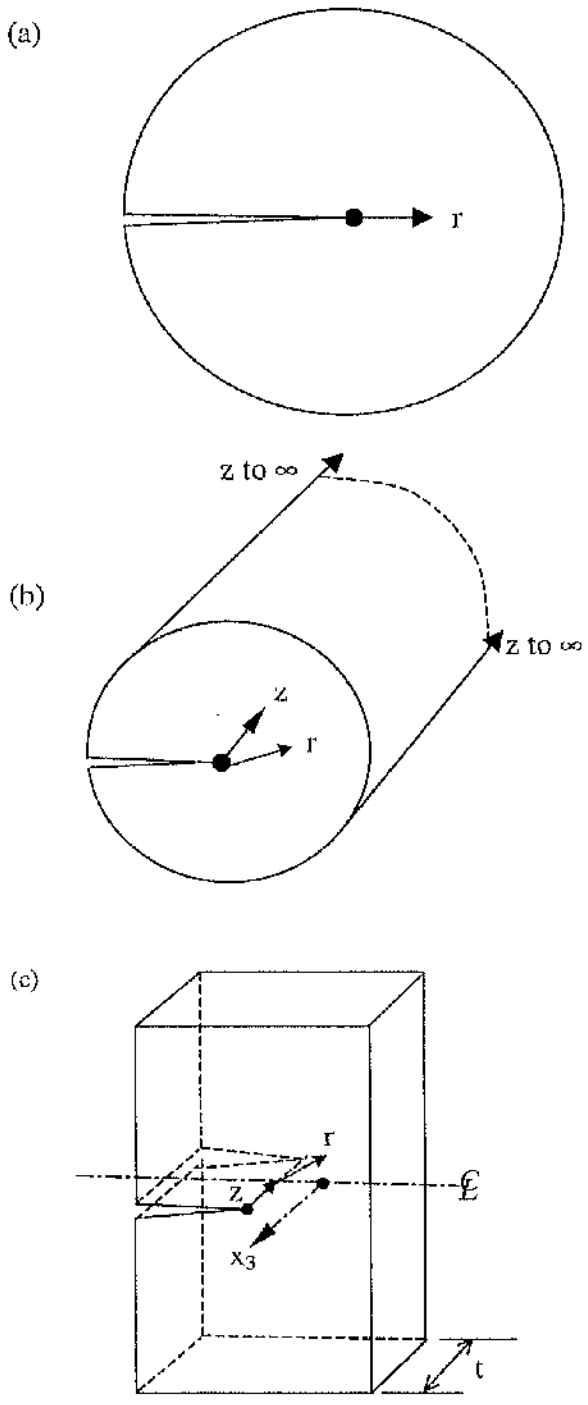


Figure 7.1: The crack tip dimensional length scales associated with (a) two-dimensional, (b) semi-infinite three-dimensional boundary layer formulations and (c) finite three-dimensional problems.

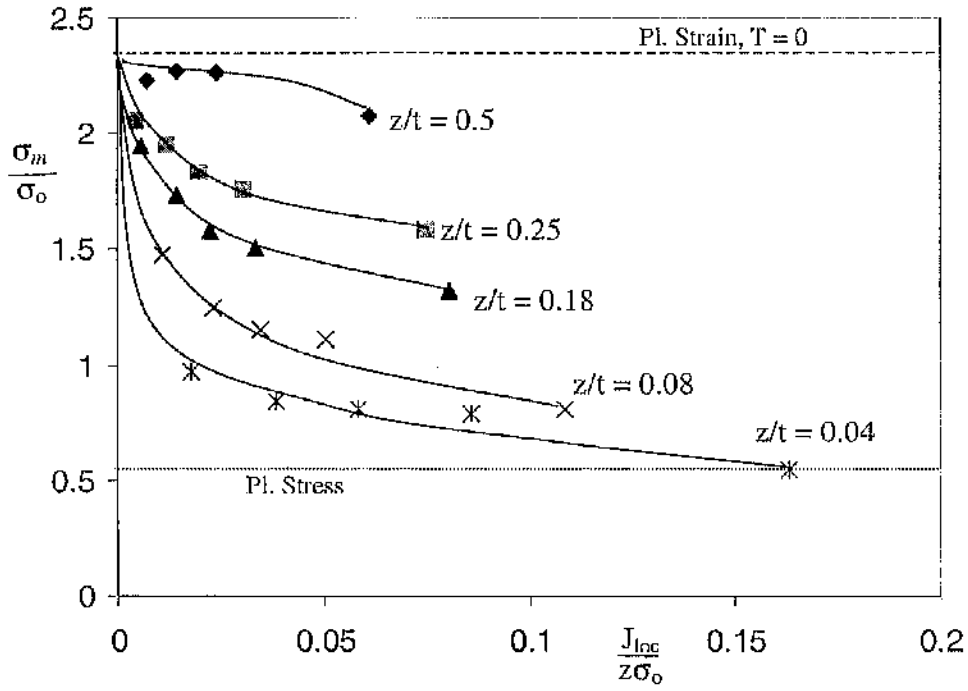


Figure 7.2: The mean stress at the crack tip, r = 0 from the midplane to near the free surface as a function of $J_{loc}/z\sigma_o$ in a boundary layer formulation at load levels $\Omega_{far}$ = 1, 3, 5, 8, 20.

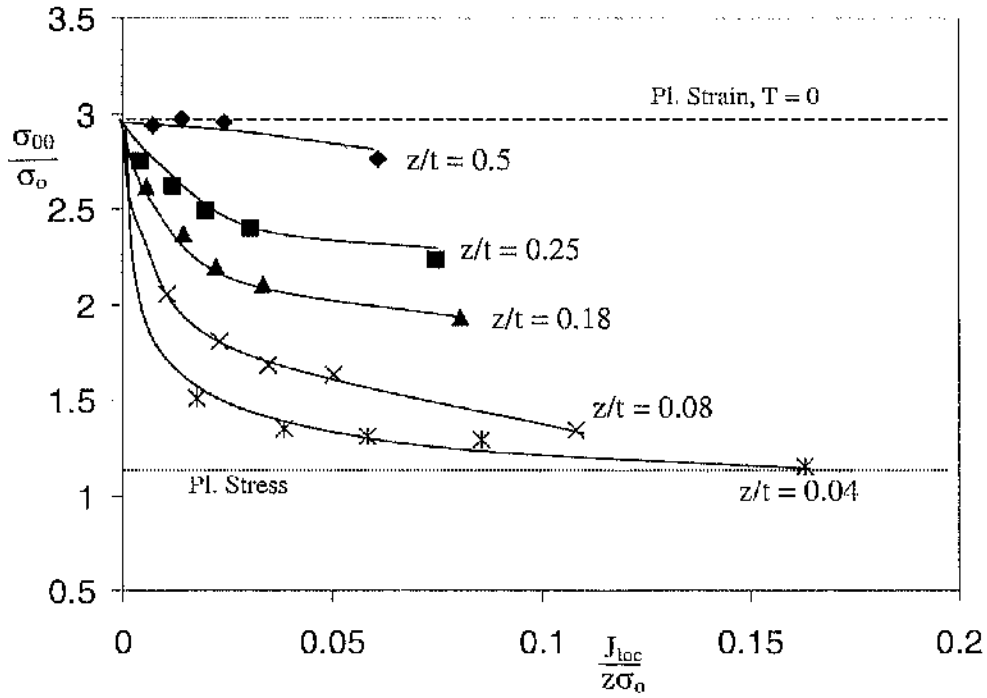


Figure 7.3: The hoop stress at the crack tip, r = 0 from the midplane to near the free surface as a function of $J_{loc}/z\sigma_o$ in a boundary layer formulation at load levels $\Omega_{far}$ = 1, 3, 5, 8, 20.

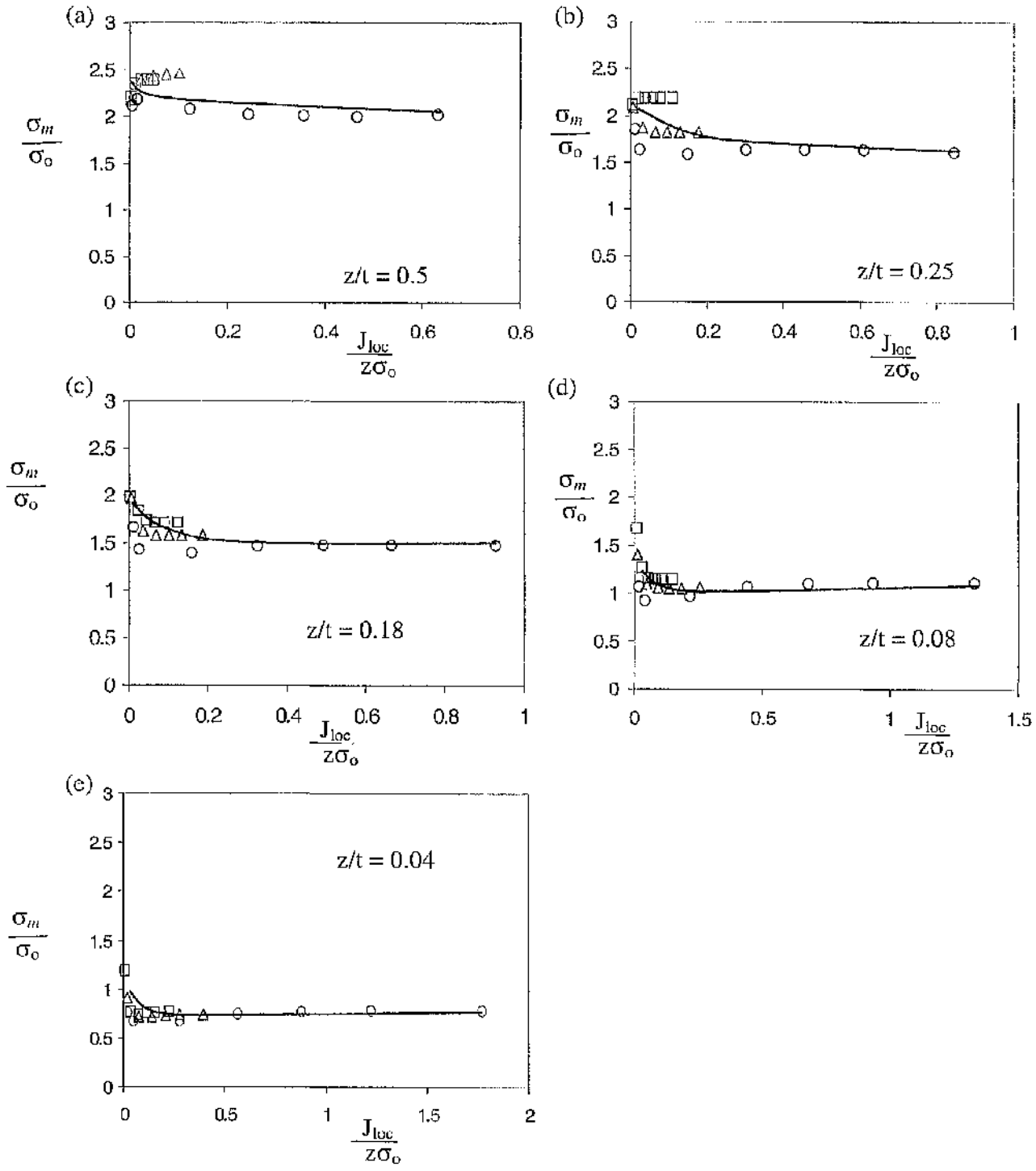


Figure 7.4: The mean stress at the crack tip (r = 0) of SENB specimens of different thickness at different sections (z/t) as a function of $J_{loc}/z\sigma_o$. The square, triangular and circular markers represent the thick, intermediate thickness and thin specimens.

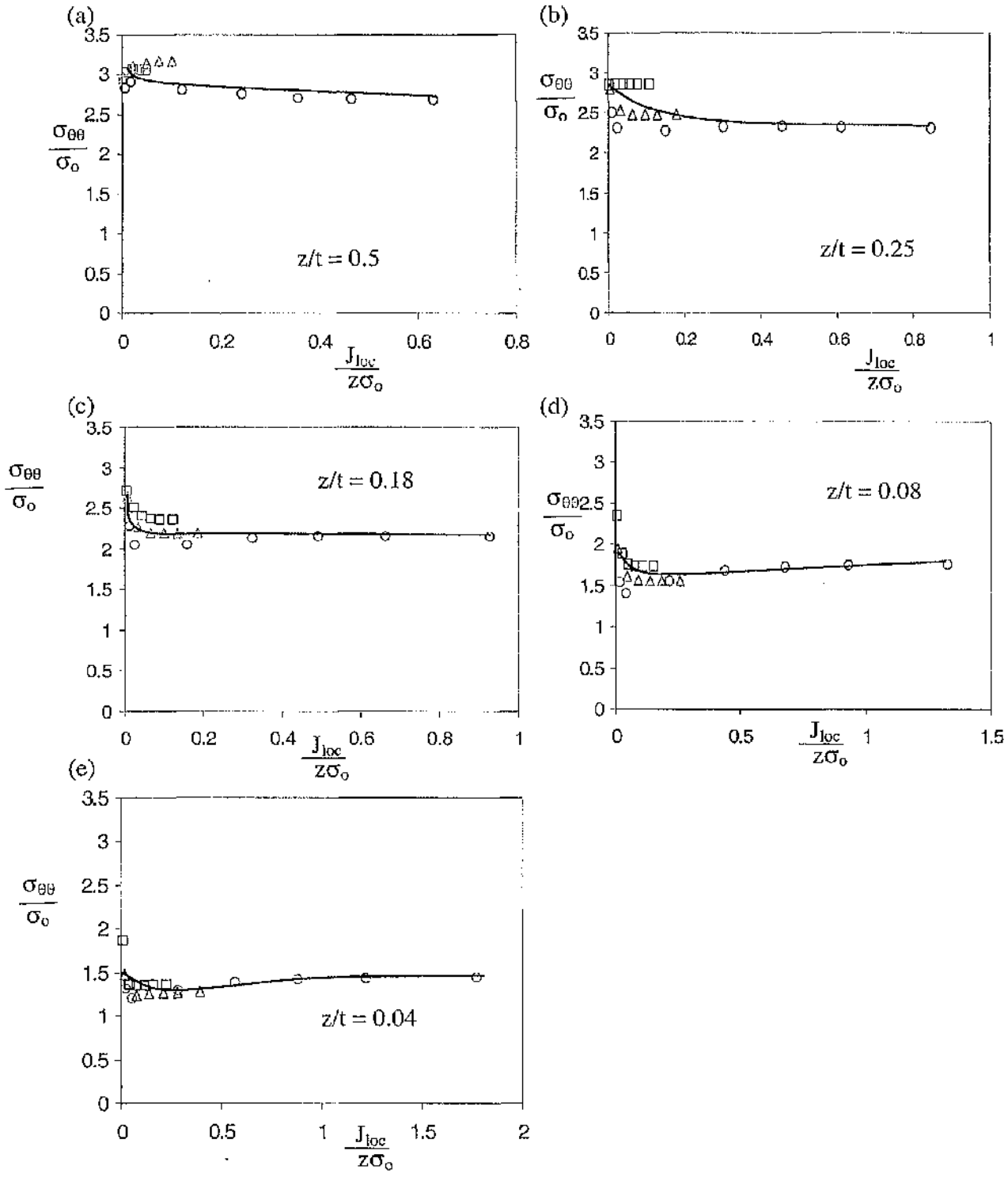


Figure 7.5: The hoop stress at the crack tip (r = 0) at different sections along the crack front as a function of $J_{loc}/z\sigma_o$, in SENB specimens of different thickness. The square, triangular and circular markers represent the thick, intermediate thickness and thin specimens.

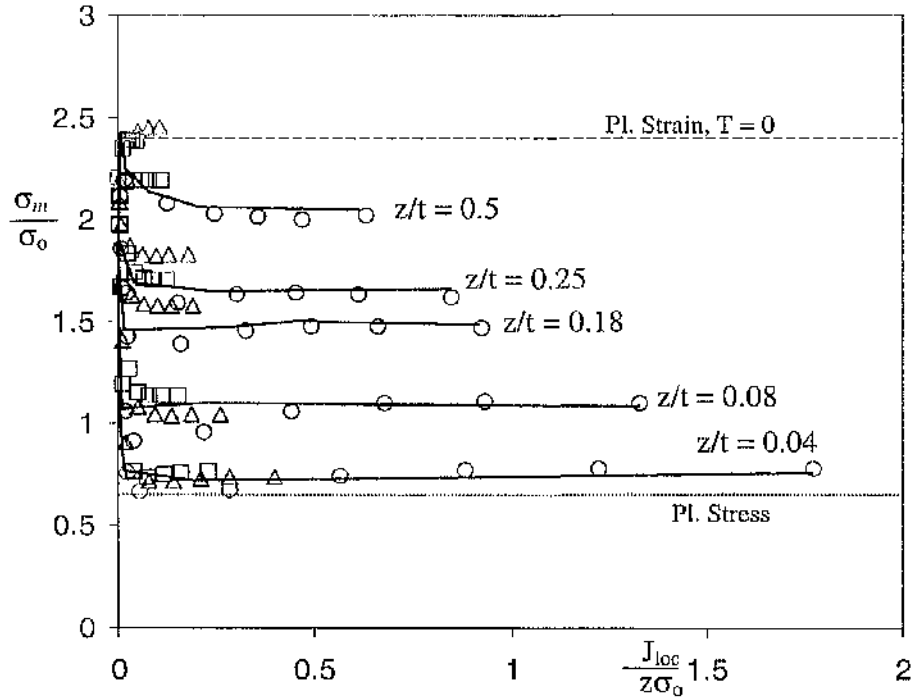


Figure 7.6: Compilation of plots from Figure 7.3 (a to f) for the mean stress at r = 0, as a function of $J_{loc}/z\sigma_o$ for SENB specimens of different thickness. The square, triangular and circular markers represent the thick, intermediate thickness and thin specimens.

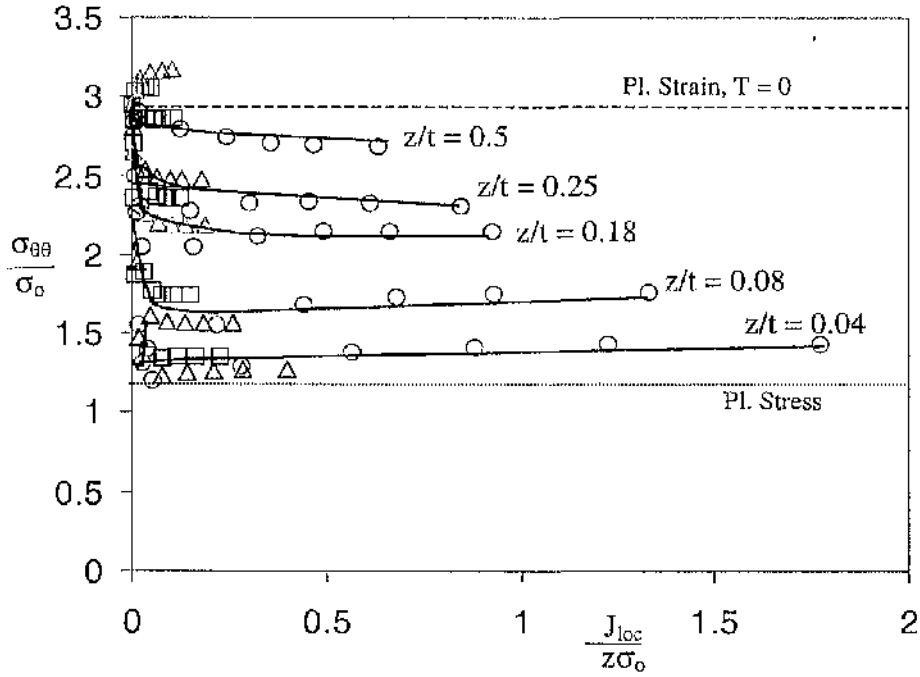


Figure 7.7: Compilation of plots from Figure 7.7 (a to f) for the hoop stress at r = 0, as a function of $J_{loc}/z\sigma_o$ for SENB specimens of different thicknesses. The square, triangular and circular markers represent the thick, intermediate thickness and thin specimens.

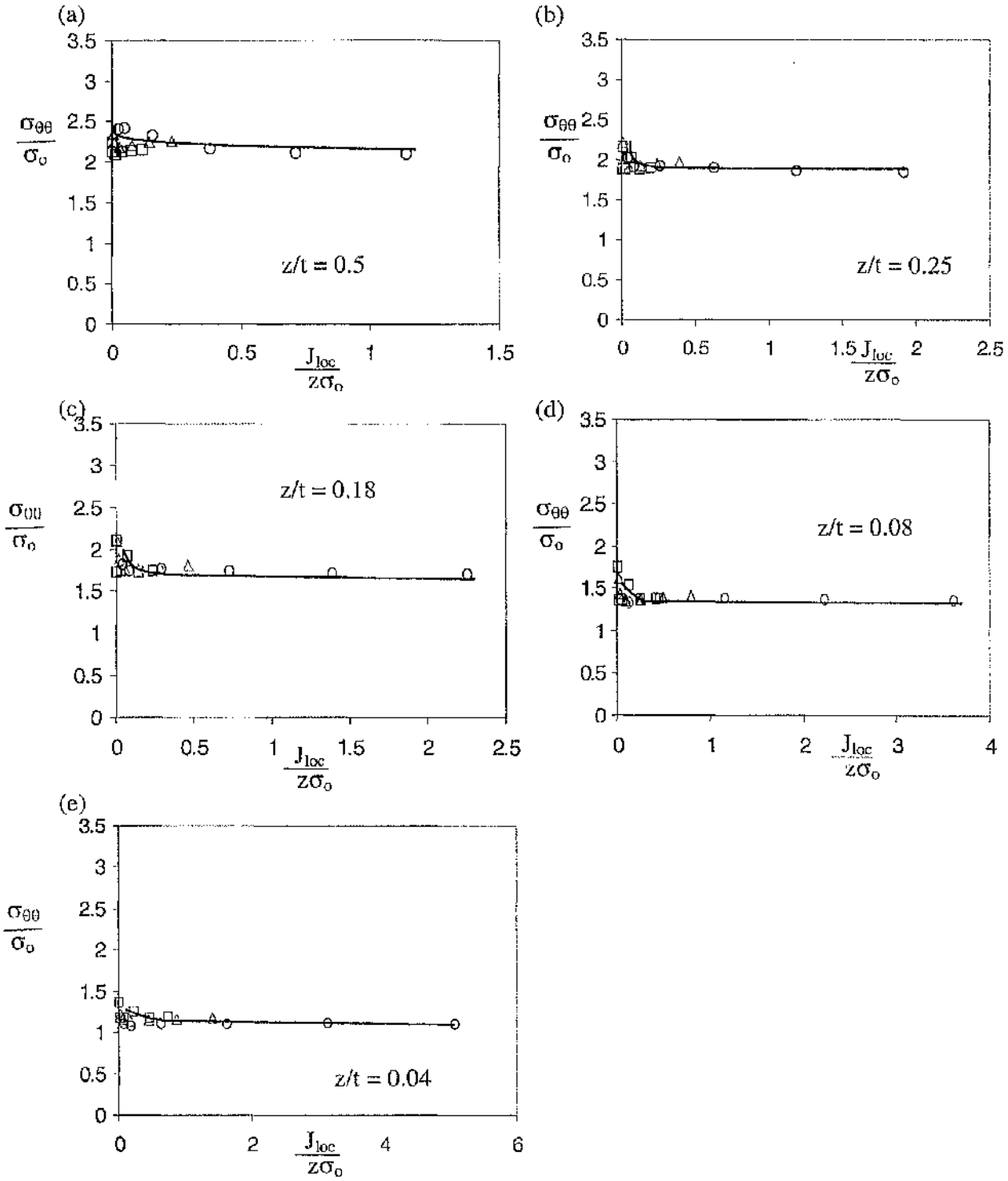


Figure 7.8: The hoop stress at the crack tip (r = 0) at different sections (z/t) as a function of $J_{loc}/z\sigma_o$ for CCP specimens of different thicknesses. The square, triangular and circular markers represent the thick, intermediate thickness and thin specimens.

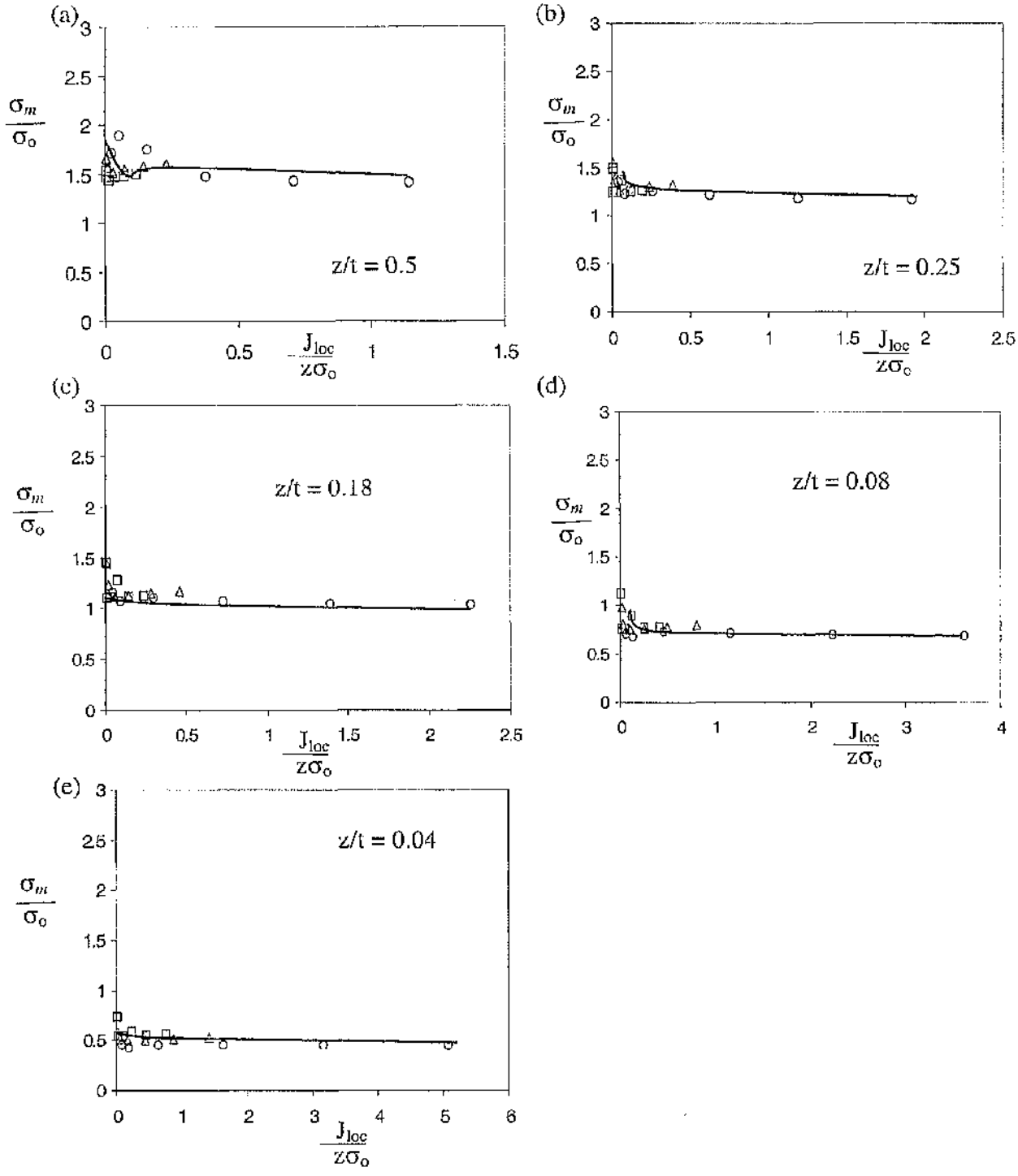


Figure 7.9: The mean stress at the crack tip (r = 0) at different sections (z/t) for CCP specimens of different thickness as a function of $J_{loc}/z\sigma_o$. The square, triangular and circular markers represent the thick, intermediate thickness and thin specimens.

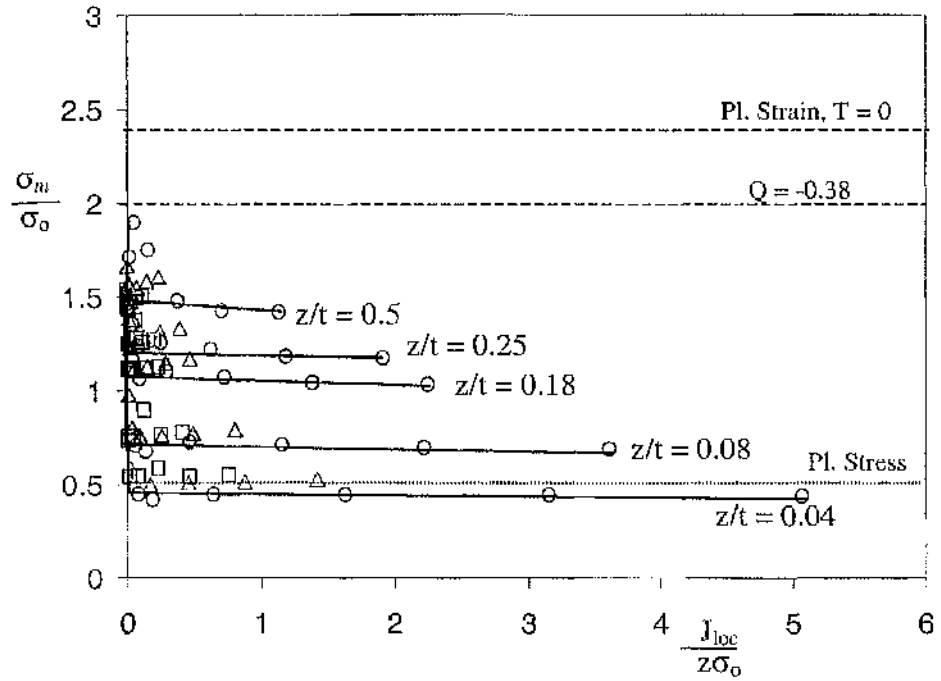


Figure 7.10: Compilation of plots from Figure 7.4 (a) to (f) for the mean stress at r = 0, as a function of $J_{loc}/z\sigma_o$ for CCP specimens of different thicknesses. The square, triangular and circular markers represent the thick, intermediate thickness and thin specimens.

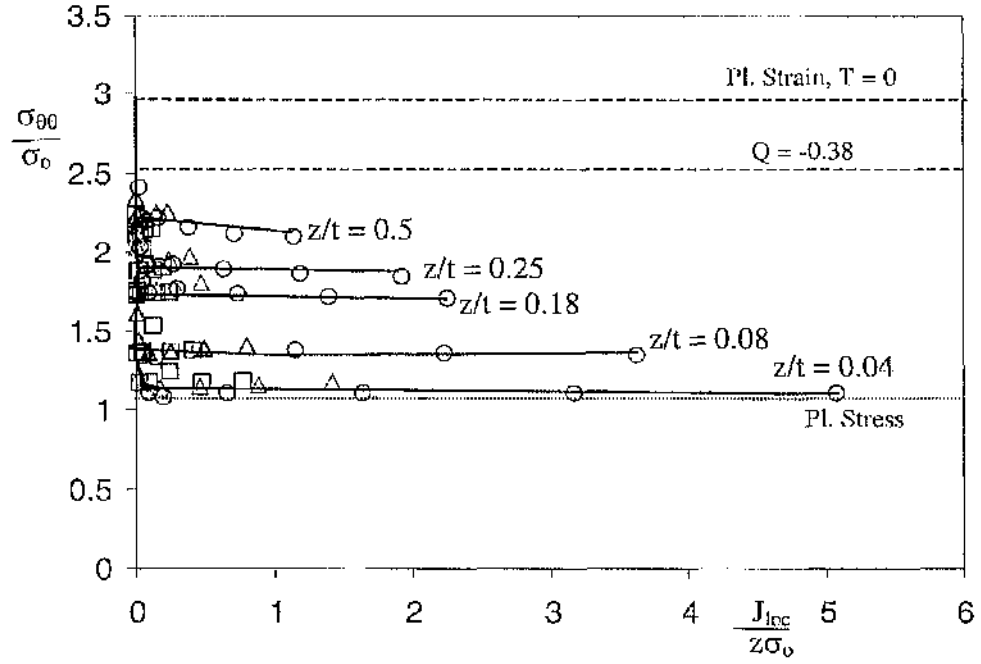


Figure 7.11: Compilation of plots from Figure 7.8 (a) to (f) for the hoop stress at r = 0, as a function of $J_{loc}/z\sigma_o$ for CCP specimens of different thicknesses. The square, triangular and plus markers represent the thick, intermediate thickness and thin specimens.

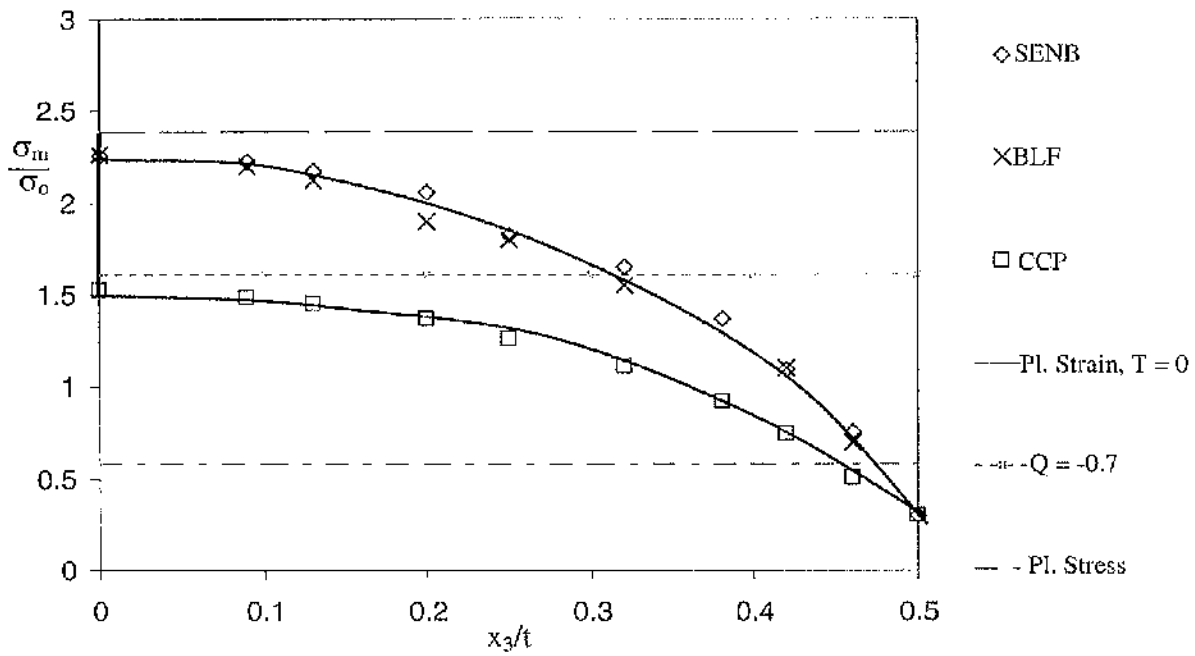


Figure 7.12: The mean stress at the crack tip (r = 0) along the crack front at deformation level, $J_{loc}/z\sigma_o \geq 0.05$ along the crack front for boundary layer formulation, SENB and CCP specimens independent of thickness.

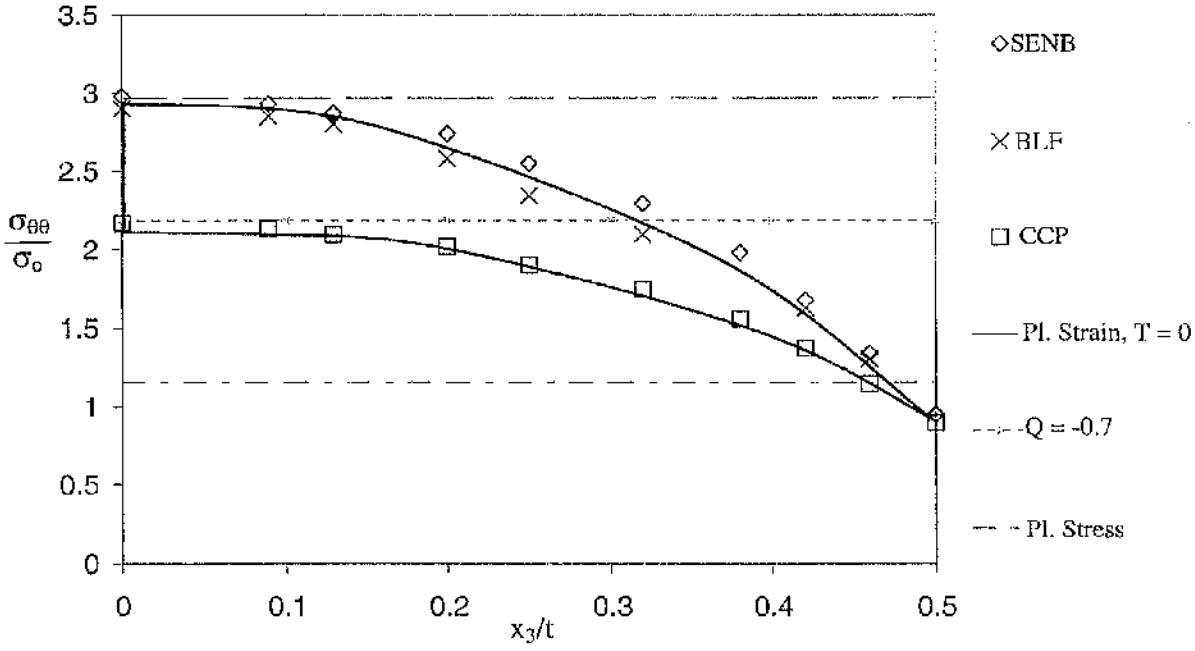


Figure 7.13: The hoop stress at the crack tip (r = 0) along the crack front at deformation level, $J_{loc}/z\sigma_o \geq 0.05$ along the crack front for boundary layer formulation, SENB and CCP specimens independent of thickness.

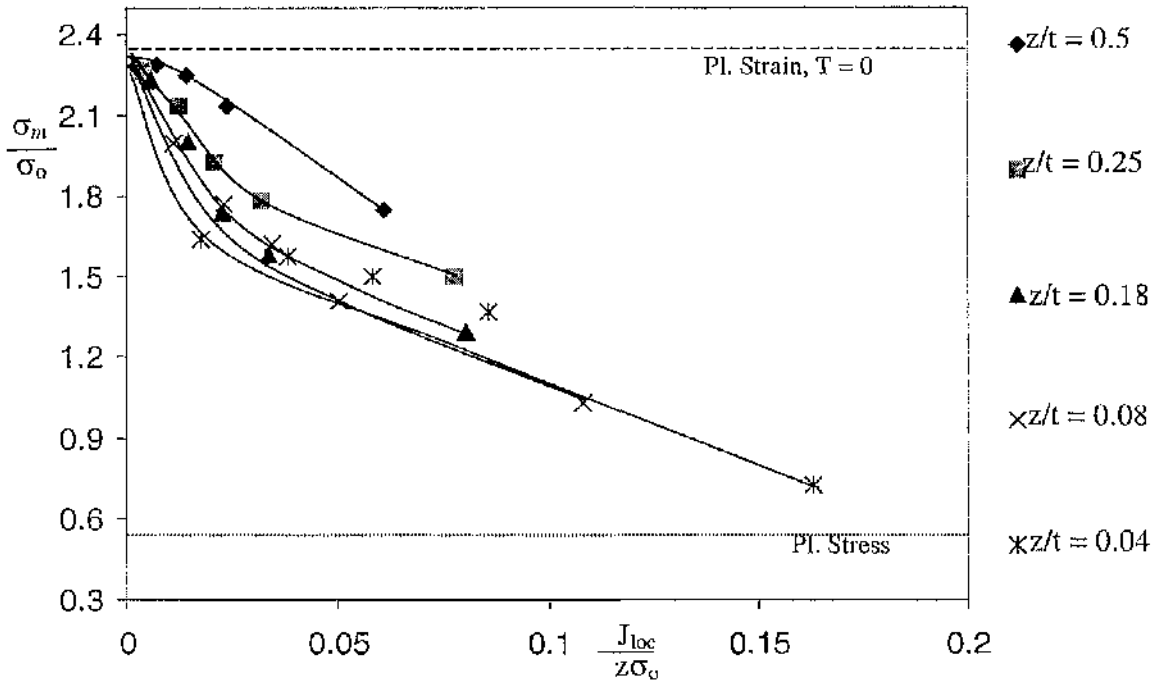


Figure 7.14: The mean stress at $r = 2J/\sigma_o$ at different sections (z/t) as a function of $J_{loc}/z\sigma_o$ at load levels, $\Omega_{far} = 1, 3, 5, 8, 20$ for a boundary layer formulation.

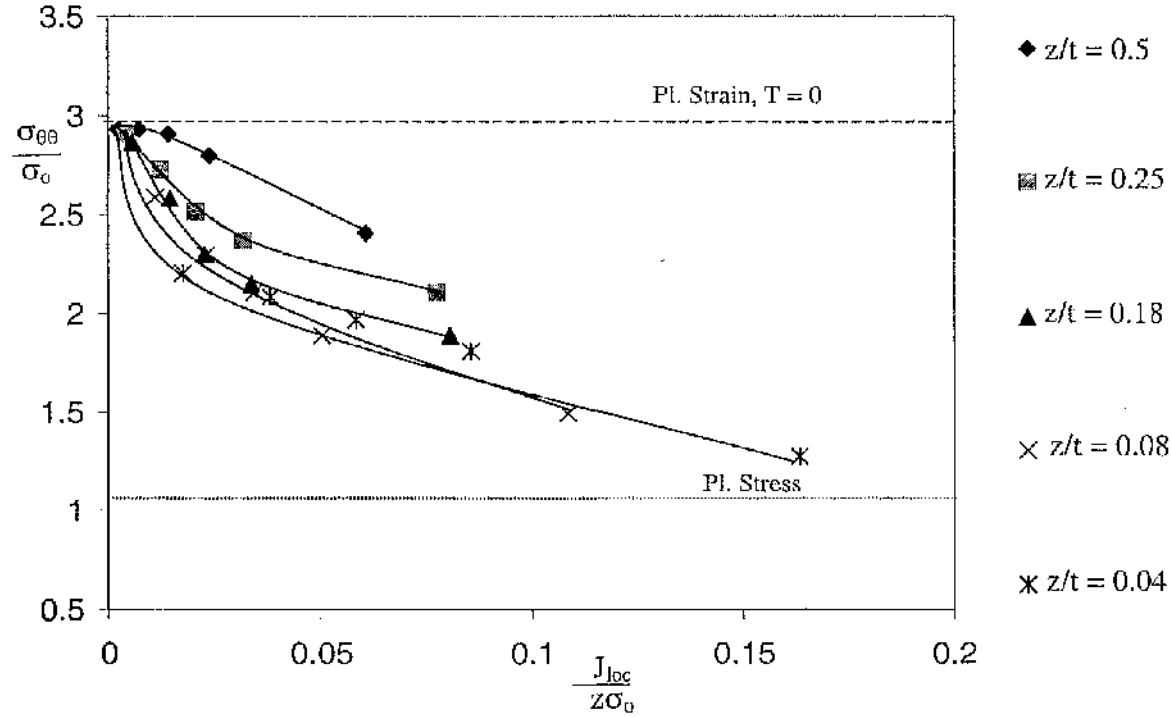


Figure 7.15: The hoop stress at $r = 2J/\sigma_o$ at different sections (z/t) as a function of $J_{loc}/z\sigma_o$ at load levels, $\Omega_{far} = 1, 3, 5, 8, 20$ for a boundary layer formulation.

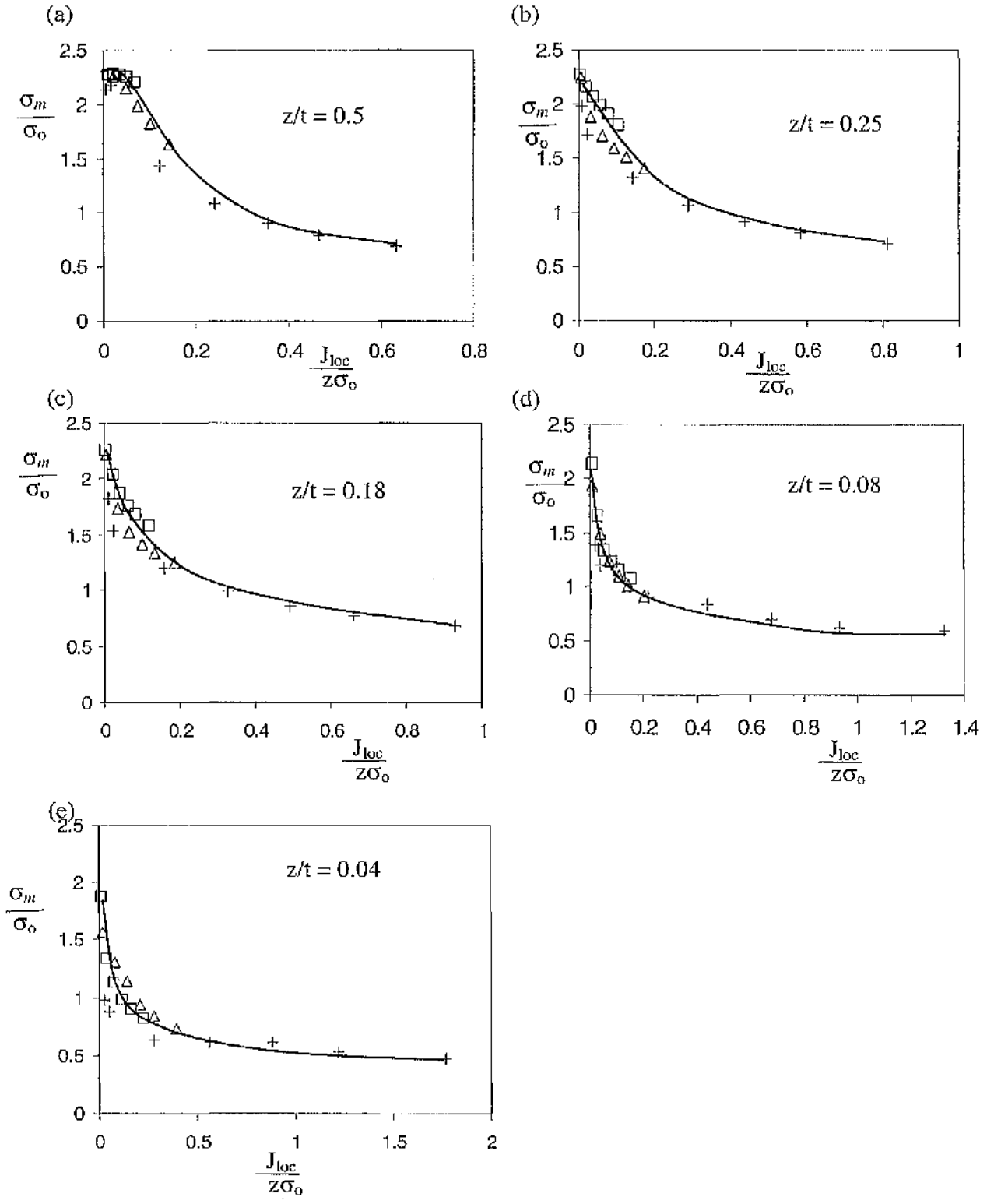


Figure 7.16: The mean stress as a function of $J_{loc}/z\sigma_o$ for SENB specimens of different thickness at different sections (z/t). The square, triangular and plus markers represent the thick, intermediate thickness and thin specimens.

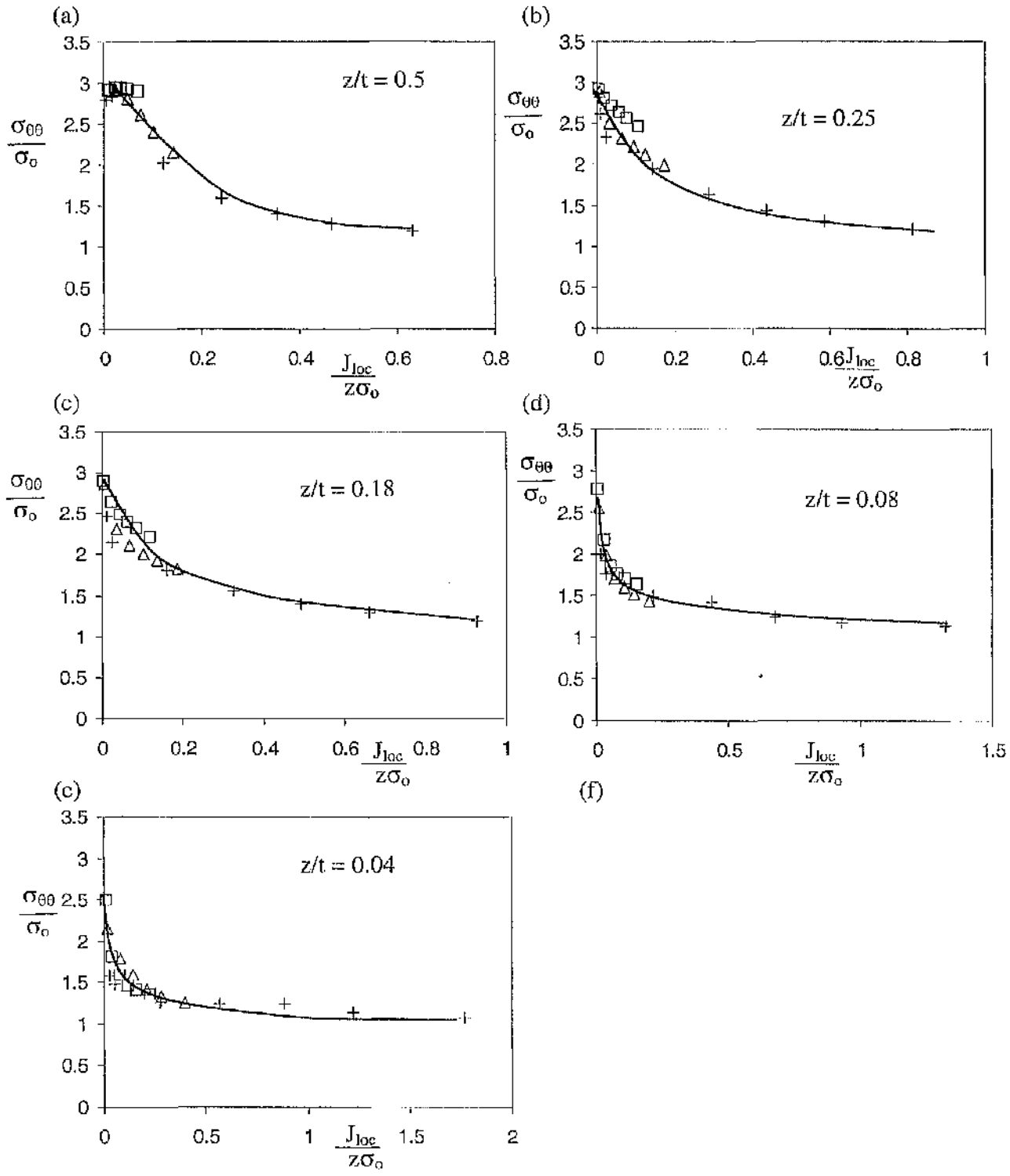


Figure 7.17: The hoop stress as a function of $J_{loc}/z\sigma_o$ for SENB specimens of different thicknesses at different sections (z/t). The square, triangular and circular markers represent the thick, intermediate thickness and thin specimens.

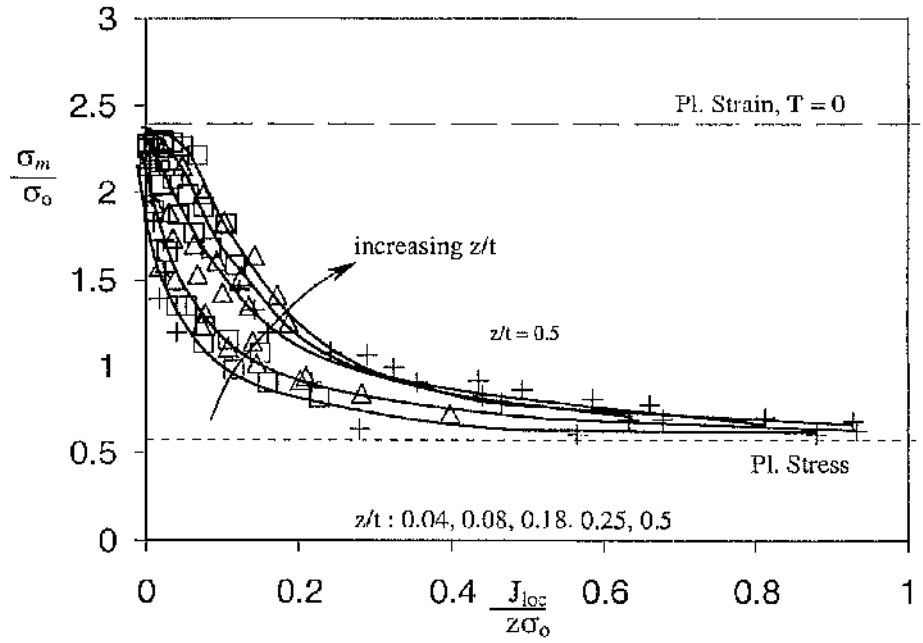


Figure 7.18: Compilation of the mean stress plots at $r\sigma_o/J = 2$ from Figure 7.16 as a function of $J_{loc}/z\sigma_o$ at different sections (z/t) for SENB specimens. The square, triangular and circular markers represent the thick, intermediate thickness and thin specimens.

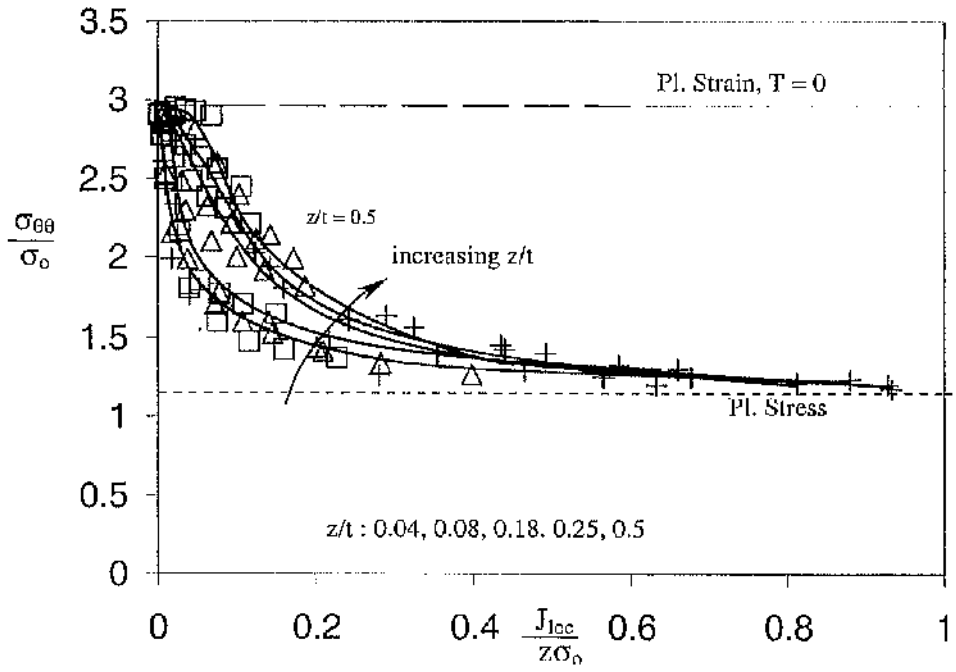


Figure 7.19: Compilation of the hoop stress plots at $r\sigma_o/J = 2$ from Figure 7.17 as a function of $J_{loc}/z\sigma_o$ at different sections (z/t) for SENB specimens. The square, triangular and circular markers represent the thick, intermediate thickness and thin specimens.

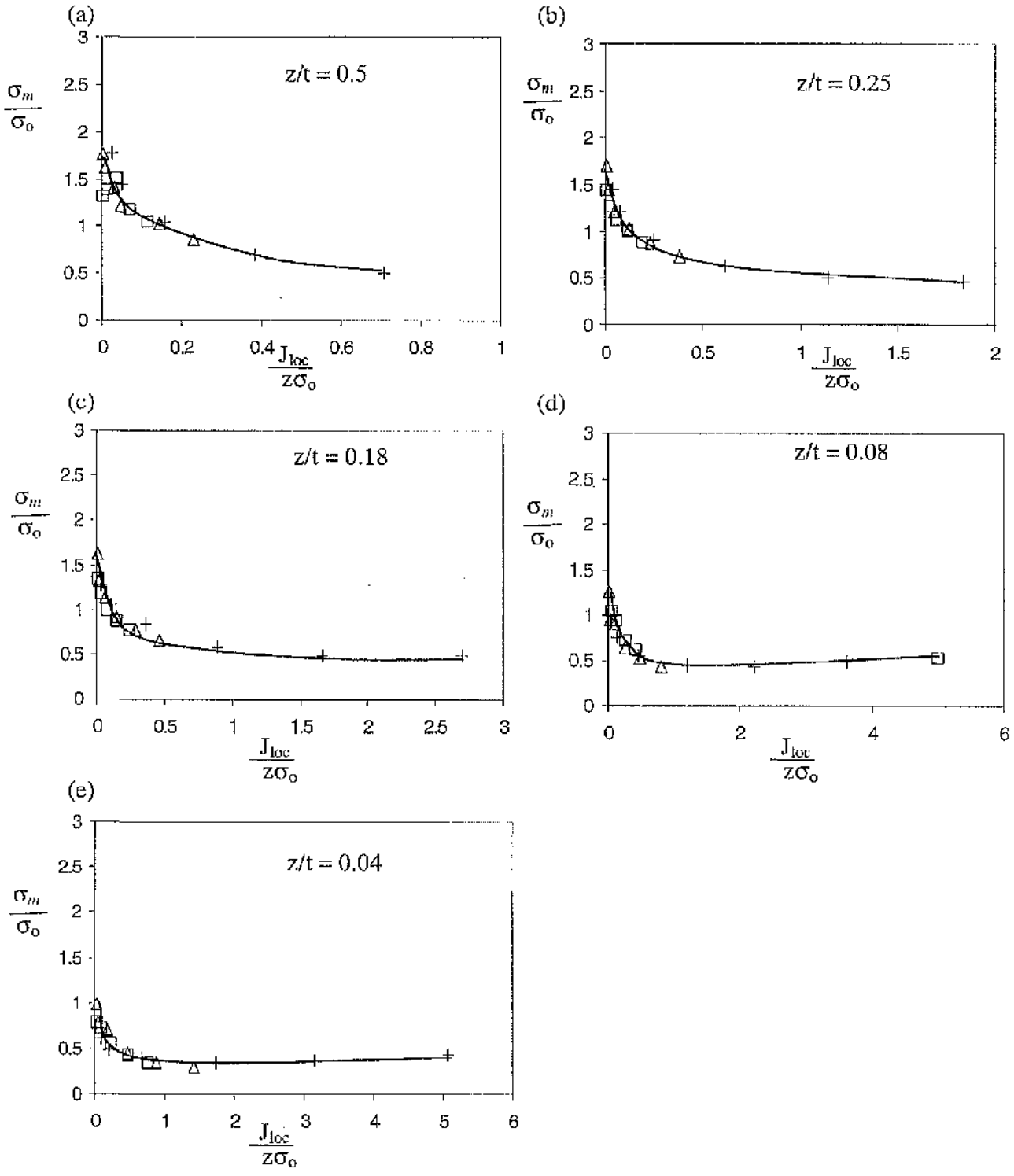


Figure 7.20: The mean stress as a function of $J_{loc}/z\sigma_o$ for CCP specimens of different thicknesses at identical sections (z/t). The square, triangular and plus markers represent the thick, intermediate thickness and thin specimens.

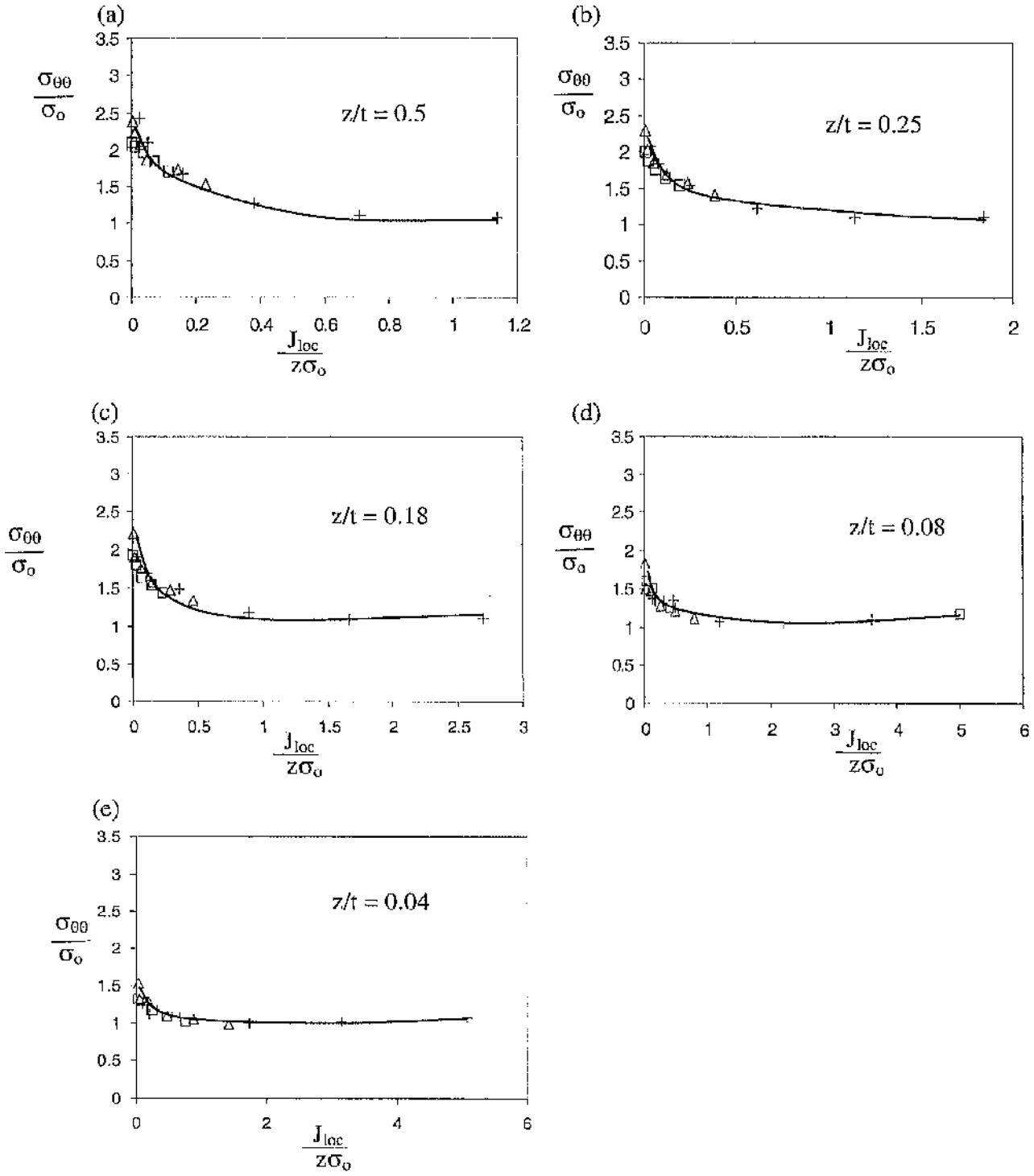


Figure 7.21: The hoop stress as a function of $J_{loc}/z\sigma_o$ for CCP specimens of different thicknesses at identical sections (z/t). The square, triangular and circular markers represent the thick, intermediate thickness and thin specimens.

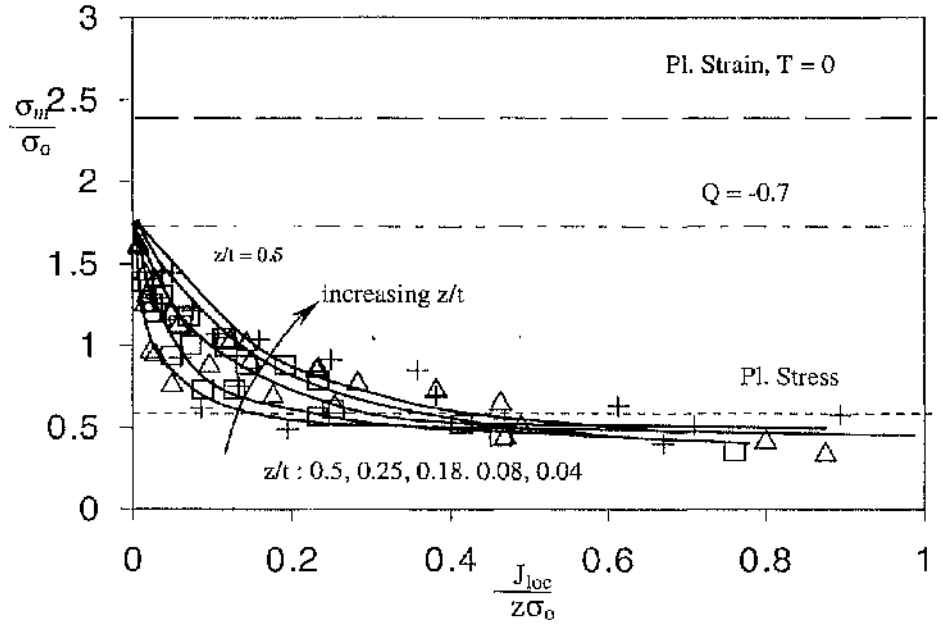


Figure 7.22: Compilation of the mean stress plots at $r\sigma_o/J = 2$ from Figure 7.20 as a function of $J_{loc}/z\sigma_o$ for CCP specimens. The square, triangular and circular markers represent the thick, intermediate thickness and thin specimens.

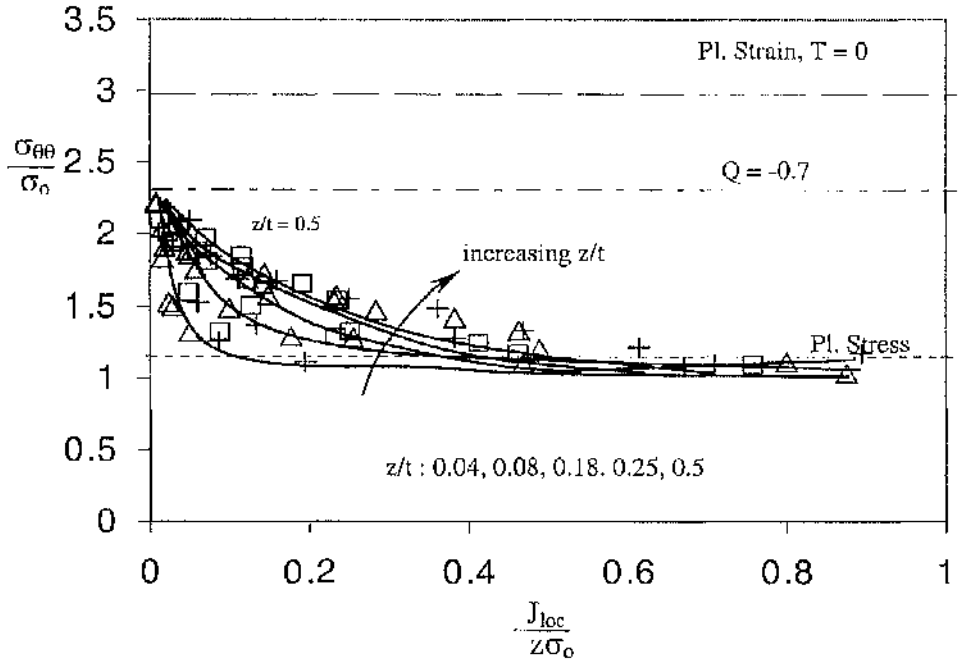


Figure 7.23: Compilation of the hoop stress plots at $r\sigma_o/J = 2$ from Figure 7.21 as a function of $J_{loc}/z\sigma_o$ for CCP specimens. The square, triangular and circular markers represent the thick, intermediate thickness and thin specimens.

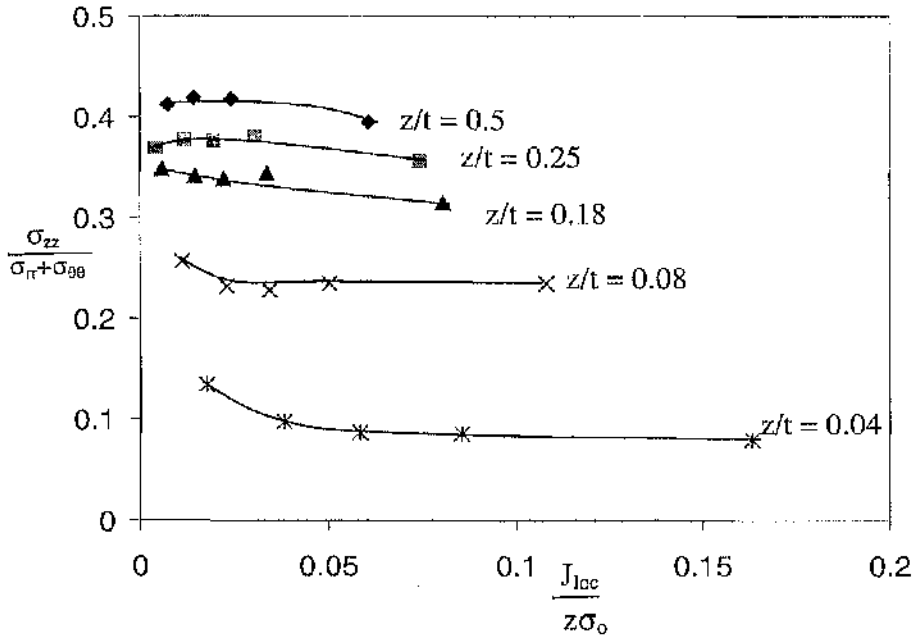


Figure 7.24: The plane strain parameter as a function of $J_{loc}/z\sigma_o$ at the crack tip (r = 0) at different sections (z/t) for a boundary layer formulation at load levels, $\Omega_{far}$ = 1, 3, 5, 8, 20.

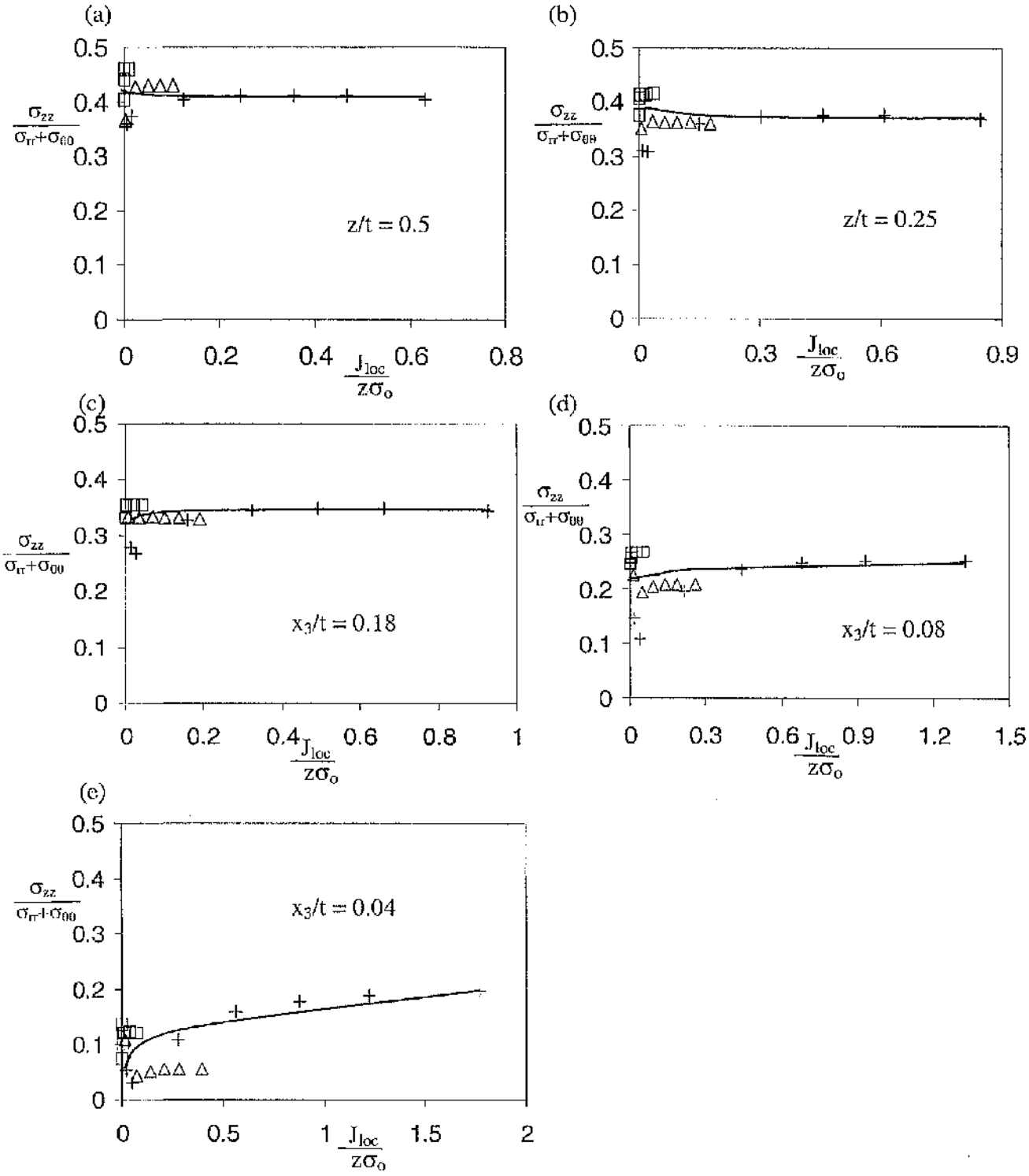


Figure 7.25: The plane strain parameter at the crack tip (r = 0) as a function of $J_{loc}/z\sigma_o$ for different thickness at identical sections (z/t) for SENB specimens. The square, triangular and plus markers represent the thick, intermediate thickness and thin specimens.

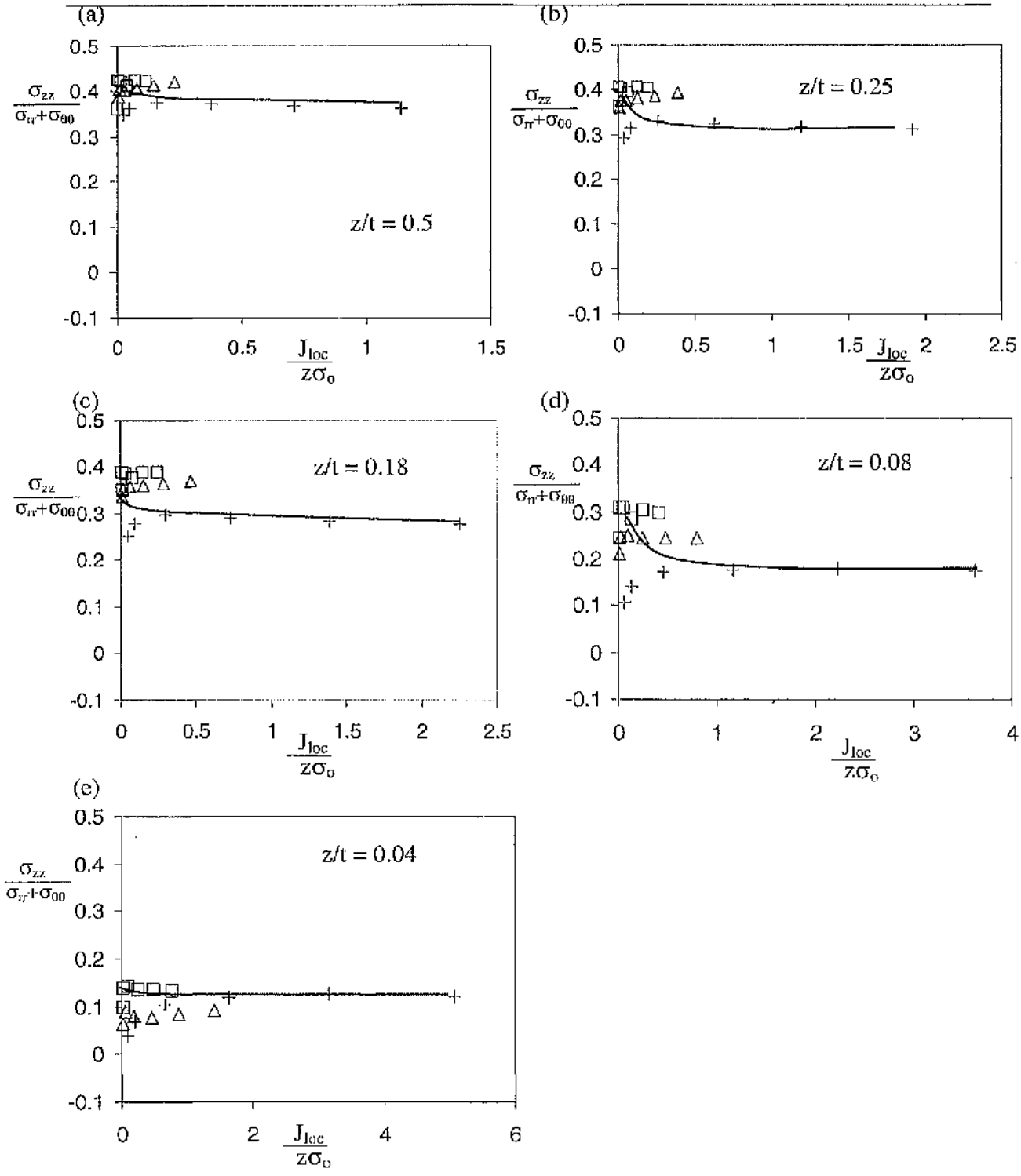


Figure 7.26: The plane strain parameter at the crack tip (r = 0) as a function of $J_{loc}/z\sigma_o$ for different thickness at identical sections (z/t) for CCP specimens. The square, triangular and plus markers represent the thick, intermediate thickness and thin specimens.

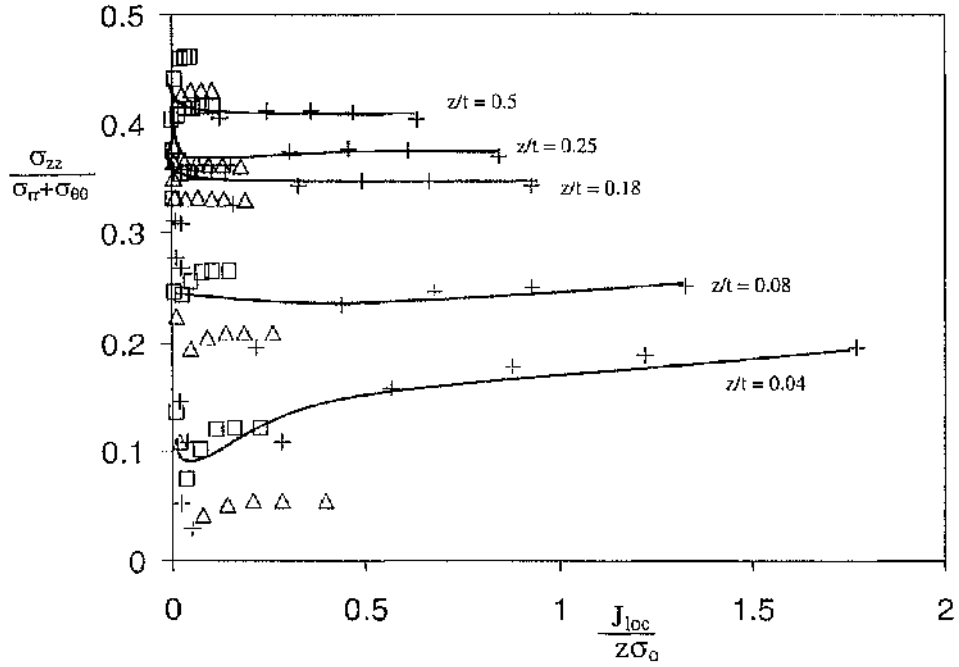


Figure 7.27: Compilation of the plane strain parameter plots from Figure 7.25 as a function of $J_{loc}/z\sigma_o$ for SENB specimens at different sections (z/t) and thickness. The square, triangular and plus markers represent the thick, intermediate thickness and thin specimens.

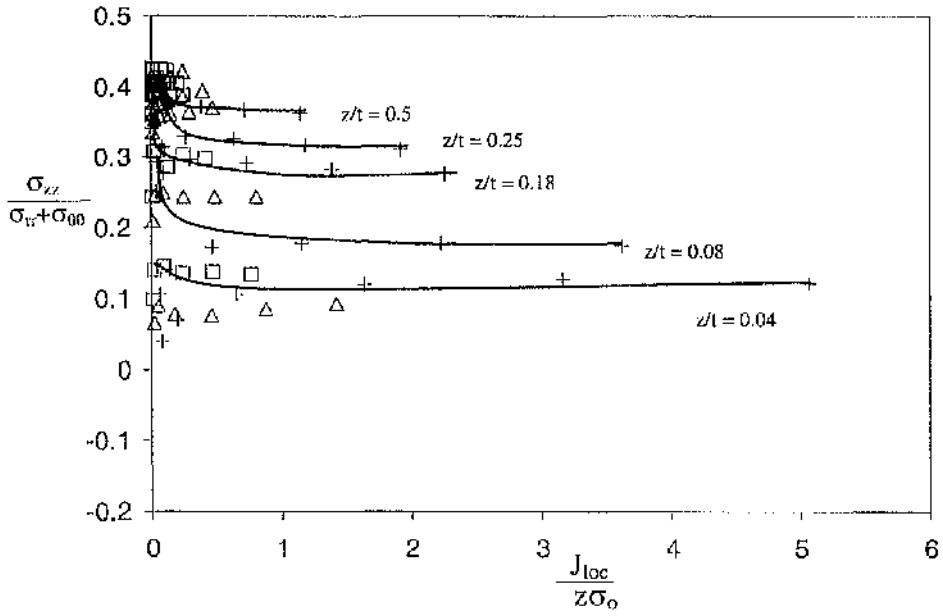


Figure 7.28: Compilation of the plane strain parameter plots from Figure 7.26 as a function of $J_{loc}/z\sigma_o$ for CCP specimens at different sections (z/t) and thickness. The square, triangular and plus markers represent the thick, intermediate thickness and thin specimens.

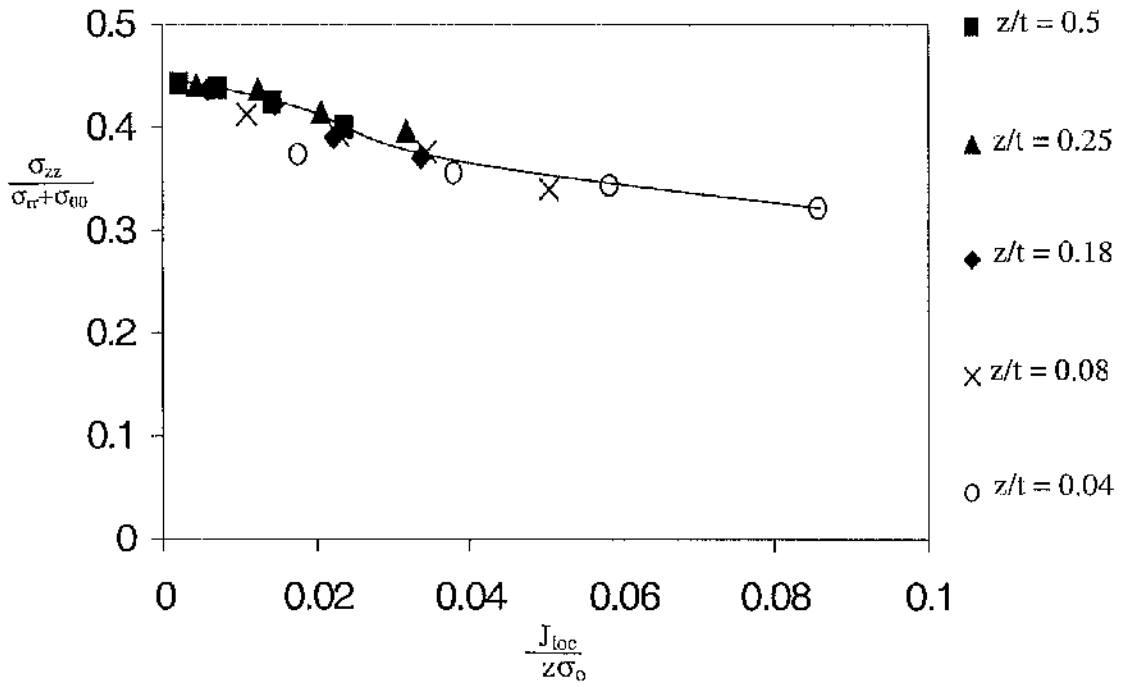


Figure 7.29: The plane strain parameter as a function of $J_{loc}/z\sigma_o$ at $r = 2J/\sigma_o$ at different sections (z/t) for a boundary layer formulation at load levels, $\Omega_{far} = 1, 3, 5, 8, 20$.

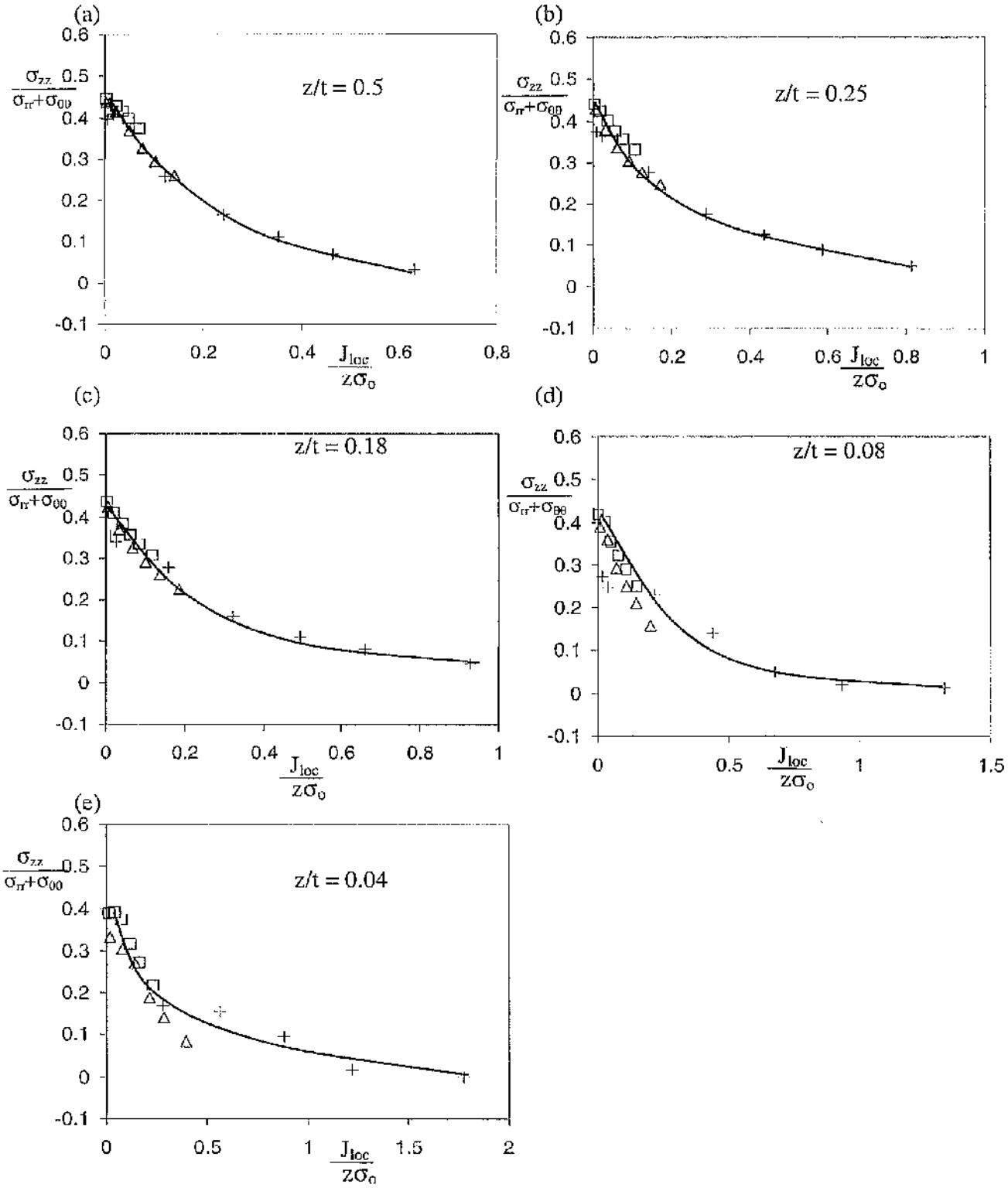


Figure 7.30: The plane strain parameter as a function of $J_{loc}/z\sigma_o$ at $r = 2J/\sigma_o$, at identical sections (z/t) for SENB specimens. The square, triangular and plus markers represent the thick, intermediate thickness and thin specimens.

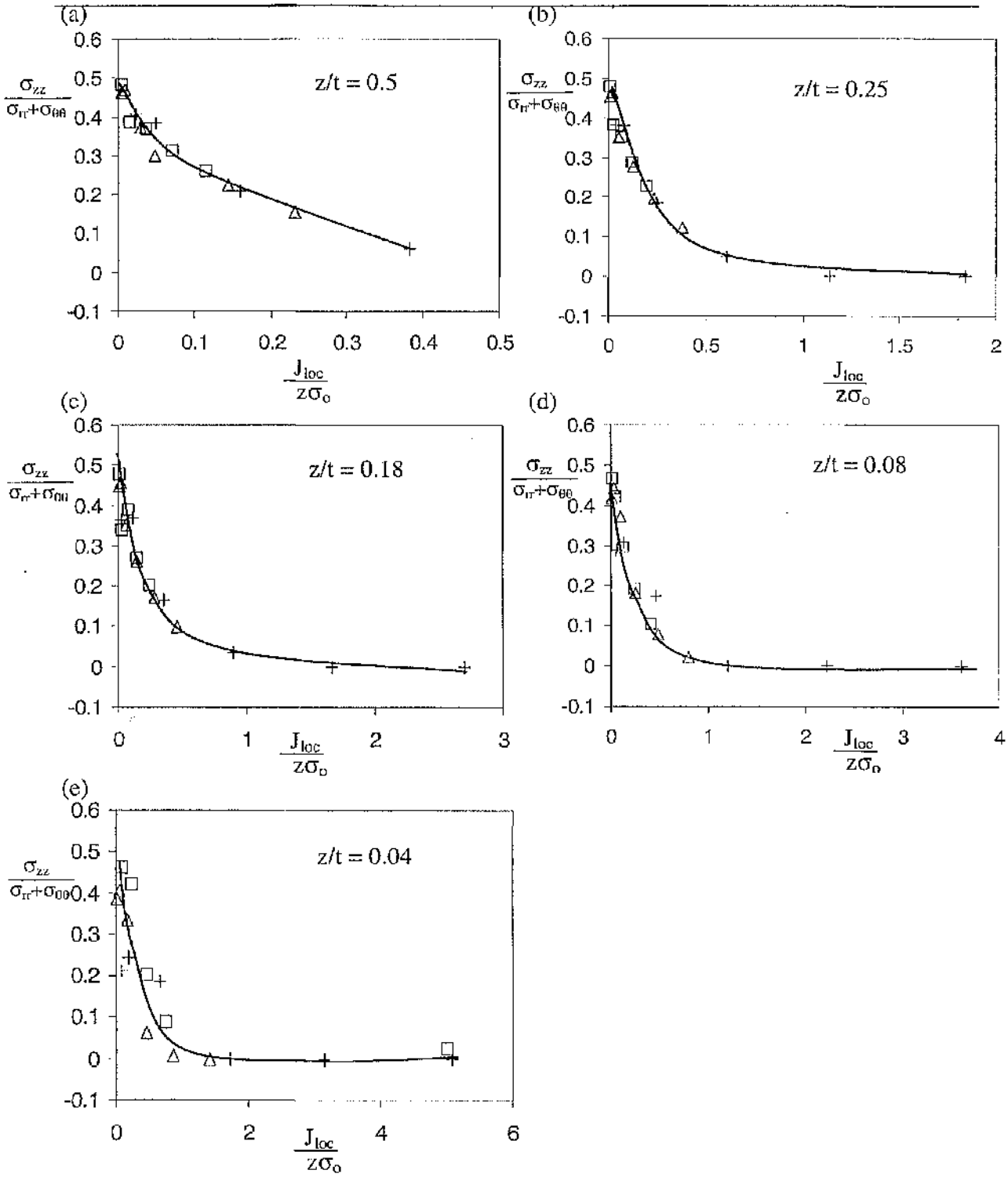


Figure 7.31: The plane strain parameter as a function of $J_{loc}/z\sigma_o$ at $r = 2J/\sigma_o$, at identical sections (z/t) for CCP specimens. The square, triangular and plus markers represent the thick, intermediate thickness and thin specimens.

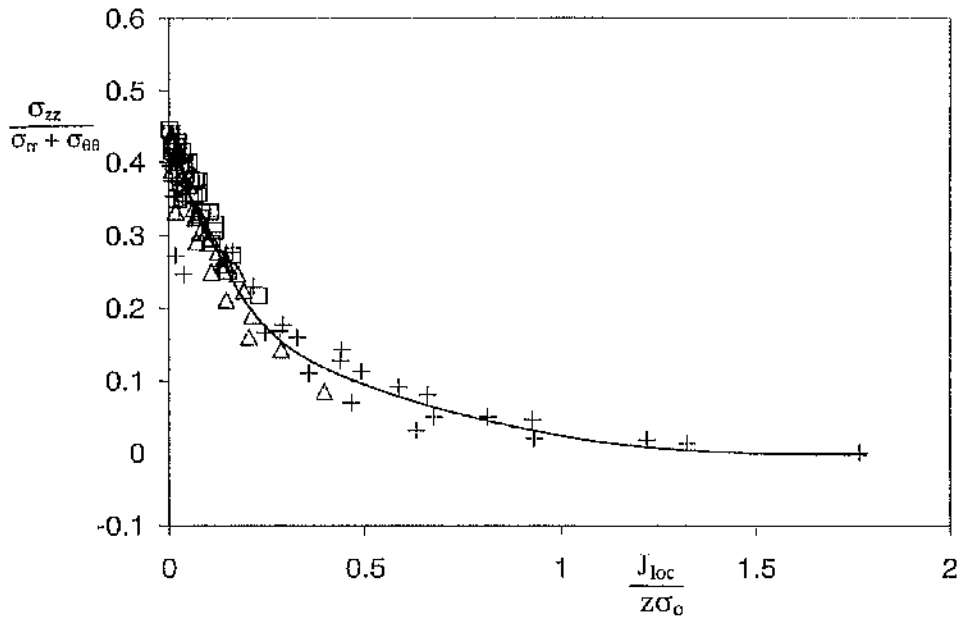


Figure 7.32: Compilation of the plane strain parameter as a function of $J_{loc}/z\sigma_o$ plots from Figure 7.30 at $r = 2J/\sigma_o$ at different sections (z/t) for SENB specimens. The square, triangular and plus markers represent the thick, intermediate thickness and thin specimens.

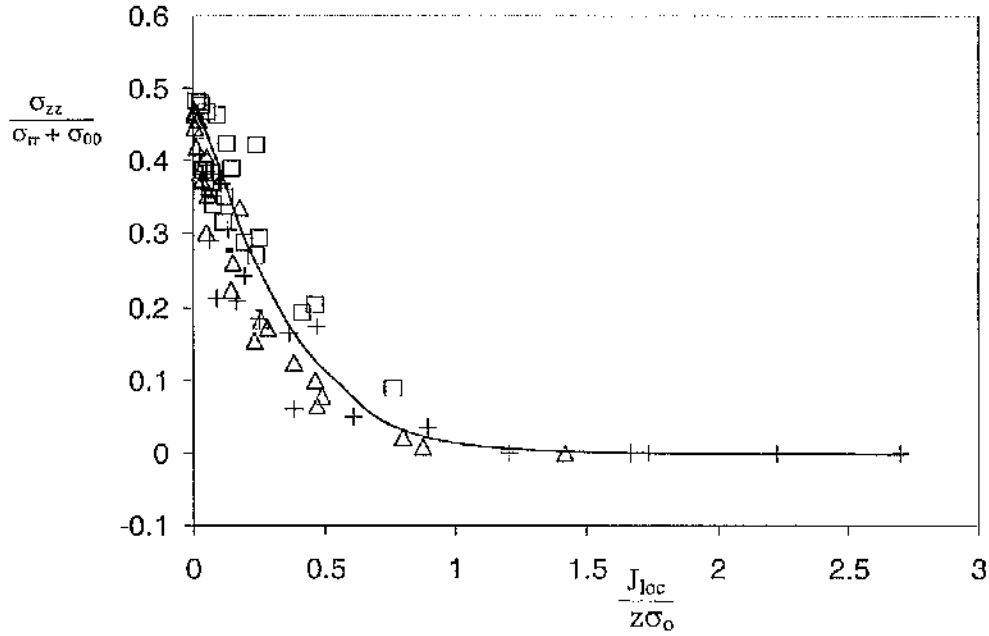


Figure 7.33: Compilation of the plane strain parameter as a function of $J_{loc}/z\sigma_o$ plots from Figure 7.31 at $r = 2J/\sigma_o$ at different sections (z/t) for CCP specimens. The square, triangular and plus markers represent the thick, intermediate thickness and thin specimens.

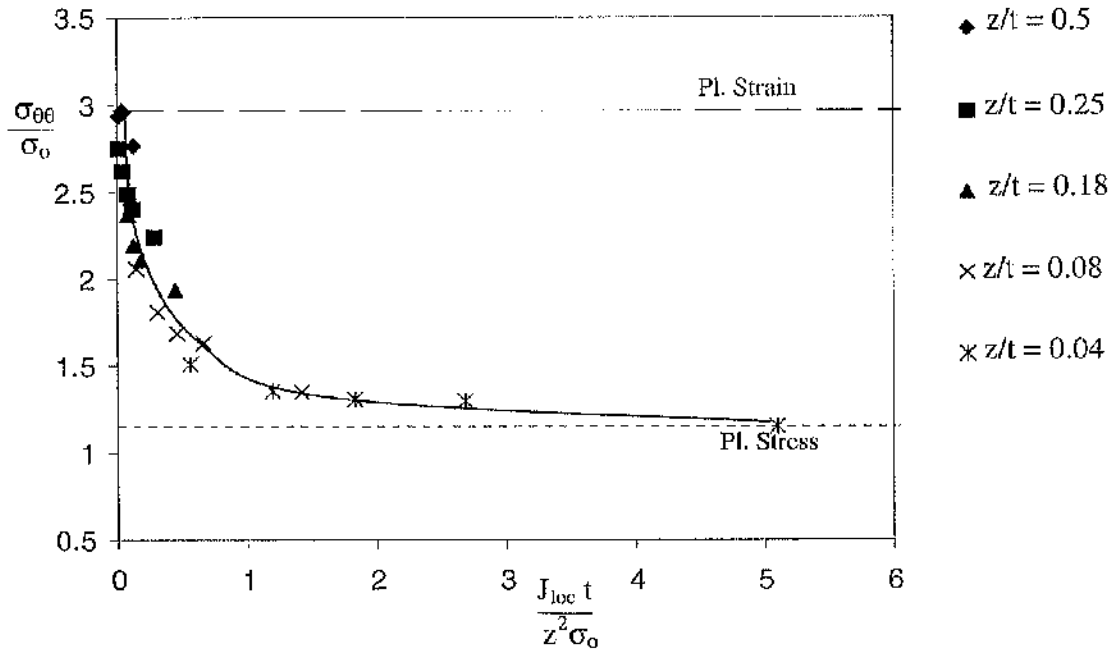


Figure 7.34: The hoop stress as a function of $J_{loc}t/z^2\sigma_o$ at different sections (z/t) for a boundary layer formulation at the crack tip at deformation, $\Omega_{far}$ = 1, 3, 5, 8, 20.

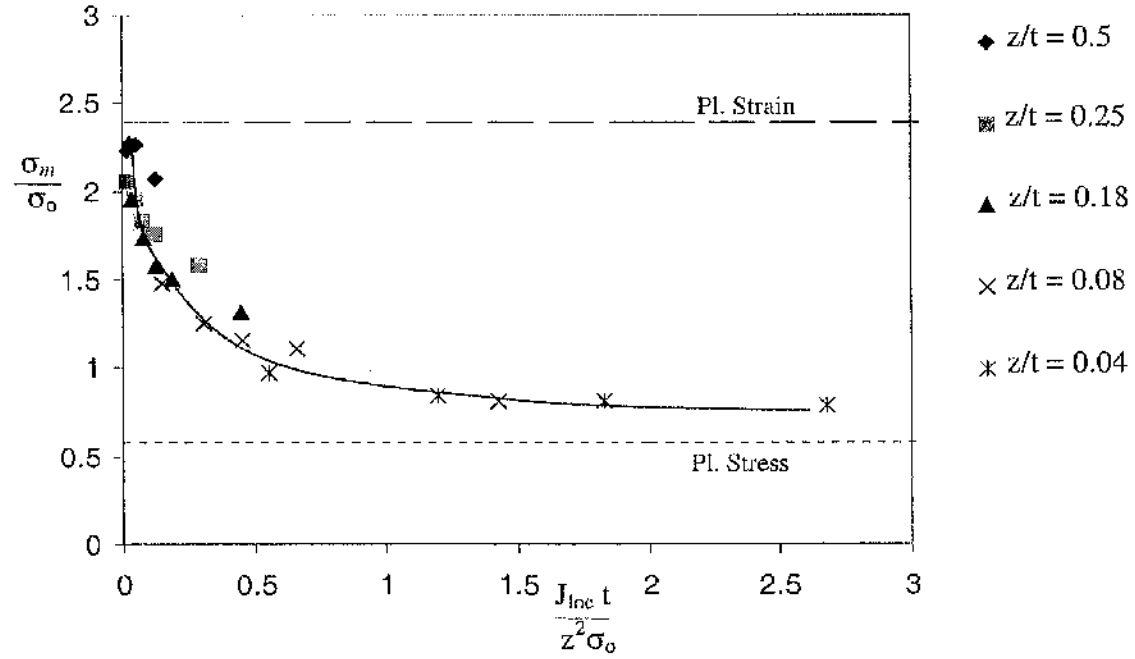


Figure 7.35: The mean stress as a function of $J_{loc}t/z^2\sigma_o$ at different sections (z/t) for a boundary layer formulation at the crack tip at deformation, $\Omega_{far}$ = 1, 3, 5, 8, 20.

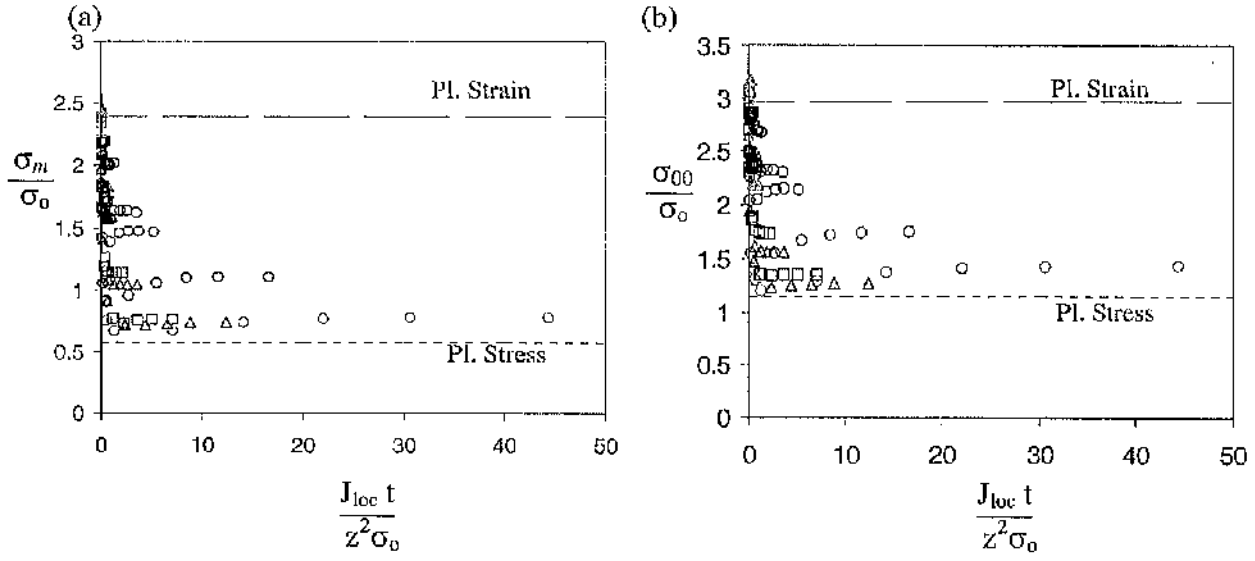


Figure 7.36: The mean and the hoop stress as a function of $J_{loc}t/z^2\sigma_o$ at different sections (z/t) for SENB specimens at the crack tip at limit load.

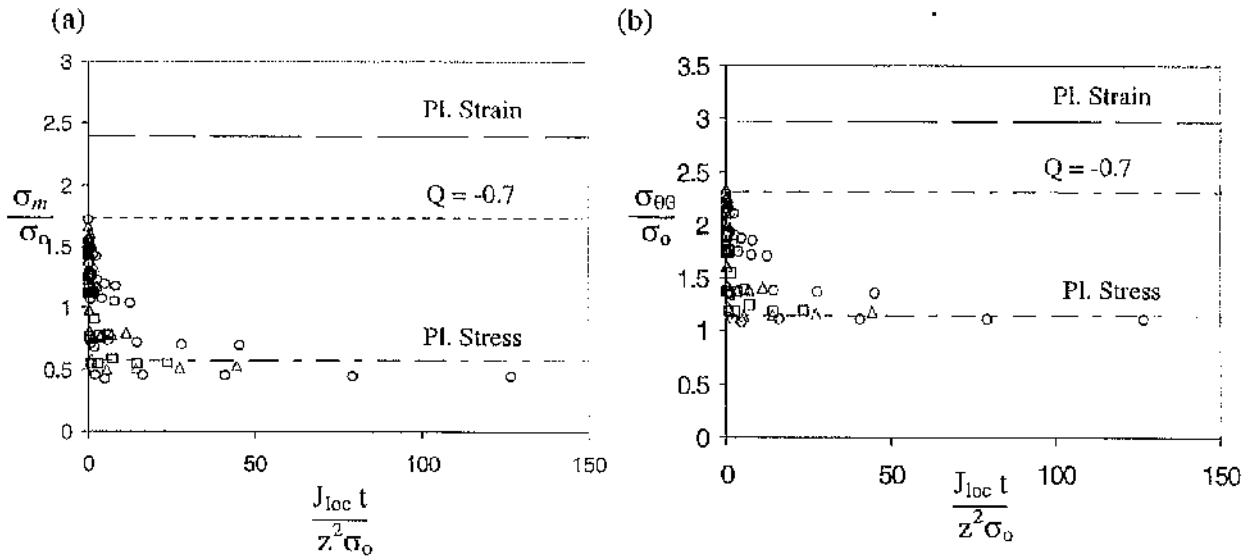


Figure 7.37: The mean and the hoop stress as a function of $J_{loc}t/z^2\sigma_o$ at different sections (z/t) for CCP specimens at the crack tip at limit load.

(a)

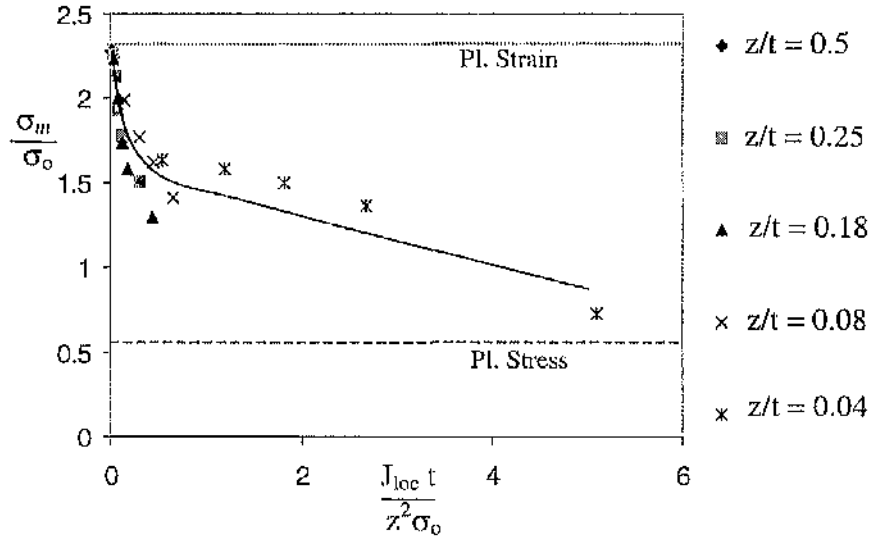


(b)

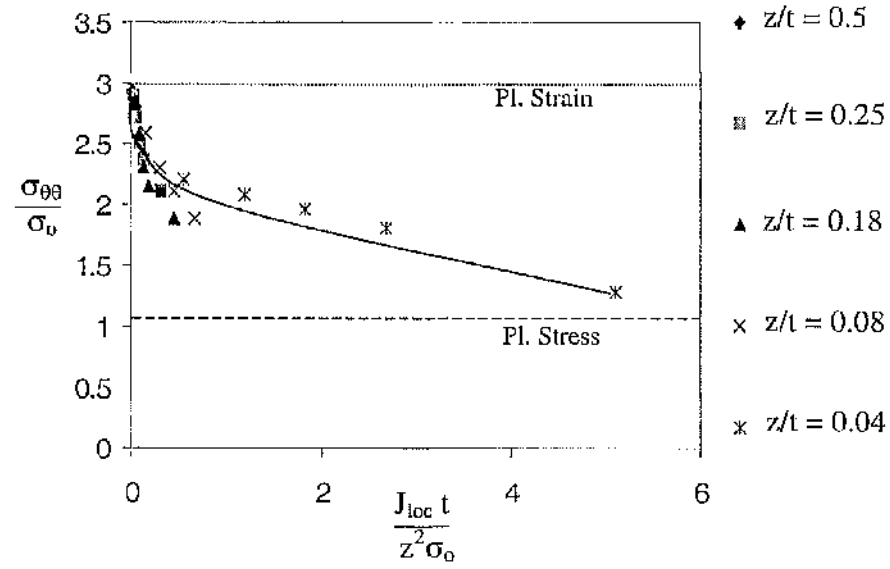


Figure 7.38: The mean and the hoop stress as a function of $J_{loc}t/z^2\sigma_o$ at different sections (z/t) for a boundary layer formulation at $r = 2J/\sigma_o$ at load levels $\Omega_{far} = 1, 3, 5, 8$ and 20.

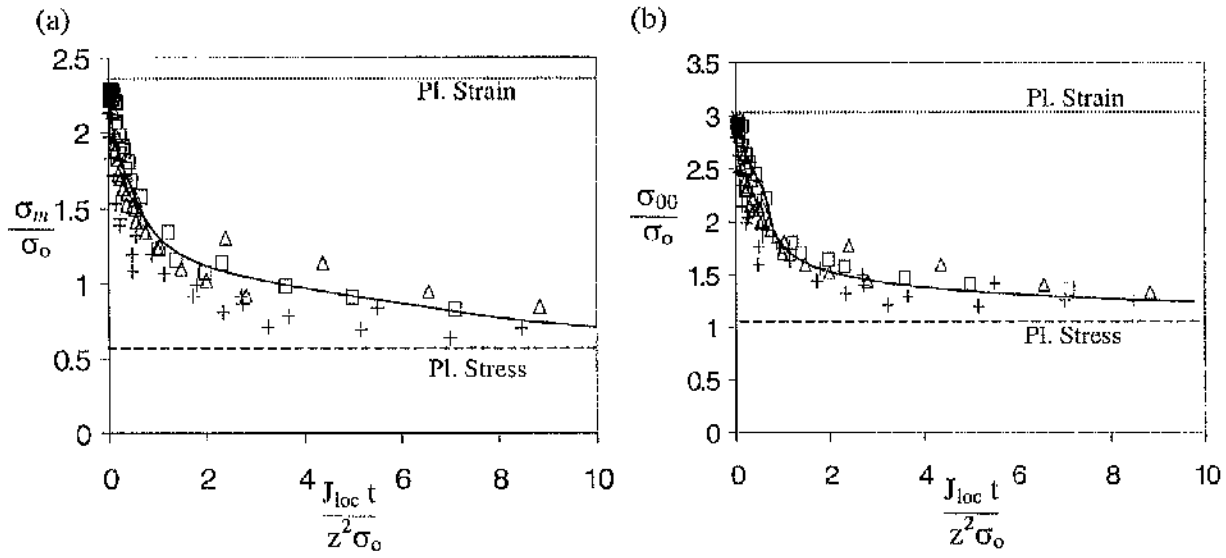


Figure 7.39: The mean and the hoop stress as a function of $J_{loc}t/z^2\sigma_o$ at different sections (z/t) for SENB specimens at $r = 2J/\sigma_o$ at limit load.

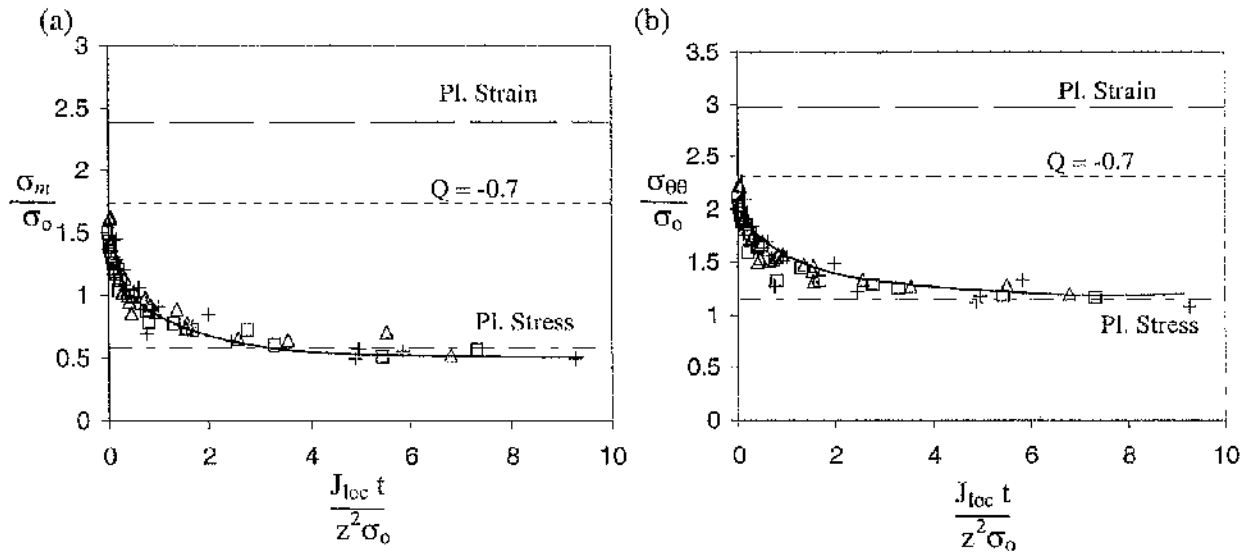


Figure 7.40: The mean and the hoop stress as a function of $J_{loc}t/z^2\sigma_o$ at different sections (z/t) for CCP specimens at $r = 2J/\sigma_o$ at limit load.

# Failure Assessment Methodologies

A widely used engineering approach to defect assessment is based on failure assessment diagrams (R6 (2001) and BS 7910 (2005)), which were originally developed within the context of single parameter fracture mechanics. The approach has been subsequently modified to take account of in-plane constraint loss within the framework of plane strain fracture mechanics (MacLennan and Hancock (1995) and Ainsworth and O'Dowd (1995)). Although part of the conservatism associated with single parameter fracture mechanics has been avoided, real structures do not necessarily fail in plane strain conditions. This chapter discusses a failure assessment scheme based on three-dimensional constraint loss which can incorporate both in-plane and out-of-plane effects.

## 8.1 Application of Out-of-Plane Constraint Loss for Failure Assessment

All the analyses in this chapter are carried out at a distance $r = 2J/\sigma_o$. This distance is chosen because constraint is distance dependent and is lost with distance from the tip. In local micromechanics analyses of cleavage failure such as Ritchie et al. (1973), it has been shown that failure initiates at a distance greater than $r = 2J/\sigma_o$. Therefore, analyses of failure at $r = 2J/\sigma_o$ are an underestimate of the constraint loss over the critical micro-structural distance. This leads to an underestimate of the constraint enhanced toughness which is conservative in defect assessment schemes.

The failure assessment scheme can also be extended to failure initiation by ductile tearing. Ductile tearing is associated with nucleation, growth and coalescence of voids which initiate within the finite strain zone ($r \leq 2J/\sigma_o$). On the assumption that the equivalent plastic strain profiles are similar in the three-dimensional crack tip field, the stress deviators in a plane strain field are -1, +1 and 0 in the $x_1$, $x_2$ and $x_3$ direction while in a plane stress field ($\theta = 0^o$), the deviators are 0, +1 and −1 in the $x_1$, $x_2$ and $x_3$ direction. The deviatoric components change directions during the transition from plane strain to plane stress, but in the limit, the strain states are identical. Hancock and Brown (1983) showed

that in circumferentially notched tension specimens, effective plastic strain to initiate failure is strongly dependent on state of stress, $\sigma_m/\overline{\sigma}$ but weakly dependent on the strain state. Ductile tearing can be assumed to depend on the state of stress at $r = 2J/\sigma_o$ which allows the three-dimensional failure assessment scheme to be applied to ductile tearing.

Two-parameter plane strain failure assessment schemes are based on a description of the crack tip field in which constraint loss is independent of distance, (Betegón and Hancock (1991) and O'Dowd and Shih (1991)). In-plane constraint loss is based on a family of fields which are hydrostatically different but deviatorically similar. However, out-of-plane constraint loss features fields which are hydrostatically and deviatorically different, and the difference is distance dependent. At this point, many researchers who have discussed three-dimensional crack tip fields have come to a conclusion that three-dimensional crack analyses can not be used to develop a viable approach for failure assessment using constraint based fracture mechanics.

To address constraint loss in three-dimensional fields, it is appropriate to consider the way in which the fields change. Interest is focused in the mean stress, $\sigma_m$ and the maximum principal stress, $\sigma_{\theta\theta}$, in the leading sector directly ahead of the crack. The loss of constraint can be expressed as the difference in mean stress, $\Delta\sigma_m$, between a given field and a reference field at a distance $r = 2J/\sigma_o$. It is natural to take the reference field as the small scale yielding field (T = 0) field under perfect plane strain conditions. A similar approach is adopted for the maximum principal stress, $\Delta\sigma_{\theta\theta}$. The stress difference between a given field and the plane strain reference field has been evaluated for three-dimensional boundary layer formulations and full-field solutions. It is important to note that if this approach is adopted under perfect plane strain conditions,

$$\frac{\Delta\sigma_m}{\sigma_o} = \frac{\Delta\sigma_{\theta\theta}}{\sigma_o} = Q \tag{8.1}$$

It is appropriate now to consider the stress system in a three-dimensional crack tip field. The stress tensor can be expressed in terms of the hydrostatic and deviatoric components following equation (2.18). Assuming, the maximum principal stress, $\sigma_{\theta\theta}$, at $\theta = 0^\circ$ is considered for discussion:

$$\sigma_{\theta\theta} = s_{\theta\theta} + \sigma_m \qquad (\theta = 0^\circ) \qquad (8.2)$$

where $s_{\theta\theta}$ is the maximum stress deviator and $\sigma_m$ is the mean stress. A change in the maximum principal stress can arise from a change in the associated stress deviator and, or, a change in the mean stress:

$$\sigma_{\theta\theta} + \Delta\sigma_{\theta\theta} = s_{\theta\theta} + \Delta s_{\theta\theta} + \sigma_m + \Delta\sigma_m \qquad (8.3)$$

Comparing equations (8.2) and (8.3), if $\Delta\sigma_{\theta\theta} = \Delta\sigma_m$, then $\Delta s_{\theta\theta} = 0$.

Figure 8.1 shows $\Delta\sigma_m/\sigma_o$ and $\Delta\sigma_{\theta\theta}/\sigma_o$ in the boundary layer formulation at $r = 2J/\sigma_o$ at sections, $z/t = 0.5$, 0.25 and 0.18 as a function of $J_{loc}t/z^2\sigma_o$. The change in the hoop stress and the mean stress is closely similar at all sections (z/t) and can simply be expressed as a single curve. The similarity of $\Delta\sigma_m$ and $\Delta\sigma_{\theta\theta}$ implies that the difference in the maximum stress deviator is zero, $\Delta s_{\theta\theta} = 0$. This implies that during out-of-plane constraint loss, the stresses in the leading sector ahead of the crack differ hydrostatically, but that the maximum stress deviators are similar. Similar results from full-field solutions are shown in Figures 8.2 and 8.3.

It is known that failure by cleavage is driven by the maximum principal stress while ductile tearing is a function of the mean stress, $\sigma_m$ and equivalent plastic strain. Constraint loss quantified by the maximum principal stress, $\sigma_{\theta\theta}$, or the mean stress, $\sigma_m$ are identical and can be used to characterise cleavage and ductile tearing. On this basis, it is possible to develop a failure criterion incorporating in-plane and out-of-plane constraint loss.

## 8.2 Analytic Expression for Out-of-Plane Constraint Loss

The change in the mean stress and the maximum principal stress has been shown to be similar. The designation for out-of-plane constraint loss, $\Delta\sigma^{op}/\sigma_o$ is proposed where $\Delta\sigma$ may be considered to be either the change in the mean stress or the maximum hoop stress. The superscript "*op*" denotes an out-of-plane effect. The general nature of out-of-plane constraint loss can be expressed by an exponential expression of the form:

$$\frac{\Delta\sigma^{op}}{\sigma_o} = \beta(e^{-\gamma\left(\frac{J_{loc}t}{z^2\sigma_o}\right)} - 1) \tag{8.4}$$

The form of exponential decay is such that at very small levels of deformation ($J \rightarrow 0$), or equivalently in sections remote from a free surface ($z \rightarrow \infty$), a fully constrained field develops, $\frac{\Delta\sigma^{op}}{\sigma_o} \rightarrow 0$. At very large levels of deformation ($J \rightarrow \infty$) or equivalently on sectors very close to the free surface ($z \rightarrow 0$), the field approaches the plane stress field.

Consequently, the value of $\beta$ in fully constrained flow fields ($T > 0$) corresponds to the difference in constraint between the plane strain ($T = 0$) and the plane stress field.

$$\beta = \frac{\sigma_m^{ssy(pl.strain)}}{\sigma_o} - \frac{\sigma_m^{pl.stress}}{\sigma_o} \tag{8.5}$$

In fully constrained geometries such as the SENB, $\beta_{SENB} = 1.82$. The other constant in equation (8.4) is $\gamma$ which is the constraint loss sensitivity. The constraint sensitivity, $\gamma$, for SENB is determined by rearranging equation (8.4) to a linear fit.

$$\ln\left(\frac{\Delta\sigma^{op}}{\beta\sigma_o} + 1\right) = \gamma\left(\frac{J_{loc}t}{z^2\sigma_o}\right) \tag{8.6}$$

Figures 8.4 show constraint sensitivity, $\gamma$, to be close to 3 for SENB specimens.

Constraint loss in CCP specimens is more complex because it is affected by both in-plane and out-of-plane effects. In-plane effects can be estimated through the two-dimensional in-plane effects based on T/Q which have been discussed in Chapter 6 and 7. Out-of-plane effects become pronounced at limit load. Using this as a reference, the out-of-plane constraint loss curve has a similar form to that given in equation (8.4). Assuming that in-plane and out-of-plane constraint loss effects affect $\beta$, $\beta_{CCP}$ for CCP can be expressed as:

$$\beta = \frac{\sigma_m^{ssy}}{\sigma_o} + Q - \frac{\sigma_m^{pl.stress}}{\sigma_o} \tag{8.7}$$

If the plane strain constraint loss, Q, is calculated from T, the applied load causes Q to become more negative with load until it becomes constant at limit load. In the present case, this leads to $\beta_{CCP} = 1.44$. The constraint loss in CCP specimen can therefore be regarded as a combination of in-plane and out-of-plane effects. The constraint sensitivity, $\gamma$, for the CCP specimen has been determined in a similar way to the SENB specimens and is shown to be 3 for perfect plasticity.

### 8.2.1 Effect of Thickness on Plane Strain J-Dominance

Any criterion for the loss of plane strain J-Dominance is largely subjective but Shih and German (1981) argued that in fully constrained plane strain flow fields, J-Dominance can be regarded as being maintained when the stresses are within ten percent of the HRR field at $r = 2J/\sigma_o$. For in-plane constraint loss, Betegón and Hancock (1991) proposed that plane strain J-Dominance should be maintained for T-stresses greater than $-0.2\sigma_o$ for a hardening exponent, $n = 13$, which is consistent with the ten percent criterion used by Shih and German (1981). However, Shih and German (1981) and Betegón and Hancock (1991) discussion is centred on J-Dominance specific to in-plane effects. The effect of thickness on plane strain J-Dominance can be discussed based on an observation which originated

from Wallin (1985), and has subsequently been adopted in the ASTM (E813-1988) standard test method for $J_{Ic}$. To maintain plane strain J-Dominance in a bend test :

$$t > 25\frac{J_c}{\sigma_o} \tag{8.8}$$

This empirical requirement has been supported by numerical and experimental results. Nevalainen and Dodds (1995) suggested the plane strain J-Dominance requirement to be $t \geq 25\text{-}50J_c/\sigma_o$ for hardening exponent, n = 5 - 10. A tighter limit on the thickness requirement to maintain plane strain J-Dominance was proposed by Koppenhoefer and Dodds (1996) at $t \geq 25\text{-}30J_c/\sigma_o$ for cleavage failure based on impact-loaded, pre-cracked Charpy specimens.

In the current three-dimensional analyses, it has been shown that on the centre plane of SENB fully thick square specimen (B/(W-a) = 1) constraint loss is almost negligible at the limit of in-plane J-Dominance ($c\sigma_o/J = 25$), where c = (W-a) is the ligament length. In order to maintain consistency for thinner specimens, the out-of-plane constraint loss curve which initiates from $J_{loc}t/z^2\sigma_o = 0$ for $\Delta\sigma^{op}/\sigma_o = 0$ can be modified to be consistent with the ten percent criterion (Shih and German (1981)). A plane strain J-Dominance limit can be drawn on the constraint loss curves as shown in Figure 8.2. If the mean stress is considered, a ten percent departure from the Prandtl corresponds to $\Delta\sigma/\sigma_o = -0.24$. Within this limit, it is reasonable to consider constraint loss to be negligible so that $\Delta\sigma/\sigma_o = 0$ when $J_{loc}t/z^2\sigma_o \leq 0.25$. The expression for out-of-plane constraint loss in the fully in-plane constrained field is now proposed to be:

$$\frac{\Delta\sigma^{op}}{\sigma_o} = 0 \qquad \text{for } \left(0 \leq \frac{3J_{loc}t}{z^2\sigma_o} \leq 0.25\right) \text{ and } \frac{T}{\sigma_o} \geq 0$$

$$\frac{\Delta\sigma^{op}}{\sigma_o} = 1.82\left(e^{-\left(\frac{3J_{loc}t}{z^2\sigma_o}\right)+0.25} - 1\right) \text{ for } \left(\frac{3J_{loc}t}{z^2\sigma_o} \leq 0.25\right) \text{ and } \frac{T}{\sigma_o} > 0 \tag{8.9}$$

The addition of 0.25 as a constant in the exponential term does not change the constraint sensitivity, γ, which remains 3. The effect of thickness on plane strain J-Dominance can now be identified by calculating the intersection of equation (8.9) to the ten percent offset shown in Figure 8.6 (a). Out-of-plane constraint loss is negligible at the midplane for thicknesses greater than:

$$t > 30\frac{J_c}{\sigma_o} \tag{8.10}$$

which is consistent with the existing thickness limit of ASTM (E813-1988). In addition, the three-dimensional analyses can be used to demonstrate plane strain J-Dominance in a three-dimensional field as shown in Figure 8.7. Plane strain J-Dominance is lost at distances z/t < 0.18 from the free surface.

In an unconstrained flow fields such as the CCP geometry, in-plane constraint loss causes J-Dominance to be lost at very small applied loads, and no offset is required $\Delta\sigma^{op}/\sigma_0 = 0$ as shown in Figure 8.6 (b). The out-of-plane constraint loss for unconstrained fields, $\Delta\sigma^{op}{}_{uc}/\sigma_0$, of a CCP specimen can be given as:

$$\frac{\Delta\sigma^{op}_{uc}}{\sigma_o} = \beta\left(e^{-3\left(\frac{J_{for}t}{z^2\sigma_o}\right)} - 1\right) \qquad (T < 0) \tag{8.11}$$

Figure 8.6 (a) and (b) show the fit of the curve of equations (8.9) and (8.11) to the SENB and CCP numerical data plotted at the midplane, z = t/2.

### 8.3 Effect of Thickness on Toughness

In order to examine the effect of thickness on toughness, data from Betegón (1990) shown in Figure 2.43 is used. From the figure, the failure locus due to in-plane constraint loss, can be reasonably expressed as:

$$\begin{aligned} J &= J_{Ic} && \frac{T}{\sigma_o} \geq 0 \\ J_c &= J_{Ic}\left(1-\alpha\frac{T}{\sigma_o}\right) && \frac{T}{\sigma_o} < 0 \end{aligned} \tag{8.12}$$

where $\alpha = 3$ is the in-plane constraint loss sensitivity for the Betegón's (1990) data and using $J_{Ic} = 200$ kN/m and $\sigma_o = 400$ MN/m$^2$. If the out-of-plane constraint loss has a similar effect to in-plane constraint loss, the out-of-plane constraint loss can be matched to the failure locus as shown schematically in Figure 8.8. The load history at the midplane for a given thickness specimen can be expressed by equation (8.9) for SENB specimens. The thickness of the cracked bend specimens was 22 mm. The load history of different thickness specimen is plotted in Figure 8.9. At a thickness of 22 mm, the load history intersects the failure locus close to $J_{Ic}$ and specimens of this thickness are almost fully constrained. As the thickness reduces, the out-out-of-plane constraint loss approaches the plane stress field.

If the intersection of the load path and the failure locus is extracted from Figure 8.9, toughness as a function of thickness failure locus can be determined using equation (8.12). Out-of-plane constraint loss saturates as plane stress is approached. The exponential expression in equation (8.9) can be expressed in a simpler form for $J_{Ic}t/z^2\sigma_o << 1$ :

$$J_c = \frac{J_{Ic}(1-0.75\beta)}{1-3\beta\gamma_{ap}\dfrac{J_{Ic}t}{z^2\sigma_o}} \tag{8.13}$$

From the variation of the J-integral along the crack front, the highest deformation occurs on the midplane and sensibly, failure can be assumed to initiate at the centre of the plate. By replacing $z = t/2$ in equation (8.13):

$$J_c = \frac{J_{Ic}(1-0.75\beta)}{1-3\beta\gamma_{op}\dfrac{4J_{Ic}}{t\sigma_o}} \qquad \text{for } \frac{4J_{Ioc}}{t\sigma_o} \le 0.3 \qquad (8.14)$$

Equations (8.13) and (8.14) essentially provides an estimation of failure at the midplane of the plate.

### 8.3.1 Experimental Validation for Thickness Effect on Toughness

It is now appropriate to use this method on experimental data to verify the predicted effect of thickness on fracture toughness. Irwin et al. (1958) have presented data for cracked bend bars of 7075-T5 and 2024-T3 Aluminium alloys, and tabulated in Irwin (1964). Originally, the toughness data versus thickness consists of notched bend and centre cracked tension panels but for comparison, only the cracked bend data is used as tabulated in Table 8.2 in order to eliminate in-plane constraint loss effects. A further caveat arises as the data were only originally analysed using LEFM which will underestimate the toughness in full plasticity.

Figures 8.10 and 8.11 show the effect of thickness on toughness using equation (8.14) at the midplane, compared with the experimental data of Irwin (1964) for 7075-T6 and 2024-T4 Aluminium alloys. The model agrees well within experimental data for SENB (fully constrained) specimens.

This is a significant step in understanding the effect of specimen thickness due to out-of-plane loss on toughness, which was discussed initially about five decades ago. The comparison between the experimental data and the analytical expression provides validation that the deformation parameter $J_{Ioc}t/z^2\sigma_o$ can successfully quantify out-of-plane constraint loss. The necessary data are the plane strain fracture toughness, $J_{Ic}$, and the yield stress in tension, $\sigma_o$ combined with a plane strain J-Q/T locus. It is pertinent to highlight the effects of $\beta$ on the $J_c$-thickness failure locus. In a through cracked problem, $\beta$ is the initial difference in constraint between the midplane and the free surface field at

asymptotically small load levels. For the present configurations, the constraint sensitivity, $\gamma$, has been shown to be similar in SENB and CCP geometries and thus only $\beta$ is shown to be dependent on geometry through the T/Q term. For different materials, the J-Q/T failure locus may differ, and the in-plane constraint sensitivity, $\alpha$ in equation (8.12) may also vary. However, Wallin (2001) suggested a simple expression for constraint loss which he argues to be universal.

The representation of toughness as a function of thickness is a useful indication of the level of toughness for a given material in a specified cracked configuration. However, a more convenient and practical method in assessing the safety margin of a flawed structure is the failure assessment diagram. This is discussed in the following section.

## 8.4 Failure Assessment Diagrams (FADs)

Although the three-dimensional crack tip analyses presented in this thesis were carried out for a non-hardening material, the expressions for the constraint loss can be used to approximate failure in real materials, as demonstrated by the effect of thickness on toughness in the preceding section. Therefore, the same approach can now be used to demonstrate a methodology of assessing failure based on failure assessment diagrams.

### 8.4.1 SENB Out-of-Plane Effects

In order to develop failure assessment diagrams to evaluate the effects of out-of-plane constraint loss in structural problems, it is appropriate initially to define the reference failure locus for the plane strain conditions. J can be decomposed as usual into elastic and plastic components:

$$J_{total} = J_{elastic} + J_{plastic} \tag{8.15}$$

Following Kumar et al. (1981), the elastic and plastic crack driving force, J is:

$$J_{elastic} = \alpha\sigma_o\varepsilon_o(W-a)h_1(a/W,n)\left(\frac{P}{P_o}\right)^2 \tag{8.16}$$

$$J_{plastic} = \alpha\sigma_o\varepsilon_o(W-a)h_1(a/W,n)\left(\frac{P}{P_o}\right)^{n+1} \tag{8.17}$$

where $\alpha$ is a constant taken as 1. The yield strain, $\varepsilon_o$, can be calculated from the yield stress, $\sigma_o$, and Young's modulus, E. $P/P_o$ is the load over limit load which is also expressed as $L_r$. The expression $h_1$ (a/W, n) is a tabulated function of geometry and strain hardening exponent, n, given by Kumar et al. (1981). For a deeply cracked bend bar (a/W = 0.5), the limit load is given by equation (4.4). For material with hardening exponent of n = 10, the $h_1^{elastic}$ = 1.41 and $h_1^{plastic}$ = 0.331. Noting that $K_r = \sqrt{\frac{J_{el}}{J_{Ic}}}$, a failure assessment line for a plane strain SENB geometry can be plotted as shown in Figure 8.12 given that failure occurs at a critical value of J. This failure assessment line is a failure locus for which t is infinite or simply a state of plane strain.

For a finite thickness SENB geometry, out-of-plane constraint loss, $\Delta\sigma^{op}/\sigma_o$, can be expressed by equation (8.9). The toughness $J_c$ due to out-of-plane constraint loss normalised by the fully constrained, $J_{Ic}$ is taken to be:

$$\frac{J_{c(\Delta\sigma/\sigma_o)}}{J_{Ic}} = 1 - \alpha\frac{\Delta\sigma^{op}}{\sigma_o} \tag{8.18}$$

where $\alpha$ is the constraint sensitivity which is dependent on the material failure locus and Betegón's data $\alpha = 3$ has been used in all calculations.

A failure assessment diagram in three-dimensional problem is represented by $L_r$ on the abscissa which is the load normalised by the limit load. The ordinate is represented by $K_r$. $K_r$ in terms of the enhanced toughness due to constraint loss has been discussed following

MacLennan and Hancock (1995) or Ainsworth and O'Dowd (1995). MacLennan and Hancock (1995) have shown that the failure assessment line derived from the EPRI scheme (equation (2.163)) is identical to the failure assessment line for constraint matched toughness given in equation (2.166). A failure assessment line that more clearly demonstrates the enhanced margins (Ainsworth and O'Dowd (1995)) is given as:

$$K_r^{ip} = K_r^{pl.strain} \sqrt{\frac{J_{(Q/T)}}{J_{Ic}}} \tag{8.19}$$

where $K_r^{pl.strain}$ has been given in equation (2.166). Following the same argument, $K_r^{op}$ for the out-of-plane constraint loss can be given as:

$$K_r^{op} = K_r^{pl.\,strain} \times \sqrt{\frac{J_{c(\Delta\sigma/\sigma_{ys})}}{J_{Ic}}} \tag{8.20}$$

where $J_{c(\Delta\sigma/\sigma_{ys})}$ is the toughness associated with constraint loss. Figure 8.13 show the effect of out-of-plane constraint loss on the failure assessment diagrams. As the thickness reduces, the toughness increases. At very low load levels, the toughness of the specimen corresponds to the plane strain $J_{Ic}$ toughness regardless of thickness. At very small loads, the extent of plasticity is small in relation to the size of the specimen and failure occurs at $K_r = K_{Ic}$. However as deformation increases, and plasticity increases prior to failure, out-of-plane constraint loss increases and this increases the toughness of the specimen towards plane stress toughness. For all specimen thickness, the failure assessment line converges to a single line which is the limit for plane stress toughness (excluding necking). The failure assessment diagrams are able to show the effect of thickness on toughness which is a significant step in identifying the transition of toughness from plane strain to plane stress, and the loss of out-of-plane constraint.

### 8.4.2 CCP In-Plane and Out-of-Plane Effects

In three-dimensional centre cracked tension panels (CCP), constraint is lost due to both in-plane and out-of-plane effects.

$$\frac{\Delta\sigma}{\sigma_o} = \frac{\Delta\sigma^{ip}}{\sigma_o} + \frac{\Delta\sigma^{op}_{itc}}{\sigma_o} \tag{8.21}$$

where, $\Delta\sigma/\sigma_o = \Delta\sigma_m/\sigma_o = \Delta\sigma_{\theta\theta}/\sigma_o$ is the total constraint loss in the leading sectors ahead of the crack tip. The superscript *ip* and *op* refer to in-plane constraint loss and out-of-plane constraint loss. The in-plane constraint loss has been determined in chapter 6. Following equations (6.1 to 6.4), in-plane constraint loss in three-dimensional CCP specimen can be estimated using the Q term given in equation (2.150). Using equation (6.4) in equation (2.150) gives:

$$\frac{\Delta\sigma^{ip}}{\sigma_o} = A_n\left(\frac{\tau}{\sqrt{3}}\frac{P}{P_o}\right) + B_n\left(\frac{\tau}{\sqrt{3}}\frac{P}{P_o}\right)^2 \tag{8.22}$$

The out-of-plane constraint loss in CCP specimens can be quantified using equation (8.11) where β is defined in equation (8.7). The failure assessment diagram for CCP can now be constructed from Kumar et al.'s (1981) expression for J given in equations (8.16) and (8.17). For a hardening exponent, n = 10, the CCP constants $h_1^{elastic} = 2.21$ and $h_1^{plastic} = 1.52$. For CCP specimens with a/W = 0.5, the toughness due to out-of-plane constraint loss $J_{c(\Delta\sigma/\sigma_o)}$ can be calculated through equation (8.18).

Figure 8.14 shows failure assessment diagrams for CCP specimens, B/(W-a) = 1 and 0.1 with a/W = 0.5 and n = 10. The failure assessment line in CCP specimens depends on the level of T/Q. At very small loads, the toughness is similar regardless of thickness. As the load increases, the failure assessment line depends on the level of T/Q. Thick CCP specimens have very negative biaxiality compared to the thin CCP specimen. It is shown

that the failure assessment line in B/(W-a) = 10 are higher than the thick CCP specimen (B/(W-a) = 1). However, at very high loads, the failure assessment lines are independent of T/Q. The CCP specimen failure assessment diagrams has been able to show the transition of plane strain to plane stress however the level of enhanced toughness is dependent on the level of T/Q. Figure 8.15 shows in-plane effect compared to the out-of-plane effect for constraint loss for CCP specimens for different thickness, which show that out-of-plane effect dominates at and after limit load.

It has been demonstrated that enhanced level of toughness associated with the loss of out-of-plane constraint can be incorporated into the failure assessment diagram scheme. Constraint loss in unconstrained flow field is dominated by in-plane effects up to limit load. At loads greater than limit load, the toughness is strongly affected by out-of-plane effects. The three-dimensional constraint based failure assessment diagram can alleviate the traditional approach of using lower bound plane strain toughness in structural integrity assessment, and avoid unnecessary conservatism.

### 8.4.3 Experimental Validation of FADs

The three-dimensional failure assessment diagram methodology is now applied to the experimental results of Irwin, Kies and Smith (1958), Rolfe and Novack (1970) and Jones and Brown (1970). These data are tabulated in Tables 8.3. Irwin et al. (1958) used 7075-T6 and 2024-T4 Aluminium alloys while Rolfe and Novack (1970) used 18 Ni Maraging Steel. Jones and Brown (1970) used a Ti 6Al-6V-2Sn Titanium alloy. All the experiments were carried out on deeply cracked SENB (three-point-bend) configurations. The failure modes of most of specimens were cleavage except for the aluminium alloys. The failure mode in the aluminium alloys has been discussed in terms of the percentage of flat or shear lip fracture, Irwin (1964). All the aluminium alloys specimens failed by flat fracture except the thinnest 7075-T6 which failed by 100% shear.

Initially the original data which is expressed in terms of $G_c$ and $K_c$ is changed to $J_c$ using equation (2.126). For all cases, a hardening exponent, n = 10 has been assumed. The out-

of-plane constraint loss is then calculated using equation (8.18) with the condition that plane strain J-Dominance is maintained for $t > 30J_c/\sigma_0$ for deeply cracked bend bars. The transformed experimental data for FADs is tabulated in Table 8.3.

Figures 8.16-8.19 show the three-point-bend failure assessment diagrams for different materials in the order given above. All the failure assessment diagrams show that the experimental data at a given thickness fall on or above the failure assessment line for the same experimental data thickness. When the calculated out-of-plane constraint loss $\Delta\sigma/\sigma_0 = 0$ for the experimental data, failures fall on the plane strain failure assessment line. This indicates that the failure methodology presented can be regarded as a conservative estimate of failure. In all diagrams, the toughness approaches a limiting failure assessment line which can be identified with a plane stress limit before necking.

As all results has been presented based on a constraint sensitivity, $\alpha = 3$, it is appropriate to discuss this effect on the limit of plane stress toughness failure assessment lines in the failure assessment diagrams. Figure 8.20 shows the effect of changing $\alpha$ for a given thickness using the data of Rolfe and Novack (1970). Increasing or decreasing value of $\alpha$ causes the plane stress toughness limit to increase or decrease correspondingly.

## 8.5 Conclusions

Within the leading sector ahead of the crack, the stress fields differ hydrostatically but the maximum stress deviators are similar. This allows a single parameter to quantify the change in the mean stress and the maximum principal stress and lead to a viable two-parameter fracture mechanics scheme.

In fully constrained crack tip fields, the limit of J-Dominance has been determined through a practical out-of-plane constraint loss scheme. In three-dimensional analyses, a thickness J-Dominance limit is maintained at $t > 30J/\sigma_0$. At a distance of $r = 2J/\sigma_0$ along the thickness J-Dominance is lost at distance $z/t < 0.18$ from the free surface.

The application of failure assessment diagrams to existing experimental data has been demonstrated. Significant advantage from the effect of out-of-plane constraint loss on toughness can now be realised through a practical method in which failure due to cleavage or ductile tearing can be described through a three-dimensional failure assessment methodology.

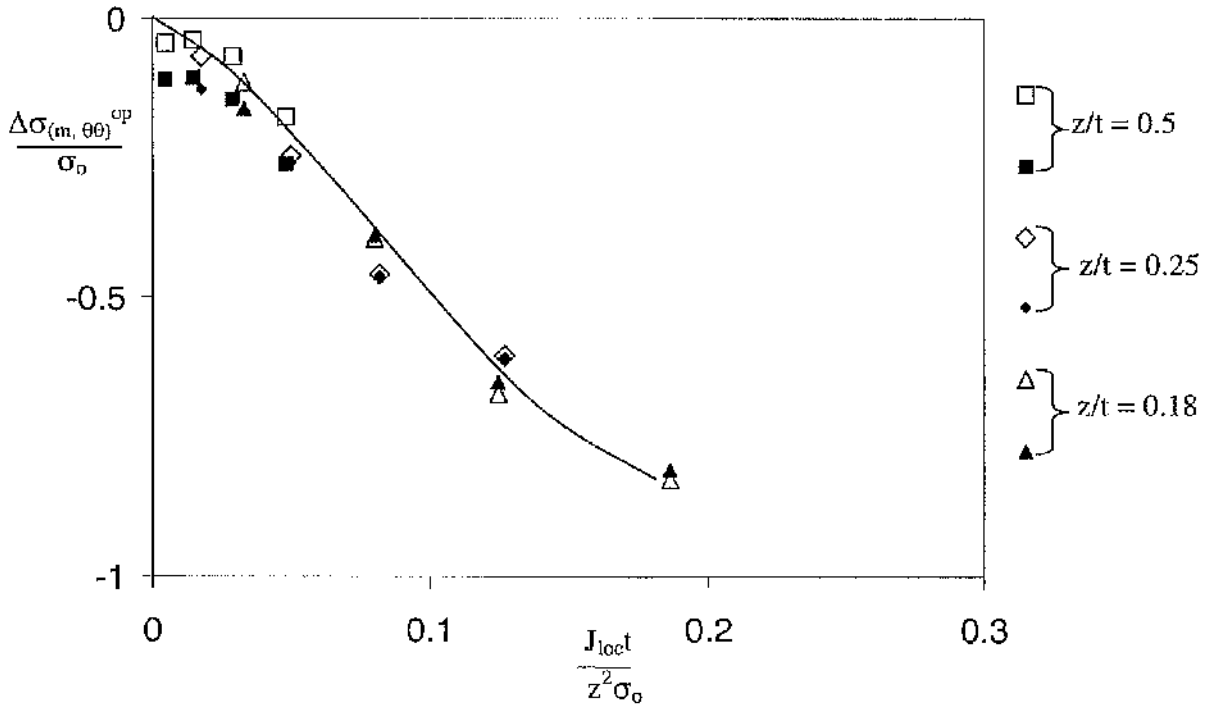


Figure 8.1: $\Delta\sigma_m{}^{op}/\sigma_o$ and $\Delta\sigma_{\theta\theta}{}^{op}/\sigma_o$ as a function of $J_{loc}t/z^2\sigma_o$ at $r = 2J/\sigma_o$ for a boundary layer formulation at z/t = 0.5, 0.25 and 0.18. The filled markers represent the mean stress, and the unfilled markers represent the hoop stress.

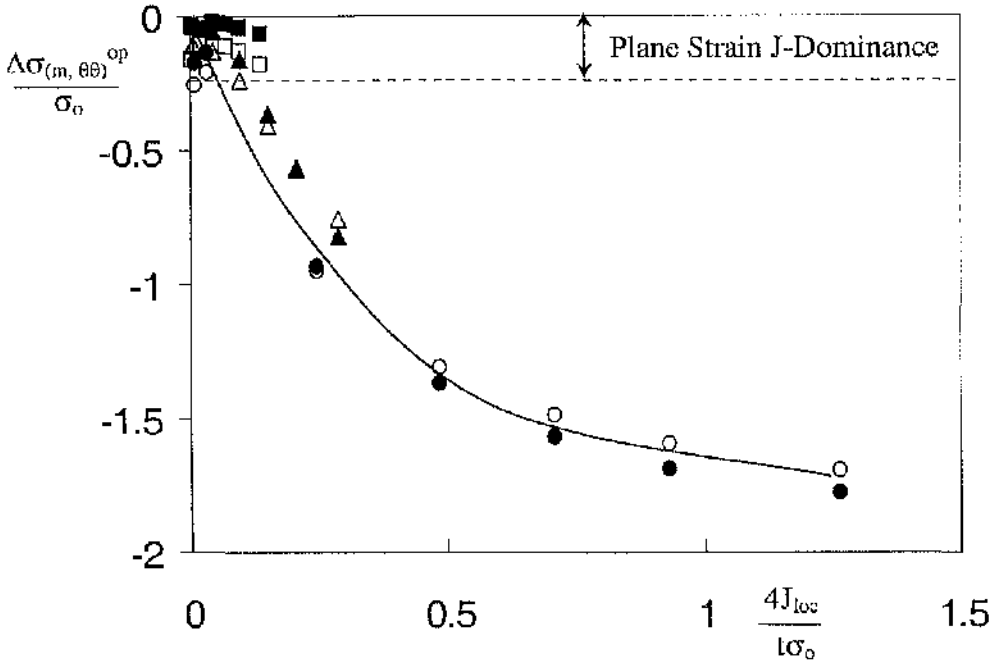


Figure 8.2: $\Delta\sigma_m^{op}/\sigma_o$ and $\Delta\sigma_{\theta\theta}^{op}/\sigma_o$ as a function of $4J_{loc}/t\sigma_o$ in SENB specimens at $r = 2J\sigma_o$ at the midplane. The square, triangular and circular markers indicate thick, intermediate thickness and thin specimens. The filled and unfilled markers represent $\Delta\sigma_m^{op}/\sigma_o$ and $\Delta\sigma_{\theta\theta}^{op}/\sigma_o$.

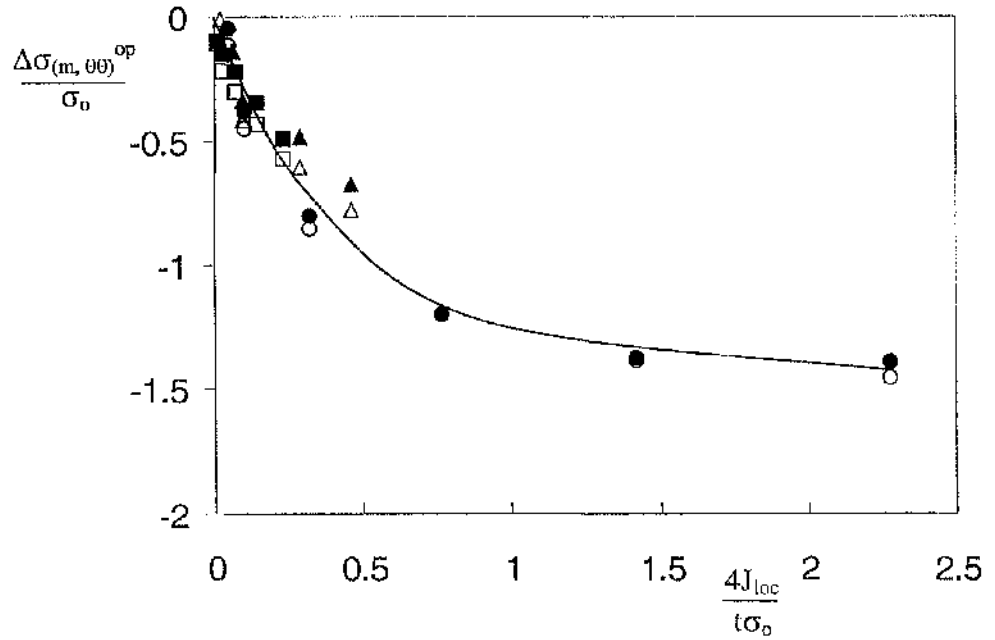


Figure 8.3: $\Delta\sigma_m^{op}/\sigma_o$ and $\Delta\sigma_{\theta\theta}^{op}/\sigma_o$ as a function of $4J_{loc}/t\sigma_o$ for CCP specimens at $r = 2J\sigma_o$ at the midplane. The square, triangular and circular markers indicate the thick, intermediate thickness and thin specimens. The filled and unfilled markers represent $\Delta\sigma_m^{op}/\sigma_o$ and $\Delta\sigma_{\theta\theta}^{op}/\sigma_o$.

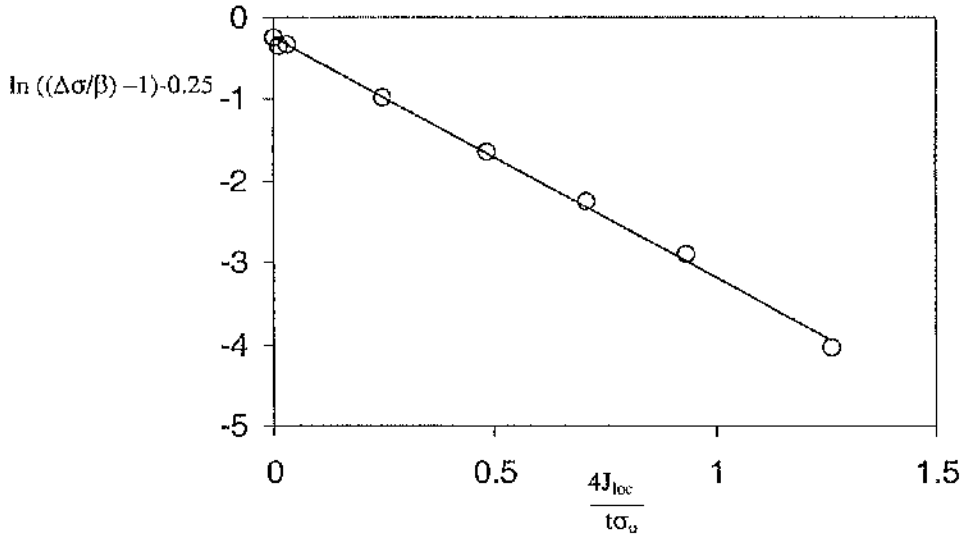


Figure 8.4: The gradient of the curve indicates the constraint sensitivity, $\gamma_{op}$, for SENB specimens.

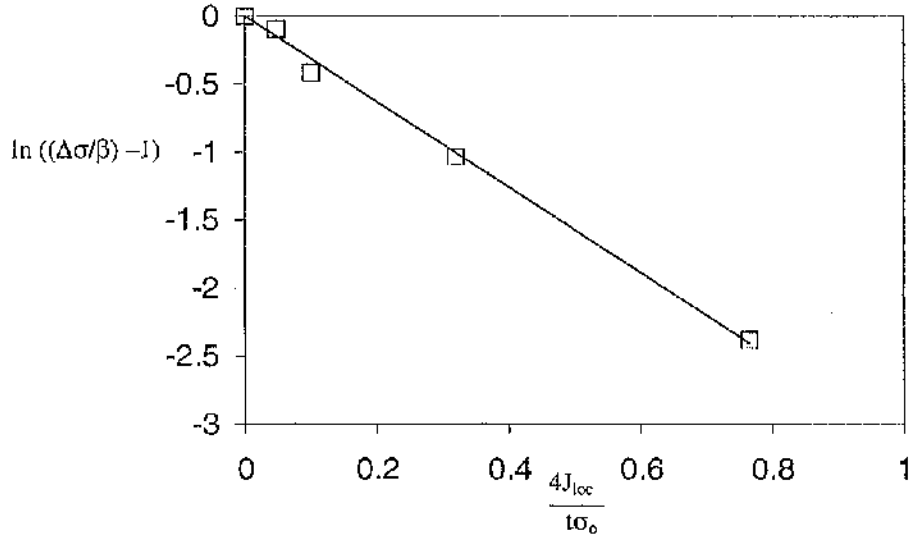


Figure 8.5: The gradient of the curve indicates the constraint sensitivity, $\gamma_{op}$ for CCP specimens.

| | SENB | CCP |
|---|---|---|
| $\beta$ | 1.82 | 1.44 |
| $\gamma_{op}$ | 3 | 3 |

Table 8.1: The out-of-plane constraint loss constant, $\beta$, and the constraint loss sensitivity, $\gamma$, for SENB and CCP specimens.

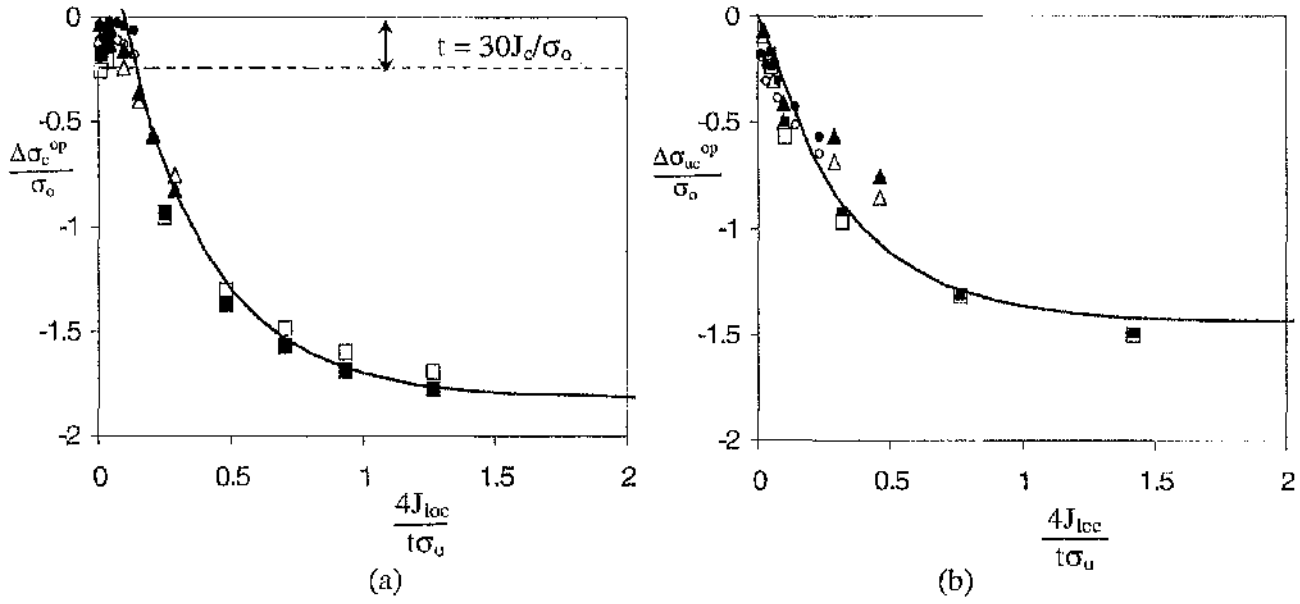


Figure 8.6: Curve fit of equations (8.9) and (8.11) at the midplane for difference of stress as a function of deformation for (a) SENB and (b) CCP in geometries with different thickness. The circular, triangular and square markers represent the thick, intermediate thickness and thin specimens while the filled and unfilled markers represent $\Delta\sigma_{\theta\theta}$, $\Delta\sigma_m$.

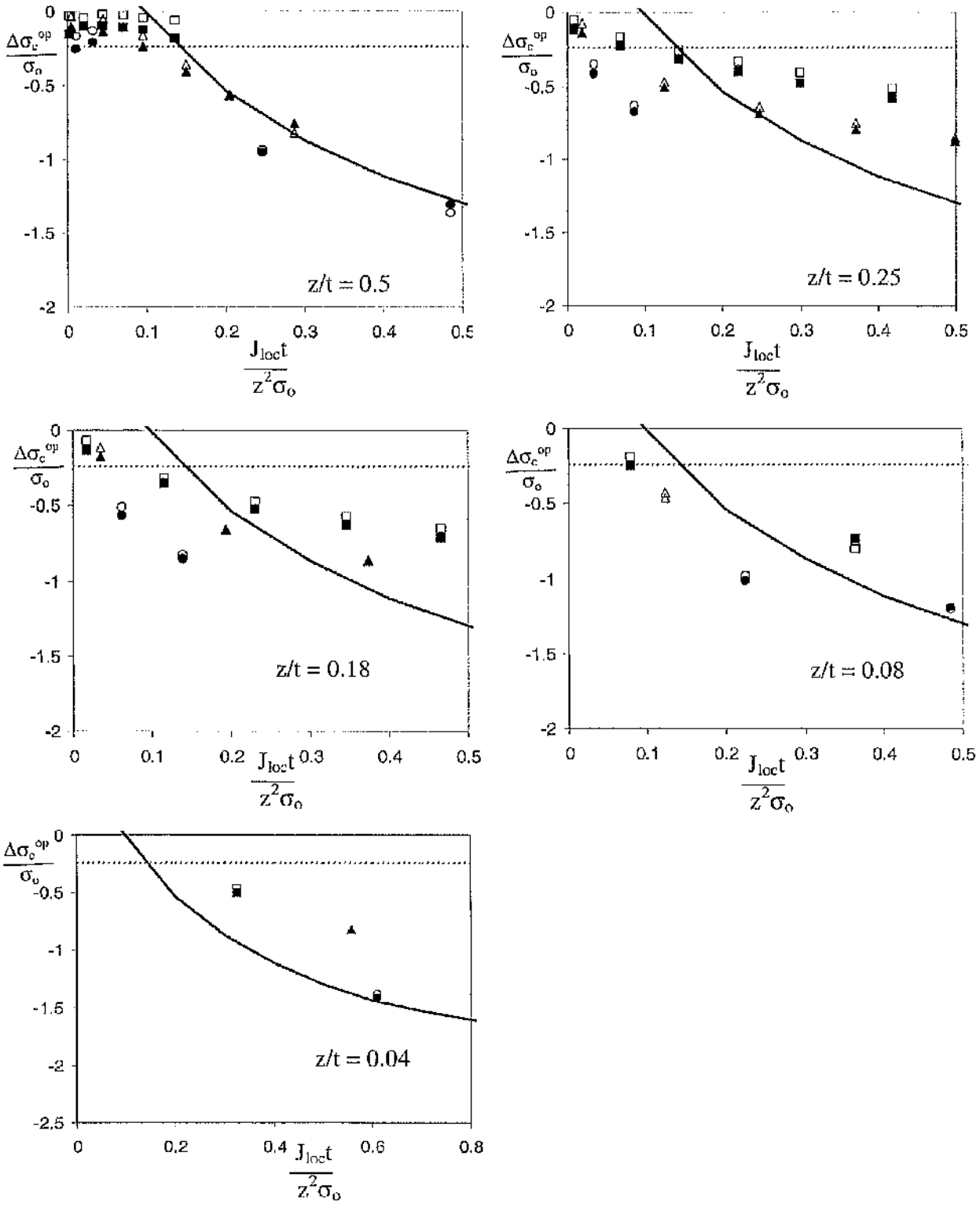


Figure 8.7: The SENB through thickness variation of the effect of thickness on J-Dominance ($t > 30\ J_c/\sigma_o$).

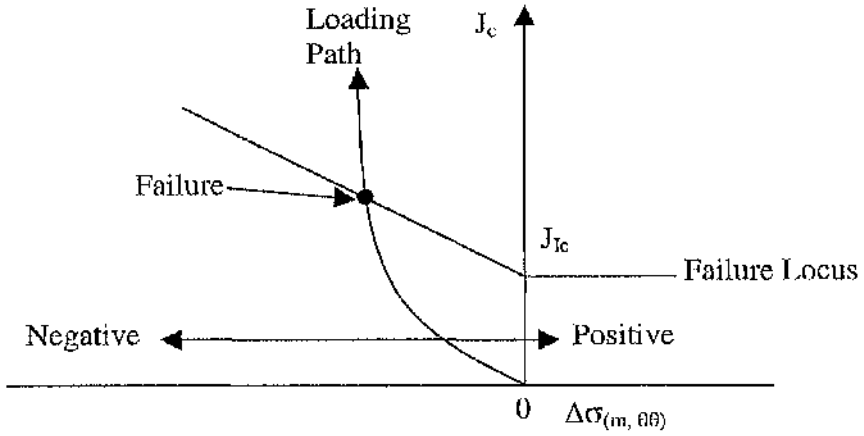


Figure 8.8: Schematic of failure locus $J_c$ as a function of $\Delta\sigma_{(m,\theta\theta)}$.

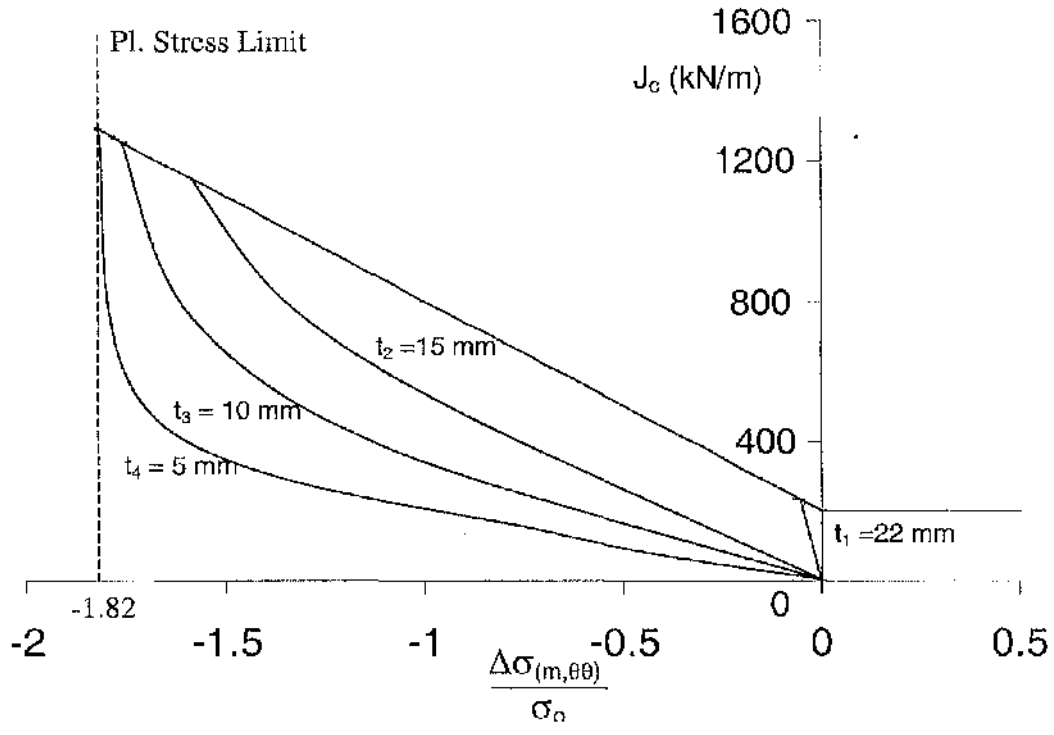


Figure 8.9: The trend of load history modelled using equations (8.9) for bend specimens using constraint sensitivity, $\gamma = 3$ and constraint loss constant, $\beta = 1.82$ at different thicknesses ($t_4 < t_3 < t_2 < t_1$) and failure locus based on Betegón's (1990) data expressed in equation (8.12).

| 7075-T6 | | 2024-T4 | |
|---|---|---|---|
| Thickness, mm | $J_c$, kN/m | Thickness, mm | $J_c$, kN/m |
| 25.4 | 22.8 | 203.2 | 57.2 |
| 19.05 | 23.5 | 101.6 | 60.7 |
| 9.32 | 27.7 | 50.8 | 64.2 |
| 3.175 | 112.1 | 25.4 | 78.6 |

Table 8.2: Effect of thickness on toughness in 7075-T6 and 2024-T4 Aluminium alloys after Irwin (1964) tabulated data. The critical crack initiation, $J_{Ic}$ = 20.2 and 52.5 kN/m and the yield stress, $\sigma_o$ = 500 and 344 MN/m$^2$.

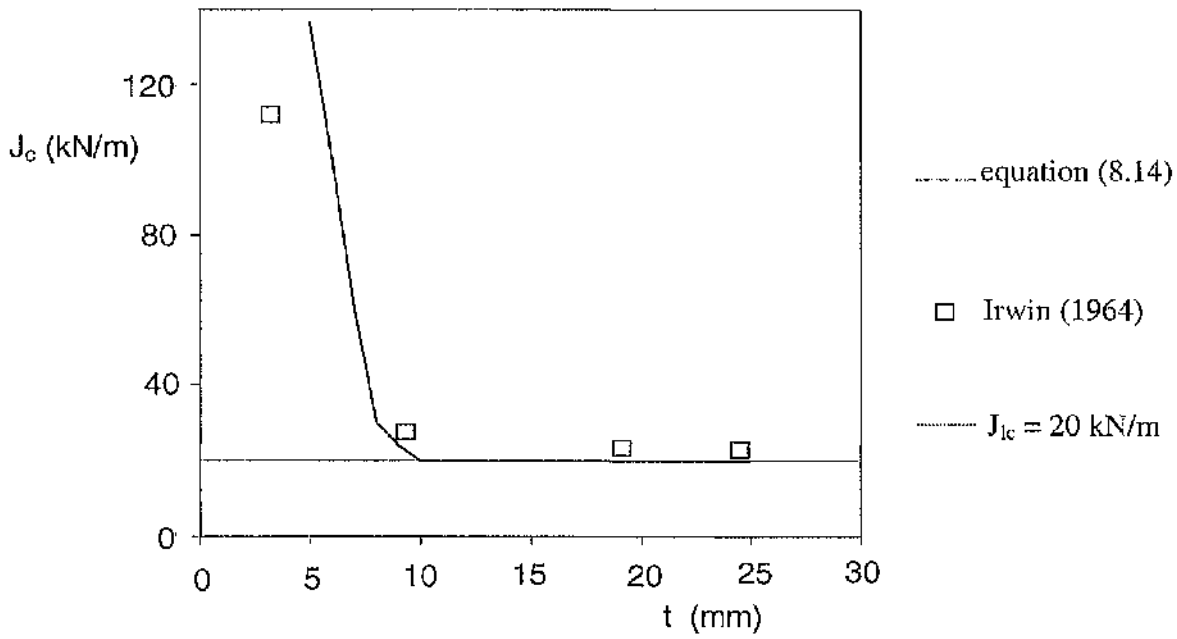


Figure 8.10: The effect of thickness on toughness from equation (8.14) representing a crack in bend bar, $\beta_{SENB}$ = 1.82, $\gamma$ = 3. The markers represent the experimental cracked bend data of Irwin (1964) for 7075-T6 Aluminium alloy tabulated in Table 8.2.

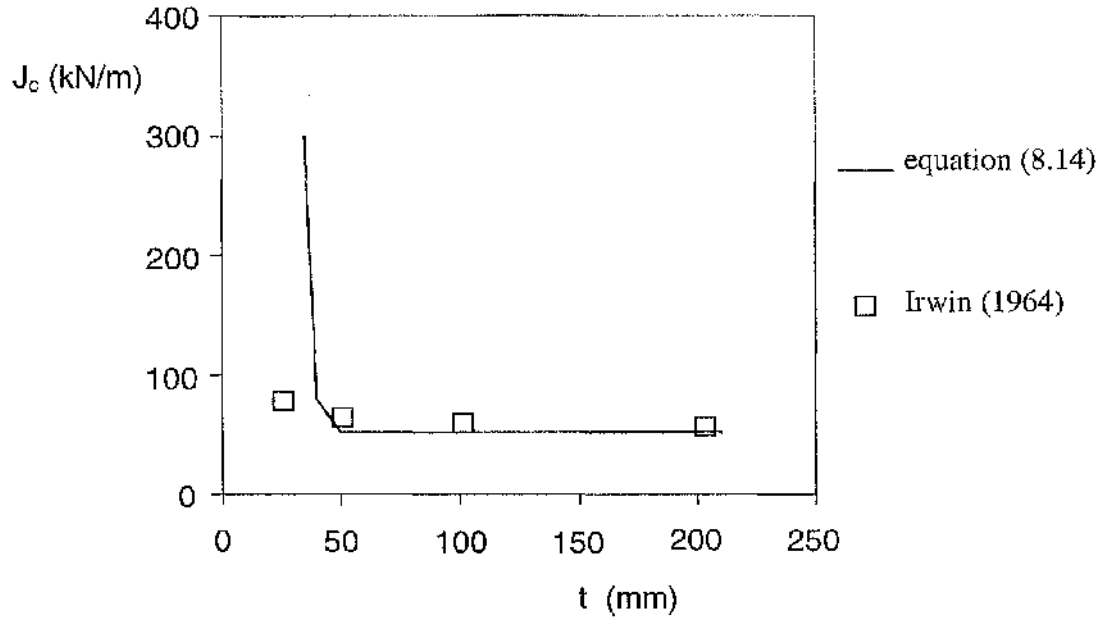


Figure 8.11: The effect of thickness on toughness of cracked bend bar from equation (8.14). The markers represent the experimental cracked bend data for 2024-T4 Aluminium alloy of Irwin (1964) tabulated in Table 8.2.

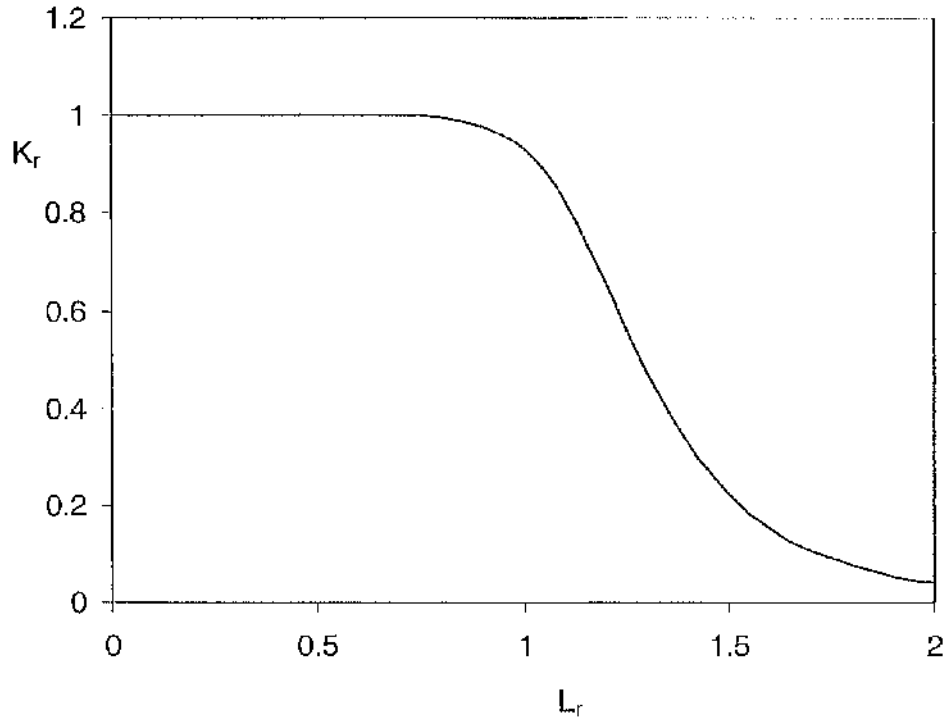


Figure 8.12: The failure assessment diagram showing failure assessment line (FAL) for SENB specimen in plane strain for a hardening exponent, n = 13.

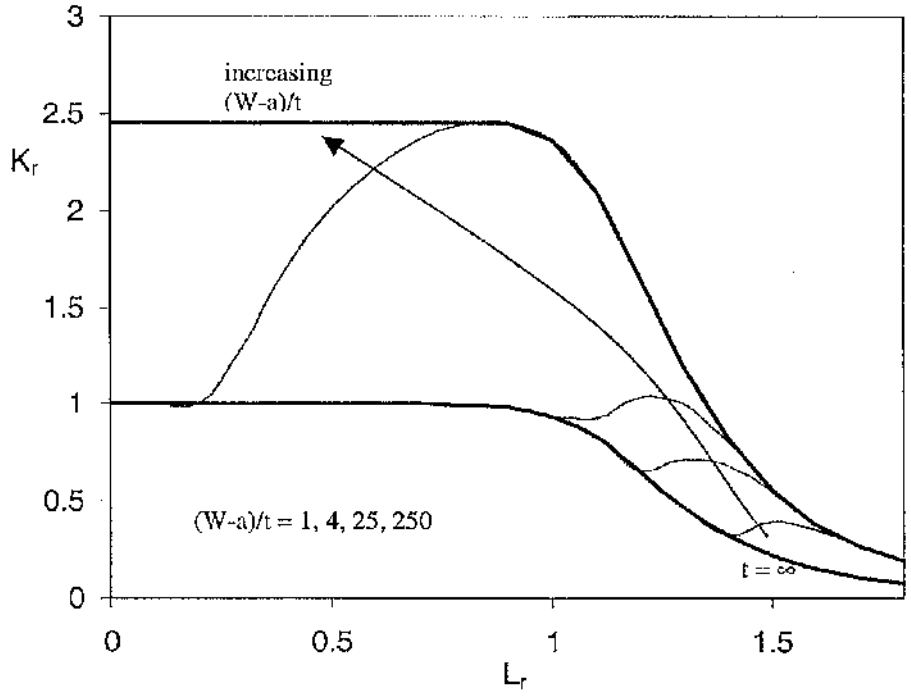


Figure 8.13: The failure assessment line for out-of-plane constraint loss in SENB specimen at different thickness, t, and at fixed ligament, (W-a), for a hardening exponent, n = 13. The continuous bold line indicates a SENB FAL in plane strain condition. (W-a) = 25 mm.

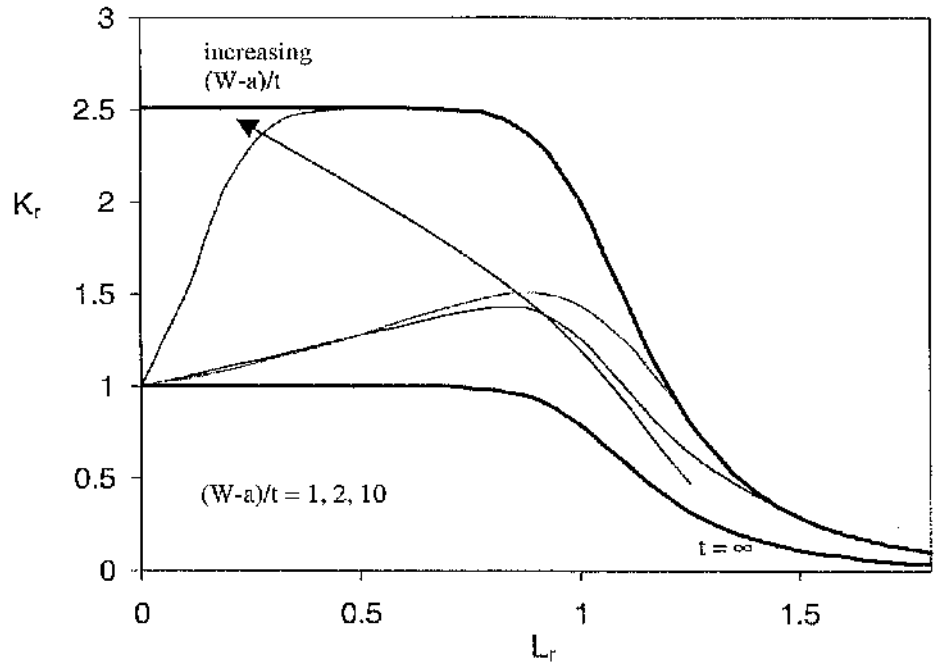


Figure 8.14: Failure assessment lines for in-plane and out-of-plane constraint loss in CCP specimen at different thickness, t, and at fixed ligament, (W-a) = 25 mm, for a hardening exponent, n = 13. The t = ∞ indicate FAL for CCP in in-plane plane strain condition.

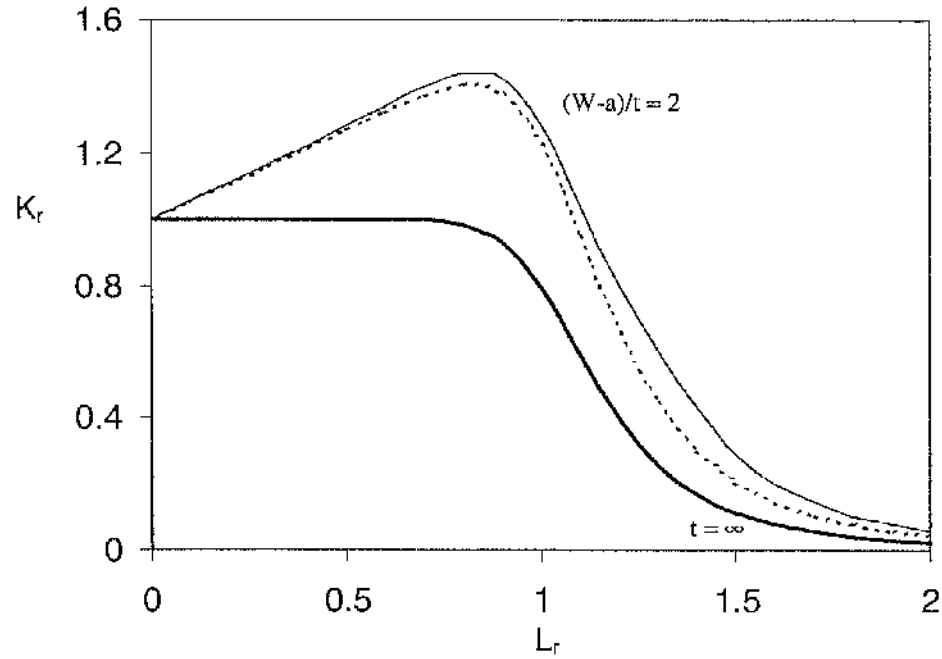


Figure 8.15: The effect of load on in-plane and out-of-plane constraint loss for CCP specimens for a hardening exponent, n = 13. The continuous lines indicate in-plane and out-of-plane effects in CCP while broken lines indicate in-plane effect in CCP for (W-a)/t = 2. The bold line indicates FAL for CCP t = ∞ which represents in-plane, plane strain condition.

| Thickness (t), mm | $\sigma_o$, MPa | E, GPa | $\sigma_U$, MPa | $J_e$, kN/m | $J_{Ic}$, kN/m | $L_r$ | $J_e$, kN/m | $\Delta\sigma/\sigma_o$ | Kr |
|---|---|---|---|---|---|---|---|---|---|
| Aluminium alloy 7075-T6, Irwin et al. (1958) | | | | | | | | | |
| 25.4 | 500 | 70 | 570 | 22.8 | 20.1 | 0.42 | 22.5 | 0 | 0.999 |
| 19.05 | | | | 23.5 | | 0.43 | 23.2 | 0 | 0.999 |
| 9.32 | | | | 27.7 | | 0.468 | 27.3 | 0 | 0.999 |
| 3.175 | | | | 112 | | 0.895 | 102.5 | -1.078 | 1.974 |
| Aluminium alloy 2024-T4, Irwin et al. (1958) | | | | | | | | | |
| 203.2 | 344 | 72 | 469 | 57.26 | 52.53 | 0.921 | 49.92 | 0 | 0.948 |
| 101.6 | | | | 60.76 | | 0.941 | 52.12 | 0 | 0.938 |
| 50.8 | | | | 64.26 | | 0.957 | 53.9 | 0 | 0.929 |
| 25.4 | | | | 78.26 | | 1.013 | 60.46 | 0 | 0.889 |
| 18 Ni Maraging Steel, Rolfe and Novack (1970) | | | | | | | | | |
| 75 | 1323 | 207 | 1379 | 695.6 | 695.6 | 0.88 | 649.2 | 0 | 0.964 |
| 55 | | | | 719.0 | | 0.89 | 661.1 | 0 | 0.961 |
| 47.5 | | | | 707.3 | | 0.885 | 653.6 | 0 | 0.963 |
| 25.4 | | | | 766.9 | | 0.91 | 694.2 | -0.042 | 1.011 |
| 12.7 | | | | 803.9 | | 0.93 | 714.1 | -0.581 | 1.567 |
| 6.25 | | | | 960.4 | | 0.98 | 801.5 | -2.07 | 2.458 |
| Titanium alloy Ti 6Al-6V-2Sn, Jones and Brown (1970) | | | | | | | | | |
| 13.76 | 1200 | 117 | 1269 | 10.13 | 10.47 | 0.145 | 9.27 | 0 | 1 |
| 13.24 | | | | 10.63 | | 0.150 | 9.92 | 0 | 1 |
| 12.7 | | | | 10.63 | | 0.150 | 9.92 | 0 | 1 |
| 12 | | | | 9.81 | | 0.150 | 9.92 | 0 | 1 |
| 6.35 | | | | 11.48 | | 0.162 | 11.49 | 0 | 1 |
| 3.17 | | | | 10.63 | | 0.155 | 10.59 | 0 | 1 |
| 1.76 | | | | 20.89 | | 0.216 | 20.56 | 0 | 0.99 |
| 1.58 | | | | 21.37 | | 0.221 | 21.52 | 0 | 0.99 |
| 0.75 | | | | 30.76 | | 0.260 | 29.79 | -0.268 | 1.34 |

Table 8.3: SENB data for construction of Failure Assessment Diagrams. The original thickness effect on toughness plots are shown in chapter 3 (Irwin et al. (1958) in Figure 3.21; Rolfe and Novack (1970) in Figure 3.26; Jones and Brown (1970) in Figure 3.27).

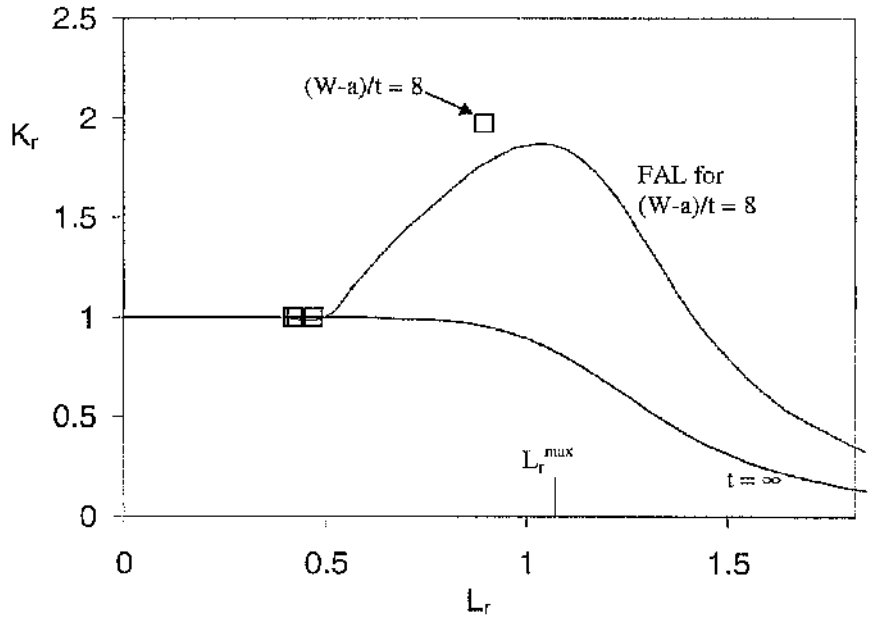


Figure 8.16: Failure Assessment Diagram, Irwin, Kies and Smith (1958), SENB 7075-T6 Aluminium alloy, n = 10. The ligament (W-a) = 25.4 mm. t = ∞ indicates the plane strain FAL limit.

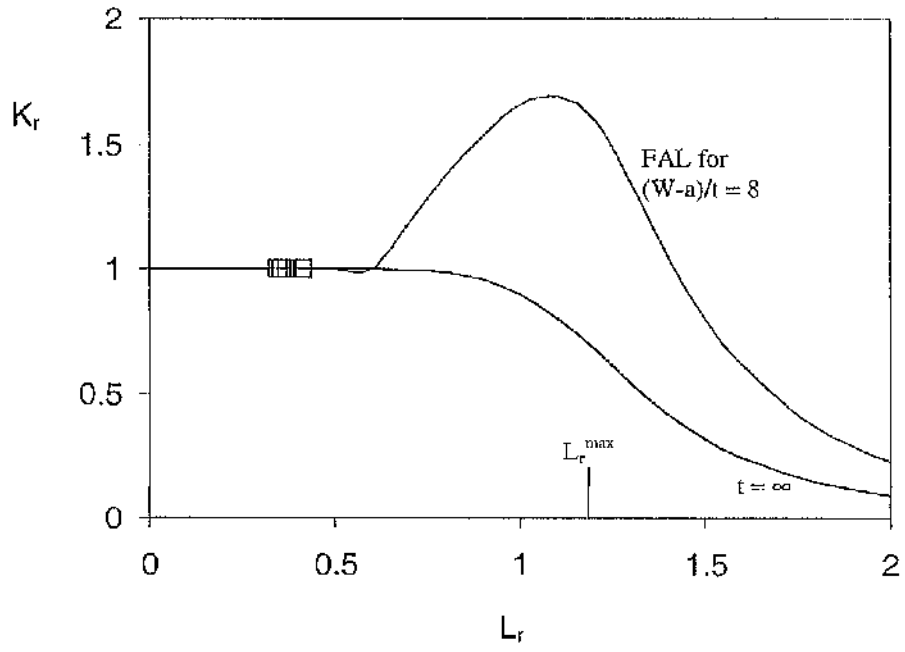


Figure 8.17: Failure Assessment Diagram, Irwin, Kies and Smith (1958), SENB 2024-T4 Aluminium alloy, n = 10. The ligament (W-a) = 203.2 mm. t = ∞ indicates the plane strain FAL limit.

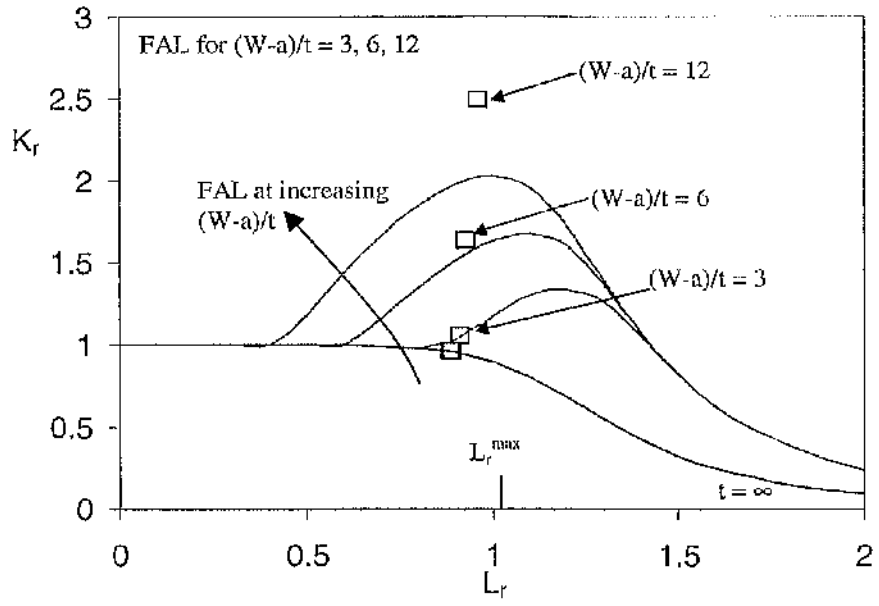


Figure 8.18: Failure Assessment Diagram, Rolfe and Novack (1970), SENB 18 Ni Maraging Steel, n = 10. The ligament (W-a) = 75 mm. t = ∞ indicates the plane strain FAL limit.

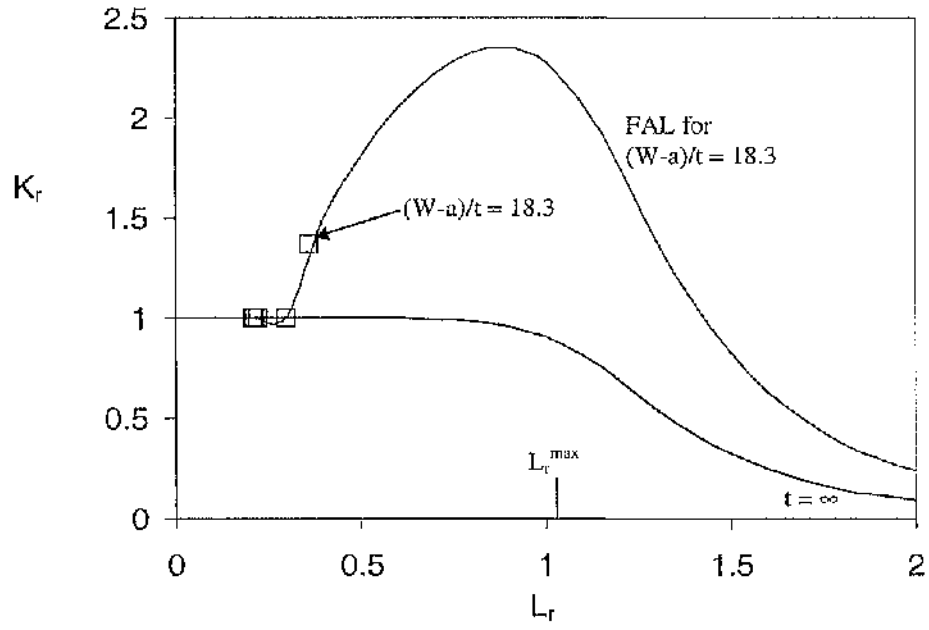


Figure 8.19: Failure Assessment Diagram, Jones and Brown (1970), SENB Ti 6Al-6V-2Sn Titanium Alloy, n = 10. The ligament (W-a) = 13.76 mm. t = ∞ indicates the plane strain FAL limit.

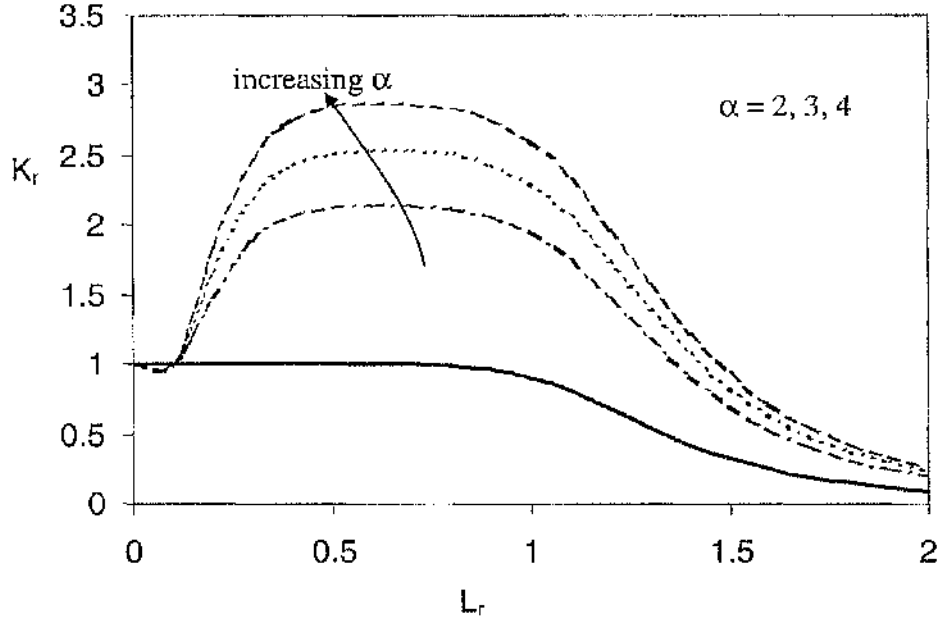


Figure 8.20: The effect of constraint sensitivity, α, using Rolfe and Novack (1970) material data at (W-a)/t = 150.

# Conclusions

The nature of three-dimensional crack tip fields has been analysed for an elastic perfectly-plastic material within the framework of small deformation theory. The geometries studied include a three-dimensional boundary layer formulation, and three-dimensional full-fields solutions of single edge notched bend bars and centre crack tension panels. The full-field solutions have different thicknesses enabling out-of-plane constraint effects to be examined through the plane strain to plane stress transition.

The nature of the stress field has been examined at two important distances; at the crack tip ($r = 0$) and at a distance $r = 2J/\sigma_0$ from the crack tip. In a constrained flow field such as the boundary layer formulation and SENB at very small load levels, a plane strain field initially develops at all sections except the free surface, which exhibit a corner field. However, as the load increases to limit load, the plane strain field is confined to the midplane while other sections (apart from the free surface) decay from the plane strain field. At the crack tip, the free surface remains a corner field but a plane stress field develops at $r = t$. In an unconstrained flow field such as CCP, the field is similar to the fully constrained flow field at very small load levels. Increase in deformation causes in-plane constraint to be lost at all sections except the free surface which remains a corner field.

Proximity to plane stress and corner field has been demonstrated to be similar in constrained and unconstrained flow fields. The corner field at the crack tip is a local effect extending over a radius of $z \leq 0.04t$ from the free surface. This allows a plane stress like field to occur on the crack tip at $z = 0.04t$ from the free surface. On the free surface, the plane stress field is recovered at a distance of $r = t$ from the crack tip.

Out-of-plane constraint loss is dependent on the distance from the crack tip, the distance from the free surface, and the applied load. The stress field ahead of the crack ($-45^\circ \leq \theta \leq 45^\circ$) is a constant stress sector in which the Cartesian stresses and stress invariants are

independent of angular co-ordinates. Out-of-plane constraint loss is associated with a family of fields which differ both hydrostatically and deviatorically. However, the maximum principal stress and the mean stress within the leading sectors at different sections (z/t) differ from the reference small scale yielding field by an identical amount implying that the maximum stress deviators are similar.

Out-of-plane constraint loss has initially been quantified through a plane strain parameter, ρ. In order to unify out-of-plane constraint loss as a function of deformation through the thickness, a dimensionless parameter $\frac{J_{loc}}{z\sigma_o}$ has been introduced. The out-of-plane constraint loss at the corresponding sections (z/t) of different thickness of the same geometry can be unified into a single constraint loss curve. However, the out-of-plane constraint loss at different sections (z/t) have different profiles. In order to unify out-of-plane constraint loss at all sections, a parameter $\frac{J_{loc}t}{z^2\sigma_o}$ has been introduced. This allows the out-of-plane constraint loss at different sections (z/t) to be united into a single relationship. An analytical expression for out-of-plane constraint loss has been developed as a function of $\frac{J_{loc}t}{z^2\sigma_o}$. This parameter has been able to quantify out-of-plane constraint loss at any section along the crack front for any specimen thickness. In geometries that lose constraint due to in-plane and out-of-plane effects such as the CCP specimens, in-plane constraint loss can be estimated through the T/Q constraint estimation scheme coupled with a scheme to assess out-of-plane constraint loss based on $\frac{J_{loc}t}{z^2\sigma_o}$.

The observation that a change in the mean stress, $\sigma_m$, and the hoop stress, $\sigma_{\theta\theta}$, from the small scale yielding field are similar allow out-of-plane constraint loss to be placed in the context of two-parameter failure scheme. Finally, a conservative failure assessment scheme from three-dimensional constraint loss crack analyses has been proposed. In fully constrained geometries, the out-of-plane constraint loss has been validated with experimental data successfully. In geometries that lose in-plane constraint, the total

constraint loss can be estimated by T/Q for in-plane loss and combined with an out-of-plane constraint loss.

The practical importance of the work is that it enables a way in which toughness data can be transferred to structures directly without depending on lower bound plane strain values. This will allow enhanced safety margins to be demonstrated in defect assessment procedures leading to judicious repair and maintenance strategies in which plant and structures can operate in optimum conditions of safe performance.

# References

ABAQUS, V.6.3 (2003) ABAQUS Manual. Hibbit, Karlsson and Sorensen Inc. Pawtucket Rhode Island.

Ainsworth, R., (1995) "A constraint-based failure assessment diagram for fracture assessment" International Journal of Pressure Vessels and Piping, vol. 64, pp. 277-285.

Ainsworth, R., O'Dowd, N.P., (1995) "Constraint in the failure assessment diagram approach for fracture assessment" Transaction of the ASME, Journal of Pressure Vessel Technology, vol.117, pp. 260-267.

Airy, G.B., (1862) "On the strains in the interior of beams" Report of the British Association for the Advancement of Science; London.

Al-Ani, A., Hancock J.W., (1991) "J-Dominance of short cracks in bending and tension" Journal of the Mechanics and Physics of Solids, vol. 39, no. 1, pp. 23-43.

Anderson, T.L., (1995) "Fracture Mechanics: Fundamentals and Applications 2nd Ed." CRC, Texas.

ASTM (1988) "E 399-83: Standard test method for plane-strain fracture toughness of metallic materials", Philadelphia.

ASTM (1988) "E 813-87: Standard Test method for $J_{Ic}$, a measure of fracture toughness", Philadelphia.

Barsom, J.M., Rolfe, S.T., (1999) "Fracture and fatigue control in structures: Applications of Fracture Mechanics - 3rd edition" ASTM, West Conshoshoken, Philadelphia.

Bazant, Z.P., Estenssoro, L.F., (1978) "Surface singularity and crack propagation." International Journal of Solids and Structures, vol. 15, pp. 405-426.

Begley, J.A. Landes, J.D., (1972) "The J-integral as a fracture criterion" ASTM STP 514, American Society for Testing and Materials, pp. 1-20.

Benthem, J.P., (1977) "State of stress at the vertex of a quarter-infinite crack in half space" International Journal of Solids and Structures, vol. 13, pp. 479-492.

Benthem, J.P., (1980) "The quarter-infinite crack in half space; Alternative and additional solutions." International Journal of Solids and Structures, vol. 16, pp. 119-130.

Betegón, C., (1990) "Two parameter elastic-plastic fracture mechanics (in Spanish) Caracterizacion biparametrica de los compos tensionales en la mecanica de la fractura elastoplastica" Phd thesis. Universidad de Oviedo, Spain.

Betegón, C., Hancock, J.W., (1991) "Two parameter characterization of elastic-plastic crack tip fields" Journal of Applied Mechanics, vol. 58, pp 104-110.

Bilby, B.A., Cardew, B.A., Goldthorpe, M.R. and Howard, I.C. (1986) "A finite element investigation of the effect of specimen geometry on the field of stress and strain at the tip of a stationary cracks. In 'Size Effect in Fracture'. Inst. Mech. Eng. London, UK, pp 37-46.

Bloom, J.M., (1983) "Validation of a deformation plasticity failure assessment diagram approach to flaw evaluation, Elastic-Plastic Fracture, second symposium, ASTM STP 803, American Society for Testing and Materials, pp. II.239-II.261, Philadelphia.

Brocks, W., Olschewski, J., (1986) "On J-Dominance of crack tip fields in largely 3D structures." International Journal of Solids and Structures, vol. 22, pp. 693-708.

Broek, D., (1974) "Elementary engineering fracture mechanics" Delft, Noordhoff Intl., Leyden.

Brothers, A.J., Yukawa, S., (1966) "Fracture test methods and their application, In application of fracture toughness parameters to structural metals, H.D. Greenberg (ed) " Metallurgical Society Conferences, vol. 31, AIME, Philadelphia, pp. 35-68.

BS 7910, (2005) "Guidance on methods for assessing the acceptability of flaws in metallic structures" British Standard Institution, London, UK.

Burton, W.S., Sinclair, G.B., Solecki, J.S., Swedlow, J.L., (1984) "On the implications for LEFM of the three-dimensional aspects in some crack/surface intersection problems." International Journal of Fracture, vol. 25, pp. 3-32.

Cardew, G.E., Goldthorpe, M.D., Howard, I.C., Kfouri, A.P., (1984) "On the elastic T-term" In fundamentals of deformation and fracture, (Eshelby memorial symposium), Cambridge University Press, pp. 456-476.

Chambers, A.E., Sinclair, G.B., (1986) "On obtaining fracture toughness values from the literature" International Journal of Fracture, vol. 30, pp. R11-R15.

Cherepanov, G. P., (1967) "On the crack propagation in continuous medium (in Russian)" Prik. Mat. Mekh. vol. 31, pp. 476-488.

Crandall, S.H., Dahl, N.C., Lardner, T.J., (eds.) (1978) "An Introduction to the Mechanics of Solids - 2nd Ed." McGraw-Hill, New York.

Cruse, T.A., (1970) "Lateral constraint in a cracked three-dimensional elastic body" International Journal of Fracture, vol. 6, pp. 326-328.

Cruse, T.A., Vanburen, W., (1971) "Three-dimensional elastic stress analysis of a fracture specimen with an edge crack" International Journal of Fracture, vol. 7, pp. 1-15.

deLorenzi, H.G., (1982) "On the energy release rate and the J-integral for three-dimensional crack configurations" International Journal of Fracture, vol. 19, pp. 183-193.

deLorenzi, H.G., Shih, C.F., (1983) "Three-dimensional elastic-plastic investigation of fracture parameters in side-grooved compact specimens," International Journal of Fracture, vol. 21, pp. 195-220.

Dodds, R.H., Jr., Shih, C.F., and Anderson, T.L., (1993) "Continuum and micromechanics treatment of constraint in fracture" International Journal of Fracture, vol. 64, pp. 101-133.

Dowling, A.R., Townley, C.H.A., (1975) " The effect of defects on structural failure: a two criteria approach". International Journal of Pressure Vessels and Piping, vol. 3, pp. 77-137.

Druce, S.G., (1980) "Effect of specimen geometry on the characterisation of ductile crack extension in C-Mn steel" AERE-R 9825, UKAEA, Harwell.

Du, Z. Z., Hancock, J.W., (1991) "The effect of non-singular stresses on crack tip constraint" Journal of the Mechanics and Physics of Solids, vol. 39, pp. 555-567.

Dugdale D.S., (1960) "Yielding of steel sheets containing slits", Journal of the Mechanics and Physics of Solids, vol. 8, pp. 100-108.

Eshelby, J.D., (1968) "Stress analysis of cracks" Journal of the Iron and Steel Institute, pp. 13-48.

Ewing, J.W., (1968) "The plastic yielding of V notched tension bars with circular roots" Journal of the Mechanics and Physics of Solids, vol. 16, pp.305.

Ewing, J.W., Hill, R., (1967) "The plastic constraint of V-notched tension bars" Journal of the Mechanics and Physics of Solids, vol. 15, pp. 115.

Fung, Y-C, (1977) "A first course in continuum mechanics, 2nd edition" Prentice-Hall, New Jersey.

Green, A.P., (1953) "The plastic yielding of notched bars due to bending" Quart. Journal of Mech. and Applied Mathematic, vol. 6, pp.223-239.

Gilmore, C.M., Provenzano, V., Smidt, Jr., F.A., Hawthorne, J.R., (1983) "Influence of thickness and temperature on stretched zone size in $J_{Ic}$ test" Metal Sci. vol. 17, pp.177-185.

Griffith, A.A., (1920) "The phenomenon of rupture and flow in solids", Philosophical Transaction of Royal Society of London, A221, pp. 163-198.

Hancock, J.W., Mackenzie, A.C., (1976) "On the mechanism of ductile failure in high-strength steels subjected to multi-axial stress-states," Journal of the Mechanics and Physics of Solids, vol. 24, pp.147-169.

Hancock, J.W., Brown, D.K., (1983) "On the role of strain and stress state in ductile failure" Journal of the Mechanics and Physics of Solids, vol. 31, pp. 1-24.

Hancock, J.W., (1992) "Constraint and stress state effects in ductile fracture: in Topics in fracture and fatigue, ed: Argon, A.S.," Springer-Verlag, New York.

Hancock, J.W., Reuter, W.A., Parks, D.M., (1993) "Constraint and toughness parameterized by T" in Hackett, E.M., Schwalbe, K.H., Dodds, R.H., Jr., Constraint Effects in Fracture, ASTM STP 1171. American Society for Testing and Materials, Philadelphia.

Hartranft, R.J., Sih, G.C., (1970) "An approximate three-dimensional theory of plates with application to crack problems" International Journal of Engineering Science, vol. 8, pp. 711-729.

Hellen, T.K., (1975) "On the method of virtual crack extension" International Journal of Numerical Methods in Engineering, vol. 9, pp. 187-207.

Henry, B.S., Luxmoore, A.R., (1995) "Three-dimensional evaluation of the T-stress in centre cracked plates" International Journal of Fracture, vol. 70, pp. 35-50.

Henry, B.S., Luxmoore, A.R., Sumpter, J.D.G., (1996) "Elastic-plastic fracture mechanics assessment of low constraint aluminium test specimens", International Journal of Fracture, vol. 81, pp. 217-234.

Henry, B.S., Luxmoore, A.R., (1997) "The stress triaxiality constraint and the Q-value as a ductile fracture parameter" Engineering Fracture Mechanics. vol. 57, pp. 375-390.

Hill, R., (1950) "The Mathematical Theory of Plasticity" Clarendon Press, Oxford, England.

Hom C.L., McMeeking, R. M., (1990) "Large crack tip opening in thin elastic-plastic sheets." International Journal of Fracture, vol. 45, pp. 103-122.

Huang, F.H., Gehes, D.D., (1984) "Influence of specimen size and microstructure on the fracture toughness of a martensitic stainless steel" Engineering Fracture Mechanics, vol. 19, pp. 1-20.

Hudson, C.M., Seward, S.K., (1978) "A compendium of sources of fracture toughness and fatigue-crack growth data for metallic alloys" International Journal of Fracture, vol. 14, pp. R151-R184.

Hudson, C.M., Seward S.K., (1982) "A compendium of sources of fracture toughness and fatigue-crack growth data for metallic alloys-Part II" International Journal of Fracture, vol. 20, pp. R59-R117.

Hutchinson J.W., (1968a) "Singular behaviour at the end of a tensile crack tip in hardening material." Journal of the Mechanics and Physics of Solids, vol. 16, pp. 13-31.

Hutchinson J.W., (1968b) "Plastic stress and strain fields at a crack tip" Journal of the Mechanics and Physics of Solids, vol. 16, pp. 337-347.

Hutchinson, J.W., (1979) "Nonlinear fracture mechanics" Department of solid mechanics, The Technical University of Denmark.

Hutchinson, J.W., (1983) "Fundamentals of the phenomenological theory of nonlinear fracture mechanics." Journal of Applied Mechanics, vol. 50, pp. 1042-1051.

Inglis, C.E., (1913) "Stresses in a plate due to the presence of cracks and sharp corners", Trans. Inst. Nav. Archit., 55, pp. 219-241.

Irwin, G.R., (1948) "Fracture dynamics" Fracture of Metals, pp. 147-166, American Society for Metals, Cleveland.

Irwin, G.R., (1957) "Analysis of stresses and strains near the end of a crack traversing a plate" Journal of Applied Mechanics, 24, pp. 361-364.

Irwin, G.R., (1958) "Fracture. In: Flugge S, editor. Encylopedia of physics, vol. VI – elasticity and plasticity." Springer, Berlin.

Irwin, G.R., Kies, J.A., Smith, H.L., (1958) "Fracture strengths relative to onset and arrest of crack propagation" Trans. American Society of Testing and Materials, vol. 58, pp. 640-660.

Irwin, G.R., (1960a) "Fracture mode transition for a crack traversing a plate" Journal of Basic Engineering, vol. 82, series D, pp. 417-423.

Irwin, G.R., (1960b) "Fracture Mechanics", Structural Mechanics, J.N. Goodier and N.J. Hoff, eds., Pergamon Press, London, pp. 557-594.

Irwin, G.R., (1964) "Dimensional and geometric aspects of fracture in Fracture of Engineering Materials" American Society for Metals, Chapman and Hall, London, pp. 211-230.

Janssen, M., Zuidema, J., Wanhill, R.J.H., (2002) "Fracture Mechanics, 2nd Ed." DUP Blue Print, Delft, The Netherlands.

Johnson, W., Sowerby, R., Venter, R.D., (1982) "Plane strain slip line fields for metal deformation processes – A source book and bibliography." Pergamon Press, Oxford.

Jones, M.H., Brown, W.F., Jr., (1970) "The influence of crack length and thickness in plane strain fracture toughness tests" Review of Developments in plane strain fracture toughness testing, ASTM STP 463 American Society for Testing and Materials, Philadelphia, pp. 63-101.

Kachanov, L. M., (1974) "Fundamentals of the theory of plasticity - Translated from Russian by M. Konyaeva," Mir Publishers, Moscow.

Kanninen, M.F., Popelar, C.H., (1985) "Advanced fracture mechanics" Oxford University Press, New York.

Karstensen, A.D., Hancock, J.W., (2002) "Constraint based fracture mechanics" Internal Report, Dept. Mech. Engineering, University of Glasgow, Glasgow.

Karstensen, A.D., (1996) "Constraint Estimation Schemes in Fracture Mechanics", PhD Thesis, Dept. Mech. Engineering, University of Glasgow, Glasgow.

Kaufmann, J.G., Hunsicker, H.Y., (1965) "Fracture toughness testing at Alcoa Research Laboratories In: Fracture toughness testing and its applications" ASTM STP 381, Philadelphia, pp. 290-309.

Keller, H.P., Munz, D., (1977) "Effect of specimen size on J-integral and stress intensity factor at the onset of crack extension" ASTM STP 631, pp. 217-231.

Kfouri, A.P., (1986) "Some evaluations of the elastic T-term using Eshelby's method" International Journal of Fracture, vol. 30, pp. 301-315.

Kim, Y., Zhu, X. K. and Chao, Y.J., (2001) "Quantification of constraint on elastic-plastic 3D crack front by the $J$-$A_2$ three term solution." Engineering Fracture Mechanics. vol. 68, pp. 895-914.

Kim, Y., Chao, Y.J., Zhu, X.K., (2003) "Effect of specimen size and crack depth on 3D crack-front constraint for SENB specimens" International Journal of Solids and Structures, vol. 40, pp. 6267-6284.

Kirk, M.T., Koppenhoefer, K.C., Shih, C.F., (1993) "Effect of constraint on specimen dimensions needed to obtain structurally relevant toughness measures. In Hackett, E.M., Schwalbe, K.H., and Dodds, R.H., Jr., (eds). Constraint Effect in Fracture, ASTM STP 1171" American Society for Testing and Materials, Philadelphia, pp. 79-103.

Knott, J.F., (1973) "Fundamentals of fracture mechanics" Butterworth & Co., England.

Koppenhoefer, K.C., Kirk, M.T., Dodds, R.H., Jr., (1995) "Size and deformation limits to maintain constraint in $K_{Ic}$ and $J_c$ testing of bend specimens. in Constraint Effects in Fracture Theory and Applications: 2nd Volume, M. Kirk and Ad Bakker eds. ASTM STP 1244, ASTM, Philadelphia.

Koppenhoefer, K.C., Dodds, R.H., Jr., (1996) "Constraint effects on fracture toughness of impact-loaded, precracked Charpy specimens" Nuclear Engineering and Design, vol. 162, pp. 145-158.

Krafft, J.M., Sullivan, A.M., Boyle, R.W., (1961) "Effect of dimensions on fast fracture instability of notched sheets" Proc. of the Crack-Propagation symposium I, pp. 8-28 Cranfield.

Kumar, V., German, M.D., Shih, C.F., (1981) "An engineering approach for elastic-plastic fracture analysis," EPRI Topical report NP 1931, Topical Report, Electric Power Research Institute, Palo Alto, CA.

Landes, J.D., Begley, J.A., (1972) "The influence of specimen geometry on $J_{Ic}$", Fracture Toughness, ASTM STP 514, American Society for Testing and Materials, Philadelphia, pp. 24-39.

Landes, J.D., Brown, K., (1998) "Results from a round robin on a standard method for measurement of fracture toughness" Journal of Testing and Evaluation, vol. 26, pp. 396-403.

Larsson, S.G., Carlsson, A.J., (1973) "Influence of non-singular stress terms and specimen geometry on small scale yielding at crack tips in elastic plastic material" Journal of the Mechanics and Physics of Solids, vol. 21, pp. 263-278.

Levy, N., Marcal, P.V., Ostergen, W.J., Rice, J.R., (1971) "Small scale yielding near a crack in Plane Strain: A finite element analysis" International Journal of Fracture, vol. 4, pp. 101-130.

Levy, N., Marcal, P.V., Rice, J.R., (1971) "Progress in three-dimensional elastic-plastic stress analysis for fracture mechanics." Nuclear Engineering and Design, vol. 17, pp. 64-75.

Leevers, P.S., Radon, J.C., (1983) "Inherent stress biaxiality in various fracture specimen geometries" International Journal of Fracture, vol. 19, pp. 311-325.

Li, F.Z., Shih, C.F., and Needleman, A., (1985) "A comparison of methods for calculating energy release rate" Engineering Fracture Mechanics, vol. 21, pp. 405-421.

Lianis, G., Ford, H., (1958) "Plastic yielding of single notched bars due to bending" Journal of the Mechanics and Physics of Solids, vol. 7, pp. 1-21.

Mackenzie, A.C., Hancock, J.W., Brown, D.K., (1977) "On the influence of state of stress on ductile failure initiation in high strength steels" Engineering Fracture Mechanics, vol. 9, pp. 167-188.

MacLennan, I.J., (1996) "Two parameter engineering fracture mechanics" PhD thesis, Dept of Mechanical Engineering, University of Glasgow.

MacLennan, I.J., Hancock, J.W., (1995) "Constraint-based failure assessment diagrams", Proc. Royal Society of London, (A), 451, pp. 757-777.

MacLennan, I.J., Hancock, J.W., (1995) "Constraint-based failure assessment diagrams" International Journal of Pressure Vessels and Piping, vol. 64, pp. 287-298.

Matlab (1998) Matlab Manual. The Math Works Inc. Version 5.8.

McClintock, F.A., Argon, A.S., (1966) "Mechanical Behaviour of Materials." Addisson-Wesley Publishing Co. Inc., Reading, Massachusetts. USA.

McClintock, F.A., (1971) "Plasticity aspects of fracture. Fracture: An Advanced Treatise (ed. H. Liebowitz), vol. III Engineering Fundamentals and Environmental Effects, pp. 47-225.

McMeeking, R.M., (1977) "Finite deformation analysis of crack-tip opening in elastic-plastic materials and implications for fracture," Journal of the Mechanics and Physics of Solids, vol.25 pp. 357-381.

McMeeking R.M., Parks D.M., (1979) "On criteria for J-Dominance of crack tip fields in large scale yielding." ASTM STP 668, American Society for Testing and Materials, Philadelphia, pp. 175-194.

Miller, A.G., (1988) "Review of limit load for structures containing defects" International Journal of Pressure Vessels and Piping, vol. 32, pp. 197-327.

Murakami, Y. (1987) "Stress Intensity Factors Handbook", Pergamon Press, New York.

Nakamura, T., Parks, D.M. (1988a), "Three-dimensional stress field near the crack front of a thin elastic plate." Journal of Applied Mechanics, vol. 55, pp. 805-813.

Nakamura, T., Parks, D.M., (1988b) "Conditions for J-Dominance in three-dimensional thin cracked plate" Analytical, numerical and experimental aspects of three-dimensional fracture processes, ASME AMD-91, ASME, pp. 227-238.

Nakamura, T., Parks, D.M., (1990) "Three-dimensional crack front fields in a thin ductile plate" Journal of the Mechanics and Physics of Solids, vol. 38, pp. 787-812.

Nakamura, T., Parks, D.M., (1992) "Determination of elastic T-stress along three-dimensional crack fronts using an interaction integral." International Journal of Solids and Structures, vol. 29, pp. 1597-1611.

Nakamura, T., Shih, C.F., Freund, L.B., (1986) "Analysis of a dynamically loaded three-point-bend ductile fracture specimen." Engineering Fracture Mechanics, vol. 25, pp. 329-339.

Nakamura, T., Shih, C.F., Freund, L.B., (1989) "Three-dimensional transient analysis of a dynamically loaded three-point-bend ductile fracture specimen." ASTM STP 995, vol. I, American Society of Testing and Materials, Philadelphia, pp. 217-241.

Nevalainen, M., Dodds, R.H., Jr., (1995) "Numerical investigation of 3-D constraint effects on brittle fracture in SE(B) and C(T) specimens." International Journal of Fracture, vol. 74, pp. 131-161.

Nye, J.F., (1985) "Physical properties of crystals: their representation by tensors and matrices" Oxford, Clarendon.

O'Dowd, N.P., Shih, C.F., (1991) "Family of crack tip fields characterized by a triaxiality parameter: Part I – structure of fields" Journal of the Mechanics and Physics of Solids, vol. 39, pp. 939-963.

O'Dowd, N.P., Shih, C.F., (1992) "Family of crack tip fields characterized by a triaxiality parameter: Part II – Fracture Applications" Journal of the Mechanics and Physics of Solids, vol. 40, pp. 989-1015.

O'Dowd, N.P., (1995) "Applications of two parameter approaches in elastic-plastic fracture mechanics" Engineering Fracture Mechanics, vol. 52, pp. 445-465.

Orowan, E., (1945) "Notch brittleness and strength of solids" Trans. Inst Eng Shipbuilders Scotland, 89, pp. 165-215.

Panasyuk, V.V., Andrejkiv, A.E., Stadnik, M.M., (1980) "Basic mechanical concepts and mathematical techniques in application to three-dimensional crack problems (A review)" Engineering Fracture Mechanics, vol. 13, pp. 925-937.

Panasyuk, V.V., Andrejkiv, A.E., Stadnik, M.M., (1981) "Three-dimensional static crack problems solution (A review)." Engineering Fracture Mechanics, vol. 14, pp. 245-260.

Pardoen, T., Marchal, Y., Delannay, F., (1999) "Thickness dependence of cracking resistance in thin aluminium plates." Journal of the Mechanics and Physics of Solids, vol. 47, pp. 2093-2123.

Paris, P.C., Sih, G.C., (1965) "Stress analysis of cracks, in: Fracture toughness testing and its applications", ASTM, Philadelphia, STP-381, pp.30-83.

Parks, D.M., (1974) "A toughness derivative finite element technique for determination of crack tip stress intensity factors" International Journal of Fracture, vol. 10, pp.487-502.

Parks, D.M., (1977) "The virtual crack extension method for nonlinear material behaviour" Computer Methods in Applied Mechanics and Engineering, vol. 12, pp.353-364.

Parks, D.M., (1991) "Three-dimensional aspects of HRR Dominance" in Defect Assessment in Components – Fundamentals and Applications, ESIS/EGF9, J.G. Blauel and K.-H.Schwalbe, Eds., Mechanical Engineering Publications, London, pp. 206-231.

Parks, D.M., (1992) "Advances in characterization of elastic-plastic crack-tip fields: in Topics in fracture and fatigue, ed: Argon, A.S.," Springer-Verlag, New York.

Patran V.2000 (2000). User's Manual. PDA Engineering, California:

R6, (2001) "Assessment of the integrity of structures containing defects" Revision 4, British Energy Generation Ltd., Gloucester, UK.

Rice, J.R., (1966) "Contained plastic deformation near cracks and notches under longitudinal shear." International Journal of Fracture, vol. 2, pp. 426-447.

Rice, J.R., (1967a) "The mechanics of crack tip deformation and extension by fatigue." in "Symposium on fatigue crack growth", STP 415, ASTM, Philadelphia.

Rice, J.R., (1967b) "Stresses due to a sharp notch in a work-hardening elastic-plastic material loaded by longitudinal shear." Journal of Applied Mechanics, vol. 34, pp. 287-298.

Rice, J.R., (1968a) "Mathematical Analysis in the Mechanics of Fracture" in "Fracture: An Advanced Treatise Vol. II. Mathematical Fundamentals." (H. Liebowitz, editor), pp. 191-311.

Rice, J.R., (1968b) "A path independent integral and the approximate analysis of strain concentration by notches and cracks." Journal of Applied Mechanics, vol. 35, pp. 379-386.

Rice, J.R., Rosengren, G.F., (1968c) "Plane strain deformation near a crack tip in a power law hardening material." Journal of the Mechanics and Physics of Solids, vol. 16, pp. 1-12.

Rice, J.R., Levy, N., (1972) "The part through surface crack in an elastic plate" ASME Journal of Applied Mechanics, vol. 39, pp. 185-194.

Rice, J.R., Tracey, D.M., (1969) "On the ductile enlargement of voids in triaxial stress fields" Journal of the Mechanics and Physics of Solids, vol. 17, pp. 201-217.

Rice, J.R., Tracey, D.M., (1973) "Computational fracture mechanics" in "Numerical and computational methods in Structural mechanics. (ed., S.J. Fenves et al.), Academic Press, New York.

Rice, J.R., (1974) "Limitations to the small scale yielding approximation for crack tip plasticity." Journal of the Mechanics and Physics of Solids, vol. 22, pp. 17-26.

Rice, J.R., (1982) "Elastic-Plastic Crack Growth" in Mechanics of Solids: The Rodney Hill 60th Anniversary volume. H.G. Hopkins and M.J. Sewell (eds.), Pergamon Press, Oxford.

Ritchie, R.O., Knott, J.F., Rice, J.R., (1973) "On the relationship between critical tensile stress and fracture toughness in mild steel," Journal of the Mechanics and Physics of Solids, vol. 21, pp. 395-410.

Riedel, H., (1987) "Fracture at high temperatures – Material research and engineering (MRE) eds: B. Ilschner and N.J.Grant" Springer-Verlag, Berlin.

Rooke, D.P., Cartwright, D.J., (1976) "Compendium of Stress Intensity Factors", HMSO.

Rolfe, S.T., Novack, S.R., (1970) "Slow-Bend $K_{Ic}$ testing of medium-strength high-toughness steels" Review of developments in plane strain fracture toughness testing, ASTM STP 463, American Society of Testing and Materials, Philadelphia, pp. 124-159.

Rosakis, A.J., Ravi-Chandar, K., (1986) "On the crack-tip stress state: an experimental evaluation of three-dimensional effects" International Journal of Solids and Structures, vol. 22, pp. 121-134.

Sham, T.L., (1991) "The determination of the elastic T-term using higher order weight functions" International Journal of Fracture, vol. 48, pp. 81-102.

Sham, T.L., Hancock, J.W., (1999) "Mode I crack tip fields with incomplete crack tip plasticity in plane stress" Journal of the Mechanics and Physics of Solids, vol. 47, pp. 2011-2027.

Sherry, A.H., France, C.C., Goldthorpe, M.R., (1995) "Compendium of T-stress solutions for two and three dimensional cracked geometries" Fatigue and Fracture of Engineering Materials and Structures, vol. 18, pp.141-155.

Sorem, W.A., Dodds, R.H., Jr., Rolfe, S.T., (1989) "An analytical and experimental comparison of rectangular and square crack-tip opening displacement fracture specimens on an A36. In: Nonlinear fracture mechanics: vol. II – Elastic-plastic fracture. ASTM STP 995, American Society of Testing and Materials, Philadelphia, pp. 470-494.

Shih, C.F., (1973) "Elastic-plastic analysis of combined mode crack problems" PhD Thesis, Harvard University, Cambridge, Massachusetts.

Shih, C.F., (1981) "Relationship between the *J*-Integral and the crack opening displacement for stationary and extending cracks." Journal of the Mechanics and Physics of Solids, vol. 29, pp. 305-326.

Shih, C.F., German, M.D., (1981) "Requirements for a one parameter characterization of crack tip fields by the HRR singularity", International Journal of Fracture, vol.17, pp. 27-43.

Shih, C.F., (1983) "Tables of Hutchinson-Rice-Rosengren singular field quantities" Technical Report (MRL-E147), Material Research Laboratory, Brown University, Providence Rhode Island.

Shih, C.F., Kumar, V., German, M.D., (1983) "Studies on the failure assessment diagram using the estimation method and J-controlled crack growth approach, Elastic-Plastic Fracture, second symposium, ASTM STP 803, American Society for Testing and Materials, pp. II.239-II.261, Philadelphia.

Shih, C.F., Moran, B., Nakamura, T., (1986) "Energy release rate along a three-dimensional crack front in a thermally stressed body" International Journal of Fracture, vol. 30, pp. 79-102.

Sih, G.C., Liebowitz, H., (1968) "Mathematical Theories of Brittle Fracture" Fracture: An advanced treatise, Ed: H. Liebowitz vol. 2 (Mathematical Fundamentals). Academic Press, New York.

Sih, G.C., (1973) "Handbook of stress intensity factors for researchers and engineers" Institute of Fracture and Solids Mechanics, Lehigh University, Bethlehem, Pennsylvania.

Srawley, J.E., "Fracture toughness as a function of thickness of high-strength sheet steel" (unpublished).

Srawley, J.E., Brown, W.F., (1967) "Plane strain crack toughness testing of high strength metallic materials" ASTM STP 410, Philadelphia.

Sumpter, J.D.G., Forbes, A.T., (1992) "Constraint based analysis of shallow cracks in mild steel. In Dawes, M.G. (ed.) 'Shallow crack fracture mechanics, Toughness tests and applications' The Welding Institute, Publishing, Abington Cambridge, England.

Sumpter, J.D.G., (1993) "An experimental investigation of the T-stress approach" in Hackett, E.M., Schwalbe, K.H., Dodds, R.H., Jr., Constraint Effects in Fracture, ASTM STP 1171. American Society for Testing and Materials, Philadelphia.

Sumpter, J.D.G., Hancock, J.W., (1994) "Status review of the J plus T-stress fracture analysis method" in 10th European Conference on Fracture, pp.617-626.

Swedlow, J.L., (1965) "The thickness effect and plastic flow in cracked plates", PhD Thesis, California Institute of Technology, California.

Tada, H., Paris, P.C., Irwin, G.R. (1985) "The stress analysis of Cracks Handbook (2nd Ed.)" Paris Productions Inc., St Louis.

Tiffany, C.F., Masters, J.N., (1965) "Applied Fracture Mechanics in Fracture Toughness Testing and its Applications" ASTM STP 381, Philadelphia, pp. 249-288.

Timoshenko, S., Goodier, J. N., (1970) "Theory of Elasticity - 3rd Ed.", McGraw-Hill, New York.

Tracey, D.M., (1971) "Finite elements for determination of crack tip elastic stress intensity factors", Engineering Fracture Mechanics, vol. 3, pp. 255-265.

Tresca, H., (1864) "On the flow of solid bodies subjected to high pressures C.r. Acad. Sci., Paris", 59, 754. Other closely connected work by Tresca is reported in C.r. Acad. Sci., 64, 809 (1867); Mem. Sav. Acad. Sci., 18, 733 (1868) and 20, 75 (1872).

Tuba, I. S., (1976) "A method of elastic-plastic plane stress and strain analysis", Journal of Strain Analysis, vol. 1, pp. 115-122.

Varias, A.G., Shih, C.F., (1993) "Quasi-static crack advance under a range of constraints – steady-state fields based on a characteristic length" Journal of the Mechanics and Physics of Solids, vol. 45, pp.835-861.

von Mises, R., (1913) "Gottinger Nachrichten, math.-phys. Klasse", 582.

Wallin, K., (1984) "The scatter in $K_{Ic}$ results" Engineering Fracture Mechanics, vol. 19, pp. 1085-1093.

Wallin, K., (1985) "The size effect in $K_{Ic}$ results" Engineering Fracture Mechanics, vol. 22, pp. 149-163.

Wallin, K., (2001) "Quantifying $T_{stress}$ controlled constraint by the master curve transition temperature $T_0$" Engineering Fracture Mechanics, vol. 68, pp. 303-328.

Wang, Y.Y., (1993) "On the two-parameter characterization of elastic-plastic crack-front fields in surface cracked plates," Constraint effects in fracture, ASTM STP 1171, Hackett, H.M., Schwalbe, K.H., and Dodds, R.H., Jr., Eds., American Society for Testing and Materials, pp. 120-138.

Wang, Huai-Wen., Kang, Yi-Lan., Zhang, Zhi-Feng., Qin, Qing-Hua., (2003) "Size effect on the fracture toughness of metallic foil" International Journal of Fracture, vol. 123, pp. 177-185.

Wells, A.A., (1961) "Unstable crack propagation in metals: Cleavage and fast fracture" Proceedings of the Crack propagation Symposium, Vol. 1, paper 48, pp. 210-230, Cranfield, UK.

Westergaard, H.M., (1939) "Bearing pressures and cracks", Journal of Applied Mechanics, vol. 6, pp. 49-53.

Williams, M. L., (1957) "On the stress distribution at the base of a stationary crack", Journal of Applied Mechanics, vol. 24, pp. 109-114.

Wellman, G.W., Dodds, R.H., Jr., Sorem, W.S. and Rolfe, S., (1985) "Three-Dimensional Elastic-Plastic finite element analysis of three-point bend specimens," ASTM STP 688, American Society for Testing and Materials, pp. 214-237.

Wellman, G.W., Sorem, W.A., Dodds, R.H., Jr., Rolfe, S.T., (1988) "Specimen thickness effects for elastic-plastic CTOD toughness of an A36 steel. In: Fracture mechanics: eighteenth symposium, ASTM STP 945, American Society of Testing and Materials, Philadelphia, pp. 535-554.

Yang, W., Freund, L.B., (1985) "Transverse shear effects for through cracks in an elastic plate" International Journal of Solids and Structures, vol. 21, pp. 977-994.

Yuan, H., Lin, G., Cornec, A., (1995) "Quantification of crack constraint effect in an austenitic steel" International Journal of Fracture, vol. 71, pp. 273-291.

Yuan, H., Brocks, W., (1998) "Quantification of constraint effects in elastic-plastic crack front fields" Journal of the Mechanics and Physics of Solids, vol. 42, no. 2, pp. 219-241.

Yusof, F., Hancock, J.W., (2005) "In-plane and out-of-plane constraint effects in three-dimensional elastic perfectly-plastic crack tip field" Proc. International Conference on Fracture, ICF 11, Turin, Italy.